CHEMICAL REVIEWS

Review

pubs.acs.org/CR

Reactivity of Surface Species in Heterogeneous Catalysts Probed by In Situ X-ray Absorption Techniques

Silvia Bordiga,[†] Elena Groppo,[†] Giovanni Agostini,[†] Jeroen A. van Bokhoven,[‡,§] and Carlo Lamberti*[,†]

[†]Department of Chemistry and NIS Centre of Excellence, Università di Torino and INSTM Reference Center, Via P. Giuria 7, 10125 Torino, Italy

[‡]ETH Zurich, Institute for Chemical and Bioengineering, HCI E127 8093 Zurich, Switzerland

[§]Laboratory for Catalysis and Sustainable Chemistry (LSK) Swiss Light Source, Paul Scherrer Instituteaul Scherrer Institute, Villigen, Switzerland

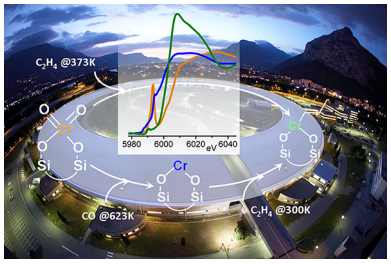

CONTENTS

Received: April 3, 2011
Published: February 28, 2013

   dx.doi.org/10.1021/cr2000898 | *Chem. Rev.* 2013, 113, 1736–1850

1. INTRODUCTION

Starting from the late seventies, the progressively increased availability of synchrotron light sources allowed the execution of experiments requiring a high X-ray flux in a continuous interval.[1−6] Among them, X-ray absorption spectroscopy (XAS, also known as X-ray absorption fine-structure, XAFS),[7−12] in both near (XANES) and post (EXAFS) edge regions, has become a powerful characterization technique in all the fields of materials science,[12−35] and in particular in catalysis.[13,16,22,23,25,30,31,36−40] After a slow start in the 1980s, mainly because of the difficulties in performing in situ experiments at the synchrotrons, the progressive development of more sophisticated and better performing experimental set-ups that allow the catalyst's state to be monitored under reactive

dx.doi.org/10.1021/cr2000898 | Chem. Rev. 2013, 113, 1736−1850

Table 1. Details on the Proceedings of the First 14 XAFS Conferences (1981−2009) and on the Fraction of Papers Related to Catalysis[a]

year	conference	location	guest editors	proceedings	total papers	catalysis papers	catalysis fraction (%)
1981	XAFS I	Daresbury (United Kingdom)	Garner, C. D., Hasnain, S. S.	*EXAFS for Inorganic Systems*, Study Weekend, Daresbury Laboratory Rep. DL/SCI/R17, 1981, pp. 1−140.	27	2[c]	7[c]
1982	XAFS II	Frascatti (Italy)	Bianconi, A., Incoccia, L., Stipcich, S.	*EXAFS and Near Edge Structure I*, Springer Series in Chemical Physics, Vol. 27, Springer, Berlin, 1983, pp. 1−420.	94	9[b]	10[b]
1984	XAFS III	Stanford (U.S.A.)	Hodgson, K.O., Hedman, B., Penner-Hahn. J.E.	*EXAFS and Near Edge Structure III*, Springer Series in Chemical Physics, Vol. 2, Springer, Berlin, 1984, pp. 1−533.	139	16[b]	12[b]
1986	XAFS IV	Fontevraud (France)	Lagarde, P., Raoux, D., Petiau, J.	*J. Phys., Colloq.* **1986**, *47*, C8-3−C8-1205.	237	27[c]	11[c]
1988	XAFS V	Seattle (U.S.A.)	Mustre de Léon, J. M., Stern, E. A., Sayers, D. E., Ma, Y., Rehr, J. J.	*Phys. B* **1995**, *158*, 1−722.	269	31[c]	11[c]
1990	XAFS VI	York (United Kingdom)	Hasnain, S.	*XAFS VI*, Ellis Horwood Ltd.: Chichester, U.K., 1990, pp. 1−792.	194	37[b]	19[b]
1992	XAFS VIII	Kobe (Japan)	Kuroda, H. et al.	*Jpn. J. Appl. Phys.* **1993** *32-2*, 3−878.	266	43[b]	17[b]
1994	XAFS VIII	Berlin (Germany)	Baberschke, K., Arvanitis, D.	*Phys. B* **1995**, *208−209*, 1−803.	310	33[c]	11[c]
1996	XAFS IX	Grenoble (France)	Goulon, J.	*J. Phys. IV* 1997, *7*, C2-1−C2-1269.	434	32[c]	7[c]
1998	XAFS X	Chicago (U.S.A.)	Bunker, B. A., Morrison T. I., Heald, S. M.	*J. Synchrotron Radiat.* **1999**, *6*, 123−804.	241	20[b]	8[b]
2000	XAFS XI	Ako (Japan)	Ohta, T., Nomura. M.	*J. Synchrotron Radiat* **2001**, *8*, 47−1013.	308	34[b]	11[b]
2003	XAFS XII	Malmö (Sweden)	Lindau, I., Mårtensson, N., Arvanitis, D., Karis, O. C.	*Phys. Scr., T*, **2005**, *115*, No. 19−1099.	333	57[b]	17[b]
2006	XAFS XIII	Stanford (U.S.A.)	Hedman, B., Pianetta, P.	*AIP Conf. Proc.*, **2007**, *882*, 1−960.	276	37[c]	13[c]
2009	XAFS XIV	Camerino (Italy)	Di Cicco, A., Filipponi, A.	*J. Phys.: Conf. Ser.* **2009**, *190*, No. 012001−012211.	211	23[b]	11[b]
2012	XAFS XV	Beijing (China)	Ziyu Wu	*J. Phys.: Conf. Ser.*, in press.			

[a]This fraction does not contain the papers published in the related surface science section. These statistics concern the published papers in the proceedings that represent only a fraction of the presented contributions. [b]Papers classified in the specific section on catalysis by the proceedings editors. [c]Papers selected by the authors of this review on the basis of the paper title and abstract.

Table 2. Details on the Proceedings of the First Three International Congresses on Operando Spectroscopy (2003−2009) and on the Fraction of Papers Related to X-ray Spectroscopies[a]

year	conference	location	guest editors	proceedings	total papers	XAS papers	XAS fraction (%)
2003	Operando I	Lunteren (the Netherlands)	Weckhuysen, B:M	*Phys . Chem. Chem. Phys.* **2003**, *5*, 4351−4742.	25	7	28
2006	Operando II	Toledo (Spain)	Bañares, M. A.	*Catal. Today* **2007**, *126*, 1−264.	32	7	22
2009	Operando III	Rostock (Germany)	Brückner, A.	*Catal. Today* **2010**, *155*, 155−330.	25	4	16
2012	Operando IV	BNL (Upton, NY, U.S.A.)		*Catal. Today* **2013**, in press.			

[a]This fraction does not contain the papers reporting results collected with other synchrotron radiation techniques (XRD, SAXS, and XPS). These statistics concern only the published papers in the proceedings that represent a fraction of the presented contributions.

conditions has increased greatly the number of XAFS experiments carried out by the catalysis community. The strong bind between catalysis and XAFS is testified by the large number of contributions related to catalysis presented in the 14 XAFS conferences that have taken place in the last three decades (since 1981 in Daresbury, United Kingdom, to 2009 in Camerino, Italy). As shown in Table 1, the contributions dealing with catalysis are a relevant fraction of the total (from 7% to 19%). The synergy between catalysis and XAFS is evident also by looking in the reverse direction. For example, Table 2 summarizes the fraction of contributions reporting XAFS results presented in the three conferences on operando spectroscopy (from 2003 in Lunteren, the Netherlands, to 2009 in Rostock, Germany); the number of contributions dealing with XAFS and catalysis is again quite high (from 16% to 28% of the total).

The data shown in Tables 1 and 2 provide clear evidence that XAFS spectroscopy (and related techniques) currently plays a fundamental role in the investigation of catalysts. In particular, XAFS techniques are extremely powerful to shed light on the structure and reactivity of surface species in *heterogeneous* catalysts, in many steps of the catalyst life and also during the catalytic act. Although many relevant contributions in the past literature authoritatively review the role of XAFS techniques in investigating specific classes of materials,[10,15,19,24,26,28,29,34,35,41−51] and some specific class of catalyst,[16,30,52−69] to the best of our knowledge there are no review articles that specifically address the role of in situ/operando XAFS techniques in the characterization of a significantly large variety of heterogeneous catalysts. We do believe that the time is right for such a review to be done.

dx.doi.org/10.1021/cr2000898 | *Chem. Rev.* 2013, 113, 1736−1850

Herein, we present a collection of case studies where the use of XAFS spectroscopy has been relevant in understanding the structure and reactivity of surface species in heterogeneous catalysis. Selected examples belong to both, industrial and academic fields. Among the industrially employed catalysts that have been deeply investigated by XAFS techniques we cite in particular (i) the titanium silicalite, TS-1, for selective oxidation reactions at low-temperature using aqueous H_2O_2 as oxidizing agent (section 3.2), (ii) the Cr/SiO_2 Phillips catalyst for ethylene polymerization (section 6); (iii) the Cu/ZnO catalyst for methanol synthesis and methanol steam-reforming (section 7.2), (iv) the $CuCl_2/Al_2O_3$ catalyst for ethylene oxychlorination (section 8.2), and (v) Pt- and Pd-supported nanoparticles for hydrogenation reactions (section 9). However, XAFS techniques have been also of great utility for investigating catalysts that are mainly of academic interest, such as (i) Ga-zeolites (section 3.3) and B-zeolites employed for acidic catalysis (section 3.4) and, more recently, (ii) metal organic frameworks (MOFs), whose industrial application is still limited but that show interesting perspectives in the catalysis field for the near future (section 5). Finally, (i) the case of Fe-zeolites for selective oxidation reactions (section 3.3) represents an intermediate situation, since at present only one industrial plant (the one-step benzene to phenol plant by Solutia) works with this catalyst. The same holds for (ii) Cu-zeolites, which show interesting properties in the direct decomposition of nitric oxide to nitrogen and oxygen and became successively relevant in the selective catalytic reduction (SCR) catalysis for DeNOx mobile applications (section 4).

All the case studies discussed in the review are materials characterized by a high surface area, which is an essential prerequisite for heterogeneous catalysts. In some cases the catalysts have a crystalline structure (such as for isomorphically substituted zeolites, cation-exchanged zeolites, and MOFs), where the active sites for both adsorption and reaction are hosted in well-defined crystallographic positions. In some other cases, the active phase is constituted by single-site transition metal grafted on an amorphous support (such as for the Cr/SiO_2 catalyst), or by metal or metal-oxide nanoparticles supported on poorly crystalline metal-oxides having a high-surface area or on active carbons (such as for Pd and Pt-based catalysts for hydrogenation reactions), or for Cu/ZnO catalysts.

From the general inspection of all the reported examples, it emerges clearly that quantitative information on the local structure of the active sites can be easily obtained on catalysts characterized by a high homogeneity of the X-ray absorbing species, such as for TS-1 and Cu-ZSM-5 catalysts. However, the majority of heterogeneous catalysts are characterized by an heterogeneity of active sites. Heterogeneity of the X-ray absorbing species can derive from several factors, such as (i) the heterogeneity of the support itself, as for the Cr sites grafted on the surface of amorphous silica in the Cr/SiO_2 Phillips catalyst (section 6); (ii) the presence of different crystallographic sites hosting the X-ray absorbing species, as for Cu^+-MOR (section 4.3); (iii) the activation treatments, as for both Fe- and Ga-zeolites (section 3.3); (iv) the presence of more than one phase containing the X-ray absorbing species, as for the Phillips catalyst at high Cr loadings (containing both, isolated Cr species and aggregated Cr_2O_3 particles, section 6.2.1. In these cases, quantitative information on the local structure of the active sites can be obtained only when XAFS data are coupled with experimental results obtained with complementary techniques, such as IR, TEM, XRD, PDF, or DAFS. In absence of complementary data, only qualitative information can be safely obtained from XAFS measurements without the risk of data overinterpretation. Several examples on the importance of a complementary approach are reported in the review. IR spectroscopy was fundamental in determining the thermodynamic conditions (temperature and CO equilibrium pressure) necessary to form carbonyl complexes having a defined stoichiometry inside the Cu^+-ZSM-5 channels (section 4.2.2). A quantitative EXAFS and XANES analysis, possible only in these conditions, was fundamental to reveal the local structure of carbonyl species. IR spectroscopy gave independent information on the fraction of chromium sites active in ethylene polymerization on the Phillips catalysts as a function of polymerization conditions, in well agreement with the values obtained by XANES (section 6.2.1.2). On the same catalyst, UV−vis spectroscopy was fundamental in highlighting the presence of a fraction of clustered Cr_2O_3 phase that has been taken into account in the EXAFS data analysis (section 6.2.1.1). UV−vis spectroscopy, combined with resonant Raman, has been necessary to support XANES and EXAFS data on the equilibrium between peroxo and hydroperoxo species formed in TS-1 upon interaction with H_2O_2/H_2O solution (section 3.2.5). This experimental picture has been further supported by ab initio calculations performed with both cluster and periodic approaches (sections 3.2.5.4 and 3.2.5.3, respectively).

Finally, the potentiality of the third generation synchrotron radiation sources allows space[66,67,70−75] and time[62,76−79] resolved experiments to be performed. Both fields are in rapid expansion, and can be of great help in the investigation of catalysts and of catalytic processes. Two selected examples will be discussed in section 7 and 8, respectively.

A review on the role of XAFS techniques in catalysis is a huge work and the selection of case studies discussed herein represents unavoidably only a subjective and partial view of the boundless topic of reactivity of surface species. This choice has been dictated mainly by the personal experience of the authors. Important overlooked systems, for which we just mention few selected references, are for example metal−organic complexes grafted on different supports,[23,80−93] model systems prepared on metal or metal-oxide vacuum cleaved single crystals or on thin oxide films grown on metal single crystals.[94−101] Nonetheless, we do believe that the selected examples cover a large fraction of catalysts categories and are useful to illustrate the increasing role that XAFS spectroscopy has in determining the properties of the active sites in heterogeneous catalysts.

2. EXPERIMENTAL METHODS

The aim of this section is not to describe in detail how the here reviewed experiments have been performed (to this purpose the reader is referred to the original literature) but to illustrate the experimental set up generally adopted to perform such kind of experiments (section 2.2.) and the methods employed to analyze the collected data (section 2.3.). These sections are anticipated by a brief one devoted to the description of the materials discussed in this work (section 2.1.).

2.1. Materials

Heterogeneous catalysts are complex systems, and the ability to reproduce the experimental results reported in the literature depends on a clear definition of the synthesis and activation procedures. For these reasons, few details are reported in this section.

dx.doi.org/10.1021/cr2000898 | Chem. Rev. 2013, 113, 1736−1850

2.1.1. Metal-Substituted MFI Frameworks. TS-1 samples (Ti content in the 0.97−3.45 TiO_2 wt. % range) were synthesized part in EniChem (Istituto "G. Donegani", Novara, Italy) and part in EniTecnologie (S. Donato Milanese, Italy) using tetrapropylammonium (TPAOH) as template, according to the original patent.[102] The "defective" silicalite-1 as been prepared with the same synthesis procedure, without adding the TiO_2 precursor in the batch.[103]

Fe-silicalite (Si/Fe = 90) catalyst was prepared by the Forni's group (University of Milano) following the hydrothermal method described in detail by Ratnasamy and Kumar,[104] as described in more detail elsewhere.[105,106]

Na-GaZSM-5 zeolite samples having Si/Ga ratio of 25, were prepared in the laboratories of the Departamento de Química, Universidad de las Islas Baleares (UIB), Palma de Mallorca, Spain, as outlined elsewhere[107] by template-assisted hydrothermal synthesis, using appropriate amounts of sodium silicate, gallium nitrate, and tetrapropylammonium bromide solutions.

2.1.2. Cu-Substituted Zeolites. Cu-exchanged zeolites (both ZSM-5[108] and MOR[109]) have been prepared following an original exchange path, based on the reaction at 573 K between the zeolite (in the protonic form) and gaseous CuCl as described elsewhere.[108−112] See also section 4.1.

2.1.3. Cr/SiO_2 Phillips catalyst. The Cr/SiO_2 catalysts were obtained by impregnating a SiO_2 support (400 m^2/g) with H_2CrO_4, following the procedure described elsewhere.[64,113−116] A Cr loading of 4 wt % was adopted to have an acceptable signal-to-noise ratio in transmission XAFS experiments.[117] A Cr loading of 0.5 wt % was used for XAFS experiments in fluorescence mode.[118] In both cases, samples were then activated according to the following procedure: (i) outgassing at 773 K; (ii) calcination in O_2 at the same temperature for 1 h (oxidized sample). After the activation and oxidation steps, two different reduction procedures have been followed: (i) a reduction step at 623 K, followed by CO removal at the same temperature, thus obtaining the hereafter called *CO-reduced* system, and (ii) a reduction step in C_2H_4 at 523 K, followed by evacuation at the same temperature, thus obtaining the hereafter called *C_2H_4-reduced* catalyst.

2.1.4. $CuCl_2/Al_2O_3$. $CuCl_2/\gamma$-Al_2O_3 catalyst has been prepared with a Cu loading of 5.0 wt % by impregnation of γ-alumina (Condea Puralox SCCa 30/170, surface area = 168 $m^2\ g^{-1}$, pore volume = 0.50 $cm^3\ g^{-1}$) with an aqueous solution of $CuCl_2/H_2O$, following the incipient wetness method, as described elsewhere.[119]

2.1.5. Metal-Supported Catalysts. Pt-supported catalysts were prepared by impregnation of supports with an aqueous solution of $Pt(NH_3)_4(NO_3)_2$ (Aldrich 27,872-6) as described elsewhere.[120] Supported Pd samples have been prepared in the Chimet laboratories on γ-Al_2O_3 (surface area = 121 $m^2\ g^{-1}$; pore volume = 0.43 $cm^3\ g^{-1}$) and on two different activated carbons, from wood (hereafter Cw; surface area = 980 $m^2\ g^{-1}$; pore volume = 0.62 $cm^3\ g^{-1}$) and peat (hereafter Cp; surface area = 980 $m^2\ g^{-1}$; pore volume = 0.47 $mm^3\ g^{-1}$) origin, following the deposition−precipitation method[121,122] with Na_2PdCl_4 as palladium precursor and Na_2CO_3 as basic agent.

2.2. Techniques and Experiential Set-ups

This section is divided in seven subsections. Sections 2.2.1 and 2.2.2 are devoted to briefly describe how the X-ray beam is "shaped" in the optic hutch to the requirements of the XAFS experiment. Sections 2.2.3. and 2.2.4 reports the set-ups for X-ray absorption and emission spectroscopies, respectively. The latter setup allows to perform high-energy resolution fluorescence detected XANES and range-extended EXAFS, as described in section 2.2.5. Finally, the set-ups needed to perform in situ (or operando) experiments and those needed for μm-resolved experiments are discussed in sections 2.2.6 and 2.2.7, respectively.

2.2.1. X-ray Beam Optimization: Energy Selection. A typical synchrotron beamline is constituted by three hutches (see Figure 1).[4,123] The first is the optic hutch, that collects the photons emitted from the machine and sets the requested beam for the experiment, in terms of energy, energy resolution, angular divergence, focusing, dimension, and others. The second is the experimental hutch, where the experiment is performed. The third is the control room, where where scientists monitor the experiment and perform a first data analysis.

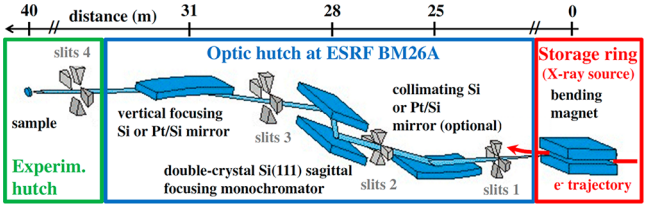

Figure 1. Scheme of the optics operative at the ESRF BM26A beamline. From right to left: (i) Storage ring, where the white X-ray beam is generated by radial acceleration of electrons; (ii) optic hutch where the white X-ray beam hits the first collimating mirror that acts as low-band-pass filter for the white X-ray beam, removing higher harmonics to reach the double crystal monochromator (section 2.2.2.), where the desired X-ray E value is selected according to eq 3 by tuning the angle θ_B, and finally the second focusing mirror collects the monochromatic X-ray beam, focuses it and sends it to the sample; (iii) Experimental hutch, containing the sample and tools to control its environment, and all detectors needed to run the experiment (see Figure 4a). The control room (not reported in the figure) contains the remote controls allowing controlling and following the experiment. Two pairs (one horizontal and one vertical) of slits are inserted along the beam path to properly define the beam dimension. Between the storage ring and the optic hutch and between this latter and the experimental hutch, for safety reasons, two X-ray absorbers are located, named front-end and safety shutter, respectively. Image kindly provided by the courtesy of W. Brass DUBBLE BM26A beamline of the ESRF.

To perform X-ray spectroscopy a monochromatic beam of desired energy E must be singled out from the white (or pink polychromatic) light emitted by the machine.[124] This is achieved by using the so-called monochromator, which consists of a crystal, usually silicon, cut along a specific (hkl) plane of known d_{hkl}-spacing and exploiting the Bragg law

$$2d_{hkl}\sin(\theta_B) = n\lambda = nhc/E \text{ where } n = 1, 2, 3, \ldots \quad (1)$$

The photon energy is linked to the photon wavelength (λ) by the relation $E = h\nu = hc/\lambda$, c being the speed of light (c = 2.9979 × 10^{+8} m/s) and h being the Planck constant (h = 6.626 × 10^{-34} Js), so that

$$hc = 12.3984 \text{ Å keV} \quad (2)$$

As a consequence, the desired energy E will be selected by tuning the angle θ_B with high precision fulfilling the relation

$$E = n[12.3984 \text{ (Å keV)}]/[2d_{hkl}\sin(\theta_B)] \quad (3)$$

dx.doi.org/10.1021/cr2000898 | Chem. Rev. 2013, 113, 1736−1850

Table 3. Selection of Si(*hkl*) Cuts, Corresponding *d*-Spacing ($d_{hkl} = a/\sqrt{(h^2 + k^2 + l^2)}$, Where a = 5.431020 Å is the Si Lattice Parameter), Bragg Reflection Angle (θ_B), Darwin Width (ω_{Darwin}), FWHM of the Double Crystal Rocking Curve ($\omega_{DC} = \sqrt{2}\omega_{Darwin}$) Computed for an Energy of E = 10 keV (λ = 1.239854 Å) in the Frame of the Dynamical Theory of X-ray Diffraction[125] with the χ0h Code[126] (http://sergey.gmca.aps.anl.gov/x0h.html) in σ-Polarization (NB = 1 arcsec = 2.7778 × 10^{-4} ° = 4.8481 × 10^{-6} rad)[a]

Si(*hkl*) reflection	d_{hkl} (Å)	θ_B (deg)	ω_{Darwin} (arcsec)	ω_{DC} (arcsec)	ΔE_{mono} (eV)	$\Delta E_{mono}/E$	E_{min} (keV) for θ_B = 25°	E_{max} (keV) for θ_B = 4°	transmitted flux (au)	*n*
Si(111)	3.1355	11.403	5.4870	7.7598	1.319	1.32 × 10^{-4}	4.678	28.343	1	3, 5
Si(220)	1.9201	18.836	4.0047	5.6635	0.569	5.69 × 10^{-5}	7.639	46.284	0.73	2, 3
Si(311)	1.6375	22.246	2.2892	3.2374	0.271	2.71 × 10^{-5}	8.958	54.271	0.42	3, 5
Si(400)	1.3577	27.167	3.4083	4.8200	0.322	3.22 × 10^{-5}	10.804	65.456	0.62	2, 3
Si(422)	1.1086	34.001	2.7647	3.9099	0.199	1.99 × 10^{-5}	13.232	80.163	0.50	2, 3
Si(511)	1.0452	36.379	1.8642	2.6364	0.123	1.23 × 10^{-5}	14.034	85.026	0.34	3, 5
Si(440)	0.96005	40.220	2.5252	3.5712	0.145	1.45 × 10^{-5}	15.279	92.567	0.46	2, 3

[a]Also reported is the covered energy range assuming that the θ_B angle of the monochromator span the 4-25° interval and the absolute (ΔE_{mono}) and relative (ΔE_{mono}/E) energy resolutions computed according to eqs 5 and 6. The last two columns report the relative photon flux transmitted by the reflection, normalized to that of Si(111) and the first two transmitted harmonics (*n*), respectively. Exhaustive lists of available crystals, cuts and related characteristics are available in the literature.[127]

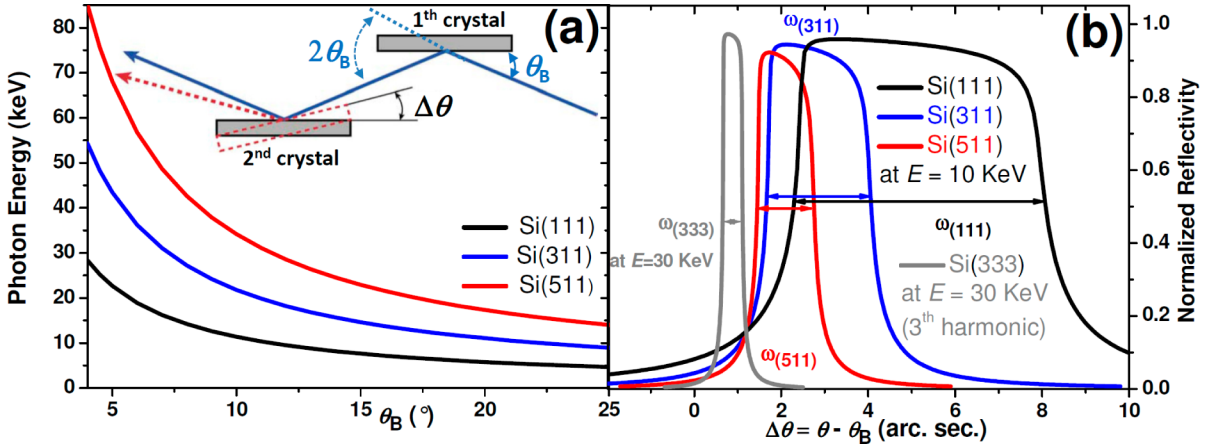

Figure 2. Part a: Photon energy delivered by a Si(*h*11) double crystal monochromator as function of the Bragg angle θ_B in the 4−25° angular range according to eq 3. h = 1 (black), h = 3 (blue), and h = 5 (red). The scheme in the upper part reports the working principle of a double crystal monochromator: the first crystal is fixed at the desired θ_B angle, while the second, performing a scan of $\Delta\theta = \theta - \theta_B$ of few arcsec, yields the so-called monochromator rocking curve where the intensity of the transmitted monochromatic beam goes from its maximum down to virtually zero in a very narrow angular range (1 arcsec = 4.8481 × 10^{-6} rad). Part b: Simulated rocking curves for Si(*h*11) double crystal monochromator for a Bragg angle allowing the selection of E = 10 keV (λ = 1.239854 Å): θ_B = 11.403°, 22.246°, and 36.379°, for h = 1 (black), 3 (blue), and 5 (red), respectively. Also reported is the simulated rocking curves for Si(333) at 30 keV (gray), corresponding to the first transmitted harmonic for the Si(111) crystal working at 10 keV. In each case the maximum of the transmitted photon flux has been normalized to unit. The positive shift of the angle of the second crystal with respect to the first one is due to the refraction phenomenon and is proportional to $\lambda^2/\sin(2\theta_B)$, while the different widths of the three curves, $\omega_{(h11)}$, reflect the different Darwin width of both first and second crystal, see Table 3. This figure reports data computed in the frame of the dynamical theory of X-rays diffraction[125] with the χ0h code[126] (http://sergey.gmca.aps.anl.gov/x0h.html) in σ-polarization.

When higher harmonics are efficiently rejected n = 1 (vide infra section 2.2.2). A second Bragg reflection is needed to maintain the beam in a horizontal direction. This device is thus called double crystal monochromator and is hosted in the optic hutch (Figure 1).

Many hard X-ray beamlines are equipped with a double crystal Si(111) monochromator however; often, the beamline can operate with different monochromator crystals, such as Si(311), Si(511), and others, see Table 3. Since the available Bragg angle that can be reached by a specific pair of monochromator crystals is limited for mechanical reasons ($\theta_{min} < \theta_B < \theta_{max}$), the choice of the (*hkl*) cut of the crystal defines the $d_{hkl} = a/\sqrt{(h^2 + k^2 + l^2)}$ parameter, and thus the range of energy ($E_{min} < E < E_{max}$) that can be reached by the beamline in that configuration according to eq 3, see Figure 2a. Also, the choice of crystals affects the intensity and energy resolution of the beam (vide infra). The selected Si(*hkl*) crystal must include a wide interval across the measured adsorption edge E_0, see the last two columns in Table 3. In general, low (high) Miller indices cover low (high) energy ranges (Figure 2a).

Even from ideally perfect crystals, the dynamical theory of diffraction foresees that each Bragg reflection has a finite line-width, called Darwin width (ω_{Darwin}):[125,128−130]

$$\omega_{Darwin} = [2r_0\lambda^2 F]/[\pi \sin(\theta_B)V] \quad (4)$$

where r_0 is the electron classical radius ($r_0 = 2.82 \times 10^{-15}$ m), F is the structural factor of the crystal and V is the unit cell volume. ω_{Darwin} is typically in the arcsec range (Table 3).

The choice of monochromator crystals depends on the specific requests of the experiment in terms of energy range, flux, or brilliance of the X-ray beam, and its energy resolution.[131,132] For a given crystal cut, the higher are the

dx.doi.org/10.1021/cr2000898 | Chem. Rev. 2013, 113, 1736−1850

(hkl) Miller indices of the cut, the sharper is the angular acceptance of the monochromator rocking curve and so the better is the energy resolution of the experiment (Figure 2b). Indeed, higher (hkl) Miller indices imply smaller d_{hkl} values, see eq 1, and so larger θ_B angles to deliver the same E (or the same λ), resulting in larger $\sin(\theta_B)$ and in smaller ω_{Darwin}, see eq 4. Any gain in energy resolution causes a reduction in photon flux, as the transmitted flux is, in first approximation, inversely proportional to the Darwin width, see Table 3.

The intrinsic energy resolution of the Si(hkl) monochromator can be estimated differentiating eq 3 and taking ω_{Darwin} as $\Delta\theta_B$:

$$\Delta E_{mono} = \omega_{Darwin}[12.3984\ (\text{Å keV})\ \cos(\theta_B)] / [2d_{hkl}\ \sin^2(\theta_B)] \quad (5)$$

Combining eqs 3 and 5, one obtains[9,129]

$$\Delta E_{mono}/E = \omega_{Darwin}\ \text{cotg}(\theta_B) \quad (6)$$

Values of $\Delta E_{mono}/E$ as low as 10^{-4}–10^{-5} are usually obtained, see Table 3. Note that eqs 5 and 6 hold when ω_{Darwin} is reported in radians. The actual energy resolution of the beamline also depends on the X-ray beam divergence, which is determined by the distance between the source and the sample and of course the optical elements in between. As an example, with a slit opening of Δl = 1 mm at a distance of D = 40 m (Figure 1) the X-ray beam divergence is $\Omega \approx \Delta l/D = 2.50 \times 10^{-5}$. If the beamline operates at E = 10 keV with a Si(111) monochromator then, in analogy to eq 6 the broadening of the energy resolution because of X-ray beam divergence is $\Delta E_{divergence}/E = \Omega\ \text{cotg}(\theta_B) = 1.29 \times 10^{-4}$, see Table 3. When both effects are taken into account, the energy resolution of the experiment is given by[129,132]

$$\Delta E/E = \text{cotg}(\theta_B)\sqrt{[\omega_{Darwin}{}^2 + \Omega^2]} \quad (7)$$

In the specific case described above, the energy broadening due to the monochromator Darwin width ($\Delta E_{mono}/E = 1.32 \times 10^{-4}$, being $\omega_{Darwin} = 2.6602 \times 10^{-5}$ rad, see Table 3) is comparable to the broadening due to the X-ray beam divergence, resulting into an overall $\Delta E/E = 1.81 \times 10^{-4}$ (ΔE = 1.81 eV).

2.2.2. X-ray Beam Optimization: Harmonic Rejection. Equations 1 and 3 contain the integer number n, which implies that, in addition to the fundamental wavelength λ (E) (transmitted with n = 1), also the higher harmonics $\lambda/2$ ($2E$), $\lambda/3$ ($3E$), etc., will pass the monochromator with n = 2, 3, etc. Higher harmonics must be rejected from the beam delivered by the optic hutch before reaching the sample, because they cause artifacts in the XAFS spectra. The spectrum emitted by bending magnets rapidly decay in intensity after the critical energy of the machine[1,133,134] (E_c), and consequently, when working at an energy E higher than the critical energy (E_c), the contamination from higher harmonics is small. However, when working at relative low energies (E < 10 keV) on a bending magnet beamline of an high energy machine, such as ESRF ($E_{electrons}$ = 6 GeV, E_c = 19.2 keV), APS ($E_{electrons}$ = 7 GeV, E_c = 19.5 keV), or SPRING-8 ($E_{electrons}$ = 8 GeV, E_c = 28.9 keV), the intensity of the second harmonic will even be higher than that of the fundamental energy and higher harmonic rejection is mandatory.

The simplest way to reject higher harmonics is the "detuning" technique. The two monochromator crystals are given a slightly different Bragg angle, θ_B. The result is a decrease of the transmitted intensity by "sliding" off the rocking curve (Figure 2b). This reduces the contribution of the higher harmonics, because for all crystals and all reflections, the angular acceptance ω_{Darwin} is much greater for the fundamental (n = 1) then for the higher harmonics ($n \geq 2$):[48,123] indeed ω_{Darwin} is proportional to λ^2, see eq 4. The intensity of the higher harmonics is thus decreased at a much faster rate. Furthermore, the use of Si($2h$ + 1, $2k$ + 1, $2l$ + 1) cuts, where all even higher harmonics are forbidden, additionally reduces the relative fraction of the higher harmonics content of the transmitted beam. As an example, for Si(111) at 10 keV $\omega_{Darwin}(n = 1)$ = 5.4870 arcsec, while $\omega_{Darwin}(n = 3)$ = 0.3347 arcsec, detuning of $\Delta\theta$ = 2.5 arcsec results in the loss of about 30% of the fundamental photons, and of almost 100% and >99% of the photons of the second and third harmonic, respectively. This can be directly appreciated comparing the rocking curve of Si(111) at 10 keV (black curve in Figure 2b) with that of the first transmitted harmonic, Si(333) reflection at 30 keV, gray curve in Figure 2b.

A second method to reject higher harmonics is the use of mirrors, also hosted in the optic hutch (Figure 1).[123,130,132,135,136] Mirrors are long crystals, usually Si, sometimes coated with a metal film (Ni, Pd, Pt, ...) to tune the electron density (ρ) that defines the surface refractive index of the mirror (n_{mirror}). They are positioned such that the X-rays incidence angle θ_1 can be adjusted in the arcsec range.

The higher harmonic rejection is based on the wavelength (and thus energy) dependence of n_{mirror}, that in the X-ray region of the electromagnetic spectrum is given by[9,137–140]

$$n_{mirror} = 1 - r_0\rho\lambda^2/2\pi - i\beta \quad (8)$$

where ρ is the electron density, r_0 is the electron classical radius, and $\beta = \mu\lambda/4\pi$, which takes into accounts the absorption phenomena (μ is linear absorption coefficient). In several textbooks[139] eq 8 is usually reported in a more concise way: $n_{mirror} = 1 - \delta - i\beta$, with $\delta = r_0\rho\lambda^2/2\pi$. Considering only the real part of refractive index, as it defines the reflection/refraction properties of the interface, and applying the Snell law, $n_1 \cos(\theta_1) = n_2 \cos(\theta_2)$,[141] to the vacuum/mirror interface, one obtains $\cos(\theta_1) = n_{mirror} \cos(\theta_{refraction})$ as n = 1 for vacuum. $Re(n_{mirror}) < 1$ because the phase velocity of X-rays in condensed matter (v_{phase}) is larger than c (generally, in optics $Re(n) = c/v_{phase}$), that is, $\delta > 0$. This implies that there is a critical angle θ_c under which total reflection occurs: $\cos(\theta_c) = n_{mirror}$ when $\theta_{refraction} = 0°$.[139] Since n_{mirror} is very close to unit ($10^{-6} < \delta < 10^{-5}$), θ_c must be very close to zero and the cosine can be approximated with the first two terms of the Taylor series in zero: $\cos(\theta_c) \approx 1 - \theta_c^2/2 \approx n_{mirror}$. Using eq 8, one obtains

$$\theta_c \approx \lambda\sqrt{(r_0\rho/\pi)} \quad (9)$$

Equation 9 implies that the critical angle for the second harmonic is one-half that of the fundamental energy and that for the third harmonic it is one-third: $\theta_c(n = 1) = 2\,\theta_c(n = 2) = 3\theta_c(n = 3)$. As a consequence, choosing an incidence angle on the second mirror θ_1 satisfying the condition: $(\lambda/2)\sqrt{(r_0\rho/\pi)} < \theta_1 < \lambda\sqrt{(r_0\rho/\pi)}$, the fundamental beam will be under total reflection conditions and will be reflected onto further optical elements (first mirror in Figure 1) or into the experimental hutch (second mirror), while second and higher harmonics will be refracted and completely adsorbed inside the mirror. The role of the first mirror (Figure 1), is to act as a low-energy-pass

dx.doi.org/10.1021/cr2000898 | Chem. Rev. 2013, 113, 1736–1850

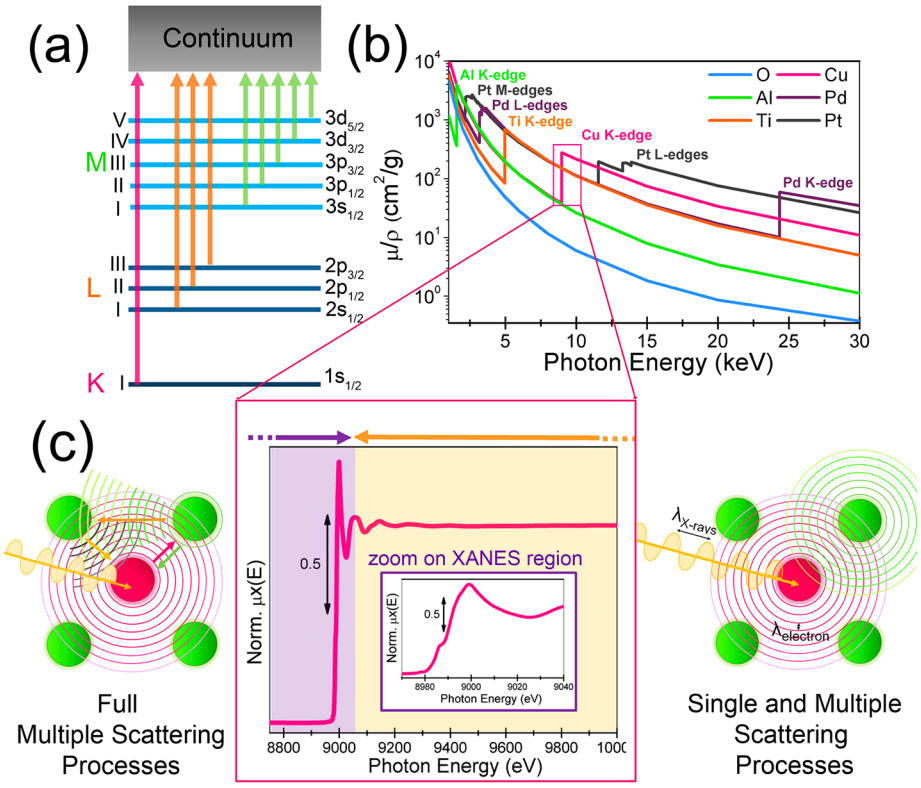

Figure 3. Part a: X-ray absorption edges nomenclature and representation of their relation with the atomic orbitals from which the electron is extracted. Part b: General behavior of the X-ray absorption coefficient μ/ρ, see eq 10, as a function of the incident X-ray energy E for O (Z = 8), Al (Z = 13), Ti (Z = 22), Cu (Z = 29), Pd (Z = 46), and Pt (Z = 78) elements. Data obtained from NIST Web site http://physics.nist.gov/PhysRefData/XrayMassCoef/tab3.html. Note the logarithmic scale of the ordinate axis. (c) Cu K-edge XAFS of activated HKUST-1 MOF. The conventional division between XANES and EXAFS region and the schematic models of full multiple and single (and multiple) scattering processes, dominating respectively the XANES and EXAFS region, are indicated (color code: absorber atom in magenta; neighbor atoms that backscatter the photoelectron wave outgoing from the absorber in green).

filter, reflecting only the fraction of the white (pink) beam[124] satisfying the relation $\theta_1 < \lambda\sqrt{(r_0\rho/\pi)}$, that is, $E < (hc/\theta_1)\sqrt{(r_0\rho/\pi)}$. An advantage of using a mirror above detuning of the double crystal monochromator is the absence of a significant loss of intensity of the $(n = 1)$-beam.

For a beam of vertical size of h the length of the mirror needed to accept the whole beam is $L = h/\sin(\theta_c) \approx h/\theta_c$. Assuming $\delta = 2 \times 10^{-6}$, $\theta_c \approx \sqrt{(2\delta)} = 2 \times 10^{-3}$, and assuming h = 1 mm we obtain L = 0.5 m. Mirrors in access of 1 m (or longer) are installed in some beamlines. Mirrors may have the additional advantage of the ability to focus the beam, increasing the number of photons per unit area (brilliance) falling onto the sample. The focusing role of the mirrors is important for the studies of highly diluted systems and for space resolved studies (see section 2.2.7).

2.2.3. X-ray Absorption Spectroscopy: Acquisition Setups for Standard and Time-Resolved Experiments. The aim of a XAFS experiment is the measure of the absorption coefficient of a given sample, $\mu(E)$, as a function of the photon energy E. For any sample, in the X-ray region of the electromagnetic spectrum, $\mu(E)$ is a monotonically decreasing function of the photon energy, given in first approximation by[49]

$$\mu(E)/\rho \approx Z^4/AE^3 \quad (10)$$

where ρ is the sample density, Z the atomic number (i.e., the number of electrons) and A the atomic mass, see Figure 3b. Equation 10 holds for a sample containing an unique chemical species like a metal foil but can be easily generalized for any sample of known composition. The featureless dependence $\mu(E)$ is interrupted by abrupt increases of the absorption at the specific energy values corresponding to the K, L, and M edges of the elements present in the sample (Figure 3a). The dependence of $\mu(E)/\rho$ on E^{-3} implies that all elements are highly absorbing in the low photon energy region, making XAFS spectroscopy on soft X-ray experimentally much more demanding than in the hard X-ray domain. As an example, for both O and Al $\mu(E)/\rho$ increases by more than 3 order of magnitude moving from 20 to 1 keV (Figure 3b). Analogously, the dependence of $\mu(E)/\rho$ on the fourth power of the atomic number makes high Z element much more absorbing than light elements. Exceptions may occur after the absorption edge of a given lighter atom: some examples are reported in Figure 3b, for example, Cu (Z = 29) is more absorbing than Pd (Z = 46) in the whole range between Cu K- and Pd K-edge (9.99−23.35 keV, see Figure 3b). Equation 10 and related Figure 3b imply that the quality of EXAFS spectrum obtained on, for example, a metal supported catalyst depends on both the metal loading (determining the edge jump) and the nature of the support, determining the featureless total absorption from the support. Light Z supports like carbons are almost transparent to hard X-rays, so that high quality S/N EXAFS spectra can be obtained up to k = 20 Å^{-1} on both 5.0 and 0.5 wt % Pd/C, just optimizing the sample thickness (9 and 35 mm, respectively).[142] SiO_2 and Al_2O_3 still are considered as medium-low Z support, still allowing good quality EXAFS spectra to be

dx.doi.org/10.1021/cr2000898 | Chem. Rev. 2013, 113, 1736−1850

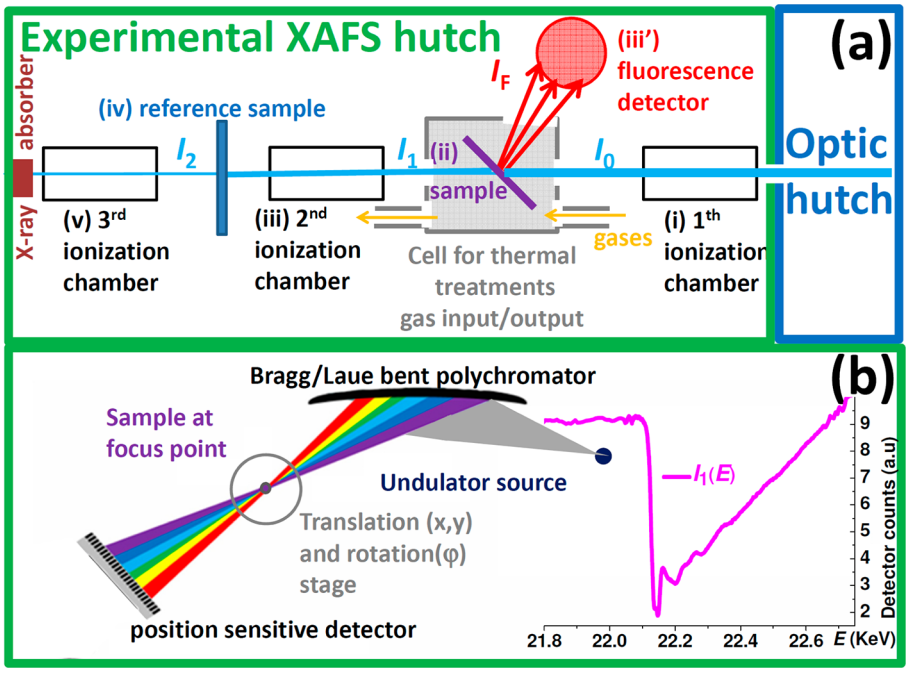

Figure 4. Schematic views of the basic setup of a XAFS experiment in conventional (part a) and dispersive geometries (part b). Part a: The harmonic-free monochromatized beam (cyan line) is delivered with the proper energy and size from the optic hutch (see Figure 1). In the experimental hutch, it crosses, from the right to the left: (i) the first ionization chamber for monitoring the intensity of the incident beam I_0; (ii) the sample, hosted in a controlled temperature/atmosphere environment (see Figure 8 for a selections of in situ cells); (iii) second ionization chamber for monitoring the intensity of the transmitted I_1 or (iii′) fluorescence detector sketched on top of the sample (electron yield detection is also possible, but not depicted); (iv) reference sample; (v) third ionization chamber for monitoring I_2. Part b left: The white or pink beam[124] is focused by a bent polychromator into a focus few μm-wide (where the sample has to be located); behind the focus the beam diverges again, allowing the simultaneous collection of the whole transmitted spectrum $I_1(E)$ in a single shot (right part). This modern acquisition is conceptually very similar to the way the very first XAFS spectra were acquired; see Figure 7a). $I_0(E)$ must be acquired a posteriori, removing the sample from the focal point. $I_2(E)$ is successively measured putting the reference in the focus. A precise translation (x,y), with z being the X-ray beam direction, and rotation (φ) stage is required for an optimal location of the sample in the focus point. This set up also allows space-resolved XAFS experiments to be performed, see section 2.2.7.

collected, but moving to zirconia or ceria experiment became more demanding, particularly for low metal loaded catalysts.

The fine structure that modulates $\mu(E)$ in proximity of a given edge (Figure 3c) is the argument of XAFS spectroscopy and thus of this review. The total $\mu(E)$ spectrum is usually divided into two different regions: (i) the near edge region or XANES region and (ii) the extended region after the edge or EXAFS region, starting ∼50−100 eV after the edge and extending until signal is avalaible (typically 400−2000 eV). As deeply discussed in the following, although usually collected in the same acquisition run, XANES (section 2.3.5) and EXAFS (section 2.3.2−2.3.4) data will be treated differently and will provide different information concerning electronic and structural properties of the atoms belonging to the selected species.

Figure 4a depicts the basic setup of a conventional XAFS experiment in catalysis, which can be schematized into the following steps. In the optic hutch, the white beam emitted from a synchrotron source is monochromatized, higher harmonics are rejected and the beam is focused, if needed, as detailed in sections 2.2.1 and 2.2.2, see Figure 1. Entering the experimental XAFS hutch, the intensity of the monochromatic beam I_0 is measured with a first ionization chamber (i); the monochromatic beam is partially absorbed by passing through the sample of thickness d (ii); the intensity of the transmitted beam I_1 is then measured with a second ionization chamber (iii); the remaining beam is further absorbed by passing through a reference sample of thickness x_R (iv); and the intensity of the beam transmitted by the reference sample $I_2(E)$ is measured by a third ionization chamber (v). In such a way, the absorption coefficient of the sample (μ) and of the reference (μ_R) can be measured for a given energy E selected by the monochromator according to the classical law of transmission phenomena, also known as Lambert−Beer law ($I_1(E) = I_0(E)\ e^{-\mu(E)d}$ and $I_2(E) = I_1(E)\ e^{-\mu_R(E)d_R}$):

$$\mu(E)d = \ln[I_0(E)/I_1(E)] \text{ and } \mu_R(E)d_R = \ln[I_1(E)/I_2(E)] \quad (11)$$

As for any transmission spectroscopy, the Lambert−Beer law holds for samples that are homogeneous in both chemical composition and sample thickness in the whole area illuminated by the X-ray beam (typically a rectangle of few mm in horizontal and a fraction of mm in vertical). If this is not the case eq 11 is no more valid and a space resolved approach has to be adopted, see section 2.2.7.

Elements iv and v are not mandatory, but when possible, they should always be present in the experimental setup because they allow direct and internal calibration of the relation between photon energy E and monochromator angle θ_B, see eq 3. Although the stability in energy of modern beamlines has improved significantly, this caution is particularly important when the reactivity of surface species is investigated, as it guarantees that the change in position of the XANES edge is actually the result of a change in the oxidation or coordination

dx.doi.org/10.1021/cr2000898 | Chem. Rev. 2013, 113, 1736−1850

Table 4. Typical Parameters Concerning the Technical Time Resolution for the Acquisition of a XAFS Spectrum in the Different Experimental Set-Ups[a]

experimental set-ups	technical time resolution (s)	factors determining the time resolution	typical N of averaged spectra	optimal ring operation mode
step scan (standard)	5×10^2	(1) N of acquired points, (2) integration time per point, and (3) monochromator dead time	3	uniform or any high current mode
Quick-XAFS	1	(1) acquired angular range, (2) monochromator speed, and (3) possible back and forth acquisitions	1	uniform or any high current mode
dispersive XAFS	10^{-3}	detector readout and erasing time	1	uniform or any high current mode
pump and probe (analyzed with differential XAFS)	10^{-10}	synchrotron bunch and laser pulse time lengths	100	(1) single bunch, (2) few separated bunches, and (3) hybrid mode (one isolated bunch)

[a]These numbers refer to the acquisition technique only and do not take the sample into account, which could require a much longer or extended (in terms of integration time, k_{max} and Δk) acquisition to obtain useful data. Usually, XAFS spectra acquired in the pump and probe set-up require a data analysis performed with the differential XAFS approach, see section 2.3.9.

state of the investigated element.[143] When transmission experiments can not be performed, for example, for highly diluted samples, the fluorescence mode is adopted. In this case the absorption coefficient is given by eq 12, where $I_F(E)$ is the intensity of the fluorescence yield emitted by the sample and detected by a fluorescence detector (step iii′ in Figure 41).

$$\mu(E) = I_F(E)/I_0(E) \tag{12}$$

EXAFS spectra collected in the fluorescence mode are susceptible to an apparent amplitude reduction due to the self-absorption of the fluorescing photons by the sample before they reach the detector. This phenomenon is negligible for diluted samples; otherwise correction for sample thickness and concentration must be applied.[144] Alternatively or simultaneously to fluorescence, electron yield EY(E), total or partial, can be measured resulting in $\mu(E) = \mathrm{EY}(E)/I_0(E)$. Fluorescence and Auger are the two complementary modes of decay of the excited atom, so that their signal is proportional to the X-ray absorption process. The decay probability is favorable to Auger in the soft X-ray range and to fluorescence in the hard X-ray region. Electron yield modes require conductive samples and vacuum conditions to result in good quality XAFS spectra. The former condition is rarely fulfilled in case of heterogeneous catalysts, while the second makes in situ or operando studies difficult, though not impossible.[145] These reasons explain why fluorescence detection mode is much more used than the electron yield one for characterization of catalysts. However, when applicable the comparison between XAFS spectra collected in the two modes can be informative because of the markedly different penetration depth of the two techniques (only the surface and a few monolayer below the surface of a catalyst can be probed in electron yield mode).[146]

The acquisition set up described in Figure 4a is usually adopted in the *step-scan* mode, where the spectra are acquired by integrating for a given time interval Δt the counts on $I_0(E)$ and $I_1(E)$ or $I_F(E)$ being the monochromator at the fixed energy E; then acquisition is stopped and the monochromator moves to the next point ($E + \Delta E$). The procedure is repeated recursively for all scheduled E points of the acquisition. Depending on the sample, EXAFS spectra with good signal/noise ratio up to high k values can be obtained in an overall integration time ranging from 20 min to some hours; 5−10 min can be sufficient for collecting a XANES spectrum.

For time-resolved studies (see section 8), such as the investigation of the catalyst reactivity as a function of the variation of the experimental conditions (e.g., feed flow or pressure or temperature), faster acquisition modes are required, see Table 4. The *quick-EXAFS* (or Q-EXAFS) acquisition mode provides an alternative way of recording XAFS spectra where the scan time is significantly reduced by moving the monochromator at a constant angular speed and recording the $I_0(E)$ and $I_1(E)$ or $I_F(E)$ data "on the fly". The method, initially realized by Frahm[147−149] at HASYLAB (Hamburg) in the late eighties, has been further implemented in several beamlines worldwide and is still under continuous implementation.[22,61,150−164] In this way, the time needed for the acquisition of a full EXAFS spectrum may be shorter than a minute, while few seconds are sufficient to acquire the XANES region. The quick-EXAFS acquisition can be applied for both transmission and fluorescence modes[151,155] and has been coupled often with XRPD technique, to provide time-resolved information on the order at short- and at long-range simultaneously.[22,61,152,153] Recent developments made possible quick-EXAFS acquisition at a subsecond time resolution.[165]

In the conventional XAFS geometry (Figure 4a), adopted by both step-scan and quick-EXAFS modes, the required energy range ($E_{min} < E < E_{max}$) is scanned stepwise or continuously by changing the monochromator Bragg angle, resulting in the simultaneous acquisition of $I_0(E)$, $I_1(E)$ and $I_2(E)$ for a given E value. Conversely, in a dispersive mode, Figure 4b left, one measures simultaneously all the energy values of a single spectrum, but the three different spectra $I_0(E)$, $I_1(E)$, and $I_2(E)$ are measured separately. The dispersive geometry uses a bent monochromator crystal, where the variation of the diffraction angle over the crystal surface can be assumed to be linear. Depending on illuminated length and Bragg angle a specific energy range is diffracted. The sample under investigation is located at the focal point of the monochromator, and the intensity of the different diffracted energies is measured by a position sensitive detector. A careful calibration process is necessary to attribute an energy interval to each detector channel.[166] Detailed descriptions of the beamlines operating in dispersive mode, of the adopted X-ray optics and of the used position sensitive detectors are available in the literature.[129,167−187] Owing to the fixed energy-position correlation on the detector, $I_0(E)$, $I_1(E)$ and $I_2(E)$ are measured separately by locating the sample, the reference, and no sample, respectively, in the focal point of the monochromator. This means that a high stability of the ring and of the beamline is required to use $I_1(E)$ and $I_o(E)$ data sets collected in different moments to obtain the corresponding $\mu(E)$ data set. For dispersive XAFS, the expression (11) of $\mu(E)$ still holds for the computation of the absorption coefficient of the sample, but $\mu_R(E)$ has to be computed as $\mu_R(E)d_R = \ln[I_0(E)/I_2(E)]$, since

dx.doi.org/10.1021/cr2000898 | Chem. Rev. 2013, 113, 1736−1850

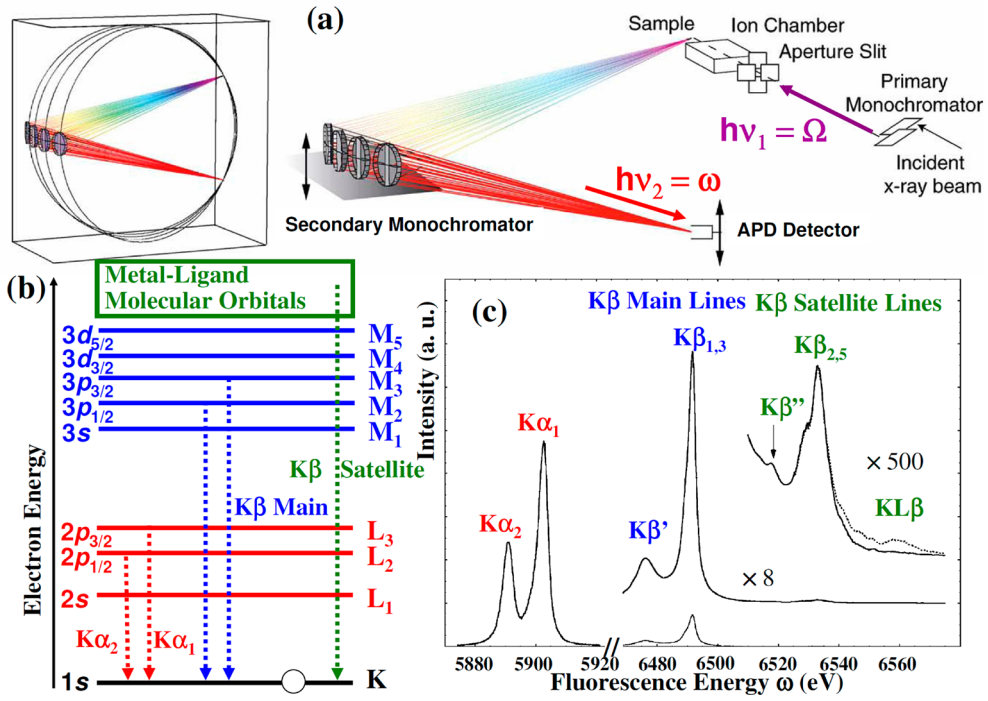

Figure 5. Part a: Scheme of the high-resolution fluorescence crystal array spectrometer (Johansson type), using six spherically bent Ge(620) crystals, available at the 18-ID (BioCAT) beamline of at the Advanced Photon Source (APS) at the Argonne National Laboratories (Chicago, U.S.). Equivalent experimental setup are available at the ID26 beamline of the ESRF synchrotron (Grenoble, F) and the SuperXAS beamline of the Swiss Light Source (Villigen, Switzerland). The arrows indicate the motion of the components when a spectrum of the emitted X-rays is taken. Ω and ω represent the incident and emitted photon energy, respectively (see Scheme 1). With this experimental setup it is possible to measure how a core hole in the 1s orbital (generated by the absorption of a primary photon of energy Ω) is filled. The second monochromator allows to discriminate between K_ω, K_β main, and K_β satellite lines (also known as valence to core lines),[219−221] as shown in Part b, where the main, dipole allowed, recombination lines for a 3d metal are reported as vertical dotted lines. Part c: Example of K shell emission lines in MnO oxide. Fixing the energy ω selected from the second monochromator to one of the emission peaks reported in part c and tuning the primary energy Ω across the K absorption edge of the metal, it is possible to collect K_α- and K_β-detected X-ray absorption spectroscopy. The relative intensities of K_ω, K_β main, and K_β satellite lines can be directly appreciated. Parts a and c were adapted with permission from ref 199. Copyright 2005 Elsevier.

the beam passing through the reference does not cross the sample anymore.

For the energy-dispersive setup, the minimum measuring time per absorption spectrum is mainly restricted by the read-out time of the detector that usually amounts to some milliseconds at most currently available dispersive spectrometers, see Table 4. As an example, ESRF has recently developed an innovative detector (FReLoN) that has cut the readout time below 100 ms. The FReLoN detector is a low noise CCD camera that combines high dynamic range, high readout speed, accuracy, and improved duty cycle in a single image.[188]

Due to the micrometric dimension of the polychromatic beam in the focus point of a dispersive EXAFS setup, sample homogeneity problems are much more critical than in standard step-scan or quick-EXAFS acquisitions, where the beam probes a much larger area of the sample (fraction of mm^3 vs some μm^3). This is particularly true for the investigation of metal supported catalysts, as the dimension of the support grains can be comparable to that of the beam. Some of the limiting parameters that need to be addressed in making a successful dispersive EXAFS experiment on heterogeneous catalysts, have been addressed in a detailed study by Newton.[189] Considerable improvements in dispersive-EXAFS data from supported metal catalysts can be achieved through manipulation of the vertical dimensions of the dispersive X-ray beam, matching the manner of sample presentation (net particle size and packing density) and the physical properties (composition, scattering ability) of the reference to that of the sample.[189] Moreover, by implementing a reference that is at least as absorbing as the support material in question, Newton demonstrated that it is possible to fully utilize more of the high photon flux available at third generation SR sources (such as ID24 at the ESRF) within the dynamic range of the 16-bit FReLoN detector.[188]

Obviously, the μm-size of the beam at the focus point makes the dispersive setup suitable also for accurate space resolved studies.[190,191] The dispersive space-resolved XAFS setup belongs to the X-ray scanning microscopy category, see sections 2.2.7 and 7.

2.2.4. X-ray Emission Spectroscopy: Acquisition Setup. X-ray emission spectroscopy (XES) provides a means of probing the partial occupied density of electronic states of a material. XES can be induced as a second order optical process (photon-in/photon-out): (i) a core electron is removed by an incident photon, then (ii) the inner shell vacancy is filled by an electron from a higher shell following the selection rules for radiative transitions (Figure 5b). When the core hole is filled by an electron from a core (valence) level, we refer to core (valence) to core XES. XES is element-specific and species-specific (or transition-specific or fluorescence decay channel-specific). Therefore XES is a powerful tool for determining detailed electronic properties of materials[192−210] in general and of transition metal-based catalysts in particular.[211−217]

The physical bases of XES have been discussed in several authoritative reviews,[193,194,198,199,205−207,217,218] herein very few

dx.doi.org/10.1021/cr2000898 | Chem. Rev. 2013, 113, 1736−1850

concepts will be summarized, which are useful for understanding the case studies discussed along the text. A schematic representation of the XES experimental set up is shown in Figure 5a: it uses a spherically bent analyzer crystals in the Johansson geometry. The ω energy is scanned moving both the crystal analyzer and the APD detector to match Bragg equation (see arrows in Figure 5a). Using a cylindrically bent crystal and a position sensitive detector the fluorescence photons are collected in the dispersive von Hamos geometry. The latter has the advantage of not needing to scan and move any motors, thus enabling to record the ω XES spectrum in a single shot for any given Ω value.[220] Parts (b) and (c) of Figure 5 refer to the excitation of a 1s electron. When the primary monochromator (right part of Figure 5a) selects an exciting photon of energy $h\nu_1 = \Omega$ higher than the chosen K-edge (or in the K-edge pre-edge peaks for resonant XES), then a core hole in the 1*s* orbital of the excited element is created and, within the given lifetime, an electron coming from some of the occupied states fills the 1s core hole. As a consequence a fluorescence photon of energy $h\nu_2 = \omega$, given by the difference in energy between the two levels, is emitted by the sample. In a standard XANES experiment, the fluorescence X-rays emitted by the sample are collected by a solid state detector that, owing to its intrinsic energy resolution (typically, few-hundred of eV), is just able to discriminate among the fluorescence photons emitted by the different chemical elements present in the sample (vide infra section 2.2.5, Figure 6a). In a XES experiment, along with the standard primary monochromator (already used before the sample for the standard XANES experiments), an additional spectrometer (composed by one or more analyzer crystals) is positioned after the sample, which acts as second monochromator (left part of Figure 5a). Using the Bragg diffraction of the analyzer crystals, the photons emitted by the sample are selected with a combined energy resolution (incident plus emitted energy resolution), typically of 0.5−1.5 eV. Selected photons will then reach a detector, such as a high efficiency Avalanche photodiode detector (APD). In such a way, the total counts are much lower than in a standard XANES fluorescence experiment, but it is possible to discriminate the energy of the electron that has filled the core hole and therefore its original atomic or the molecular orbital,[199,211] see Figure 5b. Part c of Figure 5 allows direct appreciation of the relative intensities among K_ω, K_β main, and K_β satellite lines.

When the incident X-ray energy Ω is tuned to one of the XANES pre-edge peaks, the process is called resonant X-ray emission (RXES, Scheme 1b), while if the incident energy is sufficient to excite the core electron to a high energy continuum level well above the excitation threshold (vertical gray line in Scheme 1), the process is called normal X-ray emission or non resonant X-ray emission, (NXES, Scheme 1a). RXES spectra are Ω dependent, while NXES are, in first approximation, not.

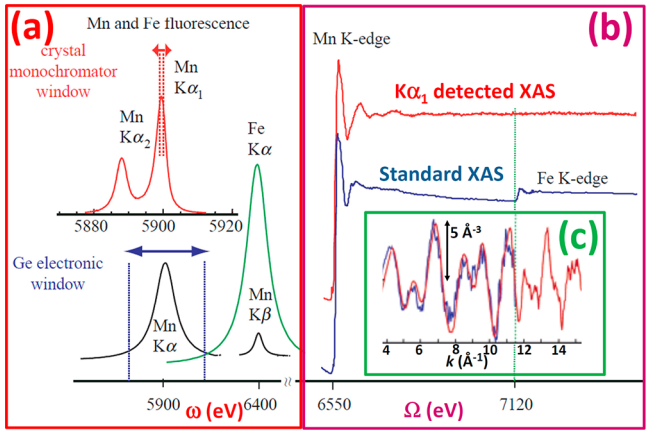

Figure 6. Principles of high-energy resolution fluorescence detected XAFS, also allowing extended EXAFS to be possible. The example refers to a sample containing both Mn and Fe elements. Part a: Schematic representation of Mn and Fe fluorescence lines. Top: selected fluorescence photons using the high energy spectrometer ($\Delta\omega$ = 1 eV) reported in Figure 5a tuning ω on the Mn Kα_1 line. Bottom: Selected fluorescence photons using a standard solid state Ge detector ($\Delta\omega$ = 200 eV) tuned on the Mn Kα lines. In this case, the low energy tail of the Fe Kα lines contribute to the photon counting, resulting in the appearance in the standard XAFS spectrum of the Fe K-edge jump that prevents the analysis of the Mn K-edge data beyond k = 11.5 Å^{-1}. Part b: Comparison between the standard (blue curves) and the HERFD (red curves) XAFS spectra of catalytic Mn_4Ca photocatalytic complex hosted inside the multiprotein membrane system known as photo system II that also contains iron centers. Part c: Corresponding k^2-weighted $\chi(k)$ functions. Adapted with permission from ref 226. Copyright 2005 American Chemical Society.

Scheme 1. Schematic Representation of Nonresonant and Resonant XES, Parts a and b, Respectively[a]

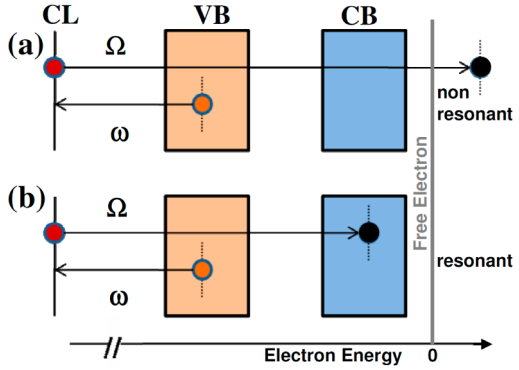

[a]In both parts, Ω and ω represent the incident and emitted photon energy, respectively. Dark red circles represent the core hole; black circles represent the final state of the excited electron; orange circles represent the valence band electron that will fill the core hole. Light orange and blue rectangles represent the fully occupied valence band (VB) and the empty conduction band (CB), respectively. CL = core level (1s, in the experiment reported in Figure 5b, c).

2.2.5. High-Energy Resolution Fluorescence Detected (HERFD) XANES and EXAFS and Range-Extended EXAFS Spectroscopy. XANES spectroscopy is employed to study the unfilled electronic states above the Fermi level. In a conventional XANES experiment, one monitors the transmitted photons, the total fluorescence yield (TFY, integrated over all the disexcitation related to the excited atomic species) or the total or partial electron (TEY or PEY) decay of the sample, while scanning the incident photon energy $h\nu_1 = \Omega$ (Figure 5a) across the edge. In such experiments, besides the limits of the X-ray optics (see section 2.2.1, eq 7), there is a limit in the energy resolution set by the lifetime broadening of the core hole of the selected edge: $\Delta E_{TFY} \approx \Gamma_{core} \equiv (h/2\pi)/\tau_{core}$, where τ_{core} is the lifetime of the core hole in the selected edge created by the absorbed X-ray. With the experimental setup reported in Figure 5a, it is possible to follow the evolution of the fluorescence emission fixing $h\nu_2 = \omega$

dx.doi.org/10.1021/cr2000898 | Chem. Rev. 2013, 113, 1736−1850

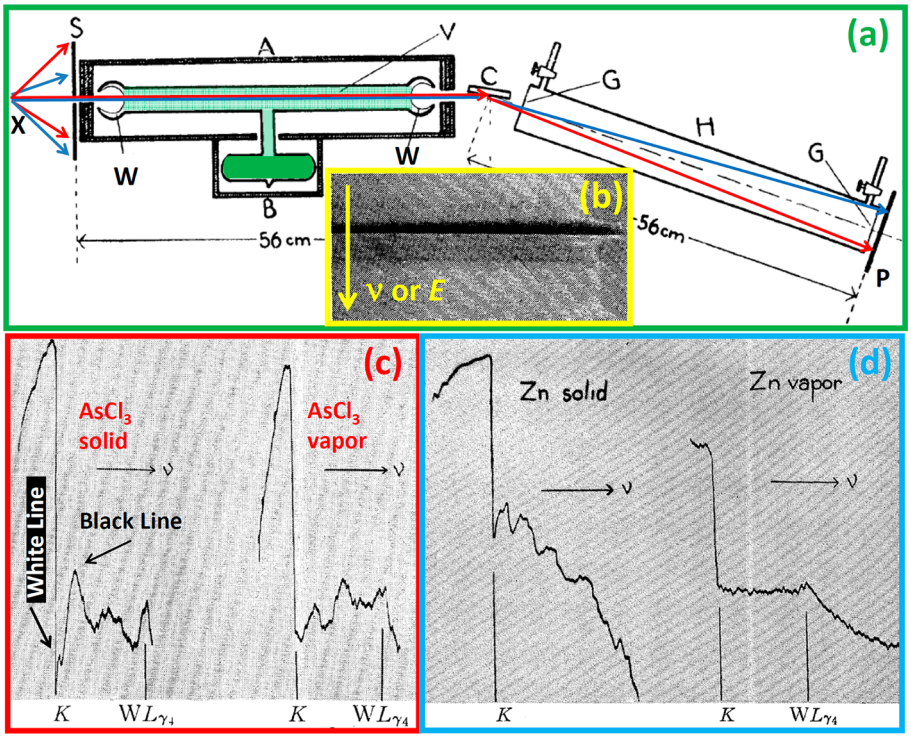

Figure 7. Part a: Scheme of the vapor cell and X-ray spectrometer used by Hanawalt[231] to measure the fine structures in K-edge X-ray absorption spectra of molecules in the vapor phase. The cell was composed of two furnaces (B and A), the former for hosting the solid phase and controlling the vapor pressure via the temperature, the latter for preventing the recondensation of the evaporated phase; a long quartz tube hosting the vapor phase (V) equipped at the end by two concave windows (W) as thin as 3 μm able to maintain the vacuum and to be sufficiently transparent to X-rays. The spectrometer consists of: an X-ray tube of the Siegbahn type (X); slits used to collimate the incoming X-rays (S); a calcite ($CaCO_3$) crystal used as monochromator (C); a quartz tube fluxed with H_2 (H) and equipped with biological X-ray transparent membranes (G) acting as windows; and a photographic plate used as detector (P). This spectrometer was able to cover the 4.9−12.4 keV spectral region, corresponding to 2.5 Å > λ > 1.0 Å and represented the historical equivalent of a dispersive spectrometer (see Figure 4b). Depending on the absorbing gas a time ranging from 4 to 30 h were needed to impress the photographic plate as shown in part b, where the energy increases from top to bottom. The adsorption edge and the successive modulations are clearly visible in part b. The photographic images were then converted into absorption-energy plots like those reported in parts c and d for $AsCl_3$ (As K-edge at 11.8 keV) and Zn (K-edge at 9.6 keV), respectively. Because only I_1 was measured in the setup, the spectra appear *inverted*. The first resonance after the edge, representing a minimum in the absorption was named *white line* while the successive maximum in the absorption spectrum was named *black line*. The former term is kept in the current terminology, whereas the latter is lost. Adapted with permission from ref 231. Copyright 1931 American Physical Society.

(corresponding to a particular fluorescence decay channel, Figure 5b) upon scanning incident photon energy $h\nu_1 = \Omega$. In such a way, the decay transition is the result of an electron coming from a higher level (HL), leaving a hole with a longer τ_{HL} lifetime ($\tau_{HL} \gg \tau_{core}$). The resulting spectrum is characterized by an intrinsic lower broadening $\Delta E_{HERFD} \approx [(\Gamma_{core})^{-2} + (\Gamma_{HL})^{-2}]^{-1/2}$, where $\Gamma_{HL} \equiv (h/2\pi)/\tau_{HL}$.[222] This effectively leads to spectra with a higher energy resolution and sharper features.[199,217,222−225] As a relevant example, XES has allowed the identification of the active sites in supported metal catalysts upon CO adsorption[216,219] see section 9.4.

Another important application of HERFD XAS consists in the so-called range-extended EXAFS spectroscopy.[226−228] It applies in case of samples containing elements with adjacent electronic numbers Z or elements where K and L edges are close in energy (e.g., Cl-doped Pt catalysts). This is for example the case of a sample containing both Mn (Z = 25; K-edge at 6539 eV) and Fe (Z = 26; K-edge at 7112 eV). The Mn K-edge spectrum will show also the undesired Fe K-edge (see blue curves in Figure 6b) that restricts the k-region of study. This holds not only for spectra collected in transmission mode but also for spectra collected in standard fluorescence mode. Indeed, the typical energy resolution of the solid detectors is ~200 eV, implying that the low energy tail of the Fe K_α lines contribute to the photon counting of the Mn K_α, (see bottom part of Figure 6a), resulting in the appearance in the standard EXAFS spectrum of the Fe K-edge jump. In such a case it is no more true that standard EXAFS is atomic specific, as the signal arising from Mn is heavily perturbed by that coming from Fe starting from k = 11.5 Å^{-1}. Conversely, HERFD XAFS can actually be considered as an atomic selective technique in all cases, because it is decay-channel selective with an energy resolution in ω of about 1 eV (see top part of Figure 6a), avoiding any contamination from whatever other decay lines. The reported example concerns the structure of the photocatalytic Mn_4Ca complex, hosted inside the multiprotein membrane system known as photo system II (also containing Fe centers), which is able to photo-oxidize H_2O to O_2. The HERFD XAFS setup used by Yano et al.[226,228] allowed collection of analyzable data up to k_{max} = 15.5 Å^{-1} (whereas standard EXAFS data could be used only up to k_{max} = 11.5 Å^{-1}), so improving the distance resolution of the data set from Δr = 0.14 to 0.10 Å, see eq 22. This improvement allows the authors to discriminate between two Mn−Mn distances at 2.67 and 2.77 Å that gave rise to an unresolved component around

dx.doi.org/10.1021/cr2000898 | *Chem. Rev.* 2013, 113, 1736−1850

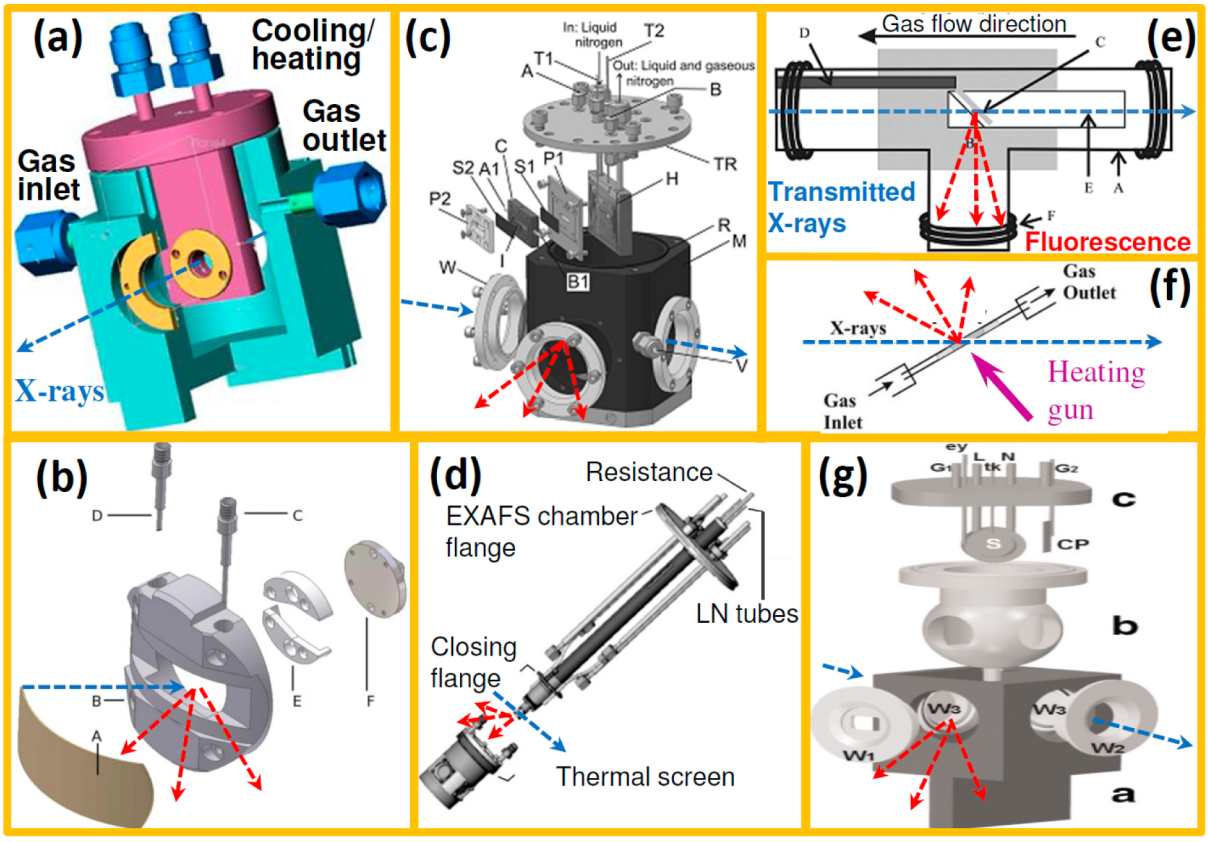

Figure 8. Selection of in situ/operando cells for XAFS measurements. Blue dashed arrows represent the incoming (and the transmitted, when present) beams; when detectable, the fluorescence emission is represented by red arrows. Part a: In situ/operando cell allowing to work in flux or in static atmosphere (10^{-2}−1.5 bar) in the 77−900 K region. The cell can work under static conditions or in flux mode. Substituting kapton with Si windows the cell was used also for far-IR synchrotron radiation experiments. Adapted with permission from ref 238 (http://www.sciencedirect.com/science/article/pii/S0168583X02017196). Copyright 2003 Elsevier. Part b: In situ/operando cell designed for fluorescence XAFS experiments measuring submonolayer model and powder catalysts under plug-flow conditions comparable to laboratory reactors (100−870 K; and 10^{-2}−3.0 bar intervals). Adapted with permission from ref 244 (http://scripts.iucr.org/cgi-bin/paper?S0909049505020261). Copyright 2005 International Union of Crystallography. Part c: In situ/operando heatable/coolable (77−973 K) fluorescence/transmission EXAFS cell for heterogeneous catalysts in gas and liquid phase. The wide windows opening allows XRD data to be simultaneously collected. Adapted with permission from ref 248 (http://scripts.iucr.org/cgi-bin/paper?S0909049507024466). Copyright 2007 International Union of Crystallography. Part d: In situ cell for reductive and oxidative treatments at different temperatures from liquid 100 to 850 K for XAFS measurements performed both in transmission and fluorescence geometry. Adapted with permission from ref 239 (http://scripts.iucr.org/cgi-bin/paper?S090904950501143X). Copyright 2005 International Union of Crystallography. Part e: Schematic drawing of the cell for in situ XAFS investigations from RT to 1250 K performed in both transmission and fluorescence geometry. Adapted with permission from ref 262 (http://scripts.iucr.org/cgi-bin/paper?S0909049504013858). Copyright 2004 International Union of Crystallography. Part f: A simple capillary of optimized diameter can be used as operando reactor allowing both transmission and fluorescence XAFS spectra to be collected. The temperature can be controlled with an heating gun. Adapted with permission from ref 261 (http://pubs.rsc.org/en/content/articlelanding/2004/cp/b403071k). Copyright 2004 the Owner Societies. Part g: In situ cell designed for XAFS measurements on catalytic systems in the soft X-ray range (1−3.5 eV) and in the 80−750 K temperature interval. Adapted with permission from ref 263 (http://rsi.aip.org/resource/1/rsinak/v71/i9/p3260_s1?isAuthorized=no). Copyright 2000 American Institute of Physics.

2.7 Å when analyzing data collected in the standard mode.[226,228]

We conclude this section with a reminder that the HERFD XES setup reported in Figure 5 makes possible the collection of oxidation state-specific EXAFS spectra. In other words, this set-up allows the discrimination of EXAFS signals coming from the same element in different oxidation sates in the same sample.[193,229] This is possible in cases where the different oxidation states of the same element are characterized by slightly different florescence lines ω, so selecting with the second monochromator (analyzer) the different emission energies ω oxidation states-specific EXAFS spectra will be collected. With the same principle, also spin-selective EXAFS spectra collection can be possible.[230] Indeed, K_β fluorescence lines arising from the high-spin and low-spin sites are shifted in energy. In both cases, the principle is similar to that reported in Figure 6a for the extended EXAFS.

2.2.6. In Situ and Operando Cells for Hard and Soft XAFS. It is worth noticing that even in the 1920−1935 pioneering period, when the very first X-ray absorption spectra were recorded on photographic plates (Figure 7b), scientists needed to develop specific cells allowing the measure of the samples under controlled conditions. This is the case of the peculiar quartz cell (Figure 7a) used by Hanawalt[231] to measure in 1931 the XAFS spectra of different molecules in the vapor phase. The XAFS spectra of $AsCl_3$ and Zn are reported in parts c and d. The cell was able to maintain the vacuum needed to avoid contamination of the measured atmosphere and to maintain the vapor temperature sufficient high to avoid vapor condensation in the solid phase on the cell windows. Quartz

dx.doi.org/10.1021/cr2000898 | Chem. Rev. 2013, 113, 1736−1850

was the material fulfilling the experimental requests and allowing to shape windows as thin as 3 μm to guarantee transparency to X-rays.

At the beginning of the age of synchrotrons (the late 1970s), the cell developed by Lytle in collaboration with the Exxon research group was a mile stone for in situ XAS characterization of catalysts.[232] Nowadays, X-ray absorption experiments aiming at investigating the reactivity of surface species require a careful control on the sample environment in terms of temperature and atmosphere and reactants flux.[233] A cell and its related gas input/output apparatus designed for this purpose must have the following characteristics: (a) sample heating up to the desired temperature, either under dynamical vacuum or in reducing/oxidizing atmosphere for catalyst activation; (b) dosage of the desired amount of gas, either in flux or in static conditions; (c) choice of the desired measurement temperature, that could be related to the reaction temperature or as low as possible (down to 77 or 4 K) for the investigation of weakly bonded adsorbates.[36,234−239] A selection of cells allowing to perform XAFS measurements on catalysts under controlled conditions is reported in Figure 8. When the activated catalyst works at the reaction temperature in flow of the reactants, then gas output can be connected to a mass spectrometer to allow the simultaneous detection of the catalyst activity.[39,68,77,238−255] This experimental setup allows to perform what has been defined "spectroscopy under operando conditions",[256−260] where the catalytic information are coupled with the spectroscopic information obtained simultaneously from, in the cases of interest for this review, EXAFS and XANES (see section 8). The simplest cell allowing operando XAFS experiments to be done is a capillary containing the catalyst, where reagents can be fluxed in and the temperature can be controlled with a heating gun (Figure 8f). More complex cells are shown in the remaining part of the Figure. When dealing with operando set-ups, it is worth noticing that traditional XAFS cells are typically not ideal catalytic reactors, since a compromise must be found between allowing the X-ray beam to probe the catalyst and keeping the bed geometry and temperature/flow/diffusion control appropriate.[250,261] The list of major difficulties that operando-cells may suffer has been recently authoritatively reviewed by Meunier[250] in terms of (i) feed impurities, (ii) feed channeling and bed bypass, (iii) temperature gradients, (iv) beam effects, (v) sample preparation effects (e.g., diffusion problems inside pressed pellets), and (vii) catalytically active cell components. However, these difficulties can often be overcome or controlled, and operando spectroscopy represents a unique tool to understand a working catalyst at the atomic level allowing quantitative structure/composition−activity/selectivity relationships and the gathering of fundamental insight in short- and long-term deactivation mechanisms of heterogeneous catalysts.[242]

Looking at heterogeneous catalytic systems from different perspectives, i.e. applying a multiple-technique approach allowing the simultaneous detection of different signals, represents a continuous challenge for in situ studies.[264−266] In this regard, some specific cells allow to couple XAFS spectroscopy with IR and/or UV−vis and/or Raman spectroscopies or with scattering techniques like XRD and SAXS. In such cases compromises must be made to allow the simultaneous detection of two or more techniques and the quality of the collected data is usually lower than what obtained in specific independent experiments. Of course care must be taken because the sampled volume and the sampling frequency may be different for the two (or more) techniques. Notwithstanding these limitations, the possibility to monitor with two or more independent techniques the catalytic system under exactly the same pressure, temperature, and flow conditions is a tremendous plus value that has driven a great instrumental effort by several users groups and by several beamline scientists worldwide. Description of the experimental setups allowing such combinations is reported in the specialized literature for XAFS/IR,[267−271] XAFS/ATR,[272] XAFS/Raman,[255,273,274] XAFS/XRD,[22,36,172,235,237,248,264,275−280] XAFS/SAXS,[266,281,282] XAFS/UV−vis/Raman,[243] XAFS/UV−vis/XRD,[283,284] XES/ATR.[272]

Very high reaction temperatures (as high as 1250 K) can be reached in the cell developed by Huwe and Froba,[262] see Figure 8e. Comparable conditions can be reached in the reactor realized at the ESRF in collaboration with the Toyota researchers.[285] The cell realized by Kawai et al.[286] is able to combine high temperature (900 K) with high pressure (10 MPa) environments, so replicating the thermodynamic conditions experienced by a working catalyst. The reader interested in the technical details of the different cells realized so far, allowing the measurement of a catalyst under in situ or operando conditions, are addressed to the reported specialized references.[68,234,238,239,241−246,248,255,285,287−290]

Most of the experimental set-ups discussed above are used for hard X-rays (E > 5 keV, that is, for K-edges of elements with Z ≥ 22, corresponding to Ti), which are rather penetrating and do not experience a too severe absorption by the windows (beryllium, mylar, or kapton is usually used) needed to maintain the chemical environment around the catalyst and by the reactants atmosphere itself. This is no more true when dealing with soft X-rays see Figure 3b, and XAFS experiments on light elements under reaction conditions were not possible for a long time. According to eq 10 the same absorbing element (window or a reaction atmosphere) increases its absorption coefficient by almost two hundred moving from the Cu to the Al K-edge: $\mu(E = 1560\ \text{eV})/\mu(E = 8980\ \text{eV}) \approx 190$.

This technical problem has been successfully overcome in the last decade e.g. by van Bokhoven et al.[263,291] (see Figure 8g), by Knop-Gericke et al.[292−297] and by Bell et al.[298] The cell by van Bokhoven et al.[291] enables in situ catalytic studies on elements with X-ray absorption edges between 1.3 and 3.0 keV range (i.e., from Mg to Cl K-edges). The apparatus consists of a vacuum vessel that contains a replaceable sealed in situ cell, whose dimensions have been minimized to reduce the X-ray beam absorption. These set-ups were used for the XANES studies on the local environment of Al (K-edge E = 1560 eV), in different zeolitic frameworks, subjected to different treatments and under different atmospheres,[299−308] see section 3.5. Of high interest were also the experiments performed at the Fe L_3-edges (707 eV) on different Fe-zeolites by the Utrecht group,[212,309,310] see section 3.3.5.1. The experimental setup developed by Knop-Gericke et al.,[292−294] covers an even lower energy range: 250 ≤ $h\nu$ ≤ 1000 eV, that is, from C to Ne K-edges. In situ investigations under reaction conditions of catalysts can be performed up to 500 K and in the mbar pressure range.

2.2.7. Experimental Set-Ups for Micrometer-Resolved Experiments. The great brilliance with reduced emittance of current third generation synchrotron sources,[4] and the new developments in optics and X-ray detector technology (such as fast-readout large area detectors with high dynamic range and low noise characteristics),[188,311] make intense subμm X-ray

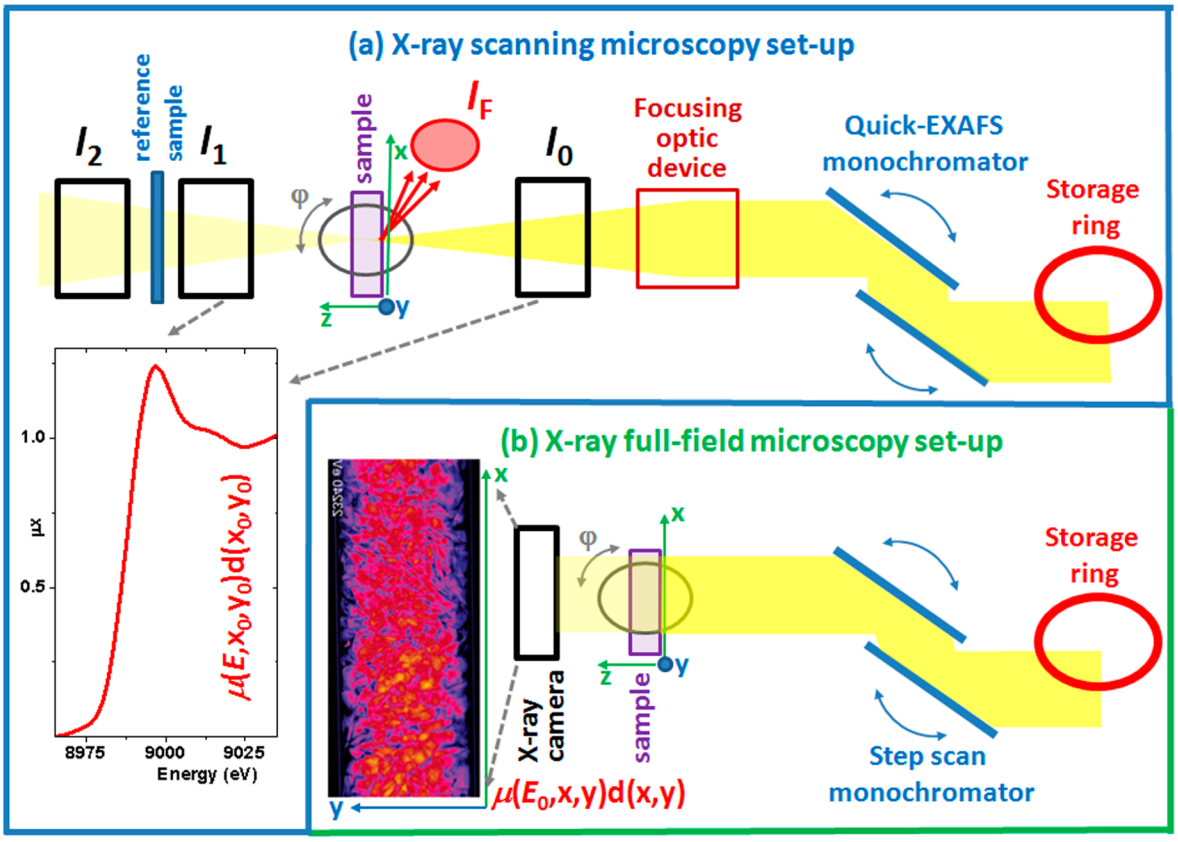

Figure 9. Schematic views of the basic setup for spatially resolved X-ray absorption spectroscopy. Part a: Scanning monochromatic μm-beam setup. This setup contains all the elements (i–v) of a conventional XAFS beamline (detection in transmission mode via I_0 and I_1, in fluorescence mode via I_0 and I_F and edge calibration via I_2, see Figure 4a). In addition, it is equipped with focusing optics (Fresnel zone plates,[313] or compound refractive lens,[314−316] or Kirkpatrick−Baez mirrors,[317] or tapered capillaries[318]), a quick-EXAFS monochromator and a sample stage with rotation (φ) and high precision (x,y) translations. Part b: Full-field imaging setup. It is equipped with a standard step-scan monochromator, a high-(x,y) resolution X-ray camera, a sample stage with rotation (φ) and medium precision (x,y) translations. Both set-ups allow tomographic data acquisitions. The insets of parts a and b reports the outputs of the single step of each acquisition: a full XAFS spectrum of a single (x_0, y_0) point and a full transmission map recorded at a single energy E_0. For a description of the scanning polychromatic μm-beam setup, see Figure 4b. This figure was inspired by the sketches reported in refs 71, 336, and 337. The inset of part b has been reproduced with permission from ref 338. Copyright 2006 American Chemical Society.

beams available today. Such beams gave birth to X-ray scanning microscopy set-ups.

We already discussed the Bragg/Laue bent polychromators (section 2.2.3., see Figure 4b), allowing a polychromatic beam to be focused in a μm-sized spot. Although conceived for time-resolved studies, the micrometer-size of the beam at the focus point makes the dispersive setup suitable for accurate space resolved studies.[190,191] In X-ray scanning microscopy the most used set-ups for focusing a monochromatic beam are:[312] (i) Fresnel zone plates,[313] (ii) compound refractive lens,[314−316] (iii) Kirkpatrick−Baez mirrors,[317] and (iv) tapered capillaries.[318] Historically, space resolved techniques have been mainly exploited in the field of solid state physics,[319−324] high pressure physics,[325−327] geology,[328−330] biology,[331,332] and medicine.[333] More recently micrometer-focused X-ray beams found applications also in the field of catalysis.[66,67,70−75,334,335]

Figure 9a reports the standard experimental setup used for scanning microscopy requiring a quick-EXAFS monochromator, a focusing device (one out of the four listed above), and a positioning stage allowing to move the sample in the two directions (x,y) perpendicular to the beam with a μm precision, plus a rotation stage (φ). A standard $\mu(E,x,y)$ spectrum is obtained for each (x,y) point. The fast scan monochromator allows to collect a Quick-XAFS spectrum in a given (x_0,y_0) point, then the monochromator moves back before the desired edge while a positioning stage moves the sample to the next point to be mapped ($x_0 + \Delta x,y_0$) or ($x_0,y_0 + \Delta y$). At the end of the process, a $\mu(E,x,y)$ map is obtained. Besides XAFS, this setup allows the use of other X-ray analytical techniques, such as X-ray fluorescence and/or diffraction (using a 2D detector instead of I_1 in Figure 9a) and thus allows to obtain a complete, micrometer-resolved, elemental, electronic, chemical, and structural information of the sample.

Figure 9b reports an alternative setup called full-field microscopy, yielding a full transmission image of the sample in a single exposure. The whole region (x,y) of interest of the sample is exposed to a flat monochromatic hard X-ray beam and its transmission image is recorded with a high-(x,y) resolution X-ray camera. The whole $I_1(E,x,y)$ map is collected for a given E value in a single shot. Successively, the monochromator moves to the next energy position and the $I_1(E + \Delta E,x,y)$ map is acquired. By recording a series of images, at different energies E across the desired absorption edge, the $I_1(E,x,y)$ maps needed for a full XANES/EXAFS spectrum can be obtained for each pixel (x,y). As was the case for the dispersive XAFS geometry (see section 2.2.3 and Figure 4b),

dx.doi.org/10.1021/cr2000898 | Chem. Rev. 2013, 113, 1736−1850

the $I_0(E,x,y)$ maps have to be collected a posteriori, repeating the step by step energy scan once the sample has been removed from the beam. This means that a high stability of the ring and of the beamline is required to use $I_1(E,x,y)$ and $I_0(E,x,y)$ data sets collected in different moments to obtain the corresponding $\mu(E,x,y)d(x,y)$ data set. Moreover, attention must be paid to correct for the dark current DC(x,y) of the detector both $I_1(E,x,y)$ and $I_0(E,x,y)$ set of images. DC(x,y) is measured by counting, for the same time, with the X-ray shutter closed. In this case, eq 11 can be rewritten for each independent (x,y) pixel of X-ray resulting in

$$\mu(E, x, y)d(x, y) = \ln\left[\frac{I_0(E, x, y) - \mathrm{DC}(x, y)}{I_1(E, x, y) - \mathrm{DC}(x, y)}\right] \quad (13)$$

The full-field microscopy setup, described in Figure 9b, does not allow the simultaneous collection of a reference sample for the energy/angle calibration, see eq 3, and is limited to transmission experiments: no μ-XRF or μ-XRD is possible with this setup. The spatial resolution of this technique is determined by that of the detector and typically lies in the micrometer range.[71] Higher spatial resolution, that is, below 100 nm, can be obtained by hard X-ray microscopy.[339,340] This technique, however, has not yet been combined with XAFS, so far.

At the end, although with a different acquisition strategy, both scanning microscopy (Figure 9a) and full-field microscopy (Figure 9b) techniques measure the $\mu(E,x,y)d(x,y)$ map of the sample defined as

$$\mu(E, x, y)d(x, y) = \int \mu(E, x, y, z)d(x, y)\, \mathrm{d}z \quad (14)$$

whereas, using standard mm-sized beams, a conventional XAFS measurement (see section 2.2.3 and Figure 4a), results in the measurement of

$$\left\langle \mu(E)d \right\rangle = \iiint \mu(E, x, y, z)d(x, y)\, \mathrm{d}x\, \mathrm{d}y\, \mathrm{d}z \quad (15)$$

where the symbol $\langle\ \rangle$ indicates a spatial averaging. The $\mu(E,x,y)d(x,y)$ map already contains an impressive number of information;[71,338] however, if the sample is inhomogeneous along the depth z crossed by the beam (either chemically: gradient in $\mu(E,x,y,z)$ along z; or geometrically: different depth $d(x,y)$ along the (x,y) plane), the interpretation of single transmission images may not be sufficient for a reasonable characterization and a tomographic approach is needed.[67,71,336,337] For tomographic imaging, the sample holder is equipped by a rotation stage allowing to collect a series of transmission images $\mu(E,x,y,\varphi)$ as a function of the rotation angle φ over 360°. From this huge data set, the three-dimensional inner structure of the sample can be reconstructed, yielding the attenuation coefficient $\mu(E,x,y,z)$ at each location inside the sample

$$\mu(E, x, y, \varphi) \xrightarrow{\text{tomographic algorithmm}} \mu(E, x, y, z) \quad (16)$$

By fitting normalized reference spectra to these data, the contribution of each chemical species to this attenuation can be extracted, see the example reported in section 7.2. Thus, the mass density of each component at each location on the virtual section can be determined quantitatively.[67,71] The error in mass density can be estimated by the residual of the fit, provided no systematic errors have been made in identifying the right reference species used in the fit.

In general, it is time-consuming to record full spectroscopic data (>6 h) in a tomographic scan, even if a single full tomogram requires but a few minutes of acquisition time and typically data for only a few characteristic X-ray energies can be recorded. Recording full XANES tomograms also results in large data sets requiring new storage and computing infrastructure as well as optimized software (see section 2.3.7). Compared to full-field imaging, scanning microscopy is significantly slower, as the sample is scanned point by point. However, it can be applied to diluted systems using the fluorescence signal for absorption spectroscopy (see Figure 9a) and, since polychromatic optics can be used in scanning microscopy (Figure 4b), it is much easier to extend the absorption spectrum to the full EXAFS region than in the case of full-field microscopy.

Both scanning microscopy (Figure 9a) and full-field microscopy (Figure 9b), techniques can combine XAFS spectroscopy with a reactants input and a products output (analyzed by mass spectrometry) and are thus well suited for operando investigations of catalytic reactions inside a chemical reactor.[67,71] Both techniques are time-consuming, so time resolution is not available with these set-ups, that have to be applied under steady-state conditions. Exceptions may be made for the full-field microscopy mode (Figure 9b) in some specific cases where monitoring the $\mu(E,x,y)d$ map at a given (fixed) E value allows to extract relevant information concerning the evolution of the reaction. This may be the case, for example, in monitoring a $Cu^+ \rightleftharpoons Cu^{2+}$ equilibrium and selecting E at the strong 1s → 4p electronic transition of Cu^+, where Cu^{2+} are almost non absorbing (vide infra Figure 49a).

2.3. EXAFS and XANES Theory and Data Analysis

2.3.1. Brief Historical Overview. The development in 1916 in Lund (Sweden) of the first vacuum X-ray spectrometer by Siegbahn and Stenström[341−344] and successive improvements[231] (Figure 7a) can be considered as the born of X-ray spectroscopy. With this kind of innovative technology the fine structure beyond the absorption edges of selected atoms was experimentally observed for the first time in 1920 by Fricke[345] on K-edges and by Hertz[346] on L-edges. In the period before the II-world war, other authors reported analogous behaviors on several different absorption edges.[347−360]

Remarkable was the observation dated 1931 by Hanawalt[231] of the effect that the chemical and physical state of the sample have on the fine structure of the XAS spectra. Using the experimental setup reported in Figure 7a and collecting XAFS spectra on a photographic plate (Figure 7b), Hanawalt was able to reach two empirical observation of fundamental importance. First, he proved that substances sublimating in the molecular form like As ($4As_{solid} \rightarrow (As_4)_{gas}$) or $AsCl_3$ (Figure 7c) are characterized by XAFS spectra exhibiting different fine structures above the edge when measured in the solid or in the vapor phases. Second, he observed that the monatomic vapors of Zn (Figure 7d), Hg, Xe, and Kr elements exhibit no secondary structure. These experiments, amazing for having been performed in 1931, already contained the main message of EXAFS spectroscopy, but several years were needed before they could be correctly interpreted and some decades were needed before the potentiality of EXAFS could be fully exploited for extracting quantitative information.

The first theoretical attempt to explain fine structure in the XAS spectra was proposed in the years 1931−32 by Kronig,[361,362] who developed a model based on the presence

dx.doi.org/10.1021/cr2000898 | Chem. Rev. 2013, 113, 1736−1850

of long-range order in the system.[363] This theory, intrinsically incorrect owing to its assumption, was found immediately to be at least incomplete, because it was unable to explain the EXAFS signals observed in gases, liquids, solutions and amorphous solids. Still, in 1932 Kronig himself, stimulated by the experiments of Hanawalt[231] (see Figure 7), presented a new theory based on the fundamental role of short-range order to explain the fine structure observed in the spectra of diatomic molecules.[364] The new approach explained the XAFS features as being the result of modulation of the wave function of the final state of a photoelectron upon its scattering from the potentials of neighboring atoms. This approach, implemented successively by Petersen[365−368] and by many other authors in the 1930s to 1960s,[369−385] represents the basis of the modern concept of XAFS, although was unable to provide quantitative information on the local structure of the absorbing atom in the investigated samples. At that stage XAFS was still just a spectroscopic curiosity and not yet a powerful characterization tool. In most of the cases,[231,345,349,354,374,384,386] the discussion was limited to a table containing a list of the observed maxima and minima of the fine structure of a given material and to a comparison of these values with those predicted by the different theories listed above.[363] No quantitative information were extracted and only qualitative conclusions could be reached. Some relevant, although qualitative, conclusions are mentioned here below. (i) Several authors observed that the amplitude of the XAFS oscillations decrease when increasing the sample temperature.[355,381,383,385] (ii) It was observed that metals with the same crystal structure had similar fine structures.[348,354,357,386] (iii) In 1957 Shiraiwa et al.[378] measured the X-ray absorption spectra of crystalline and amorphous Ge observing that the shape of the fine structure was the same for the two materials though oscillations were less intense and disappeared at lower energies in the amorphous phase than in the crystalline phase. Similar conclusion were reached in 1962 by Nelson et al.[382] who measured GeO_2 in the amorphous state and in both hexagonal and tetragonal crystalline forms. Partial and more complete reviews of the pioneering 1920−1970 period of X-ray absorption spectroscopy can be found in the literature.[5,24,129,384,387−391]

A fundamental improvement in the experimental instrumentation was achieved in the sixties when commercial diffractometers were modified so that absorption spectra of much better quality could be obtained still using conventional X-ray tubes as source.[392−394] A Si crystal, acting as a single-crystal monochromator, was positioned on the goniometer conceived to host the sample for diffraction experiments so that the step scaling of the goniometer allowed to scan through the desired absorption edge, see eq 3. By mounting and dismounting the sample in the beam path both I_1 and I_0 could be detected allowing a precise determination of the absorption coefficient μ. With this experimental setup Van Nordstrand[392,393] performed a systematic study on many transition metal compounds and classified their XANES spectra according to the atomic structure and valence of the metal element in the compound, also noting the chemical shift with valence. This fingerprint classification was used to identify the structural/valence form of elements in catalysts, which are usually so highly dispersed that their diffraction patterns cannot be measured. This work of Van Nordstrand was the first example of the application of XANES in catalysis.

The determinant advance in the interpretation of the postedge oscillations (now EXAFS) occurred in 1971, when it was shown by Sayers, Stern, and Lytle that Fourier transform of the background-subtracted oscillations gives, in *R*-space, a pattern close to the function of radial distribution of atomic density,[395] vide infra eq 19. Authors were able to extract from the EXAFS spectra collected on crystalline and amorphous Ge the following quantitative values: (i) first and second neighbors in amorphous Ge are at the crystalline distance within the accuracy of 1%; (ii) from the comparison of the relative second-shell-peak intensities for the crystalline and amorphous cases authors measured a Debye−Waller factor six times larger in the amorphous phase; from this observation authors concluded that the tetrahedral bonds are distorted by 5° in the amorphous phase.[395] It is remarkable to underline that such accurate conclusions where obtained working on experimental spectra still collected using an X-ray tube as source.

That work[395] represented the mile stone for EXAFS spectroscopy and was, still in the seventies, supported and further implemented (in more formal derivations based on Green's function and generalization to muffin-tin scattering potentials) by successive works from the same authors[7,396−399] and from independent groups.[8,400−403] Starting from the 1970s, the progressive availability of several and progressively more brilliant and broadband synchrotron radiation sources[404] determined the establishment of EXAFS and XANES spectroscopies as reliable tools to understand the structural and electronic configuration of unknown systems. Starting from the middle of the 1980s and mainly in the 1990s, the development and the distribution of codes for the data analysis (vide infra sections 2.3.4−2.3.7) allowed to enlarge significantly the scientific community using EXAFS and XANES spectroscopies for structural characterization of materials. Finally the development of cells for in situ and/or operando X-ray absorption experiments (see section 2.2.6) made EXAFS and XANES key techniques in catalysis, see Tables 1 and 2.

2.3.2. Single-Scattering Approximation. To separate the structural information from the energy dependence of the absorption cross sections, the normal EXAFS spectrum χ is usually defined as the normalized oscillatory part of $\mu(E)$. The EXAFS signal χ is extracted from the experimentally measured $\mu(E)$ function (see section 2.2.2 and Figure 3c) upon subtraction of the pre-edge and atomic-like absorptions, $\mu_0(E)$ and normalization to the edge jump (to take into account the sample thickness d).[4,37,49,50,129] The obtained EXAFS function or χ function

$$\chi(k) = [\mu(k) - \mu_0(k)]/\mu_0(k) \tag{17}$$

is conventionally expressed versus k, the wavenumber of the photoelectron outgoing from the absorber atom, according to the $k-E$ relationship reported in eq 18, where m and E_f are the mass and the kinetic energy of the photoelectron, $\hbar\omega$ is the energy of the incoming photon and E_b is the binding energy of the photoelectron

$$k = \sqrt{\frac{2m}{\hbar^2}E_f} = \sqrt{\frac{2m}{\hbar^2}(\hbar\omega - E_b)} \tag{18}$$

In the frame of the single-scattering (SS) approach, the k-weighted $\chi(k)$ function can be modeled as reported in eq 19,[7,9−11,395,405−410] known as the standard EXAFS equation

$$k\chi(k) = S_0{}^2 \sum_i \frac{N_i A_i}{r_i^2} e^{(-2r_i/\lambda)} e^{(-2\sigma_i{}^2 k^2)} \sin[2kri + 2\phi i(k)] \tag{19}$$

dx.doi.org/10.1021/cr2000898 | Chem. Rev. 2013, 113, 1736−1850

where S_0^2 is the so-called passive electron reduction factor, λ is the photoelectron mean-free path, the sum over i runs over the different coordination shells around the absorbing atom, $A_i(k)$ is the amplitude function of the scattering atom (measured in Å),[405,411] $\varphi_i(k)$ is the phase function of the couple absorber/scatterer,[405,411] N_i is the coordination number, r_i is the interatomic distance and σ_i is the relative Debye−Waller factor that quantifies the disorder of the ith shell. For each shell, σ_i consists of a dynamic term due to the thermal motion of the atoms $(\sigma_{i,T})$ and a static term due to structural disorder $(\sigma_{i,D})$[7,9−11,395,399]

$$\sigma_i^2 = \sigma_{i,T}^2 + \sigma_{i,D}^2 \tag{20}$$

The double nature of the Debye−Waller factor measured by EXAFS was already expressed in the first paper of Sayers, Stern, and Lytle[395] and was used to quantitatively explain the difference between the EXAFS spectra of crystalline and amorphous Ge. Equation 20 will play a relevant role in the interpretation of the EXAFS spectra collected on catalysts, because disorder is often an important parameter in such materials. To disentangle the temperature-dependent $\sigma^2_{i,T}$ and the temperature-independent $\sigma^2_{i,D}$ some phenomenological models have been employed, such as the correlated Einstein[412] and correlated Debye[403] models.

Equation 19 holds when single scattering (SS) paths dominate the EXAFS signal and when the pair distribution function of bond distances for each shell can be expressed using the Gaussian function $\exp(-2k^2\sigma_i^2)$. The extension of the theory in these two cases will be briefly discussed in sections 2.3.3 and 2.3.8, respectively.

The standard EXAFS formula, eq 19, provides a convenient parametrization for fitting the local atomic structure around the absorbing atom to the experimental EXAFS data.[413] The dependence of the oscillatory structure of the EXAFS signal on interatomic distance and photoelectron binding energy E_b (through eq 18) is clearly reflected in the $\sin(2kr_i)$ term. The short-range probed by an EXAFS experiment is easily explained by considering the finite lifetime of the core-hole and the limited free mean path (λ) of the photoelectron as expressed by the exponential term $e^{-2ri/\lambda}$.[414] The strength of the interfering waves depends on the type and number of neighboring atoms through the backscattering amplitude $A_i(k)$ and the coordination number N_i and, hence, is primarily responsible of the magnitude of the EXAFS signal. By performing a Fourier transform of the $\chi(k)$ function, weighted by k^n (n = 1, 2 or 3) to empirically balance the loss of EXAFS signal in the high k region, it is possible to single out the contributions of the different coordination shells in the R-space.

Once the $A_i(k)$ and $\varphi_i(k)$ functions have been independently measured on model compounds or ab initio computed, the structural parameters N_i, r_i, and σ^2_i can be determined in a least-squares approach where the difference between the experimental and the modeled $k^n\chi(k_j)$ function is minimized along all the sampled experimental points k_j. The minimization routine can be done either in k-space, directly on the measured $k^n\chi(k_j)$ function, or in R-space, working on the Fourier-transformed functions. So, for each coordination shell, the coordination number, the atomic distance and the thermal factor can be extracted from an accurate EXAFS study. According to the Nyquist theorem (also known as sampling theorem), the maximum number (n_{ind}) of optimizable parameters is defined by the product of the sampled interval in k-space (Δk) and the interval in R-space(ΔR) containing the optimized shells[415]

$$n_{ind} = 2\Delta k \Delta R/\pi \tag{21}$$

Of course care must be taken to avoid trapping in local or nonphysical minima of the minimization process. Analogously, correlation parameters between each couple of optimized parameters should ideally be lower than 0.8 in absolute value and should never exceed 0.9. From eq 19, it emerges the need to acquire an EXAFS spectrum of over the largest possible k-interval. Experimental data collected up to high k_{max} allows to (i) increase n_{ind}, as Δk increases, (ii) reduce the correlation between N_i and σ_i parameters, and (iii) increase the ability to discriminate between two close distances. The distance resolution (Δr) of an EXAFS spectrum is defined from k_{max} according to the relation

$$\Delta r = \pi/(2k_{max}) \tag{22}$$

Two equally intense signals generated by the same scatterer located at r_1 and r_2 can indeed be singled out only in case the two oscillating functions $\sin(2kr_1)$ and $\sin(2kr_2)$ are able to generate at least a beat in the sampled k-range, and this occurs for $2k(r_1 - r_2) = \pi$. To reach a distance resolution of Δr = 0.1 Å the EXAFS spectrum has to be collected up to about 16 Å^{-1}.

In some cases, when the experimental signal in R-space is particularly well-defined into distinctly different coordination shells, each observed single shell can then be back-transformed into k-space (usually called q-space) to obtain a "single frequency" $\chi_i(k)$ function. The analysis in q-space has the advantage of reducing the experimental noise, thanks to the double FT-filtering process, and of simplifying the problem, as it removes the sum symbol in eq 19. This approach was very common at the beginning of the modern age of EXAFS.[9,416] However, it leads actually to truncation errors affecting the intensity of the signal and, for shells higher than the first, it is not straightforwardly applicable when MS contributions are present in the experimental signal. As a consequence nowadays the data analysis in q-space is usually not recommended and, when adopted, care must be done in discussing the results.

2.3.3. Multiple-Scattering Expansion. The standard EXAFS formula reported in eq 19 takes into account only single scattering contributions, that is, the terms where the photoelectron is diffused by a single scattering atom before coming back to the absorbing atom: In these cases the scattering angle is 180° and we are dealing with a back-scattering or back-reflection of the photoelectron. Actually, all possible scattering paths where the photoelectron is diffused by N different neighbors can contribute to the interference phenomenon and thus to the EXAFS signal, provided that the path is ended into the absorbing atom where it starts. All the paths where the number of scattering atoms is higher than two are called multiple scattering (MS) paths. Very often MS paths have a low or very low contribution to the overall EXAFS signal with respect to SS ones, since the low free mean path of the photoelectron, λ in eq 19, penalizes longer paths. This is the normal situation found when dealing with heterogeneous catalysts where, because of the high structural heterogeneity of the absorbing species, only the atoms belonging to the first coordination sphere contribute significantly to the EXAFS signal. For this reason the EXAFS data analysis on such systems is usually performed in a SS approach.

However, although if for heterogeneous catalysts the SS approach is generally sufficient to obtain the structural

dx.doi.org/10.1021/cr2000898 | Chem. Rev. 2013, 113, 1736−1850

parameters of the active surface species, in some cases the MS contributions become important and must be included within the EXAFS data analysis in order to avoid poor, or often misleading results. Limiting the discussion to a three body path between the absorber A and two neighbors atoms B and C, beside the classical two bodies SS contributions (A → B → A and A → C → A) also MS (A → B → C → A) has to be considered. The intensity of this three body MS contribution is weighted by a factor proportional to $\cos(\theta)$, being θ the A−B−C angle.[11] This means that MS contribution will be enhanced in case of collinear arrangements of atoms such as B−A−C or A−B−C, where the so-called focusing (or shadowing) effect is fully operative. This is the situation found, for example, for all studies on fcc metal nanoparticles (section 9.), for Cu^+ carbonyls formed inside zeolites (see section 4.2.2),[417,418] and for Cr^{2+} carbonyls formed at the Cr/SiO_2 surface (Phillips catalyst, see section 6.2.2.2).[118] MS contributions have been found to be relevant also in the determination of the second shell structure around Ti atoms hosted in the MFI framework (see section 3.2.4.2)[419] and in determination of the structure of the metal centers in MOFs materials before and after molecular adsorption (section 5).[65]

The development of multiple scattering theory was a key step in the success of the modern theory of XAFS. This theory yields a unified treatment of both EXAFS and XANES.[390,420,421] Of central importance is the question of convergence, that is, how many terms are needed and which are they? A detailed study[422] shows that neither low-order nor full multiple scattering theories are fully satisfactory. Instead, a configurational average of sufficiently high-order MS contributions appears to be necessary for the convergence of both EXAFS and XANES calculations. There are three main computational difficulties in calculating MS to high order: (a) the large angular momentum basis needed at high energies, (b) the exponential proliferation of MS paths, and (c) the need for MS Debye−Waller factors. The physics which is behind the phenomenon of multiple scattering is far beyond the scopes of this work, consequently the reader should refer to the following references.[4,8,10,390,409,420,421,423−427]

2.3.4. Codes for EXAFS Data Analysis. Among the most used codes allowing to perform an EXAFS data analysis with the SS approach, we mention, for example, EXAFS pour le Mac[428] developed by Michalowicz, Viper,[429,430] developed by Klementev, RSXAP,[144] SEDEM,[431] NPI,[432] and XAS.[433] These codes are also widely used for the $\chi(k)$ extraction. In the last years, several programs have been developed allowing a MS analysis of EXAFS data, among which we mention GNXAS[425,426,434−436] by Filipponi, Di Cicco, and Natoli, EXCURVE[437−440] by Binsted et al., and FEFF, in its successive releases[390,407,422,424,441−447] developed by Rehr et al. A galaxy of codes developed in the last two decades conceived to use theoretical phases and amplitudes generated by the different releases of FEFF. Among them we mention FEFFIT,[448] UWXAFS,[449,450] XDAP,[451] XFIT,[452] EDA,[453,454] SixPACK,[455] EXAFSPAK,[456] WinXAS,[457] LASE,[458] and MAX.[459] Very recently, Meneghini, Bardelli and Mobilio reorganized the original EXAFS data analysis programs developed in the eighties by the PULS group at the Frascati National Laboratories (LNF-INFN, Italy) in a single program (ESTRA).[460] The same group also provides the FitEXA program for the data analysis.[460] Particular emphasis, because of its widespread use, has to be put on FEFFIT,[448] designed to fit experimental XAFS spectra to theoretical calculations from FEFF, that successively evolved into IFEFFIT,[461,462] with an improved graphical interface (including Athena, Artemis, and Hephaestus codes)[463] developed by Ravel and Newville. At the end of this list it is worth recalling the important peculiarity of the GNXAS code,[426,434] that include the $\chi(k)$ extraction from the experimentally measured $\mu(E)$ function, see eq 17, within the minimization process where the structural parameters (N_i, r_i, and σ_i) of the different shells, see eq 19, are optimized. In this way the correlation among the background subtraction and edge jump parameters and the structural parameter is under control.

Programs able to deal with MS approach can be divided in the following three main categories. (i) The full MS methods consider all the MS paths, treating curved-wave effects exactly and MS to all orders, thus providing an accurate self-consistent calculations of the electronic charge densities and potentials appropriate to the crystalline or molecular environment, and an accurate calculation of the Fermi energy relative to the unoccupied states.[464] However, these methods are limited to the near-edge region, because the number of basis-set functions and orbital angular momentum components that must be included rapidly increase as a function of energy above the edge. Moreover, since exact methods sum all the scattering paths, one cannot separate the contributions from specific paths, which is the condition needed to extract bond-length and bond-angle information. In other words, such exact methods are not tuned into the atomic structure of the material, but instead are focused on indirect manifestations of the structure, for example, in densities of states. (ii) The "path by path" approach, which considers only the most significant MS paths, is the most used method for analyzing EXAFS data. Its main advantages are the computational efficiency and accuracy, along with the fact that it allows a much easier determination of the structural parameters. Fourier transforms of the XAFS signal indicate that the near neighbors generally give the dominant contributions but also show that MS contributions from more distant paths eventually dominate the signal. (iii) Various alternatives to the "path by path" method have been proposed. We just mention the GNXAS method,[425,426,434−436] which systematically combines all the MS contributions for a given set of n sites within a cluster. This approach is conceptually very simple, because the MS series contains a number of distinct terms that is significantly lower than the "path by path" methods. This method overcomes the path proliferation problem and by grouping the terms in this way, leads to a faster convergence of the MS series. On the other hand, each term contains contributions having different path lengths, which complicates the treatment of vibrational and structural disorder and requires a numerical configurational average.

Finally, we briefly mention two codes able to deal with EXAFS spectra characterized by the presence of multielectron excitations: GNXAS[425,426,434−436] and XANADU.[465]

2.3.5. Codes for XANES Data Analysis. Before entering in the short discussion on the available codes, authoritative impact- or review-papers on both the XANES theory[12,42,43,390,427,445,466−474] and the application of XANES in the field of catalysis[16,47,56−58,60,392,475,476] are mentioned.

The full MS approach is the only one possible to analyze XANES data, because the mean free path of the photoelectron near the edge is much greater than that of a photoelectron emitted in the EXAFS region that has a much higher k value. Several codes have been developed so far for the XANES simulation.[477] In this regard the following specific codes are

dx.doi.org/10.1021/cr2000898 | Chem. Rev. 2013, 113, 1736−1850

Table 5. Resuming of a Selection of the Available Codes for XANES Spectra Simulation and Their Principal Characteristics.[a] Adapted, with permission, from the PhD Thesis of Gianolio,[502] University of Turin, 2012

code	method	PBC	cluster	MT	FP	SCF	fit	relax	ref
CONTINUUM	MST		X	X					479
MXAN	MST		X	X			X		503
FEFF-8	MST		X	X		X			442
XKDQ	MST		X	X					495
StoBe	LCAO		X		X	X		X	497
FDMNES	MST/FDM		X	X	X	X	X		482
PARATEC	PP+PW	X				X		X	486
PY-LMTO-LSDA	LMTO	X		X		X		X	493
WIEN2k	LAPW	X			X	X		X	484
SPRKKR	KKR	X			X	X			490
ORCA	LCMO	X			X	X		X	500

[a]MST = multiple scattering theory; LCAO = linear combination of atomic orbitals; FDM = finite difference method, PP = pseudopotential; PW = plane wave; LMTO = linear muffin tin orbitals; LAPW = linear augmented plane waves; KKR = Korringa, Kohn, Rostoker calculations; LCMO = linear combination of molecular orbitals; PBC = periodic boundary conditions; MT = muffin tin; FP = full potential; SCF = self-consistent field; Fit = possibility to fit one or more parameter matching the simulated spectrum with the experimental one; relax = possibility to optimize the structure before performing the calculation of the XANES spectrum.

mentioned: CONTINUUM,[478,479] developed by the Frascati group (Natoli, Benfatto et al.) was the first available; FEFF-8 and FEFF-9,[12,390,442,446,473,480,481] developed by the Washington group (Rehr and Ankudinov et al.); FDMNES,[482,483] developed by Joly; Wien2k,[484,485] developed by Schwarz, et al.; PARATEC[486,487] developed in Paris; BigDFT[488] developed by Genovese et al. and available in the ABINIT package;[489] the SPRKKR code developed by Ebert;[490] the PY-LMTO-LSDA code developed by Antonov et al;[491−493] the XKDQ code developed by Vedrinskii et al.[494−496] The following DFT-based codes are able to directly compute the pre-edge region: the StoBe code,[497] Stockholm−Berlin version of deMon, DFT package for atoms, molecules, and clusters initially developed by St-Amant;[498] the Amsterdam Density Function (ADF) code;[499] the ORCA code developed by Neese et al.[500] Finally, we mention CTM4XAS code developed by de Groot[501] based on the multiplet theory.[225] The characteristics of some of the listed codes are summarized in Table 5.

All reported codes are able to simulate the complete XANES spectrum, or the pre-edge structures, starting from a guessed cluster constructed around the absorber atom. Exception is made by Wien2k that, following a periodic approach, requires a .cif file as input. This implies that in order to extract structural and geometrical information from an experimental XANES spectrum, several trial structures have to be guessed and the corresponding simulated spectra compared with the experimental one. Again the Frascati group proposed a novel fitting procedure,[503−505] named MXAN, which is able to fit XANES from the edge to about 200 eV. The method is based on the comparison between the experimental spectrum and several theoretical spectra that are generated by the code by changing the relevant geometrical parameters of the site around the absorbing atom. The theoretical spectra are derived in the framework of the full multiple-scattering approach (CONTINUUM code). The MXAN procedure is able to recover information about the symmetry and atomic distances, and the solution is found to be independent of the starting conditions. Of highly interest is the successively developed method to perform a full quantitative joint analysis of both EXAFS and XANES spectra using GNXAS and MXAN codes, respectively.[506] FitIt,[507,508] a software developed by Smolentsev and Soldatov devoted to fit XANES spectra by using external codes for calculations of the spectra is also worthy of note. It can be used to determine the values of local atomic structure parameters on the basis of minimization between theoretical and experimental spectra. To reduce the number of calculations and the time consumption, multidimensional interpolation algorithm is implemented. Such approach, combined with a visual control of the fitting procedure, allows to change the geometrical parameters and to see immediately the theoretical spectrum corresponding to these structural variations.

Typically, multiple scattering theories employ an important approximation: the muffin-tin averaging of the potential needed for the expansion of the wave functions. This approximation is serious, especially when the photoelectron kinetic energy is close to the value of the approximation done on the potential. In the EXAFS region, the muffin-tin approximation is much less critical because of the much higher kinetic energy of the photoelectron. Moreover, it makes the results dependent on the size of the interstitial region between the muffin tin spheres. To avoid the restriction imposed by this approximation, several computing methods have been developed and successfully applied.[509,510] Among them, the finite difference method currently included in the FDMNES code is emerging for the reliable results and the stability of the algorithm.[482,483] Other alternative methods are possible: a plane wave's base is useful for periodic structures because it allows to employ periodic limit conditions but is not appropriate to describe the region in the neighborhood of the atomic nuclei. This problem was partially overcome by Wien2k,[484,485] using linear augmented plane, or by Paratec,[511] introducing pseudopotentials in combination with plane waves. Another approach particularly suitable for molecules is the use of mixed bases; in the code StoBe code,[497] for example, a linear combination of atomic orbitals is adopted.

Selected examples of full MS simulation of XANES spectra reviewed here concerns the structure of the $Cu^{+}(CO)_3$ complexes hosted inside ZSM-5 zeolite[417] (see section 4.2.1.) and the formation of Cr(II) carbonyls at the surface of the Cr/SiO_2 (section 6.2.2). In some other cases however, XANES spectra are extremely informative by simply analyzing the main features (pre-edge region, position of the edge, intensity and shape of the white line, etc.) in a qualitative way. In the following chapters we will demonstrate that the qualitative

dx.doi.org/10.1021/cr2000898 | Chem. Rev. 2013, 113, 1736−1850

analysis of the XANES spectra has been an important tool in understanding the local geometry of active sites in several heterogeneous catalysts. One of the most evident case of the validity of this approach is the TS-1 case (see section 3.2.2.), where the presence of pre-edge peak at 4967 eV, due to the 1s → 3pd electronic transition involving Ti(IV) atoms in tetrahedral coordination, was the first unambiguous direct proof of the isomorphous insertion of Ti atoms inside the zeolitic framework.[512−516]

2.3.6. Codes for XES Spectra Simulation. Some recent codes are available for the simulation of the XES spectra. Among them we quote the ORCA code developed by Neese et al.,[500] the versions FEFF-8.4[442] and FEFF-9[517] of the Washington code, the code SIM-RIXS, developed by Hayashi,[518] and the StoBe code developed by the Pettersson group.[497] Because of the mention of the multiplet theory[225], we also include the CTM4XAS code[501] and the graphical interface Missing of the Cowan's code[519], which are able to compute XES spectra.

2.3.7. Codes for Handling the Huge Numbers of Spectra Generated in Time or Space Resolved Experiments. When investigating the reactivity of surface species, sometimes time-dependent EXAFS experiments are performed, either in the Quick-EXAFS or in the dispersive mode (see sections 2.2.3 and 8.2.3, Figures 4b, 49, and 50). In other cases, space resolved experiments are needed (see sections 2.2.7 and 7.2 and Figures 9 and 47). Since the number of absorption spectra measured during a single time/space-resolved experiment can amount up to several hundreds or some thousand, it is evident that a code allowing to perform the data reduction steps (from background subtraction up to the FT) for a single spectrum and to apply them successively to the whole series of spectra in a controlled and straightforward manner is necessary.[520] This demand of the user community has been satisfied, for example, by San Miguel with the CDXAS code,[521] by Ressler with the WinXAS code[457,458] and Prestiprino and Figueroa the PrestoPronto code.[522] In some extend, the Athena code also fulfills this request,[463] although it is practically limited to a some tens of spectra.

When dealing with an important set of spectra, showing the space gradient or the time evolution of a system as a function of some external parameter, then the principal component analysis (PCA) method[60,523−531] is a powerful tool for determining the fraction of the different phases present on a sample. It is particularly suitable when the number of the phases and their chemical nature is unknown. Software able to treat set of XANES/EXAFS spectra with the PCA approach are, for example, the SixPACK code developed by Webb,[455] XAS,[433] and the package written by Wasserman.[524]

2.3.8. Debye−Waller Factors and Disorder. The XAFS Debye−Waller factor arises as a natural consequence of fluctuations in interatomic distances. At finite temperatures, since the atoms in solids and in molecules vibrate around their equilibrium lattice sites, the interference pattern for a given path is slightly altered. The net result is a smudge of the EXAFS amplitude that is more efficient at high k values (short wavelength). If the local disorder is small ($k^2\sigma_i^2 \ll 1$), eq 19 is valid, because the path length distribution within a coordination shell can be expressed using the Gaussian function exp($-2k^2\sigma_i^2$). Conversely, if the standard EXAFS equation is used to analyze spectra of systems characterized by a large disorder, incorrect values of the optimized parameters may be obtained.[9,409,410,532−537] According to eq 20, disorder may have two different origins: (i) at elevated temperatures, the atom vibrational amplitude increases, leading to a non-symmetric, or anharmonic, distribution in the instantaneous bond length[41,536,537] and (ii) asymmetry can also be caused by static disorder ($\sigma^2_{i,T}$ term) with a non-Gaussian pair distribution function.[535−538] The Debye−Waller factor σ^2_i and thus the determination of N_i, changes because of asymmetry or broadening of the pair distribution function. The phase shift $\varphi_i(k)$ and thus the distance r_i are also affected.[41,536,537] Such problems are especially severe in the case of some heterogeneous catalysts, which often contain highly dispersed or disordered structures with pair distribution functions quite different from well-crystalline bulk materials. In addition, in situ studies in heterogeneous catalysis, typically imply high temperatures: in such cases the shape of the pair distribution is strongly affected by anharmonic vibrations.[17,535−537,539] A commonly used procedure to face this effect is to describe the distances in a coordination shell by a probability distribution. The method is known as the cumulants method.[4,54,412,536,540] The cumulants procedure describes the various distances in a coordination shell by a probability distribution, leading to the more general equation,[537]

$$k\chi(k) = \sum_i \frac{N_i {S_0}^2 A_i(k)}{{R_i}^2} \int P(r_i) \frac{\exp(-2r_i/\lambda)}{2{r_i}^2} \sin[2kr_i + 2\delta_i(k)]\, dr_i \quad (23)$$

that replaces eq 19. In the new eq 23 $P(r_i)\, dr_i$ is the probability of finding the atoms of the ith coordination shell in the infinitesimal interval between r_i and $r_i + dr_i$. The effective distribution function is $P(r_i)\ r_i^{-2} \exp(-2r_i/\lambda)$. Expanding the terms containing r_i in a Taylor series centered on the average distance of the ith shell, $\langle r_i \rangle$, the amplitude of the EXAFS interference function for that single coordination shell containing N_i atoms of the same type may be written as[537]

$$\ln\left[\frac{A(k){kR_i}^2}{N_i {S_0}^2 F(k)}\right] = C_0 - \frac{2R_i}{\lambda} - \frac{(2k)^2}{2!}C_2 + \frac{(2k)^4}{4!}C_4 + \ldots \quad (24)$$

The coefficients C_n are called cumulants. The nth cumulant is the coefficient of the nth power of the wavenumber $(2k)$ of the Taylor series. Only the even cumulants enter into the amplitude. If the distribution is normalized, C_0 equals zero. The first correction term, C_2, is the Debye−Waller factor. Odd cumulants contribute to the phase, which may be written as

$$\phi_i(k) - \delta_i(k) = 2kR_i - \frac{(2k)^3}{3!}C_3 + \frac{(2k)^3}{3!}C_5 + \ldots \quad (25)$$

The cumulants are a measure of the deviation of the pair distribution function from the Gaussian shape.[17,422,537−539] The third cumulant measures the asymmetry and the fourth cumulant the sharpening or flattening[541] of the pair distribution function with respect to a Gaussian.[536,537,542]

Software able to analyze the EXAFS data with the cumulants approach are, for example, XDAP,[451,543] IFEFFIT,[461] and SEDEM.[431] When the data analysis is limited to the first shell, on a sample measured at different temperatures, then a very accurate analysis can be obtained using the EXTrA package developed by the Trento group.[544] The code allows to study the temperature dependence of cumulants: (i) the second cumulant C_2 can be fitted to harmonic Einstein or correlated Debye models; (ii) the comparison between EXAFS and

dx.doi.org/10.1021/cr2000898 | Chem. Rev. 2013, 113, 1736−1850

crystallographic distance allows to evaluate the perpendicular component of the relative atomic displacement; (iii) a joint analysis of second, third and fourth cumulants gives the anharmonic contributions to the mean square relative displacement of the distance distribution, the force constants of the effective pair potential and thermal expansion. Moreover, the EXTrA code[544] allows reconstruction of the characteristic function down to $k = 0$ and, by Fourier transform, the distribution of distances and the effective pair potential; it is also possible to splice the low-k reconstructed EXAFS spectrum to the high-k experimental spectrum (this procedure is particularly suited for highly distorted distributions).

2.3.9. Differential XAFS Approach. XAFS spectroscopy, as extensively discussed so far, provides detailed insights on the electronic structure of the absorber atom via XANES analysis (oxidation state, orbital occupancy, coordination geometry, valence states ligand field strength). In addition, element-specific information on coordination numbers and bond distances around the absorber can be obtained from the investigation of the EXAFS region. Quantitative results are generally obtained by fitting the experimental spectrum, but in particular cases, for example, aiming to discriminate between very similar structures or isolating information on extremely diluted species, the conventional approach can lack sensitivity. A possible solution in the analysis of such problems is the differential XAFS approach.

This methodology, deeply related to the high-stability of third generation synchrotron sources, typically relies on the acquisition of high-statistics XAFS data on both the sample of interest and a reference sample, maintaining to the best of available technical possibilities the measurement conditions unchanged. If the experiment aims to isolate the small chemical/structural modifications induced in the sample by a specific perturbation (such as: (i) light excitation, (ii) change in temperature, pressure, pH, magnetic field, (iii) presence of an adsorbate, ...), the perturbation have to be applied in a strictly controlled way, using experimental setups and acquisition strategies differently designed for each specific case. The XAFS spectra of the sample of interest $\mu(E)$ and of the reference one $\mu_0(E)$ are subtracted, thus obtaining an experimental difference spectrum

$$\Delta\mu(E) = \mu(E) - \mu_0(E) \tag{26}$$

to be theoretically interpreted. Fitting directly the $\Delta\mu x(E)$ spectra has the important advantage of increasing the sensitivity of the fit and decreasing the influence of possible systematic errors in the calculations, which come from the approximations used in the theoretical approach.[545]

The differential approach in XAFS analysis has been increasingly applied in several different research areas, and represents a challenging opportunity in pushing further the sensitivity limit of such highly informative technique. A very relevant example is the rapidly growing field of ultrafast time-resolved X-ray based studies based on the pump and probe approach, allowing to reach much higher time resolution with respect to the quick-EXAFS and dispersive EXAFS modes described in section 2.2.3., see Table 4. Over the past ten years, time-resolved XAFS in both the XANES and the EXAFS regions has been developed and implemented as a reliable tool to investigate in "real-time" the electronic and molecular structure changes of light-induced short-lived reaction intermediates in solution.[546−551] In these experiments, the system is excited by an ultrashort pump laser pulse and is probed by a short X-ray probe pulse, whose time delay with respect to the laser pump pulse can be tuned in a controlled way.[547]

In these cases, the analysis method is generally based on the determination of the transient (difference) XAFS spectra of the excited minus the unexcited (ground state) system. This method has shown its high sensitivity in detecting very small changes in the recorded data. Differential signals below 10^{-4} optical density can be identified, thanks also to the high stability of available X-ray sources, while largely reducing systematic errors such as intensity fluctuations or deterioration of the sample during the data acquisition.[552] This approach was successfully used to elucidate the structural changes resulting from an intramolecular electron-transfer process in $[Ru(bpy)_3]^{2+}$,[553] and from the ultrafast spin crossover in aqueous $[Fe(bpy)_3]^{2+}$.[554,555] Moreover, the method provided unprecedented insights in understanding the axial ligation mechanisms and the photogenerated intermediate structures in nickel(II) metalloporphyrins[556,557] and in the MLCT state of $Cu(dmp)^{2+}$ in acetonitrile.[558] Ultra-fast time resolved-EXAFS spectroscopy has been employed to elucidate the structural distortions of a photochemically active diplatinum molecule, namely $[Pt_2(P_2O_5H_2)_4]^{4-}$.[559] Van der Veen et al. in this study applied a recently proposed quantitative method for the structural analysis of the excited state,[560,561] which is based on the fitting of the transient EXAFS spectrum directly in energy space, by minimization of the square residual function between a large series of simulated transient EXAFS spectra and the experimental data. The method provides higher accuracy for the calculated structural parameters when compared to previous differential EXAFS fitting strategies, where the structural modification are generally extracted from the Fourier transform of the reconstructed excited-state EXAFS signal, thus affected by additional uncertainty due to the imprecisely known fractional population of the excited-state species.[560] Recently, a variant of this approach was used in a dispersive XAFS setup to measure the mean atomic displacement for atoms undergoing magnetostriction in an FeCo alloy, by analyzing the small changes detected in the XAFS spectrum upon variation of the relative orientation between the photon polarization and the sample magnetization vectors.[562]

These results demonstrate that EXAFS sensitivity can be extended to include atomic displacements of the order of 1 fm = 10^{-5} Å (i.e. more than 2 order of magnitude batter than usually obtained with a standard approach), hence well fitting the range of thermal expansion over a temperature of one degree, elastic phenomena, strictive-effects, and piezo-effects.[166] All these phenomena, apart the piezo-effect, are typically shown by amorphous materials, where the power of XAFS as a tool for structural characterization is maximal, in respect to other techniques, such as neutron or X-ray diffraction.

The studies summarized above highlight the potential of differential XAFS analysis, not only in the case of light-induced or magnetic-field induced structural modifications, but also when the changes are produced for instance by temperature,[563,564] pressure,[565,566] composition of the gas environment[567] or pH changes[568,569] (very relevant in biochemical problems).

Finally, coming to an application more closely related to the topic of this review, the differential XAFS approach represents an emerging strategy in the analysis of site-specific adsorption in the characterization of metal-based heterogeneous catalysts. For example, Pt L_3 XAFS is widely used for the in situ characterization of Pt-based catalyst upon hydrogen absorp-

dx.doi.org/10.1021/cr2000898 | Chem. Rev. 2013, 113, 1736−1850

tion,[570−573] and its sensitivity can be significantly enhanced by the differential analysis of the XANES features, namely, Δ-XANES approach.[573−578] As will be discussed in details in section 9.3.2, the XANES spectrum of a catalyst under adsorbate-free conditions is subtracted from XANES under conditions conducive to adsorption (e.g., by altering the potential or chemical environment). The resulting Δ-XANES spectrum is highly sensitive to changes in metal-adsorbate and metal−metal interactions and can provide detailed information on different hydrogen bonding sites (as atop, bridged, and 3-fold sites) on the metal surface.[579,580]

2.4. Atomic XAFS or AXAFS

In contrast to EXAFS and XANES, which are well established techniques, AXAFS is not yet well established. This is, essentially, due to the following reasons: (i) the technique is of rather recent origin, although the first paper appeared in 1978 by Holland et al.,[581] the phenomenon was forgotten until 1994 when a paper from the Rehr group appeared;[582] (ii) the animated debate[583,584] that appeared in the scientific community after the Rehr paper; (iii) the very low number of papers appeared until now on the topic (less than 40 in 34 years and only 4 in the 2006−2012 period); and (iv) the fact that these papers come from basically four main research groups only. For these reasons, a brief historical overview on this topic will be given in the following.

2.4.1. Brief Historical Overview. In 1978 (i.e., only 7 years after the historical paper of Sayers, Stern, and Lytle[395] representing the birth of modern EXAFS, see section 2.3.1) Holland et al.[581] observed that the $\mu(E)$ spectra of Xe and amorphous As contain structures of long period in k, particularly relevant near the edge, that could not be explained using the standard EXAFS scattering from neighbor atoms. They attributed these new structures to the scattering of the photoelectron in the periphery of the absorbing atom itself. This observation was then neglected for more than a decade. Then, in 1994, a paper by Rehr et al.[582] claimed that an oscillatory structure was found in the atomic background absorption μ_0, see section 2.3.2. The authors supported the thesis that this atomic XAFS (AXAFS) arises from scattering of the photoelectron within an embedded atom and is analogous to the Ramsauer−Townsend effect.[585,586] The physical explanation of the phenomenon resides in the potential barrier that develops when a free atom is embedded into a condensed phase; the free-atom potential is then modified and a scattering of the outcoming photoelectron produces weak oscillations in the absorption cross section. Such low frequency modulation of the $\mu_0(k)$ function, if not subtracted correctly to the experimental $\mu(k)$, will result in low R contributions (at distances shorter than those of the first neighbors atoms) in the FT of the $\chi(k)$. Rehr et al.[582] reported the experimental atomic absorption $\mu_0(k)$ for CeO_2 (Ce K-edge), BaO (Ba K-edge), and $PrBa_2Cu_3O_7$ (both Pr and Ba K-edges) and compared them with the theoretical ones computed with the ab initio FEFF5X code based on the muffin-tin approximation. They concluded that (i) the AXAFS signal can dominate multielectron excitations contributions, (ii) the AXAFS signal can interfere with the first shell data analysis, and (iii) the structure of the AXAFS signal is sensitive to chemical effects and thus can potentially provide a probe of bonding and exchange effects on the scattering potential.[582] In the proceedings of the XAFS-8 conference held in Berlin (see Table 1), a second contribution from the same group appeared on this topic.[587]

The original work of Rehr et al.[582] was successively criticized in a comment to the journal by Filipponi and Di Cicco.[583] The main arguments of the comment can be summarized following three points. (i) An alternative explanation of the nonsmooth behavior of the $\mu_0(k)$ function observed for Pr, Ce, and Ba has been given in terms of the onset of the excitation channel generating a double [1s,4d] hole. (ii) The AXAFS phenomenon, although possible, should however be accounted for in the correct framework of a non muffin-tin theory. (iii) The general relevance of the AXAFS effect for the EXAFS data analysis is negligible in comparison with the existing overwhelming number of identifications of multielectron excitation features. In their reply to the comment, Rehr et al.[584] showed that improved background calculations which suppress muffin-tin discontinuities still exhibit fine structure comparable to that reported in their first contribution.[582] In the successive XAFS conference (Grenoble 1996, see Table 1), Baberschke et al.[588,589] supported the thesis of Rehr et al.[582,587] by reporting the presence of low R contributions in the FT of the surface EXAFS signal of N adsorbed on Cu(001) surface. Authors concluded that low Z systems, such as C, N, and O, are ideal candidates to detect unambiguously the AXAFS because they are not followed by multielectron shake-ups, as it is the case for, for example, [1s,4d] in Ce, Pr, or Ba. A successive work from the same group, in collaboration with Rehr,[590] confirmed the results reported at the XAFS-9 conference in Grenoble (see Table 1). AXAFS is also discussed in the successive review of Wende,[591] one of the authors of the above-discussed papers.

It is evident that, in general, both effects (AXAFS and multielectron excitation) may be present.[592] The problem consists in the ability to discriminate between the two phenomena and between simple problems related to a noncorrect background subtraction, that could introduce low frequency signals in the $\chi(k)$ of simple mathematical origin. The only way to overcome this problem and to be sure about the information obtainable from low R contributions in the FT of the EXAFS signals, is to use a consistent set of samples where the electronic configuration of the metal can be followed by AXAFS along the series according to a logical trend, or by supporting the AXAFS results by other characterization techniques able to probe independently the electronic configuration (see the example reported in section 9.5). The work of Ramaker[593] represents a mile stone in this regard. Authors induced a perturbation on the Pt k-edge XAFS signal of metallic platinum acting on two independent parameters: (i) they investigated a series of Pt−Ru alloys as a function of the composition; they measured in situ a Pt electrode inside a working electrochemical cell as a function of the increasing applied potential. In both cases, the authors observed a systematic chemical effect in the signal at low R values, in agreement with theoretical predictions, therefore providing strong support for AXAFS, rather than for multielectronic excitations.[593] One year later, the same group[594] reported a systematic changes in the magnitude of the AXAFS signal for the in situ charging of a Pt/C electrode in H_2SO_4. Performing calculations on a (neutral, negatively and positively charged: ± 0.05 electrons were deposited per surface Pt atom in the last two cases) 13-atom Pt cluster, authors have been able to quantitatively calculate the changes observed in the AXAFS and rationalize the whole set of experimental data from an electrochemical point of view.[594]

The first application of AXAFS in catalysis appears in 1998, with a collaboration between Ramaker and Koningsberger.[595]

dx.doi.org/10.1021/cr2000898 | Chem. Rev. 2013, 113, 1736−1850

The authors showed, for a set of Pt-supported catalysts, that the variation of the support does considerably change the intensity as well as the imaginary part of the AXAFS signal, hence demonstrating that the technique can be a very useful probe of the effects of metal−support interactions in supported noble-metal catalysts. The collaboration between these two groups was very active and several successive papers appeared on the study of supported noble-metal catalysts by AXAFS.[596−602] The fact that supported noble-metal catalysts are the ideal systems for developing this new technique was further demonstrated by the appearance of successive works by the Koningsberger group,[603,604] as well as by Rehr et al.,[605,606] by Roth et al.[575,607] and by Bertagnolli et al.[608]

Successively, Koningsberger et al. investigated by AXAFS a set of catalysts obtained by supporting V_2O_5 on SiO_2, Al_2O_3, Nb_2O_5, and ZrO_2.[602,609] The authors reported a direct correlation between the intensity of the Fourier transformed AXAFS peak (SiO_2 > Al_2O_3 > Nb_2O_5 > ZrO_2) and the dehydrogenation of propane to propene in the absence of oxygen. Conversely, the oxidation of methanol to formaldehyde and the oxidative dehydrogenation of propane to propene on the same set of catalysts followed the opposite trend. The authors interpreted these observations as due to an increase of the binding energy of the vanadium valence orbitals when the ionicity of the support increases[602] (increasing electron charge on the support oxygen atoms).

Concerning the other previously discussed topics, two new papers appeared on both the in situ electrochemical studies by Ramaker et al.,[610,611] on the surface science investigation by the Baberschke group.[612,613] and in the chemistry of anions in solutions.[614] Finally, AXAFS has also been used to probe the charge redistribution within Pt-organometallic complexes, again by Ramaker and Koningsberger.[615,616]

2.4.2. Physical Principles of AXAFS. As discussed in the previous section, AXAFS has gained interest during the past decade. It is designed to extract electronic charge information from X-ray absorption data. It has been shown to be sensitive to charge on a metal[589,590,612] or metallic cluster,[593,594] to polarization by ions as far as two or three coordination shells away from the absorber atom,[593,594] and to charge redistribution in organometallic complexes.[615] The physical principles and a detailed description on how to extract the information from experimental data have been recently summarized by Ramaker and Koningsberger,[72] which we will largely follow here.

As described in sections 2.2.3 and 2.3.2 and eqs 11−18, the absorption coefficient μ is not a smooth function of the energy but exhibits fine structure, as the final state function is modulated, because of interference between the outgoing and backscattered photoelectron waves. Ramaker and Koningsberger rewrite μ as a function of the oscillatory part, χ_{ex}, which is the EXAFS function as follows:

$$\mu_{total} = \mu_{emb}[1 + \chi_{ex}] \quad (27)$$

However, even the μ_{emb} is not a smooth function, but can have structure,[581,582] which originates from the scattering of the photoelectron from the periphery of the absorbing atom itself (Figure 10). μ_{emb} is then described by the following function:

$$\mu_{emb} = \mu_{free}[1 + \chi_{ax}] \quad (28)$$

in which μ_{free} is the free and smooth atomic background and χ_{ax} represents the scattering against the bound electrons of the same absorber atom and is called AXAFS. Like EXAFS it has an oscillatory behavior, however, with a longer period (P) in k-space, because of the closer proximity of the atom periphery (r_{ax}) compared to the first neighboring atoms (r_1): $P_{ax} = \pi/r_{ax}$, see eq 19. Figure 11 shows that AXAFS is found in the Fourier transform at roughly half the distance of the first neighboring scattering atom. AXAFS is generally short-ranged in k, because it arises from scattering by the deep valence electrons, rather than the core electrons, which are dominant in EXAFS scattering. The AXAFS is sensitive to the difference in scattering of the photoelectron by the periphery of the absorbing atom relative to that of the free atom. This interatomic potential is sensitive to the bonding of the absorber

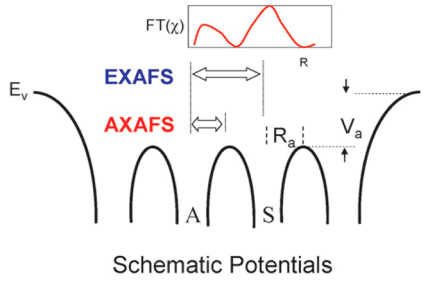

Figure 10. Schematic diagram of the scattering of the photoelectron. AXAFS originates from scattering of the photoelectron against the deep valence electrons of the atom from which the electron originates (A). EXAFS originates from scattering of the photoelectron against the core electrons of the neighboring atoms (S). Reproduced with permission from ref 72. Copyright 2010 the PCCP Owner Societies.

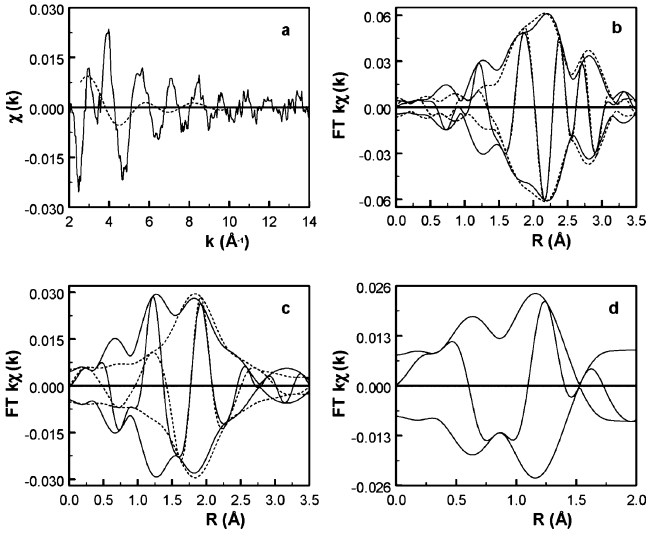

Figure 11. Isolation of an AXAFS signal from experimental data (Pt L_3 edge data of a prereduced Pt/Al_2O_3 catalyst). Part a: Raw EXAFS data (solid line) and isolated AXAFS (dashed line). Part b: k-weighted Fourier transforms of raw data (solid line), performed in the 2.5 Å^{-1} < k < 11 Å^{-1} range, and best fit (dashed line), performed in the 1.6 Å < R < 3.1 Å interval. Part c: k-weighted Fourier transforms of Pt−O corrected difference file, obtained by subtracting the first Pt−Pt shell from the raw data and Pt−O fit (dashed line), 2.5 Å^{-1} < k < 11 Å^{-1}. Part d: k-weighted Fourier transform of difference file, obtained by subtracting first Pt−Pt shell and Pt−O from the raw data, representing the AXAFS contribution. Part a shows the Fourier filtered spectrum (0 Å < R < 1.9 Å) of this AXAFS contribution (dashed curve). Reproduced with permission from ref 72 Copyright 2010 the PCCP Owner Societies.

dx.doi.org/10.1021/cr2000898 | Chem. Rev. 2013, 113, 1736−1850

atom and all other parameters that affect the electronic structure, such as polarization and hybridization.

A change in the nature or the number of bonds around the absorber atom changes the interstitial potential between the absorber and first scatterer neighbor and thus the AXAFS signal. The number of bonds will directly enhance the AXAFS signal, whereas a change in covalence of the bond will affect the interstitial potential and decrease the signal.[593,594] Overall, AXAFS is a measure of the internal electron chemical shift.[593,594]

As mentioned by Ramaker and Koningsberger, isolation of the AXAFS signal is a delicate and difficult procedure; this is probably one of the reasons why AXAFS has not found broader application. The EXAFS and AXAFS signals may overlap, which makes separation of the two signals essential because of the potential interference of the two signals in the Fourier transform. Essential is to apply a continuously adaptable smooth parameter to refine the background in the background subtraction procedure to observe the influence of this parameter on the relative intensities of the signals of the EXAFS, AXAFS, and double electron excitation in a Fourier transform.[601] Using nodal splines and polynomials makes separation of the contributions very difficult. Despite the difficulty to isolate a pure AXAFS signal, various successful applications have been described in the fields of surface science, electrochemistry, organometallic chemistry, and heterogeneous catalysis as reviewed in section 2.4.1. A specific example, particularly relevant to catalysis will be discussed in section 9.5.

A delicate but important point still remains to be discussed. When browsing through the literature, most of the FT of experimental EXAFS data reported in publications that appeared up to approximately the mid of the nineties were characterized by a *spurious peak* at about half the first neighbor distance. Later, such spurious peaks were no longer present in the FTs, because the more modern codes used for the $\chi(k)$ extraction exploit routines aimed to remove any signal in the corresponding FT below a given R value defined by the user, see, for example, the `Rbkg` parameter used in the Athena code.[463] Now, according to the interpretation of Rehr et al.[582] these peaks may have had partially an AXAFS origin. In cases where the AXAFS and the first shell EXAFS peaks are well separated in *R*-space, then the AXAFS contribution may simply be disregarded, conversely where the two contributions are partially overlapped, the absence of a proper treatment of the AXAFS contribution may cause systematic errors in the interpretation of the first shell EXAFS signal. For this reason, it would be desirable to have a larger number of independent groups involved in the study of AXAFS phenomena, in order either to definitively discard it or to settle it on more solid and recognized basis.

2.5. Other Related Techniques

Once established, the concepts of XAFS have influenced and given birth to other related techniques, such as X-ray magnetic circular dichroism (XMCD),[193,445,477,591,617−625] diffraction anomalous fine structure (DAFS),[29,445,452,626−633] photoelectron diffraction,[634−639] various electron energy-loss techniques,[640] including extended energy-loss fine structure (EXELFS)[641−646] and extended fine Auger structure,[647−649] β-decay near threshold (or beta environmental fine structure BEFS),[650] extended appearance potential fine structure,[651] photon interference XAFS (PIXAFS),[652,653] and the related X-ray `holography' effects.[654] The basic physic in all of these techniques involves similar high-order electron-atom multiple-scattering processes, which can all be treated with theoretical tools similar to those developed to understand XAFS spectroscopy.[390]

In the following short sections (2.5.1−2.5.3) few more words will be spent on XMCD, DAFS, and EXELFS, as potentially more interesting in the field of catalysis. Finally, in section 2.5.4, similarities, differences, and complementarities between EXAFS and total scattering technique (or pair distribution function (PDF) approach),[655−662] will be discussed.

2.5.1. X-ray Magnetic Circular Dichroism (XMCD). In X-ray absorption spectra, the XMCD signal $\mu_{XMCD}(E)$ is defined as the normalized difference spectrum of two XAFS spectra taken in a magnetic field, one taken with left circularly polarized beam, and one with right circularly polarized beam: $\mu_{XMCD}(E) = [\mu_L(E) - \mu_R(E)]/[\mu_L(E) + \mu_R(E)]$.[193] To maximize the XMCD signal the magnetization vector of the system is set either parallel or antiparallel to the polarization vector of the X-ray. A nonzero XMCD signal is observed only in magnetic systems and it gives information on the magnetic properties, such as spin and orbital magnetic moment. Consequently XMCD is a major characterization tool for ferromagnetic metals, oxides and their surfaces and for paramagnetic sites in bioinorganic chemistry and coordination compounds[622] and was able to bring new insight in the investigation of transition metal supported catalysts[663−665] and in biocatalysis.[666] In this regard, the Utrecht group[212,667] used XMCD in the characterization of Fe-ZSM-5, that is an heterogeneous catalysts containing a low amount of iron in form of both isolated and clustered species (vide infra section 3.3.5.2). As reviewed in section 3.3, the authors were able to estimate the fraction of isolated versus clustered Fe species, as well as the fraction of Fe(III) and Fe(II), as usually achieved with XANES.[212,667] We conclude this section by noticing that the implementation of quarter wave plates on a dispersive EXAFS beamline, such as ID24 at the ESRF, (see section 2.2.3) has allowed extremely accurate XMCD and nanosecond-resolved XMCD using the pump−probe scheme to be recorded (section 2.3.9).[183,187]

2.5.2. Diffraction Anomalous Fine Structure (DAFS). DAFS is a diffraction technique, thus useful to investigate crystalline materials characterized by long-range order. In these cases DAFS results in an EXAFS-like signal that contains information on the local environment of a selected atomic species. The intensity of a (*hkl*) diffraction peak of a crystalline material normally varies smoothly with the λ used to perform the diffraction experiment (i.e., with the photon energy $h\nu$), because the atomic form factors f_1 and f_2 are a function of λ. This statement does not hold if the λ scan goes across absorption edge of an element present in the material. This fact is at the basis of resonant (or anomalous) diffraction experiments.[661,668,669] If one measures the intensity of such a diffraction peak as a function of λ ($h\nu$), across the absorption edge of an element present in the material, he will detect an EXAFS-like signal, from which structural information around the selected atomic species can be extracted. This is actually the field of DAFS, which combines in the same experiment X-ray diffraction and X-ray absorption.[29,445,452,626−633,661] In this way, the long-range structural information contained in diffraction peaks can be combined with the chemical and local structure selectivity of X-ray absorption spectroscopy. Thus, it can provide simultaneously site-selective and chemical-selective structural information. On the experimental ground DAFS

dx.doi.org/10.1021/cr2000898 | Chem. Rev. 2013, 113, 1736−1850

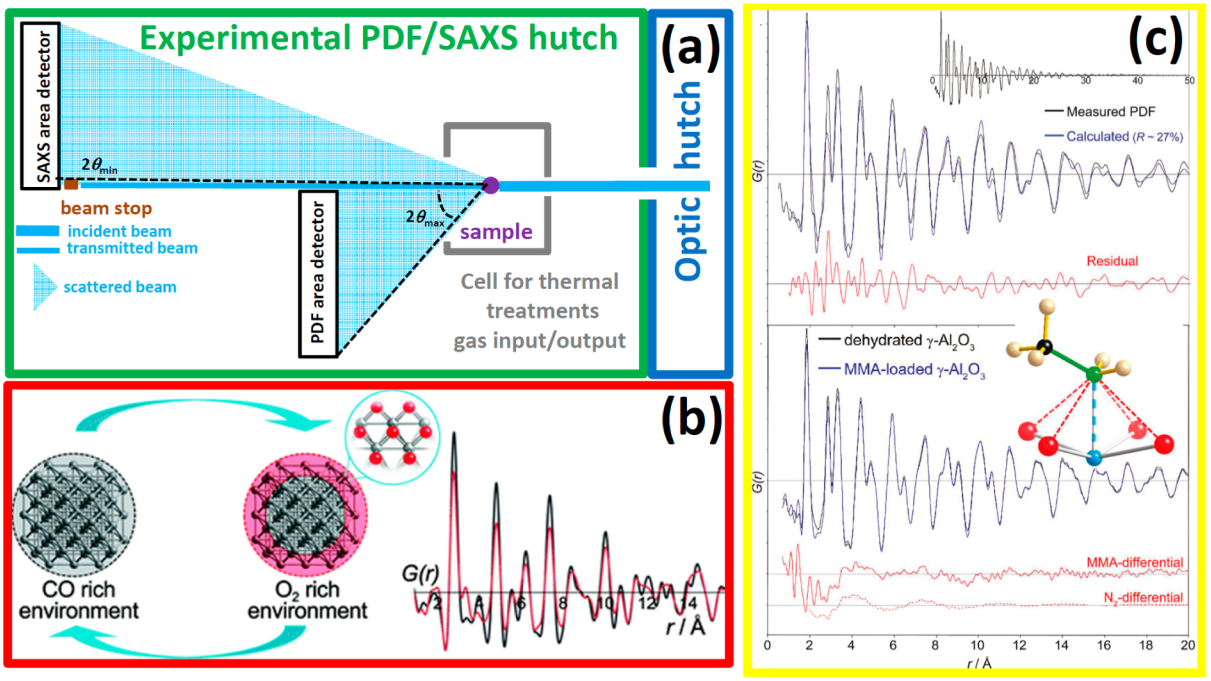

Figure 12. Part a: Scheme of an experimental hutch allowing the simultaneous data collections of PDF and SAXS. With this experimental setup operating at $\lambda = 0.2$ Å it is possible to collect PDF data (up to $Q_{max} = 4\pi \sin(\theta_{max})/\lambda = 30$ Å^{-1}) and SAXS data (down to $Q_{min} = 4\pi \sin(\theta_{min})/\lambda = 0.01$ Å^{-1}). The distances between the two detectors and the sample are not in scale (inspired by ref 673). Part b: Cyclic alternance of Pt metal and PtO/Pt shell/core configuration obtained upon cycling the CO/O_2 ration in the CO oxidation reaction catalyzed by 1 wt. % Pt/Al_2O_3 and followed under operando conditions. Left: Reaction scheme. Right: experimental differential PDF data. Reproduced with permission from ref 691. Copyright 2012 American Chemical Society. Part c (top): measured $G(r)$ for γ-Al_2O_3 (black curve), the calculated $G(r)$ for the best model fit (blue curve), and the residual to the fit (red curve). The inset reports the experimental curve in Q space. Part c (bottom): the solid red curve represents the differential $G(r)$ curve was obtained by subtracting the reference $G(r)$ collected for the dehydrated γ-Al_2O_3 (black curve) from that measured for the MMA-loaded sample (blue curve), see Eq 32 (MMM = monomethylamine). The differential corresponding to physisorbed N_2 is reported as blank experiment. The inset reports the structure of the of the adsorbed MMM as reconstructed from this study. Reproduced with permission from ref 685. Copyright 2011 American Chemical Society.

data collection needs a very high signal-to-noise ratio, as for EXAFS, to perform a quantitative oscillations analysis on a diffraction yield that is only a very small fraction of the total. So brilliant beams are required, together with a high quality diffractometer coupled to very stable absorption-dedicated optics. Once combined with EXAFS, DAFS can be used, for example, in disentangling the contribution present in a standard EXAFS spectrum of a catalyst where an amorphous phase is coexisting with a crystalline one:[632] both signals will be present in the EXAFS spectrum, while only the latter will contribute to the DAFS signal. Although DAFS contains contributions of both the real and imaginary parts of the complex anomalous scattering factors, f_1 and f_2 (XAFS being proportional to the imaginary part only), it can be analyzed, in the extended region, like EXAFS.[630,633] Codes able to handle the DAFS signal are, for example, FDMNES,[482,483] ATOMS,[631] FEFF,[445,480] XFIT,[452] FEFFIT,[448] and GNXAS,[426,434], the last one having the additional advantage of being able to directly fit the raw experimental data.

2.5.3. Extended Energy-Loss Fine Structure (EXELFS). Modern transmission electron microscopes (TEM) equipped with an electron energy-loss spectrometer allows the detection of EXELFS spectra, that are XAFS-like spectra,[641−646] that, particularly, for low Z-edges and in the near edge region, can be competitive with those collected at synchrotron sources. The technique has the further advantage of reaching the nanometer-spatial resolution typical of TEM instruments, that is, 2−3 orders of magnitude better that what can be obtained with X-ray microcopies, see sections 2.2.7 and 7. On the other hand, EXELFS is intrinsically an ultrahigh vacuum technique and the thickness of the sample investigated is limited to few tens of nanometers by the strong electron-matter interaction.

2.5.4. Total scattering: the pair distribution function (PDF) approach. *2.5.4.1. Basic considerations.* Although known and used before the theory of EXAFS was firmly defined[670] by the work of Sayers, Stern, and Lytle[395] (see section 2.3.1), and although based on a different physical process, the total scattering technique,[655−662,671] able to provide the overall pair distribution function (PDF) $G(r)$ of the material, requires a special paragraph. The experimental setup needed is that of X-ray or neutrons powder diffraction[672,673] (Figure 12a), but the scattering pattern has to be collected to much higher exchanged Q-values, up to at least 20−30 Å^{-1}. Being

$$Q = 2K \sin(\theta) = 4\pi \sin(\theta)/\lambda \quad (29)$$

low λ sources and high 2θ collections are required for PDF analysis (K is the X-ray wavenumber: $K = 2\pi/\lambda$). For standard Cu Kα ($\lambda = 1.54$ Å) and Mo Kα ($\lambda = 0.71$ Å) tubes a collection up to $2\theta = 140°$ results in $Q = 7.7$ and 16.6 Å^{-1}, respectively. Working with a synchrotron source at $\lambda = 0.5$, 0.4, 0.3, and 0.2 Å, Q values as high as 23.8, 29.8, 39.7, and 59.0 Å^{-1}, respectively, can be reached for a data collection up to $2\theta = 140°$.

A package able to handle PDF data is the set of programs PDFgetX2, PDFfit, PDFfit2, and PDFgui, developed by the

dx.doi.org/10.1021/cr2000898 | Chem. Rev. 2013, 113, 1736−1850

Billinge group.[674−676] From the experimentally collected intensity $I_{exp}(Q)$ the code extract the coherent scattering function $I_C(Q)$ after correcting for extrinsic contributions to the background intensity from such effects as Compton scattering, fluorescence, scattering from the sample holder, and other experimental artifacts. $I_C(Q)$ has sharp intensities where there are Bragg peaks, and broad features in between, the diffuse scattering. The total-scattering structure function, $S(Q)$, is then obtained from $I_C(Q)$ as follows: $S(Q) = [I_C(Q) - \langle f(Q)^2\rangle + \langle f(Q)\rangle^2]/\langle f(Q)\rangle^2$,[657,662] where the angle brackets denote an average over all the chemical species in the sample and $f(Q)$ are the X-ray atomic form factors. As $f(Q)$ decrease upon increasing Q,[677] very long integration times are needed at high Q to obtain a good statistic. For this reason, area detectors (bottom part of Figure 12a) are more suitable than point detectors because allow the integration on a wide region of the diffraction cone and because the poorer angular resolution of area detector is not a significant disadvantage in a Q-region where the diffractogram undergoes only smooth variations. Alternatively, PDF studies can be performed using neutrons because the coherent neutron scattering length is constant in the whole Q region of interest. Both $I_{exp}(Q)$ and $I_C(Q)$ data appear smooth and featureless in the high-Q region (this holds even for crystalline materials where usually no Bragg peaks are observed above $Q \approx 10$ Å^{-1}); however, after normalizing and dividing by the square of the atomic form-factor, important oscillations appear in this region of the $S(Q)$ function, similar to what happens in an EXAFS experiment comparing $\mu(E)$ and $\chi(k)$ functions at high E (high k or high Q) after the edge. Finally, the reduced pair distribution function, $G(r)$, is obtained from $S(Q)$ through a sine FT:

$$G(r) = \frac{2}{\pi}\int_{Q_{min}}^{Q_{max}} Q[S(Q) - 1]\sin(Qr)\, dQ \quad (30)$$

where Q_{min} and Q_{max} are the limits of the data collection in Q-space, being $Q_{min} \approx 0$ Å^{-1} and Q_{max} as large as possible. The PDF function (eq 30) gives the interatomic distance distribution, having peaks at positions, r, where there is a high probability to find pairs of atoms separated in the sample (solid or liquid). So PDF contains EXAFS-like information, that are however not atomically selective, so $G(r)$ contains contributions arising from the local environments of all the atomic species present in the sample. In this regard, the intrinsic differences in the nature of the $\chi(k)$ and $S(Q)$ signals obtained from EXAFS and PDF experiments on single-component disordered systems were deeply discussed by Filipponi:[678] in that work particular effort was devoted to connect the $\chi(k)$ signal with usual quantities familiar to the distribution function theory in disordered matter. As the physical phenomenon behind PDF is X-ray scattering and not photoelectron scattering, the PDF signal is not damped by the short photoelectron mean-free path and by the core hole lifetime as EXAFS is, see eq 19, so valuable structural information is contained in the pair-correlations extending to values of r much higher than those typically reachable by EXAFS (~5−8 Å). In fact, with high Q-space resolution data, PDFs can be measured out to tens of nanometers (hundreds of angstroms) and the structural information remains quantitatively reliable. With respect to EXAFS, the PDF data have not to deal with MS paths, as only SS signals are present. This represents a remarkable simplification, however complexity comes from the fact that the contribution of the local environment around all atomic species present in the sample are entangled in the PDF signal. In this regard, note that, for high Z elements ($Z > 45$, that is, $\lambda < 0.53$ Å), the lack of element sensitivity of the PDF technique can be overcome performing X-ray resonant (or anomalous) PDF data collection:[679−681] that is, acquiring two $I_{exp}(E_1,Q)$, $I_{exp}(E_2,Q)$ collections across the desired absorption edge and working on the differential pair distribution function $\Delta G(r)$ defined as

$$\Delta G(r) = G(E_1, r) - G(E_2, r) \quad (31)$$

2.5.4.2. Applications of PDF in Catalysis: Few Selected Examples. We have already underlined in section 2.2.6. that the trend and future direction of structural studies in catalysis is to probe active materials at different length-scales. This will require the combination of multiple probes that should be adapted for in situ and operando studies. In principle, PDF is well suited to operando studies as it utilizes high-energy X-rays which are highly penetrating and which allow a great degree of flexibility in the design of reaction cells. One weakness in PDF is the difficulty in analyzing particle shape, which is exacerbated with many real samples in that a dispersion of particle sizes/shapes are present. In this regard, we fully support the view of Chupas et al.,[673] who foresaw that the combination of PDF with SAXS is warranted. SAXS is indeed well suited to probe nanometer scale structure, particularly at lengths comparable to the atomic scale resolution obtained from PDF. For example, Figure 12a shows a layout that, using two area detectors located at significant different distance form the sample, would allow both high-resolution PDF (up to $Q_{max} = 4\,\pi\,\sin(\theta_{max})/\lambda = 30$ Å^{-1}) and SAXS measurements ($Q_{min} = 4\,\pi\,\sin(\theta_{min})/\lambda = 0.01$ Å^{-1}) to be performed, using a reasonable sample to detector distance (5 m) for the latter. This would enable a simultaneous probe of both particle size and shape and allow atomic-scale resolution structure to be probed.[673]

Remarkable examples of the use of PDF in understanding the structure of materials that are relevant for heterogeneous catalysis come from Chapman et al.,[673,682−688] Petkov et al.,[689,690] and Newton et al.[691]

Several works investigated supported metal nanoparticles. In such cases, because of the low weight percent of the supported metal, most of the scattering comes from the support and the extraction of the information related to the metal nanoparticles is delicate and must be performed with care. The pair distribution function of the supported nanoparticles $G_{metal}(r)$ can be obtained either performing on the same sample two data collection at different X-ray photon energies (E_1 and E_2) across the metal K-edge, see eq 31, or by performing two data collections (at the same, non resonant, photon energy E) on both the catalyst and the metal-free support, and working again on the subtracted function:

$$G_{Metal}(E, r) = G_{Catalyst}(E, r) - G_{Support}(E, r) \quad (32)$$

This differential approach allows the atom−atom correlations involving only the metal to be selectively recovered.

The formation of supported Pt nanoparticles during the reduction of $PtCl_6^{2-}$ precursors deposited on TiO_2 support under H_2 gas flow has been monitored in situ and analyzed following the differential PDF approach reported in eq 32.[673,682] The authors found that the reduction of Pt^{4+} species follows pseudo-zero-order reaction kinetics, with an activation energy of 0.52 eV.[682] Temperature-programmed data collection showed a particle growth mechanism where the initial formed

dx.doi.org/10.1021/cr2000898 | Chem. Rev. 2013, 113, 1736−1850

particles are smaller than 1 nm, then agglomerate into ensembles of many small particles and finally anneal to form larger well-ordered particles.[673] Petkov et al.[689] performed reverse Monte Carlo simulations on PDF data[692] collected on supported Ru nanoparticles, finding that particles that are around 4 nm in size exhibit the hexagonal close packed-type structure of the bulk, while particles that are only 2 nm in size are heavily disordered and consist of a Ru core and a Ru−S skin because of the usage of thiol-based capping agents. This work demonstrates that it is possible to determine the atomic-scale 3-D structure of nanosized catalysts based entirely on experimental scattering data. In a successive work, the same group used the same approach to show that 1.6-nm Au nanoparticles grown inside a dendrimeric host possess a heavily disordered, metallic glass-type structure that, upon solvent removal, evolves toward the fcc-type lattice typical of the bulk.[690] Oxford et al.[684] combined XAS, PDF, and FTIR to characterize the composition distributions of PdAu and PtCu bimetallic particles after treatment in H_2 or CO and in the presence of these gases. The authors revealed that XAS was informative in determining the component distribution of an initial sample, but PDF allowed to better follow the changes in the distribution upon changing the gas environment. Very recently, Newton et al.[691] reported an outstanding operando PDF study on diluted (1 wt.%) Pd on Al_2O_3 catalyst. Along cyclic redox (CO/O_2) conditions, the authors showed that PDF, used with subsecond time resolution, yields detailed, valuable insights into the dynamic behavior of diluted nanoscale systems. Interaction with O_2 results in the formation of double monolayer PtO oxide film on top of the nanoparticles, that keep a metal core (Figure 12b). This approach reveals how these nanoparticles respond to their environment during the catalytic process. Specific insight is gained into the structure of the highly active Pt surface oxide formed on the nanoparticles during catalysis, highlighting the nature of active sites formed and consumed along the red-ox cycle.[691]

The differential approach reported in eq 32 can also be used to determine the catalytic active sites on high surface area catalysts, using the method of dosing a probe molecule able to strongly bond on the active surface sites: $G_{\mathrm{SurfaceSite}}(E,r) = G_{\mathrm{AfterDosage}}(E,r) - G_{\mathrm{BeforeDosage}}(E,r)$. With this approach, Chupas et al. performed differential PDF analysis to resolve, with crystallographic detail, the structure of catalytic Lewis sites on the surface of the poorly crystalline, high surface area, γ-Al_2O_3 (Figure 12c). The structure was determined using the monomethylamine basic probe molecule, bound at the minority Lewis acid sites. These active sites were found to be five-coordinate, forming distorted octahedra upon monomethylamine binding.[685] Finally, Chapman et al. investigated with differential PDF the capture of I_2 molecules insides microporous materials: Ag-MOR zeolites[683] and ZIF-8 MOF.[686,687]

3. METAL ISOMORPHOUS SUBSTITUTION IN ZEOLITIC FRAMEWORKS: TI, FE, AND GA

Ti-, Fe-, and Ga-silicalite-1, characterized by the same MFI framework, are chosen as main key studies of this Section for two main reasons: (i) because of their relevance in catalysis (section 3.1) and (ii) because of the fundamental role played by XAFS techniques in understanding the structure of the active species for TS-1 (section 3.2.1). Other frameworks are also briefly discussed. Among them the case of B-CHA (section 3.4) is worth noticing as this example allows us to show that, in some specific cases, the technique can be applied also for soft X-rays. Note that the B K-edge is at 188 eV, to be compared with 4966, 7112, and 10367 eV for Ti-, Fe-, and Ga-K edges, respectively.

3.1. Relevance of Ti-, Fe-, and Ga-Silicalite-1, and B-CHA in the Field of Catalysis

Silicalite-1, synthesized first by the group of Flaningen,[693] is an aluminum free zeolite, belonging to the structure type MFI in the IUPAC nomenclature.[694,695] It shows a three-dimensional pore system consisting of two intersecting sets of tubular channels, the former linear and the latter sinusoidal, both of about 5.5 Å in diameter and defined by 10-member rings of SiO_4 tetrahedra (vide infra Figure 14b and Figure 31a).

In the last three decades, the isomorphous substitution in the zeolitic framework of Si by other tetrahedrally coordinated elements (hereafter T),[696−698] such as Al(III) (ZSM-5 zeolite),[699] Ti(IV) (TS-1),[102] Fe(III),[700−702] Ga(III)[107,703,704] and B(III),[705] provided new materials showing specific catalytic properties in oxidation reactions related to the coordination state of the heteroatom. With the only exception of Al(III), having an ionic radius very close to that of Si(IV), the remaining heteroatoms can be inserted inside the zeolitic framework only in traces (up to few wt %). When a trivalent metal substitutes Si(IV), the zeolite framework assumes a net negative charge, which can be balanced by a number of bridged Si(OH)M(III) protons (M = B, Al, Fe, Ga), giving rise to microporous solids with Brønsted acidity. Conversely, the insertion of Ti(IV) in the zeolitic framework leads to microporous solids where Brønsted acid sites are absent. Two important classes of heterogeneous catalysts for partial oxidation reaction are obtained by insertion of Ti or Fe inside the MFI zeolitic framework.

Starting from the early eighties,[102] the Ti-silicalite-1 (TS-1) has shown to be an active and selective catalyst in an impressive number of low-temperature oxidation reactions with aqueous H_2O_2 as the oxidant.[706,707] Such reactions include phenol hydroxylation,[706] benzene hydroxylation,[708] olefin epoxidation,[706,709−713] alkane oxidation,[706,714,715] oxidation of ammonia to hydroxylamine,[706,710,716] styrene oxidation,[717] cyclohexanone ammoximation,[706,716,718,719] conversion of secondary amines to dialkylhydroxylamines[706,718] and conversion of secondary alcohols to ketones.[706] The relevance of this catalyst on the industrial ground explains why the research on the catalyst improvement is still active nowadays, i.e. almost thirty years after the first patent on the material.[102] Improvements concern: (i) the growth of TS-1 crystals with controllable *b*-oriented length (sheet-like morphology, or chain-like morphology);[720,721] (ii) the synthesis of hierarchical mesoporous TS-1;[722−728] (iii) synthesis of Au/TS-1 catalysts for in situ production of hydrogen peroxide;[729−733] (iv) coinsertion of other heteroatom in the MFI framework;[734] (v) synthesis of crystalline porous titanosilicates with different topologies, such as TS-2,[735] Ti-β,[516,736−743] SSZ-33,[741] Ti-UTD-1,[741] Ti-ZSM-48[743] Ti-MOR,[744,745] Ti-FER,[746,747] Ti-ITQ-6,[746−748] delaminated Ti-ITQ-2,[742,749,750] Ti-MCM-56,[749] Ti-MCM-22 (also known as Ti-MWW),[749,751−755] Ti-JLU- 20,[756] Ti-MCM-68 (also known as Ti-MSE),[757] and more recently Ti-CHA[758] and Ti-STT;[759] (vi) synthesis of Ti-grafted amorphous mesoporous molecular sieves, such as Ti-MCM-41.[59,742,760−765]

On the other side, starting from the nineties, Fe-silicalite and Fe-ZSM-5 showed a high activity in the hydroxylation of benzene to phenol with nitrous oxide[766,767] and in the selective reduction of nitric oxide with hydrocarbons[768,769] and

dx.doi.org/10.1021/cr2000898 | Chem. Rev. 2013, 113, 1736−1850

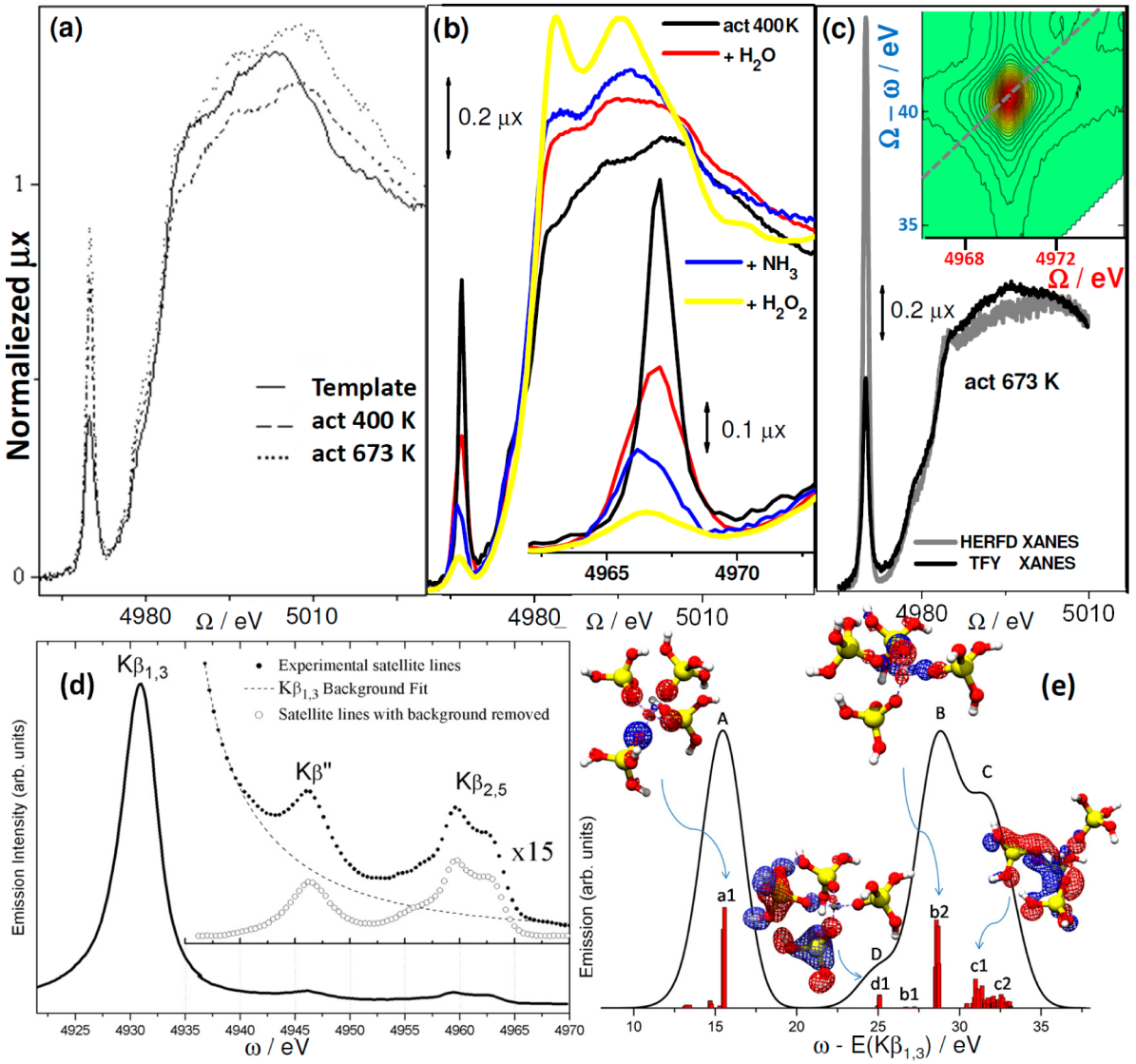

Figure 13. Part a: XANES spectra of TS-1 (x = [Ti]/([Ti] + [Si]) = 0.0179) with template (full line), and activated at 400 (dashed line), and 673 K (dotted line). Reproduced with permission from ref 781. Copyright 1999 The Japan Society of Applied Physics. Part b: Effect of interaction with molecules having increasing interaction strength with Ti(IV) sites: water (red), ammonia (blue), and hydrogen peroxide (yellow). For comparison also the spectrum of the TS-1 dehydrated at 400 K has been reported (black). Created using data previously reported in refs 857 and 872. Spectra reported in parts a and b were collected in transmission mode at the EXAFS3 station of the DCI storage ring at LURE, using a double crystal Si(311) monochromator. Part c: High energy resolution fluorescence detected (HERFD) XANES spectra collected on TS-1, activated at 673 K, at ESRF ID26 using a Si(311) double crystal monochromator and 5 Ge(331) analyzer crystals for defining Ω and ω, respectively (see Figure 5a). The standard XANES spectrum collected in total fluorescence yield (TFY, black) is compared with the HERFD spectrum obtained collecting the fluorescence photons at an energy $h\nu_2 = \omega$ = 4929.4 eV, that is, just in the low energy tail of the Ti K$\beta_{1,3}$ line at 4931 eV, see Figure 5b and part d of this Figure. The inset reports the corresponding RIXS map, where the dotted gray line shows the cut done to obtain the HERFD spectrum reported in the main part. We are grateful to E. Gallo and P. Glatzel (ESRF) for providing these data prior publication. Part d: Experimental XES spectrum of TS-1 activated at 673 K in the region of the K$\beta_{1,3}$ line (solid line). The inset reports a zoom on the valence to core (VtC) XES spectrum (full circle), the fit of the K$\beta_{1,3}$ high energy tail (dashed line), and the background removed VtC-XES lines (open circle). Part e: Theoretical VtC-XES spectrum (full black line) computed on a Ti[OSi(OH)$_3$]$_4$ cluster at TPSSh/TZVP/CP(PPP) level of theory. Red bars represent the obtained DOS of the valence molecular orbitals (MO), the most representative being graphically represented. Parts d and e were adapted with permission from ref 862. Copyright 2011 the PCCP Owner Societies.

ammonia.[770] The use of Fe-MFI for simple N_2O decomposition was also investigated.[771−776] Opposite to the TS-1 case, the active species in Fe-MFI samples are extraframework iron species that leave the lattice upon thermal activation[106,700−702,777−791] or that are introduced in the zeolite channels via postsynthesis methods.[790,792−797] For comparison with the TS-1 case, we will focus the attention on the former subset only (section 3.3).

For comparison with the Ti- and Fe-MFI systems, also Ga-containing MFI-type zeolites will be briefly discussed in section 3.3.1. Although it had not the same impact in catalysis as the similar Ti- and Fe-substitutes zeolites, Ga-silicalite-1 exhibits a high selectivity in the catalytic conversion of olefins and paraffins to aromatics following the so-called Cyclar process,[798−802] and has shown a high catalytic activity for vapor-phase conversion of phenol and ammonia mixtures into

dx.doi.org/10.1021/cr2000898 | Chem. Rev. 2013, 113, 1736−1850

aniline.[803] There is evidence that enhanced aromatization on gallium-containing zeolites is the result of a bifunctional catalytic process involving both framework and extraframework Ga atoms.[804−808]

Finally coming to zeolitic and zeotype materials based on the chabazite (CHA) topology, such as H−CHA,[809−811] H-SAPO-34,[812,813] H-SSZ-13,[814] and B-SSZ-13,[815] they possess unique shape-selectivity properties for converting methanol into light olefins.[816−821] In addition to the topology, the zeolite acidity is inherently linked to catalyst activity and selectivity.[822,823] The acidic properties of high silica chabazite (H-SSZ-13) have attracted much attention in the past decade, since the material represents an idealized model system having one acidic site per cage.[823−826]

The idea to modulate the Brønsted acidity by the isomorphous substitution of boron inside the zeolitic framework has been previously exploited with success for vapor-phase Beckmann rearrangement of cyclohexanone oxime to ε-caprolactam performed on B-ZSM-5.[827,828] It is consequently expected that B-substituted chabazite should be less acidic than the corresponding H-SAPO-34 and H-SSZ-13[814] materials, and thus possibly less prone to form coke. In order to improve catalyst performances in term of lifetime (i.e., to minimize the coke formation) and to see the effect of chemical compositions on the selectivity of C2−C4 products, a comparison between H-SAPO-34, H-SSZ-13, and B-SSZ-13 was performed by Yuen et al.[829] In this context, the recent and authoritative review by Olsbye et al. is recommended.[821]

3.2. TS-1

3.2.1. Brief Historical Overview on the Role Played by EXAFS and XANES Techniques in Understanding the Nature of Ti Sites in TS-1. On a historical ground, it is important to underline that EXAFS and XANES results on the dehydrated TS-1, originally published by Bordiga et al.[512,513] in 1994, and summarized here, represented the first direct proof that the active Ti centers in the TS-1 catalyst are isolated Ti(IV) atoms incorporated Si atoms in the tetrahedral positions and forming framework [TiO_4] units. These data closed definitively the lively debate present in the specialized literature about the structural nature of the Ti centers in TS-1. As a matter of fact, in the whole eighties and at the begin of the nineties titanyl groups, extraframework defect sites, monomeric and dimeric Ti species, Ti species incorporated in edge sharing type structures forming bridges across the zeolite channels and other hypothesis were inferred by different authors.[830−836] Different local geometries were also hypothesized ranging from tetrahedral, square pyramidal, up to octahedral were hypothesized. The origin of the initial confusion was probably related to the difficulty encountered in the synthesis of well manufactured TS-1 materials, which requires the use of extremely pure reagents and severe control in the synthesis conditions.[102] An imperfect synthesis implies an incomplete incorporation of Ti into the MFI framework, leading to a significant reduction of the catalytic performances and possibly to a misinterpretation of structural and spectroscopic data. Moreover, as already anticipated, the fact that only a very small amount of Ti, less than 3 wt % in TiO_2, corresponding to a molar ratio of x = [Ti]/([Ti] + [Si]) = 0.025, can be substitutionally incorporated into the MFI framework[837,838] does not facilitate the extraction and the attribution of the Ti contribution from the total experimental signal. Note that the [Ti]/([Ti] + [Si]) = 0.025 limit has been successively slightly improved.[839−841] In this regard, a significant improvement has recently been obtained by the Tatsumi group who, using $(NH_4)_2CO_3$ as a crystallization-mediating agent, obtained TS-1 crystals characterized by a [Ti]/([Ti] + [Si]) value as high as 0.029 without forming extraframework Ti species.[842] In any case, such a low Ti content makes the identification of vibrational, energetic and geometric features specific of TiO_4 moieties a difficult task, being all experimental data dominated by the features of the siliceous matrix.

For the reasons discussed above, the local environment around Ti(IV) species inside TS-1 was definitively assessed only more than 10 years after the discover of the material, when the atomic selectivity of X-ray absorption spectroscopies was exploited. Note that EXAFS and XANES data of Bordiga et al.[512−514] supported previous independent evidence based on XRD and on IR, Raman and UV−vis spectroscopies. In particular, diffraction experiments have evidenced an increase of the cell volume V, which is proportional to the Ti content [Ti]/([Ti] + [Si]), supporting Ti incorporation in the framework.[837] IR[737,843,844] and Raman[845] spectroscopies, showed the presence of two bands at 960 and 1025 cm^{-1}, absent in the Ti-free material, and considered as the fingerprint of substitutional Ti species. Finally, UV−vis spectra of TS-1 in vacuo exhibit a single band located at ∼48.000 cm^{-1}, assigned to the $Ti^{4+}O^{2-} \rightarrow Ti^{3+}O^{-}$ ligand-to-metal charge transfer (LMCT) of Ti(IV) ions tetrahedrally coordinated in isolated [TiO_4] sites.[512,840,846] Note that Ti(IV) species in octahedral coordination (like in anatase and rutile) exhibit a $Ti^{4+}O^{2-} \rightarrow Ti^{3+}O^{-}$ LMCT in the 31500−33000 cm^{-1} range.[847,848] Nowadays, the model assessed with XANES and EXAFS spectroscopies[512−514] has been further confirmed on the basis of (i) more refined diffraction experiments performed under in situ conditions either with synchrotron radiation[849,850] or neutron[839,851,852] sources, (ii) Raman resonant experiments,[840,841,853−855], and (iii) ab initio studies,[840,841,856−862] and XES investigation.[862]

Successive and more refined EXAFS and XANES studies have shed light on the ability of Ti sites of TS-1 to interact and react with molecules dosed from both the liquid and the gas phases,[63,781,840,857,863−866] see Figure 13b and sections 3.2.2, 3.2.4 and 3.2.5. The following sections will summarize how, due to its atomic selectivity, EXAFS spectroscopy has played a determining role in understanding the local environment and the reactivity of Ti in the parent Ti-silicalite system.[63,419,512−515,781,840,857,863−866] The remarkable success of EXAFS in such studies was mainly due to the fact that the Ti active sites in TS-1 are framework species possessing a uniform local environment, therefore all sites behave in the same way upon interactions with reactants. This implies that all Ti sites give rise to the same contribution, which thus adds constructively to the overall EXAFS signal. Conversely, we will see in the following that Fe- and Ga-silicalite-1 behave in a different way (section 3.3.1).

3.2.2. Template Burning in TS-1: XANES, EXAFS, and XES Results Compared with Adsorption of Ligand Molecules. The behavior of TS-1 upon template removal is completely different from what observed for both Ga- and Fe-MFI cases (vide infra section 3.3.1). First of all the Ti(IV) species in the MFI framework show a remarkable stability, as they do not leave it even under high temperature treatments. Second isomorphous substitution of Si with Ti in the MFI framework force Ti in a 4-fold tetrahedral coordination, while usually Ti prefers a 6-fold octahedral environment. For this reason, the "true" Ti(IV) species in tetrahedral coordination

dx.doi.org/10.1021/cr2000898 | Chem. Rev. 2013, 113, 1736−1850

can be observed in the calcined sample only. The XANES spectra of TS-1 calcined at high temperature (see dotted and dashed lines in Figure 13a) show a narrow and intense pre-edge peak at 4967 eV, due to the 1s → 3pd electronic transition involving Ti(IV) atoms in tetrahedral coordination.[512−516] The same electronic transition for Ti(IV) species in TiO_2 (anatase or rutile)[867,868] or in ETS-10 titanosilicate,[516,869,870] where Ti(IV) species are in octahedral environment, is characterized by a very low intensity because of the small pd hybridization which occurs in octahedral symmetry. Indeed, the transitions $A_{1g} \rightarrow T_{2g}$ are symmetrically forbidden in the case of octahedral coordination, while the transition $A_1 \rightarrow T_2$ is allowed in the case of tetrahedral coordination, as in the case of $[TiO_4]$ units hosted in the dehydrated MFI framework.[419,512−514,840,871] This explains why the 4967 eV pre-edge peak, very intense for the activated TS-1 samples, is strongly depressed in presence of the TPAOH template (full line curve in Figure 13a): because the nitrogen atom of the TPAOH molecule penetrates inside the first Ti(IV) coordination sphere. This picture is quantitatively confirmed by the EXAFS data summarized in Table 6, because

Table 6. Summary of the First Shell EXAFS Analysis of TS-1 in Presence of Template and As a Function of the Activation Temperature. Reproduced with Permission from Ref 781. Copyright 1999 The Japan Society of Applied Physics

activation T (K)	shell	N	R (Å)	σ (Å)
with template	O	4.0	1.83 ± 0.01	$(6 \pm 1) \times 10^{-2}$
	N	1.0	1.99 ± 0.04	$(5 \pm 2) \times 10^{-2}$
400	O	4.4 ± 0.2	1.78 ± 0.01	$(6 \pm 1) \times 10^{-2}$
673	O	4.3 ± 0.3	1.79 ± 0.01	$(6 \pm 1) \times 10^{-2}$

a second first shell contribution was needed to simulate the experimental signal collected in presence of template. The fit resulted in N = 4.0 framework oxygen atoms at 1.83 ± 0.01 Å and one nitrogen atom of the TPAOH template molecule at 1.99 ± 0.04 Å.[781] Once the template molecule has been removed, (samples activated at 400 and 673 K) the Ti−O distance of the framework undergoes a small, but well measurable, shortening (Table 6, column 3).

The ability of Ti(IV) in TS-1 to modify in a reversible (or nearly reversible) way its local environment from tetrahedral-like to octahedral-like geometries after interaction with strong ligands explains the evolution of the XANES (Figure 13a) and EXAFS (Table 6) data upon template removal, see the first part of Scheme 2 (L = TPAOH). The same reversible behavior was observed when the calcined TS-1 has been subjected to the interaction with ammonia (blue curve in Figure 13b)[63,512−514,857,864,865] or water (red line in Figure 13b)[63,857]

Scheme 2. Ability of Ti(IV) in TS-1 to Modify in a Reversible (Or Nearly Reversible) Way Its Local Environment from Tetrahedral-like to Octahedral-like Geometries after Interaction with Strong Ligands (L = TPAOH, H_2O or NH_3). Reproduced with Permission from Ref 865. Copyright 1999 American Chemical Society

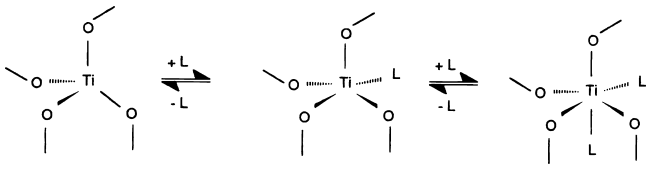

molecules. In this case, upon increasing the equilibrium pressure of the ligand molecule (L = H_2O or NH_3), a first and then a second molecule can be inserted in the Ti(IV) coordination sphere (Scheme 2). The similarities between the XANES spectra of TS-1 in presence of template (full line in Figure 13a) and after interaction with ammonia (dotted line in Figure 13b) are remarkable.

It is worth noticing that the first studies on dehydrated TS-1[512−515] were limited to the first shell only. Second shell studies appeared only later and concerned the activated sample only.[419,873] In particular, in collaboration with the colleagues of the Royal Institution (London GB), Bordiga et al.[419] showed that the four Ti−O−Si angles are not equivalent. Two couples of angles have been found, the narrower one of 143 ± 5°, and the broader of 162 ± 5°. The four second shell Ti−Si distances lie in the 3.26−3.38 ± 0.02 Å interval.[419]

Figure 13c reports the Kβ-high energy resolution fluorescence detected (HERFD) XANES spectra of TS-1, activated at 673 K (black curve). In these experimental conditions the 1s → 3pd electronic transition becomes as strong as 2.16 in normalized units, while the same peak collected simultaneously in total fluorescence yield mode (gray curve) has an intensity of 0.8, as for the spectra of the activated TS-1 reported in Figure 13a−b. The inset of Figure 13c reports the corresponding RIXS map, where the dotted gray line shows the cut done to obtain the HERFD spectrum reported in the main part.

Until now we commented the XANES features of the material. Because XANES is a XAS technique, it gives information on the unoccupied molecular orbitals (MO). Information on the occupied MO is provided by valence to core (VtC) XES spectroscopy, see the scheme in Figure 5b. Figure 13d shows the nonresonant Kβ XES lines of TS-1 activated at 673 K. The valence to core-XES spectrum (also called Kβ satellite lines) arises in the region between 4935 and 4970 eV superimposed on the K$\beta_{1,3}$ tail. A delicate background subtraction is needed to properly extract the VtC spectrum. The background-removed VtC-XES spectrum is shown in the inset of Figure 13d and presents four main features named as A, B, C, and D by Gallo et al.[862a]

A detailed DFT study allowed Gallo et al.[862] to assign the occupied MO responsible for the VtC-XES spectrum reported in the inset of Figure 13d. Using different clusters, basis sets and functionals the authors reached the following conclusions: (i) Three main spectral features A, B, and C are observed for all the simulated spectra, showing a cluster size depending fine structure, while feature D is obtained only for clusters able to reproduce also the third coordination shell around Ti(IV). (ii) In general the MOs linked to transitions responsible for A have strong O (first shell) 2s atomic character. (iii) The features labeled B and C arise from transitions involving MOs with mainly O(first shell) 2p atomic character. The main difference between B and C is that while the MOs characterizing B have mainly σ character the MOs characterizing C have mainly π character. (iv) The shoulder D is mainly due to MOs localized on the SiO_4 groups. (v) No significant spectral shape modifications is observed using clusters larger than the $Ti[OSi(OH)_3]_4$ one, reported in Figure 13e. For this reason authors concluded that only atoms up to the third coordination shell around Ti(IV) contribute to the VtC-XES spectrum of activated TS-1. In 2013, a work of Gallo et al.[862b] extended the VtC XES study of activated TS-1[862a] to the interaction with both H_2O and NH_3 ligands. Assigning the changes of the electronic structure of Ti(IV) induced by the adsorption

dx.doi.org/10.1021/cr2000898 | Chem. Rev. 2013, 113, 1736−1850

processes with DFT calculations, Gallo et al.[862b] concluded that, contrary to the widely accepted view (see right part of scheme 2 and related discussion), the Ti-sites of TS-1 can coordinate only one H_2O or one NH_3 molecule. This result underlines the potentialities of the XES technique combined with DFT calculations.

3.2.3. Effect of the Amount of Incorporated Heteroatom. The goal of this section is to underline the interplay between Ti insertion in the MFI framework and structure defectivity. It is well-known that TS-1 samples synthesized following the original patent[102] are rather defective materials showing a consistent amount of internal defects: the lack of one or more adjacent T atoms (Si or Ti) is balanced by the presence of hydroxylated nanocavities in the framework, also referred as hydroxyl nests.[103,874−877] The detailed structural and chemical role of OH groups in silicalite and TS-1 is still debated, although it is known that their presence greatly improves the interaction of the framework with guest molecules and increases the adsorption capacity of the porous material.

Ti-free silicalite (the [Ti]/([Ti] + [Si]) → 0 limit of TS-1) exhibits a low acidic behavior of Brønsted nature (because of the presence of internal hydroxyl nests), that is the origin of its ability to catalyze selective reactions, which occur only in very mild conditions, such as the Beckmann reaction,[876,877] preventing the undesired formation of coke. Models for the location and clustering of the hydroxyl groups in Ti-free silicalite have been proposed on the basis of spectroscopic (IR) and volumetric observations complemented by molecular dynamic simulations.[103,856,874,876−879] These studies have evidenced that the presence of isolated T vacancies is not able to explain the increased adsorption capabilities of silicalite and the lack of two or more adjacent T sites must be assumed. In 2000, neutron powder diffraction experiments[875,876] revealed the preferential location of Si atoms vacancies on four out of twelve independent T-sites in the orthorhombic silicalite (namely T6, T7, T10, and T11, vide infra Figure 14b). The fact that T7, T10, and T11 sites are adjacent to each other (and to the same three sites generated by the symmetry of the *Pnma* space group) implies that in principle vacancy clusters up to 6 T defects are possible, so confirming the previous indirect evidence.

In this subsection it will be discussed the effect of the Ti insertion on the nature and on the density of hydroxyl nests by following the evolution of IR, XANES, and EXAFS spectroscopies and of the neutron powder diffraction data upon increasing Ti content *x*. On the basis on the whole set of presented data, a model of the possible interplay between hydroxyl nests and framework Ti(IV) species and their synergic role in the catalytic performances of TS-1 will be presented.

3.2.3.1. Summary of Neutron Powder Diffraction and IR Studies. To better understand the role played by the microporous nature of the MFI framework hosting the active Ti sites, the Torino group has performed an extended research[103,839,864,865,874−881] on the Ti-free silicalite-1, synthesized according to the original patent for TS-1[102] (i.e., just without including TiO_2 in the reactants). It has been shown that silicalite-1 is a defective material showing a high density of bulk Si vacancies (•) resulting in the presence of hydroxylated nests: $[Si(-O-Si-)_4] \rightarrow [\bullet(HO-Si-)_4]$. The defectivity of the MFI matrix is observed for TS-1 also.[839,864,865]

In a neutron diffraction study Lamberti et al.[839,880] have shown that Ti insertion in TS-1 and Si vacancies in Ti-free silicalite-1[875,880] do not occur randomly but that they are

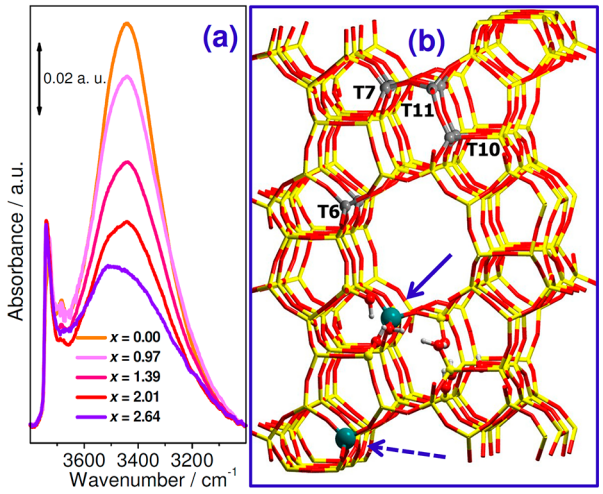

Figure 14. Part a: IR spectra, in the OH stretching region, of TS-1 samples with increasing Ti content *x* = [Ti]/([Ti] + [Si]), from 0 (silicalite-1) to 2.64. All samples have been activated at 400 K. Part b: Schematic representation of the preferential location of Ti atoms and Si vacancies in the MFI framework (upper part) and their interplay (lower part). Yellow and red sticks represents Si and O of the regular MFI lattice; green balls refer to Ti, while red and white ones refer to O and H of defective internal OH groups. Dotted and full arrows evidence regular $[Ti(OSi)_4]$ and defective $[Ti(OSi)_3OH]$ sites, see Scheme 3. Adapted with permission from ref 839. Copyright 2001 American Chemical Society.

preferentially hosted in the same four site (among the 12 of the MFI framework): T6, T7, T11, and T10 sites (see the upper part of Figure 14b). The correspondence of the four sites preferentially hosting the Si vacancies in defective silicalite-1[875,880] with those preferentially occupied by Ti atoms in TS-1[839,880] is striking. Moreover, it has been shown using several independent characterization techniques[512,863−865,873,882] (IR, UV−vis, EXAFS, microcalorimetry) that the insertion of the Ti heteroatoms in the MFI lattice has a mineralizing effect, i.e. it causes the progressive decrease of the framework defects. In particular, Figure 14a reports the OH stretching region of the IR spectra of dehydrated TS-1 samples upon increasing Ti content in the $0 \leq [Ti]/([Ti] + [Si]) \leq 2.64$ interval. The progressive incorporation of Ti atoms in the framework causes a gradual decrease of the IR absorption band due to the ν(OH) mode of the defective Si−OH groups (erosion of the broad absorption band at 3600−3200 cm^{-1}).

By combining the crystallographic evidence (obtained on defective silicalite-1 and on TS-1),[839,875,880] together with the IR spectra (Figure 14a), which put in evidence the mineralizing effect of Ti heteroatoms, it has been suggested that the incorporation mechanism of the Ti atoms in the MFI framework occurs via the insertion of titanium in defective sites of silicalite-1. In this context, it is worth reminding that the computational study of Ricchiardi et al.[856] indicates that the $[TiO_4]$ and the $[(OH)_4]$ units, substituting regular $[SiO_4]$ units in the MFI framework, have a rather similar size. In other words, $[TiO_4]$ and $[(OH)_4]$ units cause a similar local deformation when inserted in the MFI lattice. This can explain the tendency of the same sites to host either a defect (Si vacancy) or a Ti heteroatom. This also explains why the amount of incorporated Ti increases to the detriment of internal OH species: $[\bullet(HO-Si-)_4] \rightleftarrows [Ti(-O-Si-)_4]$ being the equilibrium displaced to the right-hand term by increasing

dx.doi.org/10.1021/cr2000898 | *Chem. Rev.* 2013, 113, 1736−1850

the Ti concentration during the synthesis. The fact that three out of the four preferential T sites (T7, T10, and T11), for both Ti insertion and Si vacancy, are adjacent (see top part of Figure 4b) to each other implies that, in principle, a fraction of Ti atoms could be located in proximity of a Si vacancy. So, the whole picture emerging from the combined neutron diffraction and IR studies suggests that, beside regular $[Ti(OSi)_4]$ sites, also defective $[Ti(OSi)_3OH]$ sites could be significantly present, as pictorially represented at the bottom part of Figure 14b (evidenced by dotted and full arrows, respectively).

Also theoretical chemistry has played a role in this debate. Very recently Yuan et al.[883] investigated, on an energetic ground, the location of Si vacancies and $[Ti(OSi)_4]$ and defective $[Ti(OSi)_3OH]$ sites. It was shown that the four energetically favorable sites for Si vacancies (T6, T12, T4, and T8 and) are partially the same for $[Ti(OSi)_4]$ centers (T10, T4, T8, and T11). Independently to the insertion mechanism (replacing Si vacancies or substituting the fully coordinated Si sites), the most preferential site for Ti is T10, which indicates that the insertion mechanism does not affect the favorable sites of Ti in the MFI lattice. For the defective $[Ti(OSi)_3OH]$ sites, it was found that the Si vacancy at T6 with a Ti at its neighboring T9 site (T6-def-T9-Ti pair) is the most energetically favorable one, followed by a T6-def-T5-Ti pair with a small energy gap. These findings are significant to elucidate the nature of the active sites and, in turn, the mechanism of reactions catalyzed by TS-1. In this regard, it is worth reminding the DFT study of Wells et al.[884] who showed that propylene epoxidation performed on Ti sites located adjacent to Si vacancies in the TS-1 lattice is more efficient than that occurring on fully coordinated Ti sites.

3.2.3.2. EXAFS and XANES data: evidence of the copresence of two different Ti framework sites. As summarized in section 3.2.1, EXAFS spectroscopy was fundamental in determining the local structure of Ti sites in TS-1. Although a theoretical coordination number of $N = 4$ was expected, slightly higher values were systematically observed for dehydrated TS-1[63,512,513,781,863,871] (see also Table 6). However only a defect-free TS-1 calcined and dehydrated, containing all perfect or "closed" $Ti(OSi)_4$ sites, would exhibit a theoretical value of $N = 4.0$ (Scheme 3a). On the contrary, on the basis of what debated in section 3.2.3.1, it is known that also a considerable fraction of defective "open" $Ti(OSi)_3(OH)$ sites is present and that the relative fraction of such sites is higher at low Ti concentration x. Also defective sites have four "chemically bonded" oxygen atoms, three bridging Ti with three different Si framework atoms and one hosting the titanol; however, in this case, the insertion of a fifth oxygen of the silanol, formed in the adjacent Si center when the Ti−O−Si bridge is broken, is expected (Scheme 3b). A coordination number equal to $N = 5$ is consequently expected in an ideal EXAFS measurement performed on a TS-1 sample containing only open sites. This means that the presence of a relative fraction y of open sites and of $1.0 - y$ of closed sites, would give rise to $N = 4.0 + y$, being $0 < y < 1.0$, in an ideal EXAFS measurement.

On the basis of what stated above, it is evident that, because of its atomic selectivity, EXAFS is a technique potentially able to solve the problem of the structure of Ti(IV) sites. Unfortunately, because of the small amount of incorporated Ti atoms in the MFI framework,[837] the first EXAFS spectra, obtained on well manufactured TS-1 catalysts, were affected by intrinsic low signal to noise ratio and the corresponding structural parameters obtained by data analysis were characterized by relative large error bars.[512,513,871,885] This was particularly true for the first shell coordination number: $N = 4.4 \pm 0.6$ (data collected at the PULS beamline of the ADONE storage ring in Frascati Italy),[512,513] and $N = 4.1 \pm 0.5$ (data collected at the X-11A beamline of the NSLS storage ring in the U.S.).[871] Both data were compatible, within the experimental errors, with the expected value $N = 4$ for Ti substitutionally incorporated in a defect free silicalite framework ($Ti(OSi)_4$ site). Schultz et al.,[885] worried by the low S/N ratio of the collected spectra, decided to not report the quantitative analysis of the EXAFS data.

Later on[863] new EXAFS data, characterized by a considerably improved S/N ratio, were collected. The improvement was the result of three main factors: (i) an increased photon flux (XAFS3 station at LURE, Orsay France, vs ADONE PULS beamline), (ii) the slightly higher Ti content of the sample (2.03 vs 1.94 wt.%), and (iii) the higher number (9 vs 3) of EXAFS spectra subsequently collected under the same experimental conditions to be averaged before data analysis. The new data allowed the Turin group to strongly improve their first analysis[512,513] and to affirm, after a serious evaluation of the most relevant sources of errors, of both statistical and systematic nature,[863] that the average first shell coordination number ($N = 4.45 \pm 0.25$) was significantly greater than four (see also the datum reported in Table 6, referring to a different sample).[781]

Almost ten years later, Bordiga et al.[886] reported the results of the EXAFS data analysis performed on a set of ten high quality TS-1 samples covering the 0.97−3.59 (TiO_2 wt %) titanium content range. All samples were synthesized in the Eni laboratories and dehydrated in a carefully controlled atmosphere at 400 K.[886] Although the first papers reporting EXAFS measurements on TS-1 dated back at beginning of the nineties,[512,513,834,871,885] this work was the first systematic study on the evolution of the Ti local environment in TS-1 as a function of Ti loading by means of EXAFS and XANES spectroscopies.[886] The structural parameters obtained from the first shell EXAFS data analysis are summarized in Figure 15a−c.

N values greater than 4.0 were obtained for most of the samples, demonstrating that, whichever is the Ti content, both perfect closed $Ti(OSi)_4$ and defective open [(H−O−)Ti(−O-

Scheme 3. Closed $Ti(OSi)_4$ Sites (Part a) and Defective Open $Ti(OSi)_3(OH)$ Sites (Part b).[a] Reproduced with Permission from Ref 863. Copyright 1998 American Chemical Society

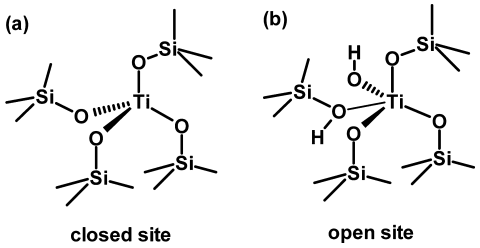

[a]The two schemes correspond to the local structure of the two Ti sites evidenced by dotted and full arrows in Figure 14b. The presence in dehydrated TS-1 of open and closed Ti sites was claimed first by the group of Bonneviot,[873,882] combining UV−visible DRS, EXAFS, and ^1H and ^{29}Si NMR spectroscopies and successively confirmed by Lamberti et al.[863]

dx.doi.org/10.1021/cr2000898 | Chem. Rev. 2013, 113, 1736−1850

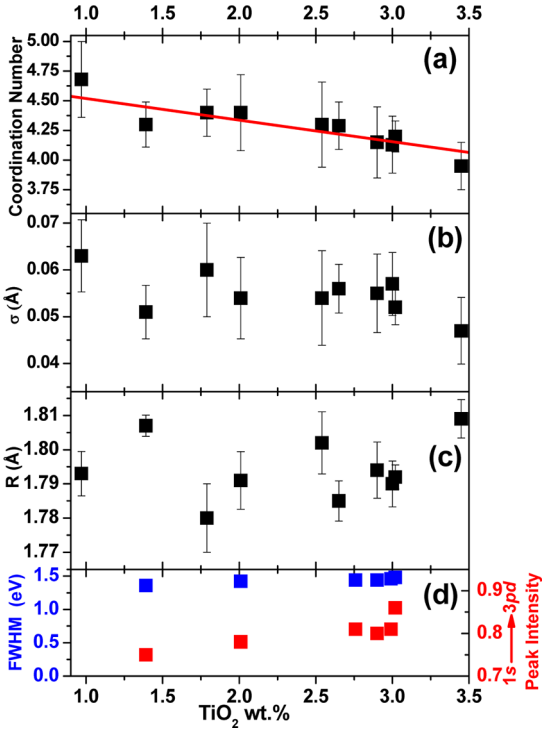

Figure 15. Parts a–c: Summary of the structural parameters extracted from first shell EXAFS data analysis, performed as described elsewhere,[863] on a set of ten high quality Ti-silicalite (TS-1) samples covering the 0.97–3.59 (TiO_2 wt %) titanium content range, synthesized in the Eni laboratories. Part a: Coordination number (N); the red line represents the best linear fit of the experimental data. Part b: Debye–Waller factor (σ). Part c: Ti–O bond distance (R). In all parts the corresponding error bars have been reported. Part d: Summary of the XANES data concerning the fingerprint pre-edge peak at 4967 eV (due to the 1s → 3pd electronic transition involving Ti atoms in T_d coordination) measured on a fraction of the high quality TS-1 samples subjected to the EXAFS study summarized in parts (a–c). Full width at half-maximum and normalized peak intensity are reported as blue (left ordinate axis) and red (right ordinate axis) squares, respectively. EXAFS and XANES data were collected at the EXAFS3 station of the DCI storage ring at LURE, Orsay France using a double crystal Si(111) and Si(311) monochromator, respectively. Adapted with permission from ref 886. Copyright 2007 the PCCP Owner Societies.

Si–)$_3$] sites are copresent. Although the error bars are still relevant, from the whole set of data an important trend can be observed: low Ti loaded TS-1 materials exhibit an N value significantly higher than the coordination number measured for the high loaded samples. This time-consuming EXAFS work indicates that the fraction of defective [(H–O–)Ti(–O-Si–)$_3$] sites progressively decreases upon increasing the Ti content x, confirming that Ti has a the mineralizing role in the MFI framework when the Eni synthesis conditions are adopted.[102] This trend perfectly matches the hypothesis put forward on the basis of the combined IR and neutron powder diffraction studies summarized in Figure 14: (i) the incorporation mechanism of the Ti atoms in the MFI framework occurs via the insertion of titanium in defective sites of silicalite-1, (ii) because silicon vacancies are clustered, a significant fraction of framework Ti species are adjacent to a Si vacancy (Scheme 3b), and (iii) the fraction of defective Ti sites decreases significantly upon reaching the maximum Ti loading, owing to the partial saturation of vacancies.

Within the error bars, no significant trends as a function of the Ti content x could be observed for both the first shell Ti–O bond length (Figure 15c) and its Debye–Waller factor (Figure 15b). The same holds for the XANES spectra (Figure 15d) . For each sample, three independent XANES spectra were collected and the average values of the normalized intensity and of the fwhm of the peak at 4967 eV are reported in Figure 15d (red and blue squares respectively). Although small increase of the normalized peak intensity upon increasing the Ti concentration x can be appreciated (red squares in Figure 15d), no important variations of the feature which is the fingerprint of tetrahedral Ti species was observed, suggesting that both open and closed sites (Scheme 3) have a T_d-like environment. High quality XANES spectra have been successively measured for four out of these ten samples at the GILDA BM8 beamline of the ESRF. The normalized intensity of the 4967 eV peak reached a value of 1.0 but this increase was related to the higher instrumental energy resolution available at the ESRF (see Equation 7) and was not reflecting any structural change in the sample.[840] High-energy resolution fluorescence detected (HERFD) XANES, see section 2.2.5 (gray curve in Figure 13c), allows to measure an 1s → 3pd peak in activated TS-1 as high as 2.16 and with a fwhm as narrow as 1.1. eV.

The model of TS-1 reviewed above (Figure 14b) was further supported from the work of Parker and Millini.[887] The authors investigated, via ^{1}H and ^{29}Si solid-state NMR spectroscopy, a series of template containing TS-1 and B-MFI samples with increasing heteroatom content x (up to 3 atoms/unit cell),[888] finding a linear negative correlation between the (SiO^-) siloxy anion content (estimated via integration of NMR deconvoluted peaks) and the Ti content x. This implies that, being the amount of TPA^+ constant (4.4/unit cell), the incorporated atoms, Ti(IV) or B(III), should contain a negative charge to allow the electrostatic neutrality of the structure. The researchers of the EniTecnologie laboratories attributed the negatively charged Ti(IV) species to $[Ti(OSi)_4OH]^-$ sites, concluding that they are the preferred counterions for TPA^+, and excluding siloxy formation up to the maximum Ti occupancy. The work of Parker and Millini[887] is very important because it reveals that Ti behaves as other incorporated heteroatoms, bearing a negative charge; it substitutes Si atoms at "defective" (siloxy) sites near the TPA^+ molecule. Furthermore, authors concluded that, since Ti must be proximal to the nitrogen atom of TPA^+, its position within the framework is not expected to be random, as found by the powder neutron diffraction studies of Lamberti et al.[839,880] and revealed also a striking correspondence between sites preferentially hosting Ti atoms and Si vacancies.[839,875,876,880]

On top of this, the study of Parker and Millini,[887] summarized above is also able to explain the 5-fold nature of Ti atoms hosted in the template-containing TS-1 revealed by both XANES (full-line curve in Figure 13a) and EXAFS (Table 6) in terms of $[Ti(OSi)_4OH]^-$ units. This implies that the original interpretation given by Lamberti et al.[781] should be slightly revised.

3.2.4. Modeling of $[Ti(OSi)_4]$ Perfect Sites in Interaction with Ligands by an Ab Initio Periodic Approach: Comparison with EXAFS Results. *3.2.4.1. Brief Overview.* In the past decade, TS-1 has been investigated in many theoretical works, either based on periodic,[861,886,889–891] semiperiodic[856,892] or cluster approaches.[840,841,857–860,862,883,886,893–898] Initially, the cluster

dx.doi.org/10.1021/cr2000898 | Chem. Rev. 2013, 113, 1736–1850

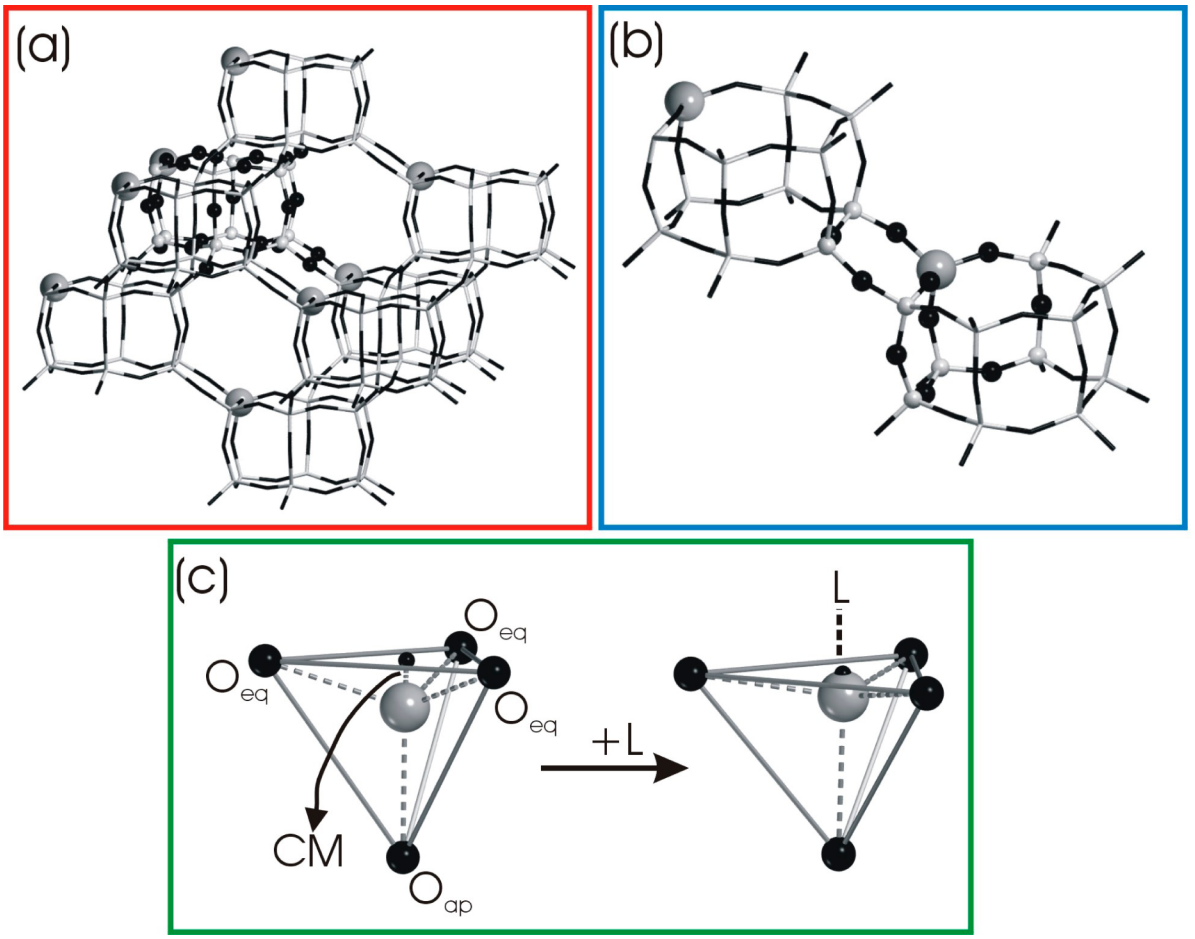

Figure 16. Parts a: Optimized periodic Ti-chabazite (Ti-CHA) with Ti/Si ratio =1/11. For sake of clarity only the unit cell (together with all Ti atoms) is rendered with balls and sticks. Part b: A particular of Ti-CHA framework reported in Part (a). Big gray spheres: Ti. Black spheres: O. Small white spheres: Si. Part c: Schematic representation of the deformation of the $[TiO_4]$ unit upon interaction with ligand molecules L (L = NH_3, H_2O, H_2CO, and CH_3CN). Gray sphere: Ti atom. Big black spheres: O atoms, divided into three equatorial (O_{eq}) and one apical (O_{ap}). The small black sphere shows the center of mass (CM) of the three O_{eq} atoms. Reproduced with permission from ref 886. Copyright 2007 the PCCP Owner Societies.

calculations were based principally on minimal models ($Ti(OH)_4$, $Ti(OSiH_3)_4$, $Ti(OSi(OH)_3)_4$),[840,841,894,897] and only successively results from calculations on more complex models, mimicking the MFI framework with clusters containing up to 18 T sites, have been published by Damin et al.[857−860,898,899] adopting the cluster/embedded cluster ONIOM method, to limit computational demand, using in all cases the $Ti(OSiH_3)_4$ portion as the high level part of the cluster. Very recently a cluster containing 40 T sites has been proposed by Yuan et al.[883] Of high interest are also the ab initio molecular dynamics approach[900,901] the time-dependent DFT for the simulation of the UV-Vis spectra[902] and the first periodic study on the insertion of Ti in the MFI lattice[891] from the Como group

When applicable, the periodic approach is certainly preferable as it is able to account for long-range effects and for the constraints acting on $[TiO_4]$ unit when inserted in a zeolitic framework. Unfortunately, due to the low symmetry of the MFI framework (which exhibits 12 T sites in the asymmetric unit and 96 T sites in the unit cell for the orthorhombic *Pnma* space group, values which moves to 24 and 192 for the monoclinic, $P2_1/n$, space group),[837,839,849,850,879] no periodic full ab initio studies have been reported up to 2009 on TS-1. Only Ricchiardi et al.[856] have reported in 2000 a hybrid molecular mechanics/quantum mechanics (MM/QM) study of TS-1 (vide infra) exploiting the QMPOT code.[903] In 2009 Gamba et al.[891] reported a first principles study on periodic TS-1 models (orthorhombic MFI framework) at Ti content corresponding to 1.35 and 2.7 wt % of TiO_2. The study reported the optimized structure of TS-1 in vacuo. By using cluster models cut from the optimized periodic DFT structures, also vibrational and electronic excitation spectra have been calculated.[891] Interaction with adsorbates was not discussed.

Due to its higher symmetry (containing 1 T site in the asymmetric unit and 12 T sites in the unit cell for the cubic $R\bar{3}m$ space group), chabazite[810,811,904] is a zeolitic structure that is more suitable to be investigated with a periodic approach. For this reason Ti-chabazite was used as a model system for full ab initio calculations of the geometric and energetic properties of molecular adsorption on Ti-zeolites. In this regard, Zicovich-Wilson[889,890] reported a full periodic ab initio calculations on Ti-chabazite, employing the CRYSTAL code.[905] In these works, Ti-chabazite was obtained by substituting six of the twelve equivalent Si atoms of the chabazite unit cell with Ti atoms (Si/Ti = 1/1): this substitution reduces the symmetry from $R\bar{3}m$ to $R\bar{3}$. Unfortunately, the so-obtained Ti-zeolite contains a high concentration of structural Ti atoms and thus is very far from TS-1: the variation in the cell parameters with respect to the

dx.doi.org/10.1021/cr2000898 | *Chem. Rev.* 2013, 113, 1736−1850

Table 7. Most Relevant Geometric Features of the [Ti(OSi)$_4$] Unit of the Ti-CHA Framework Optimized at the Periodic Restricted Hartree−Fock (RHF) Level in Vacuo (L = −) and after Adsorption of Different Ligand Molecules, L = H_2O (O), NH_3 (N), H_2CO (O), CH_3CN (N), the Ti−L Distance Refering to the Atom of the Molecule Reported in Brackets after the Molecule Formula[a]

model/method	L	R_{Ti-O} (Å)	α (deg)	β (deg)	R_{Ti-CM} (Å)	R_{Ti-Si} (Å)	Ti−O−Si (deg)	R_{Ti-L} (Å)	ref
TS-1/EXAFS		1.81 ± 0.01				(3.22−3.36) ± 0.02	(143, 162) ± 5		419
Ti-β/EXAFS		1.80							739
Ti-CHA/EXAFS[b]		1.81 ± 0.02							unpublished
Ti-STT/EXAFS[b]		1.84 ± 0.02							unpublished
Ti(SiOH$_3$)$_4$/DFT		1.803	109.5	109.5	0.601	3.461	180		859
Ti-CHA/RHF		1.790−1.802	108.6−112.9	107.9−108.8	0.569	3.239−3.301	144.9−149.9		861
TS-1/PBE-DFT[c]		1.792−1.800	110.3−113.3	105.6−108.3		3.20−3.31	138−154		891
Ti-CHA/RHF	H_2O	1.802−1.825	115.6−118.3	99.5−100.6	0.322	3.227−3.350	141.4−157.6	2.38	861
Ti-CHA/RHF	NH_3	1.805−1.841	113.1−120.5	97.8−99.3	0.267	3.237−3.357	143.0−157.2	2.36	861
Ti-CHA/RHF	H_2CO	1.797−1.822	114.4−118.7	100.4−100.6	0.331	3.233−3.337	144.2−154.9	2.42	861
Ti-CHA/RHF	CH_3CN	1.801−1.830	113.2−119.7	98.9−99.8	0.292	3.237−3.349	141.4−157.8	2.49	861

[a]For sake of comparison, the same geometric features obtained with a cluster approach on the Ti(SiOH$_3$)$_4$ cluster, where Ti lies in perfect T_d symmetry, are also listed (fifth row) together with those obtained from a recent periodic study on TS-1[891] (seventh row). Also reported are the experimental R_{Ti-O} values obtained from EXAFS studies on titanosilicates where Ti(IV) was isomorphically inserted in different frameworks. When a second shell analysis was performed also R_{Ti-Si} distances and Ti−O−Si angle are reported. For comparison also the experimental values obtained from EXAFS studies on TS-1,[419] Ti-β,[736] Ti-CHA[758] and Ti-STT[759] are reported in the first four lines. [b]The lower amount of Ti incorporated in the CHA[758] and STT[759] frameworks did not allow a second shell analysis to be made. Data collected in fluorescence mode on ESRF BM23 beamline. [c]Periodic calculation performed on orthorhombic TS-1 using the PBE gradient-corrected DFT functional and plane waves as basis set and with a 30 Ry cutoff for the plane wave expansion of the orbitals and a 180 Ry cutoff for the electronic density (PBE/VDB/30) at the Γ point.[891] 12 independent T sites are considered, only extreme values are reported here.

fully siliceous counterpart was quite high: a moves from 9.36 to 9.94 Å corresponding to $\Delta a/a = 6.2\%$ and to $\Delta V/V > 7\%$, to be compared with an experimental value of $\Delta V/V \approx 0.9\%$ for high Ti loaded TS-1.[837,849] Damin et al.[861,899] reported improved ab initio periodic calculations on Ti-CHA characterized by a higher Si/Ti ratio (11, that becomes closer to the value of 30 found in TS-1) and investigating the adsorption of a large number of molecules on the Ti site. These results still represent the most complete set of data reported so far in this field, as Damin et al.[861,899] investigated also the molecular adsorption on Ti(IV) sites, that was missing in the computationally more advanced study of Gamba et al.[891] For this reason, they will be compared in the following with the EXAFS and XANES data discussed in the previous sections.

3.2.4.2. Optimized Ti−CHA Framework and Effect of Interaction with Ligands: Comparison with EXAFS and XANES Results. After almost two decades of attempts Ti-chabazite has finally been synthesized only in 2011 by the Oslo group of Lillerud.[758] The interest in Ti-CHA was evident because its pores are not too small (eight membered rings, 3.8 Å) to limit the diffusion of small molecules; moreover a big cage, formed by connecting eight hexagonal prisms and accessible via the eight membered rings (see Figure 16a, b), is able to host the molecules interacting with Ti. As summarized above, the relatively small unit cell of the CHA framework (12 TO_2 units per cell) allows ab initio calculations to be performed at a reasonable computational cost. Damin et al.[861,899] used as starting structure the CHA framework[904] (Ti/Si = 1/11) previously optimized by using the GULP code[906] and a shell-model ion-pair potential developed by Ricchiardi et al.[856] The internal coordinates of the GULP optimized Ti-CHA model were then fully optimized at Hartree−Fock level (HF), without any symmetry constraints ($P1$ symmetry). The so obtained unit cell parameters were $a = 9.521$ Å, $b = 9.412$ Å and $c = 9.384$ Å ($\alpha = 94.3°$, $\beta = 94.0°$, $\gamma = 95.4°$, V = 832.3 Å^3). When the same approach was adopted to model the pure siliceous chabazite (hereafter Si-CHA) the following unit cell parameters were obtained: $a = b = c = 9.355$ Å, ($\alpha = \beta = \gamma = 94.6°$ and $V = 810.6$ Å^3), resulting in $\Delta a/a = 1.8\%$ and in $\Delta V/V = 2.7\%$.

An important aspect of the work of Damin et al.[861,899] is devoted to the computation of the geometric perturbation and energetic costs/gains induced either by insertion of the [TiO_4] moiety inside chabazite framework or by adsorption of a probe molecule or both. Note that a similar distortion of the Ti local environment was found by insertion of Ti inside a T site of a big cluster mimicking a fraction of a zeolite framework.[857−860] For a perfect T_d symmetry, the unique geometric variable of the TiO_4 group is the Ti−O distance, the six O−Ti−O angles being equivalent (∼ 109.5°) (see left part of Figure 16c). A rupture of the perfect T_d symmetry occurs when the TiO_4 group is inserted inside a zeolitic framework or upon adsorption of a ligand molecule L or both. In particular, when ligand molecule L approaches the Ti(IV) atom along one of the four Ti−O axes, the T_d symmetry is broken and the four oxygen ligands are no longer equivalent, being split into one apical and three equatorial (O_{ap} and O_{eq} in the left part of Figure 16c). The [TiO_4] group is now basically defined by two Ti−O distances (Ti−O_{ap} and Ti−O_{eq}) and by two angles: α = O_{eq}−Ti−O_{eq} and β = O_{eq}−Ti−O_{ap} (differing from 109.5°). Let us now define CM, the center of mass of the three O_{eq} (little black sphere in Figure 16c), and R_{Ti-CM} as the distance between Ti and CM. For perfect T_d symmetry $\alpha = \beta \approx 109.5°$ and $R_{Ti-CM} = 0.334\ R_{Ti-O}$. On the opposite side, when the TiO_4 unit is deformed to a perfect bipiramidal geometry and hence Ti lies in the O_{eq} plane, $\alpha = 120°$ and $\beta = 90°$, while $R_{Ti-CM} = 0$. It is evident that α, β, and R_{Ti-CM} are the three main parameters able to quantify the distortion of the TiO_4 unit from the T_d symmetry.[857−861,899] This geometrical description is valid under the assumption that the L···Ti(O_{eq})$_3$ moiety retains the C_3 axis (Ti−O_{ap}); if not, the symmetry is further lowered and the three

dx.doi.org/10.1021/cr2000898 | Chem. Rev. 2013, 113, 1736−1850

O_{eq} ligands are no more equivalent, resulting in four different Ti−O distances and three different α and β angles.

The values of the most important geometrical parameters emerging from the periodic HF optimization of the Ti-CHA structure are summarized in the sixth row of Table 7. Concerning the first Ti shell, the perfect T_d symmetry, typical for minimal clusters such as $Ti(SiOH_3)_4$,[859] is broken by the framework constraints, resulting in: (i) four different R_{Ti-O} distances in the 1.790−1.801 Å range, (ii) a R_{Ti-CM} distance shorter with respect to that expected for a perfect T_d symmetry by 0.032 Å, and (iii) α and β angles different from 109.5°, by less than 3°. The experimental R_{Ti-O} values observed by EXAFS on TS-1 (see also Figure 15c), Ti-Al-CHA, Ti-STT, and Ti-β (Table 7) are in good agreement with the computed values. It must be recalled that EXAFS provides average values and can not optimize four independent Ti−O contributions characterized by a small difference in R_{Ti-O}. Coming to the analysis of the second Ti shell in TS-1, the four Ti−O−Si angles of the optimized structures at periodic HF level are divided in two couples (two at about 144° and two at about 150°) which differ from each other of only 6°. A larger splitting of the Ti−O−Si angles was obtained from the experimental data on TS-1,[419] where two couples of Ti−O−Si angles located at 143 ± 5° and 162 ± 5° was determined by EXAFS. This difference is a consequence of the different framework topology (MFI vs CHA); as a matter of fact, computations performed on the MFI framework (periodic approach)[891] or on large clusters cut from the MFI framework[859,899] resulted in a splitting of the two couples of Ti−O−Si angles larger than those obtained on CHA.[861] The four Ti−Si computed distances lie in the 3.239−3.300 Å range, in good agreement with the experimental ones observed on TS-1, that are in the 3.26 ± 0.02 Å and 3.38 ± 0.02 Å interval.[419] Unfortunately, the lower Ti content of Ti-CHA[758] prevents a safe second shell analysis of the EXAFS data.

The data summarized in the top part of Table 7 demonstrate that the Ti-CHA structure (computed with Si/Ti = 11) is a good, although not perfect, model for simulating the geometrical properties of TS-1 in vacuo. Next step will be the comparison between theoretical and experimental results on the adsorption of small molecules. The structural properties of Ti-CHA model in interaction with different probes molecules (H_2O, NH_3, H_2CO, and CH_3CN) as obtained from periodic ab initio calculation on Ti-CHA[861] are summarized in the bottom part of Table 7, whereas the comparison between theoretical and experimental results[857,872] as obtained by EXAFS (Figure 17a) and XANES (Figure 13b) data is reported in Table 8 for H_2O and NH_3 ligands. The FT of the EXAFS spectra for activated TS-1 and for TS-1 in interaction with H_2O and NH_3 are shown in Figure 17a. Adsorption of both molecules causes an increase of the first shell R_{Ti-O} distances, already visible in the experimental spectra The computed ΔR_{Ti-O} (averaged on the four bonds) are in qualitative agreement with the experimental values. Calculations show that ligand adsorption causes a (further) distortion of the TiO_4 moiety from tetrahedral toward bipiramidal symmetry, as monitored by the modification of α and β angles (Table 8). Ligand adsorption modifies also the second shell environment as documented by the calculated Ti−O−Si and R_{Ti-Si} values in Table 7 and by the changes in the contribution around 3 Å in the experimental data reported in Figure 17a. Experimental and theoretical data summarized in Table 8 indicate that NH_3 is a ligand more efficient than H_2O in the distortion of the T_d symmetry, in agreement with IR evidence on the perturbation of the 960 cm^{-1} band.[857] Also the XANES spectra of activated TS-1 is strongly modified by H_2O and NH_3 adsorption (vide supra Figure 13b and related discussion). In an attempt to quantify, from the experimental XANES data, the distortion of the TiO_4 unit from the perfect T_d geometry the $F^{exp}(T_d)$ parameter was defined as[886]

$$F^{exp}(T_d) = I_{1s\rightarrow 3pd}(L)/I_{1s\rightarrow 3pd}(vacuum) \quad (33)$$

where $I_{1s\rightarrow 3pd}$ is the intensity of the XANES pre-edge band at 4967 eV. The larger is the distortion the smaller is the F value. This definition holds, at least at a first approximation, because Ti(IV) species in octahedral symmetry exhibit pre-edge features of very weak intensity.[512,867,868,870,907−912] As $I_{1s\rightarrow 3pd}$ is strongly affected by the energy resolution ($\Delta E/E$) of the measurement (which depends on the photon source, monochromator, source to sample distance and slit opening, see eq 7 in section 2.2.1), the $F^{exp}(T_d)$ parameter is meaningful only when the XANES spectra of the sample in vacuo and in presence of adsorbate L have been collected strictly under the same experimental conditions. The computational counterpart of $F^{exp}(T_d)$ is the parameter $F(T_d)$, defined as the relative contraction of the Ti−CM distance (Figure 16c) upon ligand adsorption:[886]

$$F(T_d) = Ti—CM(L)/Ti—CM(T_d) \quad (34)$$

Note that as a model for $[TiO_4]$ units in perfect T_d symmetry the $Ti(SiOH_3)_4$ cluster[859] was used,[886] therefore, a small distortion from the T_d symmetry is computed also for the Ti-CHA model in vacuum: $F(T_d)$ = 0.95. According to these definitions, a qualitative agreement between experimental and theoretical F values was obtained:[886] water results in $F^{exp}(T_d)$ = 0.51 and $F(T_d)$ = 0.54, whereas ammonia shows $F^{exp}(T_d)$ = 0.28 and $F(T_d)$ = 0.44 (Table 8).

Coming to the equilibrium distance between Ti the ligand molecules (R_{Ti-L}, L = H_2O, NH_3) periodic calculations gives a

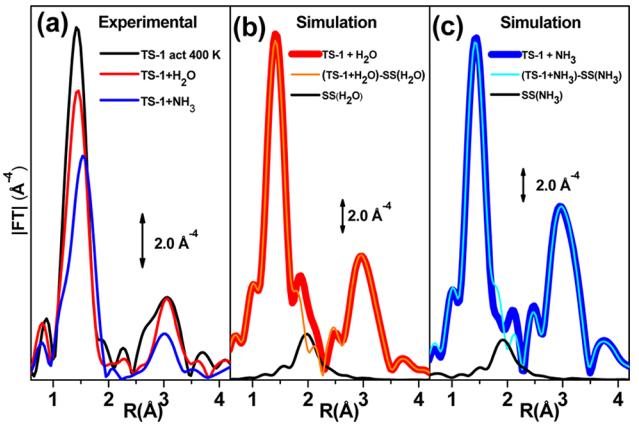

Figure 17. Part a: k^3-weighted FT of the experimental EXAFS spectra of TS-1 (x = [Ti]/([Ti] + [Si]) = 3.0 in TiO_2 wt.%) activated at 400 K (black line) and after subsequent interaction with water (red line) and ammonia (blue line). Part b: FEFF8 simulation of the MFI_T16/H_2O cluster (red bold line), of the single scattering Ti−OH_2 contribution (black line) and of the MFI_T16/H_2O cluster without the Ti−OH_2 path (orange thin line). Part c: FEFF8 simulation of the MFI_T16/NH_3 cluster, (blue bold line), of the single scattering Ti-NH_3 contribution (black line) and of the MFI_T16/NH_3 cluster without the Ti-NH_3 path (cyan thin line). The MFI_T16 cluster contains 16 T atoms (1 Ti and 15 Si), as described elsewhere.[859] Adapted with permission from ref 857. Copyright 2002 American Chemical Society.

dx.doi.org/10.1021/cr2000898 | Chem. Rev. 2013, 113, 1736−1850

Table 8. Effect of Ligand Interaction (L = H_2O, NH_3, and H_2O_2, in Aqueous Solution) on the Local Geometry of the [TiO_4] Units As Determined by EXAFS[857,872] (Columns 2 and 3), XANES[857,872] (Columns 4 and 5) and Ab Initio[861] (Columns 6−9) Techniques

		experimental EXAFS and XANES on TS-1[b]				ab initio periodic Ti-CHA[c]			
matrix	L	R_{Ti-O} (Å)	ΔR_{Ti-O} (Å)	$I_{1s\rightarrow 3pd}$	$F^{exp}(T_d)$	ΔR_{Ti-O} (Å)	$F(T_d)$	$\Delta\alpha$ (deg)	$\Delta\beta$ (deg)
TS-1		1.79 ± 0.01		0.79		−0.007	0.95	+1.2	−1.2
TS-1	H_2O	1.82 ± 0.02	+0.03	0.40	0.51	+0.02	0.54	+7.5	−9.5
TS-1	NH_3	1.88 ± 0.02	+0.09	0.22	0.28	+0.03	0.44	+7.3	−11.0
		experimental EXAFS and XANES on TS-1[a]							
TS-1[e]	H_2O/H_2O_2	1.83 ± 0.02	+0.03	0.09	0.11				
		experimental EXAFS and XANES on β[e]							
Ti-β[d]		1.79 ± 0.02		1.01					
Ti-β[d]	H_2O	1.86 ± 0.02	+0.05	0.68	0.67				

[a]From EXAFS data, we report the average Ti−O bond distance (R_{Ti-O}) and its perturbation upon ligand insertion (Δ_{Ti-O}). From XANES data we report the intensity of the pre-edge fingerprint band at 4967 eV ($I_{1s\rightarrow 3pd}$) and the evaluation of the distortion from tetrahedral geometry $F^{exp}(T_d)$ defined as $I_{1s\rightarrow 3pd}(L)/I_{1s\rightarrow 3pd}$ (vacuum). For the H_2O and NH_3 ligands, the periodic Ti-CHA model has been considered. From that study, we report the average perturbation of the Ti−O bond distance upon ligand insertion (Δ_{Ti-O}), the evaluation of the distortion from tetrahedral geometry $F(T_d)$ defined as Ti-CM(L)/Ti-CM(T_d) and the distortion of the α and β angles, ($\Delta\alpha$ and $\Delta\beta$, respectively). For comparison, also the EXAFS/XANES data reported by Blasco et al.[739] on Ti-β are here reported. Unpublished Table, reporting data from the quoted references. [b]Experimental data taken from refs 857 and 872. [c]Theoretical data taken from ref 861. [d]Only three out of four framework oxygen have been detected by EXAFS upon interaction of TS-1 with H_2O/H_2O_2.[886] [e]Experimental EXAFS and XANES data on the Ti-systems came from the Corma Group.[739] They used a different normalization to define the $I_{1s\rightarrow 3pd}$ value, so only the ratio $F^{exp}(T_d)$ can be used to compare TS-1 and Ti-β results.

shorter R_{Ti-L} for NH_3 then for H_2O (2.36 vs 2.38 Å, see Table 7),[861] in agreement with the stronger interaction. A larger difference was observed in the computations based on large clusters,[857] showing Ti···(NH_3) ≈ 2.34 vs Ti···(H_2O) ≈ 2.41 Å. On the basis of the computed Ti···(H_2O) and Ti···(NH_3) distances the contribution of adsorbed molecules to the experimental EXAFS spectra (Figure 17a) would be expected in the R region between the first Ti−O and the second Ti−Si shell peaks. Although some features appear upon water or ammonia adsorption in the 1.90−2.65 Å (phase uncorrected) range, however their low intensity prevented any attempt to obtain reliable structural data.[857] The low intensity of the ligand contribution was interpreted on the basis of a high Debye−Waller factor for the Ti···(H_2O) and Ti···(NH_3) bonds, suggested also by the very low bonding energies determined in parallel microcalorimetric[857,864,865] data and computed by ab initio methods.[857,859,861] On this basis, adsorbed water (ammonia) molecules are not directly detected by EXAFS, which is only able to measure the effect that the H_2O (NH_3) adsorption has on the Ti−O first shell bond lengths and the second shell deformation.

To verify this interpretation, Bordiga et al.[857] used the optimized geometry obtained for a large cluster ($TiSi_{15}O_{22}H_{20}$, labeled as MFI_T16) after interaction with water and ammonia (hereafter MFI_T16/H_2O and MFI_T16/NH_3 clusters) as input of the FEFF8 code[442] to generate a simulated EXAFS signal in the framework of the MS approach. The aim of these simulations was to evaluate the weight of the single scattering Ti−OH_2 (Ti−NH_3) contribution to the overall EXAFS signal of TS-1 in interaction with water (ammonia). So no geometrical optimization of the clusters nor of the Debye−Waller factors σ of the different paths has been performed in the FEFF8 simulations, the latter being arbitrarily fixed to σ = 0 Å for all paths, see eq 19. The simulated EXAFS signals are reported in bold in Figure 17b and Figure 17c for MFI_T16/H_2O and MFI_T16/NH_3 clusters, respectively, along with the single scattering Ti−OH_2 (Ti-NH_3) contribution (black curves); finally the signal of the MFI_T16/H_2O and MFI_T16/NH_3 simulated without the Ti−OH_2 (Ti−NH_3) contribution are also shown. In both cases, the spectra simulated with and without the ligand contribution are very similar. This is the proof that the modification of the overall EXAFS signal caused by insertion of a water or an ammonia molecule, into the first coordination shell of Ti(IV), is due to the modification of the framework O and Si position to accommodate the ligand molecule, and not to the additional single scattering Ti−OH_2 and Ti−NH_3 contribution. In this regard, it is worth recalling that Corma and co-workers[739] reported a two ligands EXAFS fit for the first Ti−O shell of rehydrated Ti-β samples. In that work, the first Ti−O shell was simulated by considering the contribution of both the four framework oxygen atoms and the oxygen of the adsorbed water molecule, resulting in Ti−OH_2 distances in the 2.12−2.20 Å range. Authors, however, underline that, because of the high number of optimized parameters, the results of the two ligands fit should be considered with care. They so have analyzed the experimental data using only one Ti−O distance in the fit: in such a model they just observe the increase of the average Ti−O distance of the framework oxygen (ΔR_{Ti-O} = 0.03−0.04 Å).[739] This second interpretation well agrees with the model proposed by Bordiga et al.[857] for the TS-1/H_2O system reviewed here above.

3.2.5. Reactivity of Framework Ti Species toward H_2O_2/H_2O. *3.2.5.1. Reactivity of TS-1: A General Overview.* As outlined above (section 3.1) TS-1 is a selective catalyst for mild oxidation reactions using hydrogen peroxide as oxidative agent, therefore its working condition is the H_2O_2/H_2O solution. Despite the numerous papers describing the catalytic activity of TS-1, only a few works have tried to investigate at the molecular level the nature and the properties of the active species formed in TS-1 upon interaction with H_2O_2. This lack can be ascribed to severe experimental problems, mainly due to the presence of H_2O (which precludes the extended use of IR spectroscopy) and to the lability of complexes formed by H_2O_2 on Ti(IV) centers in TS-1. The same problems occurs also for XANES and EXAFS spectroscopies, because water strongly absorb X-rays at the Ti K-edge energy (5 keV, see Figure 3b). This is the reason why, after more than thirty years from the

dx.doi.org/10.1021/cr2000898 | Chem. Rev. 2013, 113, 1736−1850

discovery of the material, the detailed structure of the active intermediate catalytic center is still debated.

The most used technique to investigate the nature of the active species is UV−vis DRS spectroscopy, because it is not affected by the presence of H_2O. This technique has revealed the formation, upon contact with H_2O_2 water solution, of a new band around 26 000 cm^{-1} (385 nm, responsible of the observed yellow color), assigned to LMCT from a O−O moiety to the Ti center,[759,872,898,913−919] see the inset in Figure 18a. Other

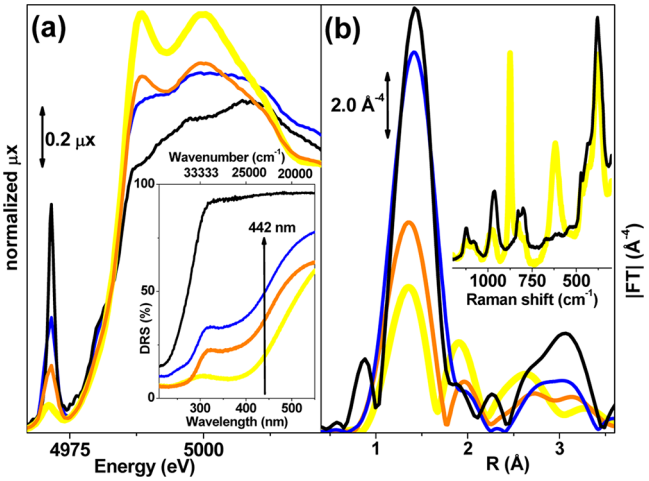

Figure 18. Part a: XANES spectra of TS-1 (black line), immediately after contact with H_2O_2/H_2O solution (yellow line), after time elapse of 24 h (blue line) and after subsequent H_2O dosage (orange line). Part b: As part a for the k^3-weighted, phase-uncorrected, |FT| of the EXAFS spectra. The spectra have been recorded at 77 K. The insets in parts a and b report the UV−vis DRS spectra and the Raman spectra (collected with the 442 nm laser, able to excite the LMCT transition, see arrow) of analogous samples subjected to the same treatments. Experimental data from in refs 898 and 913.

techniques, such as EPR,[765,917,918,920−922] Raman[759,913,914,919,923] EXAFS,[59,764,866,872,898,919,924] and ab initio calculations[764,896−899,923,925,926] have been adopted to investigate the complexes formed upon dosing H_2O_2 (or more complex species such as *tert*-butyl hydroperoxide) on titanosilicates. From all of these results, it has been established that several species can be generated at Ti sites upon H_2O_2/H_2O contact, which can have neutral (coordinated H_2O_2), peroxidic, superoxidic, and hydroperoxidic character. The most popular view is that the active species is a Ti-hydroperoxide,[709,758,759,857,866,913−915,923,925−927] which can be formed upon deprotonation of the H_2O_2 molecule on the Ti(IV) site itself, either on a perfect $[Ti-(O-Si)_4]$ site by rupture of one out of the four Ti−O−Si bridges or on a defective $[(H-O)-Ti-(O-Si)_3]$ site by elimination of a water molecule, (see Scheme 4, parts a and b, respectively). Alternatively, hydroperoxidic complexes can be formed by interaction of Ti(IV) with a HO_2^- anion (the pK_a of the $H_2O_2 + H_2O \rightleftarrows HO_2^- + H_3O^+$ equilibrium being 11.8 in water at 20 °C).[898]

The Ti-hydroperoxide species may be either end-on monodentate (η^1) or side-on bidentate (η^2), as shown in Scheme 5a, although other structures cannot be ruled out.

Scheme 5. Part a: Graphic Representation of End-on Monodentate (η^1, Left) and Side-on Bidentate (η^2, Right) TiOOH Hydroperoxo Species. Part b: Graphic Representation of Side-on η^2 Ti Peroxo Complex. Reproduced with Permission from Ref 886. Copyright 2007 the PCCP Owner Societies

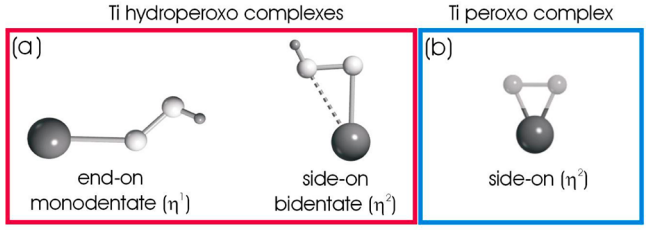

Unfortunately, there is no Ti-hydroperoxo compound of known structure to be used as model for comparison with spectroscopic and structural data. Conversely, the structure of several Ti-peroxo complexes are known by diffraction studies,[928−930] all of them showing the side-on η^2 geometry (see Scheme 5b). Peroxo complexes can be formed in TS-1 by evolution of both η^1 or η^2 hydroperoxo complexes upon a

Scheme 4. Representation of Equilibria between perfect (a) and defective (b) TiO_4 Framework Species and Corresponding Hydroperoxo Species in H_2O_2/H_2O Solutions. Reproduced with Permission from Ref 886. Copyright 2007 the PCCP Owner Societies

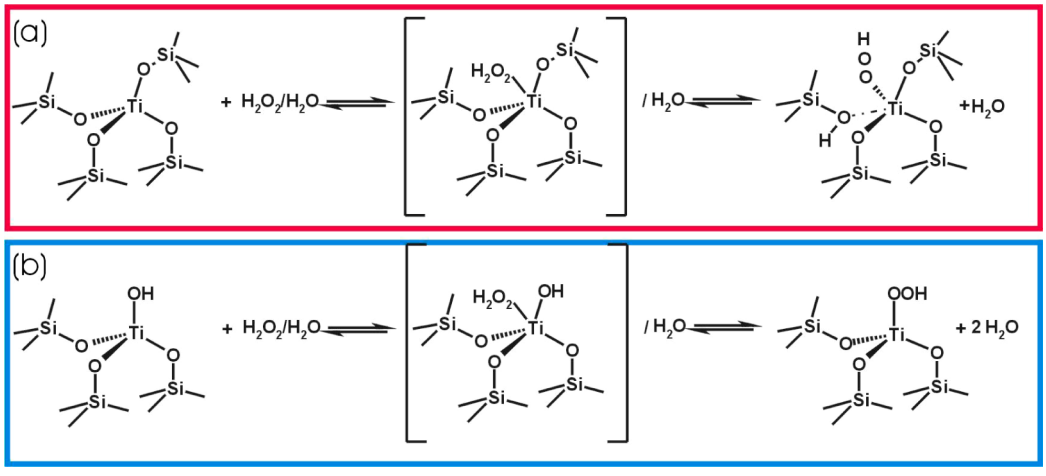

dx.doi.org/10.1021/cr2000898 | *Chem. Rev.* 2013, 113, 1736−1850

Scheme 6. Part a: Representation of Equilibria between TiO_4 Framework Species and Side-on η^2 Ti Peroxo Complexes Inside TS-1 Channels upon Dosage of H_2O_2/H_2O (left) and between Side-on η^2 Ti Peroxo and End-on η^2 Ti Hydroperoxo Complexes upon Dehydration (Right). Part b: Representation of Equilibria between TiO_4 Framework Species and η^2 End-on Ti Hydroperoxo Complexes upon Dosage of Anhydrous H_2O_2 (Left) and between End-on η^2 Ti Hydroperoxo and η^2 Side-on Ti Peroxo Complexes upon Hydration (Right). Reproduced with Permission from Ref 886. Copyright 2007 the PCCP Owner Societies

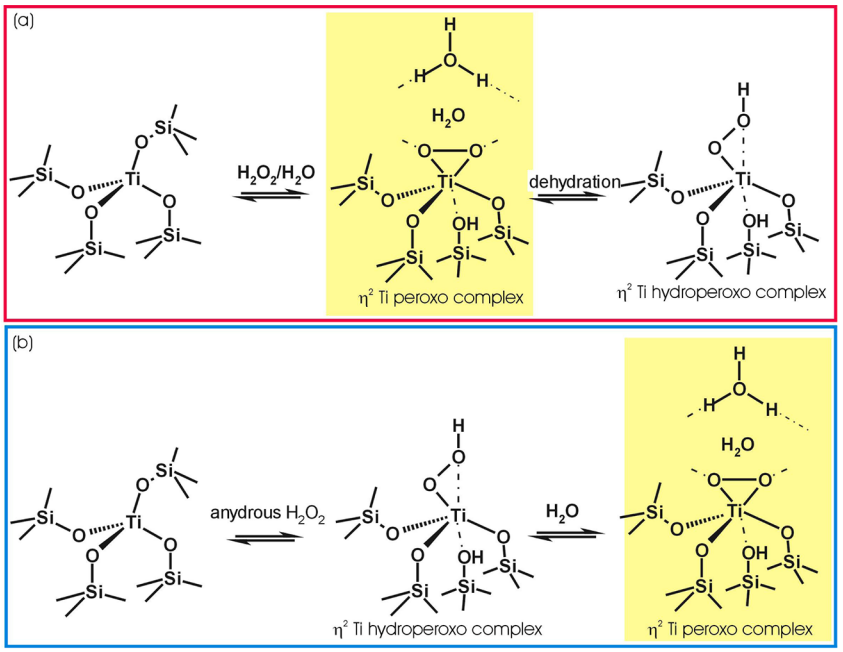

Table 9. Summary on the XANES (Columns 2−6), EXAFS (Columns 7−9), and DRS-UV−vis (Last Column) Results Shown in Figure 18.[a] Data Reported with Permission from ref 898 Copyright 2004 American Chemical Society

spectrum/ conditions	pre-edge intensity	pre-edge fwhm (eV)	$F^{exp}(T_d)$	white line intensity	white line position (eV)	shell	R (Å)	$N_{Oframework}$ ± 10%	DRS(385 nm) %
in vacuo	0.79	1.4	1.00	1.14	5004	O_F	1.79 ± 0.01	4	1
H_2O/H_2O_2	0.09	3.4	0.11	1.46 (1.45)	4984 (4995)	O_F	1.83 ± 0.02	2.8	82
						OO	2.01 ± 0.02	2	
after 24 h	0.38	2.6	0.48	1.25	4996	O_F	1.82 ± 0.01	4	49
$+H_2O$	0.23	2.8	0.29	1.24 (1.28)	4984 (4994)				66

[a]Rows 1−4 refer to TS-1 in vacuo, immediately after contact with H_2O_2/H_2O solution, after time elapse of 24 h and after subsequent H_2O dosage, respectively. Rows 2 and 4, reflecting a significant fraction of TiOO species on the TS-1 sample, are characterized by a doublet in the XANES edge (Figure 18a), so in columns 5 and 6, two values have been reported. For the sample in presence of H_2O/H_2O_2 (second row) a two ligand fit has been mandatory: O_F and OO refer to the framework oxygen and the peroxo species, respectively. The latter exhibiting a coordination number of 2. The EXAFS data analysis of spectrum after H_2O addition (last row) has not been performed owing to the heterogeneity of the Ti(IV) species in such conditions. The last column refers to the intensity of the LMCT band from the OO to Ti in then DRS UV−vis spectra (Figure 18a). .

further deprotonation in presence of water, with formation of H_3O^+/H_2O (vide infra Scheme 6b). In this respect it has been demonstrated, by titration in aqueous medium with NaOH, that the acidity of the TS-1/H_2O system is remarkably increased by addition of H_2O_2, a feature not observed for the Ti-free silicalite-1 system.[898] The increased acidity of the TS-1/H_2O_2/H_2O system must be ascribed to a peculiar interaction between H_2O_2 and Ti(IV) centers. These data find simple explanation by assuming that TiOOH species are the acidic species detected during the titration experiments and thus support the thesis of a deprotonation of the H_2O_2 molecule.

X-ray absorption spectroscopies (both in the XANES and EXAFS regions) have been determinant in highlighting the structure of the species formed by adsorption of H_2O_2 on Ti centers inside TS-1 framework. Spectra have been collected at 77 K, to prevent the thermal decomposition of the peroxo complexes. The interaction of H_2O_2/H_2O solution (yellow spectrum in Figure 18a) with the activated catalyst (black curve in Figure 18a) modified drastically all the XANES features characteristic of Ti(IV) in a tetrahedral environment (see discussion in section 3.2.2). The pre-edge feature decrease in intensity (from 0.97 to 0.09 in normalized μunits), and become broader (from 1.3 to 2.4 eV at the fwhm), testifying the complete loss of the T_d symmetry: $F^{exp}(T_d)$ = 0.11, see eq 33 and Table 8. In the meanwhile, two prominent and well-defined features around 4984 and 4995 eV appear in the edge and postedge region. The k^3-weighted, phase uncorrected, |FT| of the corresponding EXAFS spectra, reported in Figure 18b, show a complete modification of both first and second coordination shells around Ti when the H_2O_2/H_2O solution is contacted to TS-1 (compare black and yellow curves). In particular, the first shell signal is drastically reduced, while the second shell one is substantially decreased. This behavior has been interpreted in terms of the rupture of a Ti−O−Si bridge

dx.doi.org/10.1021/cr2000898 | Chem. Rev. 2013, 113, 1736−1850

(i.e., of a loss of a first shell framework ligand: $N_{Oframework} = 2.8$) and the appearance of a new side-on O−O ligand located at 2.01 Å.[866,872,898] Table 9 summarizes the XANES, EXAFS, and UV−vis data reported in Figure 18. This model will be supported by ab initio results summarized in section 3.2.5.4.

The XAFS results are supported by resonant Raman data.[913,914,919] The inset in Figure 18b reports the Raman spectra, collected with the 442 nm laser, of TS-1 before and after interaction with H_2O_2/H_2O solution (black and yellow line, respectively). It is evident that the interaction with H_2O_2 causes (i) a reduction in intensity and a blue shift in frequency of the 960 cm^{-1} mode, now at 976 cm^{-1}, (ii) the quenching of the 1125 cm^{-1} mode, due to a rupture of the T_d-like symmetry, (iii) the appearance of the strong and sharp (O−O) stretching mode at 875 cm^{-1} because of H_2O_2/H_2O solution physisorbed into the zeolite channels, and (iv) the appearance of a strong and complex new feature centered at 618 cm^{-1}. Features (i−iii) are also observed when the same experiment is performed with a 1064 nm laser source.[923] Conversely, the 618 cm^{-1} band was not observed neither on the TS-1/H_2O_2/H_2O system using a 1064 nm source nor on the Ti-free silicalite-1 molecular sieve upon interaction with H_2O_2/H_2O solution with 442 nm exciting source, and was so ascribed to a Raman enhanced vibration mode of an intermediate complex[913,914] excited using a laser with the λ in the LMCT transition of the peroxo complex. On the basis of comparison with the $(NH_4^+)_3(TiF_5O_2)^{3-}$ model compound, the Raman mode at 618 cm^{-1} has been assigned to a η^2 side-on Ti-peroxo species (see Scheme 5b).[913,914]

The combined UV−vis, resonant-Raman, and XANES characterization approach has recently been used to investigate the Ti-STT/H_2O/H_2O_2 system.[759]

3.2.5.2. Reactivity of TS-1: Equilibrium between Peroxo and Hydroperoxo Species. The XAFS (Figure 18a) and resonant Raman (inset of Figure 18b) data presented above fully demonstrate that the dominant species in the TS-1/H_2O_2/H_2O working system is a η^2 side-on Ti-peroxo species, characterized by a yellow color (inset of Figure 18a). The question is now: is the Ti-peroxo species formed in TS-1 the active one or do we have to hypothesize a conversion into a hydroperoxo active species? It is well-known that the yellow color of the TS-1/H_2O_2/H_2O system is lost within some hours (see blue line in the inset of Figure 18a).[872,898] This behavior was generally interpreted in terms of a high lability of the peroxo species. However, it has been demonstrated that the addition of water on the one-day aged catalyst is able to restore almost completely its yellow color (orange line in the inset of Figure 18a).[872,898] Since the hydroperoxo complexes are generally not colored, this suggests that water is not just a medium for transporting products on the catalytic sites but has an active role in determining the relative concentration of peroxo/hydroperoxo species present on the working catalyst. Scheme 6a summarizes the model hypothesized by Bonino et al.[898,919] on the basis of the whole set of experiments reported in Figure 18.

The UV−vis data discussed above are strongly supported by XANES and EXAFS experiments. After a 24 h aging period of the TS-1/H_2O_2/H_2O system, most of the water present on the sample evaporates and the XANES features of the side-on η^2 Ti-peroxo complex disappear (from yellow to blue curves in Figure 18a). By contacting the 1-day-aged catalyst with water all features of the side-on η^2 Ti-peroxo complex are almost restored (orange curve in Figure 18a). The reversibility of this process is clearly observed also in the k^3-weighted, phase uncorrected, |FT|s of the EXAFS spectra (Figure 18b). Table 9 summarizes the XANES, EXAFS, and UV−vis data reported in Figure 18.

Prestipino et al.[866,931] have successively reported an experimental breakthrough in this field as they where able to dose an almost anhydrous H_2O_2 vapor (using $KH_2PO_4{\cdot}H_2O_2$ as hydrogen peroxide source) in situ on the activated TS-1 catalyst (black line in Figure 19a). The XANES spectrum of TS-1

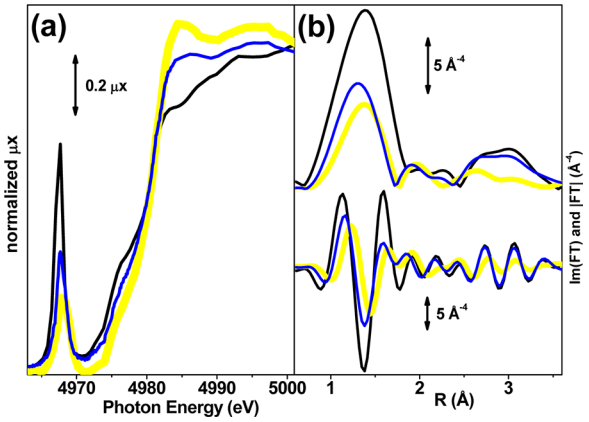

Figure 19. XANES spectra (part a) and phase-uncorrected k^3-weighted FT of the EXAFS data (part b), collected at 77 K, of activated TS-1 catalyst (black line), after contact with "anhydrous" H_2O_2 from the gas phase (blue line) and after subsequent contact with water (yellow line). Adapted with permission from ref 866. Copyright 2004 Wiley-VCH.

contacted with anhydrous H_2O_2 from the gas phase (blue line in Figure 19a) gave results very similar to that obtained after dehydration of the TS-1/H_2O_2/H_2O system by time elapsing (see blue curve in Figure 18a). Finally, when water is added to the uncolored catalyst previously contacted with anhydrous H_2O_2, the sample turns yellow and its XANES spectrum (yellow curve in Figure 19a) possesses the fingerprint features of the η^2 side-on Ti-peroxo species. Scheme 6b completes the picture, showing that the equilibrium between the uncolored end-on η^2 Ti-hydroperoxo complex and the yellow colored side-on η^2 Ti-peroxo complex is tuned by the amount of water present in the TS-1 channels. The EXAFS part of the X-ray absorption spectra (see Figure 19b) confirms the picture emerged XANES: anhydrous H2O2 modifies significantly the first coordination sphere around Ti, leaving the second one almost unaffected (compare black and blue lines in Figure 19b). Conversely, when H_2O is added a complete modification of both first and second shell signals is observed (yellow line in Figure 19b), which has been interpreted in terms of the rupture of a Ti−O−Si bridge.[872,898] The new data by Prestipino et al.[866,931] suggest that this last effect is not present in anhydrous conditions.

What observed on TS-1 and here briefly resumed is not peculiar for TS-1 only but can be observed on other titanosilicates like Ti-MSA, a mesoporous amorphous material having Ti(IV) centers exposed on the surface of the pores.[932,933] The largest pores of this material allow to form peroxo/hydroperoxo complexes by dosing *t*-butyl hydroperoxide. The XANES spectrum of Ti-MSA in vacuum (black line in Figure 20a) is typical of almost T_d-like Ti(IV) centers: the intensity of the $A_1 \rightarrow T_2$ pre-edge peak is only 0.69, to be

dx.doi.org/10.1021/cr2000898 | *Chem. Rev.* 2013, 113, 1736−1850

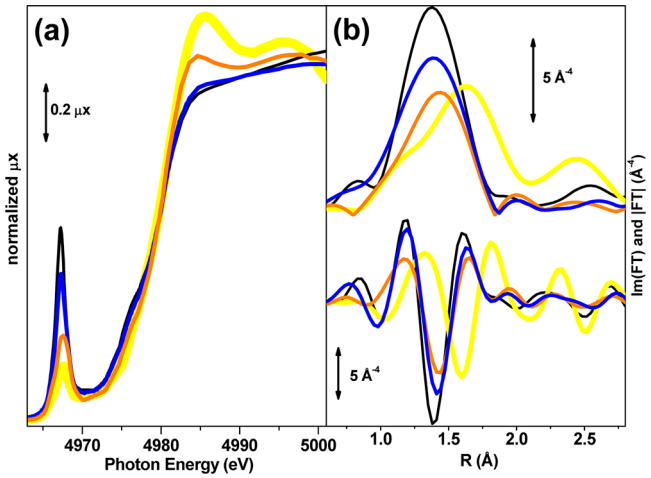

Figure 20. XANES spectra (part a) and phase-uncorrected k^3-weighted FT of the EXAFS data (part b), collected at 77 K, of activated Ti-MSA sample (black line), in interaction with ter-butyl hydroperoxide diluted in decane (blue line), in interaction with ter-butyl hydroperoxide diluted in water (orange line) and in interaction with H_2O_2/H_2O solution (yellow line). Adapted with permission from ref 866. Copyright 2004 Wiley-VCH.

compared with 0.91 for TS-1 (data obtained at the GILDA BM8 beamline at the ESRF, characterized by a better energy resolution, with respect to the data summarized in Table 8, Table 9 and Figure 15d). Upon dosing the *t*-butyl hydroperoxide in decane solution on Ti-MSA (blue curve in Figure 20a) a spectrum similar to that obtained on TS-1 contacted with anhydrous H_2O_2 is observed in both XANES and EXAFS regions (blue curve in Figure 19).[866] When the t-butyl hydroperoxide diluted in H_2O is dosed (orange curve in Figure 20a), the two features in the edge of the XANES spectrum typical of a η^2 side on peroxo complex start to be appreciable. Such features are much more evident if a H_2O_2/H_2O solution is dosed on Ti-MSA (yellow curve in Figure 20a), but such interaction causes an irreversible extraction of the Ti species from the siliceous matrix, as evidenced by the prominent elongation of the Ti−O first shell contribution (Figure 20b). This evidence explains, on the local ground, why mesoporous Ti-silicates are not suitable catalysts for the use in H_2O_2/H_2O solutions where the lost of a significant fraction of Ti species occurs. Conversely, the excellent catalytic properties of TS-1 under such conditions are paralleled by the reversible formation of the η^2 side on peroxo complex.

Summarizing, the in situ XANES and EXAFS studies, coupled with UV−vis DRS and resonant Raman experiments,[866,898] on hydrated and anhydrous peroxo/hydroperoxo complexes formed on crystalline microporous and amorphous mesoporous titanosilicates have evidenced, for the first time, the existence of an equilibrium between η^2 side-on peroxo species and η^1 end-on hydroperoxo complexes. The amount of water is the key factor in the equilibrium displacement. In this regard please note that, owing to the hydrophobic character of TS-1, substrates such as olefins are the dominant species in the channels. This fact assures a relatively low local concentration of water, which in turns guarantees a sufficient presence of the active η^1 end-on hydroperoxo complexes under working conditions.

3.2.5.3. Modeling of the Reactivity of [Ti(OSi)$_4$] Perfect Sites by an Ab Initio Periodic Approach: Comparison with EXAFS Results. The Ti-CHA model, previously discussed in section 3.2.4.2 (Figure 16), has been adopted by Bordiga et al.[886] to study H_2O_2 adsorption at Ti(IV) perfect site (Scheme 3a) by means of full ab initio periodic methods. The CRYSTAL code[934,935] has been employed to calculate energetic features and to optimize structures. In this case calculations have been performed at both restricted Hartree−Fock (RHF) and B3-LYP[936−938] levels of theory, adopting for Ti-CHA the same basis-set used in refs.[860,861,899] Atoms of the H_2O_2 molecule have been described by means of the same variational basis-set employed in refs 860, 861, and 899 to treat H_2O molecule. Ti-CHA model has been also used to study (at the same computational level and with the same code), the Ti−O−Si hydrolysis process to form Ti(IV)(−OOH) moiety.

Authors found that the formation of Ti(IV)/H_2O_2 molecular complex results in a weakly bonded species characterized by a Binding Energy, corrected by the basis set superimposition error, (ΔE) as low as 11.4 and 14.6 kJmol^{-1}, at the RHF and B3-LYP levels, respectively (Table 10). On the geometrical

Table 10. Geometric and Energetic Features of TiO_4Si_4 Moiety in Optimized Bare Ti-CHA (and of the Bare H_2O_2 Molecule) and Ti-CHA/H_2O_2 Complex Optimized at Both RHF and B3-LYP levels with CRYSTAL Code[934,935a]. Reproduced with permission from Ref.[886] Copyright 2007 the PCCP Owner Societies

	bare Ti−CHA and molecular H_2O_2		Ti−CHA/H_2O_2	
	RHF	B3-LYP	RHF	B3-LYP
Ti−O_F (Å)	1.790−1.801	1.790−1.801	1.788−1.827	1.782−1.842
⟨Ti−O_F−Si⟩ (deg)	150.2	150.5	149.2	137.8
Ti···CM (Å)	0.567	0.568	0.388	0.376
Ti···$O_{H_2O_2}$ (Å)			2.50/3.38	2.41/3.31
HO−OH (Å)	1.396	1.456	1.391	1.450
ΔE (kJ mol^{-1})			−11.4	−14.6

[a] In particular, shorter and longer distance, out of the four, Ti-framework oxygen bonds (Ti−O_F); average Ti−O_F−Si angle (⟨Ti−O_F−Si⟩); distance between Ti and CM (see Figure 16c, Ti···CM); shorter and longer distance between Ti and the two O atoms of the H_2O_2 molecule (see the two values reported for Ti···$O_{H_2O_2}$); interatomic O−O distance of the H_2O_2 molecule, either isolated or engaged, (HO−OH); formation energy of the adduct (ΔE), with respect of the bare CHA framework and isolated H_2O_2 molecule. This value has been corrected by the basis set superimposition error.

ground, the optimized complex has an end-on configuration characterized by a very long Ti···$O_{H_2O_2}$ distance of 2.50 (2.41) Å at the RHF (B3-LYP) level, Figure 21a. The perturbations of the local environment of Ti(IV) centers in Ti-CHA framework upon formation of such a molecularly adsorbed H_2O_2 molecules are comparable to those computed for the interaction of Ti(IV) with H_2O, NH_3, H_2CO, or CH_3CN (Table 7). This optimized structure was not compatible with the experimental evidence because the perturbation of the spectroscopic and structural features of such molecules (Figures 13b and 17) are much less important that those caused upon interaction with H_2O_2/H_2O solution (Figures 13a and Figure 18). Such a weakly bonded Ti···O_2H_2 complex is consequently totally unable to explain the remarkable spectroscopic XANES[866,872,898,919] (Figure 18a), UV−vis[872,913−919] (inset of Figure 18a), Raman[913,914] (inset of Figure 18b) as well as the

dx.doi.org/10.1021/cr2000898 | *Chem. Rev.* 2013, 113, 1736−1850

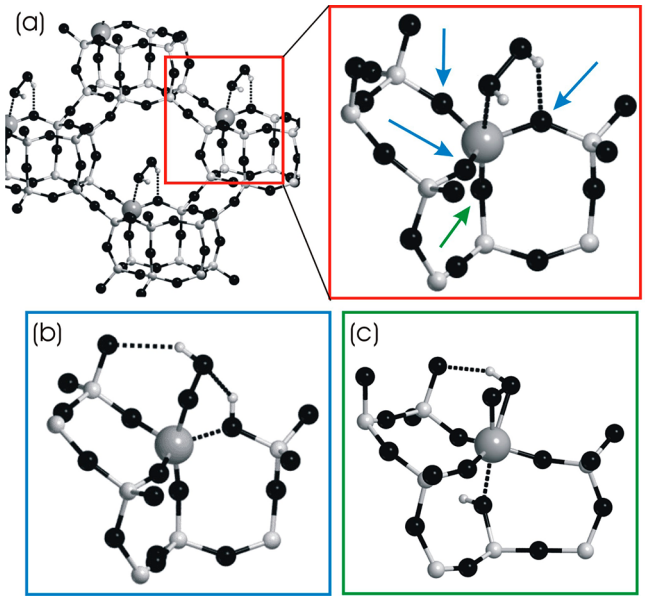

Figure 21. Part a: Optimized geometry obtained with the CRYSTAL code,[934,935] at the RHF level of theory, for the $[H_2O_2\cdots Ti(OSi)_4]$ molecular adduct formed inside the CHA framework. Left and right parts refer to two different magnifications. The definition of the 3 possible attacks on equatorial Ti−O−Si bridges (blue arrows almost equivalent) and of the attack on the unique apical Ti−O−Si bridge (green arrow) is also reported in the right part. Part b: Optimized geometry obtained with the CRYSTAL code,[934,935] at the RHF level of theory, for the $[-HO_2-Ti(OSi)_3\ ^+HOSi]$ complexes formed upon the rupture of an equatorial Ti−O−Si bridge. Part c: As in part b for the hydrolysis of the apical Ti−O−Si bridge. Reproduced with permission from ref 886. Copyright 2007 the PCCP Owner Societies.

structural (EXAFS,[59,764,866,872,913,919,924] Figure 18b) modification undergone by TS-1 upon interaction with H_2O_2/H_2O solution.

As the EXAFS data analysis, see Figure 18 and Table 9 in section 3.2.5.1, suggests the hydrolysis of a Ti−O−Si bond,[866,872,898,919] models of the hydrolyzed Ti-CHA/H_2O_2 system are probably more adequate to describe the nature of the Ti/H_2O_2 complex responsible of the yellow color of the catalyst than the simple molecular adsorption of H_2O_2 discussed above (Table 10 and Figure 21a). In this regard, it is worth noticing the work of the Royal Institution group reporting a hybrid QM/MM study of the processes of hydrolysis of Ti−O−Si linkages in Ti-substituted zeolites.[939] There are four Ti−O−Si bridges that can be potentially broken but, as described in Figure 16c, three of them (O_{eq}) are able to "see" the ligand molecule (L = H_2O_2) and are almost equivalent (see blue arrows in Figure 21a), while the fourth (O_{ap}) lies opposite to the adsorbed molecule (see green arrow in Figure 21a). Bordiga et al.[886] investigated the hydrolysis reaction $[H_2O_2\cdots Ti(OSi)_4] \rightarrow [-HO_2-Ti(OSi)_3\ ^+HOSi]$ with the CRYSTAL code,[934,935] at the RHF level of theory on both an equatorial and the apical oxygen atom. The optimized geometry are reported in parts b and c of Figure 21 and will be hereafter labeled as $HYDR_{eq}$ and $HYDR_{ap}$ systems, respectively. This theoretical study is aimed to reproduce the η^2 Ti hydroperoxo complex experimentally observed on TS-1 upon dosing anhydrous H_2O_2, see the first equilibrium in Scheme 6b and blue curves in the XANES and EXAFS spectra reported in Figure 19.

As can be seen from Figure 21b, in the optimized $HYDR_{eq}$ structure the Ti atom is only partially inserted in the chabazite framework, being one of the four starting Ti−O_F-Si moieties hydrolyzed. As reported in Table 11, the Ti−O_F distances of the three remaining Ti−O_F−Si moieties cover a range between 1.791 and 1.873 Å. Due to the framework constraints, the Si−OH moiety originated from hydrolysis remains quite near to the Ti atom and on the same plain of other two equatorial O_F atoms, being the OH−Si distance of 2.089 Å. One of the two O_{HO_2} atoms (the deprotonated one) of H_2O_2 molecule is now located at 1.941 Å from Ti, being the second (the protonated one) positioned at longer distance (2.78 Å), resulting in an end-on η^2 Ti hydroperoxo complex. A strong H-bond occurs between this second O_{HO_2} atom of the deprotonated hydrogen peroxide molecule and the silanol formed during the hydrolysis ($Si-OH\cdots O_{HO_2}$ = 1.745 Å, see Table 11). The O−OH bond is lengthened of 0.015 and 0.02 Å with respect to the bare H_2O_2 molecule and Ti-CHA/H_2O_2 complex, respectively. Moreover, the remaining H atom seems to point toward an oxygen atom belonging to a SiO_4 moiety adjacent to the Ti atom: the H···O_F distance is in this case of 2.34 Å, suggesting a very weak hydrogen-bond interaction.

The $HYDR_{eq}$ system is however very unlikely, because the hydrolysis of an equatorial Ti−O−Si bond has an energetic cost of +87.7 kJ mol^{-1}, computed with respect to the molecular adduct. Such reaction cannot occur at the mild working condition temperatures of TS-1 catalyst (below 373 K). Much less unfavored is the hydrolysis of the apical Ti−O−Si bond ($HYDR_{ap}$ system in Figure 21c), that has a cost of +26.7 kJ mol^{-1}, when computed at the RHF level of theory (Table 11). In the optimized $HYDR_{ap}$ the $[-HO_2-Ti(OSi)_3]$ moiety has a

Table 11. Geometric and Energetic Features of TiO_4Si_4 Moiety in the Optimized Ti···HO_2^- Complexes Formed in the CHA Framework upon the Rupture of an Equatorial ($HYDR_{eq}$) and of the Apical ($HYDR_{ap}$) Ti−O−Si Bridge at RHF Level with CRYSTAL Code.[934,935,a] Reproduced with permission from ref 886. Copyright 2007 the PCCP Owner Societies

system	$HYDR_{eq}$	$HYDR_{ap}$	
level of theory	RHF	RHF	B3-LYP
Ti−O_F (Å)	1.791−1.873	1.811−1.828	1.816−1.848
Ti···CM (Å)		0.411	0.378
Ti−O_{HO_2} (Å)	1.941	1.866	1.862
Ti···O_{HO_2} (Å)	2.780	2.200	2.180
O−OH (Å)	1.411	1.425	1.472
Ti···OH−Si (Å)	2.089	2.590	2.420
Si−OH···O_{HO_2} (Å)	1.745		
ΔE (kJ mol^{-1})	+87.7	+26.7	+3.4

[a]For the $HYDR_{ap}$ system calculations have been performed at the B3-LYP level also. In particular, distance between Ti and the oxygen of the silanol at the hydroxylated Ti−O−Si bond (Ti···OH-Si); distance of the hydrogen bond between the H atom of the HO_2^- moiety and the oxygen of the hydroxylated Ti−O−Si bond ($Si-OH\cdots O_{HO2}$), holding for the $HYDR_{eq}$ complex only; energy required to hydrolyze the Ti−O−Si bond (ΔE), calculated with respect to the molecular adduct described in Figure 21a and Table 10. Remaining features are reported as in Table 10, with the only exception of the oxygen atom of the hydrogen peroxide molecule, that has been labeled as O_{HO_2} owing to its deprotonated nature.

dx.doi.org/10.1021/cr2000898 | Chem. Rev. 2013, 113, 1736−1850

tripodal structure, the three Ti−O_F distances spanning a range between 1.811 and 1.828 Å. It is worth noticing that now the two Ti−O_{HO_2} distances are much closer: 1.862 (for the deprotonated O) and 2.199 Å (for the protonated O), suggesting that the interaction between Ti and the OOH^- moiety is increasing. The $HYDR_{ap}$ is potentially able to account for the strong modifications of the structural and spectroscopic features of TS-1 contacted with hydrogen peroxide.[59,764,866,872,898,913−919,924] The Ti···OH−Si distance passes from 2.089 Å in $HYDR_{eq}$ structure to 2.59 Å in $HYDR_{ap}$. The O−OH bond is lengthened of 0.014 Å with respect to O−OH bond in $HYDR_{eq}$ and of 0.029 Å with respect to HO−OH bond in bare optimized H_2O_2. Finally, the remaining H atom of OOH^- moiety is pointing toward an oxygen atom belonging to a SiO_4 moiety adjacent to the Ti atom: the H_{HO_2}···O_F distance is in this case of 2.28 Å, suggesting a very weak interaction.

Although the $[-HO_2-Ti(OSi)_3]$ moiety in $HYDR_{ap}$ structure seems to be more comparable with that expected from experimental observations[866,872,898,913,914,919] and with that obtained in other theoretical works,[895,897] however it would be reminded that $HYDR_{ap}$ is less stable with respect to the Ti-CHA/H_2O_2 molecular complex of 26.7 kJ mol^{-1}, which is still a great energy with respect to *kT*. However, because of the presence of H-bonds (as shown in Figure 21c), it should be underlined that DFT calculations based on B3-LYP Hamiltonian[936−938] give a better estimation of the energetic features of this process.[899] So more reliable energetic features of the hydrolysis reaction are obtained by DFT calculations. For this reason further calculations at B3-LYP level have been performed on the $HYDR_{ap}$ structure (Table 11). The optimized structure does not change significantly with respect to that optimized at the RHF level, consequently it will not be commented. The important point is that, using the B3-LYP Hamiltonian, the hydrolysis of the apical Ti−O−Si bond becomes almost iso-energetic, being its cost of +3.4 kJ mol^{-1} only. Authors concluded that the $[-HO_2-Ti(OSi)_3]$ moiety in $HYDR_{ap}$ structure is a reliable model of the η^2 Ti hydroperoxo complex experimentally observed on TS-1 upon dosing anhydrous H_2O_2,[886] see the first equilibrium in Scheme 6b and blue curves in the XANES and EXAFS spectra reported in Figure 19.

A final comment is devoted to the fact that most of the reactions catalyzed by TS-1 occur in water solutions.[706,913,919] For this reason Ti-CHA/H_2O_2 system investigated here in Figure 21 and in Tables 10 and 11 are unable to account for the η^2 side-on Ti peroxo complexes formed when TS-1 is contacted with H_2O_2/H_2O, see the first equilibrium in Scheme 6a and yellow curves in the XANES, EXAFS, UV−vis and Raman spectra reported in Figure 18. Added water molecules are expected to interact, via hydrogen-bonds formation, with the protons of both the hydroperoxo Ti-OOH^- moiety and the SiO-H moiety of the hydrolyzed Ti−O−Si bond. This will change completely the energetic balance of the hydrolysis reaction, due to the important role played by hydrogen-bonds.[856] In this case the adoption of the B3-LYP Hamiltonian is mandatory to have a correct description of the energetic features.

3.2.5.4. Modeling of the Reactivity of [Ti(OSi)$_4$] Perfect Sites by an Ab Initio Cluster Approach: Understanding the Effect of the Copresence of Water Molecules. Calculations on Ti-CHA/H_2O_2/nH_2O (n = 1 to 6) at B3-LYP level have been performed on a cluster representing a cage formed by 8 T centers mimicking a zeolite framework, Figure 22.[886] Note that in these cases the use of the periodic approach adopted for describing the anhydrous system is discouraged due to the much higher CPU demand. As done for the interaction of other molecules, the ONIOM approach has been used to limit the CPU demand.[857−860,898,899] In Figure 22, the sticks and balls versus the sticks notation discriminates the model zone (treated at high level) from the complementary part of the cluster treated at low level only. In all cases the model zone consists in $[^-HO_2-Ti(OSi)_3 + n\ H_2O]$.

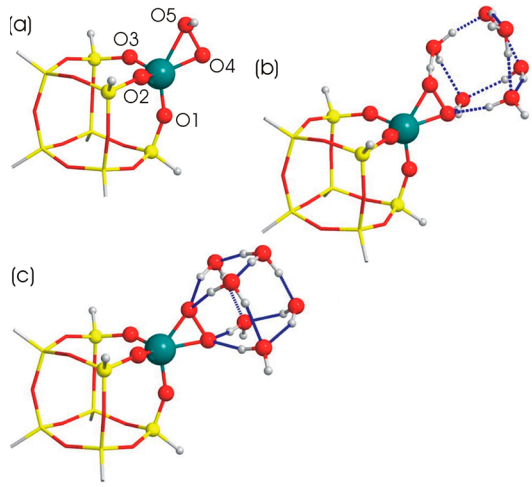

Figure 22. Part a: Optimized anhydrous $[^-HO_2-Ti(OSi)_3]$ cluster adopted for the calculation (B3-LYP/6-311+G(d,p) level) of the second deprotonation reaction of H_2O_2 on Ti(IV) sites, $[^-HO_2-Ti(OSi)_3 + 6\ H_2O] \rightarrow [^=O_2-Ti(OSi)_3 + 5\ H_2O + H_3O^+]$, to investigate the transformation of the end-on η^2 Ti hydroperoxo into the side-on η^2 Ti peroxo species (second equilibrium in Scheme 6b). The sticks and balls vs the sticks notation discriminates the model zone (treated at high level) from the complementary part of the cluster treated at low level only. Color code: green, Ti; red, O; yellow, Si; white, H; blue lines represents H-bonds. The five oxygen atoms in the first coordination shell of Ti(IV) have been labeled to allow the discrimination of the different Ti−O distances reported in Table 12. Part b: Optimized hydrated $[^-HO_2-Ti(OSi)_3 + 6\ H_2O]$ cluster. Part c: Optimized $[^=O_2-Ti(OSi)_3 + 5\ H_2O + H_3O^+]$ cluster. Reproduced with permission from ref 886. Copyright 2007 the PCCP Owner Societies.

For *n* = 1−6, Bordiga et al.[886] have investigated the energetic of the further deprotonation reaction of the $-HO_2-Ti(OSi)_3$ moiety, $[^-HO_2-Ti(OSi)_3 + n\ H_2O] \rightarrow [^=O_2-Ti(OSi)_3 + (n\text{-}1)\ H_2O + H_3O^+]$, to understand the transformation of the end-on η^2 Ti hydroperoxo into the side-on η^2 Ti peroxo species (second equilibrium in Scheme 6b). It has been found, that up to *n* = 5, the second deprotonation reaction of H_2O_2 on Ti(IV) sites is energetically disfavored and that the energy difference between the $[^=O_2-Ti(OSi)_3 + (n\text{-}1)\ H_2O + H_3O^+]$ products, and the $[^-HO_2-Ti(OSi)_3 + n\ H_2O]$ reactants progressively decreases upon increasing *n*. For *n* = 6, the $[^=O_2-Ti(OSi)_3]$ complex becomes more stable than the $[^-HO_2-Ti(OSi)_3]$ one. The optimized geometries of the hydroperoxo and peroxo species computed for *n* = 6 have been reported in parts b) and c) of Figure 22, respectively, while the most relevant bond distances are listed in Table 12. Also the geometrical features are in fair agreement with the experimental results. As already found with the periodic approach (Figure 21b,c and Table 11), the dehydrated $[^-HO_2-Ti(OSi)_3]$ cluster (Figure 22a) is an

dx.doi.org/10.1021/cr2000898 | *Chem. Rev.* 2013, 113, 1736−1850

Table 12. Optimized Distances for the Cluster Adopted for the Calculation of the Second Deprotonation Reaction of H_2O_2 on Ti(IV) Sites, $[^{-}HO_2{-}Ti(OSi)_3 + 6\ H_2O] \rightarrow [^{=}O_2{-}Ti(OSi)_3 + 5\ H_2O + H_3O^{+}]$, To Investigate the Transformation of the End-on η^2 Ti Hydroperoxo into the Side-on η^2 Ti Peroxo Species (Second Equilibrium in Scheme 6b).[a] Reproduced with Permission from Ref 886. Copyright 2007 Royal Society of Chemistry

cluster	Ti−O1 (Å)	Ti−O2 (Å)	Ti−O3 (Å)	Ti−O4 (Å)	Ti−O5 (Å)	O4−O5 (Å)
$[^{-}HO_2-Ti(OSi)_3]$	1.806	1.825	1.816	1.880	2.260	1.467
$[^{-}HO_2-Ti(OSi)_3 + 6H_2O]$	1.828	1.809	1.814	1.932	2.087	1.475
$[^{=}O_2-Ti(OSi)_3 + 5H_2O + H_3O^{+}]$	1.859	1.822	1.823	1.950	1.958	1.485

[a]See Figure 22a, b, and c for the optimized geometries of the three clusters and Figure 22a for the atom labeling. The O4−O5 bond of the bare H_2O_2 molecule is 1.454 Å at the B3-LYP/6-311+G(d,p) level used in these calculations.

end-on η^2 Ti hydroperoxo complex characterized by a large difference in the distances of the Ti centers and the two oxygen atoms of the OO^{-} moiety (Ti−O4 and Ti−O5 in Table 12), Δ_{Ti-O} = 0.380 Å. The average distance between Ti and the three framework oxygens, (O1, O2 and O3) is $\langle Ti-O_F \rangle$ = 1.816 Å. Addition of n = 6 water molecules (Figure 22b) slightly modifies the $\langle Ti-O_F \rangle$ value, now at 1.817 Å, but results in an end-on η^2 Ti hydroperoxo complex characterized by a less pronounced difference in the distances of the Ti centers and the two oxygen atoms of the OO^{-} moiety: Δ_{Ti-O} = 0.155 Å. The second deprotonation (Figure 22c) has a relevant effect on the cluster geometry, the $\langle Ti-O_F \rangle$ value is stretched at 1.835 Å and the peroxo structure results in a side-on η^2 complex characterized by two almost equivalent Ti−O4 and Ti−O5 distances (Table 12), that cannot be discriminated by EXAFS spectroscopy: Δ_{Ti-O} = 0.008 Å.

The ab initio data reported above represent an important theoretical support for the experimental evidence (XANES, EXAFS, UV−vis, and Raman, see Figure 18 and Table 9) concerning the key role played by water in determining the hydroperoxo/peroxo equilibrium in TS-1, see Scheme 6.

As a last open point it should be noticed that H_2O molecules could themselves be responsible of the hydrolysis process: this means that H_2O_2 molecule reacts principally with -TiOH moieties and not with Ti(IV) perfect site to give the final $HYDR_{ap}$ structure.

3.3. Fe- and Ga-Silicalite

3.3.1. Role of EXAFS in Understanding the Effect of Template Burning in Ga- and Fe-Substituted Silicalite. The stability of both Al and Ti as heteroatoms in the MFI framework is very high, allowing the ZSM-5 zeolite to work at high temperature and TS-1 in H_2O_2 aqueous solution. On the contrary, both Fe(III) and Ga(III) show, upon increasing the template burning temperature, an evident tendency to migrate from framework into extraframework positions in the form of small oxidic nanoaggregates trapped inside the zeolitic channels.[105,781,940] This progressive migration implies a reduction of the number of Brønsted acidic Si(OH)M(III) sites with a parallel increase of new isolated M^{3+} and clustered $M_iO_j^{x+}$ (M = Fe, Ga) acidic centers of Lewis nature. As already discussed in section 3.1, for both Fe- and Ga-MFI zeotypes, the copresence of framework and extraframework metal species has been proved to be interesting from a catalytic point of view. It is so evident that the role of postsynthesis treatments on the catalytic properties of both Fe- and Ga-MFI is of fundamental importance in the determination of the acidic, catalytic and shape-selective properties of the material, since it determines the ratio between framework and extra-framework metal species. Consequently, care must be made in comparing literature results concerning samples activated following different procedures.

Figure 23 summarizes the variation undergone by the EXAFS spectra (insets) and their corresponding k^3-weighted FT upon

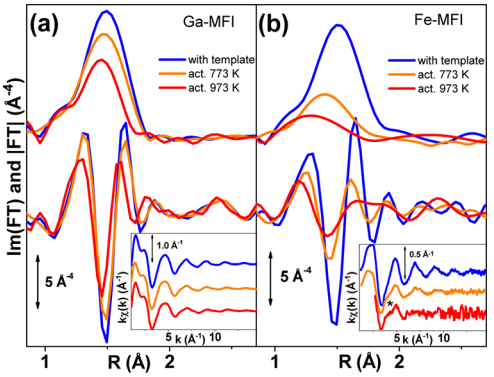

Figure 23. Effect of template removal at increasing temperature on the k^3-weighted, phase-uncorrected FTs of the EXAFS signal collected on Ga-MFI (Si/Ga = 25) and Fe-MFI (Fe/Si = 90) samples, parts a and b, respectively. Both moduli and imaginary parts (vertically downward shifted for clarity) have been reported. Blue, orange and red curves refer to the sample measured before calcination and after calcination at 773 and 973 K, respectively. In both parts, the insets report (according to the same code) $k\chi(k)$ functions. The star in the inset of part b highlights the beat in the 3.7−4.8 Å^{-1} interval, a weak evidence of the possible presence of as Fe−Fe contribution. Experimental data from refs 105, 106, 781, and 940.

template removal at increasing temperature on both Ga- and Fe-MFI systems, parts a and b, respectively. The most evident effect is the damping of the oscillation of the $k\chi(k)$ functions (most severe in the case of Fe-MFI, see insets) that implies a reduction of the intensity of the first shell peak of the corresponding |FT| and consequently a significant decrease of the first shell coordination number N optimized during the minimization routines (Table 13).

This phenomenon is due to the migration of Ga and Fe species to extraframework positions. The loss of signal is due to two main reasons. First, extraframework species are characterized by a high coordinative unsaturation, low N parameter in eq 19. Second, extraframework species are characterized by a high heterogeneity, implying a high σ^2_D factor in eq 20. When Fe (Ga) atoms occupy tetrahedral framework positions, they have a well-defined and ordered first shell environment, characterized by 4 oxygen ligands at a well-defined Fe−O (Ga−O) distance. This ordered situation gives rise to a constructive accumulation of the EXAFS signal coming from the different absorbing Fe (Ga) sites, yielding (within experimental errors) a Fe−O (Ga−O) coordination number of N = 4 (see Table 13). The situation is completely different when a fraction of Fe (Ga) atoms migrates into extraframework positions forming a complex variety of isolated and clustered species. Such heterogeneity implies that the local environment

dx.doi.org/10.1021/cr2000898 | Chem. Rev. 2013, 113, 1736−1850

Table 13. M-Substituted MFI Framework Materials (Column 1, M = Ga, Fe) and Their Activation Treatment (Column 2, with Template = No Treatment), and Results of the EXAFS Data Analysis for the Catalysts Measured in Different Conditions: Metal M Coordination Number (N), M−O Bond Length (R), and Debye−Waller Parameter (σ) (Columns 3−5)[a]

heteroatom M	activation T (K)	N	R (Å)	σ (Å)	f	ref
Ga	with template	4.2 ± 0.3	1.82 ± 0.01	(5 ± 1) × 10^{-2}	1.05 ± 0.08	940
Ga	773	3.4 ± 0.3	1.80 ± 0.01	(6 ± 1) × 10^{-2}	0.85 ± 0.08	940
Ga	973	2.5 ± 0.4	1.78 ± 0.02	(6 ± 2) × 10^{-2}	0.625 ± 0.10	940
Fe	with template	3.8 ± 0.4	1.86 ± 0.01	(4 ± 1) × 10^{-2}	0.95 ± 0.10	105
Fe	773	1.7 ± 0.3	1.82 ± 0.02	(6 ± 1) × 10^{-2}	0.42 ± 0.08	105
Fe	973	1.2 ± 0.3	1.81 ± 0.03	(6 ± 2) × 10^{-2}	0.30 ± 0.08	105

[a]As discussed in the text, the only meaningful values are those referred to the sample in presence of the template (black data); the remaining ones are biased by the fact that eq 19 is not valid for too disordered systems and should be replaced by eq 23. Column six reports the fraction of framework M (M = Ga, Fe) species as determined by the simplified model $f = N/4$. The error bars reported in column 6 have only a statistical meaning and do not include the systematic overestimation of f obtained with this method.

of Fe (Ga) atoms is characterized by a continuous spread in both Fe−O (Ga−O) bond distances, dynamic Debye−Waller factors and coordination numbers (please note that with O we mean oxygen atoms of both oxidic nanocluster and zeolitic framework sites). As a consequence, the EXAFS signal coming from extraframework Fe (Ga) species is affected by a so large Debye−Waller factor (of static origin, σ^2_D) to become practically undetectable[105,106,781,940] for high k values, because of the $\exp(-\sigma^2k^2)$ term in eq 19. In the high k region, the observed EXAFS oscillation are mainly due to the complementary fraction of Fe (Ga) atoms still occupying framework positions. Since all Fe (Ga) atoms contribute to the edge jump in the measured μd spectrum, and since the reported $\chi(k)$ functions are normalized to this jump, the dramatic decrease of the EXAFS signal is so qualitatively explained. A similar behavior has been observed for Ga(III) inserted in BEA framework.[941]

This simplified model has been used to estimate the fraction f of framework Fe (Ga) species as $f = N/4$ (see sixth column of Table 13), to be compared with results obtained from complementary techniques.[105,106,779,781,940] This model gives an overestimated f value because the complete elimination of the EXAFS oscillations holds only in the high k region, while at low k the phase difference between different Fe−O contributions is not resulting in a completely destructive interference. This is the reason why EXAFS analysis of the Fe-MFI activated at 973 K gave about 30% of framework Fe^{3+} species (Table 13), whereas IR spectroscopy, detected a nearly total erosion of the 3630 cm^{-1} absorption band due to Si(OH)Fe Brønsted groups.[779] The discrepancy between EXAFS and IR results can be explained by considering that intermediate situations probably occur between perfectly framework and totally extraframework Fe species. In fact, it is reasonable to suppose that the dislodgment from framework positions implies the progressive breaking of one of the four Fe−O−Si bridges. We can so consider partially extraframework Fe species having 3, 2 and even 1 bonds with framework oxygen atoms. None of such species do contribute to the IR band at 3630 cm^{-1}, but all of them are supposed to give a partial contribution to the EXAFS signal. A similar speculation can be done for the Ga-MFI system. The EXAFS data summarized in Table 13 can be qualitatively compared with IR data reported by Otero Areán et al.[107] and with the ^{71}Ga MAS NMR study reported by Bayense et al.,[942,943] both showing that a large fraction of Ga is removed from the framework of MFI-type gallosilicates upon steaming at 923 K. As a conclusion, although the f values reported in the sixth column of Table 13 do not have a fully quantitative character, they exhibit a reasonable and well-defined trend that qualitatively agrees with data obtained with independent techniques.

The apparent shortening of both the first shell Fe−O and Ga−O bond lengths in the samples treated at 773 and 973 K (Table 13, column 3) can also be explained in terms of structural disorder of extraframework Fe or Ga species. The effect of a large disorder is equivalent to that of a system having an asymmetrical radial distribution function, which can lead to an apparent contraction of bond length when the standard analysis of EXAFS data is performed.[532,533] In both cases, the cumulants method,[536,540] substituting eq 19 with eq 23, would be the correct approach to analyze these EXAFS data, see section 2.3.8.

3.3.2. Role of EXAFS in the Debate Concerning the Nuclearity of Extraframework Fe Species in Zeolites. Two different main preparation procedures are usually employed to disperse iron species inside the zeolite channels: (i) isomorphous insertion of Fe^{3+} into the zeolite framework during the synthesis and successive migration onto extraframework position as Fe^{2+} species[105,106,514,700−702,777,782,784−787,944] and (ii) postsynthesis insertion via ion exchange.[770,772,776,792,794−797,945−950] Until now we have discussed only samples prepared following route i. However, as the species active in catalysis are extraframework species, in this section we will discuss the role of EXAFS in the investigation of samples prepared following route ii.

Different catalytic mechanisms have been hypothesized so far to explain catalytic activity of Fe-zeolites.[951−956] Among them there is no general consensus even on the nature of the active iron site: isolated,[105,106,782,784−787,957] dinuclear[776,792,794,796,797,947,958] and polynuclear[783,788] Fe species have been put forward. The situation is complicated by the fact that the relative fraction of the three species in a given sample strongly depends on the preparation procedure, the iron content and the post synthesis treatments.

The determination of the nuclearity of the extraframework iron species in Fe-zeolites is obviously of fundamental relevance. Because of both its element selectivity and its local nature, EXAFS is in principle the technique of choice to discriminate among isolated, dimeric, and polymeric Fe species. However, severe reproducibility problems are present when looking to results coming from different laboratories. On a simple statistical ground, it is evident that dinuclear and aggregated iron species are more abundant at high iron loading, especially when postsynthesis methods are used. Conversely, Al containing Fe-ZSM-5 samples with low iron loading, and highly

dx.doi.org/10.1021/cr2000898 | Chem. Rev. 2013, 113, 1736−1850

active in selective oxidation reactions,[766,767,959] show mainly isolated extraframework Fe^{2+} species, mostly located in the vicinity of framework Al species.[784,789,955,957,960,961]

A careful look to the literature data results in the absence of an unified model to define the local structure of iron species hosted in zeolites. Figure 24 summarizes the different Fe−O, Fe−Fe, and Fe−Si/Al distances reported in the literature from EXAFS data and here plotted as a function of iron content (ordinate axis).[105,667,792,945,946,948−950,957,961−969]

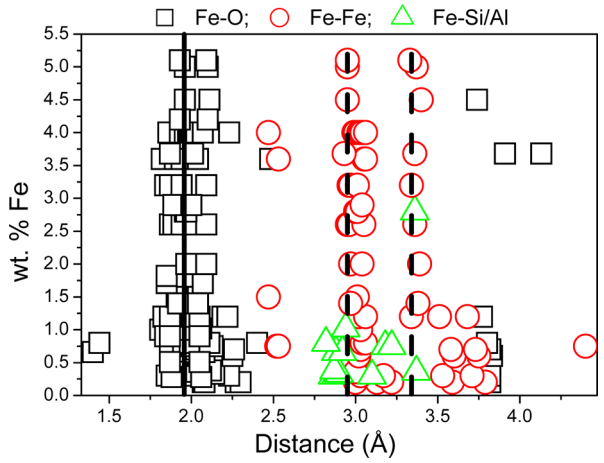

Figure 24. Summary of the diverse Fe−O (open square), Fe−Fe (open circle), and Fe−Si/Al (open triangle) distances found in the literature on the basis of the fit of EXAFS data obtained on different Fe-zeolites synthesized and treated in different ways. Distances are reported as a function of iron content. Full and dashed vertical lines indicate average Fe−O and Fe−Fe distances, respectively, obtained from XRD refinement of α-Fe_2O_3 (1.95, 2.96, and 3.34 Å). Reported data have been collected from refs 105, 667, 702, 792, 945, 946, 948−950, 957, and 961−969 This figure represents an updated version of that published in ref 956.

The results are heavily scattered: in particular, at low iron concentration (from 0.2 to 1.0 wt %), the Fe−O distances are found in the 1.78−2.40 Å range, a spread much higher than the typical accuracy of bond length distance detected by EXAFS (±0.01 or ±0.02 Å). Concerning other distances measured in EXAFS experiments, most of the Fe−Fe distances in iron containing MFI appear centered close to the values expected in of α-Fe_2O_3 (see the two vertical dashed lines in Figure 24). It is well-known that clustered iron species contribute to the FT of the EXAFS function with signals between 2 and 4 Å in the FT. By fitting the EXAFS contribution in the 2−4 Å interval with a Fe−Fe model one could in principle obtain the average Fe−Fe coordination number (N_{Fe-Fe}).[945,946,950] Unfortunately, the relationship between such N_{Fe-Fe} value and the average Fe nuclearity is far to be straightforward, because complexity is introduced by the heterogeneity of extraframework species (see above section 3.3.1). As a consequence, an average Fe−Fe coordination number of, for example, N_{Fe-Fe} = 1.0 could be interpreted as 100% of dimers, as 50% of isolated monomers and 50% of trimers (having two Fe neighbors) or as 67% of isolated monomers and 33% of tetramers, and so on. The situation is even more complex, because the 2−4 Å interval is the region where also the backscattering of framework atoms (Al or Si) is potentially expected. Consequently, the Fe−Fe contributions are superimposed to those of Fe−Si/Al in the 2.80 to 3.20 Å range. The large variability of both Fe−O and Fe−Fe distances can be explained by two main reasons. (1) the Fe-zeolites investigated by different groups might be significantly different, since the final form of Fe species is strongly affected by the preparation procedure. (2) Notwithstanding the fact that the accuracy of a first shell distance determination is in principle as good as ±0.01 or ±0.02 Å, these error bars are statistical and systematic errors are not accounted for. In the specific case of Fe-zeolites systematic errors may have a double origin. Usually phase-shifts and amplitude functions, which are crucial in determining bond distances and coordination numbers, are theoretically generated from a guessed cluster. As the actual geometry of the active Fe species is a priori unknown, phases and amplitudes generated in that way can be questionable. The second source of possible systematic errors is the assumption of a Gaussian distribution of distances, which is done in the standard EXAFS formula, eq 19, usually used in most of the cited papers. It is well-known that in systems characterized by a high degree of heterogeneity, like liquids or amorphous systems, this assumption is no longer valid. In such cases, EXAFS data should be analyzed according to the cumulant approach, so using eq 23, as discussed in section 2.3.8.

A few results among those shown in Figure 24 in the figure merit a specific comment. In particular, the Fe−O distance at about 1.4 Å found by Choi et al. on oxidized samples could be consistent with the formation of Fe(IV)═O species.[957,961] Moreover, we think that some of the distances centered at about 2.5 Å, ascribed to Fe−Fe scattering and used to argue for the presence of di-iron-oxo species, may be due to Fe−Cl groups on samples prepared from $FeCl_3$ exchanged systems. In this regard, the group of Bell[957] gave a different explanation. Authors showed that the peak at 2.5 Å, was not due to Fe−Fe contributions, but was actually due to Fe−Al contributions. Authors were able to support this thesis by arguing that (i) the imaginary part of the peak has the same characteristics as that generated theoretically for Fe−Al backscattering, whereas it differs distinctly from that generated theoretically for Fe−Fe backscattering; and (ii) the structure of the peak, measured for different samples, does not change significantly with Fe/Al ratio and was unaffected by sample treatment. They concluded that the iron in Fe-ZSM-5 is present as isolated cations associated with framework aluminum.[957] In this regard, two contributions from the group of Grünert[945,950] are worth of note. In the former,[945] the authors found a significant discrepancy between Fe nuclearity derived from EXAFS, TPR, and Mössbauer spectroscopies. Analogously, in their successive work[950] an apparent discrepancy between the results of UV−vis and the EXAFS analysis has been evidenced. The former indicated the almost exclusive presence of isolated Fe sites, whereas the latter suggested clusters of a few Fe atoms. The high N_{Fe-Fe} suggested from EXAFS may be the result of backscattering by framework Si or Al atoms being attributed to Fe. The important message coming from the works of Grünert et al. is that the use of other independent characterization techniques is important to minimize the risk of misinterpretation of the EXAFS results. We can just agree with their warning.

We conclude this section by mentioning the XMCD study (see section 2.5.1) of different Fe-ZSM-5 catalyst by Heijboer et al.[212,667] The authors showed that, in addition to the spectral shape analysis that can provide the local symmetry and bonding, the XMCD spectrum gave extra information that was very important in that case. Indeed, the XMCD signal is provided by all aligned magnetic moments in a certain system.

dx.doi.org/10.1021/cr2000898 | Chem. Rev. 2013, 113, 1736−1850

Assuming a paramagnetic system of isolated moments, full magnetization can be obtained. In contrast binuclear Fe(III) centers will couple antiferromagnetically, which thereby cancels its MCD effect. Also iron-oxide particles will be antiferromagnetic (or weakly ferrimagnetic). Consequently, the magnitude of the XMCD effect can be directly related to the amount of isolated iron species. To be quantitative, small corrections were applied to account for the partial magnetization of small iron-oxide particles. In this way, they were able to estimate the fraction of isolated vs clustered Fe species, as well as the fraction of Fe(III) and Fe(II), as usually done with XANES.[212,667]

3.3.3. Fe-Substituted Silicalite: What Has Been Learnt from XANES. The interpretation of the XANES spectra of Fe-zeolites has been less critical and more informative than that of the EXAFS spectra. Figure 25 reports the effect of template burning in air and successive activation in vacuo at increasing temperature on the XANES features of a Fe-MFI sample. The most evident variation is the red-shift of the edge position, which moves from 7123.6 eV for the sample measured with template (blue line) to 7122.4 and 7120.6 eV for the samples activated at 773 (orange line) and 973 (red line) K, respectively. An even larger shift was observed when the activation was done at 1073 K (gray curve in Figure 25). These data provide an evidence that Fe in the as prepared sample is present in form of Fe^{3+} species. After the thermal activation ferric species undergo a progressive reduction to Fe^{2+} ones.

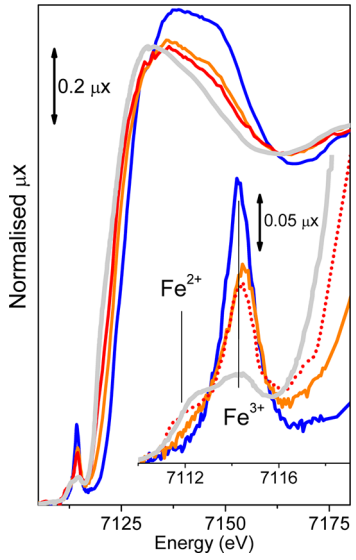

Figure 25. XANES spectra of Fe-MFI (Si/Al = 90) with template (blue line), and activated at 773 K (orange line), and 973 K (red line). The gray spectrum corresponds to a different Fe-MFI sample (Si/Al = 68) activated at 1073 K. The inset reports the magnification of the pre-edge peak. Vertical lines represent the typical position for the pre-edge features of Fe^{2+} and Fe^{3+} species. The figure contains the experimental data published in refs 105 and 106.

Besides the changes in the edge region, also the pre-edge features of the XANES spectra are affected by the thermal treatment. The spectrum of the as prepared sample is characterized by a strong and sharp 1s → 3pd pre-edge peak around 7114.2 eV (better visible in the inset), whose intensity is even higher than that of $FePO_4$ model compound (0.205 vs 0.133), indicating that the local symmetry of Fe^{3+}, in the MFI framework, is closer to the ideal T_d than the Fe sites in $FePO_4$.[105,106,702,944] This is because, in presence of the template, Fe species are characterized by 4 equivalent Fe−O bonds at 1.86 Å, while for ferric phosphate two distinct pairs of Fe−O bonds at 1.82 and at 1.87 Å are present.[970] Successive thermal treatment causes a consistent decrease of the 1s → 3pd peak intensity simultaneously, a low energy shoulder in the 1s → 3pd resonance progressively increases in intensity upon increasing activation temperature. The energy position of this new component (around 7111.8 eV) is close to that observed for the $FeCp_2$ model compound (7112.5 eV).[105,106] However, the higher full-width indicates the presence of more than one Fe^{2+} species, in agreement with the high heterogeneity of extraframework Fe species previously discussed in section 3.3.1. As a conclusion, the XANES results shown in Figure 25 demonstrate that in the in situ activated sample a significant fraction of iron species migrated from framework tetrahedral position into extra lattice Fe^{2+} species. A similar behavior has been observed by removing the template in the Fe-MCM-22 system.[786,787] Completely different results were obtained by Joyner and Stockenhuber,[964] who used XANES spectroscopy to investigate the oxidation state of iron in ion-exchanged Fe-ZSM-5 samples where only Fe^{3+} species have been detected. This fact underlines the importance of the preparation method in affecting the Fe species present in the catalyst.

Finally also the white line (first resonance after the edge) of the XANES spectra reported in Figure 25 is very informative, because its intensity basically reflects the coordination of the absorbing atom. The sample with template shows a white line intensity similar to that of $FePO_4$ (1.31 vs 1.35), much lower than that observed for 6-fold coordinated model compounds (from 1.52 to 1.60), reflecting the 4-fold coordination of iron in the as prepared sample.[105,106] Migration of Fe^{3+} to extraframework positions causes a progressive decrease of the white line intensity: from 1.23 to 1.20 for samples activated at 773 and 973 K, respectively (Figure 25). This further decrease of the white line intensity argues against the presence of a considerable fraction of iron species in aggregated clusters and suggests the dominating presence of isolated Fe species exhibiting a high coordinative unsaturation.[105,106] This picture has been strongly supported by IR data of adsorbed NO published in different contributions.[105,106,782,784,872,944]

3.3.4. Reactivity of Extraframework Fe Species Hosted in the MFI Channels toward N_2O and NO. *3.3.4.1. Reactivity toward N_2O.* On one hand, N_2O is the oxidative agent in the benzene to phenol reaction catalyzed by Fe-MFI,[766,767] on the other hand, Fe-zeolites are able to convert N_2O into oxygen and nitrogen molecules. Consequently, the interaction of N_2O in Fe-zeolites has been widely investigated with several experimental techniques like UV−vis/DRS, IR, Raman, N_2 physisorption, XRD, TEM, solid state NMR, ab initio calculations and catalytic tests.[787,956,971−980] It is thought that the reactivity toward N_2O of iron in zeolites in many oxidation reactions proceeds via the initial deposition of one oxygen atom per iron atom (the famous "α-oxygen").[766,981−983]

In this regard also XAFS techniques have played an important role.[105,106,786,787,789,948,949] Figure 26a reports the XANES spectra of a Fe-silicalite sample previously activated at 1073 K (blue line) and after interaction of N_2O at 523 K (red line). The blue shift of the edge position, the changes in the intensities of the pre-edge components (see inset), and the increased intensity of the white line testify that the extraframework Fe^{2+} species, generated during activation, are reoxidized by N_2O to Fe^{3+}.[105,106,787]

dx.doi.org/10.1021/cr2000898 | Chem. Rev. 2013, 113, 1736−1850

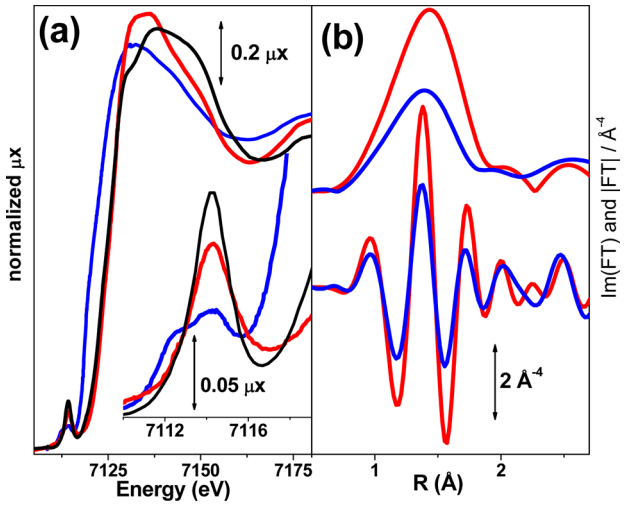

Figure 26. Part a: XANES spectra of Fe-silicalite activated at 1073 K (blue line), and subsequent oxidation with N_2O at 523 K (red line). For comparison also the spectrum of the sample with template (i.e., of Fe^{3+} in T_d symmetry) is reported as black curve. The inset shows the magnification of the pre-edge peaks. Part (b): k^3-weighted, phase uncorrected, FT of the EXAFS spectra of Fe-silicalite activated at 1073 K (blue curve), and after subsequent oxidation with N_2O at 523 K (red curve). Top and bottom curves refer to the moduli and the imaginary parts, respectively. Adapted with permission from ref 787. Copyright 2005 American Chemical Society.

By comparing the spectrum of the N_2O oxidized sample (red line) with that of the sample with template (black line, see discussion in section 3.3.3), the following observations can be drawn. The edge positions of the two spectra are found at the same energy and the same holds, within experimental uncertainty, for the maximum of the pre-edge peak at 7114.3 eV (see inset in Figure 26a). However, the shape of the XANES spectrum of the N_2O oxidized sample is significantly different, the intensity of the pre-edge peak does not reach the initial value and the fwhm is increased, see inset in Figure 26a. This is in agreement with the reoxidation of the previously reduced species but definitely excludes the reintroduction of iron in the framework. Notice that EXAFS data indicate an increase in the average coordination number of Fe sites after the N_2O oxidation, as evident in Figure 26b, where the intensity of the first shell contribution significantly increases. This suggests the presence of chemically adsorbed oxygen, coming from N_2O decomposition,[105,106,787] in agreement with the observations of Panov group on α-oxygen formation.[766,981,982]

3.3.4.2. Reactivity toward NO. The selective catalytic reduction (SCR) of NO by ammonia and hydrocarbons, observed in Fe-zeolites,[768,769,956,984−987] is of considerable practical importance to eliminate NO from traffic exhausts and is supposed to be catalyzed by the same sites active toward N_2O. For this reason, the interaction of NO with iron species in Fe zeolites has been widely investigated, particularly with FTIR. IR experiments evidenced that NO is a useful probe molecule to investigate the accessibility and coordinative unsaturation of extraframework iron ions. In fact, depending on the local environment, extraframework Fe^{3+} species can add up to 3 NO molecules, generating a mixture of $Fe^{3+}(NO)$, $Fe^{2+}(NO)$, $Fe^{2+}(NO)_2$, and $Fe^{2+}(NO)_3$ complexes,[105,106,782,784−787,790,944,956,988−990] which are completely desorbed upon outgassing at 573 K.

The interaction between Fe sites in activated Fe-silicalite and NO molecules has also been investigated by XANES spectroscopy.[787] As an example, Figure 27 shows that the dosage of NO

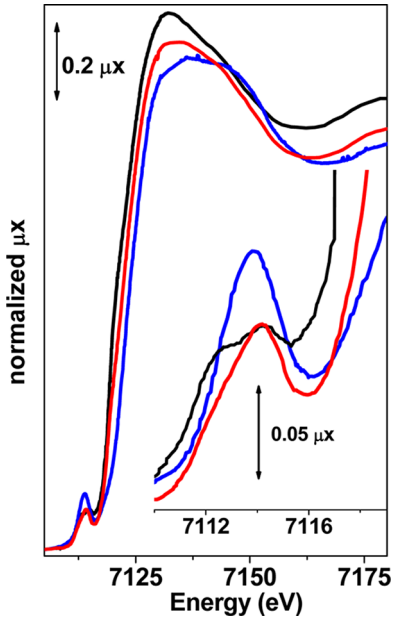

Figure 27. XANES spectra of Fe-silicalite after activation at 1073 K (black line), after dosage of 20 Torr of NO at room temperature (red line), and subsequent outgassing at 573 K (blue line). The inset shows the magnification of the pre-edge peaks. Adapted with permission from ref 787. Copyright 2005 American Chemical Society.

on the Fe-silicalite sample previously activated at 1073 K (black line) causes an important modification of the XANES spectrum (red line). Apparently, this change is roughly similar to what observed after oxidation with N_2O (see Figure 26). In particular, a definite blue shift of the edge position to higher energy can be appreciated, passing from 7119.5 to 7123.0 eV. Simultaneously, in the pre-edge region, the peak at 7112.3 eV is eroded in favor of a major peak at 7113.9 eV (see inset in Figure 27). However, at a more careful look it can be noticed that the position of the pre-edge peak (7113.9 eV) does not exactly correspond to that of the sample oxidized by N_2O (7114.3 eV, see inset in Figure 26a), which in turn closely matched the position of the sample with template (see section 3.3.3). Additionally, the peak resulting by NO adsorption is sensibly broader. The NO desorption at 573 K (red curve in Figure 27) causes the partial erosion and a small blue-shift of the major pre-edge peak, which is now found at 7114.2 eV. Notwithstanding the asymmetry of the peak, the shoulder at 7112.3 eV is far from being restored, its intensity being now 0.067 (and not 0.098). Furthermore, also the edge position is not totally restored after NO outgassing.

The edge shift and the pre-edge modifications caused by NO interaction suggest a formal oxidation of Fe^{2+}, previously reduced by thermal activation (vide supra), to Fe^{3+}; however, the oxidized Fe^{3+} species are different from those obtained upon N_2O oxidation. This was explained by the formation of complexes, characterized by a strong metal to ligands charge transfer, which can be formalized as $Fe^{3+}(NO^-)$. This in turn would imply, on the basis of the simple molecular orbital theory, a bent NO geometry.[991] The broad character of the pre-edge peak obtained by NO adsorption can be explained in

dx.doi.org/10.1021/cr2000898 | Chem. Rev. 2013, 113, 1736−1850

terms of the simultaneous presence of different nitrosyl complexes, in agreement with the complex IR spectroscopy described in literature.[106,988,989] Upon NO desorption at 573 K, the XANES spectrum of the activated sample is not totally restored (blue line in Figure 27). The combination of XANES and FTIR results implies that the interaction of NO irreversibly modified the iron sites.

3.3.5. New Frontiers of XAS/XES Techniques Applied to the Characterization of Fe-Zeolites. In the years 2003−2005, several innovative techniques have been applied to the characterization of Fe-zeolites, mainly by the Utrecht group.[211,212,309,310,667,992] In particular, three techniques will be discussed in the following subsections.

3.3.5.1. Soft X-ray Absorption Spectroscopy on Fe L-Edges. Soft X-ray absorption spectroscopy on valence metal edges is a technique largely employed by the community of solid-state physicists.[29,47,193,993] On one hand, it allows low Z atoms to be measured,[993,994] on the other hand, when applied to high Z atoms, it is intrinsically more sensitive to the atomic local environment than core-edges spectroscopy (EXAFS). It is also one of the main techniques in the field of surface science: because of the much smaller probing depth, soft X-rays are much more surface selective than hard X-rays, see eq 10 and Figure 3a. In the field of heterogeneous catalysis, it has been little used, partly because of the difficulty of in situ measurements,[291,293] see section 2.2.6.

The soft X-ray absorption experiments performed at the Fe L-edges on different Fe-zeolites[212,309,310,667] need particular experimental setup to overcome the severe absorption problems at so low photon energy (700−750 eV). Figure 28a shows the Fe L_3-edge spectra measured on a Fe-ZSM-5 overexchanged sample (Si/Al = 17; 4.4 wt.% Fe) prepared by $FeCl_3$ sublimation at 603 K and successively subjected to a mild calcination treatment.[667] The solid spectrum is obtained on the sample oxidized at 623 K in a 5% O_2-95% He flux, while the dotted spectrum concerns a sample thermally autoreduced at 623 K in a 100% He flux. The authors also measured the O K-edge spectra (around 0.5 keV) concluding that the thermal autoreduction process is accompanied by a loss of molecular oxygen and water.[309] Comparing the two spectra, a clear shift of the white line from 708.0 to 709.5 eV is observed by passing from the autoreduced to the O_2-oxidized sample. From comparison with the iron-oxide model compounds (see Figure 28b) and according to charge transfer multiplet calculations, Heijboer et al.[309,667] concluded that the two spectra measured on Fe-ZSM-5 relate to pure Fe^{3+} (full line) and Fe^{2+} (dotted line) species, respectively. The calculations showed that the Fe^{3+} site exhibits an octahedral symmetry with a crystal field of ~1.0 eV. This is less than the crystal field of 1.5 eV calculated for Fe_2O_3, indicating weaker iron−oxygen bonds in the zeolite than in the oxide phase. The Fe^{2+} site is in a tetrahedral-like geometry with a crystal field of −1.0 eV, which is similar to that calculated for the bulk oxide $FeAl_2O_4$. The Fe L_3-edges XANES spectra thus show a transformation from 6-fold Fe^{3+} under oxidized conditions to 4-fold Fe^{2+} after thermal reduction.[309,667]

Comparison between Utrecht's results (reviewed in this section) and Torino's results (reviewed in the previous sections) is not straightforward because of the different way of introducing Fe inside the zeolite. Torino's data show that Fe-MFI prepared following the hydrothermal method exhibits Fe^{3+} species in tetrahedral-like environment, occupying framework [TO_4] sites (Figure 25). Notwithstanding the difference of the local symmetry of Fe^{3+} species in the two materials, the thermal

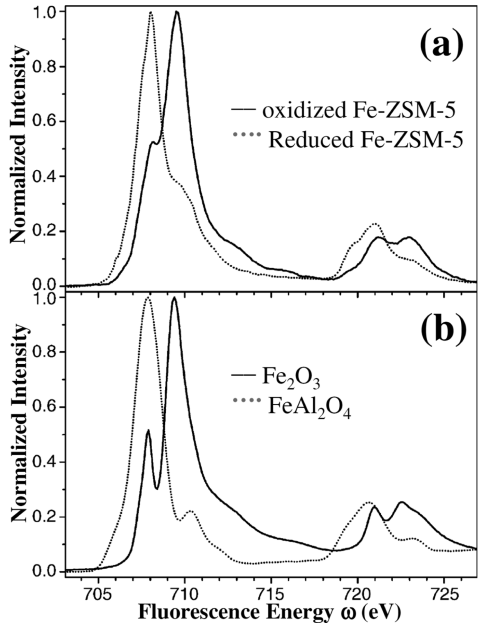

Figure 28. Part a: Fe L_3-edge spectra of Fe-ZSM-5 oxidized at 623 K in a 5% O_2-95% He flux (solid line) and autoreduced at 623 K in 100% He flux (dotted line). The sample is an overexchanged Fe-ZSM-5 (Si/Al = 17; 4.4 wt.% Fe) obtained by $FeCl_3$ sublimation at 603 K and successively subjected to a mild calcination treatment (i.e., slow heating to 473 K in He and after addition of O_2 continuing to 823 K). Part b: Fe L_3-edge spectra of Fe_2O_3 (solid line) and $FeAl_2O_4$ (dotted line) model compounds. Note that in this case the normalization of the spectra to 1.0 has been made on the white line and not on the edge jump as done for all the other near edge spectra reported in this review. Adapted with permission from ref 667. Copyright 2005 Elsevier.

treatment results in both cases to the autoreduction of Fe^{3+} to Fe^{2+} species (compare Figure 28 with Figure 25). Finally, note that Heijboer et al.[309,667] used O_2 as oxidative agent, while Torino's group used N_2O (Figure 26).[105,106]

3.3.5.2. Fe Kα- and Kβ-Detected X-ray Absorption Spectroscopy. The valence and local symmetry of iron in framework-substituted Fe-ZSM-5 with a high Fe dilution (Si/Fe = 360) has been studied by Heijboer et al.[211,212] using Kβ-detected X-ray absorption spectroscopy (see sections 2.2.4 and 2.2.5). This technique combines high-resolution ($\Delta E \approx 1$ eV) fluorescence detection of the 3p → 1s (Kβ) transition with the XANES at the Fe K-edge (see Scheme 1 and Figures 5 and 6a).[223,224] An absorption-like spectrum is recorded by fixing the secondary monochromator at the energy ω of the Kβ transition detecting the K_β fluorescence intensity as a function of the incident energy Ω that is scanned through the Fe K absorption edge (see Figures 5, 6a, and 29a). As already discussed for the XANES spectra of TS-1 (Figure 13c), Kβ-detected XANES spectra allow a more precise separation of the weak K pre-edge structure from the main edge as compared to conventional absorption spectroscopy edge (Figure 29b). Subsequent analysis and interpretation of the pre-edge spectral features, therefore, is more accurate,[199,217,222−225] see section 2.2.5.

Using this technique Heijboer et al.[211,212] have been able to quantitatively determine the degree of iron extracted from the zeolite framework upon steaming (a sample prepared following the hydrothermal method has been used in this experiment). TThe use of appropriate reference compounds allows the systematic study of the pre-edge features of the Kβ-detected

dx.doi.org/10.1021/cr2000898 | Chem. Rev. 2013, 113, 1736−1850

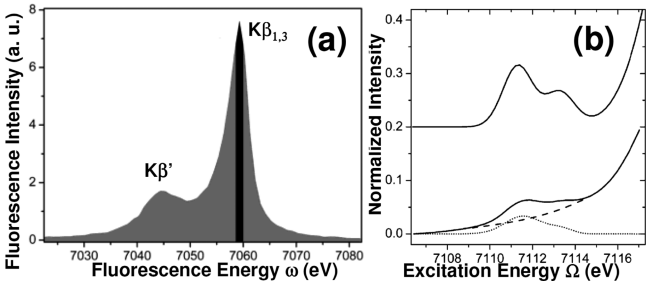

Figure 29. Part a: The integrated intensity given by the black energy window of ~1.0 eV is selected out of the overall Fe 3p → 1s X-ray fluorescence emission (gray), which is emitted upon core hole relaxation after 1s electron excitation. Part b: Comparison between the conventional fluorescence XANES spectrum of the Fe_2SiO_4 (fayalite, Fe^{2+}, O_h) model compound (bottom) and the corresponding Kβ-detected XANES spectrum (top). When conventional XANES spectroscopy is used, the "true" pre edge future (bottom dotted curve) is obtained after subtraction from the experimental spectrum (bottom full line) of the background function (dashed curve, a cubic spline function in this case). No background subtraction is conversely needed for Kβ-detected XANES spectrum (top). Adapted with permission from ref 211. Copyright 2006 American Chemical Society.

XANES spectra of framework-substituted Fe-ZSM-5, also in the case of a low iron loading (0.3 wt % Fe). Template removal and calcination cause a distortion of the zeolite framework and induce a deviation from T_d symmetry of the iron incorporated during the synthesis, reflecting their migration to extraframework positions. These results, obtained on better resolved spectra, fully confirm the results of Torino's group obtained with conventional X-ray absorption technique,[105,106] see Figure 25. Heijboer et al.[211,212] also investigated the effect of steaming by performing the high temperature treatments (>773 K) in presence of water. According to the Ferretti's results[783] they found that water facilitates the hydrolysis of the Si−O−Fe bonds and increases the formation of extraframework iron species.

3.3.5.3. Resonant Inelastic X-ray Scattering (RIXS) Spectroscopy. We conclude this section by briefly recalling that 1s → 2p resonant inelastic X-ray scattering (RIXS) spectroscopy[193,194,198,199,217,218] has been measured by de Groot et al.[992] for a series of iron oxides, including octahedral and tetrahedral Fe^{2+} and Fe^{3+} systems. As already discussed in section 2.2.4 and 2.2.5 (Figure 5), RIXS data are represented in terms of a bidimensional spectrum, where not only the usual beamline monochromator is scanned through the Fe K-edge (Ω axis in Figure 29b) but also the analyzer crystal collecting the fluorescence emitted from the sample are scanned through the Fe Kα- and Kβ-edges (ω axis in Figure 29a). The data are usually reported in a excitation/disexcitation (K-edge/L-edge) plane as contour plots or with color scales (see the inset in Figure 13c and vide infra Figure 39a,b for RIXS spectra collected on other systems). Authors used crystal-field multiplet simulations to analyze the RIXS spectral shapes of octahedral and tetrahedral Fe(II) and Fe(III) systems. The RIXS planes and the K-edge and L-edge X-ray absorption spectra related to these RIXS planes have been discussed with respect to their analytical opportunities. It is concluded that the full power and possibilities of 1s → 2p RIXS needs an overall resolution of 0.3 eV. The authors foresaw that RIXS will become a technique with more detailed information than combined conventional K-edge and L-edge X-ray absorption, with the additional advantage to be obtained in a single experiment, thus avoiding any reproducibility problem.[992] Another major advantage is that 1s → 2p RIXS involves only hard X-rays, and experiments under essentially any conditions of pressure and on any system are feasible. This last point represents a great advantage when the reactivity of surface species is the topic of the investigation, such as in the study of catalysts in working conditions.

Pirngruber et al.[213] applied the RIXS technique to a Fe-ZSM-5 catalyst during reaction with N_2O. As no $3d^4$ configuration was detected the authors concluded that formation of Fe(IV) on Fe-ZSM-5 upon reaction with N_2O can be ruled out.

3.4. B-CHA

3.4.1. Template Burning in B-SSZ-13 an example of low energy XAFS. B K-edge XANES spectra of B-SSZ-13 in presence of template (red curve), after calcination (orange curve) and after interaction with NH_3 at 373 K (blue curve) are reported in Figure 30. The as prepared B-SSZ-13 exhibits

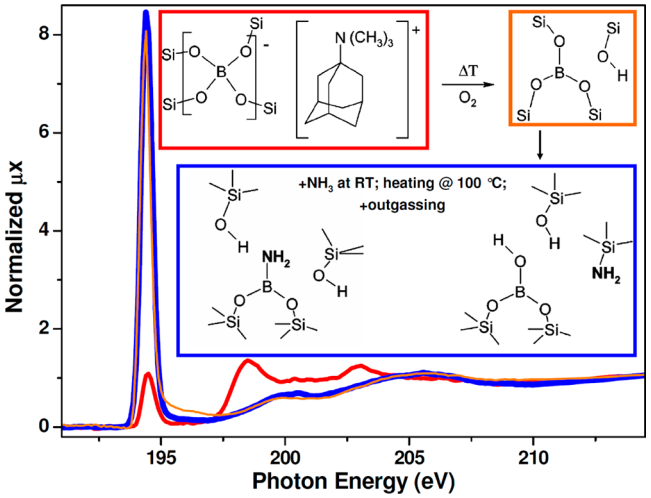

Figure 30. Normalized B K-edge NEXAFS spectra of B-SSZ-13 in presence of template (red curve), after calcination (orange curve) and after interaction with NH_3 at 373 K and successive evacuation (blue curve). Insets are used to reproduce the B species responsible for the XANES spectra reported in the main part (same color code). Adapted with permission from ref 995. Copyright 2007 American Chemical Society.

$[B(OSi)_4]$ units in T_d-like geometry (sp^3-hybridized B atoms) while, upon template burning, the break of a B−O−Si bond results in $[B(OSi)_3]$ units in D_{3h}-like geometry (sp^2-hybridized B atoms), fully confirming a parallel IR study.[815,995] This reaction scheme is depicted in the insets in Figure 30: evolution from the red to the orange one.

Indeed, the spectrum collected in presence of template is characterized by three main components at 194.4, 198.5, and 203.0 eV, whose intensities are 1.0, 1.4, and 1.3, respectively. The components at 198.5 and 203.0 eV were assigned to B in sp^3 hybridization on the basis of comparison with the spectra observed in the BO_4 tetrahedral units of bulk BPO_4,[996] in bulk c-BN,[997] and in amorphous B−P-silicate[998], where the presence of P forces B atoms in the tetrahedral coordination. In B-SSZ-13 the relatively broad nature of these bands was attributed by Regli et al.[995] to a distortion of BO_4 tetrahedra that results in the loss of the degeneracy of $\sigma^*(t_2)$ orbitals and a consequent broadening of the transitions. In particular, the component at 198.5 eV was assigned to transition from B(1s) state to antibonding (σ^*) states (T_2 and A_1 symmetry) of tetrahedral

dx.doi.org/10.1021/cr2000898 | Chem. Rev. 2013, 113, 1736−1850

BO_4 groups. Finally, the feature at 194.4 eV, was attributed to the B 1s → π^* resonance, which is associated with sp^2 hybridization and planar bonding.[997−999] It is worth noticed that, in the B-SSZ-13 sample with template, the fraction of B atoms that exhibit a planar geometry with sp^2 hybridization is very low, as the 1s → π^* resonance gives rise to very sharp and intense peaks in materials exhibiting only this phase.

In the XANES spectrum collected on the calcined B-SSZ-13 sample (orange curve in Figure 30) both features at 198.5 and 203.0 eV, ascribed to B in sp^3 hybridization, disappear and the 194.4 eV component dominates the spectrum, having an intensity as high as 8.2 and a fwhm as narrow as 0.55 eV. Actually, this component is the fingerprint band of B species having sp^2 hybridization.[997]

3.4.2. Reactivity of B-SSZ-13 toward NH_3. With the aim of creating new crystalline microporous systems with basic functionalities, Regli et al.[995] have reacted the activated B-SSZ-13 with ammonia at room temperature and then heated the sample up to 100 °C. This procedure resulted in the grafting of NH_2 groups on both B and Si framework atoms, as depicted in the blue inset of Figure 30. The reactivity of B-SSZ-13 with NH_3 was described by IR spectroscopy and supported by ab initio calculations, performed at MP2 level of theory. The same reactivity was not observed on a B-free chabazite, proving in an indirect way that in B-SSZ-13 zeolite NH_3 is able to break a B−O−Si bond. On the contrary, XANES spectra were barely modified by interaction with NH_3 (compare orange and blue curves in Figure 30). Calculation of XANES spectra with FDMNES code[482,483] showed that the spectra of both $[H_2NB(OSi)_2]$ and $[HOB(OSi)_2]$ units are very similar to that of an unreacted $[B(OSi)_3]$ unit as they are all dominated by the strong fingerprint band of sp^2-hybridized boron.[995]

3.5. Other Metal Isomorphous Substitutions

In this concise section we will first briefly enumerate some relevant X-ray absorption experiments perfomed to prove the isomorphous substitution inside zeolitic frameworks of metals different from Ti, Fe, Ga and B which have been deeply discussed in the previous sections. Successively we will summarize the few results obtained so far on the with soft X-ray on the Al K-edge for different zeolites in different conditions.

Germanium(IV) has been inserted in the MFI framework,[1000,1001] whereas tin(IV) has been introduced in the BEA framework.[1002] Vanadium(V), insertion has been testified in MFI (VS-1),[1003] in MEL (VS-2),[1004] in BEA,[1005] in ETS-10[1006] and in VAPO-5 frameworks,[698,1007,1008] as well as in MCM-41 mesoporous molecular sieve.[1009] Manganese(III) has been inserted in the MFI framework;[1010] cobalt(II) has been introduced in AlPO-5, AlPO-18, AlPO-36, and APSO-44 frameworks[1007,1011] and in mesoporous aluminophosphate molecular sieves;[1012] and copper(II) has been successfully inserted in the AlPO-5 structure,[1013] whereas zinc(II) in the MFI lattice.[1014] In all the reported cases, XAS spectroscopy has been relevant to prove the metal isomorphous substitution or to study the evolution of the metal center upon interaction with adsorbates and reactants.

As already underlined in section 2.2.6, the recent technical improvements of in situ cells, allowed the severe absorption problems related to XAFS experiments performed in reaction atmosphere in the soft X-ray region to be overcame.[263,291−298] Of particular interest are the XANES studies performed on the local environment of Al, whose K-edge is at E = 1560 eV, in different zeolitic framework, subjected to different treatments and under different atmospheres.[299−307] Recently, Agostini et al., combining in situ Al K-edge XANES with operando XRPD (analyzed using a parametric Rietveld approach) have been able to demonstrate that the dealumination process in Y-zeolite under steaming, mainly occurs at low temperature during the cooling process, when water molecules are allowed to enter again the zeolite pores.[308] This study yields to the understanding of the phenomena involved at the atomic scale in the preparation of ultrastable Y zeolites (USY) that are employed in fluid catalytic cracking (FCC), which is the most important conversion process in petroleum refineries to convert the high-boiling hydrocarbon fractions of petroleum crude oils to more valuable products like gasoline and olefinic gases. Successively, Svelle et al.[1015] performed periodical ab initio calculation on dealumination and desilication process on CHA framework, obtaining an energetic path compatible with the experimental findings of Agostini et al.[308]

4. CATION-EXCHANGED ZEOLITES: THE COPPER CASE STUDY

Copper-exchanged molecular sieves have been widely investigated after the discovery that Cu-ZSM-5 are active in the direct decomposition of nitric oxide to nitrogen and oxygen.[1016−1022] The study of this catalytic process has deserved a great practical interest, as nitric oxides are known to be a major cause of air pollution.[1023] Also other Cu-exchanged zeolites have shown to be active in the selective catalytic reduction of NOx: as an example Cu-MOR,[1024] Cu-CHA,[1025] Cu-SSZ-13,[1026] Cu-SSZ-16,[1026] Cu-X,[1027] Cu−Y,[1027] Cu-USY,[1024] and Cu-IM5.[1028] Also Cu-exchanged alumino-phosphates have been investigated, among them: Cu-SAPO-5,[1029,1030] Cu-MeAlPO-5 and Cu-MeAlPO-11 (Me = Zn, Mg, Fe, Co).[1030]

More recently, Cu-exchanged zeolites have attracted attention as good catalysts to achieve high selective catalytic reduction (SCR) activity.[1031] Ammonia SCR systems are becoming one of the favored choices for DeNOx mobile applications to meet the more stringent limits in the NOx emissions.[1032] Among the major reasons to approach this solution there are the high NOx conversion percentages possible with ammonia, and the ability to optimize the combustion process for maximum power output with minimum fuel consumption.[1033] Recently, the Cu-containing chabazite (CHA), Cu-SSZ-13, has received much attention in this regard because of its robust hydrothermal stability under SCR conditions.[1034,1035] The stability of the SSZ-13 zeolite has been attributed to its small-pore size and strong interaction between the cations and the framework walls. Conversely, the exchange of Cu into medium-pore sized zeolites (e.g., ZSM-5), seems to destabilize the zeolite structure under SCR conditions.[1026] A recent work, combining operando XAS experiments and DFT calculations, provides direct insight into the state of Cu under SCR conditions over a functioning Cu−SSZ-13 ammonia SCR catalyst.[1036] The experiments find fully hydrated Cu−SSZ-13 to be indistinguishable from hexa-aqua Cu(II). A 4-fold-coordinated Cu(II) environment persists even when the H_2O is driven from the catalyst and the Cu(II) becomes directly associated with the zeolite framework, as evidenced by the appearance of longer range structure in the EXAFS. Under Fast and Slow SCR conditions, in which NO_2 is half or all of the NOx feed, respectively, Cu(II) remains as the only evident Cu oxidation state. Under more reducing Standard

dx.doi.org/10.1021/cr2000898 | Chem. Rev. 2013, 113, 1736−1850

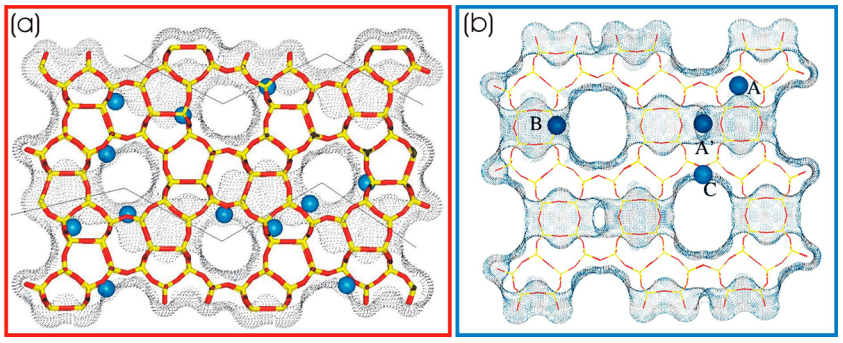

Figure 31. Sticks representation (O, red; Si or Al yellow) of the structure of ZSM-5 ([010] view) and MOR ([001] view) frameworks, parts a and b, respectively. Extraframework Cu^+ cations are represented as blue spheres. Dotted regions represent the Connolly surface[1077] of the zeolite (obtained with a probe molecule 2.8 Å in diameter). Part b is reproduced with permission from ref 1047. Copyright 2003 American Chemical Society.

SCR conditions, where there is no NO_2 in the feed, a Cu(I) species appears.

Because of their superior catalytic activity, most of the data reported up to now in literature refer to overexchanged samples prepared via a conventional ion exchange with aqueous solutions of cupric ions. As a result of this procedure, samples containing mixtures of copper ions in different aggregation and oxidation states are usually obtained.[1037−1048] The heterogeneity of copper species in catalysts prepared following this way is evident, and implies that in most cases a structural model for Cu cations cannot be confidently assessed. This makes the elucidation of structural and catalytic properties of isolated and clustered species a difficult subject. Relevant are the recent studies on the Cu-SSZ-13 system[1048b,c] and the authoritative review of the Utrecht group on the Cu location id the different zeolitic frameworks.[1048d] A significant effort in the characterization of Cu^{2+}-exchanged zeolites has been done by Schoonheydt et al. using UV−vis-DRS and EPR spectroscopies combined by ab initio calculations on model clusters.[1049−1051]

4.1. Preparation of Cu^+-Exchanged Zeolites Exhibiting a Model Compound Character

Since the early 1990s, the Turin group has developed an ongoing research[108−112,143,417,1052−1058] in the characterization of Cu^+-ZSM-5 samples prepared following an original exchange path, based on the reaction at 573 K between the zeolite (in the protonic or ammonium forms) and gaseous CuCl. This method has the advantage of directly introducing only Cu^+ cations in the zeolitic matrix, that can easily be exchanged with H^+ that leave the channels as HCl. It has been proved that the so obtained material can be considered as a model solid, containing only isolated copper species in a single, well-defined, oxidation state. Cu^+-ZSM-5 samples prepared following this method have been of great help in understanding the local structure of Cu^+ ions in zeolites. In fact, because of its model character, the Cu^+-ZSM-5 system allows to obtain clear and simple spectroscopic, energetic and structural outputs whose assignment is straightforward. This is the reason why the experimental results emerging from its characterization were used also as model to validate the computational outputs obtained by advanced quantum chemical studies.[1059−1066] This exchange method was applied by the Turin group first to the ZSM-5 matrix and was subsequently extended to faujasite,[1055,1067,1068] MOR,[109,1055,1069] *β*,[1055,1069] and ferrierite[1070] molecular sieves. An interesting variation of the gas phase exchange proposed by the Turin group was the solid-state ion exchange with CuCl, also allowing the directly introduction of Cu^+ cations inside zeolites. This method was successfully employed by e. g. Li et al.[1071] in China on MCM-41 and Y, by Kuroda et al.[1072] in Japan on ZSM-5 and by Bell et al. in the U.S.[1073−1076] on ZSM-5, Y, and USY systems. In this regard, of particular interest is the study on Cu^+-Y zeolite[1074] where authors determined the location of the copper cations in the different cationic sites of the zeolite framework and, among them, determined which are active for the oxidative carbonylation of methanol to dimethyl carbonate (DMC). The oxidation state, local coordination, and bond distances of Al and Cu were determined using Al K-edge and Cu K-edge XAFS. Observation of the catalyst under reaction conditions revealed that most of the copper cations remain as Cu^+, but some oxidation of Cu^+ to Cu^{2+} does occur.[1074] The authors concluded that only copper cations present in the supercage sites are accessible to the reactants, and hence are catalytically active.[1074]

Herein, Cu^+-ZSM-5 and Cu^+-mordenite (MOR) will be taken as two case studies to show the potential of XAFS techniques in the understanding of the local structure of hosted Cu^+ cations and in the investigation of their catalytic activity. The structure of Cu^+-ZSM-5 and Cu^+-MOR samples are schematically shown in Figure 31a−b, along with the Connolly surface[1077] of the zeolite (obtained with a spherical probe molecule 2.8 Å in diameter). The MFI structure is orthorhombic (space group: *Pnma*) and shows a three-dimensional pore system consisting of two intersecting sets of tubular channels, the former linear and the latter sinusoidal, running along the [010] and [100] directions, respectively (Figure 31a).[694,695,699] Both channels exhibit an opening of about 5.5 Å in diameter and defined by 10-member rings of [TO_4] tetrahedra. Also MOR, Figure 31b, is a zeolite with orthorhombic structure (space group: *Cmcm*), but it has only a set of parallel channels, running along the [001] direction.[694,695] These channels have an elliptical cross section, 6.5 × 7.0 Å in diameter, defined by 12-membered rings of [TO_4] tetrahedra. The channel wall has side pockets in the [010] direction, which are accessible through windows with a free entrance of 3.9 Å in diameter. Each side pocket is connected, through a distorted 8-membered ring, with two other side pockets open into the adjacent main channel. However, there is a constriction halfway along this connection with a free diameter of about 2.6 Å. The lower Si/Al ratio of MOR (5 vs 15−25) allows to host much more copper counterions in MOR than in ZSM-5.[108,109,1047]

The structural differences between ZSM-5 and MOR, determine great differences in the accessibility of extraframe-

dx.doi.org/10.1021/cr2000898 | *Chem. Rev.* 2013, 113, 1736−1850

work cations (blue spheres in Figure 31). All extra-framework cations hosted in the MFI lattice[1078] are easily accessible to small guest molecules such as CO (Figure 31a). In contrast, a great heterogeneity is found for MOR, where sites are situated[1079,1080] on the walls of the site pockets (**A**), at the access to these pockets (**B**), on the walls of the main channels (**C**), and at the bottom of the side pockets (**A′**). Cations hosted in sites **B** and **C** exhibit a coordinative unsaturation similar to those hosted in the MFI lattice, whereas cations hosted in site **A** are able to interact with a single CO molecule and **A′** cations are totally inaccessible (Figure 31b).

4.2. Cu^+-ZSM-5

Cu^+ cations inside ZSM-5 channels are able to fix N_2[108,112,1081,1082] and H_2[1083,1084] molecules even at room temperature; this high reactivity has been explained in terms of a remarkably high coordinative unsaturation.[1052] In fact, cuprous ions are able to form, depending on equilibrium pressure and temperature, $Cu^+(CO)$, $Cu^+(CO)_2$, $Cu^+(CO)_3$, $Cu^+(NO)$, and $Cu^+(NO)_2$ complexes of high structural and spectroscopic quality, to be compared with the analogous complexes typical of homogeneous chemistry.[108,110,111,1052,1053] In the following sections, we will report the XANES and EXAFS features of "well-defined" $Cu^+(CO)_n$ (n = 1−3) (sections 4.2.1 and 4.2.2) and $Cu^+(NO)_n$ (n = 1,2) (section 4.4.1) complexes formed inside ZSM-5 channels upon controlled conditions of temperature and pressure. Formation of cuprous carbonyls complexes causes a perturbation of the Cu^+ electronic structure and coordination sphere, resulting in a modification of the XANES and EXAFS spectra.[108,417,418] Interaction with NO has the same effect at low temperature only, whereas upon increasing the temperature this molecule is able to oxidize cuprous ions, thus leading to a further modification of the spectra.[1057]

4.2.1. XANES Characterization of Intrazeolitic Cuprous Carbonyl Complexes in Cu^+-ZSM-5. IR spectroscopy has been very informative on the structure of intrazeolitic $Cu^+(CO)_n$ (n =1−3) species and the main results can be summarized as follows (see inset in Figure 32a).[108,111,1052,1053] At low CO equilibrium pressures, linear $Cu^+(CO)$ complexes are formed, which are characterized by an IR absorption band at 2157 cm^{-1} (see orange curve). By increasing the CO pressure, $Cu^+(CO)_2$ adducts are formed, having C_{2v} symmetry (doublet at 2178 and 2151 cm^{-1}, due to the symmetric and antisymmetric stretching modes, red curve). Finally, by decreasing the temperature to about 80 K (i.e., increasing the CO coverage), $Cu^+(CO)_3$ complexes in C_{3v} symmetry are obtained, characterized by the appearance of a new IR doublet at 2167 and 2192 cm^{-1} (purple curve). It is worth noticing that homogeneous counterparts like $[Cu(CO)_n]^+[AsF_6]^-$ (n = 2, 3) compounds form linear ($D_{\infty h}$) and planar (D_{3h}) adducts for n = 2 and 3, respectively.[1085,1086] The distortion from the ideal linear and planar symmetry, observed for cuprous di- and tricarbonyl in ZSM-5, is due to the interaction with the zeolite walls, which acts as polidentate ligand.

Further and more direct information about the structure of the copper carbonyls and their interaction with the zeolite framework can be obtained by XAFS. The combined use of EXAFS and XANES, interpreted using a multiple scattering approach, is the only way to determine the local structure of copper carbonyls. In fact, XRPD can not be used in this case because the low Cu content in ZSM-5 (because of the high Si/Al ratio) makes the contribution of Cu nearly insignificant with respect to that of the framework.

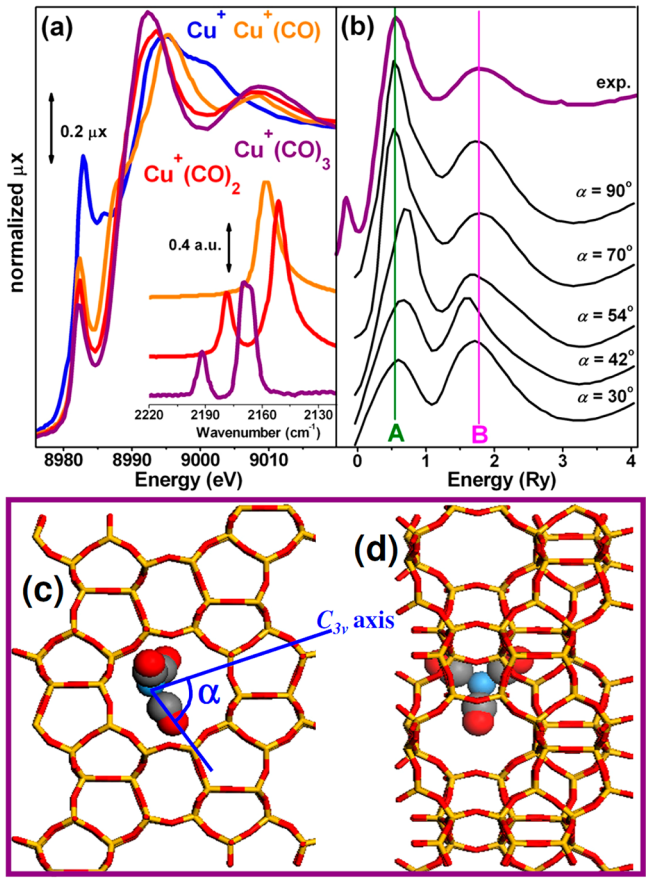

Figure 32. Part a: Normalized XANES spectra of Cu^+-ZSM-5 under vacuum (blue line), after interaction with 1 and 40 Torr of CO at RT (orange and red lines, respectively), and with 40 Torr of CO at 77 K (purple curve). The inset reports, with the same color code, the background subtracted IR spectra of $Cu^+(CO)_n$ (n = 1, 2, 3) complexes in the C−O stretching region. The spectrum of the $Cu^+(CO)_3$ adduct has been reported after further subtraction of the physisorbed component at 2138 cm^{-1}.[1087−1089] Part b: Comparison between the experimental (purple curve) and the simulated XANES curves as a function of the α angle (see part c) of the $Cu(CO)_3$ adduct in C_{3v} symmetry (1 Ry ≈ 13.6 eV). Simulated spectra are computed above the interstitial potential level only (E > 0) with CONTINUUM.[478,479] Vertical lines indicate the position of the A and B features in the experimental spectrum. Parts c and d report a schematic representation of a $Cu^+(CO)_3$ adduct formed inside the MFI channels along two perpendicular views: [010] and [100], respectively. Experimental data from in ref 417.

The XANES spectrum of the Cu^+-ZSM-5 sample under vacuum (blue line in Figure 32a) shows a very intense pre-edge peak at 8983.5 eV, together with a less intense but still well resolved component at 8986.6 eV; these two features have been attributed to the 1s → $4p_{xy}$ and 1s → $4p_z$ electronic transitions, respectively.[143,931,1057] The splitting of these two transitions (3.1 eV) indicates that bare Cu^+ cations are located in the channels of the ZSM-5 zeolite in a site characterized by an axial symmetry. Adsorption of increasing amount of CO at RT (orange and red curves in Figure 32a) causes a strong modification of both pre-edge and near-edge regions in the XANES spectra of Cu^+. As far as the pre-edge region is concerned, the 1s → $4p_{xy}$ peak significantly decreases in intensity and progressively shifts; simultaneously, the 1s → $4p_z$

dx.doi.org/10.1021/cr2000898 | Chem. Rev. 2013, 113, 1736−1850

Table 14. Quantitative Results of the EXAFS Data Analysis Performed on the Cu^+-ZSM-5 System in Vacuum and in Presence of 40 Torr of CO at RT $[Cu^+(CO)_2]$ and at 77 K $[Cu^+(CO)_3]$[a]

Cu^+ complexes	N_{CO}	R_{Cu-OF} (Å)	R_{Cu-C} (Å)	R_{C-O} (Å)	θ_{Cu-C-O} (deg)	ref.
Cu^+		2.00 ± 0.02				108
$Cu^+(CO)_2$	1.8 ± 0.3	2.11 ± 0.03	1.88 ± 0.02	1.12 ± 0.03	170 ± 10	418
$Cu^+(CO)_3$	3 (fixed)		1.93 ± 0.02	1.12 ± 0.03	180 ± 10	417

[a] N_{CO}: number of coordinated CO molecules. R_{Cu-OF}: distance of Cu^+ from the O of the framework. R_{Cu-C}: distance of Cu^+ from the C of the coordinated CO molecules. R_{C-O}: C−O bond length in the complexes. θ_{Cu-C-O}: Cu−C−O bond angle.

peak shifts at 8988 eV and becomes less visible because of overlap with the edge. Both changes indicate that the electronic configuration of copper is strongly affected by the formation of mono- and dicarbonyl adducts. By lowering the temperature down to liquid nitrogen temperature the red shift of the pre-edge peak reaches its maximum value (1.3 eV), while the 1s → $4p_z$ peak is no longer observed, indicating that it is now overshadowed by the edge. This implies that the p_{xy}/p_z splitting is increased from 3.1 eV in the pristine sample to a value greater than 4.4 eV for the $Cu^+(CO)_3$ complex. The preservation of the degeneration of p_x and p_y orbitals agrees with the IR evidence that the $Cu^+(CO)_3$ complexes formed inside the ZSM-5 zeolite are in a C_{3v}-like symmetry.[417]

Further information on the geometry of the $Cu^+(CO)_3$ complexes have been obtained by analyzing the XANES region. In fact, in this region the photoelectron has a wavelength greater than the interatomic distances and a long mean free path, resulting in a marked sensitivity of the shape and position of the edge structures upon the local geometry of CO ligands. On the basis of the IR evidence (see inset in Figure 32a), the XANES spectrum obtained in presence of the $Cu^+(CO)_3$ complexes (purple curve in Figure 32b) has been simulated by considering a series of $Cu^+(CO)_3$ clusters with C_{3v} symmetry, and characterized by a different polar angle α of the CO ligands with respect to the z axis (Figure 32c). The α angle has been progressively reduced starting from 90° (planar configuration) down to 30°. The corresponding XANES spectra have been calculated in the region between 0 and 4 Ry (54.4 eV) above the interstitial potential level and compared with the experimental results, as reported in Figure 32b. It can be immediately observed that the position and the relative intensities of the A and B features are reasonably reproduced for 70° < α < 90°. The XANES results are thus compatible with a planar or slightly bent molecule. A value close to 90° must be discarded on the basis of the IR spectroscopy[108,111] as only one IR-active band is expected for the D_{3h} symmetry. On the other hand, the steric hindrances caused by the zeolitic walls make values of α larger than 80° unreasonable from a geometric point of view. It is so concluded that, because of the interaction with the zeolitic walls, the structure of the $Cu^+(CO)_3$ complexes deviate from the planar form, typical of the homogeneous counterparts, assuming an angular value of α in the 80−60° range (Figure 32c).[417]

4.2.2. EXAFS Determination of the Structure of $Cu^+(CO)_n$ Complexes. Previous EXAFS studies conducted on Cu^+-ZSM-5 in vacuo (before CO dosage) resulted in 2.5 ± 0.3 framework oxygen atoms located at a distance of 2.00 ± 0.02 Å, see Table 14.[108,417,1054] The resulting coordination number is consistent with the presence of 2- and 3-fold coordinated Cu^+ ions in the zeolite cages, in agreement with the data reported in literature.[1072] The effect of the interaction of CO with Cu^+ sites in Cu^+-ZSM-5 on the EXAFS function is reported in Figure 33 and Figure 34b, top part. CO adsorption

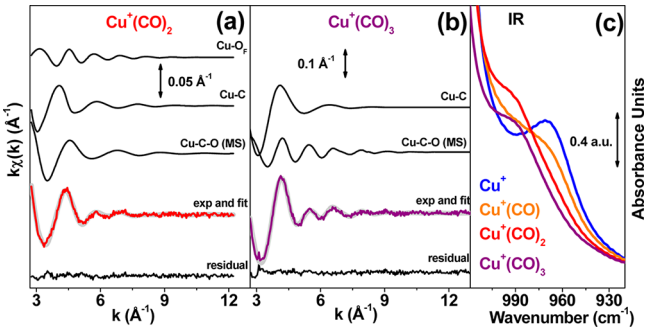

Figure 33. Part a: Results of the EXAFS data analysis for $Cu^+(CO)_2$ complexes formed inside Cu^+-ZSM-5 (data collected at room temperature with P_{CO} = 40 Torr). From top to bottom: k-weighted $\chi(k)$ functions of Cu−O_F single scattering (SS) contribution, Cu−C SS contribution, Cu−C−O MS contribution, the sum of the two previous theoretical contributions and of the Cu−O SS one (not reported for clarity) (fit, gray curve) superimposed to the experimental curve (red) and the corresponding residual function. Part b: Same for $Cu^+(CO)_3$ complexes (T = 77 K; P_{CO} = 40 Torr). In this case the experimental signal is simulated without including a contribution from the zeolitic framework. Part c: Background subtracted IR spectra of $Cu^+(CO)_n$ (n = 1, 2, 3) complexes in Cu^+-ZSM-5 zeolite in the framework stretching region: Cu^+-ZSM-5 under vacuum (blue line), after interaction with 1 and 40 Torr of CO at RT (orange and red lines, respectively), and with 40 Torr of CO at 77 K (purple curve). Experimental data from refs 417 and 418.

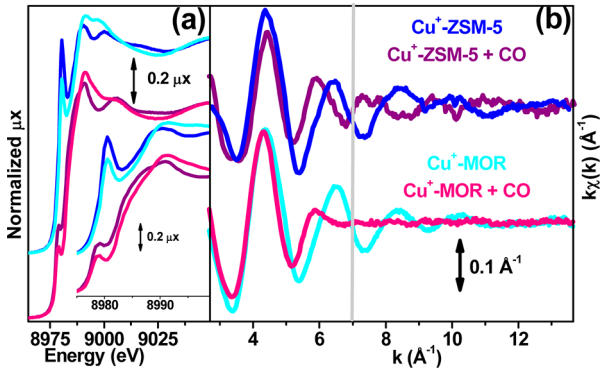

Figure 34. Part a: Comparison between room temperature XANES spectra of Cu^+-ZSM-5 (blue line) and Cu^+-MOR (cyan line) in vacuo. Vertically shifted for clarity are the XANES spectra of Cu^+-ZSM-5 (purple line) and Cu^+-MOR (pink line) after interaction with 100 Torr of CO. The inset reports a magnification of the edge region. Part b: Corresponding experimental $k\chi(k)$ functions (same color code). The gray vertical line at k = 7 $Å^{-1}$ evidence the k value above which the EXAFS signals of the samples in vacuo are nearly opposite of phase to those of the copper−carbonyl complexes hosted in ZSM-5. For the copper−carbonyl complexes hosted in MOR no signal is appreciable for k > 7 $Å^{-1}$. Experimental data from refs 108 and 109.

dx.doi.org/10.1021/cr2000898 | Chem. Rev. 2013, 113, 1736−1850

causes a modification of the $k\chi(k)$ function, both in terms of amplitude and of period of the EXAFS oscillations: this observation undoubtedly proves that EXAFS is able to detect the formation of $Cu^+(CO)_n$ adducts in Cu^+-zeolites at room temperature. In this case, a MS approach is necessary for a quantitative EXAFS data analysis[417,418] because of the linear geometry of $Cu^+\cdots C-O$ complexes.[108,1053,1058]

The results of the analysis in the MS approach, obtained by using the GNXAS code,[426,434] are illustrated in Figure 33 for both $Cu^+(CO)_2$ and $Cu^+(CO)_3$ complexes (parts a and b, respectively). The calculated and experimental EXAFS signals are reported along with the different 2 body (single scattering) and 3 body (multiple scattering) partial contributions. Starting with the $Cu^+(CO)_2$ signal (Figure 33a), a contribution at 2.11 ± 0.03 Å (see Table 14) from the zeolitic framework (O_F) has been necessary to reproduce the experimental spectrum.[418] The number of framework oxygen neighbors (2.3 ± 0.3) is in pretty agreement with that found before CO dosage (2.5 ± 0.3), while the Cu^+-O_F distance has been considerably stretched (+0.11 ± 0.03 Å) with respect to the zeolite in vacuo, suggesting a great mobility of the Cu^+ ions.[108] Moreover, the analysis gave a number of coordinated CO molecules of 1.8 ± 0.3, being so in agreement with the $Cu^+(CO)_2$ stoichiometry suggested by IR,[108,1053,1054,1058] and microcalorimetry.[1054,1058] The Cu−C distance obtained for the $Cu^+(CO)_2$ complex is 1.88 ± 0.02 Å, the C−O distance (1.12 ± 0.03 Å) is in good agreement with that of CO in the gas-phase value (1.128 Å) and the Cu−C−O bond angle is linear within the error bars (170° ± 10°), in agreement with indirect IR evidence on Cu(I)[108,1053,1054,1058] and on other metal carbonyl.[1090,1091]

Coming to the structure of $Cu^+(CO)_3$ complexes formed at liquid nitrogen temperature, the XANES study (Figure 32b) demonstrated that they are characterized by a C_{3v}-like geometry. The MS EXAFS analysis (Figure 33b) confirmed the presence of three equivalent CO molecules linearly adsorbed on Cu^+ sites (Cu−C−O = 180° ± 10°) and characterized by a Cu−C distance of 1.93 ± 0.02 Å, a C−O distance of 1.12 ± 0.03 Å.[417] In this case, the experimental spectrum was successfully simulated using the scattering contributions of $Cu^+(CO)_3$ complex only, that is without any contribution of the zeolitic framework (see Table 14). This fact has been interpreted in terms of the extraction of the Cu^+ cations by the three CO ligands into a more central position inside the channels. In other words, the Cu^+ complexation effect, already observed at RT for the $Cu^+(CO)_2$ complex and testified by the elongation of the $Cu-O_F$ bond, becomes greater in presence of 3 CO ligands so that the $Cu^+(CO)_3$ moieties have only a very weak interaction with the framework oxygen atoms.

The EXAFS data discussed above confirm the conclusion based on IR data. Figure 33c reports, in the framework stretching region, the IR spectrum of Cu^+-ZSM-5 before and after the formation of carbonyl complexes (same color code as in Figure 32). The strong interaction of Cu^+ ions with the zeolite framework is demonstrated by the presence, in the spectrum of the Cu^+-ZSM-5 system in vacuum (blue line in Figure 33c), of an IR absorption band at 980 cm^{-1}, attributed to the ν_{asym}(Si−O−Al) stretching perturbed by Cu^+ (this mode usually occurs in the 1100−1250 cm^{-1} interval in the protonic zeolites). This IR band progressively shifts in frequency and nearly disappears upon formation of $Cu^+(CO)$, $Cu^+(CO)_2$ and $Cu^+(CO)_3$ complexes (orange, red, and purple lines in Figure 33c).[417,1053,1092] In other words, the IR band at 980 cm^{-1} indicates that Cu^+ (at R_{Cu-O} = 2.00 Å) perturbs the zeolitic framework; its progressive disappearance upon formation of poli-carbonyls provides an evidence that the zeolitic framework is less perturbed (i.e., that the R_{Cu-O} distance is longer).[417,1053] We can see here that the IR skeletal mode, together with the R_{Cu-O} values measured by EXAFS, are very sensitive to "external parameters", giving information to the bonding between the $Cu^+(CO)_n$ complexes (n = 0, 1, 2, 3) and the zeolite.

These results are in line with the synchrotron radiation XRPD study on Cu^+−Y zeolite by Turnes Palomino et al.[1068] Two different cationic sites, labeled as **II** and **II***, are accessible to CO molecules in this framework. The authors showed that the more exposed Cu^+ ions, located at site **II**, migrate of 0.167(2) Å toward the center of the supercage upon $Cu^+(CO)_3$ formation while the more shielded ones, site **II***, undergo a much more relevant displacement of 0.975(1) Å. The two sites become equivalent upon formation of $Cu^+(CO)_3$ complexes.[1068,1092]

4.3. Cu^+-MOR

Cu^+-MOR is briefly discussed in this section in comparison with Cu^+−ZSM-5 to show the effect of a high heterogeneity of sites on the XAFS features. As summarized in section 4.1, the main differences between ZSM-5 and MOR are (i) the lower Si/Al ratio of MOR, which could affect the aggregation of copper ions, and (ii) the presence in MOR of cation sites having different coordination environments and accessibility, which contrast with ZSM-5, where all cation sites are equally accessible (see Figure 31).

4.3.1. XANES and EXAFS Study of $Cu^+(CO)_n$ Complexes Hosted in Cu^+−MOR: Comparison with Cu^+-ZSM-5. Figure 34a shows a comparison between the XANES spectra of Cu^+-MOR and Cu^+-ZSM-5. The pre-edge region of Cu^+-MOR is less defined than that of Cu^+-ZSM-5, reflecting the high heterogeneity of the copper species. This applies both to the samples in vacuo (top spectra) and to the copper carbonyl species (bottom spectra). Above 9030−9040 eV, where the first EXAFS oscillations start, the spectra of both zeolites become more similar, indicating a similar first shell Cu−O distance.

The EXAFS signal of the Cu^+-MOR in vacuo is reported in Figure 34b (bottom part, cyan line). The absence of any beats in the $k\chi(k)$ function suggests that the main contribution to the overall signal comes only from the first coordination shell of the Cu^+ ions. The EXAFS data analysis performed on the first coordination shell results in 2.5 ± 0.35 framework oxygen atoms, at a distance of 1.96 ± 0.02 Å, in agreement with the data obtained for Cu^+-ZSM-5. The better signal-to-noise ratio of the Cu^+-MOR spectrum is the result of the higher copper content.

When CO is adsorbed on Cu^+-MOR (pink line in the bottom part of Figure 34b) significant changes in both the frequency and amplitude of the EXAFS function are observed. In particular, for $k > 7$ $Å^{-1}$ (see gray vertical line in Figure 34b) the $k\chi(k)$ function does not show oscillations anymore. This observation provides a strong evidence that several types of carbonyl adducts are formed. The $k\chi(k)$ function is, in fact, the averaged sum of the contribution of Cu^+ ions not interacting with CO (site **A**′ in Figure 31b), of $Cu^+(CO)$ adducts formed in the side pockets (site **A** in Figure 31b), and of two slightly different $Cu^+(CO)_2$ adducts located in the main channel (sites **B** and **C**). In this respect, it is worth noticing that for Cu^+-ZSM-5 the $k\chi(k)$ oscillations of the EXAFS signal of the sample

dx.doi.org/10.1021/cr2000898 | Chem. Rev. 2013, 113, 1736−1850

in vacuo are nearly opposite in phase to those of $Cu^+(CO)_2$ adducts starting from $k = 7$ Å^{-1} (see top part of Figure 34b). This means that in the Cu^+-MOR case, for $k > 7$ Å^{-1}, the EXAFS signal coming from noninteracting Cu^+ ions in site **A′**, and those of $Cu^+(CO)_2$ adducts formed in sites **B** and **C** contribute destructively to the overall $k\chi(k)$, resulting in an almost vanished measured signal (pink curve in Figure 34b). Analogous considerations came from a comparison of the XANES spectra (Figure 34a), where the post-edge features of the Cu^+-carbonyl complexes (labeled as A and B in Figure 32b) are less defined for Cu^+-MOR. As a consequence, the heterogeneity of copper sites in MOR prevented the possibility to perform a detailed structural analysis of the carbonyl species,[109] as done for the Cu^+-ZSM-5 case (see section 4.2.2).

4.4. Reactivity toward NO: In Situ $Cu^+ \rightarrow Cu^{2+}$ Oxidation in Cu^+-ZSM-5 and Cu^+-MOR

4.4.1. Temperature Dependent NO Reaction in Cu^+-ZSM-5. As already anticipated in section 4.1, the catalytic importance of the Cu^+-ZSM-5 system is related to its ability to directly convert nitric oxide into dinitrogen and dioxygen. Although full conversion conditions are not easily realized in practical application, the decomposition reaction over Cu^+-ZSM-5 is intrinsically stoichiometric and so could be operated without formation of undesirable side-products.[1020] Moreover, unlike other catalysts (e.g., noble metals and metal oxides) Cu^+-ZSM-5 is not poisoned by oxygen developed during the reaction itself or present in the gas feed; therefore, reducing agents are not required to sustain the catalytic mechanism. Several mechanisms have been proposed in the literature to account for the reaction path. A redox mechanism, involving $Cu^+ \rightarrow Cu^{2+}$ oxidation and $Cu^{2+} \rightarrow Cu^+$ reduction steps, has been hypothesized on the basis of kinetic, EPR, and IR evidence.[1018,1037] The first in situ XANES study of Cu-ZSM-5 during NO decomposition at high temperature was reported by Liu and Robota.[1093] Successively, on the basis of combined low-temperature IR and XANES results the Turin group suggested that $Cu^+(NO)_2$ complexes are the precursors of the active sites.[108,110,1057,1092] It has been found that these species readily decompose at room temperature giving N_2O and the transient $Cu^{2+}-O^-$ species; the latter, in presence of NO, leads to the real catalytic intermediate $Cu^{2+}(NO)(NO_2)$ (where the copper is in the oxidized Cu^{2+} form) potentially capable to decompose giving nitrogen and oxygen (see Scheme 7). This scheme has been supported also by other authors.[1094−1096]

Scheme 7. Hypothesized Catalytic Cycle of NO Decomposition over Cu^+-ZSM-5, Which Leads to the Formation of Nitrogen and Oxygen. Adapted with Permission from Ref 108. Copyright 1997 American Chemical Society

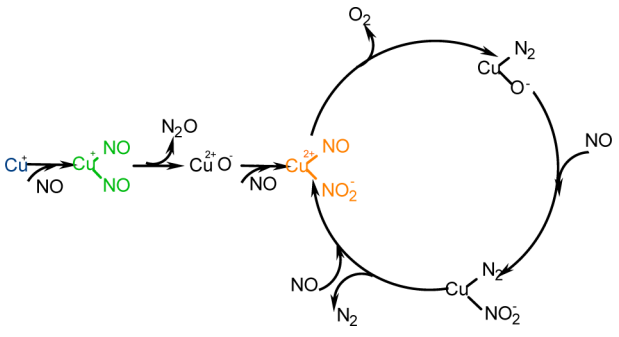

IR, EPR, and XANES temperature-dependent experiments in the 80−300 K range have been reported by Prestipino et al.[108,931,1057] to single out the precursor $Cu^+(NO)_2$ species (at 80 K) and to progressively switch on the reactivity upon increasing the temperature. IR spectroscopy has been used to define the NO equilibrium pressure needed at 80 K to safely guarantee that $Cu^+(NO)_2$ complexes are univocally present:[108,931,1057] this occurs at $P_{NO} = 8$ Torr (or higher). In these conditions the IR spectrum shows a doublet at 1827−1734 cm^{-1} (red curve in the bottom inset of Figure 35a). A

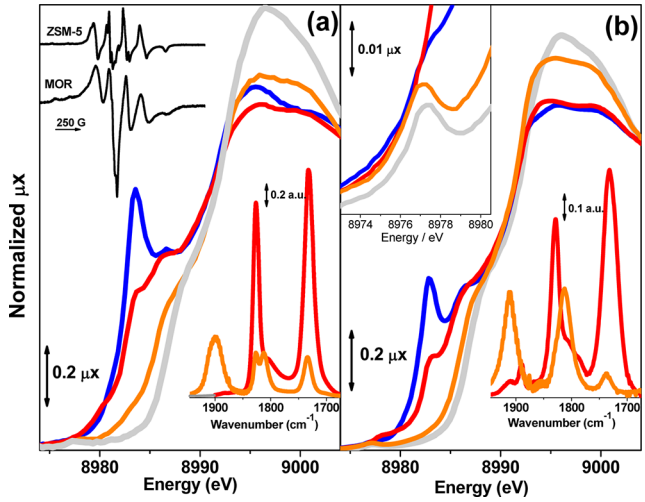

Figure 35. Part a: XANES spectra of Cu^+-ZSM-5 under vacuum (blue line), after interaction with NO at 80 K (red line, $P_{NO} = 8$ Torr), and after increasing the temperature up to 300 K (orange line). For comparison, the spectrum of a Cu^{2+}-ZSM-5 sample is also reported (light gray line). The bottom inset reports, with the same color code, the corresponding IR results. The top inset reports the EPR spectra of $Cu^+(NO)$ complexes ($P_{NO} = 0.1$ Torr; $T = 80$ K) formed on Cu^+-ZSM-5 and Cu^+-MOR, top and bottom curve, respectively. Part b: As in part a for Cu^+-MOR. The top inset reports a magnification of the region where the 1s → 3d transition of cupric ions is expected. Data from refs 1047 and 1057.

lower P_{NO} would produce a mixture of both mono- (IR absorption band at 1812 cm^{-1}) and dinitrosyl complexes, that would increase the complexity of the system. Upon increasing the temperature the 1827−1734 cm^{-1} doublet decreases in intensity in favor of a broader IR absorption band at 1900 cm^{-1} (orange curve in the bottom inset of Figure 35a) characteristic of $Cu^{2+}(NO)$ complexes. IR spectroscopy provided an evidence that the majority of Cu^+ sites (about 85%) have been oxidized by NO to Cu^{2+}.[108,931,1057] The same experiment was followed by XAFS spectroscopy using the cell reported in Figure 8a working in static conditions. Figure 35a reports the XANES spectra of Cu^+-ZSM-5 zeolite under vacuum (blue line), after interaction with NO at 80 K (red line), and after increasing the temperature up to 300 K (orange line). For comparison, the spectrum of a Cu^{2+}-ZSM-5 sample outgassed at room temperature, containing only cupric ions, is also presented (light gray line). Upon NO adsorption at 80 K (red line), the edge XANES spectrum of Cu^+-ZSM-5 is still typical of that of cuprous ions (blue curve), thus indicating that NO interacts with the Cu^+ sites of ZSM-5 without altering its oxidation state, in agreement with IR (absence of the 1900 cm^{-1} band) and EPR.[1057] More in detail, the XANES spectrum becomes more structured: a new component appears at low energy (~8979.9

dx.doi.org/10.1021/cr2000898 | Chem. Rev. 2013, 113, 1736−1850

Table 15. Position and Related Normalized Intensities of the Main Features of the XANES Spectra of Cu^+-ZSM-5 and Cu^+-MOR and Effect of Interaction with NO at 80 K[a]

	$1s \rightarrow 4p_x$		$1s \rightarrow 4p_y$		$1s \rightarrow 4p_z$	
system	position (eV)	intensity	position (eV)	intensity	position (eV)	intensity
Cu^+-ZSM-5 in vacuo[b]	degenerate with $1s \rightarrow 4p_y$		8983.5	0.92	8986.6	0.71
Cu^+-ZSM-5 + NO[b]	8979.9 (sh)	0.15	8983.7 (sh)	0.56	8986.3 (sh)	0.68
Cu^+-MOR in vacuo[c]	degenerate with $1s \rightarrow 4p_y$		8983.0	0.61	8986.7	0.59
Cu^+-MOR + NO[c]	8978.9 (sh)	0.07	8983.1	0.33	8986.1 (sh)	0.59

[a]Data taken from the spectra reported in Figure 35 (sh = shoulder). [b]Data taken from ref 1057. [c]Data taken from ref 1047.

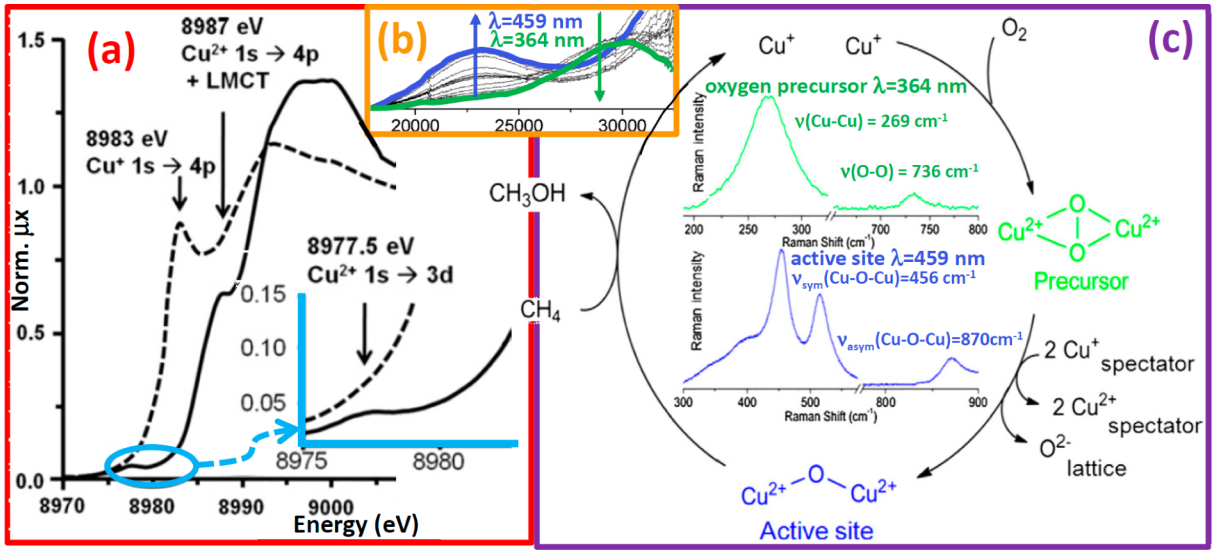

Figure 36. Part a: Cu K-edge XANES spectra of Cu-ZSM-5 treated in He at 773 K (dashed line) and after successive contact with O_2 at 623 K. The inset reports the magnification of the $1s \rightarrow 3d$ transition visible in the oxidized ample (Cu^{2+} cations). Part b: UV–vis spectra of the Cu-ZSM-5 sample treated in He at 773 K and successively contacted with O_2 at RT (green curve) and successive evolutions upon heating up to 650 K (blue curve). Part c: O_2 activation pathway in Cu-ZSM-5. The inner part of the loop reports the resonant Raman spectra of the μ-(η^2:η^2) peroxo dicopper(II) planar complex precursor (top, green curve) and of the active $[Cu_2O]^{2+}$ active core (bottom, blue curve). As shown in part b, resonant Raman conditions were obtained exciting at λ = 364 nm (27500 cm^{-1}) or at λ = 459 nm (21800 cm^{-1}) for the precursor and the active species, respectively. Adapted with permission from ref 1116. Copyright 2010 American Chemical Society.

eV), while the intense peak around 8983 eV is slightly shifted and strongly reduced in intensity. This behavior is interpreted in terms of the splitting of the p_{xy} orbital into p_x and p_y. The p_x/p_y and p_y/p_z splitting is of 3.8 and 2.6 eV, respectively,[931,1057] see Table 15. This implies that, upon interaction with NO, the symmetry of Cu^+ centers in ZSM-5 is decreased, passing from an axial to an anisotropic environment. In fact, in the case of C_{2v} or lower symmetries, three unequivalent axis are expected. Note that for $Cu^+(CO)_3$ adducts in C_{3v} symmetry the $1s \rightarrow 4p_{xy}$ XANES peak undergoes a red shift of 1.4 eV, but no splitting is observed (vide supra Figure 32a), according to the expected degeneration of p_x and p_y orbitals in C_{3v} symmetry.[417]

A XANES spectrum of the pure $Cu^+(NO)$ complex could not be collected because it was not possible to found a P_{NO} interval, where only $Cu^+(NO)$ complexes were present: increasing P_{NO}, $Cu^+(NO)_2$ complex start to form before all Cu^+ could form a mononitrosyl complex. Information on the low symmetry of $Cu^+(NO)$ complexes was obtained by EPR (top inset of Figure 35a), as both bare Cu^+ and $Cu^+(NO)_2$ complex are EPR silent. The spectrum showed an anisotropic g tensor ($g_{xx} \neq g_{yy} \neq g_{zz}$) and hyperfine tensors with noncoincident $^{Cu}\mathbf{A}$ and $^{N}\mathbf{A}$ axes.[1057,1097]

Upon increasing the temperature up to 300 K in NO atmosphere (orange spectrum in Figure 35a), a significant blue shift of both edge and pre-edge features is observed, indicating that a consistent fraction of the cuprous ions has been oxidized to the cupric state. This is the expected behavior, as the reaction of NO decomposition catalyzed by the copper sites is switched on upon increasing the temperature. By using the XANES spectrum of Cu^+-ZSM-5 (light gray line in Figure 35a) as model for 100% cuprous ions and that of a Cu^{2+}-ZSM-5 sample activated at room temperature (blue in Figure 35a) as model of ZSM-5 with 100% cupric ions, it has been determined that a fraction of ~80% of the overall Cu^+ has been oxidized by NO.[1057]

4.4.2. Temperature-Dependent NO Reaction in Cu^+-MOR. The same combined IR, EPR, and XANES temperature-dependent experiments were performed on Cu^+-MOR.[1047] Top inset in Figure 35a reports the EPR spectrum of the $Cu^+\cdots NO$ adducts formed on **A**, **B**, and **C** sites of MOR upon interaction with NO at 77 K. Though less resolved, the spectrum has the structure of that observed for Cu-ZSM-5. The same considerations are obtained after comparison of the IR spectra.

Figure 35b reports the effect on the XANES spectrum of the NO interaction with Cu^+-MOR at liquid nitrogen temperature (compare blue and red spectra). Also in this case a high P_{NO} (8 Torr) was adopted to maximize the fraction of $Cu^+\cdots(NO)_2$ complexes. As for Cu^+-ZSM-5,[1057] in these conditions cuprous dinitrosyl adducts were formed without measurable oxidation effects. Coordination with NO causes the loss of the axial

dx.doi.org/10.1021/cr2000898 | Chem. Rev. 2013, 113, 1736–1850

symmetry, here revealed by the splitting of the 1s → $4p_{xy}$ into the two 1s → $4p_x$ and 1s → $4p_y$ components at 8978.9 and 8983.1 eV, being the 1s → $4p_z$ component nearly unaffected (~8986.1 eV). This results in a p_x/p_y and p_y/p_z splitting of 3.2 and 3.0 eV, respectively, see Table 15.

To allow the catalyst to work, the temperature was raised up to 300 K in NO, then the system was outgassed and a further XANES spectrum was collected (light gray spectrum in Figure 35b). By comparing this spectrum with our reference for a 100% Cu^{2+}-MOR (dotted curve in Figure 35b), Xamena et al.[1047] concluded that NO is able to reoxidize most of the cuprous ions in MOR, in agreement with the IR study (see bottom inset in Figure 35b). This fact is testified by the blue shift of the edge, by the disappearance of the 1s → $4p_{xy}$ features of Cu^+ species and by the recovery of the 1s → 3d component of Cu^{2+} (see top inset in Figure 35b).

4.5. Bent mono-(μ-oxo)dicupric and bis(μ-oxo)dicopper Biomimetic Inorganic Models for NO Decomposition and Methane Oxidation in Cu-ZSM-5: Comparison with Fe-ZSM-5

In 2005, the Leuven group was the first one to highlight the occurrence of the selective oxidation of methane into methanol using Cu-ZSM-5.[1098] Because of the low temperature of the reaction (<200 °C), methanol remained adsorbed on the catalyst, presumably as a methoxide, but it can be recovered by extraction with a suitable solvent or solvent mixture. As was the case for Fe-ZSM-5[1099−1102] (section 3.3), the reaction in Cu-ZSM-5 was found to be stoichiometric.[1103] Both Cu-ZSM-5 and Fe-ZSM-5 catalysts have similar activation procedures and reaction conditions, the main difference being related to the formation of the active site: Fe-ZSM-5 needs to be oxidized by N_2O (see section 3.3.4), while Cu-ZSM-5 can also be activated by O_2, which is an advantage from an economical standpoint. Looking to nature, Cu- and Fe-enzymes also have the ability to selectively convert methane into methanol at ambient temperatures. These are the enzymes soluble methane mono-oxygenase[1104,1105] and particulate methane mono-oxygenase.[1106] While the former uses Fe to carry out this difficult reaction, the latter employs Cu. In both enzymes, methane oxidation occurs at a binuclear active site.[1107,1108]

On the basis of the parallelism between natural enzymatic catalysts and artificial zeolitic catalysts, the Leuven group (partially in collaboration with the Stanford group) performed an ongoing research work on Cu-exchanged zeolites supporting the thesis that the active site is a bent mono-(μ-oxo)dicupric cluster, generated from the precursor bis(μ-oxo)-dicopper cluster.[1098,1103,1109−1116] They combined EPR, DRS-UV−vis, XANES, EXAFS, resonant-Raman, and ab initio simulations to investigate the material.

The core of the multitechnical experiment performed by the groups of Schoonheydt (Leuven) and Solomon (Stanford) is summarized in Figure 36. A Cu^{2+}-ZSM-5 (Cu/Al = 0.5) is thermally reduced to Cu^+-ZSM-5 by activation in He at 723 K,[1046,1103,1116] as testified by the XANES spectrum reported in Figure 36a (dashed line). Exposure to O_2 at room temperature causes the reoxidation of Cu^+ into Cu^{2+} and the appearance in the UV−vis spectra of a component at 29 000 cm^{-1} (239 nm), see green curve in Figure 36b. This band has been attributed to a peroxo π^*_σ → Cu^{2+} CT[1117] in a μ-(η^2:η^2) peroxo dicopper(II) planar complex,[1103,1114,1116,1118] see green structure in Figure 36c. This complex is the precursor of the active species. Activation occurs by thermal heating: in the UV−vis spectra, starting from 450 K, a new component around 21 800 cm^{-1} raises at the detriment of the 29 000 cm^{-1} band (Figure 36b). This is the spectroscopic evidence of the formation of the $[Cu_2O]^{2+}$ active core (blue structure in Figure 36c). The reaction formally requires the cleavage of the O−O bond, and thus, two extra electrons (i.e., two Cu^+ react with O_2, reducing it by two electrons to the peroxo level and a second two electrons are required for complete reduction to the oxo level). Resonant Raman studies on catalysts oxidized with labeled $^{16}O_2$ and $^{18}O_2$ validated this model.[1114] The precursor μ-(η^2:η^2) peroxo dicopper(II) planar complex is characterized by ν(Cu−Cu) = 269 cm^{-1} and ν(O−O) = 736 cm^{-1}, observed exciting in the π^*_σ → Cu^{2+} CT (λ = 364 nm; 27 500 cm^{-1}), whereas the $[Cu_2O]^{2+}$ active core exhibits stretching modes at ν_{sym}(Cu−O−Cu) = 456 cm^{-1} and ν_{asym}(Cu−O−Cu) = 870 cm^{-1}, observed exciting at λ = 459 nm (21 800 cm^{-1}).

According to the reaction scheme reported in Figure 36c, the $[Cu_2O]^{2+}$ core is responsible for the methane to methanol conversion, as a correlation was found between the intensity of the 21 800 cm^{-1} component in the UV−vis spectra and the catalyst activity. The formation of both the μ-(η^2:η^2) peroxo dicopper(II) precursor and the $[Cu_2O]^{2+}$ active core is favored by a high copper loading: the authors found these dicopper species in ZSM-5 samples loaded at Cu/Al = 0.5 and, in a smaller extent, at Cu/Al = 0.3, being essentially absent in samples with Cu/Al < 0.2.

5. STRUCTURE AND REACTIVITY OF METALLORGANIC FRAMEWORKS PROBED BY IN SITU XAFS AND XES

The possibility of tuning framework porosity, topology as well as framework composition has made zeolites and zeotypes the most successful materials for a broad range of applications, such as gas adsorption and separation and for catalysis:[308,699,706,812,820,825,1022,1119−1132] sections 3 and 4 report some clear examples. But the zeolites role as the leading class of crystalline porous materials is nowadays challenged by a new emerging class of porous materials: metal organic frameworks (MOFs).[65,1132−1142] MOFs diverge from some zeolites in important aspects.[1143,1144] The most important one is their larger diversity and flexibility in composition and the less topological constraints in the formation of the porous lattice. The enormous number of new MOF frameworks reported every year reflects this flexibility and the large interest for their potential applications.[1145] Zeolites are restricted to tetrahedral networks, whereas the inorganic cornerstone in MOF topologies may be a single metal atom or a more or less complex cluster of coordinated metal atoms or complex inorganic substructures extending in one, two, or three dimensions. According to the recent classification done by Tranchemontagne et al.[1146] the coordination of the inorganic cornerstone may span the whole range from 3 up to 66. On top of this, cornerstones can be connected using different type of organic linkers, giving rise to the synthesis of isoreticular frameworks such as e.g. the IRMOF-1/IRMOF-16[1147] or the UiO-66/UiO-68[1148−1150] series.

Although the industrial application of MOFs is still limited to a few cases,[1151,1152] this new class of materials is foreseen to play an important role in the next future, in the fields of gas separation and purification,[1153−1163] liquid phase separation,[1163−1166] gas storage,[1147,1150,1167−1186] drug delivery,[1187−1189] optical and luminescent materials,[1190−1196] magnetic materials,[1197−1200] solid state ion conductors[1201] semi-

dx.doi.org/10.1021/cr2000898 | Chem. Rev. 2013, 113, 1736−1850

conductors,[1202] sensors,[1203,1204] catalysis,[1203,1205−1239] and photocatalysis.[1240] Functionalization of MOF materials remains one of the main challenges driving the MOF community,[1203,1213,1216,1223,1241−1266] even more than the optimization of the synthesis conditions to make always newer and newer structures. Indeed, the metal sites in most of the MOF structures show at maximum one coordination vacancy (and only after removal of the solvent), therefore limiting their application, for example, in catalysis, where at least two coordination vacancies are required. MOFs functionalization has been performed following two main routes: (i) by using during the synthesis linkers containing functionalized groups or (ii) by performing postsynthesis modification of MOFs framework. The latter method can be accomplished by either introducing covalent attachment to the organic linker, or by grafting of an organic molecule to the metal sites through the coordinative vacancy created after solvent elimination.[1223]

The enormous complexity and variety of MOF frameworks[1267,1268] represents an evident challenge in the characterization of MOF materials. Only a few structures were resolved from single crystal data because of the difficulty in growing large MOF crystals. In cases where only powder XRD (XRPD) data are available, additional structural information, particularly regarding local coordination within the inorganic cluster, are often mandatory to solve the structure. In several important cases EXAFS, taking benefit from its element selectivity, was able to provide complementary structural information on the inorganic cluster and the way it binds to the ligand.[65,1148−1150,1242−1246,1269−1282] The fact that MOFs are mainly constituted by low Z elements (C, O, N, H), that are almost transparent to X-rays (see Figure 3b and Eq 10), allows to collect, at the metal K- or L-edges, high quality transmission X-ray absorption spectra characterized by an optimized edge jump $\Delta\mu x$ as high as 1.0−1.5, resulting in accurate data, analyzable up to 15−18 Å^{-1}. This fact guarantees a high number of independent parameters (n_{ind}, see Eq 21) for the fit; low correlation among optimized parameters and a high ability to discriminate between two close distances, see eq 22. In this sense, MOFs represents ideal materials for EXAFS/XANES characterization.

5.1. Adsorption of CO on Cu^{2+} Sites in $Cu_3(BTC)_2$ or HKUST-1

HKUST-1, also known as $Cu_3(BTC)_2$ because of its stoichiometry, is a Cu(II) based fcc-MOF characterized by a 3D system of square-shaped pores (9 Å × 9 Å).[1283−1285] In $Cu_3(BTC)_2$ Cu^{2+} ions form dimers, where each copper atom is coordinated to four oxygen atoms, coming from the benzene-1,3,5 tricarboxylate (BTC) linkers ($[Cu_2C_4O_8]$ cage) and one water molecule.[1187,1271,1286] A schematic representation of the $Cu_3(BTC)_2$ buildings blocks and how they are connected to give rise to the three-dimensional structure is reported in Figure 37a. Prestipino et al.[1271] showed that water molecules can be removed from the first coordination shell of Cu^{2+} without loss of crystallinity and porosity. This property is extremely important, as it implies the formation of coordinatively unsaturated Cu^{2+} sites that become consequently available for additional ligands such as molecules dosed from the gas phase (Figure 37b). EXAFS analysis revealed that water removal from the first coordination shell of Cu^{2+} causes an important modification of the $[Cu_2C_4O_8]$ cage resulting in a decrease of the Cu^{2+}-Cu^{2+} distance from 2.64 ± 0.02 Å down to 2.50 ± 0.02 Å,[1271] see Table 16.

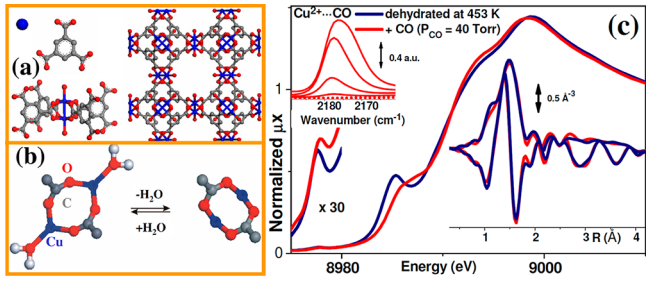

Figure 37. Part a: Schematic representation of the building blocks of HKUST-1. Two Cu^{2+} ions, and four benzene-1,3,5 tricarboxilate linkers are bounded to give rise the final 3D structure. The picture shows the typical paddle wheel coordination of Cu^{2+} sites. Water molecules directly bonded to Cu^{2+} are represented by an oxygen atom only. Part b left: Cluster of the $[Cu_2C_4O_8](H_2O)_2$ cage peculiar of the hydrated form. Part b right: Dehydrated $[Cu_2C_4O_8]$ cage. Color code: Cu^{2+}, blue; O, red; C, gray; H, white. Part c: XANES spectra of HKUST-1 collected at liquid nitrogen temperature before (dark blue curve) and after (red curve) interaction with CO (P_{CO} = 40 Torr). The bottom left inset reports a magnification of the 1s → 3d quadrupolar transition. The right inset reports the k^2-weighted, phase uncorrected, FT of the corresponding EXAFS spectra. The top left inset reports the IR spectra collected at liquid nitrogen temperature upon decreasing P_{CO} from 40 Torr down to 10^{-3} Torr (full line curves). All IR spectra have been background subtracted using the spectrum collected before CO dosage as background. Data from ref 1271.

The presence of coordinatively unsatured Cu^{2+} sites, combined with a specific framework topology, characterized by a sequence of square cages, is the key point to justify the remarkable adsorption properties toward a large variety of adsorbates. The interest in this area is broad, ranging from environmental applications in gas separation, (NOx and CO_2 traps), sensors (NO, CO_2, CO, NH_3), and H_2 storage.[1092,1187,1271,1282,1286] Very recently, the group of Corma has shown that HKUST-1 is an active and reusable solid catalysts for the cyclopropanation of alkenes with high chemo- and diastereo-selectivities.[1287] Herein we will briefly review the ability of $Cu_3(BTC)_2$ to coordinate CO molecule as monitored by in situ IR, XANES and EXAFS spectroscopies.

Already in 2002, Wang et al.[1288] observed that $Cu_3(BTC)_2$ was able to adsorb small amount of CO at room temperature and atmospheric pressure. However the paper just reported sorption isotherms, so that a direct proof of the site specific adsorption of CO on the coordinatively unsaturated Cu^{2+} sites of the dehydrated HKUST-1 was missing at that time. This evidence was reported by Prestipino et al.[1271] in 2006, who reported clear evidence of the formation of Cu^{2+}···CO adducts by both XANES and IR spectroscopies, see Figure 37c.

The main part of Figure 37c reports the XANES spectra of HKUST-1 outgassed at 453 K (dark blue curve) in comparison with that obtained after adsorption of CO at about 100 K (red curve). Upon CO interaction the first coordination sphere of Cu^{2+} undergoes a significant perturbation, as testified by the clear modification of the pre-edge features. In particular, the dipolar shakedown 1s → 3p transition becomes broader and undergoes a blue shift from 8985.3 to 8986.0 eV, testifying an increase of the covalent character in the Cu−O bond. The much weaker peak at 8977.8 eV ascribed to the quadrupolar transition 1s → 3d is less affected, being just slightly blue-shifted (see bottom left inset in Figure 37c). Interaction with CO is, however, unable to significantly perturb the extended

dx.doi.org/10.1021/cr2000898 | Chem. Rev. 2013, 113, 1736−1850

Table 16. Summary on the Structural Data of Isostructural $Cu_3(BTC)_2$ and $Cr_3(BTC)_2$ Obtained with Different Techniques. Reproduced with Permission from Ref 65. Copyright 2010 Royal Society of Chemistry

material	coordination on M site	a (Å)	V (Å^3)	R_{M-M} (Å)
$Cu_3(BTC)_2$	H_2O	26.343(5)[a]	18280(7)[a]	2.628(2)[a]; 2.64(2)[b]
$Cu_3(BTC)_2$		26.2243(5)[c]	18035(1)[c]	2.50(2)[b]
$Cr_3(BTC)_2$		26.6652(3)[d]	18959.8(6)[d]	2.06(2)[d]
$Cr_3(BTC)_2$	O_2	25.956(2)[d]	17487(4)[d]	2.8(1)[d]

[a]Single crystal X-ray diffraction.[1283] [b]Cu K-edge EXAFS.[1271] [c]Synchrotron radiation XRPD.[1271] [d]Neutron powder diffraction.[1290]

region of the X-ray absorption spectrum (right inset, reporting its FT). The authors interpreted this fact as due to the weak interaction between Cu^{2+} and CO; the resulting $Cu^{2+}\cdots CO$ complexes would be characterized by a rather long Cu−C distances and by a rather large Debye−Waller factor, that make the contribution of the CO scattering negligible with respect to that of the MOF framework, see Eq 19.

The coordination of CO molecules on Cu^{2+} ions in HKUST-1 was also evidenced by the IR spectra collected at liquid nitrogen temperature,[1271] see top left inset of Figure 37c (P_{CO} = 1 Torr), showing an increase of the IR absorption band at 2174 cm^{-1} due to the ν(CO) stretching mode of the $Cu^{2+}\cdots CO$ adducts. This assignment agrees well with the IR study of Hadjiivanov and Knozinger[1289] who reported that the labile $Cu^{2+}\cdots CO$ adducts hosted inside ZSM-5 zeolite are characterized by a $\tilde{\nu}$(CO) = 2179 cm^{-1}. The weakness of the $Cu^{2+}\cdots CO$ bond was proved by the pressure dependent IR experiment reported by Prestipino et al.,[1271] showing that CO leaves Cu^{2+}, by simply outgassing the sample at liquid nitrogen temperature.

5.2. Adsorption of O_2 on Cr^{2+} Sites in $Cr_3(BTC)_2$

5.2.1. XANES Study. The group of Long in Berkley recently succeeded in synthesizing the Cr^{2+} analogue of HKUST-1,[1290] named $Cr_3(BTC)_2$ from its stoichiometry, where the same 3D structure is obtained connecting with BTC linkers $[Cr_2C_4O_8]$ cages instead of $[Cu_2C_4O_8]$ ones. The authors used neutron powder diffraction to prove that $Cr_3(BTC)_2$ crystallizes in the same $Fm\bar{3}m$ space group as the Cu^{2+}-homologue. Insertion of Cr^{2+}, substituting Cu^{2+}, implies a slight cell expansion from a = 26.2243(5) Å, V = 18035(1) Å^3 of HKUST-1 to a = 26.6652(3) Å, V = 18959.8(6) Å^3 of $Cr_3(BTC)_2$, which is accompanied by a significant shrinking of the metal−metal distance in the dimer from R_{Cu-Cu} = 2.50 ± 0.02 Å[1271] to R_{Cr-Cr} = 2.06 ± 0.02 Å.[1290] An impressive change in structure of the $[Cr_2C_4O_8]$ cages is expected upon loss of the axial solvent,[1291] since Cr^{2+} centers can form a strong (quadruple) metal−metal bond whereas Cu^{2+} centers do not. The neutron diffraction data were definitive on this point.[1290]

The interesting aspect of this new $Cr_3(BTC)_2$ MOF material is that it is able to fix O_2 molecules from air with high selectivity and in an almost reversible way.[1290] This peculiarity is obviously of paramount importance, because the separation of O_2 from air is carried out in industry using cryogenic distillation on a scale of 100 Mtons/year, as well as using zeolites in portable devices for medical applications. Moreover, in the next future O_2 may be needed in large scale for CO_2-free energy production inside fuel cells. Thus, there is a clear benefit in developing materials that might enable this process to be carried out with a lower energy cost.

Interaction of $Cr_3(BTC)_2$ with O_2 was followed by neutron powder diffraction, IR, UV−vis-NIR and XANES spectroscopies.[1290] Neutron powder diffraction revealed a decrease of the unit cell from a = 26.6652(3) Å, V = 18959.8(6) Å^3 to a = 25.956(2) Å, V = 17487(4) Å^3, accompanied by a great elongation of the distance in the Cr−Cr dimer, that moves form R_{Cr-Cr} = 2.06 ± 0.02 Å to R_{Cr-Cr} = 2.8 ± 0.1 Å. The structural data obtained on desolvated and on O_2-interacting $Cr_3(BTC)_2$ are summarized in Table 16 and compared with similar data obtained on the isostructural $Cu_3(BTC)_2$, in both its hydrated and dehydrated forms. The removal of the water molecule coordinated to Cu^{2+} during the desolvation process in $Cu_3(BTC)_2$ resulted in a small contraction of the unit cell $\Delta a/a$ = −0.5% which is accompanied by an important shrinking of the $[Cu_2C_4O_8]$ cage of $\Delta R_{Cu-Cu}/R_{Cu-Cu}$ = −5.0%. $Cr_3(BTC)_2$ behaves differently when the coordinated O_2 molecule is removed from the Cr^{2+} site: the MOF lattice undergoes a much larger contraction $\Delta a/a$ = −2.7%, which is accompanied by a huge deformation of the $[Cr_2C_4O_8]$ cage in the opposite direction than that observed for the Cu^{2+}-homologue MOF, of $\Delta R_{Cr-Cr}/R_{Cr-Cr}$ = +35%. Such impressive behavior can be explained only on the basis of an extremely high flexibility of the $[Cr_2C_4O_8]$ cage.

To evaluate possible changes in the oxidation state of Cr upon O_2 adsorption, Long et al.[1290] have collected the Cr K-edge XANES spectra of the as prepared, desolvated and O_2-contacted material, see Figure 38a. It is known that the edge position of the XANES spectra of Cr model compounds do not correlate straightforwardly with the Cr oxidation state: indeed Tromp et al.[1292] observed that the energy shift undergone by the main absorption edge of Cr compounds having an oxidation state from Cr^0 to Cr^{6+} is similar to that of a series of Cr^{3+} complexes with different ligands. Frages et al,[1293] suggested that the centroid position (first moment energy, or baricenter)[1294] of the pre-edge feature is a better indicator of the Cr valence than the edge position. Long et al.[1290] followed this method. After the subtraction of the tail originated from the rising edge, Long et al.[1290] fitted the pre-edge region with pseudo-Voigt functions; the first moment energy (i.e., the center of mass of the pre-edge peak) was calculated from the sum of the integrated area of each peak (Figure 38c,d). For activated and O_2-loaded $Cr_3(BTC)_2$, the first moment energies occur at 5991.17 and 5991.24 eV, respectively, the latter being the weighted average between the centroids of the two pre-edge peaks at 5990.66 and 5992.40 eV, (see Figure 38d). The energy shift of the first moment (ΔE = 0.07 eV) between these two compounds is significantly smaller than that observed for the energy shift between Cr^{2+} and Cr^{3+} compounds ($\Delta E \geq$ 0.8 eV).[1293] Therefore Long et al.[1290] concluded that the observed shift was consistent with a partial charge transfer from the Cr metal center to the bound O_2 molecule and no oxidation of Cr^{2+} occurred.

5.2.2. XES Study. In this section, a few preliminary XES results collected at ID26 (ESRF) on $Cr_3(BTC)_2$ will be discussed. In particular, we will report on (i) valence to core resonant X-ray emission (VtC-RXES) maps, where both

dx.doi.org/10.1021/cr2000898 | Chem. Rev. 2013, 113, 1736−1850

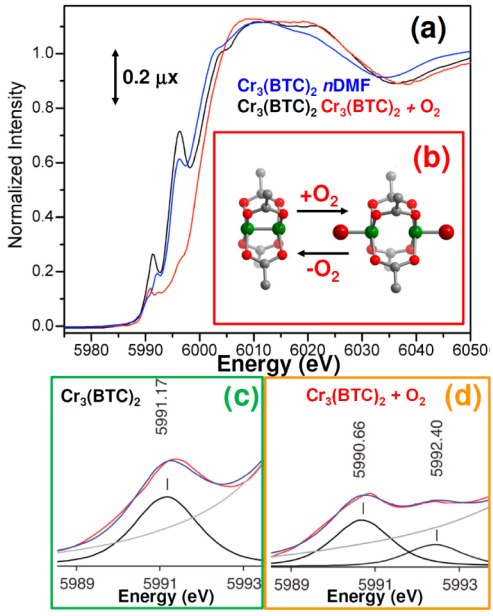

Figure 38. Part a: Normalized Cr K-edge XANES spectra of $Cr_3(BTC)_2$ MOF, as prepared (blue curve), desolvated (black curve) and after successive interaction with O_2 (red curve). Part b: Portions of the structure of $Cr_3(BTC)_2$, refined from neutron powder diffraction data, highlighting the Cr−Cr distance lengthening from 2.06(2) to 2.8(1) Å upon O_2 coordination:[1290] Cr, O, and C atoms are represented as green, red, and gray spheres, respectively. Part c: Simulation of the pre-edge data for activated $Cr_3(BTC)_2$. Red, blue, gray, and black lines represent the experimental data, simulation result, edge tail, and pseudo-Voigt components, respectively. Part d: As in part c for the O_2-loaded $Cr_3(BTC)_2$ material. Adapted with permission from ref 1290. Copyright 2010 American Chemical Society.

incident Ω and emitted ω monochromators are scanned, see Figure 5 and (ii) valence to core (VtC) Kβ satellite peaks.

The bottom part of Figure 39a shows a full VtC-RXES map of $Cr_3(BTC)_2$ sample in presence of the solvent. The dark red rectangular feature at the bottom of the map is the elastic peak. Moving vertically along the energy transfer direction $(\Omega - \omega)$, one can observe two optical peaks. These peaks arise from transitions between intermediate states achieved at about Ω = 5992 eV to final state at about $(\Omega - \omega)$ = 4 (very weak) and 8.5 eV (medium). A very strong emission appears in the 5995 eV < Ω < 6000 and 11 eV < $(\Omega - \omega)$ < 14 eV region. These features are, in part, also observed in the standard XANES spectrum (see top of Figure 39a), that shares with VtC-RXES the same Ω axis, with however, no possibility to have access to the $(\Omega - \omega)$ axis: in fact, standard XANES spectroscopy yields an 1D-spectrum that, for every Ω value, is integrated over all possible intermediate states (or ω values).

Removal of solvent, strongly modifies the VtC-RXES map of $Cr_3(BTC)_2$, see bottom part of Figure 39b. Now, three well-defined peaks lie on the constant line at Ω = 5991 eV (incident energy) at $(\Omega - \omega)$ = 4.3 (very weak), 7.8 (very strong), and 12.5 eV (medium). The presence of these XES peaks aligned at the same Ω value means that three different intermediate states are reached after excitation at Ω = 5991 eV and that three possible final states are available with different probability, the most probable one being that at $(\Omega - \omega)$ = 7.8 eV. All this information is lost in the standard XANES spectrum reported in the top part of Figure 39b. Moreover, the strong absorption described above starts now at lower Ω values (Ω ≈ 5994 eV) and has now a well-defined maximum for Ω = 5997 eV and $(\Omega - \omega)$ = 11.5 eV. A simple look at the VtC-RXES maps reported in the bottom parts of Figure 39ab, indicates that much more information on the Cr electronic structure (involving both occupied and unoccupied states) can be extracted from XES spectroscopy with respect to the standard XANES spectroscopy (see top parts in Figure 39ab). Calculation are in progress combining a DFT (ORCA code[500]) and a multiplet approach (Cowan's program[519]) in order to assign precisely the molecular orbitals involved in these transitions.[1295]

Figure 39c reports nonresonant Kβ VtC-XES satellite peaks obtained for the desolvated $Cr_3(BTC)_2$ sample before and after

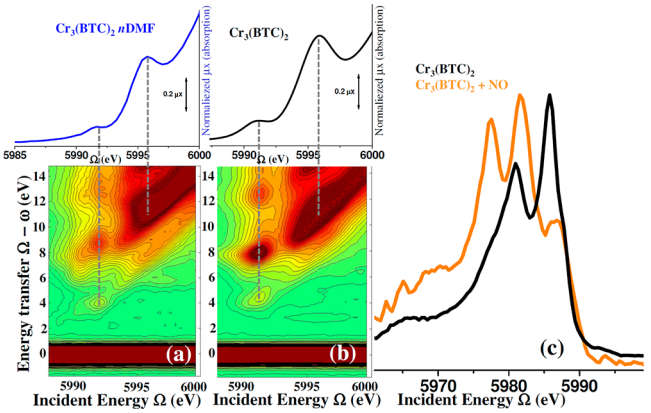

Figure 39. Standard Cr K-edge XANES spectra collected in transmission mode in the pre-edge region (ESRF BM01B, top) and valence to core (VtC) RXES map (ESRF ID26, bottom) of $Cr_3(BTC)_2$ sample before and after solvent removal: parts a and b, respectively. Vertical dotted gray lines allow to better appreciate the increased information obtained from VtC RXES with respect to standard XANES spectroscopy. Part c: A comparison between nonresonant Kβ VtC-XES satellite peaks for the desolvated $Cr_3(BTC)_2$ sample before and after interaction with NO: red and blue curves, respectively. The ordinate axis report the photon counts by the APD in arbitrary units. We are indebted to P. Glatzel and E. Gallo (ESRF, F) an to the group of J. R. Long (Berkeley, U.S.) for having allowed us to include these new data in this review before publication.

interaction with NO (red and blue curves, respectively). Again, the huge changes in the spectral features indicate that the technique is very sensitive to the changes in the coordination sphere around the absorbing atom. Indeed, nonresonant Kβ VtC-XES has been demonstrated to be a very sensitive technique in the ligand identification, that is even able to discriminate among different ligands characterized by a low Z difference, such as C, O, and N. K_β VtC-XES spectroscopy is consequently fully complementary the standard XAS in the ligand determination.[199,219−221,1296,1297]

5.3. Adsorption of NO, CO, and N_2 on Ni^{2+} sites in Ni-CPO-27

Dietzel et al.[1298] synthesized a three-dimensional honeycomb-like metallorganic framework (Figure 40a) with Ni^{2+} as the metal component: $Ni_2(dhtp)(H_2O)_2{\cdot}8H_2O$ (dhtp =2,5-dihydroxyterephthalic acid). This new material, named CPO-27-Ni, belongs to the family of CPO-27-M (Mg, Co, Ni) also known as MOF-74 (synthesized by Yaghi and co-workers) and is isostructural to framework materials with Zn^{2+}, Co^{2+} and Mg^{2+} metal component.[1299−1302]

dx.doi.org/10.1021/cr2000898 | Chem. Rev. 2013, 113, 1736−1850

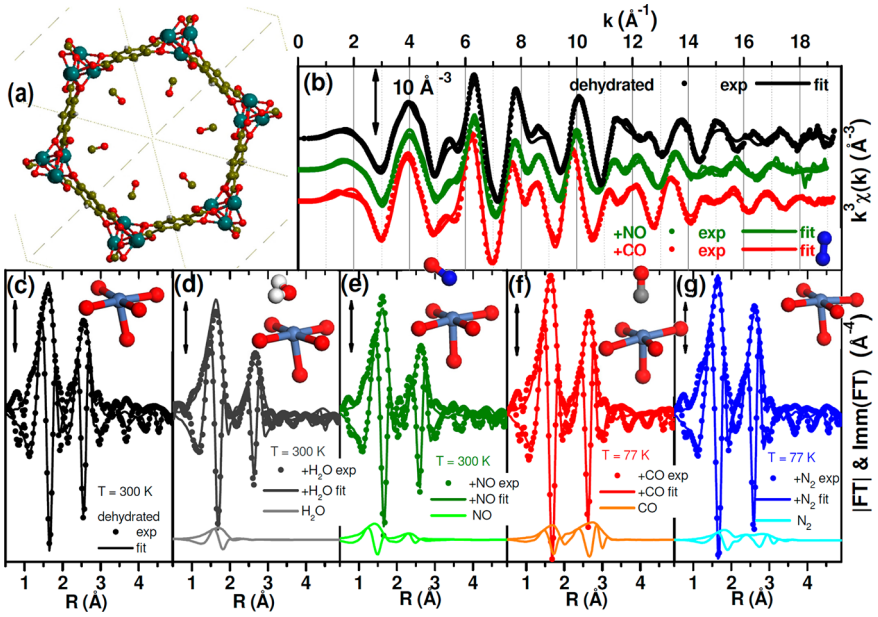

Figure 40. Part a: Structure CPO-27-Ni/CO (Ni^{2+}:CO = 1) optimized by periodic ab initio periodic approach with CRYSTAL code[1303,1304] and viewed along the *c* axis. Part b: $k^3\chi(k)$ functions of CPO-27-Ni after: desolvation (black curves); interaction with NO (green curves); and interaction with CO red curves). Parts c–g: Modulus and imaginary part of the k^3-weighted, phase uncorrected, FT of the EXAFS spectra collected on dehydrated CPO-27-Ni (c) and after interaction with H_2O (d), NO (e), CO (f), and N_2 (g). Where adsorbates are present, vertically translated also the contribution (in both modulus and imaginary parts) of the adsorbed molecule optimized in the fits is reported. The models used in the fits adopted a Ni^{2+}/adsorbate = 1:1 stoichiometry and assumed a linear adsorption geometry for CO and N_2 and a Ni–N–O angle of 130° for the NO (only the O atom of the H_2O molecule has been included in the fit). Insets report the local environment of Ni^{2+} in its dehydrated form, part c, and upon molecular adsorption parts d–g, as optimized by ab initio calculations. In parts b–g scattered and continuous curves refers to the experimental data and the best fit, respectively. The EXAFS spectra have been adapted from refs 1273–1275.

Table 17. Summary of the Parameters Optimized by Fitting the EXAFS Data Collected at 300 and 77 K[a]

sample condition	dehydrated[1273]	in vacuo[1273]	hydrated.[1273]	+NO[1273]	+CO[1274]	+N_2[1275]
T (K)	300	77	300	300	77	77
R_{factor}	0.043	0.033	0.027	0.045	0.018	0.011
N_{ind}	40	40	40	40	40	40
N_{var}	10	10	7	7	12	12
ΔE_0 (eV)	−2.5 ± 1.0	−1.7 ± 1.0	0.5 ± 0.5	−2.5 ± 1.0	0.8 ± 0.7	2.1 ± 1.0
S_0^2	1.17 ± 0.09	1.20 ± 0.08	1.17	1.17	1.18 ± 0.06	1.18 ± 0.05
$\langle R_O \rangle$ (Å)	1.99 ± 0.01	2.00 ± 0.01	2.03 ± 0.01	1.99 ± 0.01	2.024 ± 0.005	2.012 ± 0.005
σ^2(O) (Å^2)	0.0049 ± 0.0005	0.0042 ± 0.0004	0.0049	0.0049	0.0044 ± 0.0004	0.0038 ± 0.0003
R_{Ni1} (Å)	2.892 ± 0.005	2.889 ± 0.005	2.980 ± 0.005	2.95 ± 0.01	2.973 ± 0.005	2.937 ± 0.005
$\sigma^2(Ni_1)$ (Å^2)	0.0055 ± 0.0006	0.0045 ± 0.0004	0.0055	0.0055	0.0038 ± 0.0004	0.0035 ± 0.0003
R_{Ni2} (Å)	4.82 ± 0.02	4.87 ± 0.01	4.78 ± 0.03	4.79 ± 0.02	4.89 ± 0.02	4.86 ± 0.02
$\sigma^2(Ni_2)$ (Å^2)	0.0059 ± 0.0018	0.0052 ± 0.0014	0.0059	0.0059	0.008 ± 0.002	0.006 ± 0.002
α	−0.008 ± 0.009	−0.003 ± 0.007	−0.021 ± 0.005	−0.024 ± 0.007	−0.013 ± 0.009	−0.003 ± 0.007
σ^2 (Å^2)	0.009 ± 0.004	0.007 ± 0.003	0.009	0.009	0.009 ± 0.005	0.009 ± 0.004
R_{ads} (Å)			2.10 ± 0.04	1.85 ± 0.02	2.11 ± 0.02	2.27 ± 0.03
σ^2_{ads} (Å^2)			0.01 ± 0.01	0.0065 ± 0.002	0.006 ± 0.002	0.010 ± 0.005
$-\Delta H^{expt}_{ads}$(kJ mol^{-1})			100	92	58	17

[a]The fits were performed in *R*-space in the 1.0–5.0 Å range over k^3-weighted FT of the $\chi(k)$ functions performed in the 2.0–18.0 Å^{-1} interval. A single ΔE_0 and a single S_0^2 have been optimized for all SS and MS paths. The Ni–O and Ni–Ni (first and second neighbor) SS paths have been modeled with their own path length and Debye–Waller factors, while an unique σ^2 and an unique path length parameter α, common to all other SS and MS paths, have been optimized. NO, CO and N_2 adsorption have been simulated by treating the molecule as a rigid body linearly adsorbed on Ni^{2+}. Consequently only two additional parameters are needed: the Ni-molecule distance (R_{ads}) and the corresponding Debye–Waller factor (σ^2_{ads}). N_{ind} = number of independent points ($\pi\Delta R\Delta k/2$). N_{var} = number of optimized parameters. This table summarizes the data from refs 1273, 1274, and 1275.

CPO-27 framework contains one-dimensional channels (Figure 40a) filled with water that can be removed by a mild thermal treatment. Upon dehydration the crystalline structure is preserved and a material with a high surface area is obtained (about 1100 m^2/g),[1298] which contains unsaturated metal sites organized in helicoidal chains.[1298] At the intersections of the honeycomb are helical chains of cis-edge connected nickel oxygen octahedra running along the *c* axis. Nearest neighbors helices are of opposite handedness. Each chain is connected by the organic ligand with three adjacent chains, resulting in the

dx.doi.org/10.1021/cr2000898 | *Chem. Rev.* 2013, 113, 1736–1850

honeycomb motif. The channels in the honeycomb have a diameter of ~11 Å (see Figure 40a). All of the O atoms of the ligand are involved in the coordination of Ni^{2+}; these oxygens account for five out of six ligands for each nickel atom, while the sixth coordinative bond is to a water molecule which points toward the cavity.

CPO-27-Ni, in both its hydrated an dehydrated forms, was studied in detail by Bonino et al.[1273] The structure obtained from XRPD Rietveld refinement[1298] was used as input for the EXAFS model, resulting in an excellent agreement between the set of distances optimized with the two different techniques. The EXAFS signal was quite complex because constituted by several SS and MS paths. Therefore, Bonino et al.[1273] cross-checked the validity of their EXAFS model analyzing the data collected on dehydrated CPO-27-Ni at 300 and 77 K (see Table 17). The model was validated as all optimized distances were comparable in the two data sets, while the thermal parameters σ, see eq 19, increased moving from 77 to 300 K. Water removal from CPO-27−Ni affect significantly both its XANES and EXAFS spectra. In particular, the average Ni−O first shell distance decreases from 2.03 ± 0.01 Å down to 1.99 ± 0.01 Å, while an even more impressive contraction was observed for the second shell Ni−Ni distance, that moves from 2.980 ± 0.005 Å down to 2.892 ± 0.005 Å, see Table 17. The desolvation process caused the removal of the water molecule coordinated to the metal center, resulting in Ni^{2+} cations with a coordinative vacancy potentially able to coordinate ligand molecules. The interaction of NO, CO and N_2 ligands with desolvated CPO-27-Ni has been deeply investigated by means of Ni K-edge XANES and EXAFS spectroscopies, supported by parallel IR and UV−vis techniques.[1273−1275]

High quality data were obtained in transmission mode up to almost $k = 20$ Å^{-1}, see Figure 40b: this allowed to reach an high resolution in R-space, better than 0.08 Å see eq 22. The EXAFS data (and corresponding best fits) obtained on dehydrated CPO-27-Ni and after interaction with H_2O, NO, CO and N_2 are reported in *R*-spaces in Figure 40c−g and Table 17. The higher intensity of the EXAFS oscillation in the case of the CPO-27-Ni/CO and CPO-27-Ni/N_2 is evident and is due to the fact that corresponding spectra were collected at 77 K,[1274,1275] while the spectra of CPO-27-Ni contacted by H_2O and NO were collected at 300 K.[1273] This implied that authors were forced to fix much more parameter in the analysis of the this last case, see Table 17. Independent IR experiments allowed to fix the coordination number of the adsorbed molecules (NO, CO, and N_2) to 1.[1273−1275]

Adsorption of molecules on Ni^{2+} sites strongly modifies the whole framework structure inducing elongation in Ni−O and Ni−Ni distances. Figure 41a−d summarizes experimental structural data (XRPD and EXAFS) on the adsorption of H_2O, NO, CO, CO_2, and N_2, molecules on CPO-27-Ni material. Data are reported as a function of the enthalpy of adsorption measured via standard microcalorimetric[1273,1274] or via temperature-dependent IR desorption[1275] or via isosteric heat of adsorption.[1305] The figure summarizes data collected at both 77 and 300 K (open and full symbols, respectively). Comparison with the analogous values obtained from a theoretical study performed at the B3LYP-D*/TZVP level of theory (using a periodic boundary conditions) is reported in parts (e−h) of Figure 41.

From the reported set of data, it clearly emerges that computed framework distances and computed adsorption distances are systematically overestimated by the theory. Notwithstanding this fact, the trends observed in the experimental data are clearly mirrored by the theoretical data. In particular, it emerges from both experimental and theoretical data that, the larger is the adsorption energy, the larger is the perturbation induced by the adsorbed molecule to the MOF framework in terms of elongation of the $\langle R_O \rangle$, R_{Ni1}, and R_{Ni2} distances, see parts a−c and e−g of Figure 41, respectively. Regarding the adsorption distance, it follows an opposite trend: the larger is the $-\Delta H_{ads}$ ($-\Delta E^c_{ads}$), the shorter is R_{ads}, see Figure 41d and Figure 41h, respectively.

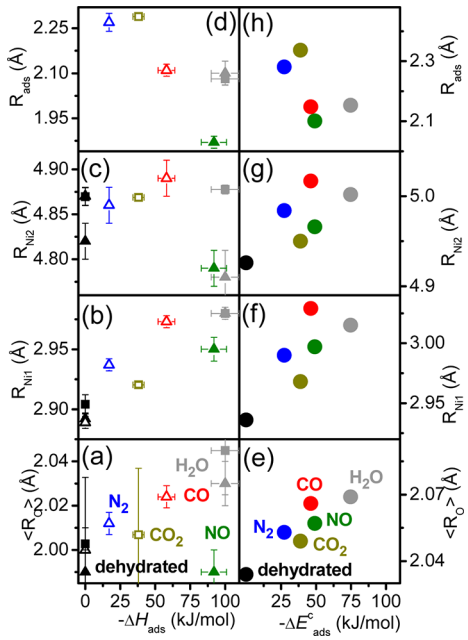

Figure 41. Correlation of the different structural parameters upon molecular adsorption on Ni^{2+} site with the corresponding adsorption energy. Left: experimental values (HRPD circles, EXAFS triangles) and corresponding incertitudes. Full and open symbols refer to data collected at 300 and 77 K, respectively. Right: Theoretical values. Note that left and right parts do not have exactly the same ordinate intervals. This reflects the systematic overestimation of the theoretical distances. Beside this fact, all trends are well reproduced. Adapted with permission from ref 1304. Copyright 2012 Elsevier.

As far as EXAFS results are concerned, it is worth noticing that $\langle R_O \rangle$, and R_{Ni2} increase by decreasing the temperature from RT (filled triangles) to 77 K (empty triangles), while R_{Ni1} does not change. An increase in the cell volume by decreasing the temperature indicates a negative thermal expansion coefficient; this rare property in solids is shared by some other MOF structures, as determined by temperature dependent diffraction experiments on MOF-5[1306−1308] or foreseen by force-field calculations on the IRMOF-1/-10/-16 family,[1309−1311] and on HKUST-1.[1312,1313]

For what concerns the calculations they predict an increase of all the framework distances upon molecule adsorption and an almost linear relationship between the adsorption energy and the distance elongation (Figure 41e−g). These findings have been confirmed by the experiments: as a general statement both XRD and EXAFS indicate an increase of all the framework distances upon molecular adsorption. However, in the experiments a larger spread of the data is observed because of the different coverages adopted in the different experiments. In fact, whereas in the calculations the coverage was fixed to

dx.doi.org/10.1021/cr2000898 | *Chem. Rev.* 2013, 113, 1736−1850

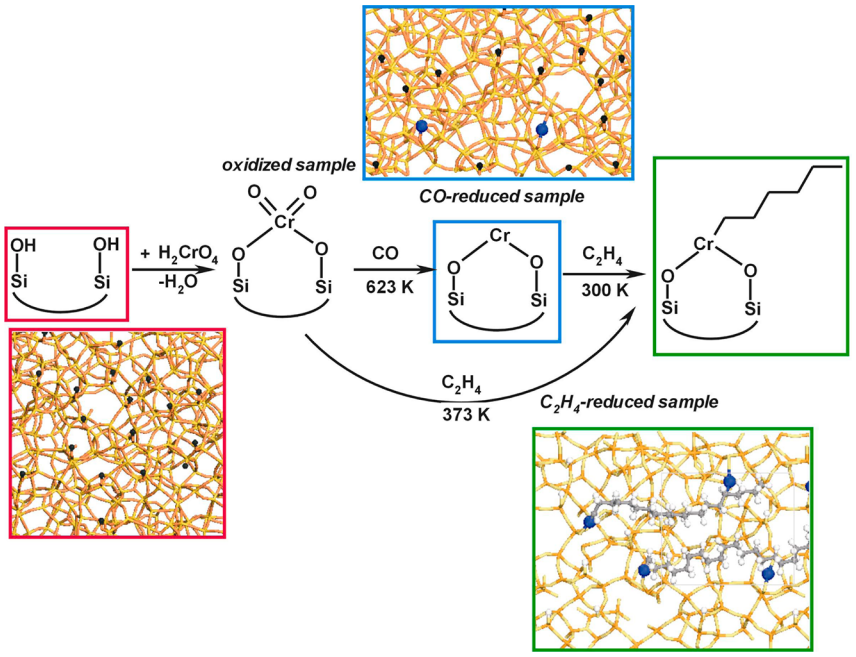

Figure 42. Schematic representation of the synthesis procedure for the Cr/SiO_2 Phillips catalyst (see text for a detailed description). In the insets, red and yellow sticks connect together silicon and oxygen atoms respectively; the big blue balls represent Cr(II) ions, while the little gray and white (black) balls represent carbon and hydrogen atoms, respectively.

Ni/molecule = 1:1, in the XRD for CO_2 and H_2O a Ni/CO_2 = 1:0.5−0.6 and Ni/H_2O = 1:5 where adopted. The different behaviour of R_{Ni2} upon H_2O absorption, as revealed from EXAFS and XRPD (indicating a shortening and a lengthening, respectively), is likely ascribable to the different coverages adopted in the two experiments. In fact, whereas the XRPD data have been recorded for the highest coverage, the EXAFS measurements have been recorded at a lower Ni/H_2O ratio and then the $Ni_{ads}-Ni_2$ shortening is a reflection of the high interaction energy. In fact a shortening of R_{Ni2} has been also observed for NO, the second molecule in terms of interaction energy among molecules considered in Figure 41. Coming to the distance between the Ni atom and the adsorbed molecules (R_{ads}), in this case an opposite trend is observed in both experiments and calculations, as expected: in fact this distance shortens by increasing the energetic of the interaction, the shortest distances being observed for the larger interacting molecules that is for H_2O and NO.

The here reviewed multitechnical approach[1273−1275,1303−1305] requiring XRPD and EXAFS for structural determination and microcalorimetry or temperature-dependent IR desorption or isosteric heat of adsorption for adsorption enthalpies determination and supported by periodic DFT calculation, is relevant in understanding and foreseeing applications to a potential practical uses of MOF materials. Indeed, the understanding of the molecular adsorption on a given surface site is the first step in understanding whether the site may have a potential catalytic reactivity or not. On the other hand, measuring (or computing) adsorption enthalpies of different molecules allows to establish an adsorption strength scale that is relevant in determining a selective adsorption ranking useful for gas separation and selective adsorption purposes. In more detail, (i) the significant difference in the $-\Delta H_{ads}$ (and $-\Delta E^c_{ads}$) for the adsorption of H_2 and CO implies that CPO-27-Ni is an interesting material for the purification of a H_2/CO mixture used to feed fuel cells. (ii) The material can clearly play a role also in the CO_2 capture, even at relatively high temperatures, that is, for *postcombustion* capture as demonstrated by the work of Dietzel et al.[1305] (iii) Finally, the ability of H_2O to progressively displace NO from the Ni^{2+} sites,[1273] makes CPO-27-Ni a good candidate for a controlled NO drug delivery inside the human body, similarly to the HKUST-1 MOF investigated by the group of Morris.[1187,1286]

6. CR/SIO$_2$ PHILLIPS CATALYST: IN SITU ETHYLENE POLYMERIZATION

6.1. Relevance of the Catalyst and Still Open Questions

The Cr/SiO_2 Phillips catalyst for ethylene polymerization[1314] accounts for a large share (more than one-third) of the world's high density polyethylene (HDPE) supply, as well as some low density polymers.[113,1315] The Phillips HDPE has a very broad molecular weight (MW) distribution that confers characteristic rheologic properties useful for specific applications. The synthesis procedure is fairly simple, as schematically shown in Figure 42. Amorphous silica is impregnated with a chromium compound (such as H_2CrO_4). The system is then activated at high temperature in oxidizing conditions, with the consequent grafting of Cr in the form of monochromate species; extensive dehydroxylation of the silica surface occurs at the same time. A typical catalyst contains about 0.5−1.0 wt % Cr.[64,113,1315−1317] The Cr(VI) precursors (oxidized sample in the following) are then reduced by C_2H_4 (industrial process, C_2H_4-reduced sample)[113] or by CO (model laboratory process, CO-reduced sample),[64,113,1318−1320] with formation of Cr(II) species, which are the active sites in ethylene polymerization.

In addition to its industrial importance, the interest in the Phillips catalyst is mainly related to its ability to polymerize C_2H_4 without the intervention of any activator, a fact which makes it unique among all the polymerization catalysts, such as the Ziegler−Natta[1321−1327] and the metallocene-based systems.[1328,1329] Notwithstanding the numerous efforts, three

dx.doi.org/10.1021/cr2000898 | *Chem. Rev.* 2013, 113, 1736−1850

main questions are still open: (i) the structure of the active sites; (ii) the fraction of the active sites, and (iii) the initiation mechanism of the polymerization reaction.[64,113,1315] It is worth noticing that the first two questions are objects of debate for the large majority of olefin polymerization catalysts, both homogeneous and heterogeneous, so that the discussion made for the Phillips catalyst has a more general validity. These three problems are strictly connected and mainly related to the high heterogeneity of the Cr sites present on the surface of the amorphous silica. In particular, it is clear that, in order to have an insight into the initiation mechanism, it is necessary to define the structure of the active sites. This represents a challenge for characterization methods, also because the low concentration of the active sites favors the observation of the spectator species instead of the working centers.[1330]

6.2. XAFS Applied on the Phillips Catalyst

The examples reported in the previous sections demonstrate that XAFS spectroscopies, owing to their atomic selectivity, represent techniques of choice in the characterization of highly diluted species.[9,13,45] Moreover, the short mean free path of the photoelectron (which is the probe of XAFS spectroscopy) limits the sensibility of the technique to few Å around the absorbing atom (see section 2.3.2). This implies that, unlike XRD, no long-range order is required and structural information can be obtained from amorphous systems also. For these reasons, XAFS spectroscopies are, in principle, powerful techniques to understand the local structure and the oxidation state of Cr species on the Phillips catalyst. Nevertheless, in contrast to the large amount of XANES studies on various chromium compounds reported in the past,[1331−1336] only few XAFS works appeared on the Phillips catalyst or on related systems,[64,117,118,1316,1337−1339] and only one is focused on in situ C_2H_4 polymerization.[1316] Three main reasons could be tentatively accounted for this lack. (i) The high reactivity of the reduced $Cr(II)/SiO_2$ catalyst toward O_2 and H_2O requires an extremely severe control of the atmosphere, that is not easily transferred from the laboratory to a synchrotron beamline. (ii) The copresence of different local environments for the Cr species, because of the heterogeneity of the support (see Figure 42), or of several Cr phases makes the data analysis extremely complex. This last point is particular true when dealing with sample characterized by a Cr loading higher than 1 wt.% (which is a necessary condition when the experiment is conducted in transmission mode), since it is well-known that in these conditions a fraction of Cr forms Cr_2O_3 aggregates inactive in ethylene polymerization (vide infra inset in Figure 43a). (iii) Finally, the low fraction of Cr sites involved in the C_2H_4 polymerization could be a limiting factor in the detection of the coordinative environment of Cr centers in working conditions (i.e., during the polymerization reaction).

In the following it will be shown that, notwithstanding all these problems, XAFS techniques have been applied with success also on the Phillips catalyst.[64,117,118,1316,1317,1337−1339] The use of a third generation synchrotron radiation source allowed to collect XAFS spectra of always increasing quality, both in terms of energy resolution and of signal-to-noise ratio. The oxidized catalyst has been the most investigated one,[117,1316,1337,1339] and the corresponding XANES spectrum has been often used to demonstrate the single-site nature of grafted Cr species. A brief summary of the main results achieved on this topic will be done in section 6.2.1.

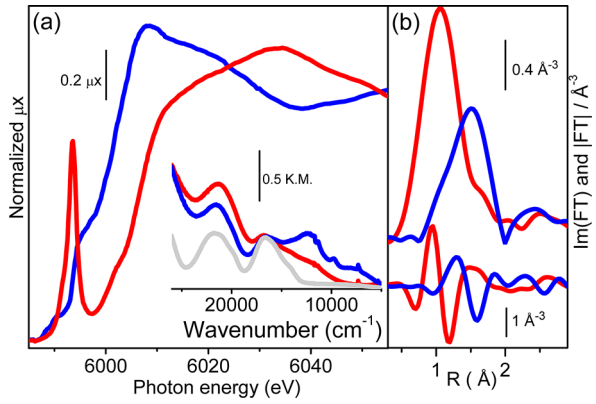

Figure 43. Part a: XANES spectra of the oxidized (red curve) and CO-reduced (blue curve) Cr/SiO_2 systems. The inset reports the DR UV−vis spectra of the oxidized (red curve) and CO-reduced sample (blue curve), together with the spectrum of α-Cr_2O_3 (gray line) for comparison. Part b: Modulus of the k^2-weighted, phase-uncorrected, Fourier transform (|FT|, 2−11 $Å^{-1}$ range) of the EXAFS signals collected together with the XANES spectra reported in part (a). In the bottom part are reported, with the same symbols, the corresponding imaginary parts. Experimental data from ref 1316.

On the contrary, to the best of our knowledge, only few works report XAFS data on the reduced $Cr(II)/SiO_2$ catalyst.[117,118,1316,1339b] Groppo et al.[1316] investigated by XAFS in transmission mode a 4 wt % Cr loaded sample. The high Cr loading was the lowest possible for transmission measurements to be performed, but caused the segregation of a fraction of Cr species in the form of clustered Cr_2O_3 phase, which complicated the successive data analysis. Nevertheless, authors succeeded in evaluating the fraction of clustered Cr_2O_3, by performing a two phases EXAFS data analysis. Moreover, the same sample was investigated after in situ ethylene polymerization. A careful analysis of the XANES data, and comparison with IR spectroscopy of adsorbed CO molecule, allowed to evaluate the fraction of Cr sites active in ethylene polymerization. A brief summary of these results will be given in sections 6.2.1.1 and 6.2.1.2. Much more recently, the same authors[118] succeeded in performing a XAFS experiment on a 0.5 wt % $Cr(II)/SiO_2$ catalyst, thus obtaining the first XAFS data of $Cr(II)/SiO_2$ without the copresence of clustered Cr_2O_3. These results will be discussed in section 6.2.2. Very recently, the group of Scott reported EXAFS spectra of a $Cr(II)/SiO_2$ catalyst obtained starting from CrO_2Cl_2 precursor collected at 10 K.[1339b] The spectra are characterized by an unprecedented quality in terms of signal/noise ratio, and allowed authors to extract very detailed structural information. When the oxidation step is performed at 500 °C, the local environment of Cr(II) was reproduced with two O atoms at 1.88 ± 0.01 Å and one O atom at 1.98 ± 0.02 Å in the first coordination shell; additionally, two O atoms at 2.49 ± 0.01 Å and 2.94 ± 0.01 Å, attributed to non-bonded adjacent siloxane groups, and a Si atom at 3.19 ± 0.08 Å were used to simulate the contributions at longer distances. Similar results were obtained for the sample activated at higher temperature (800 °C). The agreement between experimental and best-fit curves was excellent in both cases. However, the values of the optimized Debye-Waller factors are difficult to be understood. In particular, for the sample activated at 500 °C, the σ^2 factor of the non-bonded siloxane group at 2.49 Å was found to be much lower that that of bonded oxygen atoms at 1.88 Å (0.0017 vs. 0.0068 $Å^2$);

dx.doi.org/10.1021/cr2000898 | Chem. Rev. 2013, 113, 1736−1850

whereas for the sample activated at 800 °C σ^2 values of 0.0017, 0.0078 and 0.0014 Å^2 where found for O atoms located at 1.92, 2.01 and 2.90 Å, respectively.

6.2.1. A 4 wt % Cr/SiO$_2$ Sample: XAFS in Transmission Mode. Figure 43 reports the Cr K-edge XANES spectra (part a) and the k^2-weighted, phase-uncorrected, Fourier transform of the EXAFS signals (moduli and imaginary parts, top and bottom in part b) for a 4 wt % Cr/SiO$_2$ catalyst in the oxidized and reduced forms (for experimental details concerning the catalyst activation procedure see section 2.1.3 and refs 1316 and 1317). The spectra, collected in transmission mode, are affected by the presence of an unavoidable fraction of clustered α-Cr$_2$O$_3$. This is demonstrated by the DR UV−vis spectra reported in the inset of Figure 43a. Isolated Cr(VI) species on a 0.5 wt.% oxidized sample should give rise to two main components at about 30 000 and 21 500 cm^{-1}, ascribed in the literature to oxygen-to-chromium CT transitions,[64,1319] whereas the UV−vis spectrum obtained after CO-reduction should be characterized by an intense CT at about 30 000 cm^{-1} and by two d−d transitions at 12 000 and 7500 cm^{-1},[64,1319] which are the fingerprints of Cr(II) species in a distorted tetrahedral environment. For the 4 wt % loaded sample (inset in Figure 43a), both in the oxidized (full gray curve) and in the CO-reduced form (black curve), two additional bands are present around 30 000 and 21 500 cm^{-1}. These bands are typical of clustered Cr(III) in octahedral symmetry, as observed for the α-Cr$_2$O$_3$ particles (gray curve in the inset of Figure 43a).[1340] Therefore, UV−vis spectroscopy provides an evidence that a fraction of clustered α-Cr$_2$O$_3$ particles is present on both oxidized and CO-reduced samples. For this reason any quantitative EXAFS data analysis, when possible, should be performed with caution, by considering the copresence of two different phases: the isolated Cr species and the aggregated α-Cr$_2$O$_3$ particles.

The XANES spectrum of the oxidized catalyst (red curve) is characterized by an intense pre-edge peak at 5993.5 eV (see Figure 43a), characteristic of Cr(VI) species in a T_d-like symmetry,[117,1316,1317,1337−1339] in good agreement with the literature data based on different spectroscopic laboratory techniques (UV−vis, Raman and XPS).[1319,1341−1344] The corresponding |FT| of the EXAFS signal exhibits a dominant contribution centered at 1.06 Å (phase-uncorrected), which is due to the short Cr═O double bonds of the chromate structure, and a minor shoulder clearly visible at higher distances (1.55 Å, phase-uncorrected), due to longer Cr−O single bonds. Similar data have been shown previously by Weckhuysen et al.,[117] who provided two different explanations, both of them involving the presence of polychromate species. On the contrary, Groppo et al.[1316] interpreted the EXAFS data as due to the presence of a fraction of clustered α-Cr$_2$O$_3$ particles, which prevented any structural EXAFS data analysis. In fact, two kinds of species are present, which give three contributions in the same R region: Cr═O and Cr−O of isolated Cr(VI) species and Cr−O of clustered Cr(III). This heterogeneity in distances implies, in k-space, the superposition of sinusoidal signals with a substantial difference in periodicity. Under such conditions the experimental $\chi(k)$ function is rapidly extinguished by out-of-phase signals and shows only noise for k values higher than 7 Å^{-1}, in a similar way to what discussed for Fe- and Ga-MFI systems (section 3.3.1 and Figure 23). This interpretation was supported by Wang et al.,[1337] who performed an EXAFS experiment in fluorescence mode on a Cr/MCM-41 having a low Cr loading (0.35−1.7 wt %).

Upon reduction in CO, the XANES spectrum of Cr/SiO$_2$ (blue curve in Figure 43a) greatly changes. In particular, it is characterized by a remarkable red-shift of the edge, both respect to the oxidized sample (red curve, about 6.5 eV) and respect to the α-Cr$_2$O$_3$ reference (not reported, about 2.0 eV), suggesting that the treatment in CO reduced Cr(VI) to Cr species in an oxidation state lower than +3. Many independent techniques provided definite proofs that after reduction in CO isolated Cr(II) sites are present on the silica surface. However, in the present case the sample contained also clustered Cr$_2$O$_3$, and therefore the XANES spectrum shown in Figure 43a must be explained as the overlap of the signals of both Cr(II) and Cr(III). The pre-edge peak at 5993.5 eV associated with tetrahedral Cr(VI) species totally disappears and is substituted by a distinct feature at 5995.9 eV, which is considered the fingerprint of anchored Cr(II) species, as it will be discussed in section 6.2.2.1. The presence of an unstructured absorption in the 5990−5993 eV range (a region where pre-edge features of α-Cr$_2$O$_3$ appears) and the shape of the white-line, which shows a peak around 6010 eV (where the spectrum of α-Cr$_2$O$_3$ has a strong signal), confirm that the CO-reduced Cr/SiO$_2$ sample contains a not negligible fraction of clustered Cr$_2$O$_3$. Opposite to what observed for the oxidized sample, the EXAFS spectrum of the CO-reduced catalyst shows a significant signal up to 11 Å^{-1}.[1316] The corresponding k^2-weighted, phase-uncorrected, |FT| (red curve in Figure 43b) shows an almost symmetric peak, centered at 1.51 Å (phase-uncorrected), while the strong Cr═O signal characterizing the oxidized sample is totally destroyed. After reduction the Cr−O distances of the isolated species have undergone a significant elongation owing to the increased ionic radius of Cr(II) with respect to that of Cr(VI), and are now much closer to those of the clustered species.

6.2.1.1. Determination of the Fraction of Clustered Cr$_2$O$_3$: A Two-Phase EXAFS Data Analysis. EXAFS is a suitable technique for quantitative phase speciation, providing that the data analysis is properly carried out.[252,529,669,1068,1318,1345−1348] A conventional EXAFS analysis is usually performed on samples containing a single chemical species, i.e. samples where all the absorbing atoms have the same local coordination. In this case, the value obtained by EXAFS analysis is an evaluation of the real structural parameters around the absorber atom, through the formula reported in eq 19. If more than a single chemical species is present in the sample, the overall EXAFS signal is the weighted sum of the signals belonging to all phases. In such a case the fit must be performed by using a number of theoretical contributions equal to the number of chemical species present in the sample. In the simple case of a system composed by only two phases, the fitting model will include two different contributions, where the coordination number (N), the distance (r), the Debye−Waller factor (σ), and the energy shift (ΔE) should be, in principle, optimized, resulting in 8 fitting parameters. The coordination numbers obtained by the fit are proportional to the real ones according to the following relationship:

$$N_{\text{fit}}(\text{phase 1}) = N(\text{phase 1})\cdot x \quad (35)$$

$$N_{\text{fit}}(\text{phase 2}) = N(\text{phase 2})\cdot(1 - x) \quad (36)$$

where N and N_{fit} are the real coordination numbers and those obtained by the best fit procedure (in both phase 1 and phase 2), respectively, while x is the atomic fraction of the absorber in the first phase. Conversely, the distances and the Debye−Waller factors obtained by the best fit are the correct evaluation

dx.doi.org/10.1021/cr2000898 | Chem. Rev. 2013, 113, 1736−1850

of these parameters for both the two phases present in the sample. This procedure was adopted successfully in several cases, such as (i) copresence of surface copper-aluminate, $CuCl_2$, and paratacamite in catalysts for the ethylene oxychlorination reaction[1346] (vide infra section 8.2); (ii) copresence of three different Cu sites in copper-exchanged Y zeolite;[1068] and (iii) copresence of three different Ag sites in silver-exchanged Y zeolite.[669] In the last two cases, the local environment and the relative population of different cationic sites were previously determined by a Rietveld refinement of high resolution XRPD data collected at the ESRF synchrotron radiation source. The EXAFS data were fit by optimizing only Debye–Waller factors and ΔE parameters (being the coordination numbers and the distances fixed by XRPD analysis); the quality of the fits validated this multiphase approach for the EXAFS data analysis.

The same approach was adopted to analyze the EXAFS spectrum of the CO-reduced Cr/SiO_2 catalysts discusses in the previous section. The two phases present in the CO-reduced sample are isolated Cr(II) species grafted to the silica support and aggregated Cr(III) species. To reduce the number of fitting parameters, it was assumed that the aggregated Cr(III) species have an α-Cr_2O_3-like local structure. Under these assumptions, the two relationships discussed above become:

$$N_{\text{fit}}(\alpha - Cr_2O_3) = N(\alpha - Cr_2O_3)\cdot x \quad (37)$$

$$N_{\text{fit}}(Cr(II)_{\text{isolated}}) = N(Cr(II)_{\text{isolated}})\cdot(1 - x) \quad (38)$$

The EXAFS quantitative analysis has been conducted according with the following steps:[1316,1317] (i) The inverse FT of the EXAFS signal of the α-Cr_2O_3 model compound was performed in the 0.51–3.13 Å range, resulting in a filtered $\chi(k)$ function, which represents the sum of the contribution of all the scattering paths due to atoms in the first, second and part of the third coordination shells around Cr(III) in α-Cr_2O_3. Note that, using this approach, both single and multiple scattering paths are included. (ii) The so obtained signal was used for the extraction of "fictitious" phases and amplitudes that do not refer to a single Cr-scatterer contribution, but reflects the local environment of Cr atoms in the aggregated phase in an overall way. (iii) The fraction of aggregated Cr(III) species in the CO-reduced sample was fitted by using the so obtained phases and amplitudes, leaving N, σ and ΔE as free parameters. In this case, the $N_{\text{fit}}(\alpha$-$Cr_2O_3)$ directly resulted in the fraction x of aggregated species present in the catalyst, according with the relationship reported above. The σ factors were allowed to change, in contrast to the study of Prestipino et al.[1346] (where the size of the crystals of the aggregated paratacamite phase on Al_2O_3 was huge), in order to take into account that a significant fraction of the Cr_2O_3 particles have a very small size, as determined by comparing the UV–vis spectra (see inset in Figure 43a) and XRD data (data not shown). This is a crude way to account for the distributions of bond lengths because of the particle heterogeneity by using a unique fitting parameter. (iv) Finally, the isolated Cr(II) species were fitted using a single Cr–O contribution, leaving N, r, σ, and ΔE as free parameters, such values have thus to be considered on an average ground. Because of the amorphous nature of the support, isolated Cr(II) species are not supposed to contribute to the EXAFS signal at higher r values, so that in the 2.15–3.13 Å range only clustered species contribute to the experimental signal.

The fraction of α-Cr_2O_3-like particles present in the CO-reduced system was estimated to be $x = 0.38 \pm 0.04$ and the σ^2 increased from 0.0050 of crystalline α-Cr_2O_3 to 0.0065 ± 0.0005 Å^2, supporting the hypothesis of the presence of small chromia clusters. For the isolated Cr(II) species, a Cr–O contribution at 1.96 ± 0.01 Å, with a coordination number of 3.6 ± 0.3 and a Debye–Waller factor of 0.0075 ± 0.0006 Å^2 have been obtained.[1316,1317] More reliable data have been obtained more recently by Gianolio et al.,[118] analyzing the EXAFS spectrum of a 0.5 wt % $Cr(II)/SiO_2$ sample up to the second coordination sphere (see section 6.2.2.1).

6.2.1.2. An estimation of the fraction of sites active in ethylene polymerization. The problem of determination of the concentration of active sites (and hence of the turnover frequency) is not peculiar of the Phillips catalyst, but it is a general problem in catalysis. It can be solved case by case by using sensitive methods and strategies. Several efforts have been devoted in the past to develop quantitative spectroscopic methods able to quantify the fraction of active sites in the Phillips catalyst. DR UV–vis, EPR and XPS techniques and their combination have been revealed very useful to quantify the Cr^{n+} (n = 2–6) species as a function of the activation procedure.[1349−1353] However, these results give information on all the Cr species present in the sample, and no precise indication about the fraction of the active sites can be safely obtained. Only a few attempts have been made to determine the number of active sites on the $Cr(II)/SiO_2$ sample when the polymerization is performed at RT. By means of poisoning experiments, values comprised between 10 and 50% of the total Cr sites have been inferred to be active.[64,113,1354,1355] This wide range of values has been explained by considering that the selectivity of the poison toward the active site changes with the poison/site ratio. Conversely, by means of IR spectroscopy, much lower values (less than 10%) have been determined.[114,1356]

Groppo et al.[1357] have proposed a method, based on the combination of XANES and IR spectroscopy of adsorbed CO, to determine the fraction of active sites in the CO-reduced $Cr(II)/SiO_2$ Phillips catalyst. The XANES spectrum of the CO-reduced catalyst after ethylene polymerization at RT (green curve in Figure 44a) is very similar to the spectrum collected prior polymerization (blue line in Figure 43a and in Figure 44a). Only a weak erosion of the shoulder at 5995.9 eV

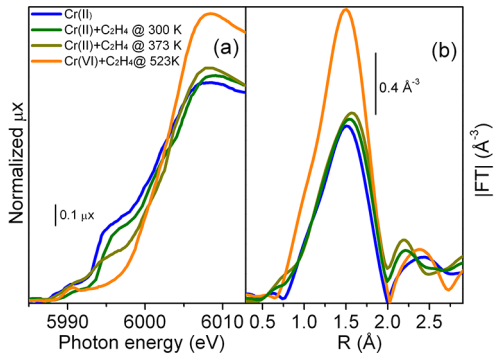

Figure 44. Estimation of the fraction of Cr(II) sites active in the ethylene polymerization. (a) Magnification of the pre-edge features of the XANES spectra of CO-reduced catalyst before (blue) and after ethylene polymerization at 300 K (light green) and 373 K (green), compared to that of C_2H_4-reduced catalyst (orange). (b) Modulus of the k^2-weighted, phase-uncorrected, Fourier transform (|FT|, 2–11 Å^{-1} range) of the EXAFS signals collected together with the XANES spectra reported in part a. Experimental data from refs 1316 and 1357.

dx.doi.org/10.1021/cr2000898 | *Chem. Rev.* 2013, 113, 1736–1850

Table 18. Cr(II) Sites Active in the C_2H_4 Polymerization on the CO-Reduced Catalyst, As Determined by Means of in Situ XANES Spectroscopy and in Situ IR of Adsorbed CO

polymerization conditions	in situ XANES spectroscopy[1316]		in situ IR spectroscopy of adsorbed CO[1357]		
temperature	300 K	373 K	300 K	300 K	373 K
$P_{C_2H_4}$	100 Torr	100 Torr	10 Torr	250 Torr	20 Torr
fraction of active Cr(II)	0.25	0.55	0.37	0.36	0.52

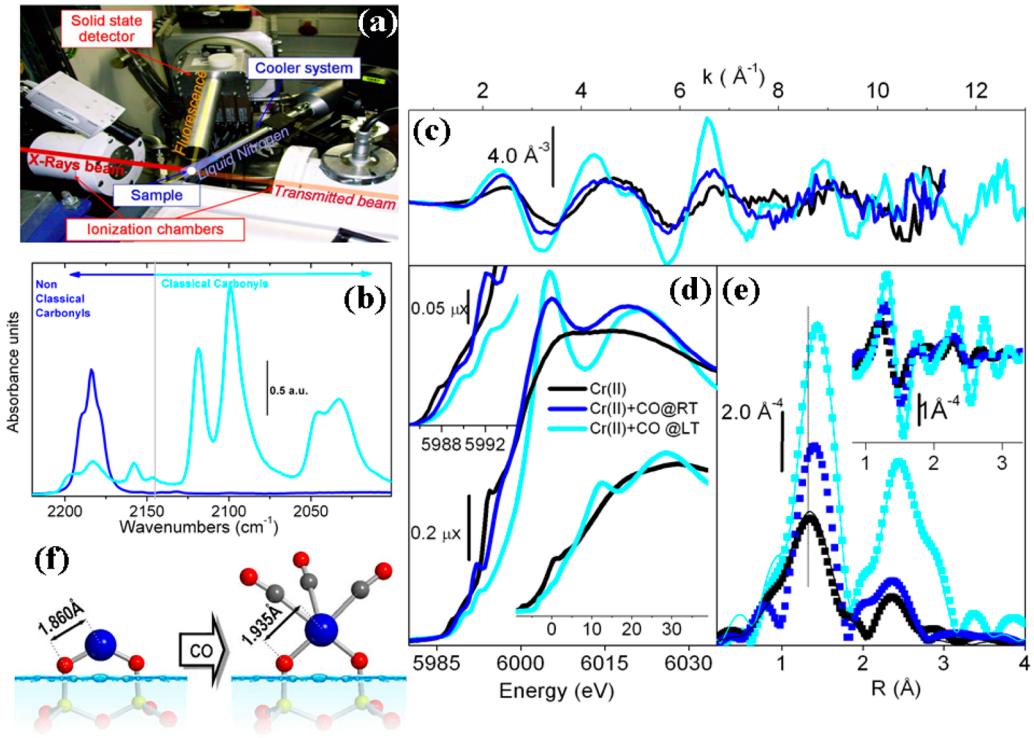

Figure 45. Part a: Experimental setup at ESRF BM26A used for fluorescence XAFS measurements showing the two ionization chambers, the fluorescence detector and the cryostream allowing to cool down the capillary hosting the activated catalyst in CO atmosphere. Part b: Evolution of IR spectra of Cr(II)/SiO_2 (in the ν_{CO} region) as a function of temperature (blue, P_{CO} = 100 Torr at 300 K; cyan, P_{CO} = 100 Torr at 100 K. The vertical gray line represents the stretching frequency of the unperturbed CO molecule, $\tilde{\nu}^0(CO)$ = 2143 cm^{-1}, and discriminates classical from non classical carbonyls. Parts c–e: Evolution of the k^3-weighted $\chi(k)$ (part c), XANES (part d), and FT of the EXAFS signals in both modulus and imaginary parts (part e) of the Cr(II)/SiO_2 system upon increasing CO coverage: black, blue, and cyan spectra refer to the system in vacuo and after interaction with P_{CO} = 150 Torr at 300 and 100 K, respectively. Scattered and full line curves refer to experimental and best fit data, respectively. Top and bottom insets in part d report a magnification of the pre-edge region and the simulated XANES spectra, respectively. Part f: Cartoon showing the solvation effect of CO on Cr(II) hosted on the silica surface. Data from ref 118.

characteristic of Cr(II) species and a slight increase in the intensity of the white line (first resonance after the edge) can be observed, which reflects a modest increase of the average coordination of Cr ions. A stronger modification of the XANES features is obtained by performing the polymerization on the CO-reduced system at 373 K (dark yellow curve in Figure 44a). In this case, both the phenomena are more evident. These results suggested that the number of Cr(II) sites involved in the ethylene polymerization reaction at RT (and low C_2H_4 pressure) is low, hence the XANES spectrum of the catalyst after polymerization reflects the majority of inactive chromium sites. On the contrary, when ethylene polymerization is performed at 373 K, a larger fraction of Cr(II) sites become active in the polymerization, and the corresponding XANES spectrum greatly changes.

The conclusions outlined before are further on demonstrated by looking at the XANES spectrum of a Cr/SiO_2 sample on which the reduction and the polymerization steps are performed simultaneously by dosing C_2H_4 at 523 K on the oxidized sample (orange curve in Figure 44a). The pre-edge peak characteristic of Cr(VI) in a T_d-like geometry (see red curve in Figure 43a) disappears, and the edge absorption shifts toward values lower than the oxidized starting point, confirming that C_2H_4 reduces Cr(VI) during the polymerization reaction. Unfortunately, as discussed above, the situation is complicated by the presence of a fraction of clustered Cr(III) ions, so that it is difficult to estimate the average oxidation state of Cr on the C_2H_4-reduced catalyst. However, by comparing the pre-edge features of the spectrum of the C_2H_4-reduced catalyst (orange curve in Figure 44a) with that of the CO-reduced catalyst after polymerization (dark yellow curve in Figure 44a), the following observations can be made: (i) The white line intensity grows up remarkably, reflecting a much higher increase of the average chromium coordination. (ii) The Cr(II) fingerprint feature at 5996 eV is totally absent, suggesting that almost all isolated chromium species have been involved by the polymerization reaction. Of course, this does not mean that all the Cr(II) sites are active in the polymerization. A large heterogeneity is expected among the isolated Cr species at this stage, including active Cr sites carrying the polymer chains, Cr sites just

dx.doi.org/10.1021/cr2000898 | Chem. Rev. 2013, 113, 1736–1850

perturbed by a polymer generated elsewhere, Cr sites still in interaction with reduction products or, eventually, Cr sites carrying some "deactivating precursors" (such as "Cr-cyclopentane" structures, which have been found to be inactive with respect to polymerization[1358]).

The decrease in intensity of the Cr(II) fingerprint at 5995.9 eV as a function of the polymerization conditions has been used to estimate an upper limit of the number of Cr(II) sites active in ethylene polymerization. By comparing the integrated area of the 5996 eV band for the CO-reduced catalyst after polymerization at RT with that measured before polymerization (Table 18), Groppo et al.[1357] estimated that a fraction of about 25% of the original Cr(II) sites was involved in the polymerization. Analogously, when the polymerization is performed on the CO-reduced catalyst at 373 K, about 55% of the initial Cr(II) sites are estimated to be involved in the polymerization Table 18. These values are in quantitative agreement with those obtained by means of IR spectroscopy of adsorbed CO (see Table 18).[1357]

The picture emerging from XANES is qualitatively confirmed by the EXAFS data. Figure 44b reports the k^2-weighted, phase-uncorrected, |FT| of the EXAFS signals (2−11 $Å^{-1}$ range) collected on the Cr/SiO_2 catalyst after polymerization. The intensity of the peak in the 0.7−2.0 Å interval increases in the order: CO-reduced catalyst (blue line) < CO-reduced catalyst after polymerization at RT (light green line) < CO-reduced catalyst after polymerization at 373 K (green line) < C_2H_4-reduced catalyst (orange line). EXAFS is unable to discriminate between Cr−O and Cr−C first shell contributions. However, as authors did not expect a change of the Cr-to-support interactions, the increase of the peak at 0.7−2.0 Å was attributed to an increase of the average number of C atoms entering in the first coordination shell of isolated Cr species after polymerization. The heterogeneity of Cr species under polymerization conditions prevented any attempt to obtain quantitative data from the corresponding EXAFS spectra and the discussion has to be concluded on a qualitative ground.

6.2.2. A 0.5 wt % Cr/SiO_2 Sample: XAFS in Fluorescence Mode. Very recently, Gianolio et al.[118] succeeded in directly determine the structural properties of $Cr(II)/SiO_2$ by means of in situ XAFS measurement. The success of the experiment was mainly related with the adopted experimental setup (Figure 45a). In that case, the $Cr(II)/SiO_2$ system was prepared inside capillaries sealed in controlled atmosphere, allowing the authors to solve contamination problems also in case of long time acquisitions, necessary for highly diluted systems (0.5 Cr wt%) measured in fluorescence mode. The low Cr loading also assured the absence of the undesired Cr_2O_3 phase that complicated the EXAFS data analysis described in section 6.2.1. The use of capillaries is standard for powder XRD measurements,[1068] but it is much more demanding for XAFS experiment because the X-ray beam must be vertically focused in the same point along the whole energy scan.[90,323] This request can be fulfilled in a third generation synchrotron radiation beamline, as discussed in section 2.2.7. The results obtained on $Cr(II)/SiO_2$ and the strategy followed to analyze the data will be discussed in section 6.2.2.1.

Following the same experimental procedure, the authors investigated also the structural modification of $Cr(II)/SiO_2$ upon adsorption of CO, used as probe molecule. Interaction of $Cr(II)/SiO_2$ with CO was studied since decades by in situ IR,[64,115,1318] probing the formation at room temperature of nonclassical[1058,1086,1092,1359,1360] (prevailing σ-donation) carbonyls on a heterogeneity of Cr(II) sites. The nature of carbonyls turns to classical one[1058,1086,1092,1359,1360] (prevailing π-back-donation) upon lowering the temperature (increasing the coverage), followed by a spectacular change in the IR spectra (from blue to cyan curves in Figure 45b). This behavior has been interpreted as the direct evidence of the unique role of the surface in the optimization of the Cr-CO interaction. In situ Raman experiments highlighted that the vibrational modes emerging from the silica background because of the resonant intensification due to the presence of the Cr(II) cations, are significantly perturbed upon CO adsorption.[1361] This was a clear, although indirect, proof that an important rearrangement of the local environment of the Cr(II) site at the silica surface occurs upon CO adsorption. Direct structural evidence were finally obtained by XAFS, as summarized in section 6.2.2.2.

6.2.2.1. Local Structure of Cr(II)/SiO_2. The XANES spectrum of the 0.5 wt % $Cr(II)/SiO_2$ in vacuo (black curve in Figure 45d) is much more defined than that of 4.0 wt % $Cr(II)/SiO_2$ sample discussed above (Figure 43a). In particular, it presents two weak pre-edge features at 5987.7 and 5990 eV (due to $Cr_{1s} \rightarrow (Cr_{3d} + O_{2p})$ dipole-forbidden transitions), and a strong one at 5994.4 eV (already assigned to $Cr_{1s} \rightarrow Cr_{4p}$ transition). This latter feature is more intense and sharper than that observed for the 4.0 wt % sample. Moreover, the white line is almost featureless, testifying the complete absence of clustered Cr_2O_3.

The corresponding EXAFS spectrum is shown in Figure 45c, whereas the FT of the EXAFS spectrum is displayed in Figure 45e (in both modulus and imaginary parts). The absence of contamination from Cr_2O_3 allowed Gianolio et al.[118] to better define the environment of Cr(II), with respect to the previous work of Groppo et al.[1316] (section 6.2.1). For $Cr(II)/SiO_2$ in vacuo (black squares in Figure 45e), the |FT| is dominated by a peak centered at 1.35 Å due to two $Cr-O_1$ contributions, where O_1 are the oxygen atoms at SiO_2 surface to which Cr is directly grafted. A first fit performed only on this first shell (first column in Table 19) confirms the coordination number of two ($S_0^2 = 0.9 \pm 0.3$) and results into $Cr-O_1$ distance of 1.86 ± 0.03 Å. The σ^2 value of 0.015 ± 0.005 $Å^2$ is in agreement with the expected heterogeneity of the grafted Cr(II) sites. Beside this main peak, a less intense component at higher distance (2.34 Å) is also evident. Among the species that could potentially contribute to this peak, there are the silicon atoms bearing the O_1 atoms and the oxygens belonging to weaker siloxane ligands (O_2). Neither of them, individually, is able to fit the experimental datum. However, when a combination of the two contributions is considered, the number of involved variables ($N_{var} = 11$) becomes higher than the number of independent parameters: $n_{ind} = 2\Delta k \Delta R/\pi \approx 10$, see eq 21. Therefore, the fit in the larger ΔR = 1.0−3.0 Å range was performed by (i) fixing the first shell variables to the values obtained from the previous fit and (ii) fixing σ^2_{Cr-O2} equal to σ^2_{Cr-O1} and N_{Cr-Si} equal to N_{Cr-O1} to avoid correlation problems. In this way, $N_{var.}$ was reduced to 4. The quality of the fit ($R_{factor} = 0.024$) is appreciable in Figure 45e (black curve), and the obtained results are reported in Table 19 (second column).

6.2.2.2. Direct Evidence of Adsorption Induced Cr(II) Mobility on the Silica Surface upon Complexation by CO. In a successive step, the interaction of $Cr(II)/SiO_2$ with CO was investigated by XAFS. Both, XANES and EXAFS spectra are strongly affected by CO interaction. In particular, upon CO

dx.doi.org/10.1021/cr2000898 | Chem. Rev. 2013, 113, 1736−1850

Table 19. Summary of the Optimized Parameters in the Analysis of EXAFS Data for the Cr(II)/SiO_2 Catalyst in Vacuo and after CO Adsorption at 100 K.[a] Reproduced with Permission from Ref 118. Copyright 2007 Royal Society of Chemistry

	Cr(II)/SiO_2		Cr(II)/SiO_2 + CO
R-range (Å)	1.00−2.20	1.00−3.00	1.00−4.20
N_{var}/N_{ind}	4/6	4/10	8/16
S_0^2	0.9 ± 0.3	0.9	0.9
ΔE_0 (eV)	−1 ± 4	−1	0 ± 1
N_{Cr-O1}	2	2	2
R_{Cr-O1} (Å)	1.86 ± 0.03	1.86	1.935 ± 0.007
σ^2_{Cr-O1} (Å^2)	0.015 ± 0.005	0.015	0.007 ± 0.001
N_{Cr-O2}		2.8 ± 0.4	
d_{Cr-O2} (Å)		2.64 ± 0.03	
σ^2_{Cr-O2} (Å^2)		0.015	
N_{Cr-Si}		2	2
R_{Cr-Si} (Å)		2.70 ± 0.02	2.76 ± 0.02
σ^2_{Cr-Si} (Å^2)		0.012 ± 0.001	0.014 ± 0.002
N_{Cr-CO}			2.3 ± 0.3
R_{Cr-CO} (Å)			1.995 ± 0.008
σ^2_{Cr-CO} (Å^2)			0.009 ± 0.001
R_{factor}	0.031	0.024	0.007

[a]Non-optimized parameters can be distinguished by the absence of the corresponding error bar. The fits were performed in the R space over a 2.0−10.0 Å^{-1} k-range.

adsorption at 300 K (blue curve) the weak pre-edge bands in the XANES spectrum blue shift of ∼2 eV and almost triplicate their intensity (top inset in Figure 45d), while the strong pre-edge band approaches the edge, becoming less visible. The featureless edge of the Cr(II)/SiO_2 becomes structured, exhibiting two well-defined components at 6005 and 6020 eV, typical of metal carbonyl complexes[417,418,1362] and due to $Cr_{1s} \rightarrow \pi_{CO}$ transitions (see the corresponding A and B components in the XANES spectra of Cu^{2+} carbonyls reported in Figure 32). When the CO coverage is increased (100 K spectrum, cyan curve), the pre-edge components further blue shift, making the $Cr_{1s} \rightarrow Cr_{4p}$ transition almost indistinguishable from the edge, and the $Cr_{1s} \rightarrow \pi_{CO}$ transitions on the edge are spectacularly intensified. The main modifications of the XANES spectrum upon carbonyl formation are well predicted by simulation (bottom inset in Figure 45d) performed with FDMNES code[482] on clusters able to correctly predict the Cr(II) carbonyl vibrational features.[1363]

In EXAFS, the overall $k^3\chi(k)$ signal (Figure 45c) increases upon carbonyl formation because of the important multiple scattering (MS) contribution of the linear Cr−CO paths. In the R space (Figure 45e), this behavior corresponds to a 2-fold increase of the first shell contribution and to the growth of a broad and intense band at higher R-values. From independent techniques, it is well-known that upon CO addition at 300 K both mono- and dicarbonyls are formed on slightly different Cr(II) sites.[64] Formation of carbonyls implies an additional contribution to the EXAFS signal (Cr−CO paths) that should be simulated with three more variables (N_{Cr-CO}, σ^2_{Cr-CO}, and R_{Cr-CO}), in addition to those needed to describe Cr(II)/SiO_2 in vacuo. Such a great number of variables prevented Gianolio e al.[118] to fit the data collected at 300 K (blue squares in Figure 45e). On the contrary, the system measured at 100 K (cyan squares in Figure 45e) is less complex. It is well-known that in these conditions multicarbonyls are formed to the detriment of weaker siloxane ligands, which are displaced;[64] this limits the number of variables. Moreover, in this last case the signal is strongly intensified by the MS contributions of linear CO ligands. For these reasons, the fit could be performed without fixing the first shell parameters (only S_0^2 is kept to the value obtained for Cr(II)/SiO_2), allowing to appreciate the change in the Cr(II) coordination sphere induced by CO adsorption.

The results of the fit (performed in the Δk = 2.0÷10.0 Å^{-1} range for consistency with the Cr(II)/SiO_2 system) are reported in the last column of Table 19 and shown in Figure 45e. An average number of carbonyls for chromium sites (N_{Cr-CO}) of 2.3 ± 0.3 is obtained, at a distance of 1.995 ± 0.008 Å. The intrinsic low accuracy of EXAFS in the determination of coordination numbers allows Gianolio e al.[118] to confirm the coexistence of mono-, di-, and tricarbonyls, but no exact stoichiometry has been formulated.[64] Conversely, the results of the fit clearly show that the carbonyl formation causes a consistent elongation of the Cr−O_1 distance of 0.08 Å, demonstrating that CO ligands "extract" Cr(II) sites from the surface. Note that this behavior is directly appreciable in the FT (both modulus and imaginary parts) of the spectra, where a shift of the first shell peak toward higher R-values is observed. As a direct consequence, an important decrease of the σ^2_{Cr-O1} (0.007 vs 0.015 Å^2) is observed, suggesting a higher homogeneity of the sites. The same effect has been recently predicted by ab initio calculation.[1363]

As a summary of this section, XANES data reported in Figure 45d show that remarkable modification in the electronic configuration of Cr(II) sites occurs during carbonyls formation, both at 300 and 100 K. The great variation observed upon lowering the temperature is the electronic image of the changes in the vibrational properties observed by IR spectroscopy (Figure 45b), and explained in terms of conversion of nonclassical into classical carbonyls. This is possible because the extraction of the Cr from the surface (R_{Cr-O1} increased by 0.08 Å) allows the optimization of the $Cr^{2+}\cdots$CO bonds by populating $Cr_{3d}-\pi_{CO}$ molecular orbital that is Cr−CO bonding and C−O antibonding. The EXAFS results were the first direct experimental evidence of adsorption induced mobility of Cr(II) sites on the SiO_2 surface. This structural flexibility has been interpreted as the key for understanding the catalytic activity of Cr(II) sites in presence of adsorbates. Reversible modification of the active sites upon adsorption/desorption of adsorbates have been already revealed by in situ EXAFS for isomorphously substituted Ti^{IV} species in TS-1[886] (section 3.2.4) and for counterions in Cu-exchanged zeolites[417,418,1068] (section 4.2.2). In both cases, EXAFS structural data, coupled with other spectroscopic results and ab initio calculations, have been of high relevance in achieving an overall comprehension of the site reactivity.

6.3. SEXAFS Applied on the Phillips Catalyst: Bridging the Gap between Heterogeneous Catalysis and Surface Science

6.3.1. Brief Overview on SEXAFS Applied to Catalysis.

The high-photon flux available on the third generation synchrotron radiation sources along with the development of beamlines ad hoc conceived to measure samples at grazing angle geometry have allowed scientists to investigate the surface of single crystals and thin films, pushing the detection limit down to the monolayer and submonolayer regime. In fact, the grazing incidence geometry of the X-ray beam on a sample (few mrad), implies that the beam does not penetrate inside the bulk

dx.doi.org/10.1021/cr2000898 | Chem. Rev. 2013, 113, 1736−1850

and thus that the only atoms excited are those lying a few nm below the surface,[17,140,1364−1373] see also the discussion on the critical angle θ_c done in section 2.2.2, eq 9, when the use of mirrors in the optic hutch was discussed. This fact allows to reduce of many orders of magnitude the background photons, both those due to the bulk fluorescence and those due to the elastic scattering of the primary beam (positioning the fluorescence detector on top of the surface). Moreover, also the photons coming from the fluorescence of the absorber atoms, representing the EXAFS signal, can be maximized by the adopted grazing incidence geometry that makes it possible to illuminate a very long sample, thus increasing the total number of surface atoms effectively probed. This technique, called ReflEXAFS or surface EXAFS (SEXAFS), makes use of ad hoc conceived reaction chamber to control the temperature and the reaction atmosphere of the sample, and therefore allows to investigate chemical reaction.[19,29,140,1374−1377]

Several authors investigated the local environments and reactivity of adsorbed atoms or more complex molecules in controlled conditions (atmosphere and temperature) on well-defined (*hkl*) metallic[94,96,1378−1383] or oxidic[1384−1393] surfaces. SEXAFS has also been used to follow catalytic reactions occurring at well-defined surfaces.[1394] As an example, the group of Schlogl et al.[293] followed with SEXAFS the oxidation of methanol on Cu(110). Authors were able to correlate the surface electronic structure of the catalyst with its performance.

6.3.2. SEXAFS Applied to a Planar Model of the Phillips Catalyst. An attempt to reduce the complexity of the Phillips catalyst surface in order to study the structure of the active sites at a molecular level was done by Thune et al.,[1343,1395] who developed a method to prepare a planar model of the catalyst. The synthesis method consists in replacing the amorphous porous silica substrate by a flat silicon wafer covered by a thermal oxide layers, hereafter SiO_2/Si(100). The SiO_2/Si(100) support was then impregnated by spin-coating with an aqueous solution of chromic acid. Agostini et al.[1396] demonstrated that operating in the ReflEXAFS mode, near the critical angle θ_c, see eq 9, it is possible to collect a fluorescence XAFS signal from 2 Cr/nm^2 distributed on a flat SiO_2/Si(100) surface, that is, far below the threshold of 1000−500 ppm concentration commonly accepted to obtain EXAFS spectra having a reasonable quality. The sample was subjected to successive oxidation/reduction cycles, according to Scheme 8, to investigate by XAFS the red-ox properties of grafted Cr sites.

Scheme 8. Schematic Representation of the Red−Ox Cycle Investigated by Agostini et al.[1396] on Cr-SiO_2/Si(100) Sample.[a] Reproduced with Permission from Ref 1396. Copyright 2007 American Chemical Society

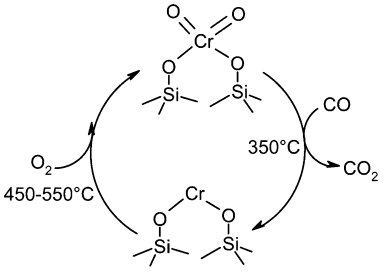

[a]The starting sample contains grafted Cr(VI) species (top) that are reduced to Cr(II) by exposure to CO at 350 °C. These latter can be reoxidized to the former by interaction with O_2 at 450−550 °C.

The sample was oxidized in situ in the ReflEXAFS chamber by O_2 at 450 °C, simulating the well-known procedure usually adopted for the standard powdered Cr/SiO_2 samples.[64] The XANES spectrum (red line in Figure 46a) is characterized by

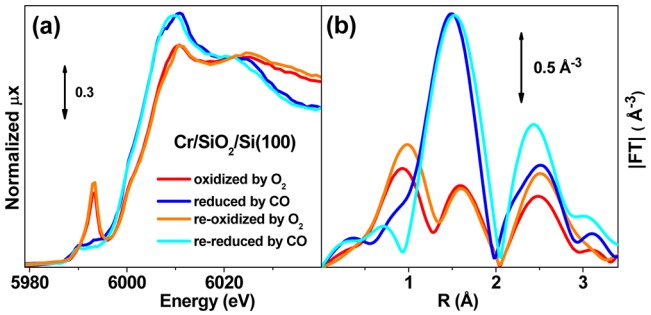

Figure 46. Normalized XANES spectra (a) and k^2-weighted, phase uncorrected, FT of the EXAFS spectra (b) of the planar Cr/SiO_2/Si(100) sample after successive red−ox cycles according to Scheme 8. Spectra collected in the ReflEXAFS chamber of the GILDA BM8 beamline at the ESERF.[140,1377] Data from ref 1396.

(i) a pre-edge peak at 5993.5 eV (that is the fingerprint of Cr(VI) in T_d-like local geometry),[64] (ii) a white line at 6011.4 eV (having a shoulder a few eV below), and (iii) the maximum of the first EXAFS oscillation at 6025 eV. Although similar to the XANES spectrum of oxidized Cr/SiO_2 sample (Figure 43a), the spectrum of oxidized Cr/SiO_2/Si(100) does not correspond to that of diluted monochromate species. In particular, (i) the pre-edge peak is lower in intensity and broader, and (ii) the postedge is not featureless as for Cr(VI)/SiO_2 sample. The postedge features described for the oxidized sample were very similar to those observed for α-Cr_2O_3,[1316] exhibiting a double white line at 6007.3 and 6011.3 eV and the maximum of the first EXAFS oscillation at 6025 eV. Agostini et al.[1396] concluded that on the oxidized sample aggregated Cr atoms forming an oxidic phase very close to that of α-Cr_2O_3 were present, along with a small fraction of isolated Cr(VI) ions in T_d-like local geometry.

After reduction in CO at 350 °C, the XANES spectrum of Cr/SiO_2/Si(100) (blue line in Figure 46a) greatly changes. In particular, (i) the absorption edge red shifts of 2.5 eV (which is much less than what observed for reduction of well dispersed monochromate species, 6.5 eV, see Figure 43a), (ii) the pre-edge peak due to Cr(VI) species in T_d-like local geometry disappears, (iii) the white line increases in intensity and red shifts of 1.0 eV, and (iv) the first EXAFS oscillation undergoes a relevant modification. The XANES spectrum of the sample reduced in CO provides an evidence that the fraction of isolated Cr(VI) species is reduced by CO to isolated Cr(II) sites (see Scheme 8), whereas the fraction of clustered Cr(III) is almost unaffected. Successive reoxidation (orange line in Figure 46a) and rereduction steps (cyan line in Figure 46a) prove the reversibility of the red−ox process on the fraction of isolated Cr species, according to the reaction cycle shown in Scheme 8. The presence of a fraction of α-Cr_2O_3 suggested that the adopted experimental conditions were not good enough to guarantee a perfect waterless activation of the sample: under the adopted reaction conditions the impurities (e.g., water) desorbing from the walls of the ReflEXAFS chamber might be accumulated in the sample atmosphere.

The conclusions reached by XANES spectroscopy were further supported by the EXAFS data. Figure 46b shows the k^2-

dx.doi.org/10.1021/cr2000898 | Chem. Rev. 2013, 113, 1736−1850

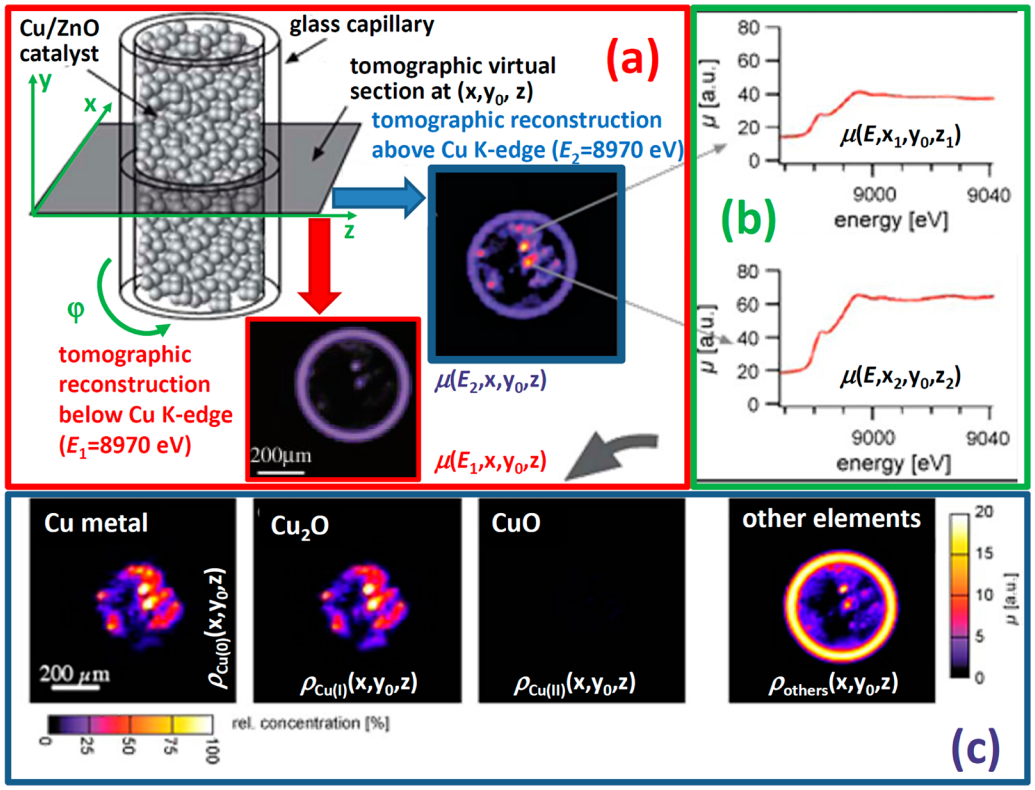

Figure 47. Scanning microtomography combined with X-ray absorption spectroscopy at the Cu K-edge collected with the experimental setup described in Figure 9a of a Cu/ZnO catalyst treated in cycles of 4% H_2/He and 2% O_2/He at 300 °C. Part a: Schematic sketch of the sample (catalyst bed containing Cu/ZnO particles in BN) showing a tomographic virtual section (x,y_0,z). With this setup, the X-ray absorption of the sample, $\mu(E,x,y,\varphi)$ was measured as function of energy by scanning the sample in translation (90 steps of 10 μm each) and rotation (101 steps over 360°), acquiring at each position a full absorption spectrum spectra (in the 8960−9040 eV range). The absorption coefficient $\mu(E,x,y,z)$ can be reconstructed for each energy at each location on the virtual slice according to eq 16. In particular, two tomographic reconstructions are shown, before and after the Cu K-edge: $\mu(E_1,x,y_0,z)$ and $\mu(E_2,x,y_0,z)$, respectively. In each location on the reconstructed slice a full XANES spectrum is obtained, as shown in Part b for the spectra corresponding to two different points: (x_1,y_0,z_1) and (x_2,y_0,z_2). From these data, the concentration of the different Cu-species, $\rho_{Cu(0)}(x,y_0,z)$, $\rho_{Cu(I)}(x,y_0,z)$, and $\rho_{Cu(II)}(x,y_0,z)$, can be extracted by fitting a linear combination of reference spectra to the spectrum at each location on the virtual slice, as shown in Part c. Fitting the pre-edge intensity also the concentration of the other elements, $\rho_{others}(x,y_0,z)$, can be obtained. For obvious graphical reasons only data concerning a $y = y_0$ plane have been reported (2D images); however, all discussed information is available on the whole (x,y,x) sampled volume (3D reconstruction). Adapted with permission from ref 71. Copyright Elsevier, 2009.

weighted, phase uncorrected, FT of the EXAFS spectra of Cr/SiO_2/Si(100) samples after oxidation/reduction treatments. The EXAFS data of the oxidized samples (red and orange curves in Figure 46a) are completely different from those of the reduced ones (blue and cyan curves in Figure 46a) in the 0−2 Å region, whereas for R > 2 Å, the spectra are very similar independently from the sample treatment. This observation supported the conclusions reached from the XANES study, that is, the presence of an unreactive aggregated phase of Cr_2O_3 (dominating the FT spectra for R > 2 Å) not involved in the red−ox mechanism, along with a reactive phase (dominating the FT spectra for R < 2 Å), able to undergo the red−ox cycle as described in Scheme 8.

In a following step, the reactivity of the Cr(VI) species on the flat Cr/SiO_2/Si(100) sample toward ethylene was investigated. The oxidized sample was contacted with ethylene (500 mbar) at 160 °C directly in the ReflEXAFS chamber. The resulting XANES and EXAFS spectra were very similar to those of the same sample reduced in CO but were also different from the spectra expected for a sample having performed a successful polymerization (see blue and orange spectra in Figure 44, respectively). Agostini et al.[1396] concluded that the treatment in ethylene was sufficient to reduce the isolated Cr(VI) species[64,1316] to Cr(II) but not to polymerize it to a large extent. Therefore, the ability of surface Cr species to undergo a red−ox cycle is not sufficient to guarantee the presence of sites active in ethylene polymerization.

7. SPACE-RESOLVED X-RAYS EXPERIMENTS

The miniaturization of in situ spectroscopic tools represented in the last years as a forefront instrumental development for the characterization of heterogeneous catalysts. With the multitude of microspectroscopic methods available fundamental insight into the structure−function relationships of catalytic processes can be obtained.[1397−1399] In the past decade, several groups have focused their efforts on miniaturization of in situ spectroscopic tools: UV−vis−NIR microscopy,[1115,1400] fluorescence microscopy,[1401−1406] NMR imaging[1407−1410] Raman microscopy,[1399,1411−1416] and IR microscopy, mainly with synchrotron radiation sources.[66,1399,1417]

On the structural ground, electron micromicroscopies play of course a relevant role, among them we mention in situ scanning transmission X-ray microscopy,[75] aberration corrected TEM,[1418] aberration-corrected scanning transmission electron

dx.doi.org/10.1021/cr2000898 | Chem. Rev. 2013, 113, 1736−1850

microscopy (STEM),[1419] and electron backscattering diffraction (EBSD)/scanning electron microscopy (SEM).[1420] Moreover, as already anticipated in section 2.5, modern transmission electron microscopes (TEM) equipped with an electron energy-loss spectrometer allows the detection XAFS-like spectra,[641−646] which, particularly for low-Z edges and in the near edge region, can be competitive with those collected at synchrotron sources. The technique has the further advantage of reaching the nm-spatial resolution typical of TEM instruments, that is, 100−1000 times better that what can be obtained with X-ray microscopies, see sections 2.2.7 and 7.1. On the other hand, EXELFS is intrinsically an ultrahigh vacuum technique and the penetration depth is limited to the few nanometer-thick catalysts.

7.1. Brief Introduction to X-ray Space-Resolved Studies in Catalysis

XAFS studies on heterogeneous catalysts mainly exploited mm-sized X-ray beams on standard beamlines (Figure 4a): this means that measured absorption coefficients were integrated over a relatively large volume, according to eq 15. The validity of this approach holds when the sample has a homogeneous thickness on the whole (x,y) surface illuminated by the beam and when the absorption coefficient $\mu(E,x,y)$ is constant in the whole sampled volume. However, in many cases spatial variations in catalyst structure can occur, for example, during impregnation of preshaped particles, during reaction in a catalytic reactor or in microstructured catalysts.[66,67,71,336,338] Therefore, spatially resolved molecular information on a microscale is required for a comprehensive understanding of these systems and experimental set-ups like those described in section 2.2.7. and in Figures 4b and 9a and b must be used. This allows to perform ex situ studies, studies under stationary reaction conditions and in some specific cases even under dynamic reaction conditions.[71]

7.2. Cu/ZnO Case Study

The relevance of the Cu/ZnO system in catalysis was related for many years to the methanol synthesis from CO/CO_2 and H_2.[1421−1425] The Cu/ZnO system was mainly supported on alumina but also other supports have been tried. Successively, the increased interest on the hydrogen economy made the Cu/ZnO system relevant for the methanol steam-reforming chemistry.[1426−1430] Surface mechanisms on the $Cu/ZnO/Al_2O_3$ catalysts account for the following three reactions: (i) methanol and steam reacting directly to form H_2 and CO_2, (ii) methanol decomposition to H_2 and CO, and (iii) the water−gas shift reaction ($CO + H_2O \rightarrow CO_2 + H_2$).

The red-ox chemistry described above is driven by the changes in the oxidation state of the copper phase present on the catalysts. Nanoparticles of Cu metal, CuO_2 and CuO were supposed to be present on the catalyst, in different relative amounts, depending on the reaction conditions. To understand the reactivity of the Cu/ZnO system, Grunwald et al.[336] performed a Cu K-edge XANES-tomographic study on the catalyst hosted inside a glass capillary of about 0.5 mm diameter. The catalyst was treated in cycles of 4% H_2/He and 2% O_2/He at 300 °C. The authors used a scanning microscopy setup (see Figure 9a) acquiring about 90 000 Cu K-edge XANES spectra (covering the 8960−9040 eV interval) in all different (x,y) points and orientation (φ) to be able to reconstruct, a posteriori, the 3D Cu XANES map of the whole sample according to the $\mu(E,x,y,\varphi) \rightarrow \mu(E,x,y,z)$ conversion schematized in eq 16. Figure 47a shows a schematic sketch of the sample together with two reconstructed attenuations maps $\mu(E_{1,2},x,y_0,z)$ through the sample at the same $y = y_0$ plane cut for two energies of E_1 = 8970 eV and E_2 = 8995 eV, that is, just before and after the Cu K-edge. The (x,y_0,z) points where an increase of the absorption coefficient μ is observed, moving from E_1 to E_2, correspond to points where copper is hosted. For each (x,y_0,z) point, the full XANES spectrum can be extracted, as shown in Figure 47b for two different (x_1,y_0,z_1) and (x_2,y_0,z_2) points.

Finally, according to the methods similar to those that will be described in section 8.2.3 about the operando experiments, applying eqs 45−48, in each (x,y_0,z) point the relative concentration of Cu metal, CuO_2 and CuO can be determined. Figure 47c reports the relative concentration of the three different Cu phases, $\rho_{Cu(0)}(x,y_0,z)$, $\rho_{Cu(I)}(x,y_0,z)$ and $\rho_{Cu(II)}(x,y_0,z)$, that have been extracted from the spatially resolved $\mu(E,x,y_0,z)$ XANES spectra after a fit with a linear combination of the reference spectra of the three pure phases. The comparison among $\rho_{Cu(0)}(x,y_0,z)$, $\rho_{Cu(I)}(x,y_0,z)$, and $\rho_{Cu(II)}(x,y_0,z)$ of a Cu/ZnO catalyst subjected to cycles of 4% H_2/He and 2% O_2/He at 300 °C, reveals that the active phase was in a reduced state either of Cu(0) or Cu(I) and that hardly any Cu(II) was observed. From the fitting of the pre-edge intensity in all (x,y_0,z) points also the concentration of the other elements, $\rho_{others}(x,y_0,z)$, can be obtained, see right map in Figure 47c. This map mainly reveals the presence of Si in the capillary container and the presence of Zn in the same regions where Cu is observed. The black internal parts observed in all four maps reported in Figure 47c refer to a void volume because of sample packing inhomogeneity.

8. TIME-RESOLVED XAFS ON CATALYST AT WORK: OPERANDO EXPERIMENTS

8.1. Brief Introduction to Time-Resolved Studies in Catalysis

In the past decade, a great boost has been given within the scientific community to develop experimental set-ups able to perform spectroscopic and structural investigation on a living catalyst, that is, during catalytic activity, that should be simultaneously monitored. This interest gave born to a series of thematic conferences: OPERANDO I, II, and III, see Table 2. In this regard, XAFS-based techniques have played an important role because the high penetration depth of hard X-rays is a great advantage in monitoring a catalyst in presence of liquid or gaseous reactants. It is therefore not by chance that the fourth series of this important conference will take place in 2012 at the Brookhaven National Laboratory (Upton, NY, U.S.A.), hosting the NSLS and constructing the NSLS-II synchrotron radiation sources.

Following catalytic reactions under OPERANDO conditions requires that the reaction products are measured simultaneously with spectroscopic and/or structural data collection. Consequently performing OPERANDO XAFS requires the ability to perform time-dependent XAFS, where the evolution of XAFS spectra is monitored as a function of external perturbation of the catalytic system, such as (i) temperature, (ii) pressure, (iii) absolute reactants flow, and (iv) relative reactant flow and others, while measuring the catalytic activity. The goal of such experiments is the correlation between the catalyst activation/deactivation and the appearance (or disappearance) of a peculiar phase, of a peculiar chemical bond, or of a peculiar oxidation state. The ideal experimental

dx.doi.org/10.1021/cr2000898 | Chem. Rev. 2013, 113, 1736−1850

set-ups for this kind of experiments are either the quick-EXAFS or the energy dispersive EXAFS (see Figure 4 and Table 4). After the first pioneering experiments of Sayers,[1431] great improvements in the understanding, at the atomic level, of the basic reactions and equilibria governing the activity of several working catalysts have been achieved in the last two decades by time dependent XAFS experiments.[62,70,76,78,79,244,247,251,259,285,577,1432−1476] To show the potential of the technique, we will report, as a case study, the investigations performed by Lamberti et al.[77,143,252,1348] on the industrial $CuCl_2/Al_2O_3$ catalyst for ethylene oxychlorination.

8.2. $CuCl_2/Al_2O_3$ Case Study

8.2.1. Industrial Relevance of the $CuCl_2/Al_2O_3$ System.

Oxychlorination of ethylene is one of the most important route to produce 1,2-dichloroethane (EDC), which is the main intermediate to produce poly vinyl chloride (PVC). Nowadays, almost all the world production of PVC chloride (PVC) is based by the polymerization of vinyl chloride, which is produced by cracking of 1,2-dichloroethane (EDC), according to the following reaction:

$$C_2H_4Cl_2 \rightarrow C_2H_3Cl + HCl \quad (39)$$

$C_2H_4Cl_2$ is in turn obtained by two parallel processes, direct chlorination (eq 40) and oxychlorination (eq 41)

$$C_2H_4 + Cl_2 \rightarrow C_2H_4Cl_2 \quad (40)$$

$$C_2H_4 + 2HCl + \frac{1}{2}O_2 \rightarrow C_2H_4Cl_2 + H_2O \quad (41)$$

The latter reaction, recycling HCl produced by the cracking of EDC, is particularly important in industrial applications because it was specifically developed to reduce the consumption of Cl_2 and the exit of useless product (HCl) outside the cycle, in agreement with the modern requests of chemical industry[1477−1479] that need more environmental friendly reactions. Oxychlorination of ethylene offers a significant economic benefit in two ways: first, it uses cheap and abundant feedstock and, second, it incorporates the recycling of waste HCl produced in the cracking EDC (eq 39). It is evident that oxychlorination is a key-process in the modern chemical industry, playing a relevant role for chlorine atom incorporation in hydrocarbons, both saturated and unsaturated, for example, in methane, ethylene, and benzene.[1480,1481] As an example, CO oxychlorination has recently been taken into consideration for the synthesis of phosgene, as an alternative to the traditional process of CO direct chlorination.[1482,1483]

Oxychlorination reaction 41 is performed at 490−530 K and 5−6 atm using both air and oxygen in fluid or fixed bed reactors. Commercial catalysts are produced by impregnation of γ-alumina with $CuCl_2$ (4−8 wt % Cu). Other metal-chlorides (mainly alkaline or alkaline earth chlorides) in a variable concentration are also added to improve the catalytic performances, making the catalyst more suitable for use in industrial reactors.[1477−1479,1484,1485] In particular, KCl is always present in the catalysts used in fixed bed technologies, sometimes together with other alkali-metal chlorides, such as CsCl, NaCl, or LiCl.[1486−1488] Rare-earth-metal chlorides, such as $LaCl_3$, added to $CuCl_2$ and KCl, are also claimed in the patent literature.[1488] $MgCl_2$ is the base additive in the catalysts used in fluid bed processes, where alkali-metal (such as LiCl) or rare-earth-metal chlorides (such as $LaCl_3$) can also be added.[1489−1491]

8.2.2. Preliminary in Situ XAFS Experiments.

Despite the abundant literature on the subject,[1477−1479,1484−1497] a significant improvement of the knowledge of the system has been achieved only in the 2000−2003 period,[119,1346,1498−1500] although limited to the base catalyst (containing only $CuCl_2$ without additives). It has been proved[119,1346,1498] that two different copper species are present on the activated catalyst (dried at 500 K in N_2 flux): a surface copper aluminate, where the copper ions are hosted in the octahedral vacancies of γ-Al_2O_3, and a highly dispersed copper chloride phase. The former phase is the only one present at low Cu loadings (up to 0.95 wt % Cu per 100 m^2 support); the latter precipitates directly from the solution once that the adsorptive capacity of alumina is exhausted. Successively it has been shown that the active phase in ethylene oxychlorination reaction 41 is the highly dispersed $CuCl_2$. following the three steps redox mechanism reported below:[1499,1500]

$$2CuCl_2 + C_2H_4 \rightarrow C_2H_4Cl_2 + 2CuCl \quad (42)$$

$$2CuCl + \frac{1}{2}O_2 \rightarrow Cu_2OCl_2 \quad (43)$$

$$Cu_2OCl_2 + 2HCl \rightarrow 2CuCl_2 + H_2O \quad (44)$$

This redox cycle, has been determined by means of an in situ Cu K-edge XANES and EXAFS study, where the three reagents (C_2H_4, O_2, and HCl) have been separately dosed on the activated $CuCl_2/\gamma$-Al_2O_3 at 500 K in the given order (see Figure 48). In particular, the chlorination of ethylene, eq 42, occurs by reduction of $CuCl_2$ to CuCl, as testified by the red-shift of the Cu K-edge, see Figure 48a top curves. The oxidation of CuCl to an oxychloride, eq 43, is proved by both the

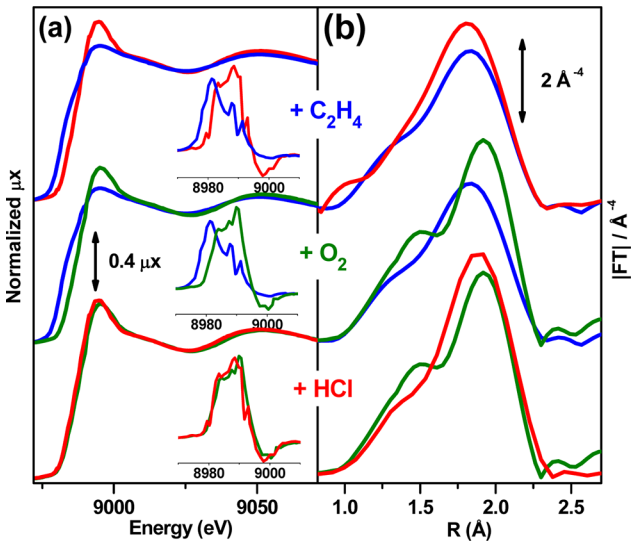

Figure 48. Three steps redox mechanism of the ethylene oxychlorination reaction, eq 42−44 followed by in situ XANES and EXAFS, parts a and b, respectively. From top to bottom the effect of the separate and successive dosage of the three reagents is reported: activated catalyst before (red line) and after (blue line) ethylene interaction; reduced catalyst before (blue line) and after (green line) interaction with O_2; oxidized catalyst before (green line) and after (red line) interaction with HCl. In all cases, the interaction temperature was 500 K. Insets in part a report the derivative of the spectra reported in the main part. The data were collected at LURE DCI (EXAFS13 beamline) and are from refs 1499 and 1500.

dx.doi.org/10.1021/cr2000898 | Chem. Rev. 2013, 113, 1736−1850

opposite blue-shift of the Cu K-edge and the appearance of a low-*R* contribution in the |FT| of the EXAFS spectra, due to the insertion of oxygen in the first coordination sphere of Cu, see middle curves in Figure 48a and b, respectively. Finally, the catalytic cycle is closed by the rechlorination of the oxychloride phase with HCl, eq 44, as demonstrated by the disappearance of the above-mentioned oxygen contribution in the FT of the EXAFS spectrum, see red curve in the bottom of Figure 48b.

The spectra shown in Figure 48a demonstrate that the oxidized and the reduced form of the catalyst are easily recognizable by XANES spectroscopy. In particular, XANES spectrum of the oxidized catalyst is characterized by an intense white line at 8995 eV, while that of the reduced catalyst shows a less intense white line at 8993 eV and exhibits a red shift of the edge of 5 eV. Even more informative are the derivative spectra (see insets), where the oxidized catalyst exhibits a strong maximum at 8988 eV and a negative peak at 8998 eV, while the reduced catalyst shows a maximum at 8981 eV.

More recently Muddada et al.[252,1348,1501,1502] extended the works of Leofanti et al.[119,1346,1498−1500] from the bare to the LiCl-, KCl-, CsCl-, $MgCl_2$-, and $LaCl_3$-doped $CuCl_2/Al_2O_3$ catalysts. Combining in situ XANES/EXAFS, IR spectroscopy of adsorbed CO, CO chemisorption, and catalytic tests performed using a pulse reactor in depletive mode authors succeeded in understanding the role of dopants (LiCl, KCl, CsCl, $MgCl_2$, and $LaCl_3$) in determining the nature, relative fraction, reducibility and dispersion of Cu-phases on $CuCl_2/\gamma$-Al_2O_3 catalysts for oxychlorination reaction (vide infra the main parts of Figure 50 for the reduction by ethylene at 500 K (eq 42). As already discussed above from the previous works, it was known that in the undoped catalyst two Cu phases coexist: Cu-aluminate and supported $CuCl_2$, being the latter the only active one.[119] In particular, the EXAFS and XANES data demonstrated the following trend in the ability of the dopant cation to compete with Cu^{2+} in the aluminate phase formation has been found: $K^+ \leq Cs^+ \leq Li^+ \ll Mg^{2+} < La^{3+}$.[1348] In particular, a fraction close to 100% of copper in the active phase is obtained by adding $MgCl_2$ or $LaCl_3$ dopants. Moreover, EXAFS directly, and IR indirectly, proved that the addition of KCl or CsCl (and less efficiently of LiCl) promotes the formation of mixed CuK_xCl_{2+x} or $CuCs_xCl_{2+x}$ phases, so altering the chemical nature of the active phase. XANES spectroscopy indicates that addition of $MgCl_2$ or $LaCl_3$ does not affect the reducibility by ethylene of the active $CuCl_2$ phase and that the reducibility of the new copper-dopant mixed chloride are in the order $CuCl_2 > CuLi_xCl_{2+x} > CuK_xCl_{2+x} > CuCs_xCl_{2+x}$,[1348] (vide infra the main parts of Figure 50).

8.2.3. Operando Experiments. The determination of the rate determining step, among reactions 42−44 has been successively achieved by a time-resolved XANES operando study by Lamberti et al.[77,143] The experiment was performed by feeding a cell containing a self-supported thin pellet of the catalyst with a diluted mixture of the three reagents (C_2H_4:HCl:O_2:N_2 = 100:36.1:7.6:180), representative of the fixed-bed process. In the course of the experiment the temperature was increased from 373 to 623 K and then decreased again to 373 K. Time resolved XANES spectra were collected in dispersive geometry, see Figure 4b, and the catalyst activity was simultaneously analyzed with a quadrupole mass spectrometer. The results of the experiment are summarized in Figure 49, part a for the heating step and part b for the cooling step of the experiment. The top curves in parts a and b report the evolution of the XANES spectra, while the bottom curves

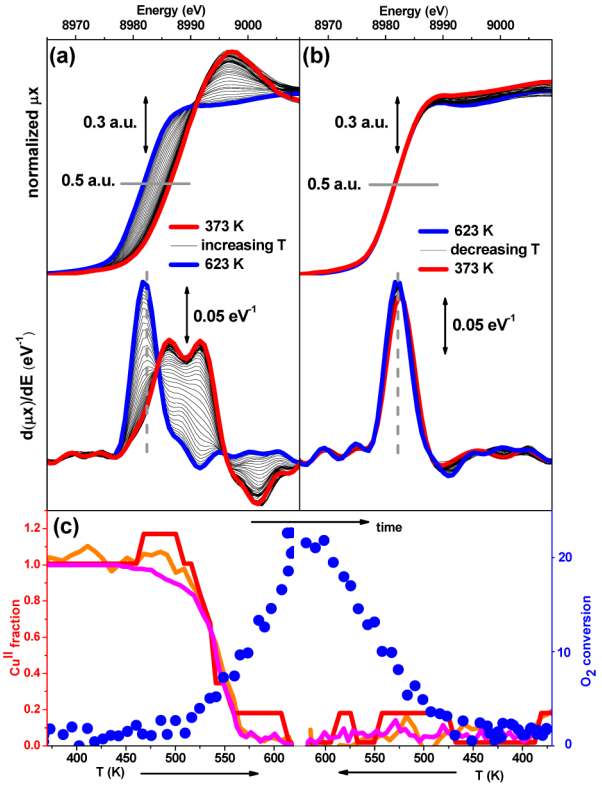

Figure 49. Part a: XANES spectra (top) and corresponding derivatives (bottom) of $CuCl_2/Al_2O_3$ system in ethylene oxychlorination environment, during the heating step of the experiment (from 373 K, blue curve, to 623 K, red curve, by 12 K min^{-1}). Part b as in part a for the cooling step of the experiment (from 623, red curve, to 373 K, blue curve, by 12 K min^{-1}). XANES spectra have been collected each 30 s, corresponding to a ΔT of 6 K. Part c summarizes the results of the operando experiment (both heating and cooling steps, left and right parts, respectively), by correlating the catalyst activity, monitored as O_2 consumption (dotted scattered blue points, right ordinate axis) with the fraction of Cu(II) (left ordinate axis) red, orange, and magenta lines, evaluated according to methods reported in eqs 45−48, respectively. The data were collected at ESRF ID24 beamline and published in refs 77 and 143.

correspond to their first derivatives Figure 49c summarizes the evolution of the Cu(II) fraction (red, orange, and magenta curves, left ordinate axis) estimated from the XANES spectra and compared with the catalyst activity reported in terms of oxygen consumption (scattered blue dots, right ordinate axis).

The XANES spectra reported in Figure 49a indicate a progressive reduction of Cu(II) into Cu(I) during the heating step whereas almost no changes are observed in the XANES spectra collected in the cooling step (Figure 49b). To evaluate the Cu(II) fraction, for each spectrum along the heating or cooling step, two model spectra are needed, one for the fully oxidized catalyst and one for the fully reduced. The catalyst itself, after activation in N_2 flux up to 500 K before and after reduction in C_2H_4 atmosphere at 500 K has been used for this purpose. Three independent methods have been used to quantify the fraction of Cu(II) belonging to the active phase on the catalyst in the i-th spectrum, x_i. The first method concerns in determining the energy (E_i) position of the edge, arbitrarily defined as the energy corresponding to normalized $\mu x = 0.5$

$$x_i = (E_i - E_{Red})/(E_{Ox} - E_{Red}) \quad (45)$$

dx.doi.org/10.1021/cr2000898 | Chem. Rev. 2013, 113, 1736−1850

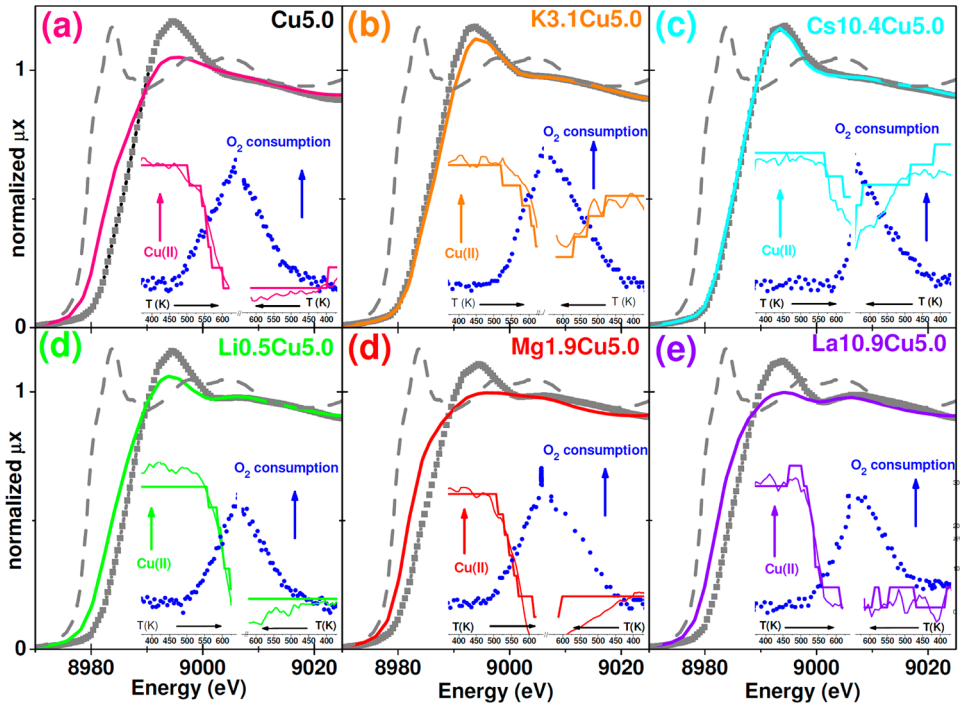

Figure 50. Main parts: XANES spectra collected in static conditions (LURE DCI, EXAFS13 beamline) of doped samples before (gray scattered curves) and after (colored solid lines) reduction by ethylene at 500 K compared with a spectrum of pure Cu^{I} chloride (dashed gray line; same curve in all frames). The insets show the results of operando experiments (ESRF ID24 beamline) reporting the evolution of the Cu^{II} fraction along the heating and cooling runs estimated from the edge shift (eq 45 bold colored line) and from the intensity of the maximum of the first derivative (eq 46 full colored line) together with the catalyst activity (scattered blue dots). Data from refs 252, 1348, and 1502.

where E_{Ox} and E_{Red} are the energy of the edge in the fully oxidized and fully reduced reference spectra respectively; and E_i the position of the edge in the i-th spectrum. Cu(II) fractions evaluated from this method are reported as red lines in Figure 49c. The value $\mu x = 0.5$ corresponds to the maximum difference in the abscissa of the two references and is obviously peculiar of the present case: for the Fe(II)/Fe(III) speciation, the $\mu x = 0.9$ value is preferred.[330]

The second method uses the intensity (I) of the first maximum due to the Cu(I) component in the derivative spectra at 8982 eV

$$x_i = 1 - I_i/I_{Red,} \tag{46}$$

where I_{Red} refers to the spectrum of the reduced reference. Cu(II) fractions evaluated from this method are reported as orange lines in Figure 49c. The peak at 8981 eV has been chosen because it is the most intense feature of the derivative XANES spectra of Cu(I) species and it falls in a region where the Cu(II) species have a null derivative. This method can not be translated to directly measure the fraction of Cu(II) using the most intense Cu(II) features at 8985 and 8992 eV, because in this region the derivative of Cu(I) species is still strong.

The last method consists in the simulation of the ith spectrum as the lineal combination of the two reference spectra according to eq 47:[143,529,1346,1347]

$$\mathrm{XANES}^{\mathrm{Theo}}{}_i(E_j, x_i) = x_1\mathrm{XANES}^{\mathrm{Ox}}(E_j) + (1 - x_i)\mathrm{XANES}^{\mathrm{Red}}(E_j) \tag{47}$$

The fraction of oxidized copper species, x_i, is optimized by a least-squares method, minimizing $\mathbf{F}(x_i)$ defined as:

$$\mathbf{F}(x_i) = \sum_{j=1}^{N} [\mathrm{XANES}_i^{\mathrm{exp}}(E_j) - \mathrm{XANES}^{\mathrm{Theo}}(E_j, x_i)]^2 \tag{48}$$

where E_j (j = 1, 2, ..., N) are the energies where the experimental spectra have been sampled. Cu(II) fractions evaluated from this method are reported as magenta lines in Figure 49c. Although this last method is more time-demanding that the previous ones, it is also more accurate, as it accounts for all the points of the spectrum.

Comparing, in Figure 49c (left axis), the fraction of Cu(II) species (x_i) evaluated according to eqs 45−48 for the series of spectra reported in Figure 49a and b, we can conclude that in all cases the agreement among the three methods is rather good, as they provide values in relative agreement within ±5%. It is interesting to note that the x_i fraction evaluated according to eq 45 (red curve in Figure 49c) has a step-like trend, because of the discreteness of the energy scale measurable with a position-sensitive detector, see Figure 4b.

From the whole set of data summarized in Figure 49c, the following can be stated: At the starting point (373 K), only Cu(II) is present and the catalyst is inactive. Both O_2 conversion and Cu(II) reduction start in the same temperature range (470−490 K) and progressively increase upon increasing the temperature. Cu(II) reduction is completed at 600 K, see Figure 49c. During the cooling step, O_2 conversion progressively declines becoming negligible in the 490−470 K range, while the oxidation state of Cu does not change anymore. These results provide evidence that at the typical oxychlorination temperature, Cu(I) is the dominant phase and the rate determining step is the oxidation of CuCl, according to eq 43. To understand the low efficiency of the oxidation process, the catalyst at the end of the cooling step has been

dx.doi.org/10.1021/cr2000898 | Chem. Rev. 2013, 113, 1736−1850

subjected to two different oxidizing treatments at increasing temperatures (373−623 K): the former with diluted O_2, the latter with a diluted O_2−HCl mixture. The first treatment causes the complete Cu oxidation already at 373 K, while the second leaves the Cu(I) unchanged up to 550 K, and, even at 623 K, a measurable fraction of Cu(I) is still present.[77] The authors concluded that HCl acts as poison for Cu(I) oxidation and is responsible for the prevailing reduced state of copper during reaction.[77]

The key role of potassium chloride dopant, present in the industrial catalysts used in fixed bed technologies, has been highlighted in a similar experiment.[77] It has been shown that the $KCl/CuCl_2/\gamma$-Al_2O_3 catalyst behaves differently from the base one, working in a prevailing oxidized state (Figure 50b). Combining operando XANES experiments with catalytic tests of ethylene conversion in pulse reactors and with IR experiments of adsorbed CO, it was concluded that the active phase of the $KCl/CuCl_2/\gamma$-Al_2O_3 is a mixed chloride (K_xCuCl_{2+x}) phase,[77] which reduces the ability of the active surface to adsorb ethylene and/or transfer two Cl atoms to each ethylene molecule. Although not detectable by XRD owing to too small crystal size,[1498] the formation of the mixed-chloride double compound, was suggested by IR spectroscopy of adsorbed CO.[77]

More recently, Muddada et al.[252,1348,1502] extended the works of Lamberti et al.[77,143] to the LiCl-, CsCl-, $MgCl_2$-, $CeCl_4$-, and $LaCl_3$-doped $CuCl_2/Al_2O_3$ catalysts. Some of these results are summarized in Figure 50. Authors coupled the catalyst activity (monitored with a pulse reactor working in both non-depletive and depletive modes) with time-resolved XANES spectroscopy performed under operando conditions (as done for the undoped catalyst, Figure 48 and Figure 49); they succeeded in understanding, at the atomic level, the role played by additives in the chemistry of the industrial catalyst used in the ethylene oxychlorination. Both KCl (Figure 50b), and CsCl (Figure 50c), form in reaction conditions a mixed phase with $CuCl_2$, which strongly modify the catalyst behavior.[252] In particular, these additives were able to reverse the rate determining step, from the CuCl oxidation (typical of the undoped catalyst) to the $CuCl_2$ reduction, that is, from eq 43 to eq 42. The change in the rate determining step is a consequence of the decrease of the rate of the latter reaction, thus of the overall activity of the system. For all remaining additives (Figure 50d−f), the rate determining step remains the CuCl oxidation, as for the undoped catalyst,[252] because the additive chlorides does not mix with $CuCl_2$, that remains the active phase.

We conclude this section by mentioning an other use $CuCl_2$ as active phase in catalysis and the role played by XAFS in understanding its structure and reactivity. PVP has been used as a good support for immobilization of $CuCl_2$ in the oxidative carboxylation of methanol to dimethylcarbonate (DMC),[1503] the oxidative coupling of 2,6-dimethylphenol,[1504] and the oxidation of tetralin.[1505] In these processes, all conducted in the liquid phase, Cu^{2+} is reduced to Cu^+ and HCl is released. Even if it was usually accepted that the basic N atoms of the pyridine (Py) rings acted as preferential sites for the Cu^{2+} grafting and several models have been proposed in literature,[1505−1508] until 2008, there were not direct proofs of the structure of the active species during the red-ox process. In that year, Groppo et al.[1509] proved that $CuCl_2$ was molecularly immobilized inside a high cross-linked P4VP. The grafting procedure and the red-ox processes involving the Cu sites were investigated by means of several complementary in situ techniques (FTIR, UV−vis, XANES, and EXAFS), allowing the determination of the structure of the system in all the steps.[1509] Note that the capability to disclose the structure surrounding Cu sites done by Groppo et al.[1509] has to be considered a non trivial result, due to the amorphous nature of the host matrix.

9. XAS AND XES STUDIES ON SUPPORTED METAL NANOPARTICLES

9.1. XAFS Applied to Supported Metal Nanoparticles: A Brief Overview

Supported metal nanoparticle systems have been among the very first catalysts investigated by XAS techniques, in this regard worth noticing are the first works performed by Lytle in collaboration with Via and Sinfelt from Exxon laboratory.[232,533,1510−1516]

Particle shape and size are the most relevant parameters in determining the adsorption and reaction properties of metal nanoparticles; therefore, a huge effort has been devoted in developing experimental tools able to give statistically significant information on these two features. Of relevance for this Review is, obviously, EXAFS spectroscopy, which exploits the fact that atoms at the surface of nanoparticles exhibit a lower coordination number than atoms in the bulk. As a consequence, by experimentally determining the coordination numbers of the different shells, N_i in eq 19, it is possible to estimate of the average particle size provided that a certain particle shape has been assumed.[36,54,79,1467,1511,1517−1529] Moreover the determination of the Debye−Waller factor [$\sigma^2 = \sigma^2_T + \sigma^2_D$, see eq 20] of the metal−metal bond, and its comparison with the value obtained from the corresponding metal foil reference (where $\sigma^2 \approx \sigma^2_T$) allows to obtain information on the disorder parameter σ^2_D and thus on the bond length heterogeneity.[533]

Among the main strengths of EXAFS are (i) the ability to probe all metal atoms crossed by the beam (overcoming limitation of XRPD, which detects only particles sufficiently large to give Bragg diffraction) and (ii) the high number of particles probed (overcoming the intrinsic statistical weakness of the TEM studies). However, only average values can be obtained by EXAFS and therefore data analysis should be performed carefully and the EXAFS results should be compared with those obtained from other independent techniques such as XRPD, TEM, STEM, chemisorption, total X-ray, or neutron scattering (also known as pair distribution function PDF, see section 2.5.4), and others.[16,1518,1519,1523,1528,1530−1546] In this regard, the works of Frenkel et al.,[253,254,1523,1527,1529,1532,1545,1547−1553] Di Cicco et al.,[1528,1533] and Longo et al.[1534−1536,1543] are of particular interest because of the highly rigorous approaches adopted.

EXAFS spectroscopy is a powerful technique also to investigate bimetallic nanoparticles, in such cases the possibility to perform a double edge data collection and analysis add more details on such complex systems and models of segregation, alloying and core/shell structures can be tested.[52,55,1473,1554−1572] In this regard, the recent review of Frenkel[69] is recommended to all scientists working in this field.

Beside the much larger surface area which is responsible of the higher chemical reactivity metal nanoparticles show many properties different form the corresponding metals in the bulk form. In this regard, temperature dependent EXAFS measurements have been particularly useful.[412,536,1550,1573] In addition

dx.doi.org/10.1021/cr2000898 | Chem. Rev. 2013, 113, 1736−1850

to the well-known contraction in the interatomic distances metal nanoparticles are characterized by a reduction in the dynamic (temperature-dependent) bond-length disorder and consequently an increase in the Debye temperature, as well as an overall decrease in the bond-length expansion coefficient coupled with nanoparticles stiffening. The increase in the Debye temperature was explained by Frenkel et al.[1550] in terms of the nanoparticles size, shape, support interactions, and adsorbate effects.

The structural investigation briefly reviewed here above played a key role in understanding the structure of supported metal nanoparticles. Some specific arguments will be treated in detail in the following. In section 9.2, we give insights into the first stages of the preparation of Pd supported catalysts during precipitation of the precursor and progressive loading on the support surface. Successively, we will focus on the nanoparticle reactivity followed by in situ XAS/XES techniques. In section 9.3, the ΔXANES technique will be used to understand the adsorption of hydrogen on Pt supported nanoparticles, while the combination of high resolution XAS and high energy RIXS techniques will shed light on the coordination of CO in section 9.4. Finally, in section 9.5, we give insights on the on a combined AXAFS and IR study of adsorbed CO on a statistically significant set of Pt supported catalysts.

9.2. Preparation of Pd-Supported Catalysts Followed by EXAFS, from the Impregnation to the Reduction Steps

The final catalytic properties of the supported metal nanoparticles (activity and selectivity toward different molecules) depend not only on the metal nature[1574−1578] but also on the metal−support interaction.[603,1577−1583] In particular, the morphology and dispersion of metal clusters can be affected by the preparation method acting on different factors: Pd-precursor, temperature and pH of the impregnating solution, kinetic factors, etc. The support can exhibit not only a direct influence on the catalytic reaction as its surface is often active toward reactants and reaction products, but also an indirect one, since the physical-chemical properties of the support can influence the metal dispersion, its resistance to sintering and the accessibility of active sites to reactants.[122,142,1539,1540,1584]

We will shortly review here the contribution of Agostini et al.[142] on Pd supported catalysts prepared via the deposition-precipitation method[121,122,1585] using Na_2PdCl_4 as precursor. The authors investigated the influence to the final catalyst of both the support nature (γ-Al_2O_3 and active carbons from both wood and peat) and of the loading of the metal−supported phase in the 0.5−5.0 in Pd wt % interval.

The investigation starts from the unsupported precipitated phase because it represents the model material for the active supported phase. Because of its amorphous nature, EXAFS spectroscopy was the only structural technique able to determine the local structure around the Pd absorbing atoms. The EXAFS spectrum of unsupported phase is shown in Figure 51b and c (orange line). Its |FT| is dominated by a first shell contribution centered around 1.6 Å and by a weaker and complex contribution at longer distance (two peaks at 2.7 and 3.2 Å, respectively), typical of the $Pd(OH)_2$ phase.[1586,1587]

The structural model used to fit the datum was based to the Pd^{2+}-polynuclearhydroxo-complexes proposed by Troitskii et al.[1586] The local environment of Pd^{2+} consists of planar coordination squares of PdO_4 units linked via two (O_{1a}) or one (O_{1b}) oxygen bridges of different geometry, the remaining Pd−O bond connects an OH group. To limit the number of the free

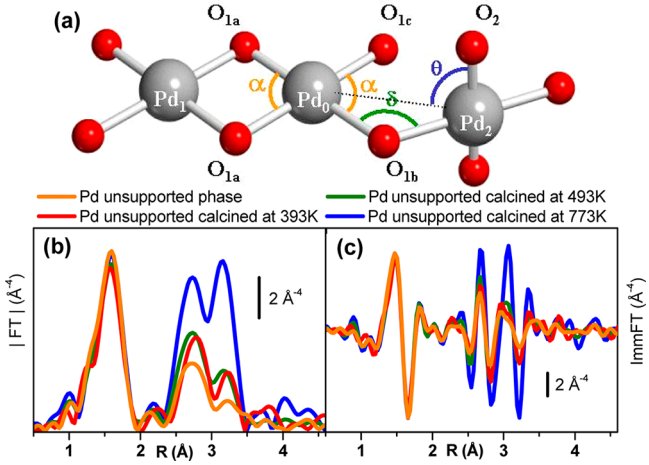

Figure 51. Part a: $Pd(OH)_2$ cluster used to model the EXAFS signal up to 4.1 Å around the absorbing Pd atom (labeled as Pd_0). Gray and red spheres represent Pd and O atoms, respectively. H atoms, unable to contribute significantly to the EXAFS signal, have been omitted. The model has been constructed from the studies of Troitskii, et al.[1586] The structural parameters optimized in the EXAFS fit are the Pd−O first shell distance (considered equivalent for O_{1a}, O_{1b}, and O_{1c} atoms), the Pd_0−Pd_1, Pd_0−Pd_2, and Pd_0−O_2 distances and the corresponding Debye−Waller factors. The angles α and δ differs from the ideal 90° of the square planar geometry in order to account for the optimized Pd_0−Pd_1, Pd_0−Pd_2, and Pd−O_1 distances. As the two PdO_4 units centered in Pd_0 and Pd_2 are linked via an unique oxygen bridge (O_{1b}) the PdO_4 unit centered in Pd_2 is, in principle, free to rotate. The optimized Pd_0-O_2 distance allows to evaluate the angle θ between the Pd_0-Pd_2 and the Pd_2−O_2 vectors. Part b: k^3-weighted, phase uncorrected modulus of the FT of the EXAFS signal of precipitated $Pd(OH)_2$ phase and subsequent heated at 393, 393, and 773 K. Part c: As in part b for the imaginary part. Data from ref 142.

parameters of the EXAFS fit, some constrains are needed: the three Pd atoms (Pd_0, Pd_1, and Pd_2 in Figure 51a) and six O atoms (O_{1a}, O_{1b}, O_{1c}, and equivalents) are forced to be lie in the same plane. Since no multiple scattering (MS) path involving Pd_0 and Pd_1 or Pd_0 and Pd_2 has a significant weight, such geometrical approximation does not affect the fit results as testify by the low value of R_{factor} = 0.027. The quantitative results of the fit reported in Table 20 validates the structural model proposed by Troitskii et al.[1586] and implies that the nature of the precipitated phase is a $[Pd(OH)_2]_n$ colloid characterized by a high local order (strong EXAFS signal up to 4.1 Å) and by a poor long-range order (XRD silent).

To study the Pd supported samples more ordered Pd^{2+} model compounds are needed, so the precipitated phase has been subjected to progressive thermal treatments at increasing temperatures (393, 493, and 773K). The thermal treatment results in a progressive crystallization and sintering process of the $Pd(OH)_2$ into more ordered Pd-oxide phases as clearly demonstrated by the XRPD patterns showing the increase of the integrated area and the decrease of the fwhm of the PdO reflections.[142]

The modulus and imaginary part of k^3-weighted phase uncorrected FT of the EXAFS spectra of precipitated palladium phase and subsequent heating at 393, 493, and 773 K are reported in Figure 51b and c and confirm what observed in the parallel XRPD investigation. The first shell signal around 1.6 Å is basically unaffected by the heating process as all Pd atoms lie in a square planar geometry, independently on the degree of hydroxylation, while the two peaks around 2.7 and 3.2 Å

dx.doi.org/10.1021/cr2000898 | Chem. Rev. 2013, 113, 1736−1850

Table 20. Summary of the EXAFS Fit of the $Pd(OH)_2$ Precipitated Phase.[a] Reproduced with permission from Ref.[142] Copyright 2010 American Chemical Society

Pd_0-O_1		Pd_0-Pd_1		Pd_0-Pd_2		Pd_0-O_2			
R(Å)	σ^2 (Å^2)	R Å)	σ^2 (Å^2)	R (Å)	σ^2 (Å^2)	R (Å)	σ^2 (Å^2)	ΔE (eV)	S_0^2
2.023 ± 0.005	0.0041 ± 0.0005	3.03 ± 0.01	0.0040 ± 0.0005	3.42 ± 0.03	0.007 ± 0.002	3.66 ± 0.04	0.008 ± 0.005	2.5 ± 0.9	0.96 ± 0.07

[a]The fit validity can be appreciated from the quality factor R = 0.027 and from the low values of main correlations among optimized variables: S_0^2/σ^2_{O1} = 0.79, $\Delta E/R_{O1}$ = 0.75 (remaining correlations below 0.7 in absolute value).

increase in intensity according to the formation of new, and more ordered, Pd−O−Pd bridges upon dehydroxylation (see Figure 51a, O_{1a} oxygen atoms). In particular, the inversion among the intensities of these two peaks can be considered as the EXAFS fingerprint of an effective dehydroxylation. Authors observed that the two phases, $Pd(OH)_2$ and PdO, have very similar EXAFS signal, both in modulus and in imaginary parts (see Figure 51b and c), and concluded that it is virtually impossible to discriminate between hydroxide and oxide phases by EXAFS.

Coming to the supported palladium catalyst, the local environment of the as precipitated Pd^{2+} phase on alumina and active carbons from wood and from peat have been investigated as a function of Pd loading, from 0.5 to 5.0 wt %. In Figure 52a,

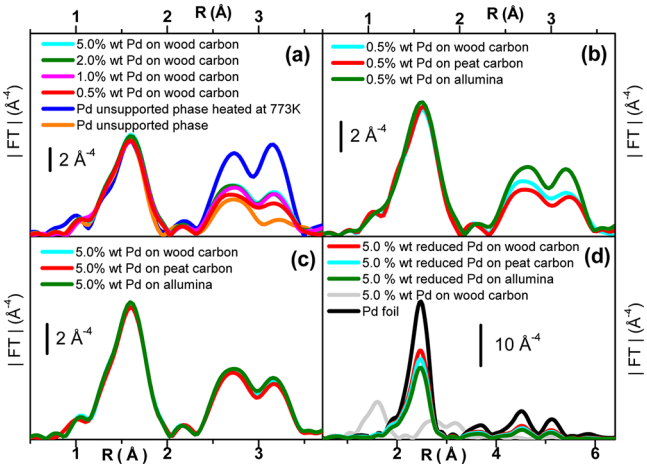

Figure 52. k^3-weighted, phase uncorrected modulus of the FT of the EXAFS signal. Part a: Pd-supported on carbon from wood with increasing Pd loading: 0.5, 1.0, 2.0, and 5.0 wt %. Part b: 0.5% Pd-supported on alumina and carbon from wood and peat. Part c: 5.0% Pd-supported on alumina and carbon from wood and peat. Part d: 5.0% Pd-supported on alumina and carbon from wood and peat reduced in H_2 atmosphere at 393K. For comparison, the spectra of as-precipitated Pd phase on carbon from wood and of Pd foil are also reported for comparison. Data from ref 142.

the modulus of k^3-weighted phase s for Pd-supported on active carbon from wood are reported. At any investigated loading, the spectra are almost intermediate between that of the $Pd(OH)_2$ and that of the PdO model compounds. The third shell contribution (centered around 3.2 Å) shows a small intensity increase upon increasing Pd loading, and saturates (already at 2.0 wt % Pd) at a value much lower than that observed for PdO heated at 773 K, indicating the dispersed nature of the oxidic Pd precursors on the support.

The effect of the support has been investigated and the spectra at the lowest and highest loadings are reported in the Figure 52b and c, respectively. At the lowest loading the effect of the support is appreciable from the intensity of the higher shells signal at 2.3−3.5 Å that increases upon moving from peat carbon through wood carbon to alumina reflecting the progressive increasing order of the supported phase. For the 5.0% Pd-loaded samples, this trend holds but becomes borderline within the sensitivity of the technique. In all as-precipitated samples, no evidence of reduced Pd metal phase is appreciable, meaning that the upper limit of the reduced metal phase is 1 to 2%.

Authors investigated the role of the support in terms of the supported phase/support interaction strength reducing the as-precipitated samples with H_2 at 393 K. The EXAFS data are reported in Figure 52d, together with the spectra of Pd foil (black curve) and of the as-precipitated Pd phase (gray curve) reference compounds. In all cases, the reducing treatment completely modifies the |FT| curves of the as-precipitated samples, showing the disappearance of the first-shell Pd−O signal around 1.6 Å and of complex one at higher distance due to the oxidic phase, accompanied by the rise in the Pd−Pd first-shell signal at 2.5 Å together with the typical higher shell peaks of the fcc structure at around 3.7, 4.5, 5.1, 5.8, and 7.0 Å. All of these features are significantly less intense than the corresponding features of the Pd metal foil (black curve), reflecting a decrease in the average coordination number, as expected in the case of nanometer-sized Pd particles.[1447,1523,1532,1539,1541,1565,1588−1590] Among reduced supported samples, a trend is observed indicating that the average Pd particle size on the three different supports is slightly different following this order: Pd on alumina < Pd on carbon from peat < Pd on carbon from wood. The observed trends reflect the higher efficiency of the alumina respect to carbons in anchoring the particles on the surface, preventing effective sintering from occurring,[1591] and was fully confirmed by the metal surface are measured by CO chemisorption reported in Figure 53.

9.3. Catalytic Reactions over Supported Metal Nanoparticles Involving Hydrogen: Application of ΔXANES

9.3.1. Relationship between Reaction Rates and Types of Surface Metal-Hydrides. Many industrially catalytic reactions involve hydrogen, the most important ones are hydrogenation, reforming, isomerization, and the water−gas shift reaction. Generally, reactions involving hydrogen are heterogeneously catalyzed by metals, such as palladium, platinum, (Raney) nickel,[1592] and more recently gold.[1593−1595] To increase the catalytically active surface areas, the catalytically active metals are supported as nanosized particles on oxidic and carbon supports (see section 9.2). In any reaction that involves hydrogen as reactant, hydrogen activation must occur. This involves splitting of dihydrogen and chemisorption of the hydrogen atoms onto the metal particles. This process readily occurs over metals, such as palladium and platinum. On the surface of these metals, hydrogen can occupy different sites, such as atop, bridged, and 3-fold sites forming surface hydrides and, in some cases (such as for palladium)

dx.doi.org/10.1021/cr2000898 | Chem. Rev. 2013, 113, 1736−1850

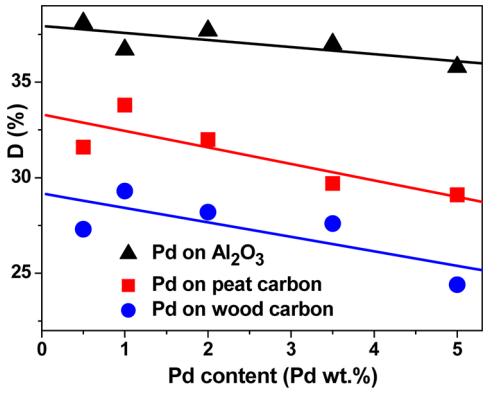

Figure 53. Pd dispersion of catalysts measured by CO chemisorption as a function of the palladium content: from 0.5% to 5%. Samples were reduced in situ with H_2 at 393 K. Blue, red, and black symbols refer to wood carbon, peat carbon, and Al_2O_3 supports, respectively. Lines with the same color report the corresponding best linear fits. Reproduced with permission from ref 142. Copyright 2010 American Chemical Society.

hydrogen penetrate into the metal lattice forming bulk hydrides.[579,580,1596]

Generally speaking, the reaction rate depends on both on the type of surface hydrides formed on the metal. For this reason, a large progress has been made in the understanding of where hydrogen is adsorbed on nanosized particles, as it will be described in this section for platinum. In some cases, relations between hydrogen coverage, the type of adsorption site and catalytic performance of the (platinum-based) catalyst has been achieved.[573,1597]

Very few experimental methods enable the determination of the adsorption site and coverage of reactants, notably hydrogen under reaction conditions. Because of its ability to probe the electronic and geometric structures under operando conditions, XAFS is one of the few methods that can do this. In this paragraph, we aim to introduce the method of ΔXANES, which is a very sensitive tool to distinguish changes in electronic structure that occur after the adsorption of reactants, such as hydrogen (see section 2.3.9 for a general introduction to the differential XAFS approach). We provide here an example how its application leads to understanding of the role of adsorbed hydrogen in catalysis.

9.3.2. ΔXANES, How It Works. As discussed in section 2.3.9, the differential XAFS approach allows the determination of small differences occurring in the XAFS (XANES or EXAFS) spectra upon some perturbation induced on the sample. In this regard, the ΔXANES method has been developed to enable the determination of the adsorption of a weak scatterer such as hydrogen;[72,1598] and later found other applications. Currently, it is most-successfully employed at the L_3 edge, because this edge probes the *d* density of states (DOS). As a matter of fact adsorption of a reactant occurs because of the overlap of atomic orbitals of the adsorbate and those of the metal, which form bonding and antibonding molecular orbitals. For the transition metals most important in catalysis, the bonding orbital is largely determined by the d orbitals of the metal. The antibonding orbital is located above the Fermi level and the *d*-DOS component can thus be detected in L_3 edge XANES. On the contrary, K-edge XANES, probing the *p*-DOS, is unable to provide information on the adsorption process. As it will be shown below, the shape of the XANES is reminiscent of the bonding site of the adsorbate. Because XAFS is a quantitative method, the adsorption sites can even be quantitatively determined.

In the past decade, the so-called ΔXANES method has been established as a versatile tool to determine the adsorption sites of adsorbed species on metal particles.[72,1597,1599,1600] The ΔXANES method is based on the assumption that all contributions that are identical in each of two XANES spectra can be removed through subtraction. The resulting difference spectrum highlights the changes between the two spectra, see eq 26:

$$\Delta\mu = \mu(1) - \mu(2) \tag{49}$$

For example, for supported nanosized platinum particles, the change in the XANES spectrum due to the adsorption of an adsorbate on the metal can be determined as $\Delta\mu$ in eq 49, being $\mu(1)$ and $\mu(2)$ XANES spectra before and after adsorption, respectively. This subtractive method has the benefit that the unchanged part of a spectrum (for example due to the atoms in the core of the particle that are not involved in the adsorption process) is removed. The result is a spectrum that is highly sensitive to what has changed; it has been suggested to be sensitive to fractions of a percent. In addition, when looking at L_3 edges, not only strongly bound (chemisorbed) species, but also weakly adsorbed species can be detected and differently adsorbed species can be simultaneously and quantitatively[575,1597,1601] determined.[1602] During the past decades, it has been established that adsorption of species on (or into) metals cause the appearance of characteristic spectral features, especially in the L_3 edge. As an example, well-known is the occurrence of a peak at about 8 eV above the absorption L_3 edge of palladium after formation of palladium hydride. This species has been assigned to the antibonding state formed between the Pd(d) and H(s) orbitals.[579] For platinum no bulk hydride is formed and hydrogen remains on the surface. Different Pt surface hydrides can be formed: atop, on bridged and 3-fold sites. When hydrogen adsorbs on an atop site, it bonds to a single platinum atom; adsorbed on bridged or 3-fold (*fcc*) site, it bonds to two respectively three platinum atoms. It has been well-established that hydrogen adsorption changes the structure of the underlying particle. Depending on how hydrogen is adsorbed, charge transfer and bond lengthening of the Pt−Pt bond occur.[1603] These changes cause the adsorption of hydrogen to have various effects on the X-ray absorption coefficient of the platinum atoms. Following the terminology introduced by Ramaker and Koningsberger,[72] eq 49 can be expressed as

$$\begin{aligned}\Delta\mu &= \mu(\mathrm{Ad/M}) - \mu(\mathrm{M}) \\ &= \Delta\mu_o + \Delta(\mu_o \cdot \chi_{\mathrm{M-M}}) + \mu_{o,\mathrm{Ad/M}} \cdot \chi_{\mathrm{M-Ad}}\end{aligned} \tag{50}$$

where μ(Ad/M) is the spectrum of metal particles with adsorbate and μ(M) that of bare particles; $\Delta\mu_o$ equals the change in atomic XAFS because of the adsorbate (see section 2.4; however note that this term is the smallest of all and generally neglected); $\Delta(\mu_o \times \chi_{\mathrm{M-M}})$ is the change in metal−metal scattering caused by chemisorption of the adsorbate; and $\mu_{o,\mathrm{Ad/M}} \times \chi_{\mathrm{M-Ad}}$ is the scattering caused by the adsorbate. Theoretical calculations[72,1604,1605] have been successful in reproducing the experimental features. The FEFF-code developed by Rehr and co-workers is the most-used one for such analysis.[442] Figure 54 shows the theoretical $\Delta\mu$ or ΔXANES signals of hydrogen adsorbed on Pt on atop and 3-

dx.doi.org/10.1021/cr2000898 | *Chem. Rev.* 2013, 113, 1736−1850

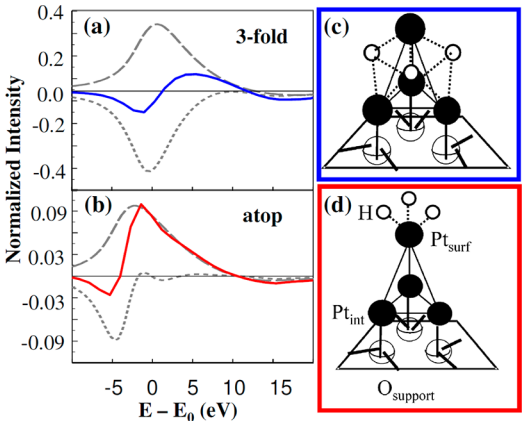

Figure 54. Theoretical signatures of ΔXANES of hydrogen adsorbed on 3-fold site (a, solid blue line) and on an atop site (b, solid red line) on platinum. The XANES signals of the platinum atoms that are closest to the hydrogen are given. The Pt−H scattering contribution ($\mu_{o,H/Pt}\,\chi_{Pt-H}$) (gray dashed light) and change in Pt−Pt contribution ($\Delta[\mu_o\,\chi_{Pt-Pt}]$) (gray dotted lines) are also indicated. Parts c and d: Structure of tetrahedral Pt_4 clusters utilized, first optimized using the Amsterdam density functional package (ADF),[499] and the used for the FEFF8[442] calculations of the XANES spectra. Adapted with permission from ref 120. Copyright 2003 Elsevier.

fold adsorption sites according to eq 49.[120] The signature of hydrogen on a bridge site resembles that of the 3-fold site and thus is not shown. When hydrogen adsorbs on the atop site, the ΔXANES consists of an almost fully positive contribution (blue curve in Figure 54a), which is indicative of the absence of a shift in the absorption edge. In contrast when hydrogen adsorbs on bridge and 3-fold sites a large negative contribution is observed, followed by a positive one (red curve in Figure 54b). The edge shift is reminiscent of charge transfer, which differs for the adsorption sites. Experimental difference spectra can be quantitatively interpreted using these established signatures (vide infra).

Using the so-called "limited absorber" assumption[1607] the agreement between theory and experiment has been very good and allowed to (partially) distinguish bonding sites, even though quantitative agreement has not been achieved yet. According to this assumption, only the metal atoms that directly contribute to the bonding with the adsorbate contribute to the difference spectrum. Obviously, a better agreement between theory and experiment can be achieved when including the changes and signatures of all platinum atoms within a particle.[1608] However this procedure requires a good understanding of the exact structure of the particle, which is in general difficult to obtain and subjected to heterogeneity problems. Further improvements in the simulation of the ΔXANES features can be achieved by configurational averaging procedure that takes into account the contribution of the adsorbate-free metal atoms.[1607]

One requirement to obtain reliable difference spectra is the use of normalized spectra, that is, pre- and post-edge subtracted and intensity normalized spectra. Moreover, a correct energy calibration is essential, see eq 3, as this will strongly influence how difference spectra look like. The latter requirement is more important than the former, because it leads to changes in the difference spectrum that directly interfere with those resulting from the adsorption or variation in the particle structure. Incorrect energy calibration leads to artifacts in the difference spectra that are difficult to be distinguished from the "real" difference spectrum and cannot be corrected for. An experimental setup allowing an exact energy calibration for each collected XANES spectrum through the simultaneous measurements of I_0, I_1, and I_2, see Figure 4a, is recommended for these studies. Also, differences that arise from a wrong background extraction can be recognized in the difference spectra by the occurrence of a residual background over a larger energy range (tens of electronvolts), and calculations can be corrected for this.

Hydrogen adsorption on supported platinum particles has been widely studied using the ΔXANES method,[72,1597,1598,1606,1609,1610] and it has now been well-established that adsorption sites can be determined as described above. We stress that application of the ΔXANES method is not restricted to hydrogen; other adsorbed species that have been studied

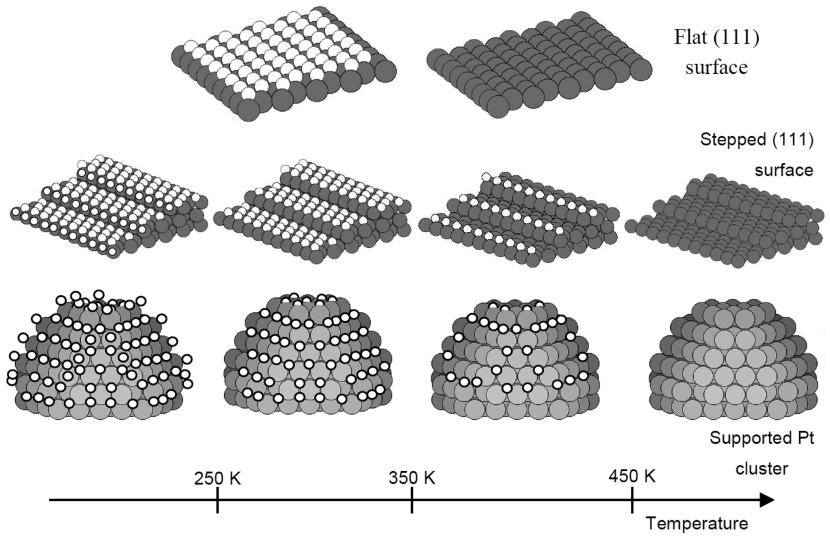

Figure 55. Hydrogen coverage on platinum as function of temperature on flat Pt(111) surface, stepped Pt(111) surface, and Pt nanoparticles. Edge and corner atoms form the strongest bonds with hydrogen. Reproduced with permission from the PhD thesis of Oudenhuijzen.[1616] Copyright 2002 Utrecht University.

dx.doi.org/10.1021/cr2000898 | Chem. Rev. 2013, 113, 1736−1850

involve carbon monoxide,[577,578,1609] oxygen,[1597] ethylene,[1600] water,[1597,1611] and hydroxide and applications are reported in actual catalytic reactions[1597] and in electrochemistry.[575,1612] Also metals different to Pt have been investigated with the ΔXANES method, such as Rh,[1613] and Ru.[577]

9.3.3. Temperature-Dependent Hydrogen Coverage on Pt Surfaces. To understand the role of hydrogen in a reaction, it is essential to determine its surface coverage during catalytic reaction. It is well established that hydrogen bonds strongly onto several transition metals and that the amount of adsorbed species depends on temperature.[1614,1615] Figure 55 illustrates the evolution, as a function of the temperature, of the hydrogen adsorption onto, from top to bottom: flat Pt(111) surface, stepped Pt(111) surface, and Pt nanoparticles. At low temperatures, all the three surfaces are completely covered with hydrogen. Decreasing coverages are observed at higher temperature. Hydrogen on flat Pt(111) surface is the weakest bound and desorbs at a temperature above 350 K. Thus, the Pt(111) surface is already empty, while the edge atoms at the stepped surfaces and those at the Pt atoms at the edges and corners of the nanoparticles are still covered with hydrogen. Above 450 K the hydrogen desorbs also from these sites. Because hydrogen bonds so strong to the catalyst surface, it plays a dominant role in the reaction kinetics.

9.3.4. Influence of Hydrogen on Hydrogenolysis: A Key Study for ΔXANES. In hydrogenolysis of alkanes, carbon−carbon bonds are broken and lighter molecules are formed. This reaction is typically metal-catalyzed and performed under hydrogen atmosphere. The reaction is generally small and positive order in the partial pressure of alkane; that of hydrogen varies strongly depending on the reaction condition and catalyst; it can be as negative as −3.[1617] The positive order in alkane and negative one in hydrogen implies that the metal surface contains very few adsorbed alkane species and that it is covered with hydrogen. Upon desorption of hydrogen, the alkane competes for the free adsorption sites. It is therefore obvious that the adsorption strength of hydrogen and the amount adsorbed, which are both influenced by the adsorption site, affect the reaction rate. In addition, the apparent activation barrier can be very high and moreover, it is related to the order in hydrogen: a high E_{act} relates to a very negative order in hydrogen and a lower E_{act} to a moderate negative order in hydrogen. For example, in ethane hydrogenolysis, an order in hydrogen of −2.5 correlates to an E_{act} of +225 kJ/mol, an order of −1.5 to +175 kJ/mol.[1618] The linear relation that is observed between order in reaction to activation barrier is reflected in the so-called *compensation effect*. This relation, also called Constable−Cremer relation,[1619] describes a linear relation between apparent activation barrier and pre-exponential factor (A_{app})

$$\mathrm{Ln}(A_{app}) = mE_{app} + c \tag{51}$$

One of the explanations of the occurrence of a compensation effect is the involvement of changes in the surface coverage of reactants[1620] as function of temperature and for a set of different catalytic systems. Thus, the binding energy and surface coverage of the adsorbed reactants and intermediates strongly affect the reaction kinetics. Temkin equation describes the influence of the adsorption of reactants on the apparent activation energy:

$$E_{app} = E_{true} + \sum n\Delta H_{ads} \tag{52}$$

where E_{true} is the intrinsic activation barrier and $\Sigma n\Delta H_{ads}$ the sum of adsorption enthalpy multiplied by the order n of that reactant.

Oudenhuijzen et al.[120] have quantitatively interpreted the compensation relation for neopentane ($C(CH_3)_4$) hydrogenolysis over supported platinum catalysts. Also in this case, there is strong inhibition by hydrogen and a positive order in the alkane pressure and the relation between negative order in hydrogen and activation barrier is observed as well. A compensation relation is observed when comparing sets of different catalysts, such as platinum on modified alumina and zeolites. Acidic supports yield rates that are orders of magnitude higher than on basic supports. In addition, the negative order in hydrogen is −1.5 for acid supports and −2.5 for basic ones.[1621] Figure 56 shows the Pt L_3 edge XANES Pt nanoparticles

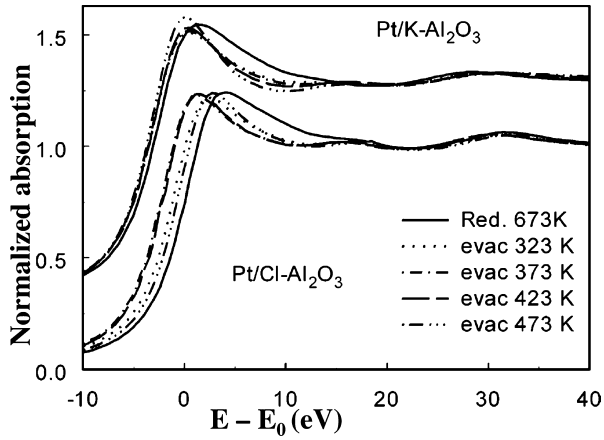

Figure 56. Pt L_3 edge XANES of supported platinum nanoparticles on basic support (K−Al_2O_3) and acid support (Cl−Al_2O_3) after reduction in hydrogen (solid line) and after evacuation at different temperatures (remaining lines refer to increasing temperature of evacuation, as reported in the legend). The spectra were recorded at 77 K. The spectra of Pt/K−Al_2O_3 are vertically offset by 0.3 for clarity. Reproduced with permission from ref 573. Copyright 2005 American Chemical Society.

supported on two different aluminas after adsorption of hydrogen and desorption at increasing temperature. In particular the same alumina was modified, making it basic by addition of potassium (Pt/K−Al_2O_3), and acidic, by addition of chlorine (Pt/Cl−Al_2O_3). Upon increasing temperature of desorption, the XANES spectra change; those of Pt/Cl−Al_2O_3 show a consistent shift toward lower energy, those of Pt/K−Al_2O_3 are markedly less shifted and changes in intensity of the whiteline dominate. It has been demonstrated that the origin of these differences is the differing preferential adsorption sites for hydrogen. Figure 57 shows the ΔXANES spectra, which are to be compared to the atop and 3-fold signatures shown in Figure 54. They identify the differing hydrogen adsorption sites in the various temperature ranges. Difference spectra with reference spectra chosen at different temperature identify either the hydrogen that is left on the surface (b and d, the reference spectrum is that of the bare platinum particles obtained by evacuation at 473 K) or the hydrogen that is desorbed in a given temperature interval and the rearrangement of the remaining hydrogens (a and c, the reference spectrum is that taken at 50 degrees higher). At the typical reaction temperature of 473 K, hydrogen adsorbs preferentially in the Pt *fcc* 3-fold hollow or bridged sites on

dx.doi.org/10.1021/cr2000898 | *Chem. Rev.* 2013, 113, 1736−1850

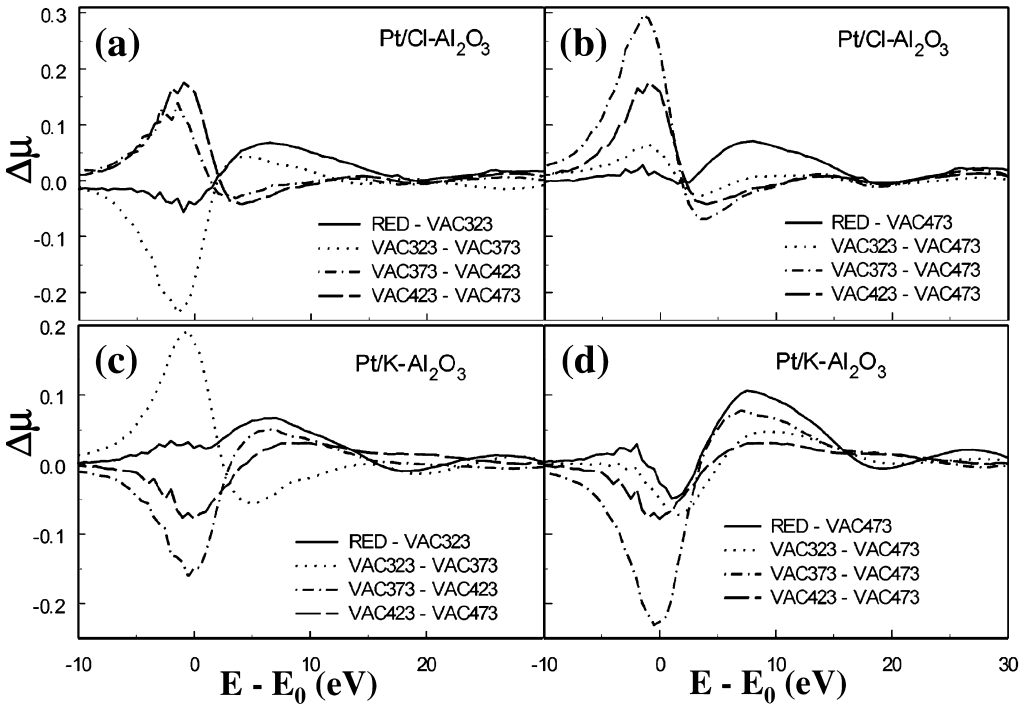

Figure 57. Difference spectra of the XANES region for the L_3 edges for Pt/Cl−Al_2O_3 and Pt/K−Al_2O_3. Parts a and b represent the signatures of the hydrogen that is desorbed, which includes the rearrangement of the hydrogen that is remaining on the surface. Parts c and d identify the signatures of the hydrogen atoms that remain on the surface. Adapted with permission from ref 573. Copyright 2005 American Chemical Society.

basic supports at high coverage; in contrast, it adsorbs on the atop site on acidic supports with a relatively low coverage. Because of the different dominant adsorption sites, the number of hydrogen atoms that need to be displaced before the neopentane can adsorb (and react) is different. As mentioned above, a platinum atom is surrounded by three fcc sites; thus for platinum on a basic support, the hydrogen atoms from the three surrounding fcc sites must desorb to enable adsorption of the alkane. On an acidic support, only the hydrogen on the atop site needs to desorb before the site is available for alkane adsorption and subsequent reaction. Consequently, one more hydrogen molecule needs to desorb from the platinum surface for basic supports, which is reflected in the difference in order of reaction, −2.5 for basic and −1.5 for acidic supports. A quantitative description of the reaction parameters such as activation barrier and pre-exponential term thus become possible, which is, however, not described here.

When ΔXANES is used, the structure of the adsorption site of reactants and intermediate has become quantitatively accessible. When the individual signatures of adsorbates, such as H, O, OH, and CO, on specific sites are known, a quantitative determination of their coverage is possible, even in case of multiply adsorbed species. Such data are perfectly complementary to methods, such as the vibrational spectroscopies, that probe the adsorbate and intermediate.

9.4. Determination of the CO adsorption sites on Pt nanoparticles Combining Experimental in Situ High-Energy-Resolution Fluorescence-Detected (HERFD), XAS and RIXS Maps

Glatzel et al.[216] reported in situ high-energy-resolution fluorescence-detected (HERFD, see section 2.2.5) X-ray XAFS[223,224] and resonant inelastic X-ray scattering (RIXS, see section 2.2.4) on 1.9 wt % H_2-reduced Pt/Al_2O_3 catalyst before and after CO adsorption. For both techniques, the energies of incident ($h\nu_1 = \Omega$) and emitted (inelastically scattered $h\nu_2 = \omega$) X-rays are analyzed by means of Bragg reflections from the second monochromator, as described in Figure 5a. In the reviewed experiment, an incident photon of energy Ω excites a Pt $2p_{3/2}$ electron into the Pt 5d level. These excited states decay with a lifetime τ upon emission of a photon with energy ω. The energy deposited in the sample in this two photon process is the energy transfer, Ω−ω, which, when sufficiently small, corresponds to a charge neutral excitation within the 5d shell. The experiments yield a two-dimensional intensity distribution, where the final state energy Ω−ω is plotted versus the incident (absorption) energy Ω as reported in Figure 58a and b.

For bare Pt nanoparticles (Figure 58a), the elastic peak and the valence-band excitations merge together, indicating a metallic electronic structure. This means that the Fermi level lies within a partially filled band. After adsorption of CO on the Pt nanoparticles (Figure 58b), an increase in intensity above 4 eV of energy transfer is observed, and a broad energy distribution develops. A gap opens up between the elastic peak at zero energy transfer and the lowest unoccupied electronic states that can be reached in the RIXS process.

Using FEFF8.4 code[390,442,1622] Glatzel et al.[216] calculated the RIXS planes for a bare Pt_6 cluster (Figure 58c) and the cluster with CO adsorbed at three different sites (Figure 58d−f). The RIXS plane for the Pt_6 cluster nicely reproduces the experimental results (Figure 58a). Adsorption of CO gives rise to a shift in the maximum RIXS intensity to higher energy transfer. The shift is approximately equal when CO is adsorbed in bridged (Figure 58e) and face-bridging sites (Figure 58f), whereas it is more pronounced for CO adsorbed to a single Pt atom in an atop configuration (Figure 58d).

Figure 58g and h combines the RIXS data with the experimental high-energy-resolution fluorescence-detected XAFS scans (see section 2.2.5). The RIXS spectral intensity

dx.doi.org/10.1021/cr2000898 | Chem. Rev. 2013, 113, 1736−1850

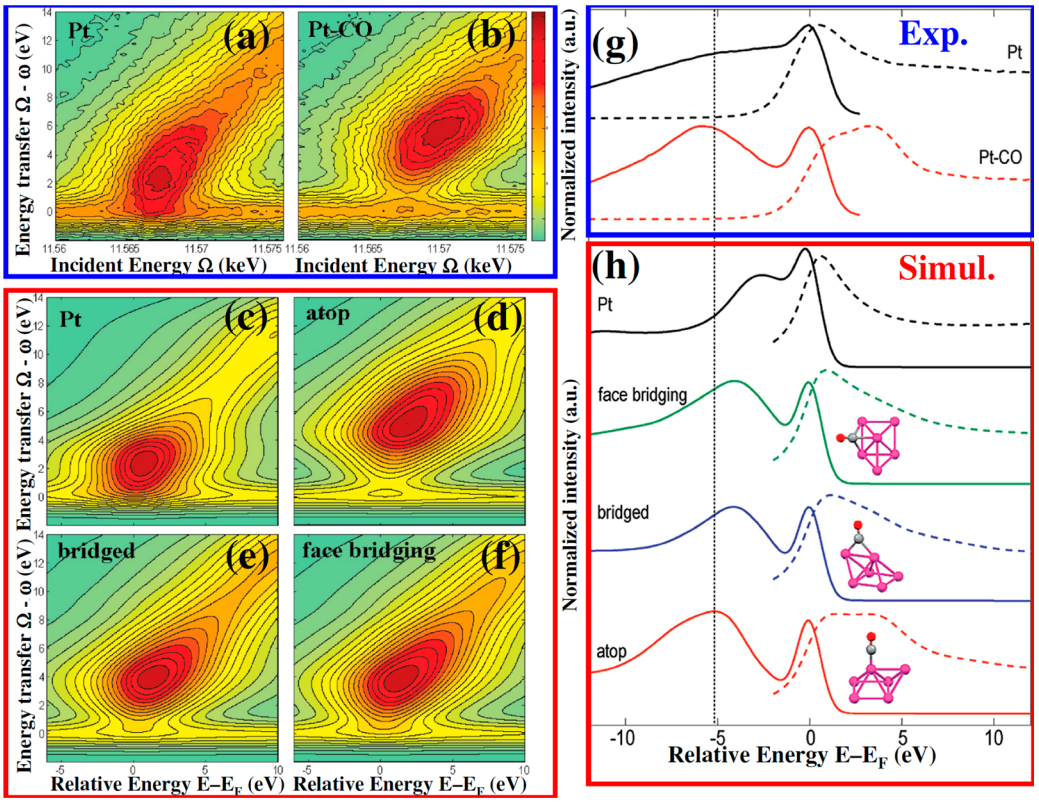

Figure 58. Parts a and b: Experimental $2p_{3/2}$ RIXS planes of H_2-reduced 1.9 wt % Pt/Al_2O_3-supported nanoparticles before and after CO adsorption, respectively. Parts c–f: Calculated $2p_{3/2}$ RIXS planes for a bare Pt_6 cluster and the cluster with CO molecule coordinated in atop, bridged and face bridging geometries, respectively. Part g: Experimental high-energy-resolution fluorescence-detected L_3 XAFS (dashed) and RIXS (solid) spectra before and after CO adsorption, top and bottom curves, respectively. Part h: Calculated high-energy-resolution fluorescence-detected L_3 XAFS (dashed) and RIXS (solid) spectra of, from top to bottom: bare Pt_6 cluster and the cluster with CO molecule coordinated in atop, bridged and face bridging geometries. Also reported are the Pt_6 and Pt_6CO clusters adopted for the calculations. The dotted vertical line is a guide to the eye. Reproduced with permission from ref 216. Copyright 2010 American Chemical Society.

in Figure 58a and b was summed along the incident energy (i.e., the horizontal direction) to give line plots with the elastic peak at zero energy. The energy transfer in Figure 58ab was multiplied by −1 for comparison with the absorption spectra. The energy of the elastically scattered peak corresponds to the energy of the Fermi level. The atop configuration provides the best agreement with the experimental absorption and RIXS data.[216] This qualitative agreement is certainly remarkable, nevertheless, it is evident that different carbonyl species are present on the surface of the nanoparticles, as clearly evidenced by IR studies,[603,1092,1623] so that the experimental spectrum could be quantitatively reproduced only using the linear combination of different theoretical curves.

9.5. Correlation between AXAFS and IR Spectroscopy of Adsorbed CO on a Set of Pt Supported Catalysts

As underlined in section 2.4, the possible recognition of AXAFS as a new tool for studying heterogeneous catalysts is hampered up to now by the lack of sufficiently broad experimental data to support the relation between the AXAFS intensity of catalytic systems and the corresponding changes in the electronic properties. The Utrecht group walked an important step in this direction.[603] They reported an important combined AXAFS/IR study on a large number (14) of different Pt-supported catalysts.

It is well-known that the IR spectroscopy of CO adsorbed on Pt nanoparticles results in two main ν(CO) stretching bands in the $\tilde{\nu}$(CO) = 2110–2000 and 1900–1700 cm^{-1} intervals due to linear and bridged CO molecules on respectively,[1092,1623,1624] see Figure 59b. From these data, it is clear that the IR linear-to-bridged intensity ratio obtained by integrating the IR bands on the different spectra decreases in the order of Pt/MCM-41 > Pt/SiO_2 > Pt/Ca–Y > Pt/K–Y, reflecting an increasing electron density on the supported Pt nanoclusters. The authors assumed that the extinction coefficients for adsorbed CO are influenced to the same extent for the linearly and bridged Pt-coordinated CO stretching vibrations, and the error in the ratio was estimated to be around 10%.[603]

The AXAFS contribution, carefully isolated from the total XAFS data by subtracting the first shell contribution (as described in section 2.4.2, Figure 11), is reported in Figure 59a for a selection of the measured samples. The error for the isolation of the AXAFS contribution was estimated to be around 10%.[603] One can notice that the AXAFS data of the different supported Pt nanoclusters differ in their AXAFS intensity, as well in the peak centroid. A decrease in the AXAFS intensity results in a shift of the peak centroid to higher R values, and the AXAFS intensity decrease follows the same order as that of the IR linear-to-bridged intensity ratio, that is, Pt/MCM-41 > Pt/SiO_2 > Pt/Ca–Y > Pt/K–Y. Figure 59c plots the AXAFS peak intensities of the 14 different samples versus their corresponding IR linear-to-bridged intensity ratio. The investigated range of the two variable is quite large, as the IR linear-to-bridged intensity ratio span a range of more than 12 units, whereas the AXAFS intensities covers the 0.8–2.6 × 10^{-2} $Å^{-2}$ interval.

dx.doi.org/10.1021/cr2000898 | Chem. Rev. 2013, 113, 1736–1850

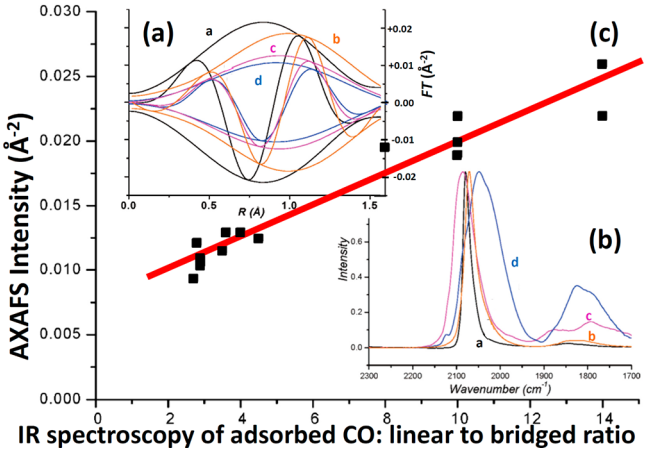

Figure 59. Part a: *k*-weighted Fourier transforms (Δk = 2.5−8.0 Å^{-1}) of the Pt L_3-edge AXAFS spectra of a selection of the 14 measured samples. Namely Pt/MCM-41, Pt/SiO_2, Pt/Ca−Y, and Pt/K−Y. samples, curves a−d, respectively. Part b: As in part a for the IR spectra of CO adsorbed at room temperature. Part c: Correlation between the AXAFS peak intensity, see part a, and the corresponding linear to bridged intensity ratio obtained from IR spectroscopy of adsorbed CO, see part b, on the whole series of 14 supported Pt nanoclusters (scattered squares). The red line represents the best linear fit among the experimental points. Adapted from with permission from ref 603. Copyright 2005 American Chemical Society.

The authors found and interesting correlation (Figure 59c) between the intensity of the AXAFS signal collected on 14 catalysts and the ratio between the IR bands of linear-to-bridged Pt-carbonyls. In other words, the AXAFS peak intensity, as well as the IR linear-to-bridged intensity ratio decrease with decreasing ionization potential of the Pt atoms in the nanoclusters. Consequently they showed that the AXAFS signal can be used to probe the electronic properties of supported Pt nanoclusters. The authors concluded that, because AXAFS does not need any probe molecule, it can be used to probe the electronic properties of supported noble metal nanoparticles under reaction conditions in real time, delivering mechanistic insight on the working catalyst. Moreover, AXAFS method can be applied to systems where the metal nanoparticles are supported on black supports like active carbons, that can hardly be investigated by IR spectroscopy.[1581]

10. CONCLUSIONS AND PERSPECTIVES

We have illustrated that X-ray absorption and emission spectroscopies have had considerable impact to understand the reactivity of surface species in heterogeneous catalysis. In situ, operando, time-, and space-resolution provide structures of species that are kinetically relevant. The use of combined methods, such as XRD, SAXS, IR, Raman, and UV−vis and ab initio calculations makes more solid and amplifies the impact of XAFS results; the on line implementation on the beamlines themselves of parallel acquisitions (XRD, SAXS IR, Raman, and UV−vis) is continuing to grow and will provide further understanding of the reactivity of surface species. For highly crystalline and complex materials, such as metal−organic frameworks, the synergy among EXAFS, XRPD, and ab initio calculations has been found to guarantee the success in the structural determination and its modification upon molecular absorption.[65,1149,1304] From the general inspection of all the reported examples, it emerges clearly that quantitative information on the local structure of the active sites can be easily obtained only on systems characterized by a high homogeneity of the X-ray absorbing species. For systems that do not fulfill this, care must be taken and generally only qualitative information can be extracted; exception can be made in case independent information is available from other techniques (IR, XRPD, DAFS, PDF, ab initio calculations, etc.). In any case, the data analysis of multiphase samples can be quantitatively performed only once a proper model of the different phases is available.

Future developments will have to further focus on developing measurement and detection schemes to exactly detect the catalytically active minority species. We foresee two directions. The first is the further development and application of modulation excitation data, which has the potential to selectively detect minority species that are sensitive to an external stimulus.[1462,1625,1626] The structural change upon modulation can be determined with enhanced accuracy.[567] The second is based on the selective detection of a fluorescence signal that correlates to the active species only,[193,229] see the description of XES spectroscopy in section 2.2.4. The construction of new and improved secondary emission spectrometers at various beamlines will spur research in this direction and to improve time resolution.

In addition to those mentioned above, we foresee the following advances in the use of XAFS techniques in catalysis in the near and more distant future: (i) Equipment to perform in situ and operando experiments to be done (section 2.2.6) will be no longer developed and used by only a selected few, highly specialized, groups but will be developed by beamline scientists (expert in both catalysis and X-rays spectroscopies) and will become readily available for the whole user community at most of the XAFS beamlines worldwide. (ii) To make point (i) fully efficient, a parallel effort will be needed on an educational ground to form new PhD students, postdoc and scientists to be able to carefully perform sophisticated experiments and to properly use the abundant codes present nowadays to analyze XAFS data (sections 2.3.4−2.3.7). (iii) Time-resolved techniques, such as fast data recording (quick-EXAFS and dispersive XAFS) (sections 2.2.3 and 8) have shown a great development in the past decade and will further develop in the future, combining more fast response with the combination of independent characterization techniques available on line and allowing parallel IR, UV−vis, Raman, etc., investigations to be carried out. Improved and readily available data-analysis programs must be developed to take full advantage of the rapid data-taking (section 2.3.7). (iv) Space-resolved, including tomographic, techniques (sections 2.2.7 and 7) will allow to have a precise three-dimensional insight into the whole catalytic bed (hosted inside a capillary) and individual catalyst grains and thus to investigate effects such as the change in the reactants/products ratio occurring along the catalytic bed. (v) Under some special conditions, where the knowledge of the absorption coefficient at a give (fixed) energy, $\mu(E_0)$, is sufficient to get relevant information on the catalyst, then combined space and time-resolved techniques may be foreseen. (vi) XES-based techniques (sections 2.2.4, 2.2.5, 3.2.2, 3.3.5, 5.2.2, and 9.4), nowadays still available on very few beamline worldwide, will allow a much deeper knowledge of the electronic structure of the active site, being able to probe with hard X-rays both occupied and nonoccupied density of states. They will allow XPS- and UV-like information, however with element specificity, to be available on catalysts in interaction with gases and liquids. Also, the combination of

dx.doi.org/10.1021/cr2000898 | *Chem. Rev.* 2013, 113, 1736−1850

XES with a diffraction-based technique, such as X-ray standing waves,[1131] will enable to detect electronic structure of elements on specific crystallographic sites. (vii) High-energy resolution fluorescence detected XANES and EXAFS (section 2.2.5) will allow: (a) range-extended EXAFS spectroscopy to be possible in samples containing elements having two absorption shells close in energy;[226,228] (b) oxidation state-specific EXAFS able to obtain separate EXAFS signals in samples containing the same element in different oxidation states;[193,229] and (c) spin-selective EXAFS spectra collection to be possible.[230] (viii) Laser pump/X−rays probe experiments, applied up to now mainly in studies related to the photodissociation of chemical bonds, may in the next future be employed to investigate photocatalysts, shed some light in the structural and electronic rearrangements of the photocatalytic site just after (visible) photon absorption or other external stimulus.[1627] In the immediate future, the incoming new X-ray free electron lasers (FEL) sources will revolutionate the physics and the chemistry of time-resolved experiments.[6,1628−1634] The development of adequate measurement technique and data-acquisition schemes for measuring X-ray absorption at incoming FEL is essential. The ultra high fluxes up to about 10^{12} photons per pulse (compared to 10^6 photons per pulse of present III generation synchrotrons) and extreme short length (tens of femtosecond, compared to hundreds of picosecond) will provide unique new opportunities, which are currently hard to imagine. (ix) Until now, in the large majority of the published papers, XANES has been often used only as a qualitative support of the hypothesized structures, discussing qualitatively the evolution of edge, pre edge and post edge features (see, e.g., the case of TS-1 in section 3.2). Quantitative results were extracted from XANES data mainly in comparison with the experimental XANES spectra of model compounds (see e.g. the Operando study of the γ-$CuCl_2/Al_2O_3$ catalyst for ethylene oxychlorination discussed in section 8). Publications where hypothesized local structures are used to compute a XANES spectrum are still rare (see, for example, results reported in Figures 32, 45, 54, and 58), but the remarkable progress made by theoretical codes (section 2.3.5) will change this situation. We foresee that in the future, the simulation of the XANES spectra will be used more and more frequently to confirm or discard local structures hypothesized from the refinement of EXAFS and diffraction data.

The first two points will probably not result in new scientific highlights but are probably the most important as they will allow to further increase the scientific community using XAS/XES spectroscopies for catalysts understanding and development, constructing a synergic interaction among large scale facilities, academia, and industries. Conversely, points iv−viii will be less widely applicable but they could lead to breakthroughs in some specific fields. We foresee, for time-resolved experiments, for points iii and ix, both a great diffusion and the possibility to reach high levels of scientific results. Coming to the related techniques (section 2.5), the following evolution are expected by the authors: (x) Extended joint EXAFS/DAFS (section 2.5.2) will allow exploration of biphasic systems and, for example, the contribution coming from coexisting amorphous and crystalline phases to be disentangled.[632] (xi) As far as metal nanoparticles are concerned, total scattering (PDF) experiments, will be able to bridge the gap between EXAFS dominating the 0−30 Å diameter interval and XRPD, informative in the 80 Å-bulk interval, see section 2.5.4.[691] (xii) X-ray magnetic circular dichroism (X-MCD), see section 2.5.1, coupled with more conventional visible light MCD and EPR, will bring new insight in the investigation of transition metal supported catalysts[663−665] and in biocatalysis.[666] (xiii) Extended energy-loss fine structure (EXELFS) spectra can be obtained in TEM equipped with an electron energy-loss spectrometer (section 2.5.3). Chemical and oxidation-state speciation can consequently be obtained with a few nanometer resolution. (xiv) BEFS is potentially a very powerful, new technique for the study of the local environment of hydrogen in catalysts, for which traditional XAFS is not achievable because of the low binding energy of the K-edge (13.6 eV) but has yet to prove to be a practical tool.[50,650]

Given the long history of X-ray absorption and emission spectroscopy applied to catalytic systems, the field is still developing remarkably rapid. We foresee an exciting future and many new discoveries in X-ray spectroscopy and concurrently in catalysis.

AUTHOR INFORMATION

Corresponding Author

*E-mail: carlo.lamberti@unito.it. Fax: +39011-6707855. Phone: 39011-6707841.

Notes

The authors declare no competing financial interest.

Biographies

Silvia Bordiga was born in 1964, obtained her degree in Chemistry in 1988, and earned her PhD in Chemistry in 1993. She obtained the position of researcher in the field of physical chemistry in 1995. She has been a Professor in Physical Chemistry at the Faculty of Sciences of the University of Turin since 2001. Her teaching activities refer to heterogeneous catalysis and spectroscopies considering both theory and applications. Her scientific activities are mainly devoted to the characterization of the physical−chemical properties of oxides, zeolites, and MOFs with particular attention to their surface properties. She has coauthored more than 250 research and 8 review papers, which have appeared in international journals and have received more than 13 000 citations (h-index 67).

Elena Groppo was born in 1978 and received her Degree in Materials Science in 2002 at the University of Torino. In 2006, she completed her PhD in Chemistry at the same University, and from 2006 to 2010, she held a PostDoc position in the group of Physical Chemistry under the supervision of Prof. Zecchina. She is now Researcher in the same research group. Her scientific interests are mainly related to in situ and operando investigation of heterogeneous catalysts for olefin polymerization by means of spectroscopic methods, including synchrotron radiation based techniques. She has coauthored more than 60 research papers (including 5 reviews), which have received more than 1000 citations (h-index 20). She received the Award for the best Young Scientist at XVI Congress of the Italian Synchrotron Radiation Society (SILS), and she was recently selected among the five best candidates for the Gerhard Ertl Young Investigator Award.

Giovanni Agostini obtained his Masters in Physics in 2006 and his PhD in Materials Science in 2010 at the Torino University under the supervision of Prof. C. Lamberti. He currently has a Post-Doc position in the same group. His main research activity consists in the structural characterization of nanostructured materials with a multitechnique approach based on combination of TEM, XRPD, and EXAFS. He recently started to use also SAXS and PDF approaches. He authored 25 research papers. He is also coediting the book *Characterization of Semiconductor Heterostructures and Nanostructures (II edition)*, Elsevier, 2013.

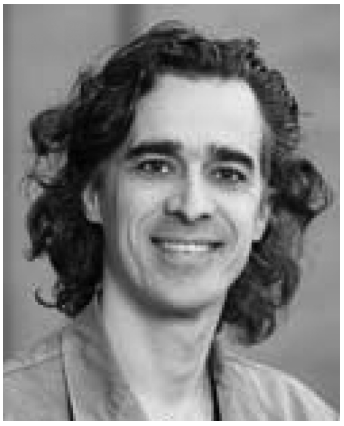

Jeroen A. Van Bokhoven is professor for Heterogeneous Catalysis at the ETH Zurich and head of the Laboratory for Catalysis and Sustainable Chemistry at the PSI Villigen, since 2010. He finished his Ph.D. cum laude at Utrecht University with professor Dr. Diek Koningsberger and Dave Ramaker and made a postdoctoral stay at the Debye Institute at Utrecht University and later with professor Dr. Roel Prins at the ETH Zurich. In 2006, he obtained an assistant professorship from the Swiss National Science Foundation. He has coauthored over 160 papers, which have received over 3000 citations (h-index 32). His main research interest focuses on synthesis of defined catalysts and active sites and on the determination of structure–performance relations in heterogeneous catalysis. He develops and explores synchrotron-based characterization methods.

Carlo Lamberti Born was born in 1964, obtained his degree in Physics in 1988, and earned his Ph.D. in solid state physics in 1993. He has been professor in Physical Chemistry at the Torino University since 2006. He has performed more than 100 experiments with synchrotron and neutron sources at ADONE, LURE DCI and SuperACO, ESRF, Elettra, SRS, SLS, APS, SOLEIL, ISIS, SOLEIL, ILL, SINQ, FRM-II, among them two Long Time projects at the ESRF. He has been member of the review committees of ESRF and SLS. His research activities are focused in the multitechnical characterization of nanostructured materials. He edited the book *Characterization of Semiconductor Heterostructures and Nanostructures*, Elsevier, 2008 (2nd edition appearing soon). He has authored and coauthored more than 250 research papers, 10 review articles, and 6 book chapters, which have received more than 9000 citations (h-index 54). He is the Italian coordinator of the European master in Materials Science MaMaSELF (http://etudes.univ-rennes1.fr/mamaself) with Torino, Rennes-1, Montoellier-2, LMU, and TUM universities

dx.doi.org/10.1021/cr2000898 | *Chem. Rev.* 2013, 113, 1736–1850

ACKNOWLEDGMENTS

We are particularly indebted to (i) E. Borfecchia, E. Gallo, D. Gianolio, and L. Mino for a critical lecture of fractions of the manuscript; (ii) A. Di Cicco, J. Evans, P. Fornasini, and S. Mobilio for giving us access to some of the oldest proceedings of the XAFS conference, so allowing us to complete the results reported in Table 1; (iii) to the beamline staff, where results here reviewed were collected ADONE (PULS), Daresbury (beamline 1.1, 3.4, 9.3), Elettra (Aloisa, Bear), ESRF (BM01B SNBL, BM08 GILDA, ID09B, BM16, ID22, BM23, ID24, ID26, BM26A DUBBLE, BM29, ID31, ID32), SLS (LUCIA, PHOENIX I, SuperXAS), LURE DCI (EXAFS 1, 3 and 13), LURE SuperACO (Sirloin, SA32), Soleil (Lucia), MAX-II (I811), and Diamond (B18). C.L. and J.A.v.B. thank the MaMaSELF consortium (http://etudes.univ-rennes1.fr/mamaself) for the financial support that has allowed us to finalize this joint work.

ACRONYM LIST

APS	advanced photon source
ATR	attenuated total reflectance
AXAFS	atomic XAFS
BEFS	beta environmental fine structure
BET	Brunauer, Emmett, and Teller (theory of adsorption)
BTC	benzene-1,3,5 tricarboxylate
CPU	central processing unit
CT	charge transfer
DAFS	diffraction anomalous fine structure
DFT	density functional theory
DMC	dimethylcarbonate
DOS	density of states
DRS	diffuse reflectance spectroscopy
EBSD	electron backscattering diffraction
EDC	1,2-dichloroethane
EPR	electron paramagnetic resonance
ESRF	European synchrotron radiation facility
EXAFS	extended X-ray absorption fine structure
EXELFS	extended energy-loss fine structure
FCC	fluid catalytic cracking
FDM	finite difference method
FP	full potential
FT	Fourier transform
FTIR	Fourier transform IR
HDPE	high density polyethylene
HERFD	high-energy resolution fluorescence detected
HF	Hartree−Fock
HL	higher level
IR	infrared
KKR	Korringa, Kohn, Rostoker calculations
LAPW	linear augmented plane waves
LCAO	linear combination of atomic orbitals
LCMO	linear combination of molecular orbitals
LMCT	ligand-to-metal charge transfer
LMTO	linear muffin tin orbitals
MLCT	metal to ligand charge transfer
MM	molecular mechanics
MO	molecular orbital
MOF	metal organic frameworks
MS	multiple scattering
MST	multiple scattering theory
MT	muffin tin
MW	molecular weight
NEXAFS	near edge X-ray absorption fine structure (XANES in the soft X-ray region)
NMR	nuclear magnetic resonance
PBC	periodic boundary conditions
PDF	pair distribution function
PEY	partial electron yield
PIXAFS	photon interference XAFS
PP	pseudopotential
PVC	poly-vinyl chloride
PW	plane wave
Q-EXAFS	quick-EXAFS
QM	quantum mechanics
RHF	restricted Hartree−Fock
ReflEXAFS	glancing-angle EXAFS
RIXS	resonant inelastic X-ray scattering
RT	room temperature
RXES	resonant XES
SAXS	small angle X-ray scattering
SCF	self-consistent field
SCR	selective catalytic reduction
SEM	scanning electron microscopy
SEXAFS	surface EXAFS
SS	single scattering
STEM	scanning transmission electron microscopy
TEM	transmission electron microscopy
TEY	total electron yield
TFY	total fluorescence yield
TPR	temperature programmed reduction
TR-EXAFS	time resolved-EXAFS
TS-1	Ti-silicalite-1
USY	ultrastable Y zeolite
UV−vis	ultraviolet−visible
VtC	valence to core
XAFS	X-ray absorption fine-structure
XANES	X-ray absorption near edge spectroscopy
XAS	X-ray absorption spectroscopy
XES	X-ray emission spectroscopy
XMCD	X-ray magnetic circular dichroism
XRD	X-ray diffraction
XRPD	X-ray powder diffraction

REFERENCES

(1) Margaritondo, G. *Introduction to Synchrotron Radiation*; Oxford: New York, 1988.
(2) Wille, K. *Rep. Prog. Phys.* **1991**, *54*, 1005.
(3) (a) Margaritondo, G. *J. Synchrotron Radiat.* **1995**, *2*, 148. (b) Bilderback, D. H.; Elleaume, P.; Weckert, E. *J. Phys. B: At., Mol., Opt. Phys* **2005**, *38*, S773.
(4) Bunker, G. *Introduction to XAFS: A Practical Guide to X-ray Absorption Fine Structure Spectroscopy*. Cambridge University Press: Cambridge, 2010.
(5) Lytle, F. W. *J. Synchrot. Radiat.* **1999**, *6*, 123.
(6) Couprie, M. E.; Filhol, J. M. *C. R. Phys.* **2008**, *9*, 487.
(7) Stern, E. A. *Phys. Rev. B* **1974**, *10*, 3027.
(8) Lee, P. A.; Pendry, J. B. *Phys. Rev. B* **1975**, *11*, 2795.
(9) Lee, P. A.; Citrin, P. H.; Eisenberger, P.; Kincaid, M. *Rev. Mod. Phys.* **1981**, *53*, 769.
(10) Teo, B. K.; Joy, D. C. *EXAFS Spectroscopy: Techniques and Applications*; Plenum: New York, 1981.
(11) Stern, E. A. Theory of EXAFS. In *X-Ray Absorption: Principles, Applications, Techniques of EXAFS, SEXAFS and XANES*; Koningsberger, D. C., Prins, R., Ed.; John Wiley & Sons: New York, 1988; Vol. 92, p 3.
(12) Rehr, J. J.; Ankudinov, A. L. *Coord. Chem. Rev.* **2005**, *249*, 131.

(13) Bart, J. C. J.; Vlaic, G. *Adv. Catal.* **1987**, *35*, 1.
(14) Diakun, G. P. *Nature* **1990**, *344*, 83.
(15) Sharpe, L. R.; Heineman, W. R.; Elder, R. C. *Chem. Rev.* **1990**, *90*, 705.
(16) Sinfelt, J. H.; Meitzner, G. D. *Acc. Chem. Res.* **1993**, *26*, 1.
(17) Crozier, E. D. *Nucl. Instrum. Methods Phys. Res. B* **1997**, *133*, 134.
(18) Linford, R. G. *Chem. Soc. Rev.* **1995**, *24*, 267.
(19) Abruna, H. D.; Bommarito, G. M.; Yee, H. S. *Acc. Chem. Res.* **1995**, *28*, 273.
(20) Tolbert, S. H.; Alivisatos, A. P. *Annu. Rev. Phys. Chem.* **1995**, *46*, 595.
(21) Mangat, P. S.; Soukiassian, P. *Surf. Rev. Lett.* **1998**, *5*, 1057.
(22) Clausen, B. S.; Topsoe, H.; Frahm, R. *Adv. Catal.* **1998**, *42*, 315.
(23) Alexeev, O.; Gates, B. C. *Top. Catal.* **2000**, *10*, 273.
(24) Filipponi, A. *J. Phys.: Condens. Matter* **2001**, *13*, R23.
(25) Bazin, D.; Guczi, L. *Appl. Catal., A* **2001**, *213*, 147.
(26) Parsons, J. G.; Aldrich, M. V.; Gardea-Torresdey, J. L. *Appl. Spectrosc. Rev.* **2002**, *37*, 187.
(27) Pellerito, L.; Nagy, L. *Coord. Chem. Rev.* **2002**, *224*, 111.
(28) Manceau, A.; Marcus, M. A.; Tamura, N. Quantitative Speciation of Heavy Metals in Soils and Sediments by Synchrotron X-ray Techniques. In *Applications of Synchrotron Radiation in Low-Temperature Geochemistry and Environmental Sciences*; Mineralogical Society of America: Chantilly, VA, 2002; Vol. *49*, p 341.
(29) Lamberti, C. *Surf. Sci. Rep.* **2004**, *53*, 1.
(30) Russell, A. E.; Rose, A. *Chem. Rev.* **2004**, *104*, 4613.
(31) Grunwaldt, J. D.; Baiker, A. *Phys. Chem. Chem. Phys.* **2005**, *7*, 3526.
(32) Hardacre, C. *Ann. Rev. Mater. Res.* **2005**, *35*, 29.
(33) Penner-Hahn, J. E. *Coord. Chem. Rev.* **2005**, *249*, 161.
(34) Strange, R. W.; Ellis, M.; Hasnain, S. S. *Coord. Chem. Rev.* **2005**, *249*, 197.
(35) Denecke, M. A. *Coord. Chem. Rev.* **2006**, *250*, 730.
(36) Couves, J. W.; Thomas, J. M.; Waller, D.; Jones, R. H.; Dent, A. J.; Derbyshire, G. E.; Greaves, G. N. *Nature* **1991**, *354*, 465.
(37) Vlaic, G.; Andreatta, D.; Colavita, P. E. *Catal. Today* **1998**, *41*, 261.
(38) Bare, S. R.; Ressler, T. *Adv. Catal.* **2009**, *52*, 339.
(39) Foster, A. J.; Lobo, R. F. *Chem. Soc. Rev.* **2010**, *39*, 4783.
(40) Bentrup, U. *Chem. Soc. Rev.* **2010**, *39*, 4718.
(41) Crozier, E. D.; Rehr, J. J.; Ingalls, R. Amorphous and Liquid Systems. In *X-Ray Absorption: Principles, Applications, Techniques of EXAFS, SEXAFS and XANES*; Koningsberger, D. C., Prins, R., Ed.; John Wiley & Sons: New York, 1988; Vol. *92*, p 373.
(42) Bianconi, A. XANES Spectroscopy. In *X-Ray Absorption: Principles, Applications, Techniques of EXAFS, SEXAFS and XANES*; Koningsberger, D. C., Prins, R., Ed.; John Wiley & Sons: New York, 1988; Vol. *92*, p 573.
(43) Bianconi, A.; Garcia, J.; Benfatto, M. *Top. Curr. Chem.* **1988**, *145*, 29.
(44) Cheetham, A. K.; Wilkinson, A. P. *Angew. Chem., Int. Ed. Engl* **1992**, *31*, 1557.
(45) Bertagnolli, H.; Ertel, T. S. *Angew. Chem., Int. Ed.* **1994**, *33*, 45.
(46) Riggsgelasco, P. J.; Stemmler, T. L.; Pennerhahn, J. E. *Coord. Chem. Rev.* **1995**, *144*, 245.
(47) Chen, J. G. *Surf. Sci. Rep.* **1997**, *30*, 5.
(48) Welter, E. Direct Speciation of Solids: X-ray Absorption Fine Structure Spectroscopy for Species Analysis in Solid Samples. In *Handbook of Elemental Speciation: Techniques and Methodology*; Cornelis, R., Caruso, J. A., Crews, H., Heumann, K. G., Ed.; John Wiley & Sons Ltd.: Chichester, U.K., 2003.
(49) Gates, W. P. X-ray Absorption Spectroscopy. In *Handbook of Clay Science*; Bergaya, F., Theng, B. K. G., Lagaly, G., Ed.; Elsevier: Amsterdam, 2006; Vol. *1*, p 789.
(50) Boscherini, F. X-ray Absorption Fine Structure in the Study of Semiconductor Heterostructures and Nanostructures. In *Characterization of Semiconductor Heterostructures and Nanostructures (II Edition)*; Lamberti, C.; Agostini, A., Eds.; Elsevier: Amsterdam, 2013, p 259.
(51) Cotte, M.; Susini, J.; Dik, J.; Janssens, K. *Acc. Chem. Res.* **2010**, *43*, 705.
(52) Sinfelt, J. H. *Acc. Chem. Res.* **1987**, *20*, 134.
(53) Prins, R.; Koningsberger, D. C. Catalysis. In *X-Ray Absorption: Principles, Applications, Techniques of EXAFS, SEXAFS and XANES*; Koningsberger, D. C., Prins, R., Ed.; John Wiley & Sons: New York, 1988; Vol. *92*, p 321.
(54) Kuroda, H.; Yokoyama, T.; Asakura, K.; Iwasawa, Y. *Faraday Discuss.* **1991**, *92*, 189.
(55) Via, G. H.; Sinfelt, J. H. Supported Bimetallic Cluster Catalysts. In *X-ray Absorption Fine Structure for Catalysts and Surfaces*; Iwasawa, Y., Ed.; World Scientific: Singapore, 1996; Vol. *2*, p 147.
(56) Englisch, M.; Lercher, J. A.; Haller, G. L. Applications of XANES to Catalyst Characterization: Supported Metal Particles. In *X-ray Absorption Fine Structure for Catalysts and Surfaces*; Iwasawa, Y., Ed.; World Scientific: Singapore, 1996; *Vol. 2*, p 276.
(57) Yoshida, S.; Tanaka, T. Applications of XANES to Catalyst Characterization: Metal Oxide Catalysts. In *X-ray Absorption Fine Structure for Catalysts and Surfaces*; Iwasawa, Y., Ed.; World Scientific: Singapore, 1996; Vol. *2*, p 304.
(58) Tanaka, T.; Yoshida, S. Applications of XANES to Catalyst Characterization: Others. In *X-ray Absorption Fine Structure for Catalysts and Surfaces*; Iwasawa, Y., Ed.; World Scientific: Singapore, 1996; Vol. *2*, p 326.
(59) Thomas, J. M.; Sankar, G. *Acc. Chem. Res.* **2001**, *34*, 571.
(60) Fernandez-Garcia, M. *Catal. Rev.* **2002**, *44*, 59−121.
(61) Newton, M. A.; Dent, A. J.; Evans, J. *Chem. Soc. Rev.* **2002**, *31*, 83.
(62) Rahman, M.; Bolton, P. R.; Evans, J.; Dent, A. J.; Harvey, I.; Diaz-Moreno, S. *Faraday Discuss.* **2003**, *122*, 211.
(63) Bordiga, S.; Damin, A.; Bonino, F.; Lamberti, C. Single Site Catalyst for Partial Oxidation Reaction: TS-1 Case Study. In *Surface and Interfacial Organometallic Chemistry and Catalysis*; Copéret, C., Chaudret, B., Ed.; Springer-Verlag GmbH: Heidelberg, Germany, 2005; Vol. *16*, p 37.
(64) Groppo, E.; Lamberti, C.; Bordiga, S.; Spoto, G.; Zecchina, A. *Chem. Rev.* **2005**, *105*, 115.
(65) Bordiga, S.; Bonino, F.; Lillerud, K. P.; Lamberti, C. *Chem. Soc. Rev.* **2010**, *39*, 4885.
(66) Beale, A. M.; Jacques, S. D. M.; Weckhuysen, B. M. *Chem. Soc. Rev.* **2010**, *39*, 4656.
(67) Grunwaldt, J. D.; Schroer, C. G. *Chem. Soc. Rev.* **2010**, *39*, 4741.
(68) Newton, M. A.; van Beek, W. *Chem. Soc. Rev.* **2010**, *39*, 4845.
(69) Frenkel, A. *Chem. Soc. Rev.* **2012**, DOI: 10.1039/c2cs35174a.
(70) Grunwaldt, J. D.; Baiker, A. *Catal. Lett.* **2005**, *99*, 5.
(71) Grunwaldt, J. D.; Kimmerle, B.; Baiker, A.; Boye, P.; Schroer, C. G.; Glatzel, P.; Borca, C. N.; Beckmann, F. *Catal. Today* **2009**, *145*, 267.
(72) Ramaker, D. E.; Koningsberger, D. C. *Phys. Chem. Chem. Phys.* **2010**, *12*, 5514.
(73) Ghigna, P.; Pin, S.; Spinolo, G.; Newton, M. A.; Zema, M.; Tarantino, S. C.; Capitani, G.; Tatti, F. *Phys. Chem. Chem. Phys.* **2010**, *12*, 5547.
(74) Kox, M. H. F.; Mijovilovich, A.; Sättler, J. J. H. B.; Stavitski, E.; Weckhuysen, B. M. *ChemCatChem* **2010**, *2*, 564.
(75) de Groot, F. M. F.; de Smit, E.; van Schooneveld, M. M.; Aramburo, L. R.; Weckhuysen, B. M. *ChemPhysChem* **2010**, *11*, 951.
(76) Evans, J. *Chem. Soc. Rev.* **1997**, *26*, 11.
(77) Lamberti, C.; Prestipino, C.; Bonino, F.; Capello, L.; Bordiga, S.; Spoto, G.; Zecchina, A.; Moreno, S. D.; Cremaschi, B.; Garilli, M.; Marsella, A.; Carmello, D.; Vidotto, S.; Leofanti, G. *Angew. Chem., Int. Ed.* **2002**, *41*, 2341.
(78) Suzuki, A.; Inada, Y.; Yamaguchi, A.; Chihara, T.; Yuasa, M.; Nomura, M.; Iwasawa, Y. *Angew. Chem., Int. Ed.* **2003**, *42*, 4795.
(79) Newton, M. A. *Chem. Soc. Rev.* **2008**, *37*, 2644.
(80) Corker, J.; Lefebvre, F.; Lecuyer, C.; Dufaud, V.; Quignard, F.; Choplin, A.; Evans, J.; Basset, J. M. *Science* **1996**, *271*, 966.

(81) Zhao, A.; Gates, B. C. *J. Am. Chem. Soc.* **1996**, *118*, 2458.
(82) Bianchini, C.; Burnaby, D. G.; Evans, J.; Frediani, P.; Meli, A.; Oberhauser, W.; Psaro, R.; Sordelli, L.; Vizza, F. *J. Am. Chem. Soc.* **1999**, *121*, 5961.
(83) Jezequel, M.; Dufaud, V.; Ruiz-Garcia, M. J.; Carrillo-Hermosilla, F.; Neugebauer, U.; Niccolai, G. P.; Lefebvre, F.; Bayard, F.; Corker, J.; Fiddy, S.; Evans, J.; Broyer, J. P.; Malinge, J.; Basset, J. M. *J. Am. Chem. Soc.* **2001**, *123*, 3520.
(84) Chabanas, M.; Baudouin, A.; Coperet, C.; Basset, J. M.; Lukens, W.; Lesage, A.; Hediger, S.; Emsley, L. *J. Am. Chem. Soc.* **2003**, *125*, 492.
(85) Guzman, J.; Gates, B. C. *Angew. Chem., Int. Ed.* **2003**, *42*, 690.
(86) Le Roux, E.; Chabanas, M.; Baudouin, A.; de Mallmann, A.; Coperet, C.; Quadrelli, E. A.; Thivolle-Cazat, J.; Basset, J. M.; Lukens, W.; Lesage, A.; Emsley, L.; Sunley, G. J. *J. Am. Chem. Soc.* **2004**, *126*, 13391.
(87) Barbaro, P.; Bianchini, C.; Dal Santo, V.; Meli, A.; Moneti, S.; Psaro, R.; Scaffidi, A.; Sordelli, L.; Vizza, F. *J. Am. Chem. Soc.* **2006**, *128*, 7065.
(88) Avenier, P.; Lesage, A.; Taoufik, M.; Baudouin, A.; De Mallmann, A.; Fiddy, S.; Vautier, M.; Veyre, L.; Basset, J. M.; Emsley, L.; Quadrelli, E. A. *J. Am. Chem. Soc.* **2007**, *129*, 176.
(89) Estephane, J.; Groppo, E.; Vitillo, J. G.; Damin, A.; Lamberti, C.; Bordiga, S.; Zecchina, A. *Phys. Chem. Chem. Phys.* **2009**, *11*, 2218.
(90) Estephane, J.; Groppo, E.; Damin, A.; Vitillo, J. G.; Gianolio, D.; Lamberti, C.; Bordiga, S.; Prestipino, C.; Nikitenko, S.; Quadrelli, E. A.; Taoufik, M.; Basset, J. M.; Zecchina, A. *J. Phys. Chem. C* **2009**, *113*, 7305.
(91) Estephane, J.; Groppo, E.; Vitillo, J. G.; Damin, A.; Gianolio, D.; Lamberti, C.; Bordiga, S.; Quadrelli, E. A.; Basset, J. M.; Kervern, G.; Emsley, L.; Pintacuda, G.; Zecchina, A. *J. Phys. Chem. C* **2010**, *114*, 4451.
(92) Tada, M.; Akatsuka, Y.; Yang, Y.; Sasaki, T.; Kinoshita, M.; Motokura, K.; Iwasawa, Y. *Angew. Chem., Int. Ed.* **2008**, *47*, 9252.
(93) Tada, M.; Muratsugu, S.; Kinoshita, M.; Sasaki, T.; Iwasawa, Y. *J. Am. Chem. Soc.* **2010**, *132*, 713.
(94) Prince, N. P.; Ashwin, M. J.; Woodruff, D. P.; Singh, N. K.; Walter, W.; Jones, R. G. *Faraday Discuss.* **1990**, *89*, 301.
(95) Rabalais, J. W. *Acc. Chem. Res.* **1994**, *27*, 26.
(96) Bowker, M.; Rowbotham, E.; Leibsle, F. M.; Haq, S. *Surf. Sci.* **1996**, *349*, 97.
(97) Nakahashi, T.; Terada, S.; Yokoyama, T.; Hamamatsu, H.; Kitajima, Y.; Sakano, M.; Matsui, F.; Ohta, T. *Surf. Sci.* **1997**, *373*, 1.
(98) Wilde, L.; Polcik, M.; Haase, J.; Brena, B.; Cocco, D.; Comelli, G.; Paolucci, G. *Surf. Sci.* **1998**, *405*, 215.
(99) Floriano, P. N.; Schlieben, O.; Doomes, E. E.; Klein, I.; Janssen, J.; Hormes, J.; Poliakoff, E. D.; McCarley, R. L. *Chem. Phys. Lett.* **2000**, *321*, 175.
(100) Jackson, G. J.; Driver, S. M.; Woodruff, D. P.; Abrams, N.; Jones, R. G.; Butterfield, M. T.; Crapper, M. D.; Cowie, B. C. C.; Formoso, V. *Surf. Sci.* **2000**, *459*, 231.
(101) Shimada, T.; Mun, B. S.; Nakai, I. F.; Banno, A.; Abe, H.; Iwasawa, Y.; Ohta, T.; Kondoh, H. *J. Phys. Chem. C* **2010**, *114*, 17030.
(102) Taramasso, M.; Perego, G.; Notari, B. U.S. Patent 4410501, 1983.
(103) Zecchina, A.; Bordiga, S.; Spoto, G.; Marchese, L.; Petrini, G.; Leofanti, G.; Padovan, M. *J. Phys. Chem.* **1992**, *96*, 4985.
(104) Ratnasamy, P.; Kumar, R. *Catal. Today* **1991**, *9*, 329.
(105) Berlier, G.; Spoto, G.; Fisicaro, P.; Bordiga, S.; Zecchina, A.; Giamello, E.; Lamberti, C. *Microchem. J.* **2002**, *71*, 101.
(106) Berlier, G.; Spoto, G.; Bordiga, S.; Ricchiardi, G.; Fisicaro, P.; Zecchina, A.; Rossetti, I.; Selli, E.; Forni, L.; Giamello, E.; Lamberti, C. *J. Catal.* **2002**, *208*, 64.
(107) Otero Areán, O.; Turnes Palomino, G.; Geobaldo, F.; Zecchina, A. *J. Phys. Chem.* **1996**, *100*, 6678.
(108) Lamberti, C.; Bordiga, S.; Salvalaggio, M.; Spoto, G.; Zecchina, A.; Geobaldo, F.; Vlaic, G.; Bellatreccia, M. *J. Phys. Chem. B* **1997**, *101*, 344.
(109) Lamberti, C.; Bordiga, S.; Zecchina, A.; Salvalaggio, M.; Geobaldo, F.; Otero Areán, C. *J. Chem. Soc. Faraday Trans.* **1998**, *94*, 1519.
(110) Spoto, G.; Bordiga, S.; Scarano, D.; Zecchina, A. *Catal. Lett.* **1992**, *13*, 39.
(111) Spoto, G.; Zecchina, A.; Bordiga, S.; Ricchiardi, G.; Martra, G.; Leofanti, G.; Petrini, G. *Appl. Catal., B* **1994**, *3*, 151.
(112) Spoto, G.; Bordiga, S.; Ricchiardi, G.; Scarano, D.; Zecchina, A.; Geobaldo, F. *J. Chem. Soc., Faraday Trans.* **1995**, *91*, 3285.
(113) McDaniel, M. P. *Adv. Catal.* **1985**, *33*, 47.
(114) Ghiotti, G.; Garrone, E.; Zecchina, A. *J. Mol. Catal.* **1988**, *46*, 61.
(115) Zecchina, A.; Spoto, G.; Ghiotti, G.; Garrone, E. *J. Mol. Catal.* **1994**, *86*, 423.
(116) Bordiga, S.; Bertarione, S.; Damin, A.; Prestipino, C.; Spoto, G.; Lamberti, C.; Zecchina, A. *J. Mol. Catal. A* **2003**, *204*, 527.
(117) Weckhuysen, B. M.; Schoonheydt, R. A.; Jehng, J. M.; Wachs, I. E.; Cho, S. J.; Ryoo, R.; Kijlstra, S.; Poels, E. *J. Chem. Soc., Faraday Trans.* **1995**, *91*, 3245.
(118) Gianolio, D.; Groppo, E.; Vitillo, J. G.; Damin, A.; Bordiga, S.; Zecchina, A.; Lamberti, C. *Chem. Commun.* **2010**, *46*, 976.
(119) Leofanti, G.; Padovan, M.; Garilli, M.; Carmello, D.; Zecchina, A.; Spoto, G.; Bordiga, S.; Palomino, G. T.; Lamberti, C. *J. Catal.* **2000**, *189*, 91.
(120) Koningsberger, D. C.; Oudenhuijzen, M. K.; de Graaf, J.; van Bokhoven, J. A.; Ramaker, D. E. *J. Catal.* **2003**, *216*, 178.
(121) Geus, J. W.; van Dillen, A. J. Preparation of Supported Catalysts by Deposition−Precipitation. In *Handbook of Heterogeneous Catalysis*; Ertl, G., Knözinger, H., Weitkamp, J., Ed.; Wiley-VCH: Weinheim, Germany, 1997; Vol. *1*, p 240.
(122) Pellegrini, R.; Leofanti, G.; Agostini, G.; Rivallain, M.; Groppo, E.; Lamberti, C. *Langmuir* **2009**, *25*, 6476.
(123) Willmott, P. *An Introduction to Synchrotron Radiation: Techniques and Applications*; John Wiley & Sons: Chichester, U.K., 2011.
(124) This holds for bending magnets and wiggler sources who exhibit a continuum energy emission following the classical synchrotron radiation spectrum (white light). Undulators emits a very intense spectrum characterized by a width of 50−500 eV centered on its fundamental energy and repeated for its harmonics (pink polychromatic light). When a long energy scan is performed at an undulator source the monochromator scan has to be coupled with the undulator gap scan in order to guarantee always the maximum emission from the machine at the desired energy.
(125) Batterman, B. W.; Cole, H. *Rev. Mod. Phys.* **1964**, *36*, 681.
(126) Lugovskaya, O. M.; Stepanov, S. A. *Kristallografiya* **1991**, *36*, 856.
(127) Underwood, J. H., *X-ray Data Booklet: Section 4.1. Multilayers and Crystals*; Center for X-ray Optics and Advanced Light Source: Berkeley, CA, 2009.
(128) Authier, A., *Dynamical Theory of X-Ray Diffraction*, International Union of Crystallography Monographs on Crystallography; Oxford University Press: Oxford, U.K., 2001; Vol. *11*.
(129) Aksenov, V. L.; Koval'chuk, M. V.; Kuz'min, A. Y.; Purans, Y.; Tyutyunnikov, S. I. *Crystallogr. Rep.* **2006**, *51*, 908.
(130) Hrdy, J. X-ray Optics for Synchrotron Radiation. In *Synchrotron Radiation: Fundamentals, Methodologies and Applications*; Mobilio, S., Vlaic, G., Ed.; Italian Physical Society (SIF): Bologna, Spain, 2003; Vol. *82*, p 677.
(131) Heald, S. M. Design of an EXAFS Experiment: EXAFS with Synchrotron Radiation. In *X-Ray Absorption: Principles, Applications, Techniques of EXAFS, SEXAFS, and XANES*; Koningsberger, D. C., Prins, R., Ed.; John Wiley & Sons: New York, 1988; Vol. *92*, p 87.
(132) Nomura, M. Measurements of XAFS: Instrumentation. In *X-ray Absorption Fine Structure for Catalysts and Surfaces*; Iwasawa, Y., Ed.; World Scientific: Singapore, 1996; Vol. *2*, p 93.
(133) Kim, K.-J. *X-ray Data Booklet: Section 2.1. Characteristics of Synchrotron Radiation*; Center for X-ray Optics and Advanced Light Source: Berkeley, CA, 2009.

(134) Koch, E.-E. *Handbook of Synchrotron Radiation, Vol. 1: Characteristics, Instrumentation and Principles of Research Applications*; North Holland: Amsterdam, 1983.
(135) Peatman, W. B., *Gratings, Mirrors and Slits: Beamline Design for Soft X-Ray Synchrotron Radiation Sources*; CRC Press: Amsterdam, 1997.
(136) Keil, P.; Lutzenkirchen-Hecht, D.; Novikov, D. V.; Hahn, U.; Frahm, R. *Nucl. Instrum. Methods Phys. Res. A* **2001**, *467*, 275.
(137) Parratt, L. G. *Phys. Rev.* **1954**, *95*, 359.
(138) James, R. W. *The Optical Principles of the Diffraction of X-rays*; Ox Bow Press: Woodbridge, CT, 1962.
(139) Born, M.; Wolf, E., *Principles of Optics: Electromagnetic Theory of Propagation, Interference and Diffraction of Light VII*; Cambridge University Press: Cambridge, U.K., 1999.
(140) D'Acapito, F.; Davoli, I.; Ghigna, P.; Mobilio, S. *J. Synchrotron. Radiat* **2003**, *10*, 260.
(141) The Snell law is usually reported as $n_1 \sin(\theta'_1) = n_2 \sin(\theta'_2)$ because referring to the angles θ'_1 and θ'_2 measured from the normal to the surface. Here, we refer to the incidence angle $\theta_{1,2} = 90 - \theta'_{1,2}$.In our case, the Snell law is consequently reported as $n_1 \cos(\theta_1) = n_2 \cos(\theta_2)$ because $\sin(\theta'_{1,2}) = \cos(\theta_{1,2})$.
(142) Agostini, G.; Groppo, E.; Piovano, A.; Pellegrini, R.; Leofanti, G.; Lamberti, C. *Langmuir* **2010**, *26*, 11204.
(143) Lamberti, C.; Bordiga, S.; Bonino, F.; Prestipino, C.; Berlier, G.; Capello, L.; D'Acapito, F.; Xamena, F. X. L. I.; Zecchina, A. *Phys. Chem. Chem. Phys.* **2003**, *5*, 4502.
(144) Booth, C. H.; Bridges, F. *Phys. Scr.* **2005**, *T115*, 202.
(145) Schroeder, S. L. M.; Moggridge, G. D.; Chabala, E.; Ormerod, R. M.; Rayment, T.; Lambert, R. M. *Faraday Discuss.* **1996**, *105*, 317.
(146) Schroeder, S. L. M. *Solid State Commun.* **1996**, *98*, 405.
(147) Frahm, R. *Nucl. Instrum. Methods Phys. Res., Sect. A* **1988**, *270*, 578.
(148) Frahm, R. *Rev. Sci. Instrum.* **1989**, *60*, 2515.
(149) Frahm, R. *Phys. B* **1989**, *158*, 342.
(150) Clausen, B. S.; Grabaek, L.; Steffensen, G.; Hansen, P. L.; Topsoe, H. *Catal. Lett.* **1993**, *20*, 23.
(151) Dobson, B. R.; Hasnain, S. S.; Neu, M.; Ramsdale, C. A.; Murphy, L. M. *Jpn. J. Appl. Phys. 1* **1993**, *32*, 192.
(152) Thomas, J. M.; Greaves, G. N. *Catal. Lett.* **1993**, *20*, 337.
(153) Sankar, G.; Wright, P. A.; Natarajan, S.; Thomas, J. M.; Greaves, G. N.; Dent, A. J.; Dobson, B. R.; Ramsdale, C. A.; Jones, R. H. *J. Phys. Chem.* **1993**, *97*, 9550.
(154) Frahm, R.; Richwin, M.; Lutzenkirchen-Hecht, D. *Phys. Scr.* **2005**, *T115*, 974.
(155) Murphy, L. M.; Dobson, B. R.; Neu, M.; Ramsdale, C. A.; Strange, R. W.; Hasnain, S. S. *J. Synchrotron Radiat.* **1995**, *2*, 64.
(156) Lee, J. M.; Sung, N. E.; Park, J. K.; Yoon, J. G.; Kim, J. H.; Choi, M. H.; Lee, K. B. *J. Synchrotron Radiat.* **1998**, *5*, 524.
(157) Bornebusch, H.; Clausen, B. S.; Steffensen, G.; Lutzenkirchen-Hecht, D.; Frahm, R. *J. Synchrotron Radiat.* **1999**, *6*, 209.
(158) Richwin, M.; Zaeper, R.; Lutzenkirchen-Hecht, D.; Frahm, R. *J. Synchrotron Radiat.* **2001**, *8*, 354.
(159) Dent, A. J. *Top. Catal.* **2002**, *18*, 27.
(160) Proux, O.; Biquard, X.; Lahera, E.; Menthonnex, J. J.; Prat, A.; Ulrich, O.; Soldo, Y.; Trevisson, P.; Kapoujyan, G.; Perroux, G.; Taunier, P.; Grand, D.; Jeantet, P.; Deleglise, M.; Roux, J. P.; Hazemann, J. L. *Phys. Scr.* **2005**, *T115*, 970.
(161) Grunwaldt, J. D.; Beier, M.; Kimmerle, B.; Baiker, A.; Nachtegaal, M.; Griesebock, B.; Lutzenkirchen-Hecht, D.; Stotzeld, J.; Frahm, R. *Phys. Chem. Chem. Phys.* **2009**, *11*, 8779.
(162) Grunwaldt, J.-D.; Frenkel, A. I. *Synchrotron Radiat. News* **2009**, *22*, 2.
(163) Khalid, S.; Caliebe, W.; Siddons, P.; So, I.; Clay, B.; Lenhard, T.; Hanson, J.; Wang, Q.; Frenkel, A. I.; Marinkovic, N.; Hould, N.; Ginder-Vogel, M.; Landrot, G. L.; Sparks, D. L.; Ganjoo, A. *Rev. Sci. Instrum.* **2010**, *81*, No. 015105.
(164) Prestipino, C.; Mathon, O.; Hino, R.; Beteva, A.; Pascarelli, S. *J. Synchrot. Radiat.* **2011**, *18*, 176.
(165) Singh, J.; Nachtegaal, M.; Alayon, E. M. C.; Stotzel, J.; van Bokhoven, J. A. *ChemCatChem* **2010**, *2*, 653.
(166) Ruffoni, M. P.; Pettifer, R. F. *J. Synchrotron Radiat.* **2006**, *13*, 489.
(167) Matsushita, T.; Phizackerley, R. P. *Jpn. J. Appl. Phys.* **1981**, *20*, 2223.
(168) Phizackerley, R. P.; Rek, Z. U.; Stephenson, G. B.; Conradson, S. D.; Hodgson, K. O.; Matsushita, T.; Oyanagi, H. *J. Appl. Crystallogr.* **1983**, *16*, 220.
(169) Oyanagi, H.; Matsushita, T.; Kaminaga, U.; Hashimoto, H. *J. Phys. Colloques* **1986**, *47*, C8−139.
(170) Hagelstein, M.; Cunis, S.; Frahm, R.; Niemann, W.; Rabe, P. *Phys. B* **1989**, *158*, 324.
(171) D'acapito, F.; Boscherini, F.; Marcelli, A.; Mobilio, S. *Rev. Sci. Instrum.* **1992**, *63*, 899.
(172) Dent, A. J.; Wells, M. P.; Farrow, R. C.; Ramsdale, C. A.; Derbyshire, G. E.; Greaves, G. N.; Couves, J. W.; Thomas, J. M. *Rev. Sci. Instrum.* **1992**, *63*, 903.
(173) Allen, P. G.; Conradson, S. D.; Pennerhahn, J. E. *J. Appl. Crystallogr.* **1993**, *26*, 172.
(174) Hagelstein, M.; Ferrero, C.; Hatje, U.; Ressler, T.; Metz, W. *J. Synchrotron Radiat.* **1995**, *2*, 174.
(175) Hatje, U.; Hagelstein, M.; Ressler, T.; Forster, H. *Phys. B* **1995**, *209*, 646.
(176) Salvini, G.; Bogg, D.; Dent, A. J.; Derbyshire, G. E.; Farrow, R. C.; Felton, A.; Ramsdale, C. *Phys. B* **1995**, *208*, 229.
(177) Salvini, G.; Dent, A. J.; Farrow, R. C.; Derbyshire, G. E.; Bogg, D. *J. Phys. IV* **1997**, *7*, 319.
(178) Hagelstein, M.; San Miguel, A.; Ressler, T.; Fontaine, A.; Goulon, J. *J. Phys. IV* **1997**, *7*, C2.
(179) Bogg, D.; Dent, A. J.; Derbyshire, G. E.; Farrow, R. C.; Ramsdale, C. A.; Salvini, G. *Nucl. Instrum. Methods Phys. Res., Sect. A* **1997**, *392*, 461.
(180) Pellicer-Porres, J.; San Miguel, A.; Fontaine, A. *J. Synchrotron Radiat.* **1998**, *5*, 1250.
(181) Allinson, N. M.; Baker, G.; Greaves, G. N.; Nicoll, J. K. *Nucl. Instrum. Methods Phys. Res., Sect. A* **1988**, *266*, 592.
(182) Pascarelli, S.; Neisius, T.; De Panfilis, S. *J. Synchrotron Radiat.* **1999**, *6*, 1044.
(183) Pascarelli, S.; Neisius, T.; De Panfilis, S.; Bonfim, M.; Pizzini, S.; Mackay, K.; David, S.; Fontaine, A.; San Miguel, A.; Itie, J. P.; Gauthier, M.; Polian, A. *J. Synchrotron Radiat.* **1999**, *6*, 146.
(184) Aksenov, V.; Gyngazov, L.; Ivanov, I.; Jeludeva, S.; Kovalchiuk, M.; Kovalenko, M.; Minashkin, V.; Scintee, N.; Shaliapin, V.; Skadorov, V.; Tiutiunnikov, S. *Nucl. Instrum. Methods Phys. Res., Sect. A* **2000**, *448*, 122.
(185) Pascarelli, S.; Mathon, O.; Munoz, M.; Mairs, T.; Susini, J. *J. Synchrotron Radiat.* **2006**, *13*, 351.
(186) Bhattacharyya, D.; Poswal, A. K.; Jha, S. N.; Sangeeta; Sabharwal, S. C. *Nucl. Instrum. Methods Phys. Res., Sect. A* **2009**, *609*, 286.
(187) Pascarelli, S.; Mathon, O. *Phys. Chem. Chem. Phys.* **2010**, *12*, 5535.
(188) Labiche, J. C.; Mathon, O.; Pascarelli, S.; Newton, M. A.; Ferre, G. G.; Curfs, C.; Vaughan, G.; Homs, A.; Carreiras, D. F. *Rev. Sci. Instrum.* **2007**, No. 091301.
(189) Newton, M. A. *J. Synchrotron Radiat.* **2007**, *14*, 372.
(190) Aquilanti, G.; Mathon, O.; Pascarelli, S. *J. Synchrotron Radiat.* **2009**, *16*, 699.
(191) Aquilanti, G.; Pascarelli, S.; Mathon, O.; Munoz, M.; Narygina, O.; Dubrovinsky, L. *J. Synchrotron Radiat.* **2009**, *16*, 376.
(192) Shirley, E. L. *Phys. Rev. Lett.* **1998**, *80*, 794.
(193) de Groot, F. *Chem. Rev.* **2001**, *101*, 1779.
(194) Kotani, A.; Shin, S. *Rev. Mod. Phys.* **2001**, *73*, 203.
(195) Schmitt, T.; Duda, L. C.; Augustsson, A.; Guo, J. H.; Nordgren, J.; Downes, J. E.; McGuinness, C.; Smith, K. E.; Dhalenne, G.; Revcolevshci, A.; Klemm, M.; Horn, S. *Surf. Rev. Lett.* **2002**, *9*, 1369.

(196) Glatzel, P.; Bergmann, U.; Yano, J.; Visser, H.; Robblee, J. H.; Gu, W. W.; de Groot, F. M. F.; Christou, G.; Pecoraro, V. L.; Cramer, S. P.; Yachandra, V. K. *J. Am. Chem. Soc.* **2004**, *126*, 9946.
(197) Ghiringhelli, G.; Brookes, N. B.; Annese, E.; Berger, H.; Dallera, C.; Grioni, M.; Perfetti, L.; Tagliaferri, A.; Braicovich, L. *Phys. Rev. Lett.* **2004**, *92*, No. 117406.
(198) Kotani, A. *Eur. Phys. J. B* **2005**, *47*, 3.
(199) Glatzel, P.; Bergmann, U. *Coord. Chem. Rev.* **2005**, *249*, 65.
(200) Augustsson, A.; Zhuang, G. V.; Butorin, S. M.; Osorio-Guillen, J. M.; Dong, C. L.; Ahuja, R.; Chang, C. L.; Ross, P. N.; Nordgren, J.; Guo, J. H. *J. Chem. Phys.* **2005**, *123*, No. 184717.
(201) Duda, L. C.; Schmitt, T.; Magnuson, M.; Forsberg, J.; Olsson, A.; Nordgren, J.; Okada, K.; Kotani, A. *Phys. Rev. Lett.* **2006**, *96*, No. 067402.
(202) Yang, W. L.; Sorini, A. P.; Chen, C. C.; Moritz, B.; Lee, W. S.; Vernay, F.; Olalde-Velasco, P.; Denlinger, J. D.; Delley, B.; Chu, J. H.; Analytis, J. G.; Fisher, I. R.; Ren, Z. A.; Yang, J.; Lu, W.; Zhao, Z. X.; van den Brink, J.; Hussain, Z.; Shen, Z. X.; Devereaux, T. P. *Phys. Rev. B* **2009**, *80*, No. 014508.
(203) Schlappa, J.; Schmitt, T.; Vernay, F.; Strocov, V. N.; Ilakovac, V.; Thielemann, B.; Ronnow, H. M.; Vanishri, S.; Piazzalunga, A.; Wang, X.; Braicovich, L.; Ghiringhelli, G.; Marin, C.; Mesot, J.; Delley, B.; Patthey, L. *Phys. Rev. Lett.* **2009**, *103*, No. 047401.
(204) Learmonth, T.; McGuinness, C.; Glans, P. A.; Downes, J. E.; Schmitt, T.; Duda, L. C.; Guo, J. H.; Chou, F. C.; Smith, K. E. *Europhys Lett.* **2007**, *79*, No. 47012 2007.
(205) Glatzel, P.; Sikora, M.; Fernandez-Garcia, M. *Eur. Phys. J. Spec. Top.* **2009**, *169*, 207.
(206) Bergmann, U.; Glatzel, P. *Photosynth. Res.* **2009**, *102*, 255.
(207) Glatzel, P.; Sikora, M.; Smolentsev, G.; Fernandez-Garcia, M. *Catal. Today* **2009**, *145*, 294.
(208) Braicovich, L.; van den Brink, J.; Bisogni, V.; Sala, M. M.; Ament, L. J. P.; Brookes, N. B.; De Luca, G. M.; Salluzzo, M.; Schmitt, T.; Strocov, V. N.; Ghiringhelli, G. *Phys. Rev. Lett.* **2010**, *104*, No. 077002.
(209) Kleymenov, E.; van Bokhoven, J. A.; David, C.; Glatzel, P.; Janousch, M.; Alonso-Mori, R.; Studer, M.; Willimann, M.; Bergamaschi, A.; Henrich, B.; Nachtegaal, M. *Rev. Sci. Instrum.* **2011**, *82*, No. 065107.
(210) Garino, C.; Gallo, E.; Smolentsev, N.; Glatzel, P.; Lamberti, C.; Gobetto, R.; Sadler, P. J.; Salassa, L. *Phys. Chem. Chem. Phys.* **2012**, *14*, 15278.
(211) Heijboer, W. M.; Glatzel, P.; Sawant, K. R.; Lobo, R. F.; Bergmann, U.; Barrea, R. A.; Koningsberger, D. C.; Weckhuysen, B. M.; de Groot, F. M. F. *J. Phys. Chem. B* **2004**, *108*, 10002.
(212) Heijboer, W. M. New frontiers in X-ray spectroscopy of FeZSM-5. PhD Thesis, Department of Inorganic Chemistry, Utrecht, the Netherlands, 2005.
(213) Pirngruber, G. D.; Grunwaldt, J. D.; van Bokhoven, J. A.; Kalytta, A.; Reller, A.; Safonova, O. V.; Glatzel, P. *J. Phys. Chem. B* **2006**, *110*, 18104.
(214) Pirngruber, G. D.; Grunwaldt, J. D.; Roy, P. K.; van Bokhoven, J. A.; Safonova, O.; Glatzel, P. *Catal. Today* **2007**, *126*, 127.
(215) Bauer, M.; Gastl, C. *Phys. Chem. Chem. Phys.* **2010**, *12*, 5575.
(216) Glatzel, P.; Singh, J.; Kvashnina, K. O.; van Bokhoven, J. A. *J. Am. Chem. Soc.* **2010**, *132*, 2555.
(217) Singh, J.; Lamberti, C.; van Bokhoven, J. A. *Chem. Soc. Rev.* **2010**, *39*, 4754.
(218) Ament, L. J. P.; van Veenendaal, M.; Devereaux, T. P.; Hill, J. P.; van den Brink, J. *Rev. Mod. Phys.* **2011**, *83*, 705.
(219) (a) Safonova, V. A.; Vykhodtseva, L. N.; Polukarov, Y. M.; Safonova, O. V.; Smolentsev, G.; Sikora, M.; Eeckhout, S. G.; Glatzel, P. *J. Phys. Chem. B* **2006**, *110*, 23192. (b) Smolentsev, G.; Soldatov, A. V.; Messinger, J.; Merz, K.; Weyhermuller, T.; Bergmann, U.; Pushkar, Y.; Yano, J.; Yachandra, V. K.; Glatzel, P. *J. Am. Chem. Soc.* **2009**, *131*, 13161.
(220) (a) Szlachetko, J.; Nachtegaal, M.; de Boni, E.; Willimann, M.; Safonova, O.; Sa, J.; Smolentsev, G.; Szlachetko, M.; van Bokhoven, J. A.; Dousse, J. C.; Hoszowska, J.; Kayser, Y.; Jagodzinski, P.; Bergamaschi, A.; Schmitt, B.; David, C.; Lucke, A. *Rev. Sci. Instrum.* **2012**, *83*, No. 103105. (b) Szlachetko, J.; Nachtegaal, M.; Sa, J.; Dousse, J. C.; Hoszowska, J.; Kleymenov, E.; Janousch, M.; Safonova, O. V.; Konig, C.; van Bokhoven, J. A. *Chem. Commun.* **2012**, *48*, 10898.
(221) Swarbrick, J. C.; Kvashnin, Y.; Schulte, K.; Seenivasan, K.; Lamberti, C.; Glatzel, P. *Inorg. Chem.* **2010**, *49*, 8323.
(222) de Groot, F. M. F.; Krisch, M. H.; Vogel, J. *Phys. Rev. B* **2002**, *66*, No. 195112.
(223) Hämäläinen, K.; Siddons, D. P.; Hastings, J. B.; Berman, L. E. *Phys. Rev. Lett.* **1991**, *67*, 2850.
(224) van Bokhoven, J. A.; C., L.; Miller, J. T.; Tromp, M.; Safonova, O. V.; Glatzel, P. *Angew. Chem., Int. Ed.* **2006**, *45*, 4651.
(225) de Groot, F. *Coord. Chem. Rev.* **2005**, *249*, 31.
(226) Yano, J.; Pushkar, Y.; Glatzel, P.; Lewis, A.; Sauer, K.; Messinger, J.; Bergmann, U.; Yachandra, V. *J. Am. Chem. Soc.* **2005**, *127*, 14974.
(227) Pushkar, Y.; Yano, J.; Glatzel, P.; Messinger, J.; Lewis, A.; Sauer, K.; Bergmann, U.; Yachandra, V. *J. Biol. Chem.* **2007**, *282*, 7198.
(228) Yano, J.; Kern, J.; Pushkar, Y.; Sauer, K.; Glatzel, P.; Bergmann, U.; Messinger, J.; Zouni, A.; Yachandra, V. K. *Philos. Trans. R. Soc., B* **2008**, *363*, 1139.
(229) de Groot, F. M. F. *Top. Catal.* **2000**, *10*, 179.
(230) Glatzel, P.; Jacquamet, L.; Bergmann, U.; de Groot, F. M. F.; Cramer, S. P. *Inorg. Chem.* **2002**, *41*, 3121.
(231) Hanawalt, J. D. *Phys. Rev.* **1931**, *37*, 715.
(232) Lytle, F. W.; Wei, P. S. P.; Greegor, R. B.; Via, G. H.; Sinfelt, J. H. *J. Chem. Phys.* **1979**, *70*, 4849.
(233) Bazin, D.; Dexpert, H.; Lynch, J. Measurements of XAFS: In Situ XAFS Measurement of Catalysts. In *X-ray Absorption Fine Structure for Catalysts and Surfaces*; Iwasawa, Y., Ed.; World Scientific: Singapore, 1996; Vol. 2, p 113.
(234) Kampers, F. W. H.; Maas, T. M. J.; van Grondelle, J.; Brinkgreve, P.; Koningsberger, D. C. *Rev. Sci. Instrum.* **1989**, *60*, 2635.
(235) Clausen, B. S.; Steffensen, G.; Fabius, B.; Villadsen, J.; Feidenhansl, R.; Topsoe, H. *J. Catal.* **1991**, *132*, 524.
(236) Meitzner, G.; Bare, S. R.; Parker, D.; Woo, H.; Fischer, D. A. *Rev. Sci. Instrum.* **1998**, *69*, 2618.
(237) Dent, A. J.; Greaves, G. N.; Roberts, M. A.; Sankar, G.; Wright, P. A.; Jones, R. H.; Sheehy, M.; Madill, D.; Catlow, C. R. A.; Thomas, J. M.; Rayment, T. *Nucl. Instrum. Methods Phys. Res., Sect. B* **1995**, *97*, 20.
(238) Lamberti, C.; Prestipino, C.; Bordiga, S.; Berlier, G.; Spoto, G.; Zecchina, A.; Laloni, A.; La Manna, F.; D'Anca, F.; Felici, R.; D'Acapito, F.; Roy, P. *Nucl. Instrum. Methods Phys. Res., Sect. B* **2003**, *200*, 196.
(239) Longo, A.; Balerna, A.; d'Acapito, F.; D'Anca, F.; Giannici, F.; Liotta, L. F.; Pantaleo, G.; Martorana, A. *J. Synchrotron Radiat* **2005**, *12*, 499.
(240) Revel, R.; Bazin, D.; Seigneurin, A.; Barthe, P.; Dubuisson, J. M.; Decamps, T.; Sonneville, H.; Poher, J. J.; Maire, F.; Lefrancois, P. *Nucl. Instrum. Methods Phys. Res., Sect. B* **1999**, *155*, 183.
(241) Odzak, J. F.; Argo, A. M.; Lai, F. S.; Gates, B. C.; Pandya, K.; Feraria, L. *Rev. Sci. Instrum.* **2001**, *72*, 3943.
(242) Weckhuysen, B. M. *Chem. Commun.* **2002**, 97.
(243) Beale, A. M.; van der Eerden, A. M. J.; Kervinen, K.; Newton, M. A.; Weckhuysen, B. M. *Chem. Commun.* **2005**, 3015.
(244) Weiher, N.; Bus, E.; Gorzolnik, B.; Moller, M.; Prins, R.; van Bokhoven, J. A. *J. Synchrotron Radiat.* **2005**, *12*, 675.
(245) Girardon, J. S.; Khodakov, A. Y.; Capron, M.; Cristol, S.; Dujardin, C.; Dhainaut, F.; Nikitenko, S.; Meneau, F.; Bras, W.; Payen, E. *J. Synchrotron Radiat* **2005**, *12*, 680.
(246) Bare, S. R.; Mickelson, G. E.; Modica, F. S.; Ringwelski, A. Z.; Yang, N. *Rev. Sci. Instrum.* **2006**, *77*, No. 023105.
(247) Tinnemans, S. J.; Mesu, J. G.; Kervinen, K.; Visser, T.; Nijhuis, T. A.; Beale, A. M.; Keller, D. E.; van der Eerden, A. M. J.; Weckhuysen, B. M. *Catal. Today* **2006**, *113*, 3.
(248) Hannemann, S.; Casapu, M.; Grunwaldt, J. D.; Haider, P.; Trussel, P.; Baiker, A.; Welter, E. *J. Synchrotron Radiat.* **2007**, *14*, 345.

(249) Bare, S. R.; Yang, N.; Kelly, S. D.; Mickelson, G. E.; Modica, F. S. *Catal. Today* **2007**, *126*, 18.
(250) Meunier, F. C. *Chem. Soc. Rev.* **2010**, *39*, 4602.
(251) Newton, M. A.; Di Michiel, M.; Kubacka, A.; Fernandez-Garcia, M. *J. Am. Chem. Soc.* **2010**, *132*, 4540.
(252) Muddada, N. B.; Olsbye, U.; Caccialupi, L.; Cavani, F.; Leofanti, G.; Gianolio, D.; Bordiga, S.; Lamberti, C. *Phys. Chem. Chem. Phys.* **2010**, *12*, 5605.
(253) Paredis, K.; Ono, L. K.; Behafarid, F.; Zhang, Z. F.; Yang, J. C.; Frenkel, A. I.; Cuenya, B. R. *J. Am. Chem. Soc.* **2011**, *133*, 13455.
(254) Paredis, K.; Ono, L. K.; Mostafa, S.; Li, L.; Zhang, Z. F.; Yang, J. C.; Barrio, L.; Frenkel, A. I.; Cuenya, B. R. *J. Am. Chem. Soc.* **2011**, *133*, 6728.
(255) Payen, E.; Barthe, L.; Berrier, E.; Blanchard, J.; Briois, V.; Carrier, X.; Che, M.; Cristol, S.; Griboval-Constant, A.; Hong, J. P.; Joly, Y.; Khodakov, A.; La Fontaine, C.; Marceau, E.; Massiani, P.; Tougerti, A. *Actual. Chim.* **2011**, 20.
(256) Weckhuysen, B. M. *Phys. Chem. Chem. Phys.* **2003**, *5*, 4351.
(257) Topsoe, H. *J. Catal.* **2003**, *216*, 155.
(258) Banares, M. A. *Catal. Today* **2005**, *100*, 71.
(259) Weckhuysen, B. M. *Chem. Soc. Rev.* **2010**, *39*, 4557.
(260) Arean, C. O.; Weckhuysen, B. M.; Zecchina, A. *Phys. Chem. Chem. Phys.* **2012**, *14*, 2125.
(261) Grunwaldt, J. D.; Caravati, M.; Hannemann, S.; Baiker, A. *Phys. Chem. Chem. Phys.* **2004**, *6*, 3037.
(262) Huwe, H.; Froba, M. *J. Synchrotron Radiat.* **2004**, *11*, 363.
(263) van der Eerden, A. M. J.; van Bokhoven, J. A.; Smith, A. D.; Koningsberger, D. C. *Rev. Sci. Instrum.* **2000**, *71*, 3260.
(264) Bruckner, A. *Catal. Rev.: Sci. Eng.* **2003**, *45*, 97.
(265) Iglesias-Juez, A.; Beale, A. M.; O'Brien, M. G.; Newton, M. A.; Bras, W.; Weckhuysen, B. M. *Synchrotron Radiat. News* **2009**, *22*, 22.
(266) Bras, W.; Andrew M. Beale, A. M. *Spectrosc. Prop. Inorg. Organomet. Compd.* **2012**, *43*, 257.
(267) Newton, M. A.; Dent, A. J.; Fiddy, S. G.; Jyoti, B.; Evans, J. *Catal. Today* **2007**, *126*, 64.
(268) Marcelli, A.; Hampai, D.; Xu, W.; Malfatti, L.; Innocenzi, P. *Acta Phys. Pol., A* **2009**, *115*, 489.
(269) Marinkovic, N. S.; Wang, Q.; Barrio, L.; Ehrlich, S. N.; Khalid, S.; Cooper, C.; Frenkel, A. I. *Nucl. Instrum. Methods Phys. Res., Sect. AA* **2011**, *649*, 204.
(270) Marinkovic, N. S.; Wang, Q.; Frenkel, A. I. *J. Synchrotron Radiat.* **2011**, *18*, 447.
(271) Becker, E.; Carlsson, P. A.; Kylhammar, L.; Newton, M. A.; Skoglundh, M. *J. Phys. Chem. C* **2011**, *115*, 944.
(272) Makosch, M.; Kartusch, C.; Sa, J.; Duarte, R. B.; van Bokhoven, J. A.; Kvashnina, K.; Glatzel, P.; Fernandes, D. L. A.; Nachtegaal, M.; Kleymenov, E.; Szlachetko, J.; Neuhold, B.; Hungerbuhler, K. *Phys. Chem. Chem. Phys.* **2012**, *14*, 2164.
(273) Briois, V.; Vantelon, D.; Villain, F.; Couzinet, B.; Flank, A. M.; Lagarde, P. *J. Synchrotron Radiat.* **2007**, *14*, 403.
(274) Vantelon, D.; Lagarde, P.; Flank, A. M.; Berrier, E.; Secordel, X.; Cristol, S.; La Fontaine, C.; Villain, F.; Briois, V. *Phase Transitions* **2009**, *82*, 322.
(275) Clausen, B. S.; Topsoe, H. Combined EXAFS/XRD Methods. In *X-ray Absorption Fine Structure for Catalysts and Surfaces*; Iwasawa, Y., Ed.; World Scientific: Singapore, 1996; Vol. 2, p 345.
(276) Shannon, I. J.; Maschmeyer, T.; Sankar, G.; Thomas, J. M.; Oldroyd, R. D.; Sheehy, M.; Madill, D.; Waller, A. M.; Townsend, R. P. *Catal. Lett.* **1997**, *44*, 23.
(277) Sankar, G.; Thomas, J. M. *Top. Catal.* **1999**, *8*, 1.
(278) Grunwaldt, J. D.; Clausen, B. S. *Top. Catal.* **2002**, *18*, 37.
(279) Aquilanti, G.; Crichton, W. A.; Pascarelli, S. *High Pressure Res.* **2003**, *23*, 301.
(280) Frenkel, A. I.; Wang, Q.; Marinkovic, N.; Chen, J. G.; Barrio, L.; Si, R.; Camara, A. L.; Estrella, A. M.; Rodriguez, J. A.; Hanson, J. C. *J. Phys. Chem. C* **2011**, *115*, 17884.
(281) Nikitenko, S.; Beale, A. M.; van der Eerden, A. M. J.; Jacques, S. D. M.; Leynaud, O.; O'Brien, M. G.; Detollenaere, D.; Kaptein, R.; Weckhuysen, B. M.; Bras, W. *J. Synchrot. Radiat.* **2008**, *15*, 632.
(282) Groppo, E.; Agostini, G.; Piovano, A.; Muddada, N. B.; Leofanti, G.; Pellegrini, R.; Portale, G.; Longo, A.; Lamberti, C. *J. Catal.* **2012**, *287*, 44.
(283) O'Brien, M. G.; Beale, A. M.; Jacques, S. D. M.; Weckhuysen, B. M. *Top. Catal.* **2009**, *52*, 1400.
(284) O'Brien, M. G.; Beale, A. M.; Jacques, S. D. M.; Di Michiel, M.; Weckhuysen, B. M. *ChemCatChem* **2009**, *1*, 99.
(285) Guilera, G.; Gorges, B.; Pascarelli, S.; Vitoux, H.; Newton, M. A.; Prestipino, C.; Nagai, Y.; Hara, N. *J. Synchrotron Radiat.* **2009**, *16*, 628.
(286) Kawai, T.; Chun, W. J.; Asakura, K.; Koike, Y.; Nomura, M.; Bando, K. K.; Oyama, S. T.; Sumiya, H. *Rev. Sci. Instrum.* **2008**, *79*, No. 014101.
(287) Bando, K. K.; Saito, T.; Sato, K.; Tanaka, T.; Dumeignil, F.; Imamura, M.; Matsubayashi, N.; Shimada, H. *J. Synchrotron Radiat.* **2001**, *8*, 581.
(288) Jentoft, R. E.; Deutsch, S. E.; Gates, B. C. *Rev. Sci. Instrum.* **1996**, *67*, 2111.
(289) Pettiti, I.; Gazzoli, D.; Inversi, M.; Valigi, M.; De Rossi, S.; Ferraris, G.; Porta, P.; Colonna, S. *J. Synchrotron Radiat* **1999**, *6*, 1120.
(290) Kispersky, V. F.; Kropf, A. J.; Ribeiro, F. H.; Miller, J. T. *Phys. Chem. Chem. Phys.* **2012**, *14*, 2229.
(291) van Bokhoven, J. A.; van der Eerden, A. M. J.; Smith, A. D.; Koningsberger, D. C. *J. Synchrotron Radiat.* **1999**, *6*, 201.
(292) Havecker, M.; Knop-Gericke, A.; Schedel-Niedrig, T. *Appl. Surf. Sci.* **1999**, *142*, 438.
(293) Knop-Gericke, A.; Havecker, M.; Schedel-Niedrig, T.; Schlogl, R. *Top. Catal.* **2001**, *15*, 27.
(294) Mayer, R. W.; Havecker, M.; Knop-Gericke, A.; Schlogl, R. *Catal. Lett.* **2001**, *74*, 115.
(295) Mayer, R. W.; Melzer, M.; Havecker, M.; Knop-Gericke, A.; Urban, J.; Freund, H. J.; Schlogl, R. *Catal. Lett.* **2003**, *86*, 245.
(296) Morales, F.; de Groot, F. M. F.; Glatzel, P.; Kleimenov, E.; Bluhm, H.; Havecker, M.; Knop-Gericke, A.; Weckhuysen, B. M. *J. Phys. Chem. B* **2004**, *108*, 16201.
(297) Borgna, A.; Anderson, B. G.; Saib, A. M.; Bluhm, H.; Havecker, M.; Knop-Gericke, A.; Kuiper, A. E. T.; Tamminga, Y.; Niemantsverdriet, J. W. *J. Phys. Chem. B* **2004**, *108*, 17905.
(298) Drake, I. J.; Liu, T. C. N.; Gilles, M.; Tyliszczak, T.; Kilcoyne, A. L. D.; Shuh, D. K.; Mathies, R. A.; Bell, A. T. *Rev. Sci. Instrum.* **2004**, *75*, 3242.
(299) van Bokhoven, J. A.; Sambe, H.; Ramaker, D. E.; Koningsberger, D. C. *J. Synchrotron Radiat.* **1999**, *6*, 207.
(300) van Bokhoven, J. A.; Sambe, H.; Ramaker, D. E.; Koningsberger, D. C. *J. Phys. Chem. B* **1999**, *103*, 7557.
(301) van Bokhoven, J. A.; Koningsberger, D. C.; Ramaker, D. E. *J. Phys.: Condens. Matter* **2001**, *13*, 10383.
(302) van Bokhoven, J. A.; Koningsberger, D. C.; Kunkeler, P.; van Bekkum, H. *J. Catal.* **2002**, *211*, 540.
(303) van Bokhoven, J. A.; van der Eerden, A. M. J.; Koningsberger, D. C. *Stud. Surf. Sci. Catal.* **2002**, *142*, 1885.
(304) van Bokhoven, J. A.; van der Eerden, A. M. J.; Koningsberger, D. C. *J. Am. Chem. Soc.* **2003**, *125*, 7435.
(305) Abraham, A.; Lee, S. H.; Shin, C. H.; Hong, S. B.; Prins, R.; van Bokhoven, J. A. *Phys. Chem. Chem. Phys.* **2004**, *6*, 3031.
(306) Bugaev, L. A.; van Bokhoven, J. A.; Sokolenko, A. P.; Latokha, Y. V.; Avakyan, L. A. *J. Phys. Chem. B* **2005**, *109*, 10771.
(307) Joyner, R. W.; Smith, A. D.; Stockenhuber, M.; van den Berg, M. W. E. *Phys. Chem. Chem. Phys.* **2004**, *6*, 5435.
(308) Agostini, G.; Lamberti, C.; Palin, L.; Milanesio, M.; Danilina, N.; Xu, B.; Janousch, M.; van Bokhoven, J. A. *J. Am. Chem. Soc.* **2010**, *132*, 667.
(309) Heijboer, W. M.; Battiston, A. A.; Knop-Gericke, A.; Havecker, M.; Mayer, R.; Bluhm, H.; Schlogl, R.; Weckhuysen, B. M.; Koningsberger, D. C.; de Groot, F. M. F. *J. Phys. Chem. B* **2003**, *107*, 13069.
(310) Heijboer, W. M.; Battiston, A. A.; Knop-Gericke, A.; Havecker, M.; Bluhm, H.; Weckhuysen, B. M.; Koningsberger, D. C.; de Groot, F. M. F. *Phys. Chem. Chem. Phys.* **2003**, *5*, 4484.

(311) Gruner, S. M. *AIP Conf. Proc.* **2010**, *1234*, 69.
(312) Martinez-Criado, G.; Borfecchia, E.; Mino, L.; Lamberti, C. Micro and Nano X-ray Beams, In *Characterization of Semiconductor Heterostructures and Nanostructures II*; Lamberti, C., Agostini, G., Ed.; Elsevier: Amsterdam, 2013, p. 413.
(313) Vila-Comamala, J.; Gorelick, S.; Farm, E.; Kewish, C. M.; Diaz, A.; Barrett, R.; Guzenko, V. A.; Ritala, M.; David, C. *Opt. Express* **2011**, *19*, 175.
(314) Lengeler, B.; Schroer, C.; Tummler, J.; Benner, B.; Richwin, M.; Snigirev, A.; Snigireva, I.; Drakopoulos, M. *J. Synchrotron Radiat.* **1999**, *6*, 1153.
(315) Schroer, C. G.; Kuhlmann, M.; Hunger, U. T.; Gunzler, T. F.; Kurapova, O.; Feste, S.; Frehse, F.; Lengeler, B.; Drakopoulos, M.; Somogyi, A.; Simionovici, A. S.; Snigirev, A.; Snigireva, I.; Schug, C.; Schroder, W. H. *Appl. Phys. Lett.* **2003**, *82*, 1485.
(316) Evans-Lutterodt, K.; Stein, A.; Ablett, J. M.; Bozovic, N.; Taylor, A.; Tennant, D. M. *Phys. Rev. Lett.* **2007**, *99*, No. 134801.
(317) Yamauchi, K.; Mimura, H.; Kimura, T.; Yumoto, H.; Handa, S.; Matsuyama, S.; Arima, K.; Sano, Y.; Yamamura, K.; Inagaki, K.; Nakamori, H.; Kim, J.; Tamasaku, K.; Nishino, Y.; Yabashi, M.; Ishikawa, T. *J. Phys.: Condens. Matter* **2011**, *23*, No. 394206.
(318) Bilderback, D. H. *X-Ray Spectrom.* **2003**, *32*, 195.
(319) Truccato, M.; Lamberti, C.; Prestipino, C.; Agostino, A. *Appl. Phys. Lett.* **2005**, *86*, No. 213116.
(320) Cagliero, S.; Piovano, A.; Lamberti, C.; Khan, M. M. R.; Agostino, A.; Agostini, G.; Gianolio, D.; Mino, L.; Sans, J. A.; Manfredotti, C.; Truccato, M. *J. Synchrotron. Radiat.* **2009**, *16*, 813.
(321) Mino, L.; Gianolio, D.; Agostini, G.; Piovano, A.; Truccato, M.; Agostino, A.; Cagliero, S.; Martinez-Criado, G.; Codato, S.; Lamberti, C. *Adv. Mater.* **2010**, *22*, 2050.
(322) Mino, L.; Agostino, A.; Codato, S.; Lamberti, C. *J. Anal. At. Spectrom.* **2010**, *25*, 831.
(323) Mino, L.; Gianolio, D.; Agostini, G.; Piovano, A.; Truccato, M.; Agostino, A.; Cagliero, S.; Martinez-Criado, G.; d'Acapito, F.; Codato, S.; Lamberti, C. *Small* **2011**, *7*, 930.
(324) Mino, L.; Agostino, A.; Codato, S.; Martinez-Criado, G.; Lamberti, C. *Nucl. Instrum. Methods Phys. Res., Sect. B* **2012**, *284*, 6.
(325) Boehler, R. *Rev. Geophys.* **2000**, *38*, 221.
(326) Hemley, R. J.; Mao, H. K. *Int. Geol. Rev.* **2001**, *43*, 1.
(327) Errandonea, D.; Manjon, F. J. *Prog. Mater. Sci.* **2008**, *53*, 711.
(328) Wenk, H. R.; Chen, K.; Smith, R. *Am. Mineral.* **2011**, *96*, 1316.
(329) Roque-Rosell, J.; Mosselmans, J. F. W.; Proenza, J. A.; Labrador, M.; Gali, S.; Atkinson, K. D.; Quinn, P. D. *Chem. Geol.* **2010**, *275*, 9.
(330) Borfecchia, E.; Mino, L.; Gianolio, D.; Groppo, C.; Malaspina, N.; Martinez-Criado, G.; Sans, J. A.; Poli, S.; Castelli, D.; Lamberti, C. *J. Anal. At. Spectrom.* **2012**, *27*, 1725.
(331) Gazzano, M.; Focarete, M. L.; Riekel, C.; Scandola, M. *Biomacromolecules* **2004**, *5*, 553.
(332) Evans, G.; Axford, D.; Waterman, D.; Owen, R. L. *Crystallogr. Rev.* **2011**, *17*, 105.
(333) Shibata, T.; Nagano, T. *Nat. Med.* **1996**, *2*, 933.
(334) de Smit, E.; Swart, I.; Creemer, J. F.; Hoveling, G. H.; Gilles, M. K.; Tyliszczak, T.; Kooyman, P. J.; Zandbergen, H. W.; Morin, C.; Weckhuysen, B. M.; de Groot, F. M. F. *Nature* **2008**, *456*, 222.
(335) de Smit, E.; Swart, I.; Creemer, J. F.; Karunakaran, C.; Bertwistle, D.; Zandbergen, H. W.; de Groot, F. M. F.; Weckhuysen, B. M. *Angew. Chem., Int. Ed.* **2009**, *48*, 3632.
(336) Schroer, C. G.; Kuhlmann, M.; Gunzler, T. F.; Lengeler, B.; Richwin, M.; Griesebock, B.; Lutzenkirchen-Hecht, D.; Frahm, R.; Ziegler, E.; Mashayekhi, A.; Haeffner, D. R.; Grunwaldt, J. D.; Baiker, A. *Appl. Phys. Lett.* **2003**, *82*, 3360.
(337) Rau, C.; Somogyi, A.; Simionovici, A. *Nucl. Instrum. Methods Phys. Res., Sect. B* **2003**, *200*, 444.
(338) Grunwaldt, J. D.; Hannemann, S.; Schroer, C. G.; Baiker, A. *J. Phys. Chem. B* **2006**, *110*, 8674.
(339) Schroer, C. G.; Meyer, J.; Kuhlmann, M.; Benner, B.; Gunzler, T. F.; Lengeler, B.; Rau, C.; Weitkamp, T.; Snigirev, A.; Snigireva, I. *Appl. Phys. Lett.* **2002**, *81*, 1527.
(340) Chu, Y. S.; Yi, J. M.; De Carlo, F.; Shen, Q.; Lee, W. K.; Wu, H. J.; Wang, C. L.; Wang, J. Y.; Liu, C. J.; Wang, C. H.; Wu, S. R.; Chien, C. C.; Hwu, Y.; Tkachuk, A.; Yun, W.; Feser, M.; Liang, K. S.; Yang, C. S.; Je, J. H.; Margaritondo, G. *Appl. Phys. Lett.* **2008**, *92*, No. 103119.
(341) Stenström, W. *Ann. Phys.* **1918**, *362*, 347.
(342) Siegbahn, M. *Ann. Phys.* **1919**, *364*, 56.
(343) Siegbahn, M. *Phil. Mag.* **1919**, *37*, 601.
(344) Siegbahn, M. *Spektroskopie der Röntgenstrahlen*; Springer: Berlin, 1931.
(345) Fricke, H. *Phys. Rev.* **1920**, *16*, 202.
(346) Hertz, G. *Z. Phys.* **1920**, *3*, 19.
(347) Lindh, A. E. *Z. Phys.* **1921**, *6*, 303.
(348) Coster, D. *Z. Phys.* **1924**, *25*, 83.
(349) Chamberlain, K. *Phys. Rev.* **1925**, *26*, 525.
(350) Lindh, A., E. *Z. Phys.* **1925**, *31*, 210.
(351) Ray, B. B. *Z. Phys.* **1929**, *55*, 119.
(352) Yost, D. M. *Subtitle* **1929**, *8*, 845.
(353) Lindh, A. E. *Z. Phys.* **1930**, *63*, 106.
(354) Kievit, B.; Lindsay, G. A. *Phys. Rev.* **1930**, *36*, 648.
(355) Hanawalt, J. D. *Z. Phys.* **1931**, *70*, 293.
(356) O'Leary, A. J. *Phys. Rev.* **1931**, *37*, 873.
(357) Coster, D.; Veldkamp, J. *Z. Phys.* **1931**, *70*, 306.
(358) Coster, D.; Veldkamp, J. *Z. Phys.* **1932**, *74*, 191.
(359) Hirsh, F. R., Jr.; Richtmyer, F. K. *Phys. Rev.* **1933**, *44*, 955.
(360) Rao, A. S. R. a. K. R. *Proc. Phys. Soc.* **1934**, *46*, 163.
(361) Kronig, R. d. L. *Z. Phys.* **1931**, *70*, 317.
(362) Kronig, R. d. L. *Z. Phys.* **1932**, *75*, 191.
(363) The Kronig long-range order theory can be summarized in the following equation: $Wn = h^2(\alpha^2 + \beta^2 + \gamma^2)/[8ma^2 \cos^2(\theta)]$, where Wn is the energy positions corresponding to the zone boundaries (i.e., not the absorption maxima or minima, but the first rise in each fine-structure maximum), h is the Plank constant, m is the electron mass, α, β, and γ are the Miller indices, a is the lattice parameter, and θ is the angle between the electron direction and the reciprocal lattice direction. The Kronig long-range order equation was simple to apply and interpret. In any experimental spectrum, it showed an approximate agreement with the theory. There were always some absorption features close to that predicted by the possible lattice planes. However, the expected stronger reflections of the lattice did not always correlate with the most intense absorption features of the EXAFS spectra as intuitively expected. Still, agreement was close enough to be tantalizing and everyone tested the agreement of their measured Kronig structures with the simple Kronig theory.
(364) Kronig, R. d. L. *Z. Phys.* **1932**, *75*, 468.
(365) Petersen, H. *Z. Phys.* **1932**, *76*, 768.
(366) Petersen, H. *Z. Phys.* **1933**, *80*, 258.
(367) Hartree, D. R.; de L. Kronig, R.; Petersen, H. *Physica* **1934**, *1*, 895.
(368) Petersen, H. *Z. Phys.* **1936**, *98*, 569.
(369) Snyder, T. M.; Shaw, C. H. *Phys. Rev.* **1940**, *57*, 881.
(370) Kostarev, A. I. *Zh. Éksp. Teor. Fiz.* **1941**, *60*, 11.
(371) Shaw, C. H. *Phys. Rev.* **1946**, *70*, 643.
(372) Kostarev, A. I. *Zh. Éksp. Teor. Fiz.* **1949**, *413*, 19.
(373) Cauchois, Y.; Mott, N. F. *Philos. Mag.* **1949**, *40*, 1260.
(374) Amar Nath, N. *Proc. Phys. Soc. B* **1955**, *68*, 472.
(375) Sawada, M.; Tsutsumi, K.; Shiraiwa, T.; Obashi, M. *J. Phys. Soc. Jpn.* **1955**, *10*, 464.
(376) Sawada, M.; Tsutsumi, K.; Hayase, A. *J. Phys. Soc. Jpn.* **1957**, *12*, 628.
(377) Tsutsumi, K.; Hayase, A.; Sawada, M. *J. Phys. Soc. Jpn.* **1957**, *12*, 793.
(378) Shiraiwa, T.; Ishimura, T.; Sawada, M. *J. Phys. Soc. Jpn.* **1957**, *12*, 788.
(379) Shiraiwa, T.; Ishimura, T.; Sawada, M. *J. Phys. Soc. Jpn.* **1958**, *13*, 847.
(380) Shiraiwa, T. *J. Phys. Soc. Jpn.* **1960**, *15*, 240.
(381) Shmidt, V. V. *Izv. Akad. Nauk. SSSR, Ser. Fiz.* **1961**, *25*, 977.
(382) Nelson, W. F.; Siegel, I.; Wagner, R. W. *Phys. Rev.* **1962**, *127*, 2025.

(383) Shmidt, V. V. *Izv. Akad. Nauk. SSSR, Ser. Fiz.* **1963**, *27*, 384.
(384) Azaroff, L. V. *Rev. Mod. Phys.* **1963**, *35*, 1012.
(385) Lytle, F. W. X-ray Absorption Fine-Structure Investigations at Cryogenic Temperatures. In *Developments in Applied Spectroscopy*; Ferraro, J. R., Ziomek, J. S., Ed.; Plenum: New York, 1963; Vol. *2*, p 285.
(386) Lindsay, G. A. *Z. Phys* **1931**, *71*, 735.
(387) Azaroff, L. V.; Pease, D. M. In *X-ray Spectroscopy*; Azaroff, L. M., Ed.; McGraw-Hill: New York, 1974; Chapter 6.
(388) Lytle, F.; Sayers, D.; Stern, E. In *Advances in X-ray Spectroscopy*; Bonnelle, C., Mande, C., Ed.; Pergamon Press: Oxford, U.K., 1982; p 267.
(389) von Bordwehr, R. S. *Ann. Phys. (Paris, Fr.)* **1989**, *14*, 377.
(390) Rehr, J. J.; Albers, R. C. *Rev. Mod. Phys.* **2000**, *72*, 621.
(391) Stern, E. A. *J. Synchrotron Radiat.* **2001**, *8*, 49.
(392) Van Nordsthand, R. A. *Adv. Catal.* **1960**, *12*, 149.
(393) Van Nordstrand, R. In *Handbook of X-rays*; Kaelble, E., Ed.; McGraw-Hill: London, 1967; p 43.
(394) Lytle, F. *Adv. X-ray Anal.* **1966**, *9*, 398.
(395) Sayers, D. E.; Stern, E. A.; Lytle, F. W. *Phys. Rev. Lett.* **1971**, *27*, 1204.
(396) Stern, E. A.; Sayers, D. E.; Lytle, F. W. *Phys. Rev. B* **1975**, *11*, 4836.
(397) Lytle, F. W.; Sayers, D. E.; Stern, E. A. *Phys. Rev. B* **1975**, *11*, 4825.
(398) Rehr, J. J.; Stern, E. A.; Martin, R. L.; Davidson, E. R. *Phys. Rev. B* **1978**, *17*, 560.
(399) Sandstrom, D. R.; Lytle, F. W. *Annu. Rev. Phys. Chem.* **1979**, *30*, 215.
(400) Schaich, W. L. *Phys. Rev. B* **1973**, *8*, 4028.
(401) Ashley, C. A.; Doniach, S. *Phys. Rev. B* **1975**, *11*, 1279.
(402) Beni, G.; Platzman, P. M. *Phys. Rev. B* **1976**, *14*, 1514.
(403) Sevillano, E.; Meuth, H.; Rehr, J. J. *Phys. Rev. B* **1979**, *20*, 4908.
(404) Hallonsten, O., *Small Science on Big Machines: Politics and Practices of Synchrotron Radiation Laboratories*; Research Policy Institute: Lund, Sweden, 2009.
(405) Teo, B.-K.; Lee, P. A. *J. Am. Chem. Soc.* **1979**, *101*, 2815.
(406) McKale, A. G.; Knapp, G. S.; Chan, S. K. *Phys. Rev. B* **1986**, *33*, 841.
(407) de Leon, J. M.; Rehr, J. J.; Zabinsky, S. I.; Albers, R. C. *Phys. Rev. B* **1991**, *44*, 4146.
(408) Vaarkamp, M.; Dring, I.; Oldman, R. J.; Stern, E. A.; Koningsberger, D. C. *Phys. Rev. B* **1994**, *50*, 7872.
(409) Fornasini, P. Introduction to X-ray Absorption Spectroscopy. In *Synchrotron Radiation: Fundamentals, Methodologies and Applications*; Mobilio, S., Vlaic, G., Ed.; Italian Physical Society (SIF): Bologna, Italy, 2003; Vol. *82*, p 129.
(410) Yokoyama, T. Theory and Parameters of EXAFS. In *X-ray Absorption Fine Structure for Catalysts and Surfaces*; Iwasawa, Y., Ed.; World Scientific: Singapore, 1996; Vol. *2*, p 9.
(411) McKale, A. G.; Veal, B. W.; Paulikas, A. P.; Chan, S. K.; Knapp, G. S. *J. Am. Chem. Soc.* **1988**, *110*, 3763.
(412) Frenkel, A. I.; Rehr, J. J. *Phys. Rev. B* **1993**, *48*, 585.
(413) Asakura, K. Analysis of EXAFS. In *X-ray Absorption Fine Structure for Catalysts and Surfaces*; Iwasawa, Y., Ed.; World Scientific: Singapore, 1996; Vol. *2*, p 33.
(414) For a compilation of electron inelastic mean free path lengths (λ) in solids for energies in the range 0−10 000 eV above the Fermi level, see, for example, Seah, M. P.; Dench, W. A. *Surf. Interface Anal.* **1979**, *1*, 2.
(415) Note that in 1993 the number of independent parameters that can be refined in an EXAFS data analysis and given in eq 21 was criticized, [Stern, E. A. *Phys. Rev. B* **1993**, *48*, 9825] and the alternative equation ($n_{ind} = 2\Delta k\Delta R/\pi + 2$) was given. This authoritative contribution has generated a long debate in the successive EXAFS conferences (see Table 1). The criteria adopted by the IXS Standards and Criteria Committee in July 26, 2000 (downloadable at http://ixs.iit.edu/subcommittee_reports/sc/err-rep.pdf,, accessed February 25, 2013) still recommend the original, more conservative, eq 21.
(416) Sayers, D. E.; Bunker, B. A. Data Analysis. In *X-Ray Absorption: Principles, Applications, Techniques of EXAFS, SEXAFS and XANES*; Koningsberger, D. C., Prins, R., Ed.; John Wiley & Sons: New York, 1988; Vol. *92*, p 211.
(417) Lamberti, C.; Palomino, G. T.; Bordiga, S.; Berlier, G.; D'Acapito, F.; Zecchina, A. *Angew. Chem., Int. Ed.* **2000**, *39*, 2138.
(418) Prestipino, C.; Capello, L.; D'Acapito, F.; Lamberti, C. *Phys. Chem. Chem. Phys.* **2005**, *7*, 1743.
(419) Gleeson, D.; Sankar, G.; Catlow, C. R. A.; Thomas, J. M.; Spanó, G.; Bordiga, S.; Zecchina, A.; Lamberti, C. *Phys. Chem. Chem. Phys.* **2000**, *2*, 4812.
(420) Natoli, C. R.; Benfatto, M.; Doniach, S. *Phys. Rev. A* **1986**, *34*, 4682.
(421) Fonda, L. *J. Phys.: Condens. Matter* **1992**, *4*, 8269.
(422) Zabinsky, S. I.; Rehr, J. J.; Ankudinov, A.; Albers, R. C.; Eller, M. J. *Phys. Rev. B* **1995**, *52*, 2995.
(423) Mustre, J.; Yacoby, Y.; Stern, E. A.; Rehr, J. J. *Phys. Rev. B* **1990**, *42*, 10843.
(424) Rehr, J. J.; Albers, R. C.; Zabinsky, S. I. *Phys. Rev. Lett.* **1992**, *69*, 3397.
(425) Filipponi, A.; Di Cicco, A.; Tyson, T. A.; Natoli, C. R. *Solid State Commun.* **1991**, *78*, 265.
(426) Filipponi, A.; Di Cicco, A.; Natoli, C. R. *Phys. Rev. B* **1995**, *52*, 15122.
(427) Benfatto, M. Multiple Scattering Approach to X-ray Absorption Spectroscopy. In *Synchrotron Radiation: Fundamentals, Methodologies and Applications*; Mobilio, S., Vlaic, G., Ed.; Italian Physical Society (SIF): Bologna, Italy, 2003; Vol. *82*, p 171.
(428) Michalowicz, A. *J. Phys. IV* **1997**, *7*, 235.
(429) Klementev, K. V. *Nucl. Instrum. Methods Phys. Res., Sect. A* **2000**, *448*, 299.
(430) Klementev, K. V. *J. Phys. D: Appl. Phys.* **2001**, *34*, 209.
(431) Aberdam, D. *J. Synchrotron Radiat.* **1998**, *5*, 1287.
(432) Delrio, M. S.; Chaboy, J.; Djerbi, R. *Comput. Chem.* **1995**, *19*, 59.
(433) Aldea, N.; Kolipaka, K. L.; Rednic, V.; Matei, F. *J. Optoelectron. Adv. Mater.* **2011**, *13*, 1581.
(434) Filipponi, A.; Di Cicco, A. *Phys. Rev. B* **1995**, *52*, 15135.
(435) Westre, T. E.; Dicicco, A.; Filipponi, A.; Natoli, C. R.; Hedman, B.; Solomon, E. I.; Hodgson, K. O. *J. Am. Chem. Soc.* **1995**, *117*, 1566.
(436) Zhang, H. H.; Filipponi, A.; DiCicco, A.; Lee, S. C.; Scott, M. J.; Holm, R. H.; Hedman, B.; Hodgson, K. O. *Inorg. Chem.* **1996**, *35*, 4819.
(437) Gurman, S. J.; Binsted, N.; Ross, I. *J. Phys. C: Solid State Phys.* **1984**, *17*, 143.
(438) Gurman, S. J.; Binsted, N.; Ross, I. *J. Phys. C: Solid State Phys.* **1986**, *19*, 1845.
(439) Binsted, N.; Cook, S. L.; Evans, J.; Greaves, G. N.; Price, R. J. *J. Am. Chem. Soc.* **1987**, *109*, 3669.
(440) Binsted, N.; Hasnain, S. S. *J. Synchrotron Radiat.* **1996**, *3*, 185.
(441) Rehr, J. J.; Deleon, J. M.; Zabinsky, S. I.; Albers, R. C. *J. Am. Chem. Soc.* **1991**, *113*, 5135.
(442) Ankudinov, A. L.; Ravel, B.; Rehr, J. J.; Conradson, S. D. *Phys. Rev. B* **1998**, *58*, 7565.
(443) Rehr, J. J.; Ankudinov, A.; Zabinsky, S. I. *Catal. Today* **1998**, *39*, 263.
(444) Cross, J. O.; Newville, M.; Rehr, J. J.; Sorensen, L. B.; Bouldin, C. E.; Watson, G.; Gouder, T.; Lander, G. H.; Bell, M. I. *Phys. Rev. B* **1998**, *58*, 11215.
(445) Rehr, J. J.; Ankudinov, A. L. *J. Synchrotron Radiat* **2001**, *8*, 61.
(446) Rehr, J. J.; Ankudinov, A. L. *J. Synchrotron Radiat* **2003**, *10*, 43.
(447) Rehr, J. J.; Kas, J. J.; Prange, M. P.; Sorini, A. P.; Takimoto, Y.; Vila, F. *C. R. Phys.* **2009**, *10*, 548.
(448) Newville, M.; Ravel, B.; Haskel, D.; Rehr, J. J.; Stern, E. A.; Yacoby, Y. *Phys. B* **1995**, *208*, 154.

(449) Stern, E. A.; Newville, M.; Ravel, B.; Yacoby, Y.; Haskel, D. *Phys. B* **1995**, *208/209*, 117.
(450) Kelly, S. D.; Stern, E. A.; Ingalls, R. *J. Synchrotron Radiat.* **2001**, *8*, 311.
(451) Vaarkamp, M.; Linders, J. C.; Koningsberger, D. C. *Phys. B* **1995**, *208−209*, 159.
(452) Ellis, P. J.; Freeman, H. C. *J. Synchrotron Radiat.* **1995**, *2*, 190.
(453) Kuzmin, A. *Phys. B* **1995**, *208*, 175.
(454) Kuzmin, A. *J. Phys. IV* **1997**, *7* (C2), 213.
(455) Webb, S. M. *Phys. Scr.* **2005**, *T115*, 1011.
(456) http://www-ssrl.slac.stanford.edu/exafspak.html (accessed February 6, 2013).
(457) (a) Ressler, T. *J. Phys. IV* **1997**, *7*, 269. (b) Ressler, T. *J. Synchrotron Radiat.* **1998**, *5*, 118.
(458) http://xlase.free.fr/ (accessed February 6, 2013).
(459) Michalowicz, A.; Moscovici, J.; Muller-Bouvet, D.; Provost, K. *J. Phys.: Conf. Series* **2009**, *190*, No. 012034.
(460) Meneghini, C.; Bardelli, F.; Mobilio, S. *Nucl. Instrum. Methods Phys. Res., Sect. B* **2012**, *285*, 153.
(461) Newville, M. *J. Synchrotron Radiat.* **2001**, *8*, 322.
(462) Newville, M. *J. Synchrotron Radiat.* **2001**, *8*, 96.
(463) Ravel, B.; Newville, M. *J. Synchrotron Radiat.* **2005**, *12*, 537.
(464) Albers, R. C. *Phys. B* **1989**, *158*, 372.
(465) Ito, Y.; Mukoyama, T.; Emura, S.; Takahashi, M.; Yoshikado, S.; Omote, K. *Phys. Rev. A* **1995**, *51*, 303.
(466) Parratt, L. G. *Rev. Mod. Phys.* **1959**, *31*, 616.
(467) Norman, D. *J. Phys. C* **1986**, *19*, 3273.
(468) Durham, P. J. Theory of XANES. In *X-Ray Absorption: Principles, Applications, Techniques of EXAFS, SEXAFS and XANES*; Koningsberger, D. C., Prins, R., Ed.; John Wiley & Sons: New York, 1988; Vol. *92*, p 53.
(469) Rehr, J. J. *Jpn. J. Appl. Phys. 1* **1993**, *32*, 8.
(470) Kosugi, N. Theory and Analysis of XANES: MO Approach. In *X-ray Absorption Fine Structure for Catalysts and Surfaces*; Iwasawa, Y., Ed.; World Scientific: Singapore, 1996; Vol. *2*, p 60.
(471) Joly, Y.; Cabaret, D.; Renevier, H.; Natoli, C. R. *Phys. Rev. Lett.* **1999**, *82*, 2398.
(472) Natoli, C. R.; Benfatto, M.; Della Longa, S.; Hatada, K. *J. Synchrotron Radiat.* **2003**, *10*, 26.
(473) Ankudinov, A. L.; Rehr, J. J. *J. Synchrotron Radiat.* **2003**, *10*, 366.
(474) Yamamoto, T. *X-Ray Spectrom.* **2008**, *37*, 572.
(475) Bart, J. C. J. *Adv. Catal.* **1986**, *34*, 203.
(476) Zeira, F. In Situ NEXAFS Characterization of Surface Intermediates. In *X-ray Absorption Fine Structure for Catalysts and Surfaces*; Iwasawa, Y., Ed.; World Scientific: Singapore, 1996; Vol. *2*, p 362.
(477) Joly, Y. Interaction of Polarized Light with Matter. In *Magnetism and Synchrotron Radiation: New Trends*; Beaurepaire, E., Bulou, H., Scheurer, F., Jean-Paul, K., Ed.; Springer: Berlin, 2010; p 77.
(478) Bianconi, A.; Garcia, J.; Benfatto, M.; Marcelli, A.; Natoli, C. R.; Ruizlopez, M. F. *Phys. Rev. B* **1991**, *43*, 6885.
(479) Tyson, T. A.; Hodgson, K. O.; Natoli, C. R.; Benfatto, M. *Phys. Rev. B* **1992**, *46*, 5997.
(480) Rehr, J. J.; Ankudinov, A. L. *J. Electron Spectrosc. Relat. Phenom.* **2001**, *114*, 1115.
(481) Ankudinov, A. L.; Bouldin, C. E.; Rehr, J. J.; Sims, J.; Hung, H. *Phys. Rev. B* **2002**, *65*, No. 104107.
(482) Joly, Y. *Phys. Rev. B* **2001**, *63*, No. 125120.
(483) Joly, Y. *J. Synchrotron Radiat.* **2003**, *10*, 58.
(484) Schwarz, K.; Blaha, P.; Madsen, G. K. H. *Comput. Phys. Commun.* **2002**, *147*, 71.
(485) Schwarz, K.; Blaha, P.; Trickey, S. B. *Mol. Phys.* **2010**, *108*, 3147.
(486) Taillefumier, M.; Cabaret, D.; Flank, A. M.; Mauri, F. *Phys. Rev. B* **2002**, *66*, No. 195107.
(487) Cabaret, D.; Gaudry, E.; Taillefumier, M.; Sainctavit, P.; Mauri, F. *Phys. Scr.* **2005**, *T115*, 131.
(488) Genovese, L.; Videau, B.; Ospici, M.; Deutsch, T.; Goedecker, S.; Mehaut, J. F. *C. R. Mec.* **2011**, *339*, 149.
(489) Gonze, X.; Amadon, B.; Anglade, P. M.; Beuken, J. M.; Bottin, F.; Boulanger, P.; Bruneval, F.; Caliste, D.; Caracas, R.; Cote, M.; Deutsch, T.; Genovese, L.; Ghosez, P.; Giantomassi, M.; Goedecker, S.; Hamann, D. R.; Hermet, P.; Jollet, F.; Jomard, G.; Leroux, S.; Mancini, M.; Mazevet, S.; Oliveira, M. J. T.; Onida, G.; Pouillon, Y.; Rangel, T.; Rignanese, G. M.; Sangalli, D.; Shaltaf, R.; Torrent, M.; Verstraete, M. J.; Zerah, G.; Zwanziger, J. W. *Comput. Phys. Commun.* **2009**, *180*, 2582.
(490) Ebert, H. In *Electronic Structure and Physical Properties of Solids: The Users of the LMTO Method*; Dreyssé, H., Ed.; Springer: Berlin, 2000; Vol. *535*, p 191.
(491) Antonov, V. N.; Harmon, B. N.; Yaresko, A. N. *Phys. Rev. B* **2002**, *66*, No. 165208.
(492) Yaresko, A. N.; Antonov, V. N.; Harmon, B. N. *Phys. Rev. B* **2003**, *68*, No. 214426.
(493) Yaresko, A. N.; Perlov, A.; Antonov, V.; Harmon, B. Band-Structure Theory of Dichroism. In *Magnetism: A Synchrotron Radiation Approach*; Beaurepaire, E., Bulou, H., Scheurer, F., Kappler, J. P., Ed.; Springer: Berlin, 2006; Vol. *697*, p 121.
(494) Bugaev, L. A.; Gegusin, I. I.; Datsyuk, V. N.; Novakovich, A. A.; Vedrinskii, R. V. *Phys. Status Solidi B* **1986**, *133*, 195.
(495) Datsyuk, V. N.; Gegusin, I. I.; Vedrinskii, R. V. *Phys. Status Solidi B* **1986**, *134*, 175.
(496) Gegusin, I. I.; Datsyuk, V. N.; Novakovich, A. A.; Bugaev, L. A.; Vedrinskii, R. V. *Phys. Status Solidi B* **1986**, *134*, 641.
(497) *StoBe-deMon*, version 3.1 (http://www.fhi-berlin.mpg.de/KHsoftware/StoBe/index.html). For a XANES application, see Hay, M. B.; Myneni, S. C. B. *J. Phys. Chem. A* **2010**, *114*, 6138. For a XES application, see Mori, R. A.; Paris, E.; Giuli, G.; Eeckhout, S. G.; Kavcic, M.; Zitnik, M.; Bucar, K.; Pettersson, L. G. M.; Glatzel, P. *Inorg. Chem.* **2010**, *49*, 6468.
(498) *The deMon2k Users' Guide*, version 3.0; Cinvestav, Mexico-City, 2011; http://www.deMon-software.com.
(499) te Velde, G.; Bickelhaupt, F. M.; Baerends, E. J.; Guerra, C. F.; Van Gisbergen, S. J. A.; Snijders, J. G.; Ziegler, T. *J. Comput. Chem.* **2001**, *22*, 931.
(500) Neese, F. *ORCA, an Ab Initio DFT and Semiempirical Electronic Structure Package*, version 2.7; University of Bonn: Bonn, Germany. 2009.
(501) Stavitski, E.; de Groot, F. M. F. *Micron* **2010**, *41*, 687.
(502) Gianolio, D. Combination of Advanced X-ray Techniques in Understanding the Structure and the Electronic Configuration of Transition Metal Complexes: Experiments vs Calculations. PhD Thesis, Department of Inorganic, Physical and Materials Chemistry, Turin, Italy, 2012.
(503) Benfatto, M.; Della Longa, S. *J. Synchrotron Radiat.* **2001**, *8*, 1087.
(504) Della Longa, S.; Arcovito, A.; Girasole, M.; Hazemann, J. L.; Benfatto, M. *Phys. Rev. Lett.* **2001**, *87*, No. 155501.
(505) Benfatto, M.; Della Longa, S.; Natoli, C. R. *J. Synchrotron Radiat.* **2003**, *10*, 51.
(506) Hayakawa, K.; Hatada, K.; D'Angelo, P.; Della Longa, S.; Natoli, C. R.; Benfatto, M. *J. Am. Chem. Soc.* **2004**, *126*, 15618.
(507) Smolentsev, G.; Soldatov, A. *J. Synchrotron Radiat.* **2006**, *13*, 19.
(508) Smolentsev, G.; Soldatov, A. V. *Comput. Mater. Sci.* **2007**, *39*, 569.
(509) Ahlers, D.; Schutz, G.; Popescu, V.; Ebert, H. *J. Appl. Phys.* **1998**, *83*, 7082.
(510) Huhne, T.; Ebert, H. *Solid State Commun.* **1999**, *109*, 577.
(511) Pfrommer, B. G.; Cote, M.; Louie, S. G.; Cohen, M. L. *J. Comput. Phys.* **1997**, *131*, 233.
(512) Bordiga, S.; Coluccia, S.; Lamberti, C.; Marchese, L.; Zecchina, A.; Boscherini, F.; Buffa, F.; Genoni, F.; Leofanti, G.; Petrini, G.; Vlaic, G. *J. Phys. Chem.* **1994**, *98*, 4125.

(513) Bordiga, S.; Boscherini, F.; Coluccia, S.; Genoni, F.; Lamberti, C.; Leofanti, G.; Marchese, L.; Petrini, G.; Vlaic, G.; Zecchina, A. *Catal. Lett.* **1994**, *26*, 195.
(514) Bordiga, S.; Geobaldo, F.; Lamberti, C.; Zecchina, A.; Boscherini, F.; Genoni, F.; Leofanti, G.; Petrini, G.; Padovan, M.; Geremia, S.; Vlaic, G. *Nucl. Instrum. Methods Phys. Res., Sect. B* **1995**, *97*, 23.
(515) Bordiga, S.; Coluccia, S.; Lamberti, C.; Marchese, L.; Zecchina, A.; Boscherini, F.; Buffa, F.; Genoni, F.; Leofanti, G.; Petrini, G.; Vlaic, G. *J. Phys. Chem.* **1995**, *99*, 16500.
(516) Davis, R. J.; Liu, Z.; Tabora, J. E.; Wieland, W. S. *Catal. Lett.* **1995**, *34*, 101.
(517) Rehr, J. J.; Kas, J. J.; Vila, F. D.; Prange, M. P.; Jorissen, K. *Phys. Chem. Chem. Phys.* **2010**, *12*, 5503.
(518) Hayashi, H. *X-Ray Spectrom.* **2011**, *40*, 24.
(519) Cowan, R. D. *The Theory of Atomic Structure and Spectra*; University of California Press: Berkeley, CA, 1981.
(520) So, I.; Siddons, D. P.; Caliebe, W. A.; Khalid, S. *Nucl. Instrum. Methods Phys. Res., Sect. A* **2007**, *582*, 190.
(521) San Miguel, A. *Physica B* **1995**, *208*, 177.
(522) Prestipino, C.; Figueroa, S. PrestoPronto (Soon Ready), 2010. PrestoPronto on Google Project Hosting. http://code.google.com/p/prestopronto/ (accessed February 6, 2013).
(523) Fernandez-Garcia, M.; Marquez Alvarez, C.; Haller, G. L. *J. Phys. Chem.* **1995**, *99*, 12565.
(524) Wasserman, S. R. *J. Phys. IV* **1997**, *7*, 203.
(525) Beauchemin, S.; Hesterberg, D.; Beauchemin, M. *Soil Sci. Soc. Am. J.* **2002**, *66*, 83.
(526) Bazin, D.; Rehr, J. J. *J. Phys. Chem. B* **2003**, *107*, 12398.
(527) Haider, P.; Grunwaldt, J. D.; Seidel, R.; Baiker, A. *J. Catal.* **2007**, *250*, 313.
(528) Wang, Q.; Hanson, J. C.; Frenkel, A. I. *J. Chem. Phys.* **2008**, *129*, No. 234502.
(529) Piovano, A.; Agostini, G.; Frenkel, A. I.; Bertier, T.; Prestipino, C.; Ceretti, M.; Paulus, W.; Lamberti, C. *J. Phys. Chem. C* **2011**, *115*, 1311.
(530) Bazin, D.; Rehr, J. J. *J. Phys. Chem. C* **2011**, *115*, 23233.
(531) Martinez-Arias, A.; Fernandez-Garcia, M. *J. Phys. Chem. C* **2011**, *115*, 23237.
(532) De Crescenzi, M.; Balzarotti, A.; Comin, F.; Incoccia, L.; Mobilio, S.; Motta, N. *Solid State Commun.* **1981**, *37*, 921.
(533) Marques, E. C.; Sandstrom, D. R.; Lytle, F. W.; Greegor, R. B. *J. Chem. Phys.* **1982**, *77*, 1027.
(534) Clausen, B. S.; Grabaek, L.; Topsoe, H.; Hansen, L. B.; Stoltze, P.; Norskov, J. K.; Nielsen, O. H. *J. Catal.* **1993**, *141*, 368.
(535) Clausen, B. S.; Norskov, J. K. *Top. Catal.* **2000**, *10*, 221.
(536) Bus, E.; Miller, J. T.; Jeremy Kropf, A.; Prins, R.; van Bokhoven, J. A. *Phys. Chem. Chem. Phys.* **2006**, *8*, 3248.
(537) Bus, E. Characterization of supported gold, platinum-gold, and platinum catalysts for hydrogenation reactions. PhD Thesis, Department of Chemical and Bioengineering, Zürich, Switzerland, 2006.
(538) Bunker, G. *Nucl. Instrum. Methods* **1983**, *207*, 437.
(539) Tranquada, J. M.; Ingalls, R. *Phys. Rev. B* **1983**, *28*, 3520.
(540) Dalba, G.; Fornasini, P. *J. Synchrotron Radiat.* **1997**, *4*, 243.
(541) Note that in the specific literature *asymmetry* is commonly referred to as *skew*, whereas *sharpening/flattening* is usually referred as *kurtosis*.
(542) van Dorssen, G. E.; Koningsberger, D. C. *Phys. Chem. Chem. Phys.* **2003**, *5*, 3549.
(543) Vaarkamp, M. *Catal. Today* **1998**, *39*, 271.
(544) Fornasini, P.; Beccara, S.; Dalba, G.; Grisenti, R.; Sanson, A.; Vaccari, M.; Rocca, F. *Phys. Rev. B* **2004**, *70*, 174301.
(545) Benfatto, M.; Della Longa, S.; Hatada, K.; Hayakawa, K.; Gawelda, W.; Bressler, C.; Chergui, M. *J. Phys. Chem. B* **2006**, *110*, 14035.
(546) Chen, L. X. *Angew. Chem., Int. Ed.* **2004**, *43*, 2886.
(547) Bressler, C.; Chergui, M. *Chem. Rev.* **2004**, *104*, 1781.
(548) Bressler, C.; Chergui, M. *Annu. Rev. Phys. Chem.* **2010**, *61*, 263.
(549) Chen, L. X. *Annu. Rev. Phys. Chem.* **2005**, *56*, 221.
(550) Borfecchia, E.; Garino, C.; Salassa, L.; Lamberti, C. *Philos. Trans. R. Soc., A* **2013**, DOI: 10.1098/rsta.2012.0132.
(551) Borfecchia, E.; Garino, C.; Salassa, L.; Ruiu, T.; Gianolio, D.; Zhang, X.; Attenkofer, K.; Chen, L. X.; Gobetto, R.; Sadler, P. J.; Lamberti, C. *Dalton Trans.*, **2013**, *42*, DOI: 10.1039/C3DT32865A.
(552) Gawelda, W.; Bressler, C.; Saes, M.; Kaiser, M.; Tarnovsky, A. N.; Grolimund, D.; Johnson, S. L.; Abela, R.; Chergui, M. *Phys. Scr.* **2005**, *T115*, 102.
(553) Gawelda, W.; Johnson, M.; de Groot, F. M. F.; Abela, R.; Bressler, C.; Chergui, M. *J. Am. Chem. Soc.* **2006**, *128*, 5001.
(554) Gawelda, W.; Cannizzo, A.; Pham, V. T.; van Mourik, F.; Bressler, C.; Chergui, M. *J. Am. Chem. Soc.* **2007**, *129*, 8199.
(555) Bressler, C.; Milne, C.; Pham, V. T.; ElNahhas, A.; van der Veen, R. M.; Gawelda, W.; Johnson, S.; Beaud, P.; Grolimund, D.; Kaiser, M.; Borca, C. N.; Ingold, G.; Abela, R.; Chergui, M. *Science* **2009**, *323*, 489.
(556) Chen, L. X.; Jager, W. J. H.; Jennings, G.; Gosztola, D. J.; Munkholm, A.; Hessler, J. P. *Science* **2001**, *292*, 262.
(557) Chen, L. X.; Zhang, X. Y.; Wasinger, E. C.; Lockard, J. V.; Stickrath, A. B.; Mara, M. W.; Attenkofer, K.; Jennings, G.; Smolentsev, G.; Soldatov, A. *Chem. Sci.* **2010**, *1*, 642.
(558) Chen, L. X.; Shaw, G. B.; Novozhilova, I.; Liu, T.; Jennings, G.; Attenkofer, K.; Meyer, G. J.; Coppens, P. *J. Am. Chem. Soc.* **2003**, *125*, 7022.
(559) Van der Veen, R. M.; Milne, C. J.; El Nahhas, A.; Lima, F. A.; Pham, V. T.; Best, J.; Weinstein, J. A.; Borca, C. N.; Abela, R.; Bressler, C.; Chergui, M. *Angew. Chem., Int. Ed.* **2009**, *48*, 2711.
(560) Gawelda, W.; Pham, V. T.; van der Veen, R. M.; Grolimund, D.; Abela, R.; Chergui, M.; Bressler, C. *J. Chem. Phys.* **2009**, *130*, No. 124520.
(561) Bressler, C.; Abela, R.; Chergui, M. *Z. Kristallogr.* **2008**, *223*, 307.
(562) Pettifer, R. F.; Mathon, O.; Pascarelli, S.; Cooke, M. D.; Gibbs, M. R. J. *Nature* **2005**, *435*, 78.
(563) Yokoyama, T.; Murakami, Y.; Kiguchi, M.; Komatsu, T.; Kojima, N. *Phys. Rev. B* **1998**, *58*, 14238.
(564) Boca, R.; Vrbova, M.; Werner, R.; Haase, W. *Chem. Phys. Lett.* **2000**, *328*, 188.
(565) Baudelet, F.; Pascarelli, S.; Mathon, O.; Itie, J. P.; Polian, A.; d' Astuto, M.; Chervin, J. C. *J. Phys.: Condens. Matter* **2005**, *17*, S957.
(566) Itie, J. P.; Baudelet, F.; Congeduti, A.; Couzinet, B.; Farges, F.; Polian, A. *J. Phys.: Condens. Matter* **2005**, *17*, S883.
(567) König, C. F. J.; van Bokhoven, J. A.; Schildhauer, T. J.; Nachtegaal, M. *J. Phys. Chem. C* **2012**, *116*, 19857.
(568) (a) Frank, P.; Carlson, R. M. K.; Carlson, E. J.; Hodgson, K. O. *Coord. Chem. Rev.* **2003**, *237*, 31. (b) Flogeac, K.; Guillon, E.; Aplincourt, M. *Eur. J. Inorg. Chem.* **2005**, 1552.
(569) Jezowska-Bojczuk, M.; Szczepanik, W.; Mangani, S.; Gaggelli, E.; Gaggelli, N.; Valensin, G. *Eur. J. Inorg. Chem.* **2005**, 3063.
(570) Ramaker, D. E.; Mojet, B. L.; Oostenbrink, M. T. G.; Miller, J. T.; Koningsberger, D. C. *Phys. Chem. Chem. Phys.* **1999**, *1*, 2293.
(571) Kubota, T.; Asakura, K.; Ichikuni, N.; Iwasawa, Y. *Chem. Phys. Lett.* **1996**, *256*, 445.
(572) Reifsnyder, S. N.; Otten, M. M.; Sayers, D. E.; Lamb, H. H. *J. Phys. Chem. B* **1997**, *101*, 4972.
(573) Oudenhuijzen, M. K.; van Bokhoven, J. A.; Miller, J. T.; Ramaker, D. E.; Koningsberger, D. C. *J. Am. Chem. Soc.* **2005**, *127*, 1530.
(574) Teliska, A.; O'Grady, W. E.; Ramaker, D. E. *J. Phys. Chem. B* **2005**, *109*, 8076.
(575) Roth, C.; Benker, N.; Buhrmester, T.; Mazurek, M.; Loster, M.; Fuess, H.; Koningsberger, D. C.; Ramaker, D. E. *J. Am. Chem. Soc.* **2005**, *127*, 14607.
(576) Teliska, M.; Murthi, V. S.; Mukerjee, S.; Ramaker, D. E. *J. Phys. Chem. C* **2007**, *111*, 9267.
(577) Scott, F. J.; Roth, C.; Ramaker, D. E. *J. Phys. Chem. C* **2007**, *111*, 11403.
(578) Scott, F. J.; Mukerjee, S.; Ramaker, D. E. *J. Electrochem. Soc.* **2007**, *154*, A396.

(579) Soldatov, A. V.; Dellalonga, S.; Bianconi, A. *Solid State Commun.* **1993**, *85*, 863.
(580) Tew, M. W.; Miller, J. T.; van Bokhoven, J. A. *J. Phys. Chem. C* **2009**, *113*, 15140.
(581) Holland, B. W.; Pettifer, R. F.; Pendry, J. B.; Bordas, J. *J. Phys. C: Solid State Phys.* **1978**, *11*, 633.
(582) Rehr, J. J.; Booth, C. H.; Bridges, F.; Zabinsky, S. I. *Phys. Rev. B* **1994**, *49*, 12347.
(583) Filipponi, A.; DiCicco, A. *Phys. Rev. B* **1996**, *53*, 9466.
(584) Rehr, J. J.; Booth, C. H.; Bridges, F.; Zabinsky, S. I. *Phys. Rev. B* **1996**, *53*, 9468.
(585) Bailey, V. A.; Townsend, J. S. *Philos. Mag.* **1921**, *42*, 873.
(586) Ramsauer, C. *Ann. Phys.* **1921**, *64*, 513.
(587) Rehr, J. J.; Zabinsky, S. I.; Ankudinov, A.; Albers, R. C. *Phys. B* **1995**, *208/209*, 23.
(588) Baberschke, K.; Wende, H.; Srivastava, P.; Chauvistre, R. *J. Phys. IV* **1997**, *7*, 469.
(589) Wende, H.; Arvanitis, D.; Tischer, M.; Chauvistre, R.; Henneken, H.; May, F.; Baberschke, K. *J. Phys. IV* **1997**, *7*, 211.
(590) Wende, H.; Srivastava, P.; Chauvistre, R.; May, F.; Baberschke, K.; Arvanitis, D.; Rehr, J. J. *J. Phys.:Condens. Matter* **1997**, *9*, L427.
(591) Wende, H. *Rep. Prog. Phys.* **2004**, *67*, 2105.
(592) Hu, T. D.; Xie, Y. N.; Jin, Y. L.; Liu, T. *J. Phys.: Condens. Matter* **1997**, *9*, 5507.
(593) O'Grady, W. E.; Qian, X.; Ramaker, D. E. *J. Phys. Chem. B* **1997**, *101*, 5624.
(594) O'Grady, W. E.; Ramaker, D. E. *Electrochim. Acta* **1998**, *44*, 1283.
(595) Ramaker, D. E.; Mojet, B. L.; Koningsberger, D. C.; O'Grady, W. E. *J. Phys.: Condens. Matter* **1998**, *10*, 8753.
(596) Koningsberger, D.; Mojet, B.; Miller, J.; Ramaker, D. *J. Synchrotron Radiat.* **1999**, *6*, 135.
(597) Mojet, B. L.; Miller, J. T.; Ramaker, D. E.; Koningsberger, D. C. *J. Catal.* **1999**, *186*, 373.
(598) Koningsberger, D. C.; de Graaf, J.; Mojet, B. L.; Ramaker, D. E.; Miller, J. T. *Appl. Catal., A* **2000**, *191*, 205.
(599) Ramaker, D. E.; van Dorssen, G. E.; Mojet, B. L.; Koningsberger, D. C. *Top. Catal.* **2000**, *10*, 157.
(600) Ramaker, D. E.; de Graaf, J.; van Veen, J. A. R.; Koningsberger, D. C. *J. Catal.* **2001**, *203*, 7.
(601) van Dorssen, G. E.; Koningsberger, D. C.; Ramaker, D. E. *J. Phys.: Condens. Matter* **2002**, *14*, 13529.
(602) Keller, D. E.; Airaksinen, S. M. K.; Krause, A. O.; Weckhuysen, B. M.; Koningsberger, D. C. *J. Am. Chem. Soc.* **2007**, *129*, 3189.
(603) van der Eerden, A. M. J.; Visser, T.; Nijhuis, A.; Ikeda, Y.; Lepage, M.; Koningsberger, D. C.; Weckhuysen, B. M. *J. Am. Chem. Soc.* **2005**, *127*, 3272.
(604) Visser, T.; Nijhuis, T. A.; van der Eerden, A. M. J.; Ji, Y.; Ikeda, Y.; Lepage, M.; Weckhuysen, B. M. *Stud. Surf. Sci. Catal.* **2005**, *158*, 1239.
(605) Ankudinov, A. L.; Rehr, J. J.; Low, J. J.; Bare, S. R. *J. Synchrotron Radiat.* **2001**, *8*, 578.
(606) Ankudinov, A. L.; Rehr, J. J.; Low, J. J.; Bare, S. R. *Top. Catal.* **2002**, *18*, 3.
(607) Roth, C.; Martz, N.; Morlang, A.; Theissmann, R.; Fuess, H. *Phys. Chem. Chem. Phys.* **2004**, *6*, 3557.
(608) Krishnan, V.; Bertagnolli, H. *Appl. Organomet. Chem.* **2007**, *21*, 161.
(609) Keller, D. E.; Weckhuysen, B. M.; Koningsberger, D. C. *Chem.—Eur. J.* **2007**, *13*, 5845.
(610) Ramaker, D. E.; O'Grady, W. E. *J. Synchrotron Radiat.* **1999**, *6*, 800.
(611) Ramaker, D. E.; Qian, X.; O'Grady, W. E. *Chem. Phys. Lett.* **1999**, *299*, 221.
(612) Wende, H.; Baberschke, K. *J. Electron Spectrosc. Relat. Phenom.* **1999**, *103*, 821.
(613) Wende, H.; Litwinski, C.; Scherz, A.; Gleitsmann, T.; Li, Z.; Sorg, C.; Baberschke, K.; Ankudinov, A.; Rehr, J. J.; Jung, C. *J. Phys.: Condens. Matter* **2003**, *15*, 5197.
(614) Harada, M.; Okada, T. *Anal. Sci.* **2001**, *17*, 233.
(615) Tromp, M.; Slagt, M. Q.; Gebbink, R.; van Koten, G.; Ramaker, D. E.; Koningsberger, D. C. *Phys. Chem. Chem. Phys.* **2004**, *6*, 4397.
(616) Tromp, M.; van Bokhoven, J. A.; Slagt, M. Q.; Gebbink, R.; van Koten, G.; Ramaker, D. E.; Koningsberger, D. C. *J. Am. Chem. Soc.* **2004**, *126*, 4090.
(617) Chen, C. T.; Sette, F.; Ma, Y.; Modesti, S. *Phys. Rev. B* **1990**, *42*, 7262.
(618) Thole, B. T.; Carra, P.; Sette, F.; Vanderlaan, G. *Phys. Rev. Lett.* **1992**, *68*, 1943.
(619) Chen, C. T.; Idzerda, Y. U.; Lin, H. J.; Smith, N. V.; Meigs, G.; Chaban, E.; Ho, G. H.; Pellegrin, E.; Sette, F. *Phys. Rev. Lett.* **1995**, *75*, 152.
(620) Ebert, H.; Schutz, G. E. *Spin-Orbit Influenced Spectroscopies of Magnetic Solids*; Springer-Verlag: Berlin, 1996.
(621) Ebert, H. *Rep. Prog. Phys.* **1996**, *59*, 1665.
(622) Funk, T.; Deb, A.; George, S. J.; Wang, H. X.; Cramer, S. P. *Coord. Chem. Rev.* **2005**, *249*, 3.
(623) Bansmann, J.; Baker, S. H.; Binns, C.; Blackman, J. A.; Bucher, J. P.; Dorantes-Davila, J.; Dupuis, V.; Favre, L.; Kechrakos, D.; Kleibert, A.; Meiwes-Broer, K. H.; Pastor, G. M.; Perez, A.; Toulemonde, O.; Trohidou, K. N.; Tuaillon, J.; Xie, Y. *Surf. Sci. Rep.* **2005**, *56*, 189.
(624) Parlebas, J. C.; Asakura, K.; Fujiwara, A.; Harada, I.; Kotani, A. *Phys. Rep.* **2006**, *431*, 1.
(625) Brune, H.; Gambardella, P. *Surf. Sci.* **2009**, *603*, 1812.
(626) Stragier, H.; Cross, J. O.; Rehr, J. J.; Sorensen, L. B.; Bouldin, C. E.; Woicik, J. C. *Phys. Rev. Lett.* **1992**, *69*, 3064.
(627) Pickering, I. J.; Sansone, M.; Marsch, J.; George, G. N. *J. Am. Chem. Soc.* **1993**, *115*, 6302.
(628) Ma, Q.; Lee, J. F.; Sayers, D. E. *Phys. B* **1995**, *208*, 663.
(629) Bazin, D. C.; Sayers, D. A.; Rehr, J. J. *J. Phys. Chem. B* **1997**, *101*, 11040.
(630) Proietti, M. G.; Renevier, H.; Hodeau, J. L.; Garcia, J.; Berar, J. F.; Wolfers, P. *Phys. Rev. B* **1999**, *59*, 5479.
(631) Ravel, B. *J. Synchrotron Radiat.* **2001**, *8*, 314.
(632) Frenkel, A. I.; Kolobov, A. V.; Robinson, I. K.; Cross, J. O.; Maeda, Y.; Bouldin, C. E. *Phys. Rev. Lett.* **2002**, *89*, No. 285503.
(633) Renevier, H.; Proietti, M. G. Grazing Incidence Diffraction Anomalous Fine Structure in the Study of Structural Properties of Nanostructures. In *Characterization of Semiconductor Heterostructures and Nanostructures II*; Lamberti, C., Agostini, G., Ed.; Elsevier: Amsterdam, 2013, p. 311.
(634) Kaduwela, A. P.; Friedman, D. J.; Fadley, C. S. *J. Electron Spectrosc. Relat. Phenom.* **1991**, *57*, 223.
(635) Chambers, S. A. *Surf. Sci. Rep.* **1992**, *16*, 261.
(636) Woodruff, D. P.; Bradshaw, A. M. *Rep. Prog. Phys.* **1994**, *57*, 1029.
(637) Henry, C. R. *Surf. Sci. Rep.* **1998**, *31*, 235.
(638) Woodruff, D. P. *Surf. Sci. Rep.* **2007**, *62*, 1.
(639) Cockayne, D. J. H. *Annu. Rev. Mater. Res.* **2007**, *37*, 159.
(640) Egerton, R. F. *Transmission Electron Energy Loss Spectroscopy*; Plenum: New York, 1986.
(641) Fujikawa, T. *J. Phys. Soc. Jpn.* **1991**, *60*, 3904.
(642) Serin, V.; Zanchi, G.; Sevely, J. *Microsc. Microanal. Microstruct.* **1992**, *3*, 201.
(643) Qian, M. X.; Sarikaya, M.; Stern, E. A. *Ultramicroscopy* **1995**, *59*, 137.
(644) Sarikaya, M.; Qian, M.; Stern, E. A. *Micron* **1996**, *27*, 449.
(645) Rez, P.; MacLaren, J. M.; Saldin, D. K. *Phys. Rev. B* **1998**, *57*, 2621.
(646) Moreno, M. S.; Jorissen, K.; Rehr, J. J. *Micron* **2007**, *38*, 1.
(647) Decrescenzi, M.; Chainet, E.; Derrien, J. *Solid State Commun.* **1986**, *57*, 487.
(648) Chainet, E.; Derrien, J.; Cinti, R. C.; Nguyen, T. T. A.; Decrescenzi, M. *J. Phys. (Paris), Colloq.* **1986**, *47* (C8), 209.
(649) Decrescenzi, M. *Phys. B* **1989**, *158*, 557.

(650) (a) Koonin, S. E. *Nature* **1991**, *354*, 468. (b) Gatti, F.; fontanelli, F.; Galeazzi, M.; Swift, A. M.; Vitale, S. *Nature* **1999**, *397*, 137. (c) Benedek, G.; Fiorini, E.; Guiliani, A.; Milani, P.; Monfardini, A.; Nucciotti, A.; Prandoni, M. L.; Sancrotti, M. *Nucl. Instrum. Methods Phys. Res. A* **1999**, *426*, 147. (d) Pergolesi, D.; Gatti, F.; Raseti, M.; D'Acapito, F.; Mobilio, S.; Gonella, F.; Maurizio, C. *AIP Conf. Proc.* **2002**, *605*, 367. (e) Arnaboldi, C.; Benedek, G.; Brofferio, C.; Capelli, S.; Capizzi, F.; Cremonesi, O.; Filipponi, A.; Fiorini, E.; Giuliani, A.; Monfardini, A.; Nucciotti, A.; Pavan, M.; Perdetti, M.; Pessina, G.; Pirro, S.; Previstali, E.; Sisti, M. *Phys. Rev. Lett.* **2006**, *96*, No. 042503.
(651) Mehl, M. J.; Einstein, T. L. *Phys. Rev. B* **1987**, *36*, 9011.
(652) Nishino, Y.; Materlik, G. *Phys. Rev. B* **1999**, *60*, 15074.
(653) Nishino, Y.; Troger, L.; Korecki, R.; Materlik, G. *Phys. Rev. B* **2001**, *64*, No. 201101.
(654) Len, P. M.; Gog, T.; Novikov, D.; Eisenhower, R. A.; Materlik, G.; Fadley, C. S. *Phys. Rev. B* **1997**, *56*, 1529.
(655) Toby, B. H.; Egami, T. *Acta Crystallogr., Sect. A* **1992**, *48*, 336.
(656) Keen, D. A. *J. Appl. Crystallogr.* **2001**, *34*, 172.
(657) Egami, T.; Billinge, S. J. L. *Underneath the Bragg Peaks: Structural Analysis of Complex Materials*; Pergamon Press: Oxford, U.K., 2003.
(658) Billinge, S. J. L.; Kanatzidis, M. G. *Chem. Commun.* **2004**, 749.
(659) Fernandez-Garcia, M.; Martinez-Arias, A.; Hanson, J. C.; Rodriguez, J. A. *Chem. Rev.* **2004**, *104*, 4063.
(660) Billinge, S. J. L.; Levin, I. *Science* **2007**, *316*, 561.
(661) Hodeau, J. L.; Guinebretiere, R. *Appl. Phys. A: Mater. Sci. Process.* **2007**, *89*, 813.
(662) Bozin, E. S.; Juhás, P.; Billinge, S. J. L. Local Structure of Bulk and Nanocrystalline Semiconductors Using Total Scattering Methods. In *Characterization of Semiconductor Heterostructures and Nanostructures II*; Lamberti, C., Agostini, G., Ed.; Elsevier: Amsterdam, 2013, p. 229.
(663) Seong, H. K.; Kim, U.; Jeon, E. K.; Park, T. E.; Oh, H.; Lee, T. H.; Kim, J. J.; Choi, H. J.; Kim, J. Y. *J. Phys. Chem. C* **2009**, *113*, 10847.
(664) Roa, D. B.; Barcelos, I. D.; de Siervo, A.; Pirota, K. R.; Lacerda, R. G.; Magalhaes-Paniago, R. *Appl. Phys. Lett.* **2010**, *96*, No. 253114.
(665) Pool, V. L.; Klem, M. T.; Chorney, C. L.; Arenholz, E. A.; Idzerda, Y. U. *J. Appl. Phys.* **2011**, *109*, No. 07B529.
(666) Staniland, S.; Ward, B.; Harrison, A.; van der Laan, G.; Telling, N. *Proc. Natl. Acad. Sci. U.S.A.* **2007**, *104*, 19524.
(667) Heijboer, W. M.; Koningsberger, D. C.; Weckhuysen, B. M.; de Groot, F. M. F. *Catal. Today* **2005**, *110*, 228.
(668) Hodeau, J. L.; Favre-Nicolin, V.; Bos, S.; Renevier, H.; Lorenzo, E.; Berar, J. F. *Chem. Rev.* **2001**, *101*, 1843.
(669) Lamberti, C.; Prestipino, C.; Bordiga, S.; Fitch, A. N.; Marra, G. L. *Nucl. Instrum. Methods Phys. Res., Sect. B* **2003**, *200*, 155.
(670) For a review, see, for example, Barker, J. A.; Henderson, D. *Rev. Mod. Phys.* **1976**, *48*, 587 that although published in 1976, reports several PDF studies performed before 1971. Note that, at that time, the radial distribution function (RDF) was more used than the PDF. The RDF, $R(r)$ is defined in such a way that $R(r)dr$ gives the number of atoms in an annulus of thickness dr at distance r from another atom. The relationship between the two distribution is given by $G(r) = R(r)/r - 4\pi r\rho_o$, being ρ_o the average number density of the material.
(671) Michel, F. M.; Ehm, L.; Antao, S. M.; Lee, P. L.; Chupas, P. J.; Liu, G.; Strongin, D. R.; Schoonen, M. A. A.; Phillips, B. L.; Parise, J. B. *Science* **2007**, *316*, 1726.
(672) Chupas, P. J.; Qiu, X. Y.; Hanson, J. C.; Lee, P. L.; Grey, C. P.; Billinge, S. J. L. *J. Appl. Crystallogr.* **2003**, *36*, 1342.
(673) Chupas, P. J.; Chapman, K. W.; Chen, H. L.; Grey, C. P. *Catal. Today* **2009**, *145*, 213.
(674) Proffen, T.; Billinge, S. J. L. *J. Appl. Crystallogr.* **1999**, *32*, 572.
(675) Qiu, X.; Thompson, J. W.; Billinge, S. J. L. *J. Appl. Crystallogr.* **2004**, *37*, 678.
(676) Farrow, C. L.; Juhas, P.; Liu, J. W.; Bryndin, D.; Bozin, E. S.; Bloch, J.; Proffen, T.; Billinge, S. J. L. *J. Phys.: Condens. Matter* **2007**, *19*, No. 335219.
(677) Cromer, D. T.; Waber, J. T. Mean Atomic Scattering Factors in Electrons for Free Atoms and Chemically Significant Ions. In *International Tables for X-ray Crystallography*, Vol. *IV*; Kynock Press: Birmingham, U.K., 1974.
(678) Filipponi, A. *J. Phys.: Condens. Matter* **1994**, *6*, 8415.
(679) Braglia, M.; Bruschi, C.; Dai, G.; Kraus, J.; Mosso, S.; Meneghini, C.; Balerna, A.; Boscherini, F.; Pascarelli, S.; Lamberti, C. *J. Non-Cryst. Solids* **1999**, *257*, 83.
(680) Petkov, V.; Selbach, S. M.; Einarsrud, M. A.; Grande, T.; Shastri, S. D. *Phys. Rev. Lett.* **2010**, *105*, No. 185501.
(681) Petkov, V.; Shastri, S. D. *Phys. Rev. B* **2010**, *81*, No. 165428.
(682) Chupas, P. J.; Chapman, K. W.; Jennings, G.; Lee, P. L.; Grey, C. P. *J. Am. Chem. Soc.* **2007**, *129*, 13822.
(683) Chapman, K. W.; Chupas, P. J.; Nenoff, T. M. *J. Am. Chem. Soc.* **2010**, *132*, 8897.
(684) Oxford, S. M.; Lee, P. L.; Chupas, P. J.; Chapman, K. W.; Kung, M. C.; Kung, H. H. *J. Phys. Chem. C* **2010**, *114*, 17085.
(685) Chupas, P. J.; Chapman, K. W.; Halder, G. J. *J. Am. Chem. Soc.* **2011**, *133*, 8522.
(686) Sava, D. F.; Rodriguez, M. A.; Chapman, K. W.; Chupas, P. J.; Greathouse, J. A.; Crozier, P. S.; Nenoff, T. M. *J. Am. Chem. Soc.* **2011**, *133*, 12398.
(687) Chapman, K. W.; Sava, D. F.; Halder, G. J.; Chupas, P. J.; Nenoff, T. M. *J. Am. Chem. Soc.* **2012**, *133*, 18583.
(688) Zhao, H. Y.; Nenoff, T. M.; Jennings, G.; Chupas, P. J.; Chapman, K. W. *J. Phys. Chem. Lett.* **2012**, *2*, 2742.
(689) Bedford, N.; Dablemont, C.; Viau, G.; Chupas, P.; Petkov, V. *J. Phys. Chem. C* **2007**, *111*, 18214.
(690) Petkov, V.; Bedford, N.; Knecht, M. R.; Weir, M. G.; Crooks, R. M.; Tang, W.; Henkelman, G.; Frenkel, A. *J. Phys. Chem. C* **2008**, *112*, 8907.
(691) Newton, M. A.; Chapman, K. W.; Thompsett, D.; Chupas, P. J. *J. Am. Chem. Soc.* **2012**, *134*, 5036.
(692) Nemeth, K.; Chapman, K. W.; Balasubramanian, M.; Shyam, B.; Chupas, P. J.; Heald, S. M.; Newville, M.; Klingler, R. J.; Winans, R. E.; Almer, J. D.; Sandi, G.; Srajer, G. *J. Chem. Phys.* **2012**, *136*, No. 074105.
(693) Flaningen, E. M.; Bennett, J. M.; Grose, R. W.; Cohen, J. P.; Patton, R. L.; Kirchner, R. M.; Smith, J. V. *Nature* **1978**, *271*, 512.
(694) Szostak, R. M., *Molecular Sieves*; Van Nostrand Reinhold: New York, 1989.
(695) Meier, W. M.; Olson, D. H.; Baerlocher, C., *Atlas of Zeolite Structure Types*; Elsevier: London, 1996.
(696) Sulikowski, B. *Heterog. Chem. Rev.* **1996**, *3*, 203.
(697) Gabelica, Z.; Valange, S. *Microporous Mesoporous Mater.* **1999**, *30*, 57.
(698) Chao, K. J.; Wei, A. C. *J. Electron Spectrosc. Relat. Phenom.* **2001**, *119*, 175.
(699) Kokotailo, G. T.; Lawton, S. L.; Meier, W. M. *Nature* **1978**, *272*, 437.
(700) Szostak, R.; Thomas, T. L. *J. Catal.* **1986**, *100*, 555.
(701) Ratnasamy, P.; Kumar, R. *Catal. Lett.* **1993**, *22*, 227.
(702) Bordiga, S.; Buzzoni, R.; Geobaldo, F.; Lamberti, C.; Giamello, E.; Zecchina, A.; Leofanti, G.; Petrini, G.; Tozzola, G.; Vlaic, G. *J. Catal.* **1996**, *158*, 486.
(703) Simmons, D. K.; Szostak, R.; Agrawal, P. K.; Thomas, T. L. *J. Catal.* **1987**, *106*, 287.
(704) Axon, S. A.; Huddersman, K.; Klinowski, J. *Chem. Phys. Lett.* **1990**, *172*, 398.
(705) Coudurier, G.; Auroux, A.; Vedrine, J. C.; Farlee, R. D.; Abrams, L.; Shannon, R. D. *J. Catal.* **1987**, *108*, 1.
(706) Notari, B. *Adv. Catal.* **1996**, *41*, 253.
(707) Clerici, M. G. Titanium Silicalite-1. In Metal Oxide Catalysis; Jackson, S. D.; Hargreaves, J. S. J., Ed.; Wiley-VCH Verlag GmbH & Co. KGaA: Weinheim, Germany, 2009; p 705.
(708) Barbera, D.; Cavani, F.; D'Alessandro, T.; Fornasari, G.; Guidetti, S.; Aloise, A.; Giordano, G.; Piumetti, M.; Bonelli, B.; Zanzottera, C. *J. Catal.* **2010**, *275*, 158.
(709) Clerici, M. G.; Bellussi, G.; Romano, U. *J. Catal.* **1991**, *129*, 159.

(710) Mantegazza, M. A.; Leofanti, G.; Petrini, G.; Padovan, M.; Zecchina, A.; Bordiga, S. *Stud. Surf. Sci. Catal.* **1994**, *82*, 541.
(711) Lane, B. S.; Burgess, K. *Chem. Rev.* **2003**, *103*, 2457.
(712) Clerici, M. G.; Ingallina, P. *J. Catal.* **1993**, *140*, 71.
(713) Cheng, W. G.; Wang, X. S.; Li, G.; Guo, X. W.; Zhang, S. J. *J. Catal.* **2008**, *255*, 343.
(714) Clerici, M. G. *Appl. Catal.* **1991**, *68*, 249.
(715) Clerici, M. G. *Top. Catal.* **2001**, *15*, 257.
(716) Mantegazza, M. A.; Petrini, G.; Spanò, G.; Bagatin, R.; Rivetti, F. *J. Mol. Catal. A* **1999**, *146*, 223.
(717) Zhuang, J. Q.; Yang, G.; Ma, D.; Lan, X. J.; Liu, X. M.; Han, X. W.; Bao, X. H.; Mueller, U. *Angew. Chem., Int. Ed.* **2004**, *43*, 6377.
(718) Roffia, P.; Tonti, S.; Cesana, A.; Mantegazza, M. A.; Padovan, M. U.S. Patent 4918194, 1990.
(719) Cavani, F.; Raabova, K.; Bigi, F.; Quarantelli, C. *Chem.—Eur. J.* **2010**, *16*, 12962.
(720) Wang, X. D.; Zhang, B. Q.; Liu, X. F.; Lin, J. Y. S. *Adv. Mater.* **2006**, *18*, 3261.
(721) Shan, Z. C.; Wang, H.; Meng, X. J.; Liu, S. Y.; Wang, L. A.; Wang, C. Y.; Li, F.; Lewis, J. P.; Xiao, F. S. *Chem. Commun.* **2011**, *47*, 1048.
(722) Schmidt, I.; Krogh, A.; Wienberg, K.; Carlsson, A.; Brorson, M.; Jacobsen, C. J. H. *Chem. Commun.* **2000**, 2157.
(723) Serrano, D.; Sanz, R.; Pizarro, P.; Moreno, I. *Chem. Commun.* **2009**, 1407.
(724) Zhou, J. A.; Hua, Z. L.; Cui, X. Z.; Ye, Z. Q.; Cui, F. M.; Shi, J. L. *Chem. Commun.* **2010**, *46*, 4994.
(725) Xin, H. C.; Zhao, J.; Xu, S. T.; Li, J. P.; Zhang, W. P.; Guo, X. W.; Hensen, E. J. M.; Yang, Q. H.; Li, C. *J. Phys. Chem. C* **2010**, *114*, 6553.
(726) Reichinger, M.; Schmidt, W.; van den Berg, M. W. E.; Aerts, A.; Martens, J. A.; Kirschhock, C. E. A.; Gies, H.; Grunert, W. *J. Catal.* **2010**, *269*, 367.
(727) Cheneviere, Y.; Chieux, F.; Caps, V.; Tuel, A. *J. Catal.* **2010**, *269*, 161.
(728) Chen, L. H.; Li, X. Y.; Tian, G.; Li, Y.; Rooke, J. C.; Zhu, G. S.; Qiu, S. L.; Yang, X. Y.; Su, B. L. *Angew. Chem., Int. Ed.* **2011**, *50*, 11156.
(729) Ma, S. Q.; Li, G.; Wang, X. S. *Chem. Lett.* **2006**, *35*, 428.
(730) Bravo-Suarez, J. J.; Bando, K. K.; Akita, T.; Fujitani, T.; Fuhrer, T. J.; Oyama, S. T. *Chem. Commun.* **2008**, 3272.
(731) Bravo-Suarez, J. J.; Bando, K. K.; Fujitani, T.; Oyama, S. T. *J. Catal.* **2008**, *257*, 32.
(732) Lu, J. Q.; Zhang, X. M.; Bravo-Suarez, J. J.; Fujitani, T.; Oyama, S. T. *Catal. Today* **2009**, *147*, 186.
(733) Liu, T.; Hacarlioglu, P.; Oyama, S. T.; Luo, M. F.; Pan, X. R.; Lu, J. Q. *J. Catal.* **2009**, *267*, 202.
(734) Klaewkla, R.; Kulprathipanja, S.; Rangsunvigit, P.; Rirksomboon, T.; Nemeth, L. *Chem. Commun.* **2003**, 1500.
(735) Thangaraj, A.; Kumar, R.; Ratnasamy, P. *J. Catal.* **1991**, *131*, 294.
(736) Blasco, T.; Camblor, M.; Corma, A.; Pérez-Parriente, J. *J. Am. Chem. Soc.* **1993**, *115*, 11806.
(737) Camblor, M. A.; Corma, A.; Perezpariente, J. *Chem. Commun.* **1993**, 557.
(738) Camblor, M. A.; Corma, A.; Perezpariente, J. *Zeolites* **1993**, *13*, 82.
(739) Blasco, T.; Camblor, M. A.; Corma, A.; Esteve, P.; Guil, J. M.; Martinez, A.; Perdigon-Melon, J. A.; Valencia, S. *J. Phys. Chem. B* **1998**, *102*, 75.
(740) Carati, A.; Flego, C.; Massara, E. P.; Millini, R.; Carluccio, L.; Parker, W. O.; Bellussi, G. *Microporous Mesoporous Mater.* **1999**, *30*, 137.
(741) Saxton, R. J. *Top. Catal* **1999**, *9*, 43.
(742) Adam, W.; Corma, A.; Garcia, H.; Weichold, O. *J. Catal.* **2000**, *196*, 339.
(743) LeBars, J.; Dakka, J.; Sheldon, R. A. *Appl. Catal., A* **1996**, *136*, 69.
(744) Wu, P.; Komatsu, T.; Yashima, T. *J. Phys. Chem.* **1996**, *100*, 10316.
(745) Wu, P.; Komatsu, T.; Yashima, T. *J. Phys. Chem. B* **1998**, *102*, 9297.
(746) Corma, A.; Diaz, U.; Domine, M. E.; Fornes, V. *Chem. Commun.* **2000**, 137.
(747) Corma, A.; Diaz, U.; Domine, M. E.; Fornes, V. *J. Am. Chem. Soc.* **2000**, *122*, 2804.
(748) Corma, A.; Diaz, U.; Domine, M. E.; Fornes, V. *Angew. Chem., Int. Ed.* **2000**, *39*, 1499.
(749) Corma, A.; Diaz, U.; Fornes, V.; Guil, J. M.; Martinez-Triguero, J.; Creyghton, E. J. *J. Catal.* **2000**, *191*, 218.
(750) Corma, A.; Diaz, U.; Fornes, V.; Jorda, J. L.; Domine, M.; Rey, F. *Chem. Commun.* **1999**, 779.
(751) Wu, P.; Tatsumi, T. *Chem. Commun.* **2001**, 897.
(752) Wu, P.; Tatsumi, T.; Komatsu, T.; Yashima, T. *J. Catal.* **2001**, *202*, 245.
(753) Wu, P.; Tatsumi, T. *J. Phys. Chem. B* **2002**, *106*, 748.
(754) Wu, P.; Tatsumi, T. *J. Catal.* **2003**, *214*, 317.
(755) Wu, P.; Nuntasri, D.; Ruan, J. F.; Liu, Y. M.; He, M. Y.; Fan, W. B.; Terasaki, O.; Tatsumi, T. *J. Phys. Chem. B* **2004**, *108*, 19126.
(756) Yang, X. Y.; Han, Y.; Lin, K. F.; Tian, G.; Feng, Y. F.; Meng, X. J.; Di, Y.; Du, Y. C.; Zhang, Y. L.; Xiao, F. S. *Chem. Commun.* **2004**, 2612.
(757) Kubota, Y.; Koyama, Y.; Yamada, T.; Inagaki, S.; Tatsumi, T. *Chem. Commun.* **2008**, 6224.
(758) Eilertsen, E. A.; Bordiga, S.; Lamberti, C.; Damin, A.; Bonino, F.; Arstad, B.; Svelle, S.; Olsbye, U.; Lillerud, K. P. *ChemCatChem* **2011**, *3*, 1869.
(759) Eilertsen, E. A.; Giordanino, F.; Lamberti, C.; Bordiga, S.; Damin, A.; Bonino, F.; Olsbye, U.; Lillerud, K. P. *Chem. Commun.* **2011**, *47*, 11867.
(760) Corma, A.; Navarro, M. T.; Pariente, J. P. *J. Chem. Soc., Chem. Commun.* **1994**, 147.
(761) Khouw, C. B.; Dartt, C. B.; Labinger, J. A.; Davis, M. E. *J. Catal.* **1994**, *149*, 195.
(762) Maschmeyer, T.; Rey, F.; Sankar, G.; Thomas, J. M. *Nature* **1995**, *378*, 159.
(763) Blasco, T.; Corma, A.; Navarro, M. T.; Pariente, J. P. *J. Catal.* **1995**, *156*, 65.
(764) Barker, C. M.; Gleeson, D.; Kaltsoyannis, N.; Catlow, C. R. A.; Sankar, G.; Thomas, J. M. *Phys. Chem. Chem. Phys.* **2002**, *4*, 1228.
(765) Chaudhari, K.; Srinivas, D.; Ratnasamy, P. *J. Catal.* **2001**, *203*, 25.
(766) Panov, G. I.; Sheveleva, G. A.; Kharitonov, A. S.; Romannikov, V. N.; Vostrikova, L. A. *Appl. Catal., A* **1992**, *82*, 31.
(767) Kharitonov, A. S.; Sheveleva, G. A.; Panov, G. I.; Sobolev, V. I.; Paukshtis, Y. A.; Romannikov, V. N. *Appl. Catal., A* **1993**, *98*, 33.
(768) Kikuchi, E.; Yogo, K.; Tanaka, S.; Abe, M. *Chem. Lett.* **1991**, 1063.
(769) Feng, X. B.; Hall, W. K. *J. Catal.* **1997**, *166*, 368.
(770) Ma, A. Z.; Grunert, W. *Chem. Commun.* **1999**, 71.
(771) Zhu, Q.; Mojet, B. L.; Janssen, R. A. J.; Hensen, E. J. M.; van Grondelle, J.; Magusin, P. C. M. M.; van Santen, R. A. *Catal. Lett.* **2002**, *81*, 205.
(772) Pirngruber, G. D. *J. Catal.* **2003**, *219*, 456.
(773) Roy, P. K.; Pirngruber, G. D. *J. Catal.* **2004**, *227*, 164.
(774) Perez-Ramirez, J.; Kumar, M. S.; Bruckner, A. *J. Catal.* **2004**, *223*, 13.
(775) Brosius, R.; Habermacher, D.; Martens, J. A.; Vradman, L.; Herskowitz, M.; Capek, L.; Sobalik, Z.; Dedecek, J.; Wichterlova, B.; Tokarova, V.; Gonsiorova, O. *Top. Catal* **2004**, *30−31*, 333.
(776) El-Malki, E. M.; van Santen, R. A.; Sachtler, W. M. H. *J. Catal.* **2000**, *196*, 212.
(777) Axon, S. A.; Fox, K. K.; Carr, S. W.; Klinowski, J. *Chem. Phys. Lett.* **1992**, *189*, 1.
(778) Lewis, D. W.; Sankar, G.; Richard, C.; Catlow, C. R. A.; Carr, S. W.; Thomas, J. M. *Nucl. Instrum. Methods Phys. Res., Sect. B* **1995**, *97*, 44.

(779) Zecchina, A.; Geobaldo, F.; Lamberti, C.; Bordiga, S.; Turnes Palomino, G.; Otero Areán, C. *Catal. Lett.* **1996**, *42*, 25.
(780) Lewis, D. W.; Catlow, C. R. A.; Sankar, G.; Carr, S. W. *J. Phys. Chem.* **1995**, *99*, 2377.
(781) Lamberti, C.; Turnes Palomino, G.; Bordiga, S.; Arduino, D.; Zecchina, A.; Vlaic, G. *Jpn. J. Appl. Phys. Part 1* **1999**, *38−1*, 55.
(782) Berlier, G.; Spoto, G.; Ricchiardi, G.; Bordiga, S.; Lamberti, C.; Zecchina, A. *J. Mol. Catal. A: Chem.* **2002**, *182*, 359.
(783) Ferretti, A. M.; Oliva, C.; Forni, L.; Berlier, G.; Zecchina, A.; Lamberti, C. *J. Catal.* **2002**, *208*, 83.
(784) Berlier, G.; Zecchina, A.; Spoto, G.; Ricchiardi, G.; Bordiga, S.; Lamberti, C. *J. Catal.* **2003**, *215*, 264.
(785) Berlier, G.; Bonino, F.; Zecchina, A.; Bordiga, S.; Lamberti, C. *ChemPhysChem* **2003**, *4*, 1073.
(786) Berlier, G.; Pourny, M.; Bordiga, S.; Spoto, G.; Zecchina, A.; Lamberti, C. *J. Catal.* **2005**, *229*, 45.
(787) Berlier, G.; Prestipino, C.; Rivallan, M.; Bordiga, S.; Lamberti, C.; Zecchina, A. *J. Phys. Chem. B* **2005**, *109*, 22377.
(788) Fejes, P.; Lazar, K.; Marsi, I.; Rockenbauer, A.; Korecz, L.; Nagy, J. B.; Perathoner, S.; Centi, G. *Appl. Catal., A* **2003**, *252*, 75.
(789) Hensen, E.; Zhu, Q. J.; Liu, P. H.; Chao, K. J.; van Santen, R. *J. Catal.* **2004**, *226*, 466.
(790) Berlier, G.; Lamberti, C.; M., R.; Mul, G. *Phys. Chem. Chem. Phys.* **2010**, *12*, 358.
(791) Bonino, F.; Damin, A.; Piovano, A.; Lamberti, C.; Bordiga, S.; Zecchina, A. *ChemCatChem* **2011**, *3*, 139.
(792) Marturano, P.; Drozdova, L.; Kogelbauer, A.; Prins, R. *J. Catal.* **2000**, *192*, 236.
(793) Marturano, P.; Kogelbauer, A.; Prins, R. *J. Catal.* **2000**, *190*, 460.
(794) Battiston, A. A.; Bitter, J. H.; Koningsberger, D. C. *Catal. Lett.* **2000**, *66*, 75.
(795) Battiston, A. A.; Bitter, J. H.; Heijboer, W. M.; de Groot, F. M. F.; Koningsberger, D. C. *J. Catal.* **2003**, *215*, 279.
(796) Battiston, A. A.; Bitter, J. H.; Koningsberger, D. C. *J. Catal.* **2003**, *218*, 163.
(797) Battiston, A. A.; Bitter, J. H.; de Groot, F. M. F.; Overweg, A. R.; Stephan, O.; van Bokhoven, J. A.; Kooyman, P. J.; van der Spek, C.; Vanko, G.; Koningsberger, D. C. *J. Catal.* **2003**, *213*, 251.
(798) Mowry, J. R.; Anderson, R. F.; Johnson, J. A. *Oil Gas J.* **1985**, *83*, 128.
(799) Thomas, J. M.; Liu, X. *J. Phys. Chem.* **1986**, *90*, 4843.
(800) Inui, T.; Matsuda, H.; Yamase, O.; Nagata, H.; Fukuda, K.; Ukawa, T.; Miyamoto, A. *J. Catal.* **1986**, *98*, 491.
(801) Kitagawa, H.; Sendoda, Y.; Ono, Y. *J. Catal.* **1986**, *101*, 12.
(802) Khodakov, A. Y.; Kustov, L. M.; Bondarenko, T. N.; Dergachev, A. A.; Kazansky, V. B.; Minachev, K. M.; Borbely, G.; Beyer, H. K. *Zeolites* **1990**, *10*, 603.
(803) Katada, N.; Kuroda, S.; Niwa, M. *Appl. Catal., A* **1999**, *180*, L1.
(804) Meriaudeau, P.; Naccache, C. *J. Mol. Catal.* **1990**, *59*, L31.
(805) Ono, Y.; Kanae, K. *J. Chem. Soc., Faraday Trans* **1991**, *87*, 669.
(806) Bayense, C. R.; Vanderpol, A.; Vanhooff, J. H. C. *Appl. Catal* **1991**, *72*, 81.
(807) Kwak, B. S.; Sachtler, W. M. H. *J. Catal.* **1994**, *145*, 456.
(808) Kwak, B. S.; Sachtler, W. M. H.; Haag, W. O. *J. Catal.* **1994**, *149*, 465.
(809) Dent, L. S.; Smith, J. V. *Nature* **1958**, *181*, 1794.
(810) Smith, J. V. *Acta Crystallogr.* **1962**, *15*, 835.
(811) Smith, J. V.; Rinaldi, F.; Glasser, L. S. D. *Acta Crystallogr.* **1963**, *16*, 45.
(812) Lok, B. M.; Messina, C. A.; Lyle Patton, R.; Gajek, R. T.; Cannan, T. R.; Flanigen, E. M. *J. Am. Chem. Soc.* **1984**, *106*, 6092.
(813) Ito, M.; Shimoyama, Y.; Saito, Y.; Tsurita, Y.; Otake, M. *Acta Crystallogr. C* **1985**, *41*, 1698.
(814) Smith, L. J.; Davidson, A.; Cheetham, A. K. *Catal. Lett.* **1997**, *49*, 143.
(815) Regli, L.; Bordiga, S.; Lamberti, C.; Lillerud, K. P.; Zones, S. I.; Zecchina, A. *J. Phys. Chem. C* **2007**, *111*, 2992.
(816) Dahl, I. M.; Kolboe, S. *J. Catal.* **1994**, *149*, 458.
(817) Stocker, M. *Microporous Mesoporous Mater.* **1999**, *29*, 3.
(818) Wilson, S.; Barger, P. *Microporous Mesoporous Mater.* **1999**, *29*, 117.
(819) Chen, D.; Moljord, K.; Fuglerud, T.; Holmen, A. *Microporous Mesoporous Mater.* **1999**, *29*, 191.
(820) Haw, J. F.; Song, W. G.; Marcus, D. M.; Nicholas, J. B. *Acc. Chem. Res.* **2003**, *36*, 317.
(821) Olsbye, O.; Svelle, S.; Bjørgen, M.; Beato, P.; Janssens, T. V. W.; Joensen, F.; Bordiga, S.; Lillerud, K. P. *Angew. Chem., Int. Ed.* **2012**, *51*, 5810.
(822) Smith, L.; Cheetham, A. K.; Marchese, L.; Thomas, J. M.; Wright, P. A.; Chen, J.; Gianotti, E. *Catal. Lett.* **1996**, *41*, 13.
(823) Bordiga, S.; Regli, L.; Cocina, D.; Lamberti, C.; Bjorgen, M.; Lillerud, K. P. *J. Phys. Chem. B* **2005**, *109*, 2779.
(824) Bordiga, S.; Regli, L.; Lamberti, C.; Zecchina, A.; Jorgen, M.; Lillerud, K. P. *J. Phys. Chem. B* **2005**, *109*, 7724.
(825) Zecchina, A.; Bordiga, S.; Vitillo, J. G.; Ricchiardi, G.; Lamberti, C.; Spoto, G.; Bjorgen, M.; Lillerud, K. P. *J. Am. Chem. Soc.* **2005**, *127*, 6361.
(826) Regli, L.; Zecchina, A.; Vitillo, J. G.; Cocina, D.; Spoto, G.; Lamberti, C.; Lillerud, K. P.; Olsbye, U.; Bordiga, S. *Phys. Chem. Chem. Phys.* **2005**, *7*, 3197.
(827) Roseler, J.; Heitmann, G.; Holderich, W. F. *Appl. Catal., A* **1996**, *144*, 319.
(828) Heitmann, G. P.; Dahlhoff, G.; Holderich, W. F. *Appl. Catal., A* **1999**, *185*, 99.
(829) Yuen, L.-T.; Zones, S. I.; Harris, T. V.; Gallegos, E. J.; Aroux, A. *Microporous Mater.* **1994**, *2*, 105.
(830) Huybrechts, D. R. C.; Debruycker, L.; Jacobs, P. A. *Nature* **1990**, *345*, 240.
(831) Huybrechts, D. R. C.; Vaesen, I.; Li, H. X.; Jacobs, P. A. *Catal. Lett.* **1991**, *8*, 237.
(832) Deo, G.; Turek, A. M.; Wachs, I. E.; Huybrechts, D. R. C.; Jacobs, P. A. *Zeolites* **1993**, *13*, 365.
(833) Behrens, P.; Felsche, J.; Vetter, S.; Schulzekloff, G.; Jaeger, N. I.; Niemann, W. *J. Chem. Soc., Chem. Commun.* **1991**, 678.
(834) Trong, On, T.; Bittar, A.; Sayari, A.; Kaliaguine, S.; Bonneviot, L. *Catal. Lett.* **1992**, *16*, 85.
(835) Trong, On, T.; Bonneviot, L.; Bittar, A.; Sayari, A.; Kaliaguine, S. *J. Mol. Catal.* **1992**, *74*, 233.
(836) Ito, T.; Kanai, H.; Nakai, T.; Imamura, S. *React. Kinet. Catal. Lett.* **1994**, *52*, 421.
(837) Millini, R.; Massara, E. P.; Perego, G.; Bellussi, G. *J. Catal.* **1992**, *137*, 497.
(838) Perego, G.; Bellussi, G.; Corno, C.; Taramasso, M.; Buonuomo, F.; Esposito, A. *Stud. Surf. Sci. Catal.* **1987**, *28*, 129.
(839) Lamberti, C.; Bordiga, S.; Zecchina, A.; Artioli, G.; Marra, G. L.; Spanò, G. *J. Am. Chem. Soc.* **2001**, *123*, 2204.
(840) Ricchiardi, G.; Damin, A.; Bordiga, S.; Lamberti, C.; Spanò, G.; Rivetti, F.; Zecchina, A. *J. Am. Chem. Soc.* **2001**, *123*, 11409.
(841) Damin, A.; Ricchiardi, G.; Bordiga, S.; Zecchina, A.; Ricci, F.; Spano, G.; Lamberti, C. *Stud. Surf. Sci. Catal.* **2001**, *140*, 195.
(842) Fan, W. B.; Duan, R. G.; Yokoi, T.; Wu, P.; Kubota, Y.; Tatsumi, T. *J. Am. Chem. Soc.* **2008**, *130*, 10150.
(843) Boccuti, M. R.; Rao, K. M.; Zecchina, A.; G., L.; Petrini, G. *Stud. Surf. Sci. Catal.* **1989**, *48*, 133.
(844) Zecchina, A.; Spoto, G.; Bordiga, S.; Padovan, M.; Leofanti, G. *Stud. Surf. Sci. Catal.* **1991**, *65*, 671.
(845) Scarano, D.; Zecchina, A.; Bordiga, S.; Geobaldo, F.; Spoto, G.; Petrini, G.; Leofanti, G.; Padovan, M.; Tozzola, G. *J. Chem. Soc., Faraday Trans.* **1993**, *89*, 4123.
(846) O'Shea, V. A. D.; Capel-Sanchez, M.; Blanco-Brieva, G.; Campos-Martin, J. M.; Fierro, J. L. G. *Angew. Chem., Int. Ed.* **2003**, *42*, 5851.
(847) Borello, E.; Lamberti, C.; Bordiga, S.; Zecchina, A.; Otero Areán, C. *Appl. Phys. Lett.* **1997**, *71*, 2319.
(848) Lamberti, C. *Microporous Mesoporous Mater.* **1999**, *30*, 155.

(849) Lamberti, C.; Bordiga, S.; Zecchina, A.; Carati, A.; Fitch, A. N.; Artioli, G.; Petrini, G.; Salvalaggio, M.; Marra, G. L. *J. Catal.* **1999**, *183*, 222.
(850) Marra, G. L.; Artioli, G.; Fitch, A. N.; Milanesio, M.; Lamberti, C. *Microporous Mesoporous Mater.* **2000**, *40*, 85.
(851) Hijar, C. A.; Jacubinas, R. M.; Eckert, J.; Henson, N. J.; Hay, P. J.; Ott, K. C. *J. Phys. Chem. B* **2000**, *104*, 12157.
(852) Henry, P. F.; Weller, M. T.; Wilson, C. C. *J. Phys. Chem. B.* **2001**, *105*, 7452.
(853) Li, C.; Xiong, G.; Xin, Q.; Liu, J.; Ying, P.; Feng, Z.; Li, J.; Yang, W.; Wang, Y.; Wang, G.; Liu, X.; Lin, M.; Wang, X.; Min, E. *Angew. Chem., Int. Ed.* **1999**, *38*, 2220.
(854) Fan, F. T.; Feng, Z. C.; Li, C. *Acc. Chem. Res.* **2010**, *43*, 378.
(855) Fan, F. T.; Feng, Z. C.; Li, C. *Chem. Soc. Rev.* **2010**, *39*, 4794.
(856) Ricchiardi, G.; de Man, A.; Sauer, J. *Phys. Chem. Chem. Phys.* **2000**, *2*, 2195.
(857) Bordiga, S.; Damin, A.; Bonino, F.; Zecchina, A.; Spanò, G.; Rivetti, F.; Bolis, V.; Lamberti, C. *J. Phys. Chem. B* **2002**, *106*, 9892.
(858) Bonino, F.; Damin, A.; Bordiga, S.; Lamberti, C.; Zecchina, A. *Langmuir* **2003**, *19*, 2155.
(859) Damin, A.; Bordiga, S.; Zecchina, A.; Lamberti, C. *J. Chem. Phys.* **2002**, *117*, 226.
(860) Damin, A.; Bonino, F.; Ricchiardi, G.; Bordiga, S.; Zecchina, A.; Lamberti, C. *J. Phys. Chem. B* **2002**, *106*, 7524.
(861) Damin, A.; Bordiga, S.; Zecchina, A.; Doll, K.; Lamberti, C. *J. Chem. Phys.* **2003**, *118*, 10183.
(862) (a) Gallo, E.; Lamberti, C.; Glatzel, P. *Phys. Chem. Chem. Phys.* **2011**, *13*, 19409. (b) Gallo, E.; Bonino, F.; Swarbrick, J. C.; Petrenko, T.; Piovano, A.; Bordiga, S.; Gianolio, D.; Groppo, E.; Neese, F.; Lamberti, C.; Glatzel, P. *ChemPhysChem.* **2013**, *14*, 79.
(863) Lamberti, C.; Bordiga, S.; Arduino, D.; Zecchina, A.; Geobaldo, F.; Spanò, G.; Genoni, F.; Petrini, G.; Carati, A.; Villain, F.; Vlaic, G. J. *J. Phys. Chem. B* **1998**, *102*, 6382.
(864) Bolis, V.; Bordiga, S.; Lamberti, C.; Zecchina, A.; Carati, A.; Rivetti, F.; Spano, G.; Petrini, G. *Microporous Mesoporous Mater.* **1999**, *30*, 67.
(865) Bolis, V.; Bordiga, S.; Lamberti, C.; Zecchina, A.; Carati, A.; Rivetti, F.; Spano, G.; Petrini, G. *Langmuir* **1999**, *15*, 5753.
(866) Prestipino, C.; Bonino, F.; Usseglio Nanot, A.; Damin, A.; Tasso, A.; Clerici, M. G.; Bordiga, S.; D'Acapito, F.; Zecchina, A.; Lamberti, C. *ChemPhysChem* **2004**, *5*, 1799.
(867) Wu, Z. Y.; Ouvrard, G.; Gressier, P.; Natoli, C. R. *Phys. Rev. B* **1997**, *55*, 10382.
(868) Cabaret, D.; Joly, Y.; Renevier, H.; Natoli, C. R. *J. Synchrotron Radiat.* **1999**, *6*, 258.
(869) Sankar, G.; Bell, R. G.; Thomas, J. M.; Anderson, M. W.; Wright, P. A.; Rocha, J. *J. Phys. Chem.* **1996**, *100*, 449.
(870) Prestipino, C.; Solari, P. L.; Lamberti, C. *J. Phys. Chem. B* **2005**, *109*, 13132.
(871) Pei, S.; Zajac, G. W.; Kaduk, J. A.; Faber, J.; Boyanov, B. I.; Duck, D.; Fazzini, D.; Morrison, T. I.; Yang, D. S. *Catal. Lett.* **1993**, *21*, 333.
(872) Zecchina, A.; Bordiga, S.; Spoto, G.; Damin, A.; Berlier, G.; Bonino, F.; Prestipino, C.; Lamberti, C. *Top. Catal* **2002**, *21*, 67.
(873) Le Noc, L.; Trong On, D.; Solomykina, S.; Echchahed, B.; Bél, F.; Cartier dit Moulin, C.; Bonneviot, L. *Stud. Surf. Sci. Catal.* **1996**, *101*, 611.
(874) Zecchina, A.; Bordiga, S.; Spoto, G.; Marchese, L.; Petrini, G.; Leofanti, G.; Padovan, M. *J. Phys. Chem.* **1992**, *96*, 4991.
(875) Artioli, G.; Lamberti, C.; Marra, G. L. *Acta Crystallogr., Sect. B* **2000**, *56*, 2.
(876) Bordiga, S.; Roggero, I.; Ugliengo, P.; Zecchina, A.; Bolis, V.; Artioli, G.; Buzzoni, R.; Marra, G. L.; Rivetti, F.; Spanò, G.; Lamberti, C. *J. Chem. Soc., Dalton Trans.* **2000**, 3921.
(877) Bordiga, S.; Ugliengo, P.; Damin, A.; Lamberti, C.; Spoto, G.; Zecchina, A.; Spanò, G.; Buzzoni, R.; Dalloro, L.; Rivetti, F. *Top. Catal.* **2001**, *15*, 43.
(878) Zecchina, A.; Bordiga, S.; Spoto, G.; Marchese, L.; Petrini, G.; Leofanti, G.; Padovan, M.; Otero Areàn, C. *J. Chem. Soc., Faraday Trans.* **1992**, *88*, 2959.
(879) Marra, G. L.; Tozzola, G.; Leofanti, G.; Padovan, M.; Petrini, G.; Genoni, F.; Venturelli, B.; Zecchina, A.; Bordiga, S.; Ricchiardi, G. *Stud. Surf. Sci. Catal.* **1994**, *84*, 559.
(880) Marra, G. L.; Spanò, G.; Artioli, G.; Bordiga, S.; Zecchina, A.; Lamberti, C. *Highlights of ISIS Science*, ISIS Facility Annual Report 2000−2001; Science & Technology Facilities Council: Swindon, U.K., 2001; p 26.
(881) Bolis, V.; Busco, C.; Bordiga, S.; Ugliengo, P.; Lamberti, C.; Zecchina, A. *Appl. Surf. Sci.* **2002**, *196*, 56.
(882) Trong, On, D.; Le Noc, L.; Bonneviot, L. *Chem. Commun.* **1996**, 299.
(883) Yuan, S. P.; Si, H. Z.; Fu, A. P.; Chu, T. S.; Tian, F. H.; Duan, Y. B.; Wang, J. G. *J. Phys. Chem. A* **2011**, *115*, 940.
(884) Wells, D. H.; Delgass, W. N.; Thomson, K. T. *J. Am. Chem. Soc.* **2004**, *126*, 2956.
(885) Schultz, E.; Ferrini, C.; Prins, R. *Catal. Lett.* **1992**, *14*, 221.
(886) Bordiga, S.; Bonino, F.; Damin, A.; Lamberti, C. *Phys. Chem. Chem. Phys.* **2007**, *9*, 4854.
(887) Parker, W. O.; Millini, R. *J. Am. Chem. Soc.* **2006**, *128*, 1450.
(888) Millini, R.; Perego, G.; Berti, D.; Parker, W. O.; Carati, A.; Bellussi, G. *Microporous Mesoporous Mater.* **2000**, *35−36*, 387.
(889) Zicovich-Wilson, C. M.; Dovesi, R. *J. Phys. Chem. B* **1998**, *102*, 1411.
(890) Zicovich-Wilson, C. M.; Dovesi, R.; Corma, A. *J. Phys. Chem. B* **1999**, *103*, 988.
(891) Gamba, A.; Tabacchi, G.; Fois, E. *J. Phys. Chem. A* **2009**, *113*, 15006.
(892) Deka, R. C.; Nasluzov, V. A.; Shor, E. A. I.; Shor, A. M.; Vayssilov, G. N.; Rosch, N. *J. Phys. Chem. B* **2005**, *109*, 24304.
(893) Vayssilov, G. N. *Catal. Rev.: Sci. Eng.* **1997**, *39*, 209.
(894) de Man, A. J. M.; Sauer, J. *J. Phys. Chem.* **1996**, *100*, 5025.
(895) Sinclair, P. E.; Sankar, G.; Catlow, C. R. A.; Thomas, J. M.; Maschmeyer, T. *J. Phys. Chem. B* **1997**, *101*, 4232.
(896) Sinclair, P. E.; Carlow, C. R. A. *J. Phys. Chem. B* **1999**, *103*, 1084.
(897) Vayssilov, G. N.; van Santen, R. A. *J. Catal.* **1998**, *175*, 170.
(898) Bonino, F.; Damin, A.; Ricchiardi, G.; Ricci, M; Spanò, G; D'Aloisio, R; Zecchina, A; Lamberti, C; Prestipino, C; Bordiga, S. *J. Phys. Chem. B* **2004**, *108*, 3573.
(899) Damin, A. Ab initio based methods applied to the studyof MgO and TS-1 case systems. PhD Thesis, Department of Inorganic, Physical and Materials Chemistry, Turin, Italy, 2003.
(900) Fois, E.; Gamba, A.; Spano, E. *J. Phys. Chem. B* **2004**, *108*, 9557.
(901) Fois, E.; Gamba, A.; Spano, E. *J. Phys. Chem. B* **2004**, *108*, 154.
(902) Fois, E.; Gamba, A.; Tabacchi, G. *ChemPhysChem* **2005**, *6*, 1237.
(903) Sierka, M.; Sauer, J. *J. Chem. Phys.* **2000**, *112*, 6983.
(904) Calligaris, M.; Nardin, G.; Randaccio, L.; Comin Chiaramonti, P. *Acta Crystallogr., Sect. B* **1982**, *38*, 602.
(905) (a) Dovesi, R.; Saunders, V. R.; Roetti, C.; Causà, M.; Harrison, N. M.; Orlando, R.; Aprà, E. *CRYSTAL-95 User Documentation*; Università di Torino: Torino, Italy, 1995. (b) Dovesi, R.; Orlando, R.; Civalleri, B.; Roetti, C.; Saunders, V. R.; Zicovich-Wilson, C. M. *Z. Kristallogr.* **2005**, *220*, 571.
(906) Gale, J. D. *J. Chem. Soc., Faraday Trans.* **1997**, *93*, 629.
(907) Paris, E.; Mottana, A.; Dellaventura, G.; Robert, J. L. *Eur. J. Mineral.* **1993**, *5*, 455.
(908) Dingwell, D. B.; Paris, E.; Seifert, F.; Mottana, A.; Romano, C. *Phys. Chem. Miner.* **1994**, *21*, 501.
(909) Farges, F.; Brown, G. E.; Rehr, J. J. *Geochim. Cosmochim. Acta* **1996**, *60*, 3023.
(910) Farges, F. *Am. Mineral.* **1997**, *82*, 44.
(911) Farges, F.; Brown, G. E.; Rehr, J. J. *Phys. Rev. B* **1997**, *56*, 1809.
(912) Romano, C.; Paris, E.; Poe, B. T.; Giuli, G.; Dingwell, D. B.; Mottana, A. *Am. Mineral.* **2000**, *85*, 108.

(913) Bordiga, S.; Damin, A.; Bonino, F.; Ricchiardi, G.; Lamberti, C.; Zecchina, A. *Angew. Chem., Int. Ed.* **2002**, *41*, 4734.
(914) Bordiga, S.; Damin, A.; Bonino, F.; Ricchiardi, G.; Zecchina, A.; Tagliapietra, R.; Lamberti, C. *Phys. Chem. Chem. Phys.* **2003**, *5*, 4390.
(915) Zecchina, A.; Bordiga, S.; Lamberti, C.; Ricchiardi, G.; Lamberti, C.; Ricchiardi, G.; Scarano, D.; Petrini, G.; Leofanti, G.; Mantegazza, M. *Catal. Today* **1996**, *32*, 97.
(916) Clerici, M. G.; Ingallina, P.; Millini, R. In *Proceedings of the 9th International Zeolite Conference*, Montreal, Canada, 1992; von Ballmoos, R., Higgins, J. B., Treacy, M. M. J., Ed.; Butterworth-Heinemann: Boston, 1993; Vol. *1*, p 445.
(917) Geobaldo, F.; Bordiga, S.; Zecchina, A.; Giamello, E.; Leofanti, G.; Petrini, G. *Catal. Lett.* **1992**, *16*, 109.
(918) Bonoldi, L.; Busetto, C.; Congiu, A.; Marra, G.; Ranghino, G.; Salvataggio, M.; Spanò, G.; Giamello, E. *Spectrochim. Acta, Part A* **2002**, *58*, 1143.
(919) Bonino, F. TS-1 oxidation catalyst: a spectroscopic characterization in working conditions. PhD Thesis, Department of Inorganic, Physical and Materials Chemistry, Turin, Italy, 2003.
(920) Bal, R.; Chaudhari, K.; Srinivas, D.; Sivasanker, S.; Ratnasamy, P. *J. Mol. Catal. A* **2000**, *162*, 199.
(921) Srinivas, D.; Manikandan, P.; Laha, S. C.; Kumar, R.; Ratnasamy, P. *J. Catal.* **2003**, *217*, 160.
(922) Shetti, V. N.; Manikandan, P.; Srinivas, D.; Ratnasamy, P. *J. Catal.* **2003**, *216*, 461.
(923) Tozzola, G.; Mantegazza, M. A.; Ranghino, G.; Petrini, G.; Bordiga, S.; Ricchiardi, G.; Lamberti, C.; Zulian, R.; Zecchina, A. *J. Catal.* **1998**, *179*, 64.
(924) Sankar, G.; Thomas, J. M.; Catlow, C. R. A.; Barker, C. M.; Gleeson, D.; Kaltsoyannis, N. *J. Phys. Chem. B* **2001**, *105*, 9028.
(925) Sever, R. R.; Root, T. W. *J. Phys. Chem. B* **2003**, *107*, 4080.
(926) Sever, R. R.; Root, T. W. *J. Phys. Chem. B* **2003**, *107*, 4090.
(927) Lin, W. Y.; Frei, H. *J. Am. Chem. Soc.* **2002**, *124*, 9292.
(928) Wang, G.-C.; Sung, H. H. Y.; Williams, I. D.; Leung, W.-H. *Inorg. Chem.* **2012**, *51*, 3640.
(929) Jeske, P.; Haselhorst, G.; Weyhermuller, T.; Wieghardt, K.; Nuber, B. *Inorg. Chem.* **1994**, *33*, 2462.
(930) Hagadorn, J. R.; Arnold, J. *Organometallics* **1998**, *17*, 1355.
(931) Prestipino, C. The use of synchrotron radiation techniques in the characterization of active materials for catalytic reactions. PhD Thesis, Department of Inorganic, Physical and Materials Chemistry, Turin, Italy, 2004.
(932) Bellussi, G.; Perego, C.; Carati, A.; Peratello, S.; Previdi Massara, E.; Perego, G. *Stud. Surf. Sci. Catal.* **1994**, *84*, 85.
(933) Carati, A.; Ferraris, G.; Guidotti, M.; Moretti, G.; Psaro, R.; Rizzo, C. *Catal. Today* **2003**, *77*, 315.
(934) Saunders, V. R.; Dovesi, R.; Roetti, C.; Causà, M.; Harrison, N. M.; Orlando, R.; Zicovich-Wilson, C. M. *CRYSTAL-98 User's Manual*; Università di Torino: Torino, Italy, 1999.
(935) Civalleri, B.; D'Arco, P.; Orlando, R.; Saunders, V. R.; Dovesi, R. *Chem. Phys. Lett.* **2001**, *348*, 131.
(936) Lee, C.; Yang, W.; Parr, R. G. *Phys. Rev. B* **1988**, *37*, 785.
(937) Becke, A. D. *J. Chem. Phys.* **1993**, *98*, 1372.
(938) Becke, A. D. *J. Chem. Phys.* **1993**, *98*, 5648.
(939) To, J.; Sherwood, P.; Sokol, A. A.; Bush, I. J.; Catlow, C. R. A.; van Dam, H. J. J.; French, S. A.; Guest, M. F. *J. Mater. Chem.* **2006**, *16*, 1919.
(940) Lamberti, C.; Turnes Palomino, G.; Bordiga, S.; Zecchina, A.; Spano, G.; Otero Areán, C. *Catal. Lett.* **1999**, *63*, 213.
(941) Prieto, C.; Blasco, T.; Camblor, M.; Perez-Pariente, J. *J. Mater. Chem.* **2000**, *10*, 1383.
(942) Bayense, C. R.; Vanhooff, J. H. C.; Kentgens, A. P. M.; Dehaan, J. W.; Vandeven, L. J. M. *J. Chem. Soc. Chem. Commun.* **1989**, 1292.
(943) Bayense, C. R.; Kentgens, A. P. M.; Dehaan, J. W.; Vandeven, L. J. M.; Vanhooff, J. H. C. *J. Phys. Chem.* **1992**, *96*, 775.
(944) Berlier, G. Structure and reactivity of iron clusters in microporous systems. PhD Thesis, Department of Inorganic, Physical and Materials Chemistry, Turin, Italy, 2001.
(945) Heinrich, F.; Schmidt, C.; Loffler, E.; Menzel, M.; Grünert, W. *J. Catal.* **2002**, *212*, 157.
(946) Hensen, E. J. M.; Zhu, Q.; Hendrix, M. M. M.; Overweg, A. R.; Kooyman, P. J.; Sychev, M. V.; van Santen, R. A. *J. Catal.* **2004**, *221*, 560.
(947) Marturano, P.; Drozdova, L.; Pirngruber, G. D.; Kogelbauer, A.; Prins, R. *Phys. Chem. Chem. Phys.* **2001**, *3*, 5585.
(948) Pirngruber, G. D.; Roy, P. K.; Weiher, N. *J. Phys. Chem. B* **2004**, *108*, 13746.
(949) Pirngruber, G. D.; Luechinger, M.; Roy, P. K.; Cecchetto, A.; Smirniotis, P. *J. Catal.* **2004**, *224*, 429.
(950) Schwidder, M.; Kumar, M. S.; Klementiev, K.; Pohl, M. M.; Brückner, A.; Grünert, W. *J. Catal.* **2005**, *231*, 314.
(951) Ryder, J. A.; Chakraborty, A. K.; Bell, A. T. *J. Phys. Chem. B* **2002**, *106*, 7059.
(952) Ryder, J. A.; Chakraborty, A. K.; Bell, A. T. *J. Catal.* **2003**, *220*, 84.
(953) Kachurovskaya, N. A.; Zhidomirov, G. M.; Hensen, E. J. M.; van Santen, R. A. *Catal. Lett.* **2003**, *86*, 25.
(954) Liang, W. Z.; Bell, A. T.; Head-Gordon, M.; Chakraborty, A. K. *J. Phys. Chem. B* **2004**, *108*, 4362.
(955) Wichterlova, B.; Sobalik, Z.; Dedecek, J. *Appl. Catal., B* **2003**, *41*, 97.
(956) Zecchina, A.; Rivallan, M.; Berlier, G.; Lamberti, C.; Ricchiardi, G. *Phys. Chem. Chem. Phys.* **2007**, *9*, 3483.
(957) Choi, S. H.; Wood, B. R.; Ryder, J. A.; Bell, A. T. *J. Phys. Chem. B* **2003**, *107*, 11843.
(958) El-Malki, E. M.; van Santen, R. A.; Sachtler, W. M. H. *Microporous Mesoporous Mater.* **2000**, *35*−*6*, 235.
(959) Pirutko, L. V.; Chernyavsky, V. S.; Uriarte, A. K.; Panov, G. I. *Appl. Catal., A* **2002**, *227*, 143.
(960) Hensen, E. J. M.; Zhu, Q.; van Santen, R. A. *J. Catal.* **2003**, *220*, 260.
(961) Choi, S. H.; Wood, B. R.; Bell, A. T.; Janicke, M. T.; Ott, K. C. *J. Phys. Chem. B* **2004**, *108*, 8970.
(962) Krylov, A. S.; Poliakoff, J. F.; Stockenhuber, M. *Phys. Chem. Chem. Phys.* **2000**, *2*, 5743.
(963) Pirngruber, G. D.; Roy, P. K.; Prins, R. *Phys. Chem. Chem. Phys.* **2006**, *8*, 3939.
(964) Joyner, R.; Stockenhuber, M. *J. Phys. Chem. B* **1999**, *103*, 5963.
(965) Jia, J. F.; Sun, Q.; Wen, B.; Chen, L. X.; Sachtler, W. M. H. *Catal. Lett.* **2002**, *82*, 7.
(966) Popov, A. G.; Smirnov, A. V.; Knyazeva, E. E.; Yuschenko, V. V.; Kalistratova, E. A.; Klementiev, K. V.; Grunert, W.; Ivanova, I. I. *Microporous Mesoporous Mater.* **2010**, *134*, 124.
(967) Hoj, M.; Beier, M. J.; Grunwaldt, J. D.; Dahl, S. *Appl. Catal., B* **2009**, *93*, 166.
(968) Janas, J.; Gurgul, J.; Socha, R. P.; Shishido, T.; Che, M.; Dzwigaj, S. *Appl. Catal., B* **2009**, *91*, 113.
(969) Park, J. H.; Choung, J. H.; Nam, I. S.; Ham, S. W. *Appl. Catal., B* **2008**, *78*, 342.
(970) Long, G. J.; Cheetham, A. K.; Battle, P. D. *Inorg. Chem.* **1983**, *22*, 3012.
(971) Perez-Ramirez, J.; Kapteijn, F.; Bruckner, A. *J. Catal.* **2003**, *218*, 234.
(972) Yuranov, I.; Bulushev, D. A.; Renken, A.; Kiwi-Minsker, L. *J. Catal.* **2004**, *227*, 138.
(973) Pirngruber, G. D.; Roy, P. K. *Catal. Today* **2005**, *110*, 199.
(974) Heyden, A.; Peters, B.; Bell, A. T.; Keil, F. J. *J. Phys. Chem. B* **2005**, *109*, 4801.
(975) Sun, K. Q.; Xia, H.; Hensen, E.; van Santen, R.; Li, C. *J. Catal.* **2006**, *238*, 186.
(976) Li, Y.; Feng, Z. C.; Xin, H. C.; Fan, F. T.; Zhang, J.; Magusin, P.; Hensen, E. J. M.; van Santen, R. A.; Yang, Q. H.; Li, C. *J. Phys. Chem. B* **2006**, *110*, 26114.
(977) Kondratenko, E. V.; Perez-Ramirez, J. *Appl. Catal., B* **2006**, *64*, 35.
(978) Kondratenko, E. V.; Perez-Ramirez, J. *J. Phys. Chem. B* **2006**, *110*, 22586.

(979) Heyden, A.; Hansen, N.; Bell, A. T.; Keil, F. J. *J. Phys. Chem. B* **2006**, *110*, 17096.
(980) Melian-Cabrera, I.; Espinosa, S.; Groen, J. C.; van de Linden, B.; Kapteijn, F.; Moulijn, J. A. *J. Catal.* **2006**, *238*, 250.
(981) Dubkov, K. A.; Ovanesyan, N. S.; Shteinman, A. A.; Starokon, E. V.; Panov, G. I. *J. Catal.* **2002**, *207*, 341.
(982) Starokon, E. V.; Dubkov, K. A.; Pirutko, L. V.; Panov, G. I. *Top. Catal* **2003**, *23*, 137.
(983) Starokon, E. V.; Parfenov, M. V.; Malykhin, S. E.; Panov, G. I. *J. Phys. Chem. C* **2011**, *115*, 12554.
(984) Marturano, P.; Kogelbauer, A.; Prins, R. *Stud. Surf. Sci. Catal.* **1999**, *125*, 619.
(985) Krocher, O.; Devadas, M.; Elsener, M.; Wokaun, A.; Soger, N.; Pfeifer, M.; Demel, Y.; Mussmann, L. *Appl. Catal., B* **2006**, *66*, 208.
(986) Devadas, M.; Krocher, O.; Elsener, M.; Wokaun, A.; Soger, N.; Pfeifer, M.; Demel, Y.; Mussmann, L. *Appl. Catal., B* **2006**, *67*, 187.
(987) Devadas, M.; Krocher, O.; Elsener, M.; Wokaun, A.; Mitrikas, G.; Soger, N.; Pfeifer, M.; Demel, Y.; Mussmann, L. *Catal. Today* **2007**, *119*, 137.
(988) Lobree, L. J.; Hwang, I. C.; Reimer, J. A.; Bell, A. T. *J. Catal.* **1999**, *186*, 242.
(989) Mul, G.; Perez-Ramirez, J.; Kapteijn, F.; Moulijn, J. A. *Catal. Lett.* **2002**, *80*, 129.
(990) Krishna, K.; Seijger, G. B. F.; van den Bleek, C. M.; Makkee, M.; Mul, G.; Calis, H. P. A. *Catal. Lett.* **2003**, *86*, 121.
(991) Hawker, P. N.; Twigg, M. V. Iron(II) and Lower States. In *Comprehensive Coordination Chemistry: The Synthesis, Reactions, Properties and Applications of Coordination Compounds*; Wilkinson, G., Gillard, R. D., McCleverty, J. A., Ed.; Pergamon: Oxford, U.K., 1987, p 1179.
(992) de Groot, F. M. F.; Glatzel, P.; Bergmann, U.; van Aken, P. A.; Barrea, R. A.; Klemme, S.; Havecker, M.; Knop-Gericke, A.; Heijboer, W. M.; Weckhuysen, B. M. *J. Phys. Chem. B* **2005**, *109*, 20751.
(993) Luches, P.; D'Addato, S.; Valeri, S.; Groppo, E.; Prestipino, C.; Lamberti, C.; Boscherini, F. *Phys. Rev. B* **2004**, *69*, No. 045412.
(994) Groppo, E.; Prestipino, C.; Lamberti, C.; Carboni, R.; Boscherini, F.; Luches, P.; Valeri, S.; D'Addato, S. *Phys. Rev. B* **2004**, *70*, 165408.
(995) Regli, L.; Bordiga, S.; Busco, C.; Prestipino, C.; Ugliengo, P.; Zecchina, A.; Lamberti, C. *J. Am. Chem. Soc.* **2007**, *129*, 12131.
(996) Kasrai, M.; Fleet, M. E.; Muthupari, S.; Li, D.; Bancroft, G. M. *Phys. Chem. Miner.* **1998**, *25*, 268.
(997) Hemraj-Benny, T.; Banerjee, S.; Sambasivan, S.; Fischer, D. A.; Han, W.; Misewichd, J. A.; Wong, S. S. *Phys. Chem. Chem. Phys.* **2005**, *7*, 1103.
(998) Carboni, R.; Pacchioni, G.; Fanciulli, M.; Giglia, A.; Mahne, N.; Pedio, M.; Nannarone, S.; Boscherini, F. *Appl. Phys. Lett.* **2003**, *83*, 4312.
(999) Stöhr, J. *NEXAFS spectroscopy*; Springer-Verlag: Berlin, 1992.
(1000) Tuilier, M. H.; Lopez, A.; Guth, J. L.; Kessler, H. *Zeolites* **1991**, *11*, 662.
(1001) Ghosh, A.; Vargas, N. G.; Mitchell, S. F.; Stevenson, S.; Shantz, D. F. *J. Phys. Chem. C* **2009**, *113*, 12252.
(1002) Bare, S. R.; Kelly, S. D.; Sinkler, W.; Low, J. J.; Modica, F. S.; Valencia, S.; Corma, A.; Nemeth, L. T. *J. Am. Chem. Soc.* **2005**, *127*, 12924.
(1003) Higashimoto, S.; Matsuoka, M.; Zhang, S. G.; Yamashita, H.; Kitao, O.; Hidaka, H.; Anpo, M. *Microporous Mesoporous Mater.* **2001**, *48*, 329.
(1004) Anpo, M.; Zhang, S. G.; Higashimoto, S.; Matsuoka, M.; Yamashita, H.; Ichihashi, Y.; Matsumura, Y.; Souma, Y. *J. Phys. Chem. B* **1999**, *103*, 9295.
(1005) Dzwigaj, S.; Matsuoka, M.; Anpo, M.; Che, M. *Res. Chem. Intermed.* **2003**, *29*, 665.
(1006) (a) Nash, M. J.; Rykov, S.; Lobo, R. F.; Doren, D. J.; Wachs, I. *J. Phys. Chem. C* **2007**, *111*, 7029. (b) Yeates, R. M.; Murdoch, M. J.; Southon, P. D.; McLaughlin, A. C.; Howe, R. F.; Bonino, F.; Bordiga, S.; Damin, A. *Dalton Trans.* **2009**, 8025.
(1007) Chao, K. J.; Wei, A. C.; Wu, H. C.; Lee, J. F. *Catal. Today* **1999**, *49*, 277.
(1008) Cheng, H. Y.; Yang, E.; Lai, C. J.; Chao, K. J.; Wei, A. C.; Lee, J. F. *J. Phys. Chem. B* **2000**, *104*, 4195.
(1009) Wei, D.; Wang, H.; Feng, X. B.; Chueh, W. T.; Ravikovitch, P.; Lyubovsky, M.; Li, C.; Takeguchi, T.; Haller, G. L. *J. Phys. Chem. B* **1999**, *103*, 2113.
(1010) Tusar, N. N.; Logar, N. Z.; Arcon, I.; Thibault-Starzyk, F.; Ristic, A.; Rajic, N.; Kaucic, V. *Chem. Mater.* **2003**, *15*, 4745.
(1011) Barrett, P. A.; Sankar, G.; Catlow, C. R. A.; Thomas, J. M. *J. Phys. Chem.* **1996**, *100*, 8977.
(1012) Selvam, P.; Mohapatra, S. K. *J. Catal.* **2005**, *233*, 276.
(1013) Mathisen, K.; Nicholson, D. G.; Fitch, A. N.; Stockenhuber, M. *J. Mater. Chem.* **2005**, *15*, 204.
(1014) Hagen, A.; Hallmeier, K. H.; Hennig, C.; Szargan, R.; Inui, T.; Roessner, F. *Stud. Surf. Sci. Catal.* **1995**, *94*, 195.
(1015) Malola, S.; Svelle, S.; Bleken, F. L.; Swang, O. *Angew. Chem., Int. Ed.* **2012**, *51*, 652.
(1016) Iwamoto, M.; Yahiro, H.; Torikai, Y.; Yoshioka, T.; Mizuno, N. *Chem. Lett.* **1990**, 1967.
(1017) Sato, S.; Yoshihiro, Y.; Yahiro, H.; Mizuno, N.; Iwamoto, M. *Appl. Catal.* **1991**, *70*, L1.
(1018) Iwamoto, M.; Yahiro, H.; Tanda, K.; Mizuno, N.; Mine, Y.; Kagawa, S. *J. Phys. Chem.* **1991**, *95*, 3727.
(1019) Iwamoto, M.; Yahiro, H.; Mizuno, N.; Zhang, W. X.; Mine, Y.; Furukawa, H.; Kagawa, S. *J. Phys. Chem.* **1992**, *96*, 9360.
(1020) Li, Y. J.; Hall, W. K. *J. Phys. Chem.* **1990**, *94*, 6145.
(1021) Li, Y. J.; Hall, W. K. *J. Catal.* **1991**, *129*, 202.
(1022) Shelef, M. *Chem. Rev.* **1995**, *95*, 209.
(1023) Li, J. H.; Chang, H. Z.; Ma, L.; Hao, J. M.; Yang, R. T. *Catal. Today* **2011**, *175*, 147.
(1024) Cheung, T.; Bhargava, S. K.; Hobday, M.; Foger, K. *J. Catal.* **1996**, *158*, 301.
(1025) Korhonen, S. T.; Fickel, D. W.; Lobo, R. F.; Weckhuysen, B. M.; Beale, A. M. *Chem. Commun.* **2011**, *47*, 800.
(1026) Fickel, D. W.; Fedeyko, J. M.; Lobo, R. F. *J. Phys. Chem. C* **2010**, *114*, 1633.
(1027) Rejmak, P.; Broclawik, E.; Gora-Marek, K.; Radon, M.; Datka, J. *J. Phys. Chem. C* **2008**, *112*, 17998.
(1028) Palomares, A. E.; Marquez, F.; Valencia, S.; Corma, A. *J. Mol. Catal., A* **2000**, *162*, 175.
(1029) Mathisen, K.; Nicholson, D. G.; Beale, A. M.; Sanchez-Sanchez, M.; Sankar, G.; Bras, W.; Nikitenko, S. *J. Phys. Chem. C* **2007**, *111*, 3130.
(1030) Dedecek, J.; Vondrova, A.; Cejka, J. *Collect. Czech. Chem. Commun.* **1998**, *63*, 1755.
(1031) Granger, P.; Parvulescu, V. I. *Chem. Rev.* **2011**, *111*, 3155.
(1032) Brandenberger, S.; Krocher, O.; Tissler, A.; Althoff, R. *Catal. Rev.: Sci. Eng* **2008**, *50*, 492.
(1033) Patchett, J. A.; Verbeek, R. P.; Grimston, K. R.; Rice, G. W.; Calabrese, J. L.; Van Genderen, M. U.S. Patent 6581374, 2003.
(1034) Fickel, D. W.; D'Addio, E.; Lauterbach, J. A.; Lobo, R. F. *Appl. Catal., B* **2011**, *102*, 441.
(1035) Kwak, J. H.; Tonkyn, R. G.; Kim, D. H.; Szanyi, J.; Peden, C. H. F. *J. Catal.* **2010**, *275*, 187.
(1036) McEwen, J. S.; Anggara, T.; Schneider, W. F.; Kispersky, V. F.; Miller, J. T.; Delgass, W. N.; Ribeiro, F. H. *Catal. Today* **2012**, *184*, 129.
(1037) Giamello, E.; Murphy, D.; Magnacca, G.; Morterra, C.; Shioya, Y.; Nomura, T.; Anpo, M. *J. Catal.* **1992**, *136*, 510.
(1038) Kuroda, Y.; Kotani, A.; Maeda, H.; Moriwaki, H.; Morimato, T.; Nagao, M. *J. Chem. Soc. Faraday Trans.* **1992**, *88*, 1583.
(1039) Grünert, W.; Hayes, N. W.; Joyner, R. W.; Shpiro, E. S.; Siddiqui, M. R. H.; Baeva, G. N. *J. Phys. Chem.* **1994**, *98*, 10832.
(1040) Dedecek, J.; Wichterlova, B. *J. Phys. Chem.* **1994**, *98*, 5721.
(1041) Dedecek, J.; Sobalik, Z.; Tvaruzkova, Z.; Kaucky, D.; Wichterlova, B. *J. Phys. Chem.* **1995**, *99*, 16327.
(1042) Wichterlova, B.; Dedecek, J.; Vondrova, A. *J. Phys. Chem.* **1995**, *99*, 1065.

(1043) Beutel, T.; Sarkany, J.; Lei, G. D.; Yan, J. Y.; Sachtler, W. M. H. *J. Phys. Chem.* **1996**, *100*, 845.
(1044) Yamashita, H.; Matsuoka, M.; Tsuji, K.; Shioya, Y.; Anpo, M.; Che, M. *J. Phys. Chem.* **1996**, *100*, 397.
(1045) Kumashiro, P.; Kuroda, Y.; Nagao, M. *J. Phys. Chem. B* **1999**, *103*, 89.
(1046) Turnes Palomino, G.; Fisicaro, P.; Bordiga, S.; Zecchina, A.; Giamello, E.; Lamberti, C. *J. Phys. Chem. B* **2000**, *104*, 4064.
(1047) Llabrés i Xamena, F. X.; Fisicaro, P.; Berlier, G.; Zecchina, A.; Palomino, G. T.; Prestipino, C.; Bordiga, S.; Giamello, E.; Lamberti, C. *J. Phys. Chem. B* **2003**, *107*, 7036.
(1048) (a) Ene, A. B.; Bauer, M.; Archipov, T.; Roduner, E. *Phys. Chem. Chem. Phys.* **2010**, *12*, 6520. (b) Fickel, D. W.; Lobo, R. F. *J. Phys. Chem. C* **2010**, *114*, 1633. (c) Deka, U.; Juhin, A.; Eilertsen, E. A.; Emerich, H.; Green, M. A.; Korhonen, S. T.; Weckhuysen, B. M.; Beale, A. M. *J. Phys. Chem. C* **2012**, *116*, 4809. (d) Deka, U.; Lezcano-Gonzalez, I.; Weckhuysen, B. M.; Beale, A. N. *ACS Catal.* **2013**, *3*, 413.
(1049) Pierloot, K.; Delabie, A.; Groothaert, M. H.; Schoonheydt, R. A. *Phys. Chem. Chem. Phys.* **2001**, *3*, 2174.
(1050) Delabie, A.; Pierloot, K.; Groothaert, M. H.; Schoonheydt, R. A.; Vanquickenborne, L. G. *Eur. J. Inorg. Chem.* **2002**, 515.
(1051) Delabie, A.; Pierloot, K.; Groothaert, M. H.; Weckhuysen, B. M.; Schoonheydt, R. A. *Phys. Chem. Chem. Phys.* **2002**, *4*, 134.
(1052) Zecchina, A.; Bordiga, S.; Salvalaggio, M.; Spoto, G.; Scarano, D.; Lamberti, C. *J. Catal.* **1998**, *173*, 540.
(1053) Zecchina, A.; Bordiga, S.; Palomino, G. T.; Scarano, D.; Lamberti, C.; Salvalaggio, M. *J. Phys. Chem. B* **1999**, *103*, 3833.
(1054) Bolis, V.; Maggiorini, S.; Meda, L.; D'Acapito, F.; Palomino, G. T.; Bordiga, S.; Lamberti, C. *J. Chem. Phys.* **2000**, *113*, 9248.
(1055) Turnes Palomino, G.; Zecchina, A.; Giamello, E.; Fisicaro, P.; Berlier, G.; Lamberti, C.; Bordiga, S. *Stud. Surf. Sci. Catal.* **2000**, *130*, 2915.
(1056) Bolis, V.; Bordiga, S.; Palomino, G. T.; Zecchina, A.; Lamberti, C. *Thermochim. Acta* **2001**, *379*, 131.
(1057) Prestipino, C.; Berlier, G.; Llabrés i Xamena, F. X.; Spoto, G.; Bordiga, S.; Zecchina, A.; Palomino, G. T.; Yamamoto, T.; Lamberti, C. *Chem. Phys. Lett.* **2002**, *363*, 389.
(1058) Bolis, V.; Barbaglia, A.; Bordiga, S.; Lamberti, C.; Zecchina, A. *J. Phys. Chem. B* **2004**, *108*, 9970.
(1059) Rodriguez-Santiago, L.; Sierka, M.; Branchadell, V.; Sodupe, M.; Sauer, J. *J. Am. Chem. Soc.* **1998**, *120*, 1545.
(1060) Nachtigallova, D.; Nachtigall, P.; Sierka, M.; Sauer, J. *Phys. Chem. Chem. Phys.* **1999**, *1*, 2019.
(1061) Nachtigall, P.; Nachtigallova, D.; Sauer, J. *J. Phys. Chem. B* **2000**, *104*, 1738.
(1062) Nachtigallova, D.; Nachtigall, P.; Sauer, J. *Phys. Chem. Chem. Phys.* **2001**, *3*, 1552.
(1063) Calzaferri, G.; Leiggener, C.; Glaus, S.; Schurch, D.; Kuge, K. *Chem. Soc. Rev.* **2003**, *32*, 29.
(1064) Davidova, M.; Nachtigallova, D.; Bulanek, R.; Nachtigall, P. *J. Phys. Chem. B* **2003**, *107*, 2327.
(1065) Bludsky, O.; Silhan, M.; Nachtigallova, D.; Nachtigall, P. *J. Phys. Chem. A* **2003**, *107*, 10381.
(1066) Davidova, M.; Nachtigallova, D.; Nachtigall, P.; Sauer, J. *J. Phys. Chem. B* **2004**, *108*, 13674.
(1067) Lamberti, C.; Spoto, G.; Scarano, D.; Paze, C.; Salvalaggio, M.; Bordiga, S.; Zecchina, A.; Palomino, G. T.; DAcapito, F. *Chem. Phys. Lett.* **1997**, *269*, 500.
(1068) Turnes Palomino, G.; Bordiga, S.; Zecchina, A.; Marra, G. L.; Lamberti, C. *J. Phys. Chem. B* **2000**, *104*, 8641.
(1069) Bordiga, S.; Pazé, C.; Berlier, G.; Scarano, D.; Spoto, G.; Zecchina, A.; Lamberti, C. *Catal. Today* **2001**, *70*, 91.
(1070) Turnes Palomino, G.; Bordiga, S.; Lamberti, C.; Zecchina, A.; Otero Arean, C. *Stud. Surf. Sci. Catal.* **2002**, *142*, 199.
(1071) Li, Z.; Xie, K. C.; Slade, R. C. T. *Appl. Catal., A* **2001**, *209*, 107.
(1072) Kuroda, Y.; Yagi, K.; Horiguchi, N.; Yoshikawa, Y.; Kumashiro, R.; Nagao, M. *Phys. Chem. Chem. Phys.* **2003**, *5*, 3318.
(1073) Zhang, Y. H.; Drake, I. J.; Briggs, D. N.; Bell, A. T. *J. Catal.* **2006**, *244*, 219.
(1074) Drake, I. J.; Zhang, Y. H.; Briggs, D.; Lim, B.; Chau, T.; Bell, A. T. *J. Phys. Chem. B* **2006**, *110*, 11654.
(1075) Drake, I. J.; Zhang, Y. H.; Gilles, M. K.; Liu, C. N. T.; Nachimuthu, P.; Perera, R. C. C.; Wakita, H.; Bell, A. T. *J. Phys. Chem. B* **2006**, *110*, 11665.
(1076) Zhang, Y. H.; Drake, I. J.; Bell, A. T. *Chem. Mater.* **2006**, *18*, 2347.
(1077) Connolly, M. L. *Science* **1983**, *221*, 707.
(1078) Olson, D. H.; Khosrovani, N.; Peters, A. W.; Toby, B. H. *J. Phys. Chem. B* **2000**, *104*, 4844.
(1079) Mortier, W. J. *Compilation of Extra Framework Sites in Zeolites*; Butterworth: London, 1982.
(1080) Attfield, M. P.; Weigel, S. J.; Cheetham, A. K. *J. Catal.* **1997**, *170*, 227.
(1081) Kuroda, Y.; Yoshikawa, Y.; Konno, S.; Hamano, H.; Maeda, H.; Kumashiro, R.; Nagao, M. *J. Phys. Chem.* **1995**, *99*, 10621.
(1082) Itadani, A.; Tanaka, M.; Kuroda, Y.; Nagao, M. *New J. Chem.* **2007**, *31*, 1681.
(1083) Spoto, G.; Gribov, E.; Bordiga, S.; Lamberti, C.; Ricchiardi, G.; Scarano, D.; Zecchina, A. *Chem. Commun.* **2004**, 2768.
(1084) Solans-Monfort, X.; Branchadell, V.; Sodupe, M.; Zicovich-Wilson, C. M.; Gribov, E.; Spoto, G.; Busco, C.; Ugliengo, P. *J. Phys. Chem. B* **2004**, *108*, 8278.
(1085) Rack, J. J.; Webb, J. D.; Strauss, S. H. *Inorg. Chem.* **1996**, *35*, 277.
(1086) Strauss, S. H. *J. Chem. Soc., Dalton Trans.* **2000**, 1.
(1087) Bordiga, S.; Escalona Platero, E.; Otero Arean, C.; Lamberti, C.; Zecchina, A. *J. Catal.* **1992**, *137*, 179.
(1088) Bordiga, S.; Scarano, D.; Spoto, G.; Zecchina, A.; Lamberti, C.; Otero Arean, C. *Vib. Spectrosc.* **1993**, *5*, 69.
(1089) Lamberti, C.; Morterra, C.; Bordiga, S.; Cerrato, G.; Scarano, D. *Vib. Spectrosc.* **1993**, *4*, 273.
(1090) Zecchina, A.; Bordiga, S.; Lamberti, C.; Spoto, G.; Carnelli, L.; Otero Arean, C. *J. Phys. Chem.* **1994**, *98*, 9577.
(1091) Bordiga, S.; Garrone, E.; Lamberti, C.; Zecchina, A.; Otero Arean, C.; Kazansky, V. B.; Kustov, L. M. *J. Chem. Soc., Faraday Trans.* **1994**, *90*, 3367.
(1092) Lamberti, C.; Zecchina, A.; Groppo, E.; Bordiga, S. *Chem. Soc. Rev.* **2010**, *39*, 4951.
(1093) Liu, D. J.; Robota, H. J. *Catal. Lett.* **1993**, *21*, 291.
(1094) Petunchi, J. O.; Marcelin, G.; Hall, W. K. *J. Phys. Chem.* **1992**, *96*, 9967.
(1095) Valyon, J.; Hall, W. K. *J. Phys. Chem.* **1993**, *97*, 7054.
(1096) Aylor, A. W.; Larsen, S. C.; Reimer, J. A.; Bell, A. T. *J. Catal.* **1995**, *157*, 592.
(1097) Sojka, Z.; Che, M.; Giamello, E. *J. Phys. Chem. B* **1997**, *101*, 4831.
(1098) Groothaert, M. H.; Smeets, P. J.; Sels, B. F.; Jacobs, P. A.; Schoonheydt, R. A. *J. Am. Chem. Soc.* **2005**, *127*, 1394.
(1099) Sobolev, V. I.; Dubkov, K. A.; Panna, O. V.; Panov, G. I. *Catal. Today* **1995**, *24*, 251.
(1100) Panov, G. I.; Sobolev, V. I.; Dubkov, K. A.; Parmon, V. N.; Ovanesyan, N. S.; Shilov, A. E.; Shteinman, A. A. *React. Kinet. Catal. Lett.* **1997**, *61*, 251.
(1101) Dubkov, K. A.; Sobolev, V. I.; Talsi, E. P.; Rodkin, M. A.; Watkins, N. H.; Shteinman, A. A.; Panov, G. I. *J. Mol. Catal. A-Chem.* **1997**, *123*, 155.
(1102) Starokon, E. V.; Parfenov, M. V.; Pirutko, L. V.; Abornev, S. I.; Panov, G. I. *J. Phys. Chem. C* **2011**, *115*, 2155.
(1103) Vanelderen, P.; Hadt, R. G.; Smeets, P. J.; Solomon, E. I.; Schoonheydt, R. A.; Sels, B. F. *J. Catal.* **2011**, *284*, 157.
(1104) Green, J.; Dalton, H. *Biochem. J.* **1986**, *236*, 155.
(1105) Green, J.; Dalton, H. *Biochem. J.* **1989**, *259*, 167.
(1106) Rosenzweig, A. C. *Biochem. Soc. Trans.* **2008**, *36*, 1134.
(1107) White, M. C.; Doyle, A. G.; Jacobsen, E. N. *J. Am. Chem. Soc.* **2001**, *123*, 7194.

(1108) Pirngruber, G. D.; Frunz, L.; Luchinger, M. *Phys. Chem. Chem. Phys.* **2009**, *11*, 2928.
(1109) Groothaert, M. H.; Lievens, K.; van Bokhoven, J. A.; Battiston, A. A.; Weckhuysen, B. M.; Pierloot, K.; Schoonheydt, R. A. *ChemPhysChem* **2003**, *4*, 626.
(1110) Groothaert, M. H.; van Bokhoven, J. A.; Battiston, A. A.; Weckhuysen, B. M.; Schoonheydt, R. A. *J. Am. Chem. Soc.* **2003**, *125*, 7629.
(1111) Groothaert, M. H.; Lievens, K.; van Bokhoven, J. A.; Battiston, A. A.; Weckhuysen, B. M.; Pierloot, K.; Schoonheydt, R. A. *Stud. Surf. Sci. Catal.* **2004**, *154*, 2449.
(1112) Groothaert, M. H.; Pierloot, K.; Delabie, A.; Schoonheydt, R. A. *Phys. Chem. Chem. Phys.* **2003**, *5*, 2135.
(1113) Smeets, P. J.; Groothaert, M. H.; van Teeffelen, R. M.; Leeman, H.; Hensen, E. J. M.; Schoonheydt, R. A. *J. Catal.* **2007**, *245*, 358.
(1114) Woertink, J. S.; Smeets, P. J.; Groothaert, M. H.; Vance, M. A.; Sels, B. F.; Schoonheydt, R. A.; Solomon, E. I. *Proc. Natl. Acad. Sci. U.S.A.* **2009**, *106*, 18908.
(1115) (a) Schoonheydt, R. A. *Chem. Soc. Rev.* **2010**, *39*, 5051. (b) Smeets, P. J.; Woertink, J. S.; Sels, B. F.; Solomon, E. I.; Schoonheydt, R. A. *Inorg. Chem.* **2010**, *49*, 3753. (c) Vanelderen, P.; Vancauwenbergh, J.; Sels, B. F.; Schoonheydt, R. A. *Coord. Chem. Rev.* **2013**, *257*, 483.
(1116) Smeets, P. J.; Hadt, R. G.; Woertink, J. S.; Vanelderen, P.; Schoonheydt, R. A.; Sels, B. F.; Solomon, E. I. *J. Am. Chem. Soc.* **2010**, *132*, 14736.
(1117) Where π^* σ is a π^* orbital of the peroxo species that undergoes a σ-bonding interaction with the half-occupied copper d orbital).
(1118) Baldwin, M. J.; Root, D. E.; Pate, J. E.; Fujisawa, K.; Kitajima, N.; Solomon, E. I. *J. Am. Chem. Soc.* **1992**, *114*, 10421.
(1119) Davis, M. E.; Lobo, R. F. *Chem. Mater.* **1992**, *4*, 756.
(1120) Ozin, G. A. *Adv. Mater.* **1992**, *4*, 612.
(1121) van Santen, R. A.; Kramer, G. J. *Chem. Rev.* **1995**, *95*, 637.
(1122) Corma, A. *J. Catal.* **2003**, *216*, 298.
(1123) Corma, A. *Chem. Rev.* **1995**, *95*, 559.
(1124) Morris, R. E.; Weigel, S. J. *Chem. Soc. Rev.* **1997**, *26*, 309.
(1125) Arends, I. W. C. E.; Sheldon, R. A.; Wallau, M.; Schuchardt, U. *Angew. Chem., Int. Ed. Engl.* **1997**, *36*, 1144.
(1126) Krishna, R.; Smit, B.; Calero, S. *Chem. Soc. Rev.* **2002**, *31*, 185.
(1127) Davis, M. E. *Nature* **2002**, *417*, 813.
(1128) Stein, A. *Adv. Mater.* **2003**, *15*, 763.
(1129) Bjorgen, M.; Bonino, F.; Kolboe, S.; Lillerud, K. P.; Zecchina, A.; Bordiga, S. *J. Am. Chem. Soc.* **2003**, *125*, 15863.
(1130) Perez-Ramirez, J.; Christensen, C. H.; Egeblad, K.; Christensen, C. H.; Groen, J. C. *Chem. Soc. Rev.* **2008**, *37*, 2530.
(1131) van Bokhoven, J. A.; Lee, T. L.; Drakopoulos, M.; Lamberti, C.; Thiess, S.; Zegenhagen, J. *Nat. Mater.* **2008**, *7*, 551.
(1132) Morris, R. E.; Bu, X. H. *Nat. Chem* **2010**, *2*, 353.
(1133) Cheetham, A. K.; Ferey, G.; Loiseau, T. *Angew. Chem., Int. Ed.* **1999**, *38*, 3268.
(1134) James, S. L. *Chem. Soc. Rev.* **2003**, *32*, 276.
(1135) Bradshaw, D.; Claridge, J. B.; Cussen, E. J.; Prior, T. J.; Rosseinsky, M. J. *Acc. Chem. Res.* **2005**, *38*, 273.
(1136) Ferey, G. *Chem. Soc. Rev.* **2008**, *37*, 191.
(1137) O'Keeffe, M. *Chem. Soc. Rev.* **2009**, *38*, 1215.
(1138) Perry, J. J., IV; Perman, J. A.; Zaworotko, M. J. *Chem. Soc. Rev.* **2009**, *38*, 1400.
(1139) Furukawa, H.; Ko, N.; Go, Y. B.; Aratani, N.; Choi, S. B.; Choi, E.; Yazaydin, A. O.; Snurr, R. Q.; O'Keeffe, M.; Kim, J.; Yaghi, O. M. *Science* **2010**, *329*, 424.
(1140) Farha, O. K.; Hupp, J. T. *Acc. Chem. Res.* **2010**, *43*, 1166.
(1141) Seeber, G.; Cooper, G. J. T.; Newton, G. N.; Rosnes, M. H.; Long, D. L.; Kariuki, B. M.; Kogerler, P.; Cronin, L. *Chem. Sci* **2010**, *1*, 62.
(1142) Zhou, H. C.; Long, J. R.; Yaghi, O. M. *Chem. Rev.* **2012**, *112*, 673.
(1143) Ferey, G. *Chem. Mater.* **2001**, *13*, 3084.
(1144) Eddaoudi, M.; Moler, D. B.; Li, H. L.; Chen, B. L.; Reineke, T. M.; O'Keeffe, M.; Yaghi, O. M. *Acc. Chem. Res.* **2001**, *34*, 319.
(1145) Long, J. R.; Yaghi, O. M. *Chem. Soc. Rev.* **2009**, *38*, 1213.
(1146) Tranchemontagne, D. J.; Mendoza-Cortes, J. L.; O'Keeffe, M.; Yaghi, O. M. *Chem. Soc. Rev.* **2009**, *38*, 1257.
(1147) Eddaoudi, M.; Kim, J.; Rosi, N.; Vodak, D.; Wachter, J.; O'Keeffe, M.; Yaghi, O. M. *Science* **2002**, *295*, 469.
(1148) Cavka, J. H.; Jakobsen, S.; Olsbye, U.; Guillou, N.; Lamberti, C.; Bordiga, S.; Lillerud, K. P. *J. Am. Chem. Soc.* **2008**, *130*, 13850.
(1149) Valenzano, L.; Civalleri, B.; Bordiga, S.; Nilsen, M. H.; Jakobsen, S.; Lillerud, K.-P.; Lamberti, C. *Chem. Mater.* **2011**, *23*, 1700.
(1150) Chavan, S.; Vitillo, J. G.; Gianolio, D.; Zavorotynska, O.; Civalleri, B.; Jakobsen, S.; Nilsen, M. H.; Valenzano, L.; Lamberti, C.; Lillerud, K. P.; Bordiga, S. *Phys. Chem. Chem. Phys.* **2012**, *14*, 1614.
(1151) Müller, U.; Schubert, M.; Teich, F.; Puetter, H.; Schierle-Arndt, K.; Pastre, J. *J. Mater. Chem.* **2006**, *16*, 626.
(1152) Czaja, A.; Trukhan, T.; Müller, U. *Chem. Soc. Rev.* **2009**, *38*, 1284.
(1153) Dinca, M.; Long, J. R. *J. Am. Chem. Soc.* **2005**, *127*, 9376.
(1154) Pan, L.; Olson, D. H.; Ciemnolonski, L. R.; Heddy, R.; Li, J. *Angew. Chem., Int. Ed.* **2006**, *45*, 616.
(1155) Li, J.-R.; Luppler, R. J.; Zhou, H. C. *Chem. Soc. Rev.* **2009**, *38*, 1477.
(1156) Britt, D.; Furukawa, H.; Wang, B.; Glover, T. G.; Yaghi, O. M. *Proc. Natl. Acad. Sci. U.S.A.* **2009**, *106*, 20637.
(1157) Tanaka, D.; Henke, A.; Albrecht, K.; Moeller, M.; Nakagawa, K.; Kitagawa, S.; Groll, J. *Nat. Chem* **2010**, *2*, 410.
(1158) Sato, H.; Matsuda, R.; Sugimoto, K.; Takata, M.; Kitagawa, S. *Nat. Mater.* **2010**, *9*, 661.
(1159) Shimomura, S.; Higuchi, M.; Matsuda, R.; Yoneda, K.; Hijikata, Y.; Kubota, Y.; Mita, Y.; Kim, J.; Takata, M.; Kitagawa, S. *Nat. Chem* **2010**, *2*, 633.
(1160) Matsuda, R.; Tsujino, T.; Sato, H.; Kubota, Y.; Morishige, K.; Takata, M.; Kitagawa, S. *Chem. Sci* **2010**, *1*, 315.
(1161) Keskin, S.; van Heest, T. M.; Sholl, D. S. *ChemSusChem* **2010**, *3*, 879.
(1162) Ferey, G.; Serre, C.; Devic, T.; Maurin, G.; Jobic, H.; Llewellyn, P. L.; De Weireld, G.; Vimont, A.; Daturi, M.; Chang, J. S. *Chem. Soc. Rev.* **2011**, *40*, 550.
(1163) Li, J. R.; Sculley, J.; Zhou, H. C. *Chem. Rev.* **2012**, *112*, 869.
(1164) Cychosz, K. A.; Ahmad, R.; Matzger, A. J. *Chem. Sci* **2010**, *1*, 293.
(1165) Li, Y. S.; Liang, F. Y.; Bux, H.; Feldhoff, A.; Yang, W. S.; Caro, J. *Angew. Chem., Int. Ed.* **2010**, *49*, 548.
(1166) An, J.; Geib, S. J.; Rosi, N. L. *J. Am. Chem. Soc.* **2010**, *132*, 38.
(1167) Kondo, M.; Yoshitomi, T.; Seki, K.; Matsuzaka, H.; Kitagawa, S. *Angew. Chem., Int. Ed. Engl* **1997**, *36*, 1725.
(1168) Millward, A. R.; Yaghi, O. M. *J. Am. Chem. Soc.* **2005**, *127*, 17998.
(1169) Sun, D. F.; Ma, S. Q.; Ke, Y. X.; Collins, D. J.; Zhou, H. C. *J. Am. Chem. Soc.* **2006**, *128*, 3896.
(1170) Li, Y. W.; Yang, R. T. *J. Am. Chem. Soc.* **2006**, *128*, 726.
(1171) Dinca, M.; Dailly, A.; Liu, Y.; Brown, C. M.; Neumann, D. A.; Long, J. R. *J. Am. Chem. Soc.* **2006**, *128*, 16876.
(1172) Forster, P. M.; Eckert, J.; Heiken, B. D.; Parise, J. B.; Yoon, J. W.; Jhung, S. H.; Chang, J. S.; Cheetham, A. K. *J. Am. Chem. Soc.* **2006**, *128*, 16846.
(1173) Dietzel, P. D. C.; Johnsen, R. E.; Fjellvag, H.; Bordiga, S.; Groppo, E.; Chavan, S.; Blom, R. *Chem. Commun.* **2008**, 5125.
(1174) Vitillo, J. G.; Regli, L.; Chavan, S.; Ricchiardi, G.; Spoto, G.; Dietzel, P. D. C.; Bordiga, S.; Zecchina, A. *J. Am. Chem. Soc.* **2008**, *130*, 8386.
(1175) Ma, S. Q.; Sun, D. F.; Simmons, J. M.; Collier, C. D.; Yuan, D. Q.; Zhou, H. C. *J. Am. Chem. Soc.* **2008**, *130*, 1012.
(1176) Nelson, A. P.; Farha, O. K.; Mulfort, K. L.; Hupp, J. T. *J. Am. Chem. Soc.* **2009**, *131*, 458.
(1177) Murray, L. J.; Dinca, M.; Long, J. R. *Chem. Soc. Rev.* **2009**, *38*, 1294.

(1178) Han, S. S.; Mendoza-Cortes, J. L.; Goddard, W. A. *Chem. Soc. Rev.* **2009**, *38*, 1460.
(1179) Hu, Y. H.; Zhang, L. *Adv. Mater.* **2010**, *22*, E117.
(1180) D'Alessandro, D. M.; Smit, B.; Long, J. R. *Angew. Chem., Int. Ed.* **2010**, *49*, 6058.
(1181) Sumida, K.; Horike, S.; Kaye, S. S.; Herm, Z. R.; Queen, W. L.; Brown, C. M.; Grandjean, F.; Long, G. J.; Dailly, A.; Long, J. R. *Chem. Sci.* **2010**, *1*, 184.
(1182) Sumida, K.; Brown, C. M.; Herm, Z. R.; Chavan, S.; Bordiga, S.; Long, J. R. *Chem. Commun.* **2011**, *47*, 1157.
(1183) Getman, R. B.; Bae, Y. S.; Wilmer, C. E.; Snurr, R. Q. *Chem. Rev.* **2012**, *112*, 703.
(1184) Sumida, K.; Rogow, D. L.; Mason, J. A.; McDonald, T. M.; Bloch, E. D.; Herm, Z. R.; Bae, T. H.; Long, J. R. *Chem. Rev.* **2012**, *112*, 724.
(1185) Suh, M. P.; Park, H. J.; Prasad, T. K.; Lim, D. W. *Chem. Rev.* **2012**, *112*, 782.
(1186) Wu, H. H.; Gong, Q. H.; Olson, D. H.; Li, J. *Chem. Rev.* **2012**, *112*, 836.
(1187) Xiao, B.; Wheatley, P. S.; Zhao, X. B.; Fletcher, A. J.; Fox, S.; Rossi, A. G.; Megson, I. L.; Bordiga, S.; Regli, L.; Thomas, K. M.; Morris, R. E. *J. Am. Chem. Soc.* **2007**, *129*, 1203.
(1188) Horcajada, P.; Chalati, T.; Serre, C.; Gillet, B.; Sebrie, C.; Baati, T.; Eubank, J. F.; Heurtaux, D.; Clayette, P.; Kreuz, C.; Chang, J. S.; Hwang, Y. K.; Marsaud, V.; Bories, P. N.; Cynober, L.; Gil, S.; Ferey, G.; Couvreur, P.; Gref, R. *Nat. Mater.* **2010**, *9*, 172.
(1189) Horcajada, P.; Gref, R.; Baati, T.; Allan, P. K.; Maurin, G.; Couvreur, P.; Ferey, G.; Morris, R. E.; Serre, C. *Chem. Rev.* **2012**, *112*, 1232.
(1190) Bunzli, J. C. G.; Piguet, C. *Chem. Rev.* **2002**, *102*, 1897.
(1191) Serre, C.; Millange, F.; Thouvenot, C.; Gardant, N.; Pelle, F.; Ferey, G. *J. Mater. Chem.* **2004**, *14*, 1540.
(1192) Imbert, D.; Comby, S.; Chauvin, A. S.; Bunzli, J. C. G. *Chem. Commun.* **2005**, 1432.
(1193) Bordiga, S.; Lamberti, C.; Ricchiardi, G.; Regli, L.; Bonino, F.; Damin, A.; Lillerud, K. P.; Bjorgen, M.; Zecchina, A. *Chem. Commun.* **2004**, 2300.
(1194) Allendorf, M. D.; Bauer, C. A.; Bhakta, R. K.; Houk, R. J. T. *Chem. Soc. Rev.* **2009**, *38*, 1330.
(1195) Wang, C.; Zhang, T.; Lin, W. B. *Chem. Rev.* **2012**, *112*, 1084.
(1196) Cui, Y. J.; Yue, Y. F.; Qian, G. D.; Chen, B. L. *Chem. Rev.* **2012**, *112*, 1126.
(1197) Maspoch, D.; Ruiz-Molina, D.; Wurst, K.; Domingo, N.; Cavallini, M.; Biscarini, F.; Tejada, J.; Rovira, C.; Veciana, J. *Nat. Mater.* **2003**, *2*, 190.
(1198) Maspoch, D.; Domingo, N.; Molina, D. R.; Wurst, K.; Hernandez, J. M.; Vaughan, G.; Rovira, C.; Lloret, F.; Tejada, J.; Veciana, J. *Chem. Commun.* **2005**, 5035.
(1199) Kurmoo, M. *Chem. Soc. Rev.* **2009**, *38*, 1353.
(1200) Zhang, W.; Xiong, R. G. *Chem. Rev.* **2012**, *112*, 1163.
(1201) Ferey, G.; Millange, F.; Morcrette, M.; Serre, C.; Doublet, M. L.; Greneche, J. M.; Tarascon, J. M. *Angew. Chem., Int. Ed.* **2007**, *46*, 3259.
(1202) Silva, C. G.; Corma, A.; Garcia, H. *J. Mater. Chem.* **2010**, *20*, 3141.
(1203) Qiu, S. L.; Zhu, G. S. *Coord. Chem. Rev.* **2009**, *253*, 2891.
(1204) Xie, Z. G.; Ma, L. Q.; deKrafft, K. E.; Jin, A.; Lin, W. B. *J. Am. Chem. Soc.* **2010**, *132*, 922.
(1205) Forster, P. M.; Cheetham, A. K. *Top. Catal* **2003**, *24*, 79.
(1206) Kesanli, B.; Lin, W. B. *Coord. Chem. Rev.* **2003**, *246*, 305.
(1207) Schlichte, K.; Kratzke, T.; Kaskel, S. *Microporous Mesoporous Mater.* **2004**, *73*, 81.
(1208) Wu, C. D.; Hu, A.; Zhang, L.; Lin, W. B. *J. Am. Chem. Soc.* **2005**, *127*, 8940.
(1209) Hermes, S.; Schröter, M.-K.; Schmid, R.; Khodeir, L.; Muhler, M.; Tissler, A.; Fischer, R. W.; Fischer, R. A. *Angew. Chem., Int. Ed.* **2005**, *44*, 6237.
(1210) Dybtsev, D. N.; Nuzhdin, A. L.; Chun, H.; Bryliakov, K. P.; Talsi, E. P.; Fedin, V. P.; Kim, K. *A Angew. Chem., Int. Ed.* **2006**, *45*, 916.
(1211) Llabrés i Xamena, F. X.; Abad, A.; Corma, A.; Garcia, H. *J. Catal.* **2007**, *250*, 294.
(1212) Xiao, B.; Hou, H. W.; Fan, Y. T. *J. Organomet. Chem.* **2007**, *692*, 2014.
(1213) Goto, Y.; Sato, H.; Shinkai, S.; Sada, K. *J. Am. Chem. Soc.* **2008**, *130*, 14354.
(1214) Proch, S.; Herrmannsdorfer, J.; Kempe, R.; Kern, C.; Jess, A.; Seyfarth, L.; Senker, J. *Chem.—Eur. J.* **2008**, *14*, 8204.
(1215) Horike, S.; Dinca, M.; Tamaki, K.; Long, J. R. *J. Am. Chem. Soc.* **2008**, *130*, 5854.
(1216) Savonnet, M.; Aguado, S.; Ravon, U.; Bazer-Bachi, D.; Lecocq, V.; Bats, N.; Pinel, C.; Farrusseng, D. *Green Chem.* **2009**, *11*, 1729.
(1217) Das, S.; Kim, H.; Kim, K. *J. Am. Chem. Soc.* **2009**, *131*, 3814.
(1218) Gascon, J.; Aktay, U.; Hernandez-Alonso, M. D.; van Klink, G. P. M.; Kapteijn, F. *J. Catal.* **2009**, *261*, 75.
(1219) Jiang, D. M.; Urakawa, A.; Yulikov, M.; Mallat, T.; Jeschke, G.; Baiker, A. *Chem.—Eur. J* **2009**, *15*, 12255.
(1220) Lee, J.; Farha, O. K.; Roberts, J.; Scheidt, K. A.; Nguyen, S. T.; Hupp, J. T. *Chem. Soc. Rev.* **2009**, *38*, 1450.
(1221) Shultz, A. M.; Farha, O. K.; Hupp, J. T.; Nguyen, S. T. *J. Am. Chem. Soc.* **2009**, *131*, 4204.
(1222) Ma, L.; Abney, C.; Lin, W. *Chem. Soc. Rev.* **2009**, *38*, 1248.
(1223) Corma, A.; Garcıa, H.; Llabres i Xamena, F. X. *Chem. Rev.* **2010**, *110*, 4606.
(1224) Juan-Alcaniz, J.; Ramos-Fernandez, E. V.; Lafont, U.; Gascon, J.; Kapteijn, F. *J. Catal.* **2010**, *269*, 229.
(1225) Jiang, D. M.; Mallat, T.; Meier, D. M.; Urakawa, A.; Baiker, A. *J. Catal.* **2010**, *270*, 26.
(1226) Luz, I.; Xamena, F.; Corma, A. *J. Catal.* **2010**, *276*, 134.
(1227) Gao, S. X.; Zhao, N.; Shu, M. H.; Che, S. N. *Appl. Catal., A* **2010**, *388*, 196.
(1228) Song, F. J.; Wang, C.; Falkowski, J. M.; Ma, L. Q.; Lin, W. B. *J. Am. Chem. Soc.* **2010**, *132*, 15390.
(1229) Dhakshinamoorthy, A.; Alvaro, M.; Garcia, H. *Adv. Synth. Catal.* **2010**, *352*, 3022.
(1230) Dang, D. B.; Wu, P. Y.; He, C.; Xie, Z.; Duan, C. Y. *J. Am. Chem. Soc.* **2010**, *132*, 14321.
(1231) Liu, Y.; Xuan, W. M.; Cui, Y. *Adv. Mater.* **2010**, *22*, 4112.
(1232) Li, Y. Q.; Song, P.; Zheng, J.; Li, X. G. *Chem.—Eur. J* **2010**, *16*, 10887.
(1233) Liu, H. L.; Liu, Y. L.; Li, Y. W.; Tang, Z. Y.; Jiang, H. F. *J. Phys. Chem. C* **2010**, *114*, 13362.
(1234) Makiura, R.; Motoyama, S.; Umemura, Y.; Yamanaka, H.; Sakata, O.; Kitagawa, H. *Nat. Mater.* **2010**, *9*, 565.
(1235) Lillerud, K. P.; Olsbye, U.; Tilset, M. *Top. Catal.* **2010**, *53*, 859.
(1236) Oxford, G. A. E.; Dubbeldam, D.; Broadbelt, L. J.; Snurr, R. Q. *J. Mol. Catal. A: Chem.* **2011**, *334*, 89.
(1237) Vermoortele, F.; Ameloot, R.; Vimont, A.; Serre, C.; De Vos, D. *Chem. Commun.* **2011**, *47*, 1521.
(1238) Ranocchiari, M.; van Bokhoven, J. A. *Phys. Chem. Chem. Phys.* **2011**, *13*, 6388.
(1239) Yoon, M.; Srirambalaji, R.; Kim, K. *Chem. Rev.* **2012**, *112*, 1196.
(1240) Silva, C. G.; Luz, I.; Llabres i Xamena, F. X.; Corma, A.; Garcia, H. *Chem.—Eur. J.* **2010**, *16*, 11133.
(1241) Kamegawa, T.; Sakai, T.; Matsuoka, M.; Anpo, M. *J. Am. Chem. Soc.* **2005**, *127*, 16784.
(1242) Dathe, H.; Peringer, E.; Roberts, V.; Jentys, A.; Lercher, J. A. *C. R. Chim.* **2005**, *8*, 753.
(1243) Dathe, H.; Jentys, A.; Lercher, J. A. *Phys. Chem. Chem. Phys.* **2005**, *7*, 1283.
(1244) Dathe, H.; Jentys, A.; Lercher, J. A. *Stud. Surf. Sci. Catal.* **2005**, *158*, 995.

(1245) Szeto, K. C.; Lillerud, K. P.; Tilset, M.; Bjorgen, M.; Prestipino, C.; Zecchina, A.; Lamberti, C.; Bordiga, S. *J. Phys. Chem. B* **2006**, *110*, 21509.
(1246) Szeto, K. C.; Prestipino, C.; Lamberti, C.; Zecchina, A.; Bordiga, S.; Bjorgen, M.; Tilset, M.; Lillerud, K. P. *Chem. Mater.* **2007**, *19*, 211.
(1247) Szeto, K. C.; Kongshaug, K. O.; Jakobsen, S.; Tilset, M.; Lillerud, K. P. *Dalton Trans.* **2008**, 2054.
(1248) Kaye, S. S.; Long, J. R. *J. Am. Chem. Soc.* **2008**, *130*, 806.
(1249) Tanabe, K. K.; Wang, Z. Q.; Cohen, S. M. *J. Am. Chem. Soc.* **2008**, *130*, 8508.
(1250) Morris, W.; Doonan, C. J.; Furukawa, H.; Banerjee, R.; Yaghi, O. M. *J. Am. Chem. Soc.* **2008**, *130*, 12626.
(1251) Doonan, C. J.; Morris, W.; Furukawa, H.; Yaghi, O. M. *J. Am. Chem. Soc.* **2009**, *131*, 9492.
(1252) Yamada, T.; Kitagawa, H. *J. Am. Chem. Soc.* **2009**, *131*, 6312.
(1253) Gadzikwa, T.; Farha, O. K.; Mulfort, K. L.; Hupp, J. T.; Nguyen, S. T. *Chem. Commun.* **2009**, 3720.
(1254) Ingleson, M. J.; Heck, R.; Gould, J. A.; Rosseinsky, M. J. *Inorg. Chem.* **2009**, *48*, 9986.
(1255) Gadzikwa, T.; Farha, O. K.; Malliakas, C. D.; Kanatzidis, M. G.; Hupp, J. T.; Nguyen, S. T. *J. Am. Chem. Soc.* **2009**, *131*, 13613.
(1256) Ingleson, M. J.; Barrio, J. P.; Guilbaud, J. B.; Khimyak, Y. Z.; Rosseinsky, M. J. *Chem. Commun.* **2008**, 2680.
(1257) Hong, D. Y.; Hwang, Y. K.; Serre, C.; Ferey, G.; Chang, J. S. *Adv. Funct. Mater.* **2009**, *19*, 1537.
(1258) Wang, Z.; Cohen, S. M. *Chem. Soc. Rev.* **2009**, *38*, 1315.
(1259) Chavan, S.; Vitillo, J. G.; Uddin, M. J.; Bonino, F.; Lamberti, C.; Groppo, E.; Lillerud, K. P.; Bordiga, S. *Chem. Mater.* **2010**, *22*, 4602.
(1260) Deng, H. X.; Doonan, C. J.; Furukawa, H.; Ferreira, R. B.; Towne, J.; Knobler, C. B.; Wang, B.; Yaghi, O. M. *Science* **2010**, *327*, 846.
(1261) Chen, B. L.; Xiang, S. C.; Qian, G. D. *Acc. Chem. Res.* **2010**, *43*, 1115.
(1262) Kandiah, M.; Usseglio, S.; Svelle, S.; Olsbye, U.; Lillerud, K. P.; Tilset, M. *J. Mater. Chem.* **2010**, *20*, 9848.
(1263) Garibay, S. J.; Cohen, S. M. *Chem. Commun.* **2010**, *46*, 7700.
(1264) Tanabe, K. K.; Cohen, S. M. *Chem. Soc. Rev.* **2011**, *40*, 498.
(1265) Shekhah, O.; Liu, J.; Fischer, R. A.; Woll, C. *Chem. Soc. Rev.* **2011**, *40*, 1081.
(1266) Cohen, S. M. *Chem. Rev.* **2012**, *112*, 970.
(1267) Ferey, G.; Serre, C. *Chem. Soc. Rev.* **2009**, *38*, 1380.
(1268) Stock, N.; Biswas, S. *Chem. Rev.* **2012**, *112*, 933.
(1269) Kitagawa, H.; Nagao, Y.; Fujishima, M.; Ikeda, R.; Kanda, S. *Inorg. Chem. Commun.* **2003**, *6*, 346.
(1270) Surble, S.; Millange, F.; Serre, C.; Ferey, G.; Walton, R. I. *Chem. Commun.* **2006**, 1518.
(1271) Prestipino, C.; Regli, L.; Vitillo, J. G.; Bonino, F.; Damin, A.; Lamberti, C.; Zecchina, A.; Solari, P. L.; Kongshaug, K. O.; Bordiga, S. *Chem. Mater.* **2006**, *18*, 1337.
(1272) Hafizovic, J.; Bjorgen, M.; Olsbye, U.; Dietzel, P. D. C.; Bordiga, S.; Prestipino, C.; Lamberti, C.; Lillerud, K. P. *J. Am. Chem. Soc.* **2007**, *129*, 3612.
(1273) Bonino, F.; Chavan, S.; Vitillo, J. G.; Groppo, E.; Agostini, G.; Lamberti, C.; Dietzel, P. D. C.; Prestipino, C.; Bordiga, S. *Chem. Mater.* **2008**, *20*, 4957.
(1274) Chavan, S.; Vitillo, J. G.; Groppo, E.; Bonino, F.; Lamberti, C.; Dietzel, P. D. C.; Bordiga, S. *J. Phys. Chem. C* **2009**, *113*, 3292.
(1275) Chavan, S.; Bonino, F.; Vitillo, J. G.; Groppo, E.; Lamberti, C.; Dietzel, P. D. C.; Zecchina, A.; Bordiga, S. *Phys. Chem. Chem. Phys.* **2009**, *11*, 9811.
(1276) Seredyuk, M.; Gaspar, A. B.; Ksenofontov, V.; Verdaguer, M.; Villain, F.; Gutlich, P. *Inorg. Chem.* **2009**, *48*, 6130.
(1277) de Combarieu, G.; Hamelet, S.; Millange, F.; Morcrette, M.; Tarascon, J. M.; Ferey, G.; Walton, R. I. *Electrochem. Commun.* **2009**, *11*, 1881.
(1278) Masciocchi, N.; Galli, S.; Colombo, V.; Maspero, A.; Palmisano, G.; Seyyedi, B.; Lamberti, C.; Bordiga, S. *J. Am. Chem. Soc.* **2010**, *132*, 7902.
(1279) Gross, S.; Bauer, M. *Adv. Funct. Mater.* **2010**, *20*, 4026.
(1280) Rossin, A.; Di Credico, B.; Giambastiani, G.; Peruzzini, M.; Pescitelli, G.; Reginato, G.; Borfecchia, E.; Gianolio, D.; Lamberti, C.; Bordiga, S. *J. Mater. Chem.* **2012**, *22*, 10335.
(1281) Jakobsen, S.; Gianolio, D.; Wragg, D. S.; Nilsen, M. H.; Emerich, H.; Bordiga, S.; Lamberti, C.; Olsbye, U.; Tilset, M.; Lillerud, K. P. *Phys. Rev. B* **2012**, *86*, No. 125429.
(1282) Borfecchia, E.; Maurelli, S.; Gianolio, D.; Groppo, E.; Chiesa, M.; Bonino, F.; Lamberti, C. *J. Phys. Chem. C* **2012**, *116*, 19839.
(1283) Chui, S. S. Y.; Lo, S. M. F.; Charmant, J. P. H.; Orpen, A. G.; Williams, I. D. *Science* **1999**, *283*, 1148.
(1284) Vishnyakov, A.; Ravikovitch, P. I.; Neimark, A. V.; Bulow, M.; Wang, Q. M. *Nano Lett.* **2003**, *3*, 713.
(1285) Peterson, V. K.; Liu, Y.; Brown, C. M.; Kepert, C. J. *J. Am. Chem. Soc.* **2006**, *128*, 15578.
(1286) Bordiga, S.; Regli, L.; Bonino, F.; Groppo, E.; Lamberti, C.; Xiao, B.; Wheatley, P. S.; Morris, R. E.; Zecchina, A. *Phys. Chem. Chem. Phys.* **2007**, *9*, 2676.
(1287) Corma, A.; Iglesias, M.; Xamena, F.; Sanchez, F. *Chem.—Eur. J* **2010**, *16*, 9789.
(1288) Wang, Q. M.; Shen, D. M.; Bulow, M.; Lau, M. L.; Deng, S. G.; Fitch, F. R.; Lemcoff, N. O.; Semanscin, J. *Microporous Mesoporous Mater.* **2002**, *55*, 217.
(1289) Hadjiivanov, K.; Knozinger, H. *J. Catal.* **2000**, *191*, 480.
(1290) Murray, L. J.; Dinca, M.; Yano, J.; Chavan, S.; Bordiga, S.; Brown, C. M.; Long, J. R. *J. Am. Chem. Soc.* **2010**, *132*, 7856.
(1291) Cotton, F. A.; Hillard, E. A.; Murillo, C. A.; Zhou, H. C. *J. Am. Chem. Soc.* **2000**, *122*, 416.
(1292) Tromp, M.; aoulin, J.; Reid, G.; Evans, J. *AIP Conf. Proc.* **2007**, *882*, 699.
(1293) Farges, F. *Phys. Chem. Miner.* **2009**, *36*, 463.
(1294) The centroid of a XANES peak is the energy of the baricenter of the peak (E_B), it is so defined as $E_B = \Sigma(I_i \times E_i)/\Sigma(I_i)$, where I_i is the intensity of the XANES pek at the energy of E_i, and where the sums run over all the sampled points.
(1295) Gallo, E.; Glatzel, P.; Long, J. R.; Bordiga, S.; Lamberti, C.; et al.et al.Unpublished work.
(1296) Bergmann, U.; Horne, C. R.; Collins, T. J.; Workman, J. M.; Cramer, S. P. *Chem. Phys. Lett.* **1999**, *302*, 119.
(1297) Eeckhout, S. G.; Safonova, O. V.; Smolentsev, G.; Biasioli, M.; Safonov, V. A.; Vykhodtseva, L. N.; Sikora, M.; Glatzel, P. *J. Anal. At. Spectrom.* **2009**, *24*, 215.
(1298) Dietzel, P. D. C.; Panella, B.; Hirscher, M.; Blom, R.; Fjellvag, H. *Chem. Commun.* **2006**, 959.
(1299) Rosi, N. L.; Kim, J.; Eddaoudi, M.; Chen, B. L.; O'Keeffe, M.; Yaghi, O. M. *J. Am. Chem. Soc.* **2005**, *127*, 1504.
(1300) Dietzel, P. D. C.; Morita, Y.; Blom, R.; Fjellvag, H. *Angew. Chem., Int. Ed.* **2005**, *44*, 6354.
(1301) Dietzel, P. D. C.; Johnsen, R. E.; Blom, R.; Fjellvåg, H. *Chem.—Eur. J.* **2008**, *14*, 2389.
(1302) Valenzano, L.; Civalleri, B.; Chavan, S.; Palomino, G. T.; Arean, C. O.; Bordiga, S. *J. Phys. Chem. C* **2010**, *114*, 11185.
(1303) Valenzano, L.; Civalleri, B.; Sillar, K.; Sauer, J. *J. Phys. Chem. C* **2011**, *115*, 21777.
(1304) Valenzano, L.; Vitillo, J. G.; Chavan, S.; Civalleri, B.; Bonino, F.; Bordiga, S.; Lamberti, C. *Catal. Today* **2012**, *182*, 67.
(1305) Dietzel, P. D. C.; Besikiotis, V.; Blom, R. *J. Mater. Chem.* **2009**, *19*, 7362.
(1306) Rowsell, J. L. C.; Spencer, E. C.; Eckert, J.; Howard, J. A. K.; Yaghi, O. M. *Science* **2005**, *309*, 1350.
(1307) Zhou, W.; Wu, H.; Yildirim, T.; Simpson, J. R.; Walker, A. R. H. *Phys. Rev. B* **2008**, *78*, No. 054114.
(1308) Lock, N.; Wu, Y.; Christensen, M.; Cameron, L. J.; Peterson, V. K.; Bridgeman, A. J.; Kepert, C. J.; Iversen, B. B. *J. Phys. Chem. C* **2010**, *114*, 16181.

(1309) Dubbeldam, D.; Walton, K. S.; Ellis, D. E.; Snurr, R. Q. *Angew. Chem., Int. Ed.* **2007**, *46*, 4496.
(1310) Han, S. S.; Goddard, W. A. *J. Phys. Chem. C* **2007**, *111*, 15185.
(1311) Greathouse, J. A.; Allendorf, M. D. *J. Phys. Chem. C* **2008**, *112*, 5795.
(1312) Tafipolsky, M.; Amirjalayer, S.; Schmid, R. *J. Phys. Chem. C* **2010**, *114*, 14402.
(1313) Amirjalayer, S.; Tafipolsky, M.; Schmid, R. *J. Phys. Chem. C* **2011**, *115*, 15133.
(1314) Hogan, J. P.; Banks, R. L. U.S. Patent 2,825,721, 1958.
(1315) McDaniel, M. P. *Adv. Catal.* **2010**, *53*, 123.
(1316) Groppo, E.; Prestipino, C.; Cesano, F.; Bonino, F.; Bordiga, S.; Lamberti, C.; Thüne, P. C.; Niemantsverdriet, J. W.; Zecchina, A. *J. Catal.* **2005**, *230*, 98.
(1317) Groppo, E. Structure and Reactivity of the Active Centres on the Cr/SiO_2 Phillips Catalyst: A Challenge for Characterization Methods. Department of Inorganic, Physical and Materials Chemistry, Turin, Italy, 2005.
(1318) Zecchina, A.; Garrone, E.; Ghiotti, G.; Coluccia, S. *J. Phys. Chem.* **1975**, *79*, 972.
(1319) Weckhuysen, B. M.; Wachs, I. E.; Shoonheydt, R. A. *Chem. Rev.* **1996**, *96*, 3327.
(1320) Zecchina, A.; Scarano, D.; Bordiga, S.; Spoto, G.; Lamberti, C. *Adv. Catal.* **2001**, *46*, 265.
(1321) Ziegler, K. Belgian Patent 533,362, 1954.
(1322) Ziegler, K.; Holzkamp, E.; Martin, H.; Breil, H. *Angew. Chem.* **1955**, *67*, 541.
(1323) Natta, G. *J. Polym. Sci.* **1955**, *16*, 143.
(1324) Natta, G. *Angew. Chem.* **1956**, *68*, 393.
(1325) Kissin, Y. V. *Isospecific Polymerization of Olefins with Heterogeneous Ziegler–Natta Catalysts*; Springer-Verlag: New York, 1985.
(1326) Böhm, L. L. *Angew. Chem., Int. Ed.* **2003**, *42*, 5010.
(1327) Wilke, G. *Angew. Chem., Int. Ed.* **2003**, *42*, 5000.
(1328) Theopold, K. H. *Eur. J. Inorg. Chem.* **1998**, 15.
(1329) Brintzinger, H. H.; Fischer, D.; Mulhaupt, R.; Rieger, B.; Waymouth, R. M. *Angew. Chem., Int. Ed.* **1995**, *34*, 1143.
(1330) Lamberti, C.; Groppo, E.; Spoto, G.; Bordiga, S.; Zecchina, A. *Adv. Catal.* **2007**, *51*, 1.
(1331) Pantelouris, A.; Modrovw, H.; Pantelouris, M.; Hormes, J.; Reinen, D. *Chem. Phys.* **2004**, *300*, 13.
(1332) Jousseaume, C.; Vivien, D.; Kahn-Harari, A.; Derouet, J.; Ribot, F.; Villain, F. *J. Appl. Phys.* **2003**, *93*, 6006.
(1333) Jousseaume, C.; Ribot, F.; Kahn-Harari, A.; Vivien, D.; Villain, F. *Nucl. Instrum. Methods Phys. Res., Sect. B* **2003**, *200*, 425.
(1334) Arcon, I.; Mirtic, B.; Kodre, A. *J. Am. Chem. Soc.* **1998**, *81*, 222.
(1335) Juhin, A.; Calas, G.; Cabaret, D.; Galoisy, L.; Hazemann, J. L. *Phys. Rev. B* **2007**, *76*, No. 054105.
(1336) Garcia, L.; Benfatto, M.; Natoli, C. R.; Bianconi, A.; Davoli, I.; Marcelli, A. *Solid. State Commun.* **1986**, *58*, 595.
(1337) Wang, Y.; Ohishi, Y.; Shishido, T.; Zhang, Q. H.; Yang, W.; Guo, Q.; Wan, H. L.; Takehira, K. *J. Catal.* **2003**, *220*, 347.
(1338) Pak, C.; Haller, G. L. *Microporous Mesoporous Mater.* **2001**, *48*, 165.
(1339) (a) Demmelmaier, C. A.; White, R. E.; van Bokhoven, J. A.; Scott, S. L. *J. Phys. Chem. C* **2008**, *112*, 6439. (b) Zhong, L.; Lee, M. Y.; Liu, Z.; Wanglee, Y. J.; Liu, B. P.; Scott, S. L. *J. Catal.* **2012**, *293*, 1.
(1340) Scarano, D.; Spoto, G.; Bordiga, S.; Carnelli, L.; Ricchiardi, G.; Zecchina, A. *Langmuir* **1994**, *10*, 3094.
(1341) Weckhuysen, B. M.; Verberckmoes, A. A.; DeBaets, A. R.; Schoonheydt, R. A. *J. Catal.* **1997**, *166*, 160.
(1342) Thune, P. C.; Linke, R.; van Gennip, W. J. H.; de Jong, A. M.; Niemantsverdriet, J. W. *J. Phys. Chem. B* **2001**, *105*, 3073.
(1343) Thune, P. C.; Verhagen, C. P. J.; vandenBoer, M. J. G.; Niemantsverdriet, J. W. *J. Phys. Chem. B* **1997**, *101*, 8559.
(1344) Vuurman, M. A.; Wachs, I. E.; Stufkens, D. J.; Oskam, A. *J. Mol. Catal.* **1993**, *80*, 209.
(1345) Frenkel, A. I.; Kleifeld, O.; Wasserman, S. R.; Sagi, I. *J. Chem. Phys.* **2002**, *116*, 9449.
(1346) Prestipino, C.; Bordiga, S.; Lamberti, C.; Vidotto, S.; Garilli, M.; Cremaschi, B.; Marsella, A.; Leofanti, G.; Fisicaro, P.; Spoto, G.; Zecchina, A. *J. Phys. Chem. B* **2003**, *107*, 5022.
(1347) Le Toquin, R.; Paulus, W.; Cousson, A.; Prestipino, C.; Lamberti, C. *J. Am. Chem. Soc.* **2006**, *128*, 13161.
(1348) Muddada, N. B.; Olsbye, U.; Leofanti, G.; Gianolio, D.; Bonino, F.; Bordiga, S.; Fuglerud, T.; Vidotto, S.; Marsella, A.; Lamberti, C. *Dalton Trans.* **2010**, *39*, 8437.
(1349) Fubini, B.; Ghiotti, G.; Stradella, L.; Garrone, E.; Morterra, C. *J. Catal.* **1980**, *66*, 200.
(1350) Weckhuysen, B. M.; Deridder, L. M.; Schoonheydt, R. A. *J. Phys. Chem.* **1993**, *97*, 4756.
(1351) Weckhuysen, B. M.; Verberckmoes, A. A.; Buttiens, A. L.; Schoonheydt, R. A. *J. Phys. Chem.* **1994**, *98*, 579.
(1352) Weckhuysen, B. M.; Deridder, L. M.; Grobet, P. J.; Schoonheydt, R. A. *J. Phys. Chem.* **1995**, *99*, 320.
(1353) Hercules, D. M.; Proctor, A.; Houalla, M. *Acc. Chem. Res.* **1994**, *27*, 387.
(1354) Myers, D. L.; Lunsford, J. H. *J. Catal.* **1985**, *92*, 260.
(1355) Myers, D. L.; Lunsford, J. H. *J. Catal.* **1986**, *99*, 140.
(1356) Kantcheva, M.; Bushev, V.; Klissurski, D. *J. Catal.* **1994**, *145*, 96.
(1357) Groppo, E.; Lamberti, C.; Cesano, F.; Zecchina, A. *Phys. Chem. Chem. Phys.* **2006**, *8*, 2453.
(1358) Espelid, O.; Borve, K. J. *J. Catal.* **2002**, *205*, 366.
(1359) Lupinetti, A. J.; Frenking, G.; Strauss, S. H. *Angew. Chem., Int. Edit* **1998**, *37*, 2113.
(1360) Lupinetti, A. J.; Strauss, S. H.; Frenking, G. *Prog. Inorg. Chem.* **2001**, *49*, 1.
(1361) Damin, A.; Bonino, F.; Bordiga, S.; Groppo, E.; Lamberti, C.; Zecchina, A. *ChemPhysChem* **2006**, *7*, 342.
(1362) Engemann, C.; Hormes, J.; Longen, A.; Dotz, K. H. *Chem. Phys.* **1998**, *237*, 471.
(1363) Damin, A.; Vitillo, J. G.; Ricchiardi, G.; Bordiga, S.; Lamberti, C.; Groppo, E.; Zecchina, A. *J. Phys. Chem. A* **2009**, *113*, 14261.
(1364) Macdowell, A. A.; Norman, D.; West, J. B.; Campuzano, J. C.; Jones, R. G. *Nucl. Instrum. Methods Phys. Res., Sect. A* **1986**, *246*, 131.
(1365) Macdowell, A. A.; Norman, D.; West, J. B. *Rev. Sci. Instrum.* **1986**, *57*, 2667.
(1366) Jiang, D. T.; Alberding, N.; Seary, A. J.; Crozier, E. D. *Rev. Sci. Instrum.* **1988**, *59*, 60.
(1367) Macdowell, A. A.; Hashizume, T.; Citrin, P. H. *Rev. Sci. Instrum.* **1989**, *60*, 1901.
(1368) Mythen, C. S.; Vanderlaan, G.; Padmore, H. A. *Rev. Sci. Instrum.* **1992**, *63*, 1313.
(1369) Heald, S. M. *Rev. Sci. Instrum.* **1992**, *63*, 873.
(1370) Smith, A. D.; Roper, M. D.; Padmore, H. A. *Nucl. Instrum. Methods Phys. Res., Sect. B* **1995**, *97*, 579.
(1371) Baudoing-Savois, R.; De Santis, M.; Saint-Lager, M. C.; Dolle, P.; Geaymond, O.; Taunier, P.; Jeantet, P.; Roux, J. P.; Renaud, G.; Barbier, A.; Robach, O.; Ulrich, O.; Mougin, A.; Berard, G. *Nucl. Instrum. Methods Phys. Res., Sect. B* **1999**, *149*, 213.
(1372) Lopez-Flores, V.; Ansell, S.; Bowron, D. T.; Diaz-Moreno, S.; Ramos, S.; Munoz-Paez, A. *Rev. Sci. Instrum.* **2007**, *78*, No. 013109.
(1373) Benzi, F.; Davoli, I.; Rovezzi, M.; d'Acapito, F. *Rev. Sci. Instrum.* **2008**, *79*, No. 103902.
(1374) Citrin, P. H. *J. Phys. (Paris)* **1986**, *47*, 437.
(1375) Abruna, H. D. *Adv. Chem. Phys.* **1990**, *77*, 255.
(1376) Haase, J. *J. Chem. Soc., Faraday Trans.* **1996**, *92*, 1653.
(1377) D'Acapito, F. Introduction to the ReflEXAFS Technique. In *Synchrotron Radiation: Fundamentals, Methodologies and Applications*; Mobilio, S., Vlaic, G., Ed.; Italian Physical Society (SIF): Bologna, Italy, 2003; Vol. *82*, p 191.
(1378) Atrei, A.; Johnson, A. L.; King, D. A. *Surf. Sci.* **1991**, *254*, 65.
(1379) Adler, D. L.; Collins, I. R.; Liang, X.; Murray, S. J.; Leatherman, G. S.; Tsuei, K. D.; Chaban, E. E.; Chandavarkar, S.; McGrath, R.; Diehl, R. D.; Citrin, P. H. *Phys. Rev. B* **1993**, *48*, 17445.

(1380) Fernandez, A.; Espinos, J. P.; Gonzalezelipe, A. R.; Kerkar, M.; Thompson, P. B. J.; Ludecke, J.; Scragg, G.; Decarvalho, A. V.; Woodruff, D. P.; Fernandezgarcia, M.; Conesa, J. C. *J. Phys.: Condens. Matter* **1995**, *7*, 7781.
(1381) D'Acapito, F.; Mobilio, S.; Cikmacs, P.; Merlo, V.; Davoli, I. *Surf. Sci.* **2000**, *468*, 77.
(1382) Srivastava, P.; Baberschke, K. *Top. Catal* **2000**, *10*, 199.
(1383) Battocchio, C.; Fratoddi, I.; Venditti, I.; Yarzhemsky, V. G.; Norov, Y. V.; Russo, M. V.; Polzonetti, G. *Chem. Phys.* **2011**, *379*, 92.
(1384) Gota, S.; GautierSoyer, M.; Douillard, L.; Duraud, J. P.; LeFevre, P. *Surf. Sci.* **1996**, *352*, 1016.
(1385) Bourgeois, S.; LeSeigneur, P.; Perdereau, M.; Chandesris, D.; LeFevre, P.; Magnan, H. *Thin Solid Films* **1997**, *304*, 267.
(1386) Harte, S. P.; Woodhead, A. P.; Vinton, S.; Evans, T.; Haycock, S. A.; Muryn, C. A.; Wincott, P. L.; Dhanak, V. R.; Marsden, C. E.; Thornton, G. *Surf. Sci.* **1999**, *424*, 179.
(1387) Blesa, M. A.; Weisz, A. D.; Morando, P. J.; Salfity, J. A.; Magaz, G. E.; Regazzoni, A. E. *Coord. Chem. Rev.* **2000**, *196*, 31.
(1388) Fenter, P.; Cheng, L.; Rihs, S.; Machesky, M.; Bedzyk, M. J.; Sturchio, N. C. *J. Colloid Interface Sci.* **2000**, *225*, 154.
(1389) Lindsay, R.; Thornton, G. *Top. Catal.* **2002**, *18*, 15.
(1390) Weiher, N.; Willneff, E. A.; Figulla-Kroschel, C.; Jansen, M.; Schroeder, S. L. M. *Solid State Commun.* **2003**, *125*, 317.
(1391) D'Acapito, F.; Ghigna, P.; Alessandri, I.; Cardelli, A.; Davoli, I. *Nucl. Instrum. Methods Phys. Res., Sect. B* **2003**, *200*, 421.
(1392) Ghigna, P.; Spinolo, G.; Alessandri, I.; Davoli, I.; D'Acapito, F. *Phys. Chem. Chem. Phys.* **2003**, *5*, 2244.
(1393) Pang, C. L.; Muryn, C. A.; Woodhead, A. P.; Raza, H.; Haycock, S. A.; Dhanak, V. R.; Thornton, G. *Surf. Sci.* **2005**, *583*, L147.
(1394) Roberts, M. W. *Catal. Lett.* **2000**, *67*, 39.
(1395) van Kimmenade, E. M. E.; Kuiper, A. E. T.; Tamminga, Y.; Thune, P. C.; Niemantsverdriet, J. W. *J. Catal.* **2004**, *223*, 134.
(1396) Agostini, G.; Groppo, E.; Bordiga, S.; Zecchina, A.; Prestipino, C.; D'Acapito, F.; van Kimmenade, E.; Thune, P. C.; Niemantsverdriet, J. W.; Lamberti, C. *J. Phys. Chem. C* **2007**, *111*, 16437.
(1397) Urakawa, A.; Baiker, A. *Top. Catal.* **2009**, *52*, 1312.
(1398) Somorjai, G. A.; Frei, H.; Park, J. Y. *J. Am. Chem. Soc.* **2009**, *131*, 16589.
(1399) Stavitski, E.; Weckhuysen, B. M. *Chem. Soc. Rev.* **2010**, *39*, 4615.
(1400) Kox, M. H. F.; Stavitski, E.; Weckhuysen, B. M. *Angew. Chem., Int. Ed.* **2007**, *46*, 3652.
(1401) Stavitski, E.; Kox, M. H. F.; Weckhuysen, B. M. *Chem.—Eur. J.* **2007**, *13*, 7057.
(1402) Karwacki, L.; Stavitski, E.; Kox, M. H. F.; Kornatowski, J.; Weckhuysen, B. M. *Angew. Chem., Int. Edit.* **2007**, *46*, 7228.
(1403) Kox, M. H. F.; Stavitski, E.; Groen, J. C.; Perez-Ramirez, J.; Kapteijn, F.; Weckhuysen, B. M. *Chem.—Eur. J.* **2008**, *14*, 1718.
(1404) Mores, D.; Stavitski, E.; Kox, M. H. F.; Kornatowski, J.; Olsbye, U.; Weckhuysen, B. M. *Chem.—Eur. J.* **2008**, *14*, 11320.
(1405) De Cremer, G.; Sels, B. F.; De Vos, D. E.; Hofkens, J.; Roeffaers, M. B. J. *Chem. Soc. Rev.* **2010**, *39*, 4703.
(1406) Chen, P.; Zhou, X. C.; Shen, H.; Andoy, N. M.; Choudhary, E.; Han, K. S.; Liu, G. K.; Meng, W. L. *Chem. Soc. Rev.* **2010**, *39*, 4560.
(1407) Gladden, L. F. *Top. Catal.* **2003**, *24*, 19.
(1408) Koptyug, I. V.; Lysova, A. A.; Sagdeev, R. Z.; Kirillov, V. A.; Kulikov, A. V.; Parmon, V. N. *Catal. Today* **2005**, *105*, 464.
(1409) Lysova, A. A.; Koptyug, I. V.; Sagdeev, R. Z.; Parmon, V. N.; Bergwerff, J. A.; Weckhuysen, B. M. *J. Am. Chem. Soc.* **2005**, *127*, 11916.
(1410) Britton, M. M. *Chem. Soc. Rev.* **2010**, *39*, 4036.
(1411) Kox, M. H. F.; Domke, K. F.; Day, J. P. R.; Rago, G.; Stavitski, E.; Bonn, M.; Weckhuysen, B. M. *Angew. Chem., Int. Edit.* **2009**, *48*, 8990.
(1412) Kim, H.; Kosuda, K. M.; Van Duyne, R. P.; Stair, P. C. *Chem. Soc. Rev.* **2010**, *39*, 4820.
(1413) Harvey, C. E.; Lantman, E. M. V.; Mank, A. J. G.; Weckhuysen, B. M. *Chem. Commun.* **2012**, *48*, 1742.
(1414) Domke, K. F.; Day, J. P. R.; Rago, G.; Riemer, T. A.; Kox, M. H. F.; Weckhuysen, B. M.; Bonn, M. *Angew. Chem., Int. Ed.* **2012**, *51*, 1343.
(1415) Karreman, M. A.; Buurmans, I. L. C.; Geus, J. W.; Agronskaia, A. V.; Ruiz-Martinez, J.; Gerritsen, H. C.; Weckhuysen, B. M. *Angew. Chem., Int. Ed.* **2012**, *51*, 1428.
(1416) Zandbergen, M. W.; Jacques, S. D. M.; Weckhuysen, B. M.; Beale, A. M. *Angew. Chem., Int. Ed.* **2012**, *51*, 957.
(1417) Stavitski, E.; Kox, M. H. F.; Swart, I.; de Groot, F. M. F.; Weckhuysen, B. M. *Angew. Chem., Int. Ed.* **2008**, *47*, 3543.
(1418) Liu, J. Y. *ChemCatChem* **2011**, *3*, 934.
(1419) Zhou, W.; Wachs, I. E.; Kiely, C. J. *Curr. Opin. Solid State Mater. Sci.* **2012**, *16*, 10.
(1420) Stavitski, E.; Drury, M. R.; de Winter, D. A. M.; Kox, M. H. F.; Weckhuysen, B. M. *Angew. Chem., Int. Ed.* **2008**, *47*, 5637.
(1421) Forzatti, P.; Tronconi, E.; Pasquon, I. *Catal. Rev.: Sci. Eng.* **1991**, *33*, 109.
(1422) Waugh, K. C. *Catal. Today* **1992**, *15*, 51.
(1423) Solomon, E. I.; Jones, P. M.; May, J. A. *Chem. Rev.* **1993**, *93*, 2623.
(1424) Hansen, P. L.; Wagner, J. B.; Helveg, S.; Rostrup-Nielsen, J. R.; Clausen, B. S.; Topsoe, H. *Science* **2002**, *295*, 2053.
(1425) Spivey, J. J.; Egbebi, A. *Chem. Soc. Rev.* **2007**, *36*, 1514.
(1426) Jiang, C. J.; Trimm, D. L.; Wainwright, M. S.; Cant, N. W. *Appl. Catal., A* **1993**, *93*, 245.
(1427) Breen, J. P.; Meunier, F. C.; Ross, J. R. H. *Chem. Commun.* **1999**, 2247.
(1428) Gunter, M. M.; Ressler, T.; Jentoft, R. E.; Bems, B. *J. Catal.* **2001**, *203*, 133.
(1429) Purnama, H.; Ressler, T.; Jentoft, R. E.; Soerijanto, H.; Schlogl, R.; Schomacker, R. *Appl. Catal., A* **2004**, *259*, 83.
(1430) Turco, M.; Bagnasco, G.; Costantino, U.; Marmottini, F.; Montanari, T.; Ramis, G.; Busca, G. *J. Catal.* **2004**, *228*, 43.
(1431) Sayers, D.; Cantrell, J.; Bazin, D.; Dexpert, H.; Fontaine, A.; Lagarde, P.; Lynch, J.; Bournonville, J. *Phys. B* **1989**, *158*, 206.
(1432) Bogg, D.; Conyngham, M.; Corker, J. M.; Dent, A. J.; Evans, J.; Farrow, R. C.; Kambhampati, V. L.; Masters, A. F.; McLeod, D. N.; Ramsdale, C. A.; Salvini, G. *Chem. Commun.* **1996**, 647.
(1433) Fiddy, S. G.; Newton, M. A.; Dent, A. J.; Salvini, G.; Corker, J. M.; Turin, S.; Campbell, T.; Evans, J. *Chem. Commun.* **1999**, 851.
(1434) Fiddy, S. G.; Newton, M. A.; Campbell, T.; Corker, J. M.; Dent, A. J.; Harvey, I.; Salvini, G.; Turin, S.; Evans, J. *Chem. Commun.* **2001**, 445.
(1435) Newton, M. A.; Burnaby, D. G.; Dent, A. J.; Diaz-Moreno, S.; Evans, J.; Fiddy, S. G.; Neisius, T.; Pascarelli, S.; Turin, S. *J. Phys. Chem. A* **2001**, *105*, 5965.
(1436) Evans, J.; O'Neill, L.; Kambhampati, V. L.; Rayner, G.; Turin, S.; Genge, A.; Dent, A. J.; Neisius, T. *J. Chem. Soc., Dalton Trans.* **2002**, 2207.
(1437) Iwasawa, Y. *J. Catal.* **2003**, *216*, 165.
(1438) Groothaert, M. H.; Lievens, K.; Leeman, H.; Weckhuysen, B. M.; Schoonheydt, R. A. *J. Catal.* **2003**, *220*, 500.
(1439) Okumura, K.; Yoshimoto, R.; Uruga, T.; Tanida, H.; Kato, K.; Yokota, S.; Niwa, M. *J. Phys. Chem. B* **2004**, *108*, 6250.
(1440) Newton, M. A.; Jyoti, B.; Dent, A. J.; Fiddy, S. G.; Evans, J. *Chem. Commun.* **2004**, 2382.
(1441) Newton, M. A.; Jyoti, L.; Dent, A. J.; Diaz-Moreno, S.; Fiddy, S. G.; Evans, J. *ChemPhysChem* **2004**, *5*, 1056.
(1442) Newton, M. A.; Fiddy, S. G.; Guilera, G.; Jyoti, B.; Evans, J. *Chem. Commun.* **2005**, 118.
(1443) Groust, J. F.; Pommier, C.; Stievano, L.; Villain, F.; Giorgetti, C.; Baudelet, F.; Massiani, P. *Catal. Lett.* **2005**, *102*, 257.
(1444) Iglesias-Juez, A.; Martinez-Arias, A.; Newton, M. A.; Fiddy, S. G.; Fernandez-Garcia, M. *Chem. Commun.* **2005**, 4092.
(1445) Newton, M. A.; Dent, A. J.; Diaz-Moreno, S.; Fiddy, S. G.; Jyoti, B.; Evans, J. *Chem.—Eur. J.* **2006**, *12*, 1975.
(1446) Guilera, G.; Newton, M. A.; Polli, C.; Pascarelli, S.; Guino, M.; Hii, K. K. *Chem. Commun.* **2006**, 4306.

(1447) Caravati, M.; Meier, D. M.; Grunwaldt, J. D.; Baiker, A. *J. Catal.* **2006**, *240*, 126.
(1448) Ressler, T.; Hagelstein, M.; Hatje, U.; Metz, W. *J. Phys. Chem. B* **1997**, *101*, 6680.
(1449) Fulton, J. L.; Linehan, J. C.; Autrey, T.; Balasubramanian, M.; Chen, Y.; Szymczak, N. K. *J. Am. Chem. Soc.* **2007**, *129*, 11936.
(1450) Newton, M. A.; Dent, A. J.; Fiddy, S. G.; Jyoti, B.; Evans, J. *Phys. Chem. Chem. Phys.* **2007**, *9*, 246.
(1451) Newton, M. A.; Belver-Coldeira, C.; Martinez-Arias, A.; Fernandez-Garcia, M. *Nat. Mater.* **2007**, *6*, 528.
(1452) Gamarra, D.; Belver, C.; Fernandez-Garcia, M.; Martinez-Arias, A. *J. Am. Chem. Soc.* **2007**, *129*, 12064.
(1453) Mondelli, C.; Ferri, D.; Grunwaldt, J. D.; Krumeich, F.; Mangold, S.; Psaro, R.; Baiker, A. *J. Catal.* **2007**, *252*, 77.
(1454) Newton, M. A.; Belver-Coldeira, C.; Martinez-Arias, A.; Fernandez-Garcia, M. *Angew. Chem., Int. Ed.* **2007**, *46*, 8629.
(1455) Evans, J.; Tromp, M. *J. Phys.: Condens. Matter* **2008**, *20*, No. 184020.
(1456) Klasovsky, F.; Hohmeyer, J.; Bruckner, A.; Bonifer, M.; Arras, J.; Steffan, M.; Lucas, M.; Radnik, J.; Roth, C.; Claus, P. *J. Phys. Chem. C* **2008**, *112*, 19555.
(1457) Dent, A. J.; Evans, J.; Fiddy, S. G.; Jyoti, B.; Newton, M. A.; Tromp, M. *Faraday Discuss.* **2008**, *138*, 287.
(1458) Liang, A. J.; Gates, B. C. *J. Phys. Chem. C* **2008**, *112*, 18039.
(1459) Nagai, Y.; Dohmae, K.; Ikeda, Y.; Takagi, N.; Tanabe, T.; Hara, N.; Guilera, G.; Pascarelli, S.; Newton, M. A.; Kuno, O.; Jiang, H. Y.; Shinjoh, H.; Matsumoto, S. *Angew. Chem., Int. Ed.* **2008**, *47*, 9303.
(1460) Frahm, R.; Stötzel, J.; Lützenkirchen-Hecht, D. *Synchrotron Radiat. News* **2009**, *22*, 6.
(1461) Kubacka, A.; Martinez-Arias, A.; Fernandez-Garcia, M.; Di Michiel, M.; Newton, M. A. *J. Catal.* **2010**, *270*, 275.
(1462) Ferri, D.; Kumar, M. S.; Wirz, R.; Eyssler, A.; Korsak, O.; Hug, P.; Weidenkaff, A.; Newton, M. A. *Phys. Chem. Chem. Phys.* **2010**, *12*, 5634.
(1463) Koziej, D.; Hubner, M.; Barsan, N.; Weimar, U.; Sikora, M.; Grunwaldt, J. D. *Phys. Chem. Chem. Phys.* **2009**, *11*, 8620.
(1464) Kimmerle, B.; Grunwaldt, J. D.; Baiker, A.; Glatzel, P.; Boye, P.; Stephan, S.; Schroer, C. G. *J. Phys. Chem. C* **2009**, *113*, 3037.
(1465) Guerrero, S.; Miller, J. T.; Kropf, A. J.; Wolf, E. E. *J. Catal.* **2009**, *262*, 102.
(1466) Gamarra, D.; Fernandez-Garcia, M.; Belver, C.; Martinez-Arias, A. *J. Phys. Chem. C* **2010**, *114*, 18576.
(1467) Ellis, P. J.; Fairlamb, I. J. S.; Hackett, S. F. J.; Wilson, K.; Lee, A. F. *Angew. Chem., Int. Ed.* **2010**, *49*, 1820.
(1468) Iglesias-Juez, A.; Beale, A. M.; Maaijen, K.; Weng, T. C.; Glatzel, P.; Weckhuysen, B. M. *J. Catal.* **2010**, *276*, 268.
(1469) O'Brien, M. G.; Beale, A. M.; Jacques, S. D. M.; Di Michiel, M.; Weckhuysen, B. M. *Appl. Catal., A* **2011**, *391*, 468.
(1470) Hubner, M.; Koziej, D.; Bauer, M.; Barsan, N.; Kvashnina, K.; Rossell, M. D.; Weimar, U.; Grunwaldt, J. D. *Angew. Chem., Int. Ed.* **2011**, *50*, 2841.
(1471) Korhonen, S. T.; Beale, A. M.; Newton, M. A.; Weckhuysen, B. M. *J. Phys. Chem. C* **2011**, *115*, 885.
(1472) Nagai, Y.; Dohmae, K.; Ikeda, Y.; Takagi, N.; Hara, N.; Tanabe, T.; Guilera, G.; Pascarelli, S.; Newton, M. A.; Takahashi, N.; Shinjoh, H.; Matsumoto, S. *Catal. Today* **2011**, *175*, 133.
(1473) Uemura, Y.; Inada, Y.; Niwa, Y.; Kimura, M.; Bando, K. K.; Yagishita, A.; Iwasawa, Y.; Nomura, M. *Phys. Chem. Chem. Phys.* **2012**, *14*, 2152.
(1474) Lee, A. F.; Ellis, C. V.; Naughton, J. N.; Newton, M. A.; Parlett, C. M. A.; Wilson, K. *J. Am. Chem. Soc.* **2011**, *133*, 5724.
(1475) Iglesias-Juez, A.; Kubacka, A.; Fernandez-Garcia, M.; Di Michiel, M.; Newton, M. A. *J. Am. Chem. Soc.* **2011**, *133*, 4484.
(1476) Newton, M. A.; Di Michiel, M.; Kubacka, A.; Iglesias-Juez, A.; Fernandez-Garcia, M. *Angew. Chem., Int. Ed.* **2012**, *51*, 2363.
(1477) Naworski, J. S.; Evil, E. S. In *Applied Industrial Catalysis*; Leach, B. E., Ed.; Accademic Press: New York, 1983; Vol. *1*, p 239.
(1478) Newmann, M. N. *Encyclopedia of Polymer Science and Engineering*; Wiley: New York, 1985; Vol. *17*.
(1479) Garilli, M.; Fatutto, P. L.; Piga, F. *Chim. Ind. (Milan, Italy)* **1998**, *80*, 333.
(1480) Cavani, F.; Centi, G.; Perathoner, S.; Trifiro, F., *Sustainable Industrial Chemistry*; Wiley-VCH: Wenheim, Germany, 2009.
(1481) Cavani, F.; Teles, J. H. *ChemSusChem* **2009**, *2*, 508.
(1482) Zhang, T. Z.; Troll, C.; Rieger, B.; Kintrup, J.; Schluter, O. F. K.; Weber, R. *Appl. Catal., A* **2009**, *365*, 20.
(1483) Zhang, T. Z.; Troll, C.; Rieger, B.; Kintrup, J.; Schluter, O. F. K.; Weber, R. *Appl. Catal., A* **2009**, *357*, 51.
(1484) Mross, W. D. *Catal. Rev. Sci. Eng* **1983**, *25*, 591.
(1485) Arcoya, A.; Cortes, A.; Seoane, X. L. *Can. J. Chem. Eng.* **1982**, *60*, 55.
(1486) Shiozaki, K.; Onischi, A. European Patent 62320, 1982.
(1487) Laurer, P. R.; Krome, G.; Cordemans, L.; Seifert, R.; Danz, E. European Patent 54674, 1981.
(1488) Fatutto, I.; Carmello, D.; Marsella, A. European Patent 1053789, 2000.
(1489) Derieth, H.; Walter, R.; Weidenbach, G.; Strebbele, M. European Patent 255156, 1988.
(1490) Eden, J. S.; Cowfer, J. A. U.S. Patent 4849393, 1989.
(1491) Carmello, D.; Grilli, M.; Fatutto, P.; Caccialupi, L. European Patent 1045731, 1999.
(1492) Baiker, A.; Holstein, W. L. *J. Catal.* **1983**, *84*, 178.
(1493) Rollins, K.; Sermon, P. A. *J. Chem. Soc., Chem. Commun.* **1986**, 1171.
(1494) Fortini, E. M.; Garcia, C. L.; Resasco, D. E. *J. Catal.* **1986**, *99*, 12.
(1495) Sermon, P. A.; Rollins, K.; Reyes, P. N.; Lawrence, S. A.; Martin Luengo, M. A.; Davies, M. J. *J. Chem. Soc., Faraday. Trans. 1* **1987**, *83*, 1347.
(1496) Sai Prasad, P. S.; Kanta Rao, P. *J. Chem. Soc., Chem. Commun.* **1987**, 951.
(1497) Garcia, C. L.; Resasco, D. E. *J. Catal.* **1990**, *122*, 151.
(1498) Leofanti, G.; Padovan, M.; Garilli, M.; Carmello, D.; Marra, G. L.; Zecchina, A.; Spoto, G.; Bordiga, S.; Lamberti, C. *J. Catal.* **2000**, *189*, 105.
(1499) Leofanti, G.; Marsella, A.; Cremaschi, B.; Garilli, M.; Zecchina, A.; Spoto, G.; Bordiga, S.; Fisicaro, P.; Berlier, G.; Prestipino, C.; Casali, G.; Lamberti, C. *J. Catal.* **2001**, *202*, 279.
(1500) Leofanti, G.; Marsella, A.; Cremaschi, B.; Garilli, M.; Zecchina, A.; Spoto, G.; Bordiga, S.; Fisicaro, P.; Prestipino, C.; Villain, F.; Lamberti, C. *J. Catal.* **2002**, *205*, 375.
(1501) Muddada, N. B.; Olsbye, U.; Fuglerud, T.; Vidotto, S.; Marsella, A.; Bordiga, S.; Gianolio, D.; Leofanti, G.; Lamberti, C. *J. Catal.* **2012**, *284*, 236.
(1502) Gianolio, D.; Muddada, N. B.; Olsbye, U.; Lamberti, C. *Nucl. Instrum. Methods Phys. Res., Sect. B* **2012**, *284*, 53.
(1503) Sato, Y.; Kagotani, M.; Souma, Y. *J. Mol. Catal. A: Chem.* **2000**, *151*, 79.
(1504) Meinders, H. C. *J. Mol. Catal.* **1980**, *7*, 321.
(1505) Galiasso Tailleur, R.; Garcia, C. J. G. *J. Catal.* **2007**, *250*, 110.
(1506) McCurdie, M. P.; Belfiore, L. A. *Polymer* **1999**, *40*, 2889.
(1507) Belfiore, L. A.; McCurdie, M. P.; Das, P. K. *Polymer* **2001**, *42*, 9995.
(1508) Pardey, A. J.; Rojas, A. D.; Yanez, J. E.; Betancourt, P.; Scott, C.; Chinea, C.; Urbina, C.; Moronta, D.; Longo, C. *Polyhedron* **2005**, *24*, 511.
(1509) Groppo, E.; Uddin, M. J.; Bordiga, S.; Zecchina, A.; Lamberti, C. *Angew. Chem., Int. Ed.* **2008**, *47*, 9269.
(1510) Sinfelt, J. H.; Via, G. H.; Lytle, F. W. *J. Chem. Phys.* **1978**, *68*, 2009.
(1511) Via, G. H.; Sinfelt, J. H.; Lytle, F. W. *J. Chem. Phys.* **1979**, *71*, 690.
(1512) Sinfelt, J. H.; Via, G. H.; Lytle, F. W. *J. Chem. Phys.* **1980**, *72*, 4832.
(1513) Sinfelt, J. H.; Via, G. H.; Lytle, F. W.; Greegor, R. B. *J. Chem. Phys.* **1981**, *75*, 5527.

(1514) Sinfelt, J. H.; Via, G. H.; Lytle, F. W. *J. Chem. Phys.* **1982**, *76*, 2779.
(1515) Meitzner, G.; Via, G. H.; Lytle, F. W.; Sinfelt, J. H. *J. Chem. Phys.* **1983**, *78*, 882.
(1516) Via, G. H.; Meitzner, G.; Lytle, F. W.; Sinfelt, J. H. *J. Chem. Phys.* **1983**, *79*, 1527.
(1517) Duivenvoorden, F. B. M.; Kip, B. J.; Koningsberger, D. C.; Prins, R. *J. Phys., Colloq.* **1986**, *47* (C8), 227.
(1518) Kip, B. J.; Duivenvoorden, F. B. M.; Koningsberger, D. C.; Prins, R. *J. Am. Chem. Soc.* **1986**, *108*, 5633.
(1519) Kip, B. J.; Duivenvoorden, F. B. M.; Koningsberger, D. C.; Prins, R. *J. Catal.* **1987**, *105*, 26.
(1520) Benfield, R. E. *J. Chem. Soc., Faraday Trans.* **1992**, *88*, 1107.
(1521) Vanzon, F. B. M.; Maloney, S. D.; Gates, B. C.; Koningsberger, D. C. *J. Am. Chem. Soc.* **1993**, *115*, 10317.
(1522) Che, M.; Cheng, Z. X.; Louis, C. *J. Am. Chem. Soc.* **1995**, *117*, 2008.
(1523) Frenkel, A. I.; Hills, C. W.; Nuzzo, R. G. *J. Phys. Chem. B* **2001**, *105*, 12689.
(1524) Jentys, A. *Phys. Chem. Chem. Phys.* **1999**, *1*, 4059.
(1525) Bezemer, G. L.; Bitter, J. H.; Kuipers, H.; Oosterbeek, H.; Holewijn, J. E.; Xu, X. D.; Kapteijn, F.; van Dillen, A. J.; de Jong, K. P. *J. Am. Chem. Soc.* **2006**, *128*, 3956.
(1526) Miller, J. T.; Kropf, A. J.; Zha, Y.; Regalbuto, J. R.; Delannoy, L.; Louis, C.; Bus, E.; van Bokhoven, J. A. *J. Catal.* **2006**, *240*, 222.
(1527) Karim, A. M.; Prasad, V.; Mpourmpakis, G.; Lonergan, W. W.; Frenkel, A. I.; Chen, J. G. G.; Vlachos, D. G. *J. Am. Chem. Soc.* **2009**, *131*, 12230.
(1528) Principi, E.; Witkowska, A.; Dsoke, S.; Marassi, R.; Di Cicco, A. *Phys. Chem. Chem. Phys.* **2009**, *11*, 9987.
(1529) Mostafa, S.; Behafarid, F.; Croy, J. R.; Ono, L. K.; Li, L.; Yang, J. C.; Frenkel, A. I.; Cuenya, B. R. *J. Am. Chem. Soc.* **2010**, *132*, 15714.
(1530) Vargaftik, M. N.; Moiseev, I. I.; Kochubey, D. I.; Zamaraev, K. I. *Faraday Discuss.* **1991**, *92*, 13.
(1531) Yuan, Y. Z.; Kozlova, A. P.; Asakura, K.; Wan, H. L.; Tsai, K.; Iwasawa, Y. *J. Catal.* **1997**, *170*, 191.
(1532) Frenkel, A. *Z. Kristallogr.* **2007**, *222*, 605.
(1533) Witkowska, A.; Di Cicco, A.; Principi, E. *Phys. Rev. B* **2007**, *76*, No. 104110.
(1534) Deganello, G.; Giannici, F.; Martorana, A.; Pantaleo, G.; Prestianni, A.; Balerna, A.; Liotta, L. F.; Longo, A. *J. Phys. Chem. B* **2006**, *110*, 8731.
(1535) Casaletto, M. P.; Longo, A.; Venezia, A. M.; Martorana, A.; Prestianni, A. *Appl. Catal., A* **2006**, *302*, 309.
(1536) Longo, A.; Martorana, A. *J. Appl. Crystallogr.* **2008**, *41*, 446.
(1537) Knecht, M. R.; Weir, M. G.; Myers, V. S.; Pyrz, W. D.; Ye, H. C.; Petkov, V.; Buttrey, D. J.; Frenkel, A. I.; Crooks, R. M. *Chem. Mater.* **2008**, *20*, 5218.
(1538) Sanchez, S. I.; Menard, L. D.; Bram, A.; Kang, J. H.; Small, M. W.; Nuzzo, R. G.; Frenkel, A. I. *J. Am. Chem. Soc.* **2009**, *131*, 7040.
(1539) Agostini, G.; Pellegrini, R.; Leofanti, G.; Bertinetti, L.; Bertarione, S.; Groppo, E.; Zecchina, A.; Lamberti, C. *J. Phys. Chem. C* **2009**, *113*, 10485.
(1540) Pellegrini, R.; Leofanti, G.; Agostini, G.; Bertinetti, L.; Bertarione, S.; Groppo, E.; Zecchina, A.; Lamberti, C. *J. Catal.* **2009**, *267*, 40.
(1541) Groppo, E.; Liu, W.; Zavorotynska, O.; Agostini, G.; Spoto, G.; Bordiga, S.; Lamberti, C.; Zecchina, A. *Chem. Mater.* **2010**, *22*, 2297.
(1542) Smeekens, S.; Heylen, S.; Villani, K.; Houthoofd, K.; Godard, E.; Tromp, M.; Seo, J. W.; DeMarco, M.; Kirschhock, C. E. A.; Martens, J. A. *Chem. Sci.* **2010**, *1*, 763.
(1543) Longo, A.; Liotta, L. F.; Di Carlo, G.; Giannici, F.; Venezia, A. M.; Martorana, A. *Chem. Mater.* **2010**, *22*, 3952.
(1544) Corma, A.; Iborra, S.; Xamena, F.; Monton, R.; Calvino, J. J.; Prestipino, C. *J. Phys. Chem. C* **2010**, *114*, 8828.
(1545) Cuenya, B. R.; Croy, J. R.; Mostafa, S.; Behafarid, F.; Li, L.; Zhang, Z. F.; Yang, J. C.; Wang, Q.; Frenkel, A. I. *J. Am. Chem. Soc.* **2010**, *132*, 8747.
(1546) Pellegrini, R.; Agostini, G.; Groppo, E.; Piovano, A.; Leofanti, G.; Lamberti, C. *J. Catal.* **2011**, *280*, 150.
(1547) Frenkel, A. I. *J. Synchrotron Radiat.* **1999**, *6*, 293.
(1548) Vila, F.; Rehr, J. J.; Kas, J.; Nuzzo, R. G.; Frenkel, A. I. *Phys. Rev. B* **2008**, *78*, No. 121404.
(1549) Yevick, A.; Frenkel, A. I. *Phys. Rev. B* **2010**, *81*, No. 115451.
(1550) Cuenya, B. R.; Frenkel, A. I.; Mostafa, S.; Behafarid, F.; Croy, J. R.; Ono, L. K.; Wang, Q. *Phys. Rev. B* **2010**, *82*, No. 155450.
(1551) Frenkel, A. I.; Yevick, A.; Cooper, C.; Vasic, R. *Annu. Rev. Anal. Chem.* **2011**, *4*, 23.
(1552) Small, M. W.; Sanchez, S. I.; Menard, L. D.; Kang, J. H.; Frenkel, A. I.; Nuzzo, R. G. *J. Am. Chem. Soc.* **2011**, *133*, 3582.
(1553) Sasaki, K.; Kuttiyiel, K. A.; Barrio, L.; Su, D.; Frenkel, A. I.; Marinkovic, N.; Mahajan, D.; Adzic, R. R. *J. Phys. Chem. C* **2011**, *115*, 9894.
(1554) Via, G. H.; Drake, K. F.; Meitzner, G.; Lytle, F. W.; Sinfelt, J. H. *Catal. Lett.* **1990**, *5*, 25.
(1555) Toshima, N.; Harada, M.; Yamazaki, Y.; Asakura, K. *J. Phys. Chem.* **1992**, *96*, 9927.
(1556) Nashner, M. S.; Somerville, D. M.; Lane, P. D.; Adler, D. L.; Shapley, J. R.; Nuzzo, R. G. *J. Am. Chem. Soc.* **1996**, *118*, 12964.
(1557) Nashner, M. S.; Frenkel, A. I.; Adler, D. L.; Shapley, J. R.; Nuzzo, R. G. *J. Am. Chem. Soc.* **1997**, *119*, 7760.
(1558) Wang, Y.; Toshima, N. *J. Phys. Chem. B* **1997**, *101*, 5301.
(1559) Nashner, M. S.; Frenkel, A. I.; Somerville, D.; Hills, C. W.; Shapley, J. R.; Nuzzo, R. G. *J. Am. Chem. Soc.* **1998**, *120*, 8093.
(1560) Fung, A. S.; Kelley, M. J.; Koningsberger, D. C.; Gates, B. C. *J. Am. Chem. Soc.* **1997**, *119*, 5877.
(1561) Toshima, N.; Yonezawa, T. *New J. Chem.* **1998**, *22*, 1179.
(1562) Hills, C. W.; Nashner, M. S.; Frenkel, A. I.; Shapley, J. R.; Nuzzo, R. G. *Langmuir* **1999**, *15*, 690.
(1563) Sinfelt, J. H. *Surf. Sci.* **2002**, *500*, 923.
(1564) Wang, L. L.; Khare, S. V.; Chirita, V.; Johnson, D. D.; Rockett, A. A.; Frenkel, A. I.; Mack, N. H.; Nuzzo, R. G. *J. Am. Chem. Soc.* **2006**, *128*, 131.
(1565) Knecht, M. R.; Weir, M. G.; Frenkel, A. I.; Crooks, R. M. *Chem. Mater.* **2008**, *20*, 1019.
(1566) Kowal, A.; Li, M.; Shao, M.; Sasaki, K.; Vukmirovic, M. B.; Zhang, J.; Marinkovic, N. S.; Liu, P.; Frenkel, A. I.; Adzic, R. R. *Nat. Mater.* **2009**, *8*, 325.
(1567) Myers, S. V.; Frenkel, A. I.; Crooks, R. M. *Chem. Mater.* **2009**, *21*, 4824.
(1568) Menard, L. D.; Wang, Q.; Kang, J. H.; Sealey, A. J.; Girolami, G. S.; Teng, X. W.; Frenkel, A. I.; Nuzzo, R. G. *Phys. Rev. B* **2009**, *80*, No. 064111.
(1569) Alayoglu, S.; Zavalij, P.; Eichhorn, B.; Wang, Q.; Frenkel, A. I.; Chupas, P. *ACS Nano* **2009**, *3*, 3127.
(1570) Teng, X. W.; Feygenson, M.; Wang, Q.; He, J. Q.; Du, W. X.; Frenkel, A. I.; Han, W. Q.; Aronson, M. *Nano Lett.* **2009**, *9*, 3177.
(1571) Beale, A. M.; Weckhuysen, B. M. *Phys. Chem. Chem. Phys.* **2010**, *12*, 5562.
(1572) Guczi, L.; Boskovic, G.; Kiss, E. *Catal. Rev.: Sci. Eng.* **2010**, *52*, 133.
(1573) Kang, J. H.; Menard, L. D.; Nuzzo, R. G.; Frenkel, A. I. *J. Am. Chem. Soc.* **2006**, *128*, 12068.
(1574) Hegedus, L.; Mathe, T.; Tungler, A. *Appl. Catal., A* **1996**, *143*, 309.
(1575) Hegedus, L.; Mathe, T.; Tungler, A. *Appl. Catal., A* **1996**, *147*, 407.
(1576) Wiersma, A.; van de Sandt, E. J. A. X.; den Hollander, M. A.; van Bekkum, H.; Makkee, M.; Moulijn, J. A. *J. Catal.* **1998**, *177*, 29.
(1577) Bernas, A.; Kumar, N.; Mäki-Arvela, P.; Kul'kova, N. V.; Holmbom, B.; Salmi, T.; Murzin, D. Y. *Appl. Catal., A* **2003**, *245*, 257.
(1578) Panagiotopoulou, P.; Kondarides, D. I. *Catal. Today* **2006**, *112*, 49.
(1579) Venezia, A. M.; La Parola, V.; Pawelec, B.; Fierro, J. L. G. *Appl. Catal., A* **2004**, *264*, 43.
(1580) Markus, H.; Plomp, A. J.; Maki-Arvela, P.; Bitter, J. H.; Murzin, D. Y. *Catal. Lett.* **2007**, *113*, 141.

(1581) Bertarione, S.; Prestipino, C.; Groppo, E.; Scarano, D.; Spoto, G.; Zecchina, A.; Pellegrini, R.; Leofanti, G.; Lamberti, C. *Phys. Chem. Chem. Phys.* **2006**, *8*, 3676.
(1582) Groppo, E.; Bertarione, S.; Rotunno, F.; Agostini, G.; Scarano, D.; Pellegrini, R.; Leofanti, G.; Zecchina, A.; Lamberti, C. *J. Phys. Chem. C* **2007**, *111*, 7021.
(1583) Ruta, M.; Semagina, N.; Kiwi-Minsker, L. *J. Phys. Chem. C* **2008**, *112*, 13635.
(1584) Rotunno, F.; Prestipino, C.; Bertarione, S.; Groppo, E.; Scarano, D.; Zecchina, A.; Pellegrini, R.; Leofanti, G.; Lamberti, C. *Stud. Surf. Sci. Catal.* **2006**, *162*, 721.
(1585) Simonov, P. A.; Likholobov, V. A. Physicochemical Aspects of Preparation of Carbon-Supported Noble Metal Catalysts. In *Catalysis and Electrocatalysis at Nanoparticle Surfaces*; Wieckowski, A., Savinova, E. R., Vayenas, C. G., Ed.: Marcel Dekker Inc.: New York, 2003, p 409.
(1586) Troitskii, S. Y.; Chuvilin, A. L.; Kochubei, D. I.; Novgorodov, B. N.; Kolomiichuk, V. N.; Likholobov, V. A. *Russ. Chem. Bull.* **1995**, *44*, 1822.
(1587) Troitskii, S. Y.; Chuvilin, A. L.; Bogdanov, S. V.; Moroz, E. M.; Likholobov, V. A. *Russ. Chem. Bull.* **1996**, *45*, 1296.
(1588) Keresszegi, C.; Grunwaldt, J. D.; Mallat, T.; Baiker, A. *J. Catal.* **2004**, *222*, 268.
(1589) Grunwaldt, J. D.; Caravati, M.; Baiker, A. *J. Phys. Chem. B* **2006**, *110*, 25586.
(1590) Sun, Y.; Frenkel, A. I.; Isseroff, R.; Shonbrun, C.; Forman, M.; Shin, K. W.; Koga, T.; White, H.; Zhang, L. H.; Zhu, Y. M.; Rafailovich, M. H.; Sokolov, J. C. *Langmuir* **2006**, *22*, 807.
(1591) Prelazzi, G.; Cerboni, M.; Leofanti, G. *J. Catal.* **1999**, *181*, 73.
(1592) Ertl, G.; Knözinger, H.; Schüth, F.; Weitkamp, J. *Handbook of Heterogeneous Catalysis*; Wiley-VCH: Weinheim, Germany, 2008.
(1593) Mohr, C.; Hofmeister, H.; Radnik, J.; Claus, P. *J. Am. Chem. Soc.* **2003**, *125*, 1905.
(1594) Bus, E.; Prins, R.; van Bokhoven, J. A. *Catal. Commun.* **2007**, *8*, 1397.
(1595) Bus, E.; Prins, R.; van Bokhoven, J. A. *Phys. Chem. Chem. Phys.* **2007**, *9*, 3312.
(1596) Scarano, D.; Bordiga, S.; Lamberti, C.; Ricchiardi, G.; Bertarione, S.; Spoto, G. *Appl. Catal., A* **2006**, *307*, 3.
(1597) Guo, N.; Fingland, B. R.; Williams, W. D.; Kispersky, V. F.; Jelic, J.; Delgass, W. N.; Ribeiro, F. H.; Meyer, R. J.; Miller, J. T. *Phys. Chem. Chem. Phys.* **2010**, *12*, 5678.
(1598) Ankudinov, A. L.; Rehr, J. J.; Low, J. J.; Bare, S. R. *J. Chem. Phys.* **2002**, *116*, 1911.
(1599) van Bokhoven, J. A. *Phys. Chem. Chem. Phys.* **2010**, *12*, 5502.
(1600) Bus, E.; Ramaker, D. E.; van Bokhoven, J. A. *J. Am. Chem. Soc.* **2007**, *129*, 8094.
(1601) Melke, J.; Schoekel, A.; Dixon, D.; Cremers, C.; Ramaker, D. E.; Roth, C. *J. Phys. Chem. C* **2010**, *114*, 5914.
(1602) The difference method has also been applied to the EXAFS part of the spectrum collected on modern synchrotrons. In these cases, the detection of extremely small changes in the $k^3\chi(k)$ function is well-accepted to emphasize the very weak oscillations that occur at higher k values. At $k = 10$ Å^{-1} this corresponds to multiply of the intensity by a factor of thousand. Thus changes in spectra smaller than one-thousandth are able to be detected. Contributions of minority species to the spectra can thus be determined and, in case of supported metal particles, the method is not restricted to the extremely small particles with relatively large surface areas.
(1603) Mager-Maury, C.; Bonnard, G.; Chizallet, C.; Sautet, P.; Raybaud, P. *ChemCatChem* **2011**, *3*, 200.
(1604) Ramaker, D. E.; Koningsberger, D. C. *Phys. Rev. Lett.* **2002**, *89*, No. 139701.
(1605) Ankudinov, A. L.; Rehr, J. J.; Low, J. J.; Bare, S. R. *Phys. Rev. Lett.* **2002**, *89*, No. 139702.
(1606) Teliska, M.; O'Grady, W. E.; Ramaker, D. E. *J. Phys. Chem. B* **2004**, *108*, 2333.
(1607) Stoupin, S. *J. Chem. Theory Comput.* **2009**, *5*, 1337.
(1608) Lewis, E. A.; Segre, C. U.; Smotkin, E. S. *Electrochim. Acta* **2009**, *54*, 7181.
(1609) Stakheev, A. Y.; Zhang, Y.; Ivanov, A. V.; Baeva, G. N.; Ramaker, D. E.; Koningsberger, D. C. *J. Phys. Chem. C* **2007**, *111*, 3938.
(1610) Ji, Y. Y.; Koot, V.; van der Eeirden, A. M. J.; Weckhuysen, B. M.; Koningsberger, D. C.; Ramaker, D. E. *J. Catal.* **2007**, *245*, 415.
(1611) Gatewood, D. S.; Schull, T. L.; Baturina, O.; Pietron, J. J.; Garsany, Y.; Swider-Lyons, K. E.; Ramaker, D. E. *J. Phys. Chem. C* **2008**, *112*, 4961.
(1612) Scott, F. J.; Mukerjee, S.; Ramaker, D. E. *J. Phys. Chem. C* **2010**, *114*, 442.
(1613) Ziegelbauer, J. M.; Gatewood, D.; Gulla, A. F.; Guinel, M. J. F.; Ernst, F.; Ramaker, D. E.; Mukerjee, S. *J. Phys. Chem. C* **2009**, *113*, 6955.
(1614) Lu, K. E.; Rye, R. R. *Surf. Sci.* **1974**, *45*, 677.
(1615) Davis, S. M.; Somorjai, G. A. *Surf. Sci.* **1980**, *91*, 73.
(1616) Oudenhuijzen, M. K. Support Effects in Heterogeneous Catalysis. PhD Thesis, Department of Inorganic Chemistry, Utrecht, the Netherlands, 2002.
(1617) Sinfelt, J. H. *Catal. Rev. Sci. Eng.* **1970**, *3*, 175.
(1618) Martin, G. A.; Dutartre, R.; Yuan, S.; Márquez-Alvarez, C.; Mirodatos, C. *J. Catal.* **1998**, *177*, 105.
(1619) Constable, F. H. *Proc. R. Soc. A (London)* **1925**, *108*, 355.
(1620) Bond, G. C.; Keane, M. A.; Kral, H.; Lercher, J. A. *Catal. Rev.: Sci. Eng.* **2000**, *42*, 323.
(1621) Bond, G. C. *Catal. Today* **1993**, *17*, 399.
(1622) Ankudinov, A. L.; Rehr, J. J.; Low, J.; Bare, S. R. *Phys. Rev. Lett.* **2001**, *86*, 1642.
(1623) Visser, T.; Nijhuis, T. A.; van der Eerden, A. M. J.; Jenken, K.; Ji, Y.; Bras, W.; Nikitenko, S.; Ikeda, Y.; Lepage, M.; Weckhuysen, B. M. *J. Phys. Chem. B* **2005**, *109*, 3822.
(1624) Lepage, M.; Visser, T.; van der Eerden, A. M. J.; Soulimani, F.; Weckhuysen, B. M. *Vib. Spectrosc.* **2008**, *48*, 92.
(1625) Ferri, D.; Newton, M. A.; Nachtegaal, M. *Top. Catal* **2011**, *54*, 1070.
(1626) Eyssler, A.; Kleymenov, E.; Kupferschmid, A.; Nachtegaal, M.; Kumar, M. S.; Hug, P.; Weidenkaff, A.; Ferri, D. *J. Phys. Chem. C* **2011**, *115*, 1231.
(1627) Chen, L. X.; Liu, D.-J. *Synchrotron Radiat. News* **2009**, *22*, 17.
(1628) O'Shea, P. G.; Freund, H. P. *Science* **2001**, *292*, 1853.
(1629) Feldhaus, J.; Arthur, J.; Hastings, J. B. *J. Phys. B: At., Mol. Opt. Phys.* **2005**, *38*, S799.
(1630) Pfeifer, T.; Spielmann, C.; Gerber, G. *Rep. Prog. Phys.* **2006**, *69*, 443.
(1631) Gaffney, K. J.; Chapman, H. N. *Science* **2007**, *316*, 1444.
(1632) Huang, Z. R.; Kim, K. J. *Phys. Rev. Spec. Top.—Accel. Beams* **2007**, *10*, No. 034801.
(1633) Berrah, N.; Bozek, J.; Costello, J. T.; Dusterer, S.; Fang, L.; Feldhaus, J.; Fukuzawa, H.; Hoener, M.; Jiang, Y. H.; Johnsson, P.; Kennedy, E. T.; Meyer, M.; Moshammer, R.; Radcliffe, P.; Richter, M.; Rouzee, A.; Rudenko, A.; Sorokin, A. A.; Tiedtke, K.; Ueda, K.; Ullrich, J.; Vrakking, M. J. J. *J. Mod. Opt.* **2010**, *57*, 1015.
(1634) Marangos, J. P. *Contemp. Phys.* **2011**, *52*, 551.